Climate Monitoring and Diagnostics Laboratory

Summary Report No. 24
1996-1997

Trends of Controlled Ozone-Depleting Substances

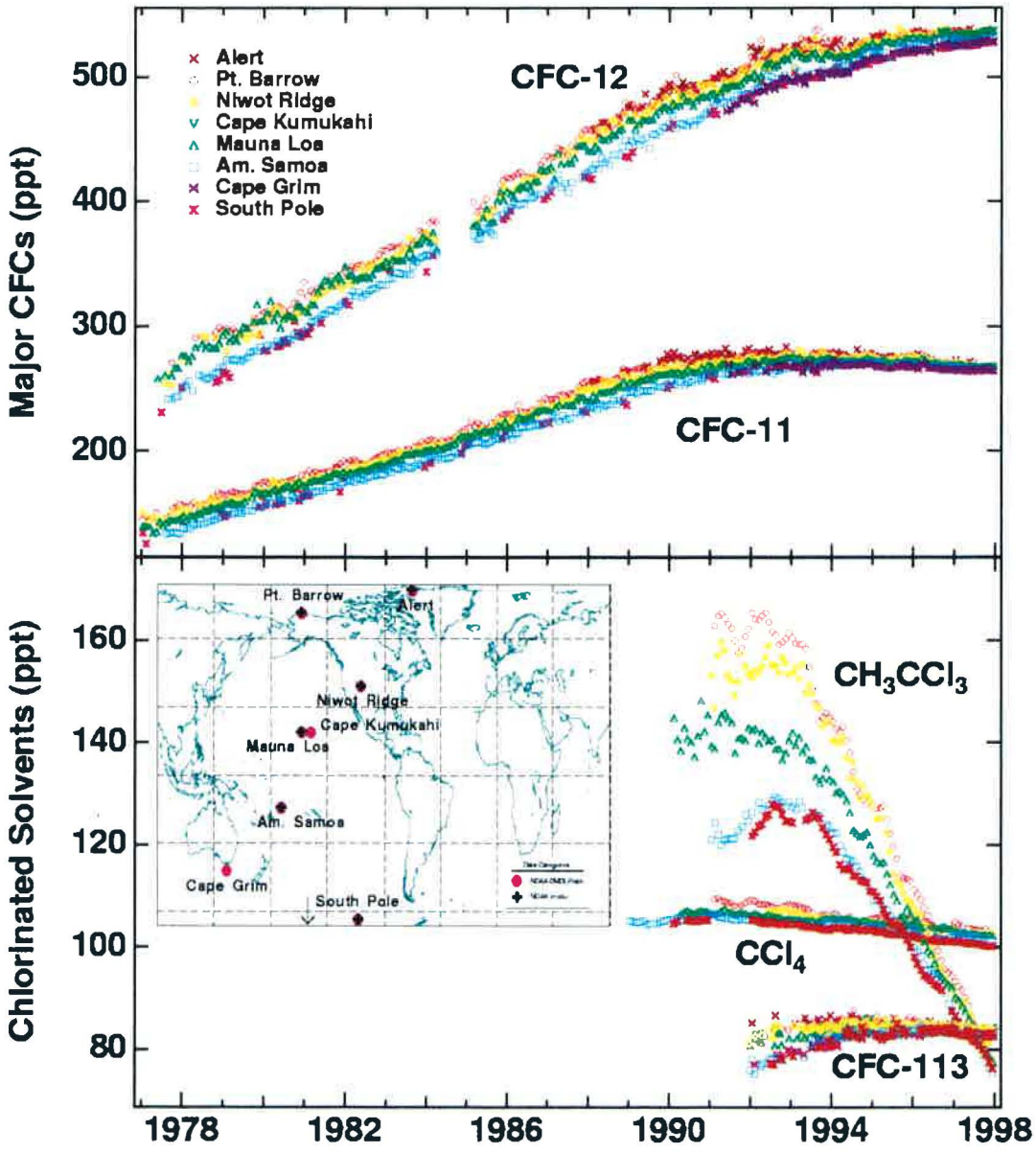

U.S. Department of Commerce
National Oceanic and Atmospheric Administration
Environmental Research Laboratories

Climate Monitoring and Diagnostics Laboratory Summary Report No. 24

1996-1997

David J. Hofmann, Editor
James T. Peterson, Editor
Rita M. Rosson, Assistant Editor

Boulder, Colorado

December 1998

U.S. DEPARTMENT OF COMMERCE
William Daley, Secretary

National Oceanic and Atmospheric Administration
D. James Baker, Under Secretary for Oceans and Atmosphere/Administrator

Environmental Research Laboratories
James L. Rasmussen, Director

NOTICE

Mention of a commercial company or product does not constitute an endorsement by NOAA Environmental Research Laboratories. Use for publicity or advertising purposes of information from this publication concerning proprietary products or the tests of such products is not authorized.

For sale by the National Technical Information Service, 5285 Port Royal Road
Springfield, VA 22161

Preface

The Climate Monitoring and Diagnostics Laboratory (CMDL) is located in Boulder, Colorado, with observatories in Barrow, Alaska; Mauna Loa, Hawaii; Cape Matatula, American Samoa; and South Pole, Antarctica. It is one of twelve components of the Environmental Research Laboratories (ERL) within the Office of Oceanic and Atmospheric Research (OAR) of the National Oceanic and Atmospheric Administration (NOAA). CMDL conducts research related to atmospheric constituents that are capable of forcing change in the climate of the earth through modification of the atmospheric radiative environment, for example greenhouse gases and aerosols, and those that may cause depletion of the global ozone layer.

This report is a summary of activities of CMDL for calendar years 1996 and 1997. It is the 24th consecutive report issued by this organization and its Air Resources Laboratory/Geophysical Monitoring for Climatic Change predecessor since formation in 1972. From 1972 through 1993 (numbers 1 through 22), reports were issued annually. For 1994-1995 we began a 2-year reporting cycle, which stems from a need to most efficiently use the time and financial resources of our staff and laboratory and from a general trend towards electronic media. In this respect, CMDL has developed a comprehensive internet home page during the past several years. There you will find information about our major groups and observatories, latest events and press releases, publications, data availability, and personnel. Numerous data graphs and ftp data files are available. The URL address is http://www.cmdl.noaa.gov. Information (program descriptions, accomplishments, publications, plans, data access, etc.) on CMDL parent organizations can best be obtained via the internet. Their URL addresses are ERL: http://www.erl.noaa.gov; OAR: http://www.oar.noaa.gov; NOAA: http://www.noaa.gov.

This report is organized into the following major sections:

1. Observatory, Meteorology, and Data Management
2. Carbon Cycle
3. Aerosols and Radiation
4. Ozone and Water Vapor
5. Nitrous Oxide and Halocompounds
6. Cooperative Programs

These are followed by a list of CMDL staff publications for 1996-1997.

Inquiries and/or comments are welcomed and should be addressed to:

Director, R/E/CG
NOAA/Climate Monitoring and Diagnostics Laboratory
325 Broadway
Boulder, CO 80303-3328
(303) 497-6074
e-mail: dhofmann@cmdl.noaa.gov

Contents

Preface v
CMDL Organization, 1997 viii
CMDL Staff, 1997 ix
CMDL Station Information x

1. Observatory, Meteorology, and Data Management Operations 1
   1.1. Mauna Loa Observatory 1
      1.1.1. Operations 1
      1.1.2. Programs 3
   1.2. Barrow Observatory 8
      1.2.1. Operations 8
      1.2.2. Programs 9
   1.3. Samoa Observatory 12
      1.3.1. Operations 12
      1.3.2. Programs 12
   1.4. South Pole Observatory 14
      1.4.1. Operations 14
      1.4.2. Programs 15
   1.5. Meteorological Measurements 17
      1.5.1. Meteorology Operations 17
      1.5.2. Station Climatologies 19
   1.6. References 29

2. Carbon Cycle 30
   2.1. Overview 30
   2.2. Carbon Dioxide 31
      2.2.1. In Situ Carbon Dioxide Measurements 31
      2.2.2. Flask Sample Carbon Dioxide Measurements 32
      2.2.3. Carbon Dioxide Reference Gas Calibrations 34
      2.2.4. Measurements of Stable Isotopes of CO_2 34
      2.2.5. Measurement of the Oxygen Isotopic Ratio of Soil CO_2 and Soil-Respired CO_2 39
   2.3. Methane 40
      2.3.1. In Situ Methane Measurements 40
      2.3.2. Discrete Sample Measurements of Methane 41
      2.3.3. Measurement of $^{13}C/^{12}C$ of Methane 43
   2.4. Carbon Monoxide 43
      2.4.1. In Situ Carbon Monoxide Measurements 43
      2.4.2. Flask Measurements of Carbon Monoxide 44
   2.5. Hydrogen 46
   2.6. Nitrous Oxide and Sulfur Hexafluoride 47
   2.7. MAGICC Analysis System 47
   2.8. Measurements on Tall Towers 48
   2.9. Aircraft Profiles 49
   2.10. Data Integration (Globalview) 49
   2.11. Inverse Modeling 50
   2.12. References 50

3. Aerosols and Radiation 52
3.1. Aerosol Monitoring 52
3.1.1. Scientific Background 52
3.1.2. Experimental Methods 53
3.1.3. Annual Cycles 55
3.1.4. Long-Term Trends 58
3.1.5. Lidar Measurements at Mauna Loa Observatory 58
3.1.6. Special Studies 60
3.2. Solar and Thermal Atmospheric Radiation 64
3.2.1. Radiation Measurements 64
3.2.2. Solar Radiation Calibration Facility 65
3.2.3. Aerosol Optical Depth Remote Sensing 67
3.2.4. MLO UV Spectroradiometer 67
3.2.5. MLO Broadband UV 69
3.2.6. Baseline Surface Radiation Network (BSRN) 71
3.2.7. WMO Global Atmosphere Watch (GAW) Stations 72
3.2.8. Barrow Snow Melt Date 72
3.2.9. Arctic UV Monitoring 73
3.3. References 74

4. Ozone and Water Vapor 76
4.1. Continuing Programs 76
4.1.1. Total Ozone Observations 76
4.1.2. Umkehrs 76
4.1.3. Calibration of Dobson Spectrophotometers 77
4.1.4. Surface and Tropospheric Ozone 78
4.1.5. Ozonesondes 79
4.1.6. Atmospheric Water Vapor 80
4.1.7. Atmospheric Transport 83
4.2. Special Projects 83
4.2.1. Characterization of the ECC Ozonesonde 83
4.2.2. Stratospheric Water Vapor as Part of the Observations of the Middle Stratosphere (OMS) Program 86
4.2.3. MLO Seasonal Transport Characteristics 86
4.3. References 89

5. Nitrous Oxide and Halocompounds 91
5.1. Continuing Programs 91
5.1.1. Introduction 91
5.1.2. Flask Samples 91
5.1.3. RITS Continuous Gas Chromatograph Systems 97
5.1.4. Gravimetric Standards 100
5.2. Stratospheric Measurements 101
5.2.1. Aircraft Projects-ACATS-IV 101
5.2.2. High Altitude GC Tracer Measurements Project: OMS/STRAT/POLARIS 106
5.3. Ocean Projects 112
5.3.1. Southern Ocean Expedition – BLAST III 112
5.3.2. Ocean Uptake of Atmospheric Trace Gases 113
5.4. GC Measurements at Two Tall towers in the U.S. 115
5.5. Firn Air Measurements 116
5.5. References 119

6. Cooperative Programs 122
Spectral Albedo Observation on the Snow Field at Barrow, Alaska
Teruo Aoki, Tadao Aoki, M. Fukabori, Y. Zaizen, Y. Tachibana, and F. Nishio 122
Latitudinal Tropospheric Concentration Distribution of Selected Halocarbons and Hydrocarbons
D.R. Blake, and F.S. Rowland 124
Ultrahigh Resolution Infrared Solar Spectroscopy From Mauna Loa Observatory: Update
S.J. David and F.J. Murcray 125
Polar Regions UV Spectroradiometer Monitoring Program: Observations in UV Irradiance at the South Pole and Barrow, Alaska
J. Ehramijian, C.R. Booth, L.W. Cabasug, J.S. Robertson, and T. Mestechkina 126
The National Satellite Testbed Receiver at Mauna Loa
P. Enge 129
Measurements of Short-Period Magnetic Field Data
K. Hayashi 130
Total Nitrate, NSS, and MSA Variation at Mauna Loa
B.J. Huebert, C.R. Adams, and L. Zhuang 131
Monthly Average Surface Air Concentrations of ^{210}PB and ^{7}Be at BRW, MLO, SMO, and SPO
J. Kada 133
Operation of Brewer Instruments at Mauna Loa Observatory
J.B. Kerr 136
The Global Distribution of Atmospheric Methyl Chloride
M.A.K. Khalil and R.A. Rasmussen 139
Artificial Windshielding of Precipitation Gauges in the Arctic
R.J. McClure 141
Investigation of the Transfer Function Between Atmosphere and Snow Concentrations of Hydrogen Peroxide at South Pole
J.R. McConnell and R.C. Bales 142
Middle Atmosphere Temperature Climatology at Mauna Loa from Rayleigh/Raman Lidar Measurements
S. McDermid, T. Leblanc, R. Cageao, G. Beyerle, and T.D. Walsh 145
Intercomparison of UV-B Spectroradiometer at Mauna Loa During 1995-1996
P.J. Neale, V.R. Goodrich, and D.R. Hayes, Jr 149
Middle Atmospheric Water Vapor Measurements From Mauna Loa, 1996-1998
G.E. Nedoluha, R.M. Bevilacqua, R.M. Gomez, and B.C. Hicks 152
An Active Layer Thermal Regime at Barrow, Alaska
F.E. Nelson, K.M. Hinkel, and R. Paetzold 154
The NDSC Microwave Ozone Profiling Instrument at Mauna Loa Observatory
A. Parrish, B.J. Connor, and J.J. Tsou 156
NSWC Point Barrow Geomagnetic Observatory
J.F. Scarzello and D.S. Lenko 157
Barrow Magnetic Observatory
J. Townshend 158
The ANSTO CMDL Radon Program at MLO
S. Whittlestone, D. Kuniyuki, and S. Ryan 159
Aerosol Size Distribution and Gaseous Species in April at Barrow
Y. Zaizen, K. Okada, M. Ikegami, T. Aoki, and Y. Sawa 161

7. Publications and Presentations by CMDL Staff, 1996-1997 163

CMDL Organization, 1997

The CMDL organization structure features five research areas organized according to scientific discipline as follows: (1) Carbon Cycle; (2) Nitrous Oxide and Halocompounds; (3) Ozone and Water Vapor; (4) Aerosols and Radiation; and (5) Observatory Operations. At the end of 1997, the laboratory staff consisted of 46 civil service personnel (excluding part-time student assistants), 33 CIRES/University of Colorado personnel, and two NOAA Corps officers as well as several visitors and people on special appointments.

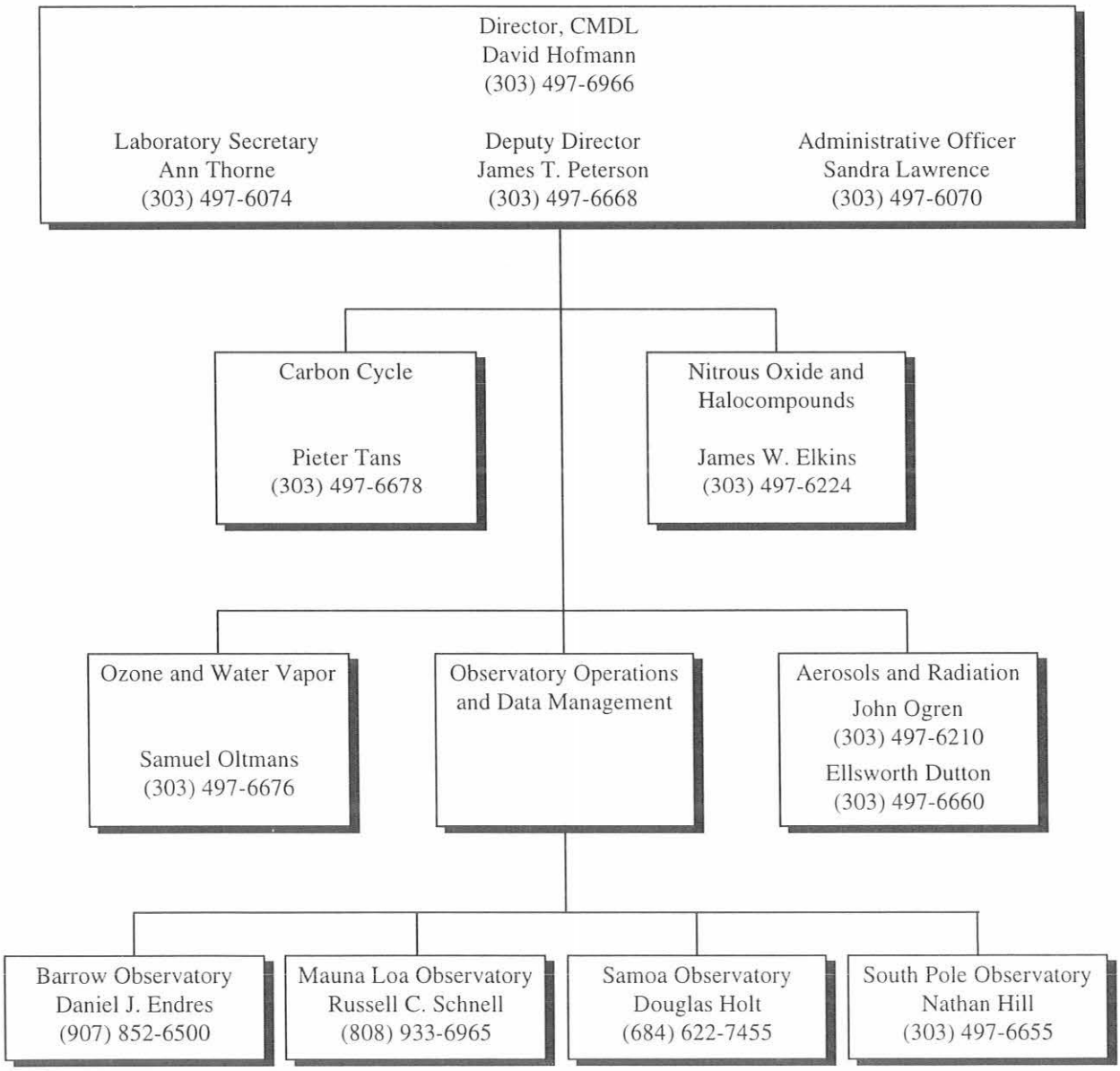

CMDL Staff, 1996/1997

Director's Office

David Hofmann, Director
James T. Peterson, Deputy Director
Sandra Lawrence, Administrative Officer
Eric McLaughlin, Office Automation Clerk
Rita Rosson, Editorial Assistant
Ann Thorne, Secretary
Kay Villars, Administrative Assistant

Special Projects

Mark Bieniulis, CIRES
Laurie Bruhwiler, Physical Scientist
Bradley Halter, CIRES
Thomas Mefford, CIRES
Eldon Ferguson, Guest Scientist

Aerosols and Radiation Division

Ellsworth Dutton, Meteorologist
John Ogren, Physical Scientist
Jill Foose, Secretary
Sharon Anthony, CIRES
Michael Bergin, DOE Post Doc.
Barry Bodhaine, Meteorologist
Rudy Haas, Mathematician
Brian Hagan, CIRES
Wen Huang, Physical Science Aid
Anne Jefferson, CIRES
Jan Kleinn, Guest Scientist
David Longenecker, CIRES
Lynn McInnes, NRC Post Doc.
Charles Myers, CIRES
Donald Nelson, Meteorologist
Jay Shah, CIRES
Patrick Sheridan, CIRES
Herman Sievering, Guest Scientist
Robert Stone, CIRES
Shad Thaxton, CIRES
Renee Tatusko, Physical Scientist
James Wendell, Electronic Technician

Ozone and Water Vapor Division

Samuel Oltmans, Physicist
Jill Foose, Secretary
Kirsten Borbe, CIRES
Mark Clark, CIRES
Robert Evans, CIRES
Eric Hackathorn, Engineering Aid
Joyce Harris, Physical Scientist
Bryan Johnson, CIRES
Gloria Koenig, Physical Scientist
Walter Komhyr, Contractor
Jeffrey Lathrop, Physical Scientist
Michael O'Neill, CIRES
Dorothy Quincy, CIRES
Eric Rice, Contractor
Holger Vömel, CIRES
Matthew Wood, Physical Science Technician

Carbon Cycle Division

Pieter Tans, Chief
Debra Hansen , Secretary
Yvette Ayhens, CIRES
Peter Bakwin, Physicist
Louise Belnay, Intern
Thomas Conway, Research Chemist
Richard Dissly, NRC Post Doc.
Ed Dlugokencky, Research Chemist
Alison Feingold, C.U. Work Study
Laurie Geller, CIRES
Douglas Guenther, CIRES
Michael Hahn, CIRES
Dale Hurst, NRC Associate
Janice Imanaka, Phys. Science Technician
Duane Kitzis, CIRES
Patricia Lang, Physical Scientist
Joshua Martin, Phys. Science Aid
Kenneth Masarie, CIRES
John Miller, CIRES
Paul Novelli, Res. Chemist
Constance Prostko-Bell, CIRES
Michel Ramonet, Guest Scientist
Durelle Scott, CCHE Intern
Kirk Thoning, Physicist
Michael Trolier, INSTAAR
Lee Waterman, Research Chemist
Dan Yakir, NRC Post Doc.
Ni Zhang, CIRES
Conglong Zhao, CIRES

Nitrous Oxide and Halocarbons Division

James Elkins, Chief
Debra Hansen, Secretary
James Butler, Research Chemist
Andrew Clarke, CIRES
Nicholas Condon, CIRES
Matthew Dicorleto, CIRES
Raymond Dunn, CIRES
Geoffrey Dutton, CIRES
Ryan Flores, C.U. Work Study
Jackson Fox, CIRES
Arnold Hayden, CIRES
Frank Lee, AISES Intern
Jürgen Lobert, CIRES
Loreen Lock, CIRES
Michele McCarthy, C.U. Work Study
Steve Montzka, Research Chemist
Fred Moore, CIRES
Richard Myers, Phys. Sci. Technician
Matthew Pender, CIRES
Michael Perry, C.U. Work Study
Eric Ray, NRC Post Doc.
Pavel Romashkin, CIRES
Robin Sam, CIRES
Thomas Swanson, CIRES
Thayne Thompson, Physicist
Michael Volk, CIRES
Eric Wood, CU Work Study
Shari Yvon-Lewis, CIRES

Observatory Operations Division

James T. Peterson
Linda Sachetti, Secretary

Daniel Endres, Station Chief, **Barrow**
Malcom Gaylord, Electronic Engineer

Russell Schnell, Director, **Mauna Loa**
Judith Pereira, Program Support Technician
John Barns, Physical Scientist
John Chin, Physicist
Darryl Kuniyuki, Electronic Engineer
Leslie Pajo, Office Automation Clerk
Steven Ryan, Physical Scientist
Robert Uchida, Electronic Technician
Alan Yoshinaga, Chemist

Mark Winey, Station Chief, **Samoa**
Gerald Yung, Elect. Engineer

Ricardo Ramos, NOAA Corps, **South Pole**
Jeffrey Otten, Engineering Technician
Nathan Hill, NOAA Corps
Mark Boland, NOAA Corps
Glen McConville, Electronic Technician
Thomas Jacobs, NOAA Corps

CMDL Station Information

	Barrow (BRW)	**Mauna Loa (MLO)**
Name:		
Latitude:	71.323°N	19.539°N
Longitude:	156.609°W	155.578°W
Elevation:	8 m	3397 m
Time Zone:	GMT -9	GMT -10
Office Hours:	8:00 am-5:00 pm	8:00 am-5:00 pm
Telephone		
Office hours:	(907) 852-6500	(808) 933-6965
Fax:	(907) 852-4622	(808) 933-6967
Postal Address:	Officer in Charge NOAA/ERL/CMDL Pouch 888 Barrow, AK 99723	U.S. Dept. of Commerce NOAA - Mauna Loa Observatory, Rm. 202 P.O. Box 275 Hilo, HI 96721
Freight Address:	Officer in Charge NOAA/ERL/CMDL 617 Cunningham Barrow, AK 99723	U.S. Dept. of Commerce NOAA - Mauna Loa Observatory 154 Waianuenue Ave. Hilo, HI 96720-2452

	Samoa (SMO)	**South Pole (SPO)**
Name:		
Latitude:	14.232°S	89.997°S
Longitude:	170.563°W	102.0°E
Elevation:	77 m	2837 m
Time Zone:	GMT -11	GMT +12
Office Hours:	8:00 am-5:00 pm	8:00 am - 5:00 pm
Telephone:		
Office hours:	011 (684) 622-7455	Relayed through CMDL Boulder
After hours:	011 (684) 699-9953	
Fax:	011 (684) 699-4440	
Postal Address:	Officer in Charge U.S. Dept. of Commerce NOAA - CMDL Samoa Observatory Pago Pago, American Samoa 96799	Officer in Charge NOAA/CMDL Clean Air Facility S-257 South Pole, Antarctica PSC 468 Box 402 FPO AP 96598-5402
Freight Address:	Same as above	Same as above

1. Observatory, Meteorology, and Data Management Operations

1.1. Mauna Loa Observatory

R. Schnell, J. Barnes, J. Chin, D. Kuniyuki, L. Pajo, J. Pereira, S. Ryan, B. Uchida, and A. Yoshinaga

1.1.1. Operations

The construction of the new Network for the Detection of Stratospheric Change (NDSC) building near the center of the Mauna Loa Observatory, Hawaii (MLO) site dominated the nonscientific activities of the MLO staff throughout 1996-1997. The building was completed in November 1997 in time for an international gathering of celebrants to enjoy a week of festivities in Hilo that included dedication of the NDSC building; the 40th anniversary of MLO; renaming of the original MLO building the "Keeling Building" in honor of Dave Keeling who initiated CO_2 measurements at MLO 40 years prior; and a 2-day Climate Monitoring and Diagnostic Laboratory (CMDL) review. The NDSC building houses or will house a majority of the NDSC programs at MLO in addition to most of the CMDL programs once located in the original MLO building. In connection with the anniversary, the Lyman Museum in Hilo presented a well-attended month-long exhibit on the history of MLO that included a display of MLO instruments dating from the 1950s.

A major shift in MLO operations and activities over the past 2 years has been brought about by the absorption of Internet technology and direct computer control and communications into all but a few relic programs. Only a few years ago, MLO data were mainly recorded on disks and paper tapes, with a few programs accessible to off-site principal investigators (PIs) by using a dial-up telephone modem. Today MLO has about 50 computers with most data going by way of the Internet direct to PIs located around the world. This includes large lidar data files and Fourier transform interferometer (FTIR) spectra. Two years ago MLO installed a camera overlooking the mountain site and made the images available on the Internet. In early 1996 only a few dozen people per week logged onto the site, whereas by late 1997 this grew to a peak of 25,000 per month. At present the primary efforts of two MLO staff are required to keep the computer/Internet systems operating and updated.

The number of flasks being collected at the Cape Kumukahi Lighthouse Tower MLO flask sampling facility on the easternmost point of the Big Island has increased over the past 2 years because it is an excellent site for sampling marine boundary layer air. This has necessitated sending two staff to the site on alternate weeks to augment the normal weekly schedule. The Cape Kumukahi site has long been a target for vandalism and for littering in the form of abandoned cars. This continued into 1996 to the point of being discouraging for MLO staff and expensive for the Coast Guard staff who maintain the tower. On one occasion the rotating beacon was shot out, costing $10,000 for repairs.

MLO staff initiated a number of activities aimed at combating this problem including having the Coast Guard block the beacon from shining toward a housing development, welding protective covers over padlocks, arranging for the National Weather Service (NWS) to use MLO power to replace its theft-attractive solar cells on the co-located NWS weather station, and holding a community meeting in the Puna area to explain what our measurements are all about. Through these actions, aided possibly by the perpetrators leaving the area, or youths growing up, etc., vandalism and littering has essentially ceased. There has not been a notable incident for a year.

Within the Hilo facility, the electronics repair area in the corner of the basement was walled in and air conditioning installed. This was a long overdue improvement that now provides security and a less corrosive environment for valuable electronic equipment. The adjacent data storage room was cleaned out, and much of the archive was shipped to Boulder for storage under less humid conditions. This room was carpeted, painted, and turned into an overflow office that is now used for staff computer/Internet training. The room shared by the MLO Director and secretary was partitioned to provide privacy and better temperature control.

The County of Hawaii trained MLO staff on the correct procedures for entering and exiting a helicopter in anticipation of rescue missions at MLO when Mauna Loa volcano erupts again. This training included a flight to, and an attempted landing at, the MLO site. As a result of the test, a larger helicopter pad with clear landing approaches was constructed at MLO and a secondary pad prepared at the 2438 m (8000 ft) level. The volcano eruption escape plan was updated and better coordinated with the Hawaii County Civil Defense Agency. The last Mauna Loa volcano eruption in 1984 cut the power line to MLO, and flowing lava reached the outskirts of Hilo. It is just a matter of time before Mauna Loa erupts again.

In 1996, Global Positioning System (GPS) measurements (two different systems, two different times) at the same elevation at MLO produced data that were 70 m (210 ft) off the conventional and generally accepted rod and level survey height of the MLO "Stair" benchmark. GPS algorithms do not account for the local geoid-ellipsoid differences introduced by the mass of Mauna Kea and Mauna Loa, which distort the globe in this part of the world. To address this discrepancy MLO arranged funding from the National Aeronautics and Space Administration (NASA) to obtain an elevation survey using a new benchmark placed between Mauna Kea and Mauna Loa in the recent survey for the Saddle Road realignment. This survey determined that the Stair benchmark is recorded as being 3.66 m (12 ft) higher than present survey methods place it. The following are the elevations of various locations at MLO based upon the most recent survey: Stair marker, 3391.81 m (11,128 ft); floor of the MLO main (Keeling) building, 3395.8 m (11,141 ft); floor of the NASA lidar trailer, 11,138 ft. (3394.9 m). These elevations are considered to be accurate within 0.3 m (1 ft).

On August 15, 1997, the most costly lightning strike in MLO history damaged almost every instrument connected to a data or communication line. The charge bypassed safety devices by fusing a path through electronic circuits in surge protectors, servers, modems and computers. The overall cost to MLO and NDSC equipment was more than $100,000 spread over a few dozen projects. The local telephone company (GTE) experienced an additional $50,000 loss to their switching equipment. The new NDSC building has extra lightning protection on both communication and electrical lines, but it appears that MLO may never be completely safe from the larger strikes.

Outreach

About 700 people from 23 different countries visited MLO in 1996-1997. In November 1996 MLO assisted in hosting the NDSC Steering Committee Meeting in Kona and gave the attendees a tour of MLO. In August 1997 the Chairman of the House Appropriations Committee for Commerce, State, and Judiciary along with two other Congressmen visited MLO (transported most of the way up by a National Guard helicopter from Hilo) and were greeted and briefed by the Director of CMDL. Part of their education included a web display of El Niño and its probable effects on the Congressmen's respective home districts. The largest group of about 125 visitors, which included many National Oceanic and Atmospheric Administration (NOAA) and Department of Commerce (DOC) dignitaries and congressional staffers, visited during the MLO 40th anniversary celebrations in November 1997.

A small, but information-filled, four-fold handout on the goals and activities of MLO, including a bit of station history and current graphs of trends in halocarbon and carbon cycle species, was developed in early 1996 as a visitor and public relations handout. This has proved to be a popular item with more than 1500 distributed to date. The brochure is maintained in a computer file and updated periodically.

Four TV documentaries including footage of MLO activities and data were shot onsite over the past 2 years, including a local National Broadcasting Company (NBC) affiliate report on ozone depletion broadcast live from MLO for the Hawaii 6:00 P.M. news broadcast. This was a first for MLO because it included two-way dialogue with the studio anchor in Honolulu. In late 1997 the British Broadcasting Corporation (BBC) filmed extensively at MLO for a series on El Niño. The broadcast of this series on the Discovery Channel raised the awareness of the MLO home page to such a level that the number of visits to the page (up to 25,000 per month) are now overwhelming the ability of the MLO server to handle the traffic. MLO staff were interviewed live on the phone three times for radio programs, discussing climate change and ozone depletion issues.

The MLO director spoke to about 18 civic clubs such as Rotary, Lions, Civitan, etc., bringing the MLO message to interested parties. In addition he spoke to six university and two high school classes on the same subject.

A new cooperative effort between five Big Island public and private high schools and MLO was begun by a MLO staff member in September 1996. In the program, called VOGNET, students make regular observations of volcanic aerosols from a network of five locations evenly spaced around the island in order to study the distribution and relative levels of volcanic acidic haze or "vog" in Hawaii. Science teachers from the five schools were trained in condensation nucleus (CN) and aerosol optical depth measurements, and each school was lent a Gardner CN counter and a 2-wavelength sunphotometer. Each school takes hourly observations and periodically submits these to the lead school, Hawaii Preparatory Academy, which maintains a database and distributes copies back to all the schools. Aerosol optical depth and CN measurements from MLO, along with radiosonde data from the Hilo weather service, are included in the database. Every few months, a 1-day conference is held in which all the participants get together to discuss results and participate in an instrument intercalibration session. It is hoped that besides being an educational tool, VOGNET will become a scientific resource. No existing vog monitoring networks are in place in Hawaii, despite years of concern over the public health effects of the volcanic particles.

Computers/Network

By the end of 1997 MLO had 57 PCs, 45 of which are functioning on the network. Twenty-four of the 57 are running under Windows 95, 8 under Windows 3.X, 12 under DOS, 4 under Windows NT, and 9 under other operating systems such as a Unix type, OS/2, or Novell Netware. The increase in the number of computers at MLO in 1996-1997 was due to an increase in new programs such as the NDSC Brewer system (two), the water vapor program (one), and a new lidar analysis computer (one) coming to MLO. In the Hilo office graphics workstation, CD recording, network monitoring, and guest scientist computers were added. Two Web camera systems were set up at the observatory to process real-time images that are sent to the Web server in Hilo and on to the Internet (another new computer) every 10 minutes. In August 1996 the installation of a new Web server program and a major revision of the MLO Web page were completed. The Web page now contains pictures and information about current MLO programs, history, staff, station attributes, publications, and contact procedures. The latest meteorological data are updated every hour and current satellite images of Hawaii and the Pacific Ocean are linked to the MLO home page.

The NT server in the Hilo office was upgraded with additional hard drive space and memory. The graphics workstation has an HP scanner, a digitizing pad, and an optical disk drive. This computer proved essential in creating the MLO brochures, pamphlets for the NDSC and 40th anniversary meetings, and the Web page graphics, and for the archiving of data and images on optical disks. A new concentrator was set up at the mountain site allowing for more connections to the fiber optic cabling. Additional fiber optic lines were run to the basement from the second floor in the Hilo facility.

A monthly maintenance schedule for backing up computers on the network was established in April 1996 with the backups on (DAT) tapes initiated and controlled

from the NT server in Hilo. The old magnetic tape unit was disconnected from the VAX system and removed in early 1997.

In November 1996 a mini-network was set up at the NDSC Steering Committee Meeting held in Waikoloa, Kona. The mini-network consisted of two PCs, one laser printer, and a color inkjet printer. One PC was set up to run the NDSC database and to create signs, transparencies, etc. The other PC was used for e-mail access through the telephone system. A third computer was set up with a 27-inch TV to broadcast live images from the mountain to the hotel convention room.

In January 1997 a videoconference system was set up to test its viability for use with the other observatories and Boulder. A test conference was held with Boulder; video images were good but the sound needed considerable improvement. This technology was considered of marginal value to MLO, and the computer was reconfigured for use by guests and visiting scientists.

The August 1997 lighting strike caused the worst damage and expense from any single natural event ever recorded at MLO, probably even more than the volcanic eruption of 1984. Thirteen of the MLO-supplied computers on the mountain were affected. Two network hubs and the router box were burnt out, as were the cordless telephone, fax machine, and two phone switch boxes. Most repairs were completed quickly, but some systems took months to repair or replace. The above losses do not include damage to equipment belonging to CMDL Boulder, NDSC, and MLO cooperative programs.

1.1.2. PROGRAMS

Table 1.1 summarizes the programs in operation or terminated at MLO during 1996-1997. Relevant details of note on some of the respective programs are as follows:

Gases

Carbon Dioxide. The CMDL Siemens Ultramat-3 IR CO_2 analyzer and the Scripps Institution of Oceanography (SIO) Applied Physics IR CO_2 analyzer (see listing under Cooperative Programs in Table 1.1) were operated in parallel without major problems throughout 1996-1997. Routine maintenance and calibrations were undertaken on both instruments as scheduled. SIO upgraded their CO_2 data acquisition system in 1994 but had problems with power surges at MLO that caused frequent computer downtime. An uninterruptible power supply (UPS) was installed in 1996 to correct that problem. Data are recorded on a strip chart recorder and stored on a PC hard disk and a floppy disk that are mailed to SIO weekly. The CMDL CO_2 data acquisition system worked through 1996-1997 without major problems, except that the network card in the computer was damaged in the August lightning strike.

The weekly CO_2, CH_4, and other gas sampling programs, using flasks at MLO and at Cape Kumukahi, were carried out according to schedule throughout the year without major problems. An AIRKIT sampling unit at Cape Kumukahi, upgraded from the MAKS unit, uses flask types and sampling procedures that are the same as for the MAKS method. Both the MAKS and the AIRKIT sampled simultaneously next to each other through 1996-1997 without problems.

Carbon dioxide emissions from the Mauna Loa volcano measured at MLO, resumed their steady decline in 1996-1997 after a brief factor-of-2 rise in 1994-1995 that was probably due to new emissions from the upper southwest rift. The ratio of SO_2 to CO_2 measured in the plume remained steady at about 4×10^{-5} between mid-1994 and the end of 1996. Since magma exsolves CO_2 at a much greater depth than SO_2, this observation suggests that there has been no magma ascent to shallow depths since 1994. The temporary increase in CO_2 in 1994-1995 must have come from a small intrusion of magma at a great depth.

Because outgassing from the volcanic vents at the Mauna Loa caldera and along the northeast rift zone at Mauna Loa has fallen to negligible levels, the tables for MLO outgassing that appeared in prior reports have been discontinued. They will be reinstated should MLO outgassing become active again, as is the case following major eruptions.

Carbon Monoxide. The Trace Analytical RBA3 reduction gas analyzer for the continuous measurement of CO mixing ratios developed a major problem in 1997. The unit was shipped back to the Boulder laboratory on March 26, 1997, and has been out of service through December 1997.

Methane. Chromatograms from the HP6890 methane gas chromatograph (GC) system are stored on the Carbon Cycle Group (CCG) hard disk. Since April 1996, instead of shipping all the required gases needed for this program from the Boulder laboratory, MLO has been purchasing the nitrogen carrier gas and the oxidizer in Hilo at discounted prices. The price for grade 5 ultra pure nitrogen (99.999%) and oxidizer (40% oxygen in balanced nitrogen, with analytical accuracy of $\pm$2% and analysis precision of $\pm$1%) in size 200 cylinders is about $100 per cylinder. The amount of these gases used is one cylinder of nitrogen per 5 weeks and one cylinder of oxidizer per 2.5 weeks.

The CH_4 data continued to show variations of clearly defined frequency. The typical diurnal cycle was well correlated with up- and downslope winds, with the marine boundary layer air having the higher CH_4 concentrations. Multi-day or synoptic-scale CH_4 cycles were also observed, which apparently relate to different air mass source regions.

Sulfur Dioxide. In February 1997 the TECO SO_2 analyzer was returned to the NOAA Air Resources Laboratory ending 2.5 years of measurements at MLO. Another analyzer was lent to MLO from the University of Miami in June, and a new system that overcomes most of the problems encountered with the earlier program was developed in the following months. Sampling lines and solenoid valves in the new system are entirely made of Teflon. The lines are heated and regulated by computer to allow for constant temperature or constant relative humidity samples. Air is alternately drawn from heights of 4, 10, 23, and 40 m. By measuring the SO_2 profile above the ground, we can determine if enhanced levels at night are coming from beneath the surface temperature inversion (Mauna Loa volcano) or outside the temperature inversion

TABLE 1.1. Summary of Measurement Programs at MLO in 1996-1997

Program	Instrument	Sampling Frequency
Gases		
CO_2	Siemens Ultramat-3 IR analyzer†	Continuous
	0.5-L glass flasks, through analyzer	1 pair wk^{-1}
CO	Trace Analytical RGA3 reduction gas analyzer no. R5†	Continuous
CO_2, CH_4, CO, ^{13}C, ^{18}O of CO_2	2.5-L glass flasks, MAKS pump unit*	1 pair wk^{-1}
	AIRKIT pump unit, 2.5-L glass flasks‡	1 pair wk^{-1}
CH_4	3-L evacuated glass flasks‡	1 pair wk^{-1}
	HP6890GC†	Continuous
SO_2	TECO model 435 pulsed-florescence analyzer†	Continuous
Surface O_3	Dasibi 1003-AH UV absorption ozone monitor†	Continuous
Total O_3	Dobson spectrophotometer no. 76†	3 day^{-1}, weekdays
O_3 profiles	Dobson spectrophotometer no. 76† (automated Umkehr method)	2 day^{-1}
	Balloonborne ECC sonde	1 wk^{-1}
N_2O, CFC-11, CFC-12, CFC-113, CH_3CCl_3, CCl_4	300-mL stainless steel flasks (phased out 1996-1997)	1 sample wk^{-1}
N_2O, CFC-11, CFC-12, CFC-113, CH_3CCl_3, CCl_4, SF_6, HCFC-22, HCFC-141b, HCFC-142b, CH_3Br, CH_3Cl, CH_2Cl_2, $CHCl_3$, C_2HCl_3, C_2Cl_4, H-1301, H-1211, H-2402, HFC-134a	850-mL stainless steel flasks	1 sample wk^{-1}
	2.5-L stainless steel flasks	1 sample wk^{-1}
CFC-11, CFC-12, CFC-113, N_2O, CCl_4, CH_3CCl_3	HP5890 automated GC†	1 sample h^{-1}
N_2O	Shimadzu automated GC†	1 sample h^{-1}
Radon	Two-filter system	Continuous integrated 30-min samples
Aerosols		
Condensation nuclei	Pollak CNC	1 day^{-1}
	TSI CNC†	Continuous
Optical properties	Four-wavelength nephelometer†: 450, 550, 700, 850 nm; three-wavelength nephelometer: 450, 550, 700 nm	Continuous
Aerosol light absorption (black carbon)	Aethalometer†	Continuous
Stratospheric and upper tropospheric aerosols	Nd:YAG lidar: 532-, 1064-nm wavelengths	1 profile wk^{-1}
	Ruby lidar: 694-nm wavelength	1 profile wk^{-1}
Solar Radiation		
Global irradiance	Eppley pyranometers with Q, OG1, and RG8 filters†	Continuous
Direct irradiance	Eppley pyrheliometer with Q filter†	Continuous
	Eppley pyrheliometer with RG8 filter†	Continuous
	Eppley pyrheliometer with Q, OG1, RG2, and RG8 filters†	3 day^{-1}
	Eppley/Kendall active cavity radiometer†	1 mo^{-1}
Diffuse irradiance	Eppley pyrgeometer with shading disk and Q filter†	Continuous
UV solar radiation	Yankee Environmental UVB pyranometer (280-320 nm)†	Continuous
Terrestrial (IR) radiation	Global downwelling IR pyrgeometer†	Continuous
Turbidity	J-202 and J-314 sunphotometers with 380-, 500-, 778-, 862-nm narrowband filters	3 day^{-1}, weekdays
	PMOD three-wavelength sunphotometer†: 380, 500, 778 nm; narrowband	Continuous
Column water vapor	Two-wavelength tracking sunphotometer: 860, 940 nm†	Continuous
Meteorology		
Air temperature	Aspirated thermistor, 2-, 9-, 37-m heights†	Continuous
	max.-min. thermometers, 2-m height	1 day^{-1}
Air temperature (30-70 km)	Lidar	1 profile wk^{-1}
Temperature gradient	Aspirated thermistors, 2-, 9-, 37-m heights†	Continuous
Dewpoint temperature	Dewpoint hygrometer, 2-m height†	Continuous

TABLE 1.1. Summary of Measurement Programs at MLO in 1996-1997—Continued

Program	Instrument	Sampling Frequency
Meteorology - Continued		
Relative humidity	TSL 2-m height†	Continuous
Pressure	Capacitance transducer†	Continuous
	Mercurial barometer	5 wk^{-1}
Wind (speed and direction)	8.5-, 10-, and 38-m heights†	Continuous
Precipitation	Rain gauge, 20-cm	5 wk^{-1}
	Rain gauge, 20-cm§	1 wk^{-1}
	Rain gauge, tipping bucket†	Continuous
Total precipitable water	Foskett IR hygrometer†	Continuous
Precipitation Chemistry		
pH	pH meter	wk^{-1}
Conductivity	Conductivity bridge	wk^{-1}
Cooperative Programs		
CO_2 (SIO)	Applied Physics IR analyzer†	Continuous
CO_2, ^{13}C, N_2O (SIO)	5-L evacuated glass flasks*	1 pair wk^{-1}
CO_2, CO, CH_4, $^{13}C/^{12}C$ (CSIRO)	Pressurized glass flask sample	1 mo^{-1}
CH_4, CH_3CCl_3, CH_3Cl, F-22, F-12, F-11, F-113, CO, CO_2, N_2O, $CHCl_3$, CCl_4 (OGIST)	Pressurized stainless steel flasks*	3 wk^{-1}
O_2 analyses (SIO)	5-L glass flasks through tower line and pump unit*	3 $(2\ mo)^{-1}$
O_2 analyses (URI)	3-L glass flasks through tower line and pump unit	2 $(2\ mo)^{-1}$
CH_4 ($^{13}C/^{12}C$) (Univ. of Washington)	35-L evacuated flask	2 mo^{-1}
Total suspended particulates (DOE)	High-volume sampler	Continuous (1 filter wk^{-1})
Ultraviolet radiation (Smithsonian)	Eight-wavelength UV radiometer: 290-325 nm; narrowband (out for repairs June 1996-present)	Continuous
Ultraviolet radiation (CSU-USDA)	Multi-wavelength radiometer (direct, diffuse, shadowband) (began 11/97)	Continuous
Precipitation collection (DOE)	Exposed collection pails (ended 7/97)	Integrated monthly sample
Radionuclide deposition (DOE)	Ion-exchange column (began 8/97)	Monthly
Aerosol chemistry (Univ. of Calif.-Davis)	Programmed filter sampler	Integrated 3-day sample, 1 continuous and 1 downslope sample $(3\ days)^{-1}$
Sulfate, nitrate, aerosols (Univ. of Hawaii)	Filter system	Daily, 2000-0600 LST
Radon (ANSTO)	Aerosol scavenging of Rn daughters†; 2-filter system	Continuous; integrated 30-min samples
AERONET sunphotometers (NASA Goddard)	Automated solar-powered sunphotometers (began April 1996)	Continuous
Global Positioning System (GPS) Test Bed (FAA and Stanford University)	GPS-derived column water vapor profiles (began 9/97)	Continuous
Network for Detection of Stratospheric Change (NDSC)		
Ultraviolet radiation (NOAA and NIWA)	UV spectrometer (280-450 nm), 1-nm resolution†	Continuous
Stratospheric O_3 profile, 20-64 km (Univ. of Mass, Amherst)	Millitech Corp., 110.8-GHz microwave ozone spectroscopy	3 profiles h^{-1}
Stratospheric O_3 profiles (15-55 km), temperature (20-75 km), aerosol profiles (15-40 km) (JPL)	UV lidar†	3-4 profiles wk^{-1}
Stratospheric water vapor profiles, 40-80 km, 10-15 km resolution (NRL)	Millimeterwave spectrometer (began 3/96)	Continuous
UV/visible radiation (NIWA and NOAA)	Slant column NO_2 spectrometer (began 7/96)	Continuous, day
Column O_3, UV (AES, Canada)	Brewer spectrophotometers (two)(began 3/97 and 11/97)	Daily
Solar spectra (Univ. of Denver)	FTIR spectrometer, automated†	5 days wk^{-1}

All instruments are at MLO unless indicated.
*MLO and Kumukahi.
†Data from this instrument recorded and processed by microcomputers.
‡Kumukahi only.
§Kulani Mauka

(Kilauea volcano), or are uniformly mixed (e.g., long-range transport of anthropogenic pollution). In conjunction with existing multilevel wind and temperature measurements, this information will be useful in studying the properties of the downslope wind and air circulation above MLO.

During system development and testing in the Hilo office from September through December 1997, prior to deployment at MLO, a quasi-continuous record of SO_2 was obtained in Hilo for that period. Concentrations as low as a few tens of a part per trillion were sometimes measured in clean downslope air at night. Episodes of volcanic pollution from Kilauea had concentrations that could exceed 200 parts per billion (ppb). In comparison, up to 50 ppb were observed at MLO in upslope winds contaminated by Kilauea volcano emissions.

Ozone Monitoring. The 1996-1967 MLO ozone monitoring program consisted of three measurement focii: continuous MLO surface ozone monitoring using a Dasibi model 1003-AH UV absorption ozone monitor; daily total and Umkehr ozone profile measurements using a computer-based automated Dobson instrument (Dobson no. 76); and ozone profile measurements based on weekly ascents of balloonborne electrochemical concentration cell (ECC) ozonesondes released from the NWS station at the Hilo airport.

Dobson no. 76, the MLO instrument, was operated daily during weekdays throughout the period including AM/PM Umkehr profiles. A new computer was installed in June 1996, and data acquisition upgrades and network connections were finalized at that time. Summer intercomparisons with the world standard Dobson no. 83 occurred in both 1996 and 1997. The instrument was shut down from March 1997 to May 1997 because of dust and vibrations from the construction of the NDSC building.

The Dasibi program operated normally throughout the period and the data transmission software was upgraded in August 1996. The Dasibi was calibrated and yearly maintenance was carried out by Boulder-based staff in March 1997, and absorption tubes were cleaned by other Boulder-based CMDL employees in November 1997 at which time analog/digital checks were also completed.

Ozonesondes were launched weekly whenever supplies were available from Boulder. In 1996 there were 47 ozonesonde flights and in 1997 there were 45.

Halocompounds and Nitrous Oxide. The Nitrous Oxide and Halocompounds (NOAH) system had its semiannual maintenance by Boulder staff in June 1996. Besides making the normal maintenance checks, the staff installed an electronic actuator to replace an air-actuated model for the stream select valve. In August round-robin tank measurement and precision checks were run by MLO. The UPS unit started to have problems in December. Minor repairs and adjustments and new batteries in March 1997 returned the system to normal operation. The lightning storm in August 1997 damaged the serial card, the network card, and a CPU fan. These were replaced and the system placed back on line.

Radon. The CMDL-Department of Energy (DOE) radon program operated normally in 1996 and during the first half of 1997. The lightning strike in August destroyed the instrument electronics and computer. In early 1997, reorganization within DOE ended its involvement in radon monitoring. Without spare parts, schematics, or documentation, the DOE radon program was terminated at MLO. Radon continues to be measured continuously with the Australian Nuclear Science and Technology Organization (ANSTO) instrument, which has a similar time response and a four times greater sensitivity than the DOE detector. The ANSTO program (see Table 1.1, Cooperative Programs) now has an 8-year record of radon measurements at MLO.

Aerosols

Condensation Nuclei. The Thermo Systems Incorporated (TSI) unit is a continuously operating CN counter (CNC) in which condensation occurs in butyl alcohol vapor with light scattering detection and single-particle counting statistics as a basis for determining CN concentrations. The Pollock CNC continues to be used as a primary daily calibration.

Aerosol Light Scattering. The four-wavelength nephelometer for determining aerosol optical properties continues to run without considerable down time. A three-wave TSI nephelometer with much better resolution now operates in parallel with it, sampling the same air stream.

Aerosol Absorption. The aethalometer performed satisfactorily during most of 1996-1997. On September 12, 1996, it was sent back to the manufacturer to be upgraded. It was returned on January 9, 1997. The new instrument has a built-in computer and an automatic filter-changing system.

Stratospheric and Upper Tropospheric Aerosols. Weekly observations continued with both the CMDL and NDSC ruby and Nd:YAG lidars throughout 1996 and 1997. The ruby laser (694-nm wavelength) had various electronic problems but no optical problems except for the usual flashlamp changes. Two of three high-voltage transformers burned out in the power supply rebuilt by the prior lidar operator. The laser still works well with only one transformer to charge the large capacitors. A source of replacement transformers was located in the event the last unit on hand fails. A significant change was made in the data acquisition electronics in the spring of 1997. After many years of service, the 8-bit Biomation was replaced with an Analogic FAST 16 board (16-bit conversion at 1 MHz). The new board plugs into the PC. The 16-bit conversion captures the entire altitude range from about 7 to 45 km at one detector sensitivity. Previously the laser shots (typically 200) were spread between several different detector sensitivities requiring splicing of the altitude ranges.

The Nd:YAG laser power supply also had a few failures. The problems were corrected without a service call from California. The four flashlamps were replaced on two occasions when the power dropped significantly. In preparation for the move into the new NDSC building some of the lidar control functions were automated. General Purpose Interface Bus (GPIB) control of some of the lidar electronics was added as well as remote tuning of the laser power. Polarization measurements of cirrus clouds at 532 nm were taken on occasion to demonstrate the technique for future studies. An Avalanche Photodiode

(APD) was tried for the aerosol measurement at 1064-nm laser wavelength using the FAST 16 board, but the response was far too slow for the lidar signal. A photomultiplier tube (Hamamatsu R632) with an S-1 cathode was then installed. The sensitivity of the tube at 1064 nm is low, but the laser emits most of its power at that wavelength. The detector must also be cooled (-30°C) to reduce the dark noise. The first profiles were taken in October 1996. The accuracy is already better than that of the ruby lidar system.

A time-dependent atmospheric model was developed from Hilo radiosonde data and upper stratospheric models for the aerosol calculation that requires molecular density as a function of altitude. The ruby analysis has always used a fixed model, but the higher accuracy and altitude range of the YAG 532-nm channel required a better molecular density profile. The 532-nm observations have all been processed using the appropriate daily radiosonde values extrapolated to high altitudes with the new model. The temperature analysis was improved by comparisons with the Goddard and Jet Propulsion Laboratory (JPL) lidars that were operated at the observatory during the Mauna Loa ozone (MLO3) campaign. Nonlinearities in high count rates were noticed, and it was found that initializing the calculation at 75 km produced better agreement than at 80 km. The temperature record has been reanalyzed with these corrections.

The lidar laboratory in the new building has been designed with separate control, laser, and telescope rooms, providing about twice the space of the current building. A large rollaway hatch, ~1.8 m × 2.1 m (9 ft × 9 ft) for the telescopes was installed with a screw drive for automatic operation. The smaller laser hatch ~0.6 m × 1.8 m (2 ft × 6 ft) is hinged and driven by an electric actuator. An optical rack for multiple telescopes and both lasers was built from existing aluminum components.

Solar Radiation

Excavation of the NDSC building foundation in the spring of 1997 caused a heavy loading of fine dust that was cleaned off of the radiation windows daily. Plumes of diesel exhaust from heavy equipment on the site caused occasional intermittent increases in aerosol optical depth determined to be as great as 0.2. Even after construction was completed, high winds were lifting dust from areas of the site that had been back-filled by fine sand.

In August 1997 a new computerized tracker was installed on the radiation tower. This tracker carries the primary MLO normal incidence pyrheliometer (NIP), a second NIP, a diffuse pyranometer, and a diffuse pyrgeometer. It uses an altitude-azimuth mount that is controlled by a computer.

The lightning strike in mid-August damaged the solar dome computer, the new tracker, and the Campbell data acquisition system. These were repaired in the following weeks. In November 1997 new grid tables were built on the new solar radiation platform above the NDSC building, and most of the instruments and data systems were relocated there. The only instrument that remained in its original place was the diffuse pyranometer located on the solar radiation wall on the walkway above the station.

Meteorology

A computer-based "New Met System" measures temperatures at the 2-, 9-, and 37-m levels, dewpoint at the 2-m level, and wind speeds and directions at the 8.5-, 10-, and 38-m levels of the MLO Observation Tower. This new system has remained in operation with high reliability to date. MLO meteorological data are presented and discussed in section 1.5 of this report.

Precipitation Chemistry

The MLO modified program of precipitation chemistry collection and analyses was continued throughout 1996-1997 within the basic MLO operational routine. This program consists of collections of a weekly integrated precipitation sample from the Hilo NWS station and the collection of precipitation event samples at MLO. Analyses of these samples are undertaken in the Hilo laboratory for pH and conductivity.

Cooperative Programs

MLO Cooperative programs are listed in Table 1.1. New programs and changes not discussed in the NDSC section (next), are presented here.

In March 1996 MLO began calibrating automated sunphotometers for the NASA Aerosol Robotics Network (AERONET) program which will provide ground-truth optical depth measurements for the upcoming Earth Observing System (EOS) satellites. The photometers are self-contained units powered by solar panels that use a robot to make direct sun and sky measurements. Data is transmitted to a Geostationary Operational Environmental Satellite (GOES) once every hour. In September 1997 the Federal Aviation Administration (FAA) installed high quality GPS and meteorology sensors on the MLO Observation Tower in a study of atmospheric effects on GPS positioning. From this program MLO will receive nearly continuous column water vapor measurements. In November 1997 the Colorado State University-U.S. Department of Agriculture (CSU-USDA) UVB monitoring instruments were installed.

Network for the Detection of Stratospheric Change

In the past 4 years the amount of NDSC equipment and the number of NDSC programs installed at MLO are approaching those of the long-established MLO activities. A short description of current NDSC programs and activities at MLO with relevant dates of installation and modifications to the programs follows. The NOAA lidar, ozonesonde, and Dobson operations, which are also part of the MLO NDSC facility, are described in other sections of this report.

UV Spectroradiometer. The UV spectroradiometer described in the previous *Summary Report (No. 23)* continued to operate satisfactorily through October 1997, at which time it was replaced by a new model. This new instrument was also developed by the National Institute for Water and Atmosphere (NIWA) in Lauder, New Zealand, and was put into operation in the new MLO NDSC building in November 1997. Routine operations for the new instrument are quite similar to those of the old one. The instrument uses a double monochromator to measure

UV irradiance over the interval 280-450 nm, with a resolution of about 1 nm, and is programmed to perform a scan every 5° of solar zenith angle. Weekly quality control calibrations are performed with a mercury lamp and a 45-W quartz lamp. An absolute-standard 1000-W FEL lamp calibration is performed several times each year. The first 2 years of data from the original UV spectroradiometer are presented in section 3 of the present *Summary Report*.

Ozone Microwave Spectrometer. The University of Massachusetts microwave instrument measures the vertical profile of ozone from 20 to 70 km with a vertical resolution of 10 km or less up to 40 km, degrading to 15 km at 64 km. The ozone altitude distribution is retrieved from the details of the pressure-broadened line shape. The instrument has been well validated.

This instrument is the only ground-based ozone profile instrument capable of making measurements in the upper stratosphere and mesosphere. Its measurements are unaffected by aerosols, an important property following a major volcanic eruption such as that of Mount Pinatubo in June 1991.

UV Lidar. Much of the short-term work of NDSC revolves around providing correlative and validation measurements for satellite and aircraft instruments, in particular the Upper Atmosphere Research Satellite (UARS). Other recent validation efforts have included those for instruments onboard the NASA DC8 during the Tropical Ozone Transport Experiment/Vortex Experiment (TOTE/VOTE) mission. In August 1997 the JPL lidar made coordinated measurements of ozone and temperature profiles in support of the Cryogenic Infrared Spectrometers and Telescopes for the Atmosphere (CRISTA) Space Shuttle mission, which was launched August 7, 1997. Preliminary intercomparisons of temperature profiles obtained by lidar at MLO and CRISTA show very good agreement over the altitude range from 20 to 60 km.

During the last 2 years the JPL UV lidar has conducted several extensive studies of the dynamics of the middle atmosphere above MLO. Using the lidar, one can observe gravity waves, planetary waves, atmospheric tides, and mesospheric inversions. Temperature climatologies have also been developed using these results. In 1996 and 1997 the JPL system made 177 and 259 lidar measurements, respectively, at MLO. Each measurement provides three profiles: one ozone, one temperature, and one aerosol.

It is assumed that the more stable concrete floor in the new NDSC building will allow JPL to slightly improve data quality. JPL will also use the opportunity offered by the move and the rebuilding of the lidar to try to extend the range of its measurements to lower altitudes. The additional space will make the lidar easier to operate and maintain.

Water Vapor Millimeter-Wave Spectrometer. The water vapor millimeter-wave spectrometer (WVMS) at Mauna Loa has been measuring middle-atmospheric water vapor nearly continuously since March 1, 1996. As expected, the observed seasonal variations in water vapor profiles at MLO are smaller than those observed by WVMS instruments at higher latitude sites at Table Mountain, California (34.4°N), and Lauder, New Zealand (45.0°S). Although the data record at MLO is as yet too short to provide much useful information on multi-year trends, it is expected that the small seasonal variation and excellent observing conditions at the MLO site will make it the prime location for estimating long-term trends.

NO_2 UV/Vis Spectrometer. Since July 9, 1996, total column nitrogen dioxide (NO_2) has been measured at MLO using the twilight zenith technique with a NIWA ultraviolet/visible (UV/Vis) spectrometer. Continuous data have been obtained except for a short period in mid-November 1996 when a viewing window failed and a 4-week period in September-October 1997 when a computer problem occurred. Data through December 31, 1997, have been analyzed and quality confirmed, and will be submitted to the NDSC archive by June 30, 1998. It is planned to upgrade this spectrometer so that in addition to the NO_2 and O_3 currently measured, stratospheric BrO and OCIO, as required to meet the NDSC UV/Vis specification, will also be measured. November 1998 is the target date for this upgrade.

Brewer Ozone/UV Spectrophotometer. A single monochromator Brewer instrument was installed by the Canadian Atmospheric Environment Service (AES) at MLO and began routine measurements of O_3 and UV-B radiation on March 24, 1997. A second instrument was added in November 1997. The measurements are supplemented by all-sky images that are recorded every 10 minutes in order to assist in the analysis of the UV-B data. Overviews of the automatic operation of the instrument and data retrievals have since been carried out remotely from AES in Toronto over the Internet.

The data are archived at the World Ozone and Ultraviolet Data Centre (WOUDC) in Toronto. Up-to-date preliminary data are available over the Internet from AES. Publication of some new results is planned after thorough analysis of a longer data record is completed.

Solar FTIR Spectrometer. The University of Denver FTIR spectrometer routinely monitors total column concentrations of HCl, HNO_3, O_3, N_2O, F-22, HF, CH_4, NO, HCN, CO, C_2H_2, and C_2H_6. Because of the automatic nature of the instrument, the program is able to investigate diurnal variations in the species. Data are not collected on Sundays or Monday mornings unless special operators are on site to load liquid nitrogen into the instrument.

1.2. Barrow Observatory

D. Endres and M. Gaylord

1.2.1. Operations

The 1996-1997 season was a time of growth for arctic research in general and for the Barrow Observatory, Pt. Barrow, Alaska (BRW) in particular. Upgraded instrumentation and data acquisition systems at the observatory increased the quality and accessibility of data to researchers in Boulder, Colorado. Many programs can now be controlled, and software modified, from Boulder to meet special needs as conditions change in the sampling

regime. Internet access for most programs has led to a greater interest in BRW data than ever before with many requests for data being filled from the CMDL homepage.

The observatory building has undergone a major renovation with the addition of new windows, doors, paint inside and out, and two new entryways to allow for storage of compressed gas tanks. Previously, tanks were stored at the DEW Line site 0.8 km away and tanks were hauled by snowmachine when needed. The new storage area will permit easier access to carrier and calibration gas tanks during periods of inclement weather.

Personnel at the station remained unchanged since the last summary report, showing the longest period of stability since the station began operation in 1973. The station chief continues to serve on the Barrow Restoration Advisory Board for military base closures as well as being a member of the Barrow Environmental Observatory (BEO) Management Committee. The BEO Management Committee was appointed by the Barrow Arctic Science Consortium to coordinate research in the BEO and advise the Consortium on matters of scientific interest.

All vehicles ran well throughout the year. The 1990 Chevy Blazer was scheduled to be replaced by General Services Administration (GSA) but was in good enough condition to warrant keeping it in operation at least another year, saving several thousand dollars in shipping.

When older wooden windows in CMDL housing unit B would no longer seal, new high-efficiency thermal windows were procured and will be installed as soon as weather permits. The windows in unit A will be replaced in 1999. Since the house was connected to city water in 1995, there have been no problems with freezing pipes; therefore, the water storage tank in the entryway was cut into manageable-size pieces and removed. The walls were painted, new vinyl flooring was installed, and lights and outlets were added.

During 1996-1997, BRW was visited by 285 registered guests. Among these were researchers from China and Japan. There were two different television crews at BRW, one from an Arkansas news program and the other from a Japanese science show. There were several visits by personnel from the National Science Foundation (NSF), the Arctic Research Consortium of the U.S. (ARCUS), and the U.S. Air Force.

1.2.2. PROGRAMS

A more detailed analysis of all data collected at BRW can be found in the section detailing each of the major programs.

Aerosols

The single biggest change in the measurement curriculum was in the aerosol program. During September 1997 the entire aerosol system was upgraded with new equipment that fits into one 483 mm (19-in.) rack. A Thermal Systems Inc. (TSI) 3-channel integrating nephelometer replaced the 25-year old Meteorology Research Inc. 4-channel nephelometer that was the station instrument. The TSI condensation nucleus counter (CNC) was replaced with another unit of the same design and soon developed problems. A spare will be installed as soon as one becomes available. The Magee Scientific aethalometer was replaced by a Radiance Research particle soot absorption photometer for measurement of optical absorption coefficient, and a system of size-resolved impactor and filter samples were collected for gravimetric and chemical analysis at NOAA's Pacific Marine Environmental Laboratory in Seattle. A selectable time base was used as well as sector-selected sampling to allow for differing lengths of sample exposure depending on time of year and external conditions such as out-of-sector wind. Both programs will run concurrently for 1 year to allow for instrument comparisons. See *CMDL No. 23 Summary Report 1994-1995*, chapter 3, for a more detailed description of regional aspects of the program. Routine maintenance and calibrations were performed as scheduled.

Funding of the new equipment was provided by a grant from the Atmospheric Radiation Measurement Program (ARM) of the Department of Energy. For a description of the ARM program, see the section listed in the Barrow Cooperative programs.

Solar Radiation

Two new instruments were added to the suite of solar radiation measurements at BRW. The new instruments are used to monitor ultraviolet (UV) radiation. In addition to the global and direct irradiance, albedo, and IR radiation, BRW will now monitor biologically-active UV using a Yankee Environmental Systems (YES) UVB-1. The UVB-1 measures the erythemal spectra between 280 and 320 nm. The second instrument is a Biospherical Instruments Inc. (BSI) GUV-511C ground-based UV radiometer. The BSI instrument measures five discreet wavelength intervals at 305, 320, 340, and 380 nm and PAR from 400 to 700 nm at a rate of 2 Hz. PAR is the portion of the spectrum associated with plant growth.

Because no useful data can be collected in the visible spectrum between sunset in mid-November to sunrise in mid-January, solar radiation instruments were sent to Boulder for calibration and cleaning in November. The terrestrial infrared (IR) radiation program, both up- and downwelling, continued throughout the winter using Eppley pyrgeometers.

Carbon Cycle

Carbon Dioxide Nondispersive Infrared Analyzer. The Siemens Ultramat 5-E continued to be the station instrument and ran well the entire period. The data continue to show normal seasonal variations. Highs of up to 370 ppm and lows to 340 ppm were observed. System calibrations were performed as scheduled.

An HP-Unix workstation replaced the CAMS unit as the control and data acquisition system for recording data for the CMDL Carbon Cycle Group. Realtime data can be monitored at the station both in digital format and

graphically, providing useful information on system performance. The data can now be transferred daily over the Internet and updated regularly on the CMDL homepage. Control and modification of the data acquisition program and operating parameters are available to Boulder personnel in a manner never before possible at BRW.

Methane. A major upgrade to the equipment was made when the Hach-Carle gas chromatograph (GC) was replaced with an HP-6890 GC. The instrument is connected to the data acquisition system described previously. Once again, realtime data plots assist in troubleshooting the system and ensuring that the GC is maintained in an optimal running configuration. All data are stored on a 3.5 in. rewritable optical disk that is mailed to Boulder once a month.

Carbon Monoxide. A Trace Analytical GC has been in continuous operation since 1991. No major problems were noted. The CO analyzer is connected to the carbon cycle data acquisition system described previously. As with the other carbon cycle data, CO data are transmitted to Boulder daily using the Internet. Data are also stored on the 3.5 in. optical disk described previously. Realtime data are displayed graphically on the computer monitor and aid in quality control and troubleshooting the system.

Flask Samples. Flask samples were collected as scheduled. The data concerning flask samples can be found in sections 2 and 5 of this report. No major problems were encountered.

^{13}C. Isotopic carbon analysis was performed on samples collected at the CMDL global network of which BRW is a part. Data are available since 1990. See section 2 of this report.

Meteorology

There were no major changes in the meteorology program during 1996-1997. The system continued to run with minimal problems. The data are updated daily on the Observatory Operations page of the CMDL homepage. Calibrations were performed twice each year, once in the spring and once in the fall, to ensure correct operation of all sensors. Temperature probes were checked and corrected, if needed, to 0.2°C. Alignment of the wind sensor was checked and the speed accuracy was traceable to National Institute of Standards and Technology standards.

The winters of 1996-1997 and 1997-1998 were among the warmest on record with several new record high temperatures being recorded. During the summer of 1997 there were 25 straight days of rain with a total of 63.5 mm (2.5 in.) falling during this time.

CAMS

With the replacement of the final CAMS unit during the summer of 1997 there are no longer any CAMS units in BRW. They had an operational life of over 10 years and performed well the entire time. Newer PC-based data acquisition systems (DAS) have become the standard and allow for unprecedented data quality control and transfer to Boulder.

Ozone

Surface Ozone. Surface ozone, as measured by the Dasibi ultraviolet absorption photometer, continues to be one of the long-term staples of the BRW measurement complement. During July of 1997 the CAM unit used for the Dasibi was replaced by a PC-based system. It was connected to the BRW Local Area Network (LAN) and data are now transferred to Boulder via the Internet. Calibrations and maintenance were performed as scheduled and no major problems have arisen.

Total Column Ozone. BRW continued to operate Dobson no. 91 for total column ozone measurements. Seasonal variation of total ozone continued as in past years with highs in the spring and lows occurring in the fall. Values in April were as high as 440 Dobson Units (DU) and lows in September were as low as 290 DU. The Dobson was not operated during the winter months due to lack of sunlight, but calibration continued to ensure proper functioning when the sun rises the next year. Observations are usually made from February until October.

On March 17, 1997, station personnel recorded a reading of 300 DU which was a record low for March. The March average from 1974 until 1982 was 430 DU. The low values in March 1997 coincided with record low ozone in the arctic polar vortex region as recorded by the NASA TOMS satellite instrument.

Nitrous Oxide and Halocarbons

Gas Chromatographs. Both the Shimadzu GC-8A and the HP-5890 gas chromatographs ran well during the 1996-1997 season. Data continued to show decreased growth rates noted in past years related to the decreased use of CFC's attributed to the Montreal Protocol, which phased out production of certain CFC's.

Data were stored on 3.5 in. floppy disks and mailed to Boulder once per week. The primary data transfer scheme continued via the Internet.

Flask Samples. Flask samples were collected as scheduled. Data showed a very distinct reduction in the CFC-12 growth rate attributed to the Montreal Protocol. A more detailed list of the chemicals analyzed can be found in Table 1.2.

Cooperative Projects

A comprehensive list of all BRW cooperative projects and affiliations can be found in Table 1.2.

DOE/ARM. On July 1, 1997, the Department of Energy (DOE) Atmospheric Radiation Measurement (ARM) program dedicated the North Slope of Alaska and Adjacent Arctic Ocean (NSA/AAO) Cloud and Radiation Testbed (CART) site. The site is located downwind of BRW on NOAA property and consists of a modular unit to house instrumentation and three instrument platforms. ARM's data acquisition system and offices are located in the Ukpeagvik Inupiat Corporation-NARL (UIC-NARL)

facility about 2 km from the sensors. A 40-m tower was erected during the summer of 1997 and will have three levels of meteorology sensors as well as several solar radiation sensors mounted by the spring of 1998.

TABLE 1.2. Summary of Measurement Programs at BRW in 1996-1997

Program	Instrument	Sampling Frequency
Gases		
CO_2	Siemens Ultramat 5E analyzer	Continuous
	3-L glass flasks	1 pair wk^{-1}
	0.5-L glass flasks, through analyzer	1 pair wk^{-1}
CO_2, CH_4, CO, and $^{13}C/^{12}C$ and $^{18}O/^{16}O$ of CO_2	0.5-L glass flasks, P^3 pump unit	1 pair wk^{-1}
CH_4	Carle automated GC	1 sample $(12\ min)^{-1}$
Surface O_3	Dasibi ozone meter	Continuous
Total O_3	Dobson spectrophotometer no. 91	3 day^{-1}
CO_2	Siemens Ultramat 5E analyzer	Continuous
N_2O, CFC-11, CFC-12, CFC-113, CH_3CCl_3, CCl_4	300-mL stainless steel flasks	1 sample mo^{-1}
N_2O, CFC-11, CFC-12, CFC-113, CH_3CCl_3, CCl_4, SF_6, HCFC-22, HCFC-141b, HCFC-142b, CH_3Br, CH_3Cl, CH_2Cl_2, $CHCl_3$, C_2HCl_3, C_2Cl_4, H-1301, H-1211, H-2402, HFC-134a	850-mL stainless steel flasks	1 sample mo^{-1}
CFC-11, CFC-12, CFC-113, N_2O CCl_4, CH_3CCl_3	HP5890 automated GC	1 sample h^{-1}
N_2O	Shimadzu automated GC	1 sample h^{-1}
CO	Trace Analytical GC	1 sample $(6\ min)^{-1}$
Aerosols		
Condensation nuclei	Pollak CNC	1 day^{-1}
	T.S.I. CNC	Continuous
Optical properties	Four-wavelength nephelometer	Continuous
Black carbon	Aethalometer	Continuous
Solar Radiation		
Global irradiance	Eppley pyranometers with Q and RG8 filters	Continuous
Direct irradiance	Tracking NIP	Continuous
	Eppley pyrheliometer with Q, OG1 RG2, and RG8 filters	Discrete
Albedo	Eppley pyranometer	Continuous
Terrestrial (IR) Radiation		
Upwelling and downwelling	Eppley pyrgeometers	Continuous
Meteorology		
Air temperature	Thermistor, 2 levels	Continuous
	Max.-min. thermometers	1 day^{-1}
Dewpoint temperature	Dewpoint hygrometer	Continuous
Pressure	Capacitance transducer	Continuous
	Mercurial barometer	Discrete
Wind (speed and direction)	R.M. Young Aerovane	Continuous
Precipitation	Rain gauge, tipping bucket	
Cooperative Programs		
Total surface particulates (DOE)	High-volume sampler (1 filter wk^{-1})	Continuous
Precipitation gauge (USDA)	Nipher shield, Alter shield, 2 buckets	1 mo^{-1}
Magnetic fields (USGS)	3-Component fluxgate magnetometer and total field proton magnetometer	Continuous
	Declination/inclination magnetometer sample	6 sets mo^{-1}
Various trace gases (OGIST)	Stainless steel flasks	1 set wk^{-1} (3 flasks set^{-1})

TABLE 1.2. Summary of Measurement Programs at BRW in 1996-1997—Continued

Program	Instrument	Sampling Frequency
Cooperative Programs - Continued		
CO_2, ^{13}C, N_2O (SIO)	5-L evacuated glass flasks	1 pair wk^{-1}
CH_4 (Univ. of Calif., Irvine)	Various stainless steel flasks	1 set $(3\ mo)^{-1}$
Earthquake detection (Univ. of Alaska)	Seismograph	Continuous, check site 1 wk^{-1}
$^{13}CH_4$ ($^{13}C/^{12}C$) (Univ. of Washington)	35-L stainless steel flasks	1 $(2\ wk)^{-1}$
^{14}CO (Univ. of Washington)	A150 aluminum cylinders filled to 2000 psi	1 $(3\ wk)^{-1}$
UV monitor (NSF)	UV spectrometer	1 scan per 0.5 hour
Magnetic fields (NAVSWC)	^{3}He sensors	Continuous
Sound source (DOE)	RASS	1 hr^{-1}
CO_2 flux (San Diego State Univ.)	CO_2 and H_2O infrared gas analyzer and sonic anemometer	Continuous
O_2 in air (Univ. of Rhode Island)	3-L glass flasks	1 pair $(2\ wk)^{-1}$
Magnetic micropulsations (Univ. of Tokyo)	Magnetometer and cassette recorder	Continuous
Study thaw depth in permafrost (SUNY)	Temperature probe	Continuous
Size distribution and chemical composition of atmospheric aerosols (MRI, Japan)	CNC, size selectable filters	Continuous
Radiation observations (MRI, Japan)	Pyranometer	Continuous
Aerosol chemistry (Univ. of Alaska)	High-volume sampler	3 wk^{-1}

1.3. Samoa Observatory

D. Holt and G. McConville

1.3.1. Operations

The station chief position at the American Samoa Observatory (SMO) was vacated in July 1997 when the incumbent chief completed his 2-year term. The post was occupied with temporary managers from August until October 1997 when the permanent chief arrived. The engineer that served as station technician completed his 2-year tour in November 1997 and was replaced by an electronics technician in December 1997. The fresh ideas brought forward by these two new personnel has resulted in optimism for the future of the facility.

Internet and e-mail access at this remote site continued to be an unstable operation. The local telephone company promised substantial connection improvements through a microwave relay or fiber optic cables, but actual and/or timely implementation of either was uncertain. The National Aeronautics and Space Administration (NASA), which funds three projects here, promised assistance in acquisition of an Internet connection because of their requirements for data acquisition; however, with funding constraints was unable to be of assistance at this time.

In December 1996 the new remote building, housing two separate gas chromatograph (GC) systems and ozone and aerosol measuring equipment, was finally completed with all its data acquisition systems operational. This building's construction was started in November 1995 and was fraught with many delays because of material shortages and misinterpretation of construction methods. The long delay was frustrating but worth the wait, because the result was a well built, dry, secure environment for important atmospheric data instrumentation.

Funds were approved to rehabilitate the termite-eaten house for the station chief and hopefully funds will be approved soon to upgrade the deteriorated condition of the station technician's house. The tropical conditions of humidity, salty air, insect infestations, frequent rain, and incessant mold and mildew takes its toll on most everything.

The emergency generator was given a tune-up and reported by the mechanic to be in surprisingly good condition after being in service for over 20 years. This electrical back-up provider still got frequent use because of continued power lapses by the local electricity provider.

Over the past 2 years many visiting school classes were welcomed to the Observatory to learn more about the ongoing projects that are conducted here. The teachers appreciated the students' learning experience, and the students enjoyed this type of field trip. In addition to the educational benefit of these visits, and since this site is very remote, most of the children on the island learned what was contained in the facility and generally refrained from an inquisitive, forcible entry at a later mischievous opportunity. Although the new National Park of American Samoa is basically undeveloped, it was quite ironic that the employees of the Park asked permission to picnic on the observatory grounds instead of utilizing their own Park facilities. It only proved that the observatory is located upon one of the most beautiful locations in American Samoa.

1.3.2. Programs

Table 1.3 summarizes the programs at SMO for 1996-1997. Operational highlights follow.

TABLE 1.3. Summary of Measurement Programs at SMO in 1996-1997

Program	Instrument	Sampling Frequency
Gases		
CO_2	Siemens Ultramat-5E analyzer	Continuous
CO_2, CH_4	0.5-L glass flasks, through analyzer	1 pair wk^{-1}
	2.5-L glass flasks, MAKS pump unit	1 pair wk^{-1}
CO_2, CH_4, CO, and ^{13}C, ^{18}O of CO_2	2.5-L glass flasks, AirKit	1 pair wk^{-1}
Surface O_3	Dasibi ozone meter	Continuous
	TEI UV photometric ozone analyzer	Continuous
Total O_3	Dobson spectrophotometer no. 42	4 day^{-1}
N_2O, CFC-11, CFC-12, CFC-113, CH_3CCl_3, CCl_4	850-mL stainless steel flasks	1 sample wk^{-1}
N_2O, CFC-11, CFC-12, CFC-113, CH_3CCl_3, CCl_4, SF_6, HCFC-22, HCFC-141b, HCFC-142b, CH_3Br, CH_3Cl, CH_2Cl_2, $CHCl_3$, C_2HCl_3, C_2Cl_4, H-1301, H-1211, H-2402, HFC-134a	2.4-mL stainless steel flasks	1 sample wk^{-1}
CFC-11, CFC-12, CFC-113, N_2O, CCl_4, CH_3CCl_3	HP5890 automated GC	2 sample h^{-1}
N_2O	Shimadzu automated GC	2 sample h^{-1}
Aerosols		
Condensation nuclei	Pollak CNC	1 day^{-1}
	TSI CNC	Continuous
Solar Radiation		
Global irradiance	Eppley pyranometers with Q and RG8 filters	Continuous
Direct irradiance	Eppley pyrheliometer with Q filter	Continuous
	Eppley pyrheliometer with Q, OG1, RG2, and RG8 filters	Discrete
Diffuse irradiance	Eppley pyrgeometer with shading disk and Q filter	Continuous
Meteorology		
Air temperature	Thermistors (2)	Continuous
Dewpoint temperature	Polished mirror	Continuous
Pressure	Capacitance transducer	Continuous
	Mercurial barometer	1 wk^{-1}
Wind (speed and direction)	R.M. Young Windbird	Continuous
Precipitation	Rain gauge, tipping bucket	Continuous
	Rain gauge, plastic bulk	1 day^{-1}
Cooperative Programs		
CO_2, ^{13}C, N_2O (SIO)	5-L evacuated glass flasks	1 set wk^{-1} (3 flasks set^{-1})
GAGE/AGAGE project: CFC-11, CFC-12, CFC-113, N_2O, CCl_4, CH_3CCl_3, CH_4 (SIO)	HP5880/HP5890 Series II gas chromatograph	3 h^{-1}
Various trace gases (OGIST)	Stainless steel flasks	1 set wk^{-1} (3 flasks set^{-1})
Bulk deposition (DOE)	Ion exchange column	Continuous (1 filter mo^{-1})
Total suspended particulates (DOE)	High-volume sampler	Continuous (1 filter wk^{-1})
Total suspended particulates (SEASPAN)	High-volume sampler	Continuous (1 filter wk^{-1})
CH_4,($^{13}C/^{12}C$ ratio) (Univ. of Wash.)	30-L pressurized cylinder	Biweekly
Light hydrocarbons (UCI)	1-L evacuated stainless steel flasks	3-4 flasks qtr^{-1}
O_2 (URI)	2.5-L glass flasks	2 pair mo^{-1}
O_2 (SIO)	3-L glass flasks	2 sets mo^{-1} (3 flasks set^{-1})

SIO - Scripps Institution of Oceanography
OGIST - Oregon Graduate Institute of Science and Technology
UCI - University of California, Irvine
URI - University of Rhode Island

Carbon Dioxide

The Control and Monitoring System (CAMS) for the CO_2 Siemens analyzer continued to cause many interruptions in data collection throughout 1996-1997. This control system will soon be retired and replaced with a newer type control system. This lone remaining CAMS will be the last to be replaced at this facility.

The Martin and Kitzis Sampler (MAKS) continued to be operated in tandem with the new automated AirKit until October 1996 when the MAKS was retired. The AirKit did an admirable job and produced the desired comparable data that the MAKS had produced.

Surface Ozone

The Dasibi ozone measuring system experienced several data interruptions during 1996-1997, but after subsequent repairs it continued to operate reliably for extended periods of time. The unreliable frequency control and voltage spikes of the local power caused frequent uneven traces in the recorded data.

In July 1997 a Thermo Electron Instruments (TEI) UV photometric ozone analyzer was installed to operate in parallel with the Dasibi system. This instrument has operated in a reliable manner.

Total Ozone

The Dobson spectrophotometer continued to operate reliably throughout this 2-year term. Between December 1996 and April 1997, the instrument was shipped round-trip to Australia for a thorough calibration. Several computer program upgrades in 1996-1997 made data collection more precise and useful. The dome covering the instrument has reached the end of its life expectancy because of the humid, salty atmosphere and will be replaced soon.

Ozonesonde Balloons

The National Weather Service supplied hydrogen for the ozonesonde balloon launches that were routinely performed weekly, and for a short time, twice weekly. There was a standby supply of helium available when hydrogen was not. This is one location where hydrogen-filled balloons were launched with reduced risk, because the high humidity suppresses the occurrence of static sparks.

Nitrous Oxide and Halocompounds

Two gas chromatographs operated continuously with little serious maintenance required. Paper printouts and electronic recorded data were closely monitored and sent to Boulder at periodic intervals. The continuously running air pumps and several different compressed gases utilized by the systems required daily monitoring and occasional attention.

Aerosols

In July 1997 the Thermal System, Inc. (TSI) condensation nuclear counter (CNC) was removed and sent to Boulder because of its continued maintenance problems. It has not been replaced. The Pollak counter continued to be troublesome on occasion because of its age and difficult-to-replace parts.

Solar Radiation and Meteorology

The solar radiation and meteorology instruments operated reliably with only daily adjustments and occasional maintenance required. Automatic data transmission to Boulder continued to be very reliable as long as the telephone/modem line connections remained satisfactory. International communication system quality continued to be the uncontrollable weakness in these two operations.

Cooperative Programs

A comprehensive list of SMO cooperative projects is given in Table 1.3. Only projects that experienced special problems or unusual activity are mentioned here.

SIO GAGE/AGAGE. The Scripps Institution of Oceanography (SIO) Global Atmospheric Gases Experiment (GAGE) project ended when the new remote building was completed. The new Advanced Global Atmospheric Gases Experiment (AGAGE) project replaced it and was a well-engineered, mostly maintenance-free system after the initial installation inconveniences were resolved.

SEASPAN. The SEAREX South Pacific Aerosol Network (SEASPAN) wind/sector system and circuits required maintenance several times during this reporting period. The system was quite reliable in most other respects.

DOE. The Department of Energy (DOE) reduced the frequency of its ion exchange column sampling after the French government ceased nuclear testing near Tahiti. The once-a-week sampling was reduced to once a quarter. Their high volume air sampler was replaced in October 1996 with a very reliable, low maintenance system.

University of Washington. The University of Washington ended its flask/methane collection project with the last flask being filled in June 1997.

1.4. South Pole Observatory

R. Ramos and M. Boland, NOAA Corps

1.4.1. Operations

The Amundsen-Scott South Pole Station is located at 90°S on the Polar Plateau at an elevation of 2838 m above sea level. The station is managed by the National Science Foundation (NSF) Office of Polar Programs. CMDL has operated a South Pole Observatory (SPO) at this station since 1972.

Nearly all of the CMDL projects are housed in the Clean Air Facility (CAF). The 1996 summer field season marked the last year that a CMDL crew would occupy the "old" CAF. Construction began in November 1995 on the

Atmospheric Research Observatory (ARO) and was completed in January 1997. The new ARO houses CMDL's "new" CAF, the Biospherical Instruments, Inc., San Diego, ultraviolet (UV) monitoring instrument, and the University of Illinois lidar instrument. The ARO also has an additional 25 m^2 for future atmospheric monitoring science.

The ARO was built on a previously surveyed site inside the Clean Air Sector (CAS), approximately 183 m and grid 070° from the "old" CAF. In November 1995 the walk-up meteorological (MET) tower was moved. The tower was excavated from its location along the old CAS boundary line at grid 110° to its new location along the new CAS boundary line at grid 340°. After the tower was erected at the new site, all meteorological instruments were reinstalled.

During construction of the ARO, an electrical generator was placed in the CAS to supply power to the construction site. In addition, numerous vehicles were required inside the CAS to assist with construction. Most of CMDL's projects were shut down on January 22, 1997, during the move into the new building. By February 10, 1997, all projects and equipment were set-up and running in the ARO building.

A new facility for CMDL's stratospheric ozonesonde and Antarctic Support Associates (ASA) meteorological program was also constructed in the 1997 summer season. The new building is a heated facility with an inflation room large enough for CMDL's 540 m^3 volume plastic balloons and a separate data acquisition room. It has unofficially been named the Balloon Inflation Facility (BIF).

Upgrades to the station electric generators continued through the austral summers of 1995-1996 and 1996-1997. There were several scheduled blackouts during this period to facilitate the upgrades.

Data continued to be transferred digitally via satellite throughout the year with no significant problems encountered. Increased demand from the South Pole science community is expected to continue. In anticipation of the removal of the South Pole VAX computer system, all CMDL data and e-mail traffic were transferred to the UNIX system.

1.4.2. PROGRAMS

Table 1.4 is a summary of the measurement programs at SPO during 1996-1997. Operational highlights are as follows.

Carbon Cycle

The Siemens continuous carbon dioxide (CO_2) analyzer ran continuously without significant problems. During the 1996 winter an intermittent (wandering) output was traced to the Multi-Cool system. The magnetic stirrer was disabled and the spurious output was eliminated. A new Hewlett Packard data acquisition system was installed when the system was moved to the new building, January 1997. The use of the Linseis chart recorder ceased in August 1997 due to the lack of paper. Sample flasks were filled through the analyzer once per week and through a portable Martin and Kitzis Sampler (MAKS) unit twice per month.

Aerosols

The Meteorology Research, Inc. (MRI) four-wavelength nephelometer, the Pollak condensation nucleus counter (CNC), and the Thermo Systems Inc. (TSI) CNC all ran continuously without significant problems. Discrete observations with the Pollak CNC took place twice daily and compared within historical averages with data from the TSI CNC.

Solar and Terrestrial Radiation

During the austral summer, all Epply pyranometers, pyrgeometers, and the tracking normal incidence phyrheliometer (NIP) ran continuously with minimal problems. Occasional (24-48 hours) adjustments had to be made to both tracking instruments to align them with the sun. Discrete observations with the filter wheel NIP took place three times daily during especially clear conditions. After sunset each March, the short-wave instruments were taken off-line for the winter.

Ozone and Water Vapor

The Dasibi ultraviolet absorption ozone monitor ran continuously without significant problems. The new computer-based data acquisition system (PC-DAS) was brought on-line in mid-February 1996 and was run concurrently with the CAMS unit. After 6 weeks of simultaneous operation, the CAMS unit was removed in March. Minor changes were made to the PC-DAS software to correct some minor errors.

Discrete observations with the Dobson ozone spectrophotometer took place three times daily during the austral summer and again during the winter months when the full moon was at least 5° above the horizon and at least 50% full. In June 1996 the mercury thermometer was accidentally broken. Without a spare mercury thermometer, an alcohol thermometer had to be used. In late October repeated mercury lamp tests were outside acceptable limits. The Q setting table was adjusted by -0.36. Weekly mercury lamp tests were performed to verify that the instrument had stabilized. A new mercury thermometer was installed in November 1996 and the old Q setting table was used again. With the move into the ARO building Dobson no. 82 was replaced with Dobson no. 80 in January 1997. Side-by-side observations with the two instruments were conducted for a number of days during the changeover.

The ozonesonde program ran well during the year. Rubber balloons (1500 g) were launched during the warmer summer months, November–March, while the larger 540 m^3 plastic balloons were used in the colder winter months, April–October. Launches occurred once per week except during the months of stratospheric ozone depletion (August-November) when the schedule was increased to every 3 days and then to every other day. Periodically, plastic balloons were flown with both CMDL sondes and ASA Meteorological Department sondes. It is strongly recommended that tandem (dual instrument)

TABLE 1.4. Summary of Measurement Programs at SPO in 1995-1996

Programs	Instrument	Sampling Frequency
Gases		
CO_2	Siemans IR analyzer	Continuous
CO_2, CH_4	2.5-L glass flasks, through analyzer	1 pair week^{-1}
	2.5-L glass flasks, MAKS pump unit	1 pair twice mo^{-1}
Surface O_3	Dasibi ozone meter	Continuous
Ozone profiles	Balloonborne ECC sonde	1 wk^{-1}, summer, autumn, winter; 3 day^{-1}, spring
N_2O, CFC-11, CFC-12, CFC-113 CH_3CCl_3, CCl_4	300-mL stainless steel flasks	1 pair mo^{-1}
N_2O, CFC-11, CFC-12, CFC-113, CH_3CCl_3, CCl_4, SF_6, HCFC-22, HCFC-141b, HCFC-142b, CH_3Br, CH_3Cl, CH_2Cl_2, $CHCl_3$, C_2HCl_3, C_2Cl_4, H-1301, H-1211, H-2402, HFC-134a	850-mL stainless steel flasks and 2.5-L stainless steel flasks	1 pair mo^{-1}
CFC-11, CFC-12, CFC-113, N_2O, CH_3CCl_3, CCl_4	Shimadzu automated GCs	1 sample h^{-1}
Aerosols		
Condensation nuclei	Pollack CNC	2 day^{-1}
	TSI CNC	Continuous
Optical properties	Four-wavelength nephelometer	Continuous
Solar Radiation		
Global irradiance	Eppley pyranometers with Q and RG8 filters	Continuous, summer
	Eppley pyranometer with Q filter	Continuous, summer
	Net radiometer	Continuous, summer
Direct irradiance	Eppley pyrheliometer with Q, OG1, RG2, and RG8 filters	3 day^{-1}
	Eppley pyrheliometer with Q and RG8 filters	Continuous, summer
Albedo	Eppley pyranometer with Q and RG8 filters, downward facing	Continuous
Diffuse irradiance	Eppley pyranometer with shading disk and Q filter	Continuous
Terrestrial (IR) Radiation		
Upwelling and downwelling	Eppley pyrgeometers	Continuous
Meteorology		
Air temperature	Platinum resistor, 2- and 20-m heights	Continuous
Pressure	Capacitance transducer	Continuous, week^{-1}
	Mercurial barometer	
Wind (speed and direction)	Bendix Aerovane	Continuous
Frost-point temperature	Hygrometer	Continuous
Cooperative Programs		
CO_2, ^{13}C, N_2O (SIO)	5-L evacuated glass flasks	2 mo^{-1} (3 flasks sample^{-1})
O_2, N_2 (Scripps)	Air sampling pump and flasks	2 mo^{-1} (3 flasks set^{-1})
Total surface particulate (DOE)	High-volume pump and filters	Continuous (4 filters mo^{-1})
Interhemispheric $^{13}C/^{14}C$ (CSIRO)	Pump unit, 0.5-L and 5-L flasks	2 mo^{-1} (2 flasks set^{-1})
H_2O_2 (Univ. of Arizona)	Snow sample collection	1 week^{-1}, 2 week^{-1}- spring
Isotope production (SUNY)	Pressurized cylinders	N/A, checked once mo^{-1}
Polar stratospheric clouds (NASA/Goddard)	Lidar: 830 nm	Continuous, Feb. – Sept. 1996

launches be undertaken as much as possible during the non-ozone hole season. Tandem launches save on the helium supply and ASA meteorological balloons. Balloon launches from the new BIF began in late February 1997.

Nitrous Oxide and Halocarbons

The two Shimadzu Mini-2 electron capture gas chromatographs (GC) ran continuously with no significant problems.

During the MET tower move in November 1996, the GC sampling lines were discovered to be connected to the intakes that were attached to the outside of the aerosol stack. After the tower was erected at its new location, new sampling lines were spliced to the lines running out to the tower. These lines (at mid-tower and top-of-tower) were then used as the intakes for the GCs. These same lines were used after the move into the ARO building; however, they were shortened by about half their length.

A spurious signal appeared on the trailing edge of the CFC-113 trace. This contamination was traced to the CAL1 cylinder regulator. CMDL-Boulder was notified and the contamination signal was removed mathematically during analysis.

There was a noticeable effect on the GC system from room temperature changes in the new ARO building; limiting the use of the double doors to the storage room significantly reduced this problem.

Meteorology

The meteorology system ran continuously without significant problems. During the MET tower relocation, all instruments were removed and placed on the roof windward railing of the "old" CAF. Also during this time, yearly maintenance and calibrations were performed.

Data Acquisition

The use of an automatic file transfer protocol (FTP) process began in December 1996 for sending data to CMDL-Boulder. The satellite rise times change on a weekly basis. In previous years this required CMDL South Pole personnel to manually FTP the data back at different times throughout the year. With the new set-up, the data files are automatically sent when the satellites rise above the horizon.

Cooperative Programs

SIO. The Scripps Institution of Oceanography (SIO) conducts long-term monitoring of CO_2, $^{13}C/^{12}C$ ratio, and N_2O. Twice per month, three evacuated glass flasks were exposed to ambient air.

Three glass flasks were pressurized with ambient air twice per month for the long-term monitoring of O_2 and N_2. A new pump unit was brought down in February 1997. Throughout the 1997 winter the new pump unit was used for the first-of-the month sample and the old unit for the mid-month sample.

DOE. The Department of Energy (DOE) conducts long-term monitoring of the spatial and temporal distribution of specific and anthropogenic radionuclides in surface air. The DOE pumps on the first floor of the ARO building required that the intake pipe be extended about 5 m. The DOE pump ran continuously without problems; filters were replaced each week.

CSIRO. Commonwealth Scientific and Industrial Research Organization (CSIRO) monitors the long-term ratio of $^{13}C/^{12}C$ in atmospheric CO_2. Two glass flasks were filled with ambient air every 2 weeks. There were no problems with this system.

State University of New York (SUNY). Air-filled cylinders remained on platforms approximately 800 m downwind of the main station for the quantification of the production rate of radiocarbon by galactic cosmic rays. The cylinders were inspected and cleared of snow once per month. One of the two support stands was raised in September 1997 due to significant snow drifting.

University of Arizona. Snow samples were collected to study the snow/atmosphere exchange of H_2O_2. Surface snow and micropit samples were collected weekly, except during the spring when they were collected twice per week. Beginning in January 1996, two additional, deeper (30 and 50 mm) samples were collected. Additionally, snow heights were measured from a "sampling grid" inside the CAS. A new sampling grid was set up in the new CAS in October 1996. Concurrent snow-height measurements were made in the old and new grids for about 1 month before sampling began in the new grid. In October 1997 another sampling grid was set up in the new CAS due to significant snow drifting in the old one. Concurrent snow-height measurements were again made in both grids.

1.5. Meteorological Measurements

T. Mefford (Editor) and B. Halter

1.5.1. Meteorology Operations

Introduction

The climatology of surface meteorological observations at the four CMDL observatories is based on hourly average measurements of the resultant wind direction and speed, barometric pressure, ambient and dewpoint temperatures, and the precipitation amount. The meteorological sensors in use were selected for their high accuracy as well as their ability to withstand the extreme conditions of the polar regions. Data is recorded as 1-min averages so that the variability within the hourly averages can be determined. To the extent that is possible, World Meteorological Organization (WMO) siting standards [*WMO*, 1969] are followed. Thermometers are also positioned at the top of the sampling towers at BRW, MLO, and SPO to measure the temperature gradient to determine the stability of the surface boundary layer.

A detailed description of the PC-based data acquisition system may be found in *Peterson and Rosson* [1994]. Table 1.5 describes the instrument deployment as of December 31, 1997.

At BRW the complement of sensors measuring meteorological variables remained unchanged. Corrections to the configuration of the digital data cables and the communications board in the computer were made to bring the system into conformance with standards for the stable RS-485 data communications between sensor interface modules and the computer.

At MLO, maintenance of the array of meteorological sensors included the replacement of some weather beaten components such as AC power cords and the R.M. Young anemometers at the 10.2 and 38.2-m levels in May 1997. In mid-August 1997 a lightning strike, which interrupted

TABLE 1.5. CMDL Meteorological Sensor Deployment December 31, 1997

Sensor	BRW		MLO		SMO		SPO	
	Serial No.	Elevation, m	Serial No.	Elevation, m	Serial No.	Elevation, m	Serial No.	Elevation, m
Primary anemometer†	14584	10.5	23186	10.2	15945	13.7	14583	10.0
Secondary anemometer†			15946	38.2				
Pressure transducer‡	374199	9.5	374198	3398.4	374200	78.5	358960	2841.0
Mercurial barometer	641	9.5	278	3398.4	961	78.5	1215A	2841.0
Air temperature A§		2.2		2.0		14.0		2.0
Air temperature B§¶		16.3		37.4				22.0
Air temperature C**		2.0		2.0		12.8		2.0
Dewpoint temperature	G0001	2.0	G0004	2.0	G0008	12.8	G0007	2.0
Rain gauge		~4		0.8		~4		

Heights are in meters above surface, except for the pressure transducer and mercurial barometer, which is with respect to MSL.
†Propeller Anemometer, model no. 05103, R. M. Young Company, Traverse City, Michigan.
‡Pressure Transducer, model no. 270, Setra Systems, Acton Massachusetts.
§Platinum Resistance Probe, Logan 4150 Series, Logan Enterprises, Liberty, Ohio.
¶Thermometer, positioned at the top of the local sampling tower to facilitate an estimation of boundary layer stability.
**Hygrothermometer, Technical Services Laboratory model no. 1088-400, Fort Walton Beach, Florida.

many of the projects at the observatory, damaged the meteorological data acquisition computer as well as some of the electrical components on the tower. The computer was replaced and spare sensor parts were sent to MLO. The system was back up and running about a month after the lightning strike. The data cable from the tower to the data acquisition computer was replaced in October 1997.

At SMO a new data cable connecting the tower sensor to the computer in the main observatory building was pulled through an underground conduit and put into operation in May 1997. At the same time, some deficiencies in the interconnections among sensor interface modules and the computer were corrected. Calibration checks on wind and temperature sensors were performed, while periodic comparison of the pressure sensor with the observatory's mercurial barometer continued. Corrosion by sea salt aerosol, which continually hits the outdoor components, continued to cause occasional instrument malfunction. Most susceptible are those components associated with sensors which must have a continuous stream of outside air drawn past them in order to make valid measurements, such as the Technical Services Laboratory (TSL) dewpoint hygrometer with its exposed chilled mirror and printed circuit board. Replacement of this sensor is being considered.

At SPO the meteorological data acquisition computer and barometric sensor were transferred from the old Clean Air Facility to the new Atmospheric Research Observatory in January 1997. An Antarctic Support Associates (ASA) surveyor determined a change in elevation of +2.35 m for the pressure sensor. The other meteorological sensors had been remounted on the meteorological tower that was moved in December 1995 [*Peterson and Rosson*, 1994]. Table 1.6 summarizes the changes to the sensor heights after the tower move. The tower is located approximately 91.4-m grid north-northwest from the new building. Data cables and the AC power line running to the relocated tower from the old Clean Air Facility were removed, and new cables were run from the new building to the tower along a line of wooded stanchions. A separation of 1 to 2 feet was maintained between the AC power and data lines. The mercurial barometer, used as a check on the long-term stability of the pressure sensor, was returned to the manufacturer for reconditioning and calibration. The barometer in the ASA meteorology office was used to make these periodic checks until November 1997 when the CMDL barometer was received and installed in the new building. Calibration checks of temperature and wind sensors, including interface electronics, were performed.

TABLE 1.6. SPO Sensor Instrument Heights Before and After Tower Move

Instrument	Height Before Move (m)	Height After Move (m)
Primary anemometer	10.0	10.0
Pressure transducer	2841.0	2841.0
Air temperature A	1.1	2.0
Air temperature B	20.0	22.0
Air temperature C	1.6	2.0
Dewpoint temperature	1.6	2.0
Non-aspirated temperature	1.4	2.0

Heights are in meters above snow surface, except for barometric pressure, which is with respect to MSL.
Refer to Table 1.5 for sensor information.

Heights of the tower sensors were maintained by raising them to compensate for drifted snow accumulation around the tower.

Data Management

The meteorological data acquisition system gathers data from sensors that operate continuously at each of the four CMDL observatories. Data are transferred to Boulder on a daily basis via the Internet. Preliminary hourly averages of wind direction and speed, barometric pressure, ambient and dewpoint temperature, and precipitation amounts are sent to the station personnel. Each month, a climatic summary is prepared from edited data and distributed within CMDL and to each of the observatories.

A comparison of the number of data points recorded against that expected for the year was used to monitor the system's performance. Table 1.7 shows the performance of each system during 1996 and 1997. On average the meteorological data acquisition system for the four observatories operated 98.16% and 95.99% of the time for 1996 and 1997 respectively. Due to the remoteness of the observatories, power outages are common and are the main reason for data loss. Hardware failure, system restarts, and system maintenance are the other reasons for data loss. At BRW, during the winter periods, rime, snow, and ice occasionally would build up on the sensors and have to be removed by the station personnel. At MLO high winds can cause electrostatic buildup on the 38-m anemometer. The solution was to temporarily disconnect the AC power that would reset the sensor modules. The biggest cause of data loss at MLO was due to the lightning strike in August 1997 when the system was down for about a month until it was replaced. At SMO, the biggest cause of data loss was due to the buildup of corrosion on the sensor connector pins and moisture getting into the RS-485 communications line. This produced noise in the communications line that the data acquisition system was not able to handle.

1.5.2. Station Climatologies

The 21-year station climatologies are an important record for the interpretation of measured values of aerosols, trace gases, atmospheric turbidity, solar radiation, and in the long-term changes in the records themselves. The records also serve to outline periods of local contamination.

TABLE 1.7. CMDL Meteorological Operations Summary

Station	Expected Number of Data Points	Percent Data Capture	Number of Missing Data Points
		1996	
BRW	4,216,320	99.42%	24,442
MLO	6,851,520	96.51%	239,005
SMO	3,689,280	97.23%	102,340
SPO	4,216,320	99.47%	22,243
Average		98.16%	
		1997	
BRW	4,204,800	99.80%	8,386
MLO	6,832,800	88.61%	777,921
SMO	3,679,200	97.40%	95,579
SPO	4,204,800	98.16%	77,196
Average		95.99%	

Barrow

In Figure 1.1 wind roses of hourly average resultant wind direction and speed at BRW are presented in 16

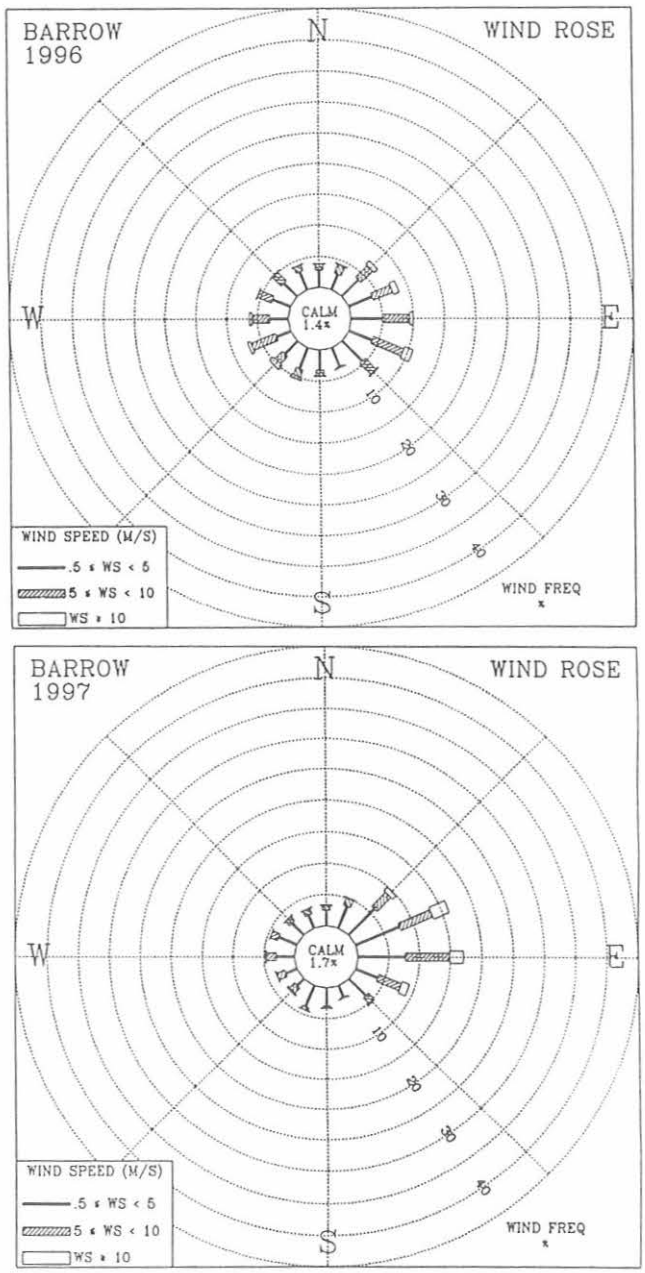

Fig. 1.1. Wind roses of surface winds for BRW for 1996 (top) and 1997 (bottom). The distribution of resultant wind direction and speed are given in units of percent occurrence. Wind speed is displayed as a function of direction in three speed classes.

direction classes and 4 speed classes. Winds from the "clean air" sector, north-northeast to southeast occurred 48.5% of the time in 1996 and 63.5% in 1997 as compared to 61.9% for the 19-year period from 1977 through 1995 (Figure 1.2). Wind speeds that were greater than 10 ms^{-1} in 1996 (6.9%) and 1997 (7.9%) were less frequent than the 19-year climatology (11.7%). The average speed of 5.1 ms^{-1} in 1996 (Table 1.8) was the second lowest average while the 5.0 ms^{-1} in 1997 was the lowest average in the 21 years at the station.

The average air temperatures of –10.7°C in 1996 and –11.2°C (Table 1.8) in 1997 were both warmer than the 19-year average of –12.5°C. New record high temperatures were recorded in 1996 during the months of June (23°C) and November (1°C) while March tied its record high (-1°C). June 1996 was the warmest ever recorded in the 21-year history of the observatory, and June 1997 set a new record low temperature (-12°C). The barometric pressure for 1996 was 1.8 hPa above the 19-year average while the average for 1997 was close to normal. February 1996 (-40°C), April 1997 (-36°C), and November 1997 (-24°C) set new record lows. The summertime precipitation was measured at 41 mm in 1996; this was below the long-term average of 63 mm, while the 65 mm measured in 1997 was slightly above normal.

Mauna Loa

The climatology of MLO is best understood when it is considered in two distinctive wind direction regimes, the night (downslope) period (1800–0559) Hawaiian Standard Time (HST) and the day (upslope) period (0600–1759 HST). The 19-year night and day wind roses illustrate the two distinct wind patterns (Figure 1.3)

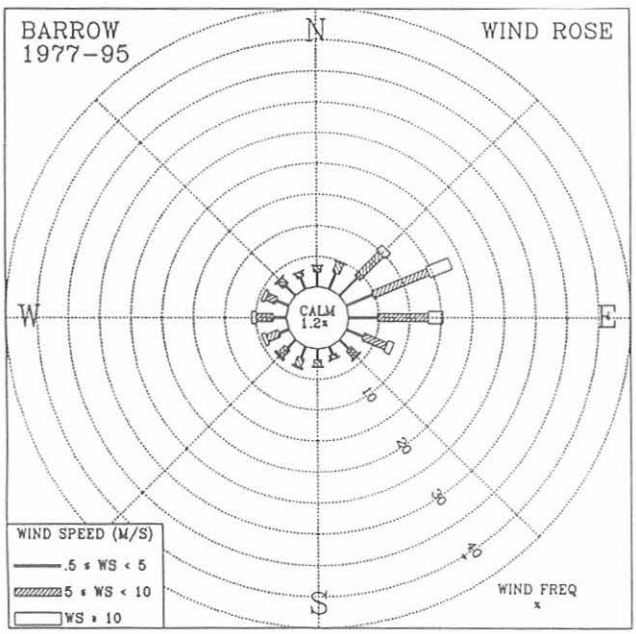

Fig. 1.2. Wind rose of surface winds for BRW for 1977 through 1995. The distribution of resultant wind direction and speed are given in units of percent occurrence for the 19-year period. Wind speed is displayed as a function of direction in three wind classes.

For the night regime, the 19-year wind rose (Figure 1.3) shows that 91.3% of all winds observed had a southerly component. The percentage of occurrence of southerly winds in 1996 was 91.8% (Figure 1.4) and 90.9% in 1997 (Figure 1.5). Pressure gradient controlled winds (WS ≥ 10 ms^{-1}) from predominately westerly and southeasterly directions occurred 10.0% in 1996 and 8.8% in 1997 while the 19-year average shows a 7.0% occurrence. The annual average wind speed for both 1996 and 1997 was slightly above the long term mean (Tables 1.9 and 1.10). The upslope or northerly component winds (north-northwest through east-northeast) that occurred 2.4% of the time in 1996 and 1.8% in 1997, are the result of daytime, upslope flow extending into the early evening hours.

For the day regime, the 1996 and 1997 wind roses (Figures 1.4 and 1.5) indicate that winds from the west-northwest through east-northeast occurred 55.9% of the time in 1996 and 53.8% of the time in 1997, compared with 58.6% for the 19-year climatology (Figure 1.3). Pressure gradient controlled winds (WS ≥ 10 ms^{-1}) occurred 9.2% of the time in 1996 and 7.8% in 1997 while the 19-year average shows an occurrence of 5.8%. In 1996 and 1997, the pressure gradient winds, which are usually associated with storms, followed the expected pattern of fewer occurrences during the day regime. The day wind rose is more uniformly distributed in the light wind classes than the night wind rose. This is due to the occurrence of variable wind directions during the transition periods at dawn and dusk, most of which are included in this regime.

The average ambient temperature for 1996 and 1997 (Tables 1.9 and 1.10), combining both day and night records, was 7.0°C, which is close to the long-term average of 7.1°C. February 1997 tied the record low temperature for the month (7°C). The average barometric pressure for 1996 (679.5 hPa) and 1997 (679.6 hPa) were both lower than the long-term average of 680.5 hPa. May and June 1996 each tied its high-pressure record. March 1996 and February 1997 set new record low pressures while June and July 1997 tied their record low pressures. The precipitation amount for 1996 (671 mm) was significantly higher than the long-term average of 460 mm while the amount for 1997 (391 mm) was slightly lower than normal.

Samoa

A comparison of SMO's 1996 and 1997 wind roses (Figure 1.6) to that of the 19-year period (Figure 1.7) shows a considerably higher percentage (69.8%) of "clean air" sector winds (north-northwest through southeast) in 1996 while 1997 (60.5%) was closer to the long-term average of 59.7%. The occurrence of winds in the 10 ms^{-1} or greater class was 2.5% in 1996 and 5.0% in 1997 while the expected occurrence based on the 19-year average is 4.9%. The annual average wind speed for 1996 (4.7 ms^{-1}) was close to normal while 1997 (5.5 ms^{-1}) (Table 1.11) was above normal.

TABLE 1.8. BRW 1996 and 1997 Monthly Climate Summary

	Jan.	Feb.	March	April	May	June	July	Aug.	Sept.	Oct.	Nov.	Dec.	Year
							1996						
Prevailing wind direction	SE	ESE	SW	ENE	ESE	WSW	WSW	E	NE	ESE	SE	ENE	ESE
Average wind speed (m s^{-1})	4.3	5.7	5.1	3.9	4.7	4.5	5.4	5.8	5.6	5.4	5.8	5.4	5.1
Maximum wind speed* (m s^{-1})	13	17	17	12	13	13	14	12	13	18	14	17	18
Direction of max. wind* (deg.)	207	197	265	76	229	235	222	95	41	114	240	65	114
Average station pressure (hPa)	1021.6	1010.4	1022.1	1018.9	1018.0	1010.5	1012.1	1011.0	1015.9	1014.7	1016.4	1019.1	1015.9
Maximum pressure* (hPa)	1037	1038	1046	1036	1034	1029	1023	1024	1030	1036	1033	1043	1046
Minimum pressure* (hPa)	997	975	1004	1000	1002	996	996	994	1004	994	1004	989	975
Average air temperature (°C)	-21.3	-25.9	-20.4	-17.5	-3.6	2.3	4.8	1.7	-2.7	-14.6	-12.8	-19.9	-10.7
Maximum temperature* (°C)	-2	-7	-1	-9	5	23	19	11	7	1	1	-8	23
Minimum temperature* (°C)	-35	-40	-43	-30	-17	-4	-1	-4	-12	-31	-26	-29	-43
Average dewpoint temperature (°C)	-23.7	-28.8	-22.6	-19.6	-4.9	0.7	3.0	0.3	-4.3	-16.6	-14.6	-22.0	-13.0
Maximum dewpoint temperature (°C)	-3	-9	-1	-10	3	10	12	10	7	0	-1	-9	12
Minimum dewpoint temperature (°C)	-38	-44	-47	-32	-19	-7	-4	-7	-13	-33	-29	-32	-47
Precipitation (mm)	0	0	2	0	3	2	18	7	8	0	0	0	41
							1997						
Prevailing wind direction	SSW	ENE	W	E	E	E	E	ENE	E	SE	E	ENE	E
Average wind speed (m s^{-1})	4.7	4.5	4.2	4.5	4.5	4.4	4.6	5.5	6.3	5.0	5.9	6.2	5.0
Maximum wind speed* (m s^{-1})	14	15	17	15	10	13	11	15	16	15	15	14	17
Direction of max. wind* (deg.)	71	74	231	105	94	100	216	221	84	115	102	62	231
Average station pressure (hPa)	1017.4	1017.1	1025.1	1015.4	1020.8	1012.6	1012.4	1009.7	1008.5	1015.0	1002.3	1012.7	1014.1
Maximum pressure* (hPa)	1038	1038	1045	1038	1032	1024	1030	1020	1021	1029	1024	1040	1045
Minimum pressure* (hPa)	994	999	1009	981	1005	1003	1003	996	989	988	977	997	977
Average air temperature (°C)	-27.7	-25.4	-25.0	-16.4	-7.4	-0.3	3.4	4.8	1.3	-6.5	-11.4	-24.2	-11.2
Maximum temperature* (°C)	-11	-18	-4	-4	2	10	16	15	10	1	0	-9	16
Minimum temperature* (°C)	-41	-39	-37	-36	-20	-12	-2	-1	-3	-20	-24	-37	-41
Average dewpoint temperature (°C)	-31.0	-28.3	-27.8	-18.4	-8.9	-2.2	2.2	3.5	0.1	-8.8	-13.1	-26.9	-13.9
Maximum dewpoint temperature (°C)	-12	-21	-4	-5	0	9	10	14	9	1	0	-11	14
Minimum dewpoint temperature (°C)	-45	-43	-41	-39	-22	-14	-2	-4	-6	-22	-26	-40	-45
Precipitation (mm)	0	0	0	0	1	11	8	36	8	0	1	0	65

Instrument heights: wind, 10.5 m; pressure, 9.5 m (MSL); air temperature, 2.2 m; dewpoint temperature, 2.0 m. Wind and temperature instruments are on a tower 25 m northeast of the main building.

*Maximum and minimum values are hourly averages.

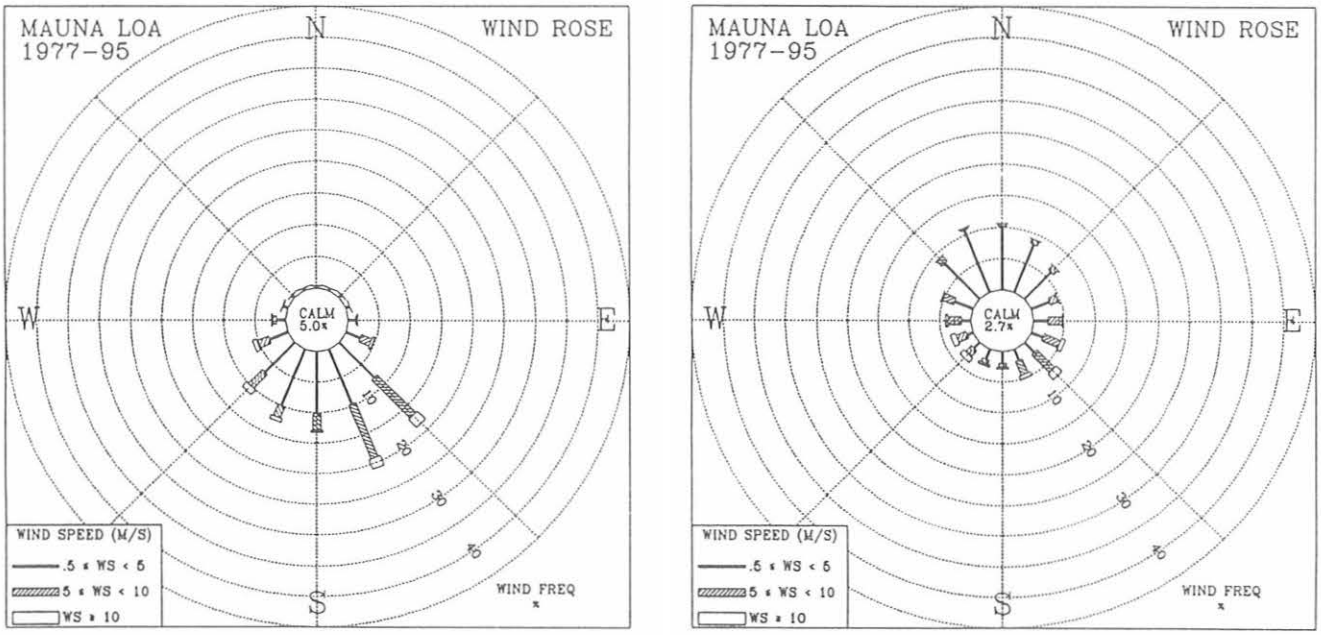

Fig. 1.3. Wind roses of the surface winds for MLO for 1977 through 1995 night (left) and day (right). The distribution of resultant wind direction and speed are given in units of percent occurrence for the 19-year period. Wind speed is displayed as a function of direction in three speed classes.

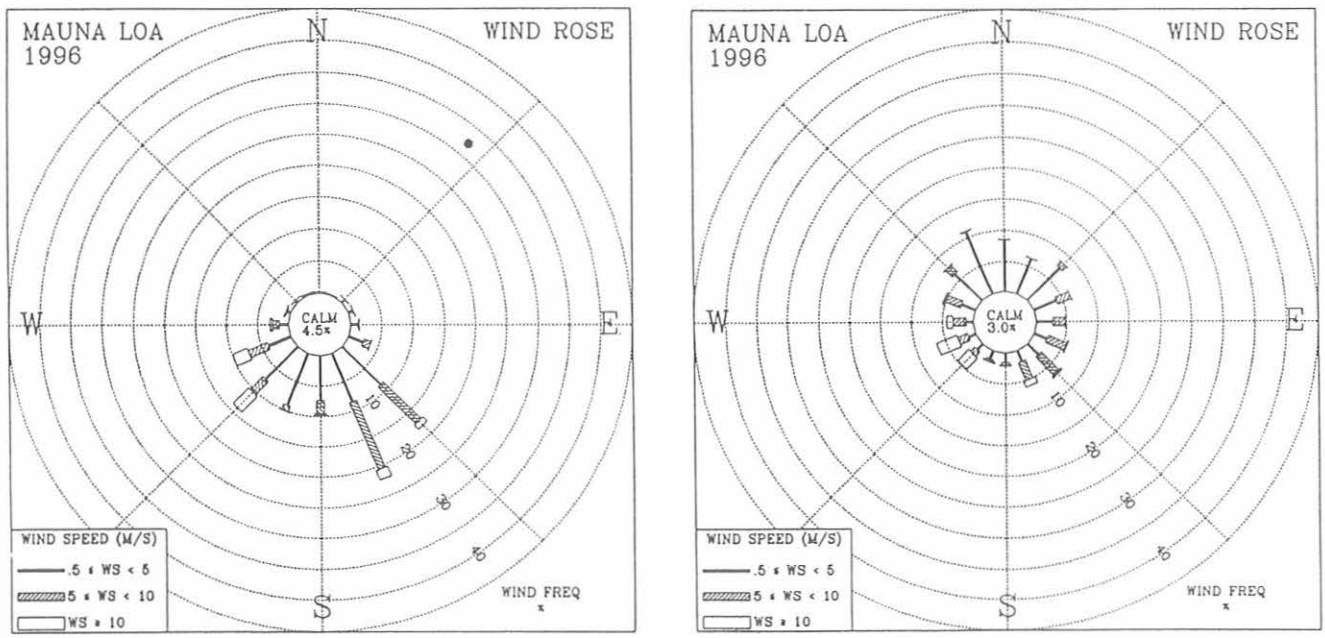

Fig. 1.4. Wind roses of the surface winds for MLO for 1996 night (left) and day (right). The distribution of resultant wind direction and speed are given in units of percent occurrence. Wind speed is displayed as a function of direction in three wind speed classes.

TABLE 1.9. MLO 1996 Monthly Climate Summary

	Jan.	Feb.	March	April	May	June	July	Aug.	Sept.	Oct.	Nov.	Dec.	Year
							Night						
Prevailing wind direction	SSE	SW	SW	SSE	SSE	SSE	SE	SSE	SSE	SE	SSE	SW	SSE
Average wind speed (m s^{-1})	4.9	6.1	6.3	4.6	6.9	4.0	4.2	4.7	2.9	4.5	3.6	7.7	5.1
Maximum wind speed* (m s^{-1})	18	17	22	13	16	12	13	13	10	12	14	19	22
Direction of max. wind* (deg.)	226	235	232	227	250	164	162	164	159	160	156	224	232
Average station pressure (hPa)	678.1	677.5	677.3	680.4	681.1	681.1	680.8	680.9	680.1	680.5	679.1	677.1	679.5
Maximum pressure* (hPa)	682	682	684	684	686	686	685	684	682	684	683	681	686
Minimum pressure* (hPa)	672	673	669	675	674	678	678	678	678	676	675	670	669
Average air temperature (°C)	3.3	3.1	2.4	5.5	7.0	5.8	6.1	6.7	6.8	6.0	4.8	3.6	5.1
Maximum temperature* (°C)	8	10	8	12	13	13	14	14	14	11	9	8	14
Minimum temperature* (°C)	0	-2	-2	1	4	1	2	2	2	2	1	-1	-2
Average dewpoint temperature (°C)	-7.8	-9.4	-14.7	-14.2	-12.0	-9.3	-10.3	-9.2	-7.2	-11.2	-4.2	-12.6	-10.2
Maximum dewpoint temperature (°C)	3	5	4	5	7	7	7	8	8	8	7	6	8
Minimum dewpoint temperature (°C)	-28	-32	-33	-30	-31	-29	-30	-27	-27	-27	-30	-33	-33
Precipitation (mm)	35	68	57	0	0	0	2	1	1	0	21	64	249
							Day						
Prevailing wind direction	SSE	WSW	WNW	N	NW	NNW	N	NE	NNW	ENE	NNW	WSW	NNW
Average wind speed (m s^{-1})	4.7	5.7	6.7	3.9	6.3	3.3	3.3	4.4	2.7	3.8	3.5	7.4	4.7
Maximum wind speed* (m s^{-1})	20	16	21	10	17	11	12	12	8	11	15	20	21
Direction of max. wind* (deg.)	229	232	223	122	261	164	157	139	165	161	157	240	223
Average station pressure (hPa)	678.1	677.5	677.4	680.5	681.3	681.3	681.0	681.1	680.1	680.5	679.0	677.0	679.5
Maximum pressure* (hPa)	683	682	684	684	685	685	684	684	682	683	683	682	685
Minimum pressure* (hPa)	671	673	668	676	675	679	678	679	678	676	675	670	668
Average air temperature (°C)	6.1	6.2	6.7	10.0	12.0	10.1	10.4	11.1	10.6	9.9	7.6	7.0	8.9
Maximum temperature* (°C)	14	12	13	16	17	17	17	18	16	15	14	14	18
Minimum temperature* (°C)	0	-1	-1	2	5	3	3	3	4	3	1	-1	-1
Average dewpoint temperature (°C)	-4.5	-6.3	-9.5	-7.2	-6.9	-3.9	-3.4	-3.4	-2.0	-6.3	-2.0	-9.0	-5.4
Maximum dewpoint temperature (°C)	6	7	5	6	8	8	9	9	9	8	8	8	9
Minimum dewpoint temperature (°C)	-28	-32	-33	-27	-25	-28	-28	-26	-26	-24	-33	-31	-33
Precipitation (mm)	44	47	116	2	2	20	54	0	6	21	49	59	422

Instrument heights: wind, 10.2 m; pressure, 3398.4 m (MSL); air temperature, 2.0 m; dewpoint temperature, 2.0 m. Wind and temperature instruments are on a tower 15 m southwest of the main building.

*Maximum and minimum values are hourly averages.

TABLE 1.10. MLO 1997 Monthly Climate Summary

	Jan.	Feb.	March	April	May	June	July	Aug.	Sept.	Oct.	Nov.	Dec.	Year
							Night						
Prevailing wind direction	SW	SSE	SSE	SE	SW	SE	SSE	SSE	SSE	SSE	SSW	SSE	SSE
Average wind speed ($m\ s^{-1}$)	7.0	5.5	4.7	3.3	5.7	6.6	5.2	3.3	3.2	4.5	3.5	4.7	4.9
Maximum wind speed* ($m\ s^{-1}$)	21	16	13	10	15	13	16	7	8	12	16	12	21
Direction of max. wind* (deg.)	262	171	236	129	231	128	159	153	152	162	233	164	262
Average station pressure (hPa)	677.8	678.3	678.2	679.6	678.4	680.7	680.2	681.4	681.3	680.7	680.4	680.1	679.6
Maximum pressure* (hPa)	683	683	683	683	683	683	683	685	684	683	684	683	685
Minimum pressure* (hPa)	673	667	674	675	675	677	677	679	677	679	675	677	667
Average air temperature (°C)	4.1	3.2	2.5	4.3	5.4	6.3	7.0	6.6	6.1	6.0	4.7	4.9	5.0
Maximum temperature* (°C)	9	11	8	11	13	13	15	13	11	12	10	10	15
Minimum temperature* (°C)	-2	-3	-1	-2	0	1	2	3	2	1	1	1	-3
Average dewpoint temperature (°C)	-14.3	-16.4	-4.7	-11.6	-9.8	-8.6	-10.0	-7.9	-9.4	-14.7	-7.9	-27.3	-12.2
Maximum dewpoint temperature (°C)	7	1	5	7	7	7	8	7	7	7	8	3	8
Minimum dewpoint temperature (°C)	-33	-33	-23	-27	-30	-26	-29	-20	-28	-32	-25	-39	-39
Precipitation (mm)	83	5	12	6	0	9	36	0	1	0	48	0	201
							Day						
Prevailing wind direction	WSW	ENE	NNW	NNW	WSW	SE	NNW	NNW	NNW	SE	NNW	SE	NNW
Average wind speed ($m\ s^{-1}$)	6.7	4.6	4.7	3.1	6.5	5.6	4.4	3.2	3.0	4.0	3.4	3.7	4.5
Maximum wind speed* ($m\ s^{-1}$)	17	15	14	10	16	13	16	8	8	9	16	12	17
Direction of max. wind* (deg.)	259	171	246	280	241	143	153	158	151	145	230	290	259
Average station pressure (hPa)	677.9	678.2	678.2	679.6	678.5	680.8	680.5	681.6	681.3	680.7	680.3	680.1	679.7
Maximum pressure* (hPa)	683	682	683	683	682	684	683	684	684	683	684	684	684
Minimum pressure* (hPa)	672	668	673	676	675	677	677	679	678	678	674	677	668
Average air temperature (°C)	7.7	7.0	5.8	8.7	9.9	10.9	11.2	11.7	10.2	10.4	8.4	8.8	9.1
Maximum temperature* (°C)	14	15	13	16	17	18	18	18	16	16	15	15	18
Minimum temperature* (°C)	-2	-1	-1	0	1	2	4	4	3	3	1	1	-2
Average dewpoint temperature (°C)	-10.3	-12.0	-1.8	-5.7	-3.8	-3.9	-3.3	-3.3	-2.9	-8.9	-2.5	-18.6	-6.7
Maximum dewpoint temperature (°C)	6	5	6	8	8	9	9	9	11	7	9	5	11
Minimum dewpoint temperature (°C)	-31	-33	-23	-26	-29	-25	-27	-22	-26	-29	-24	-37	-37
Precipitation (mm)	9	2	63	22	1	11	31	7	6	32	5	0	191

Instrument heights: wind, 10.2 m; pressure, 3398.4 m (MSL); air temperature, 2.0 m; dewpoint temperature, 2.0 m. Wind and temperature instruments are on a tower 15 m southwest of the main building.

*Maximum and minimum values are hourly averages.

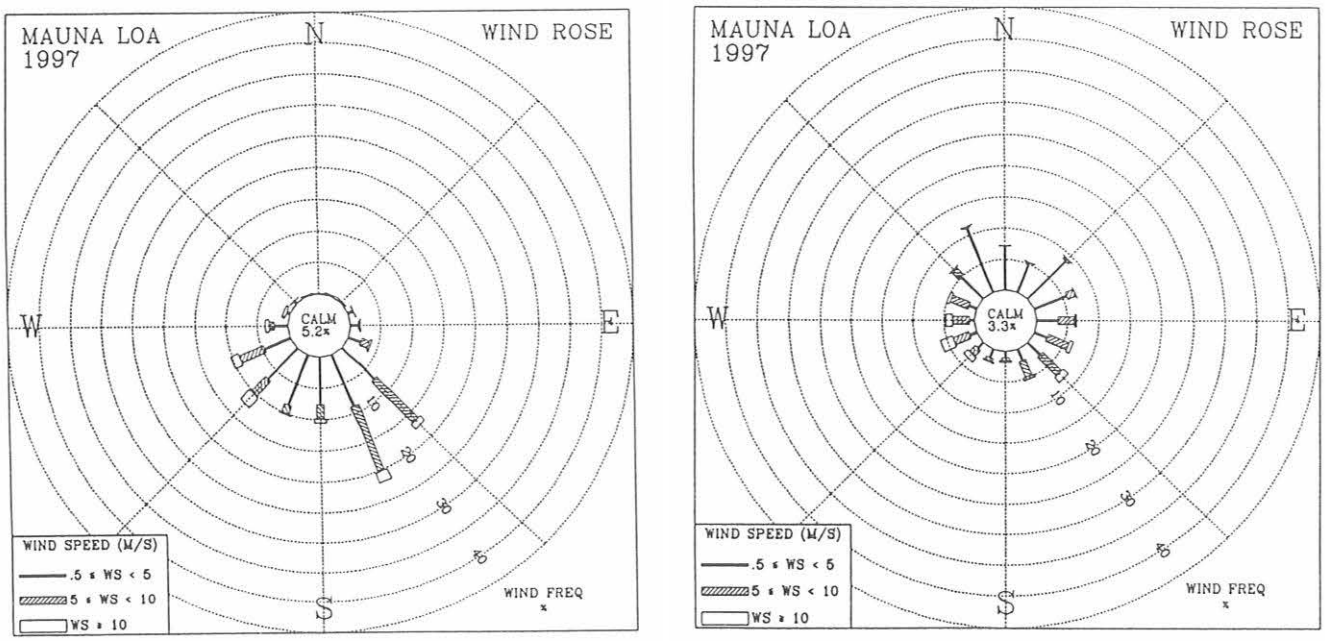

Fig. 1.5. Wind roses of the surface winds for MLO for 1997 night (left) and day (right). The distribution of resultant wind direction and speed are given in units of percent occurrence. Wind speed is displayed as a function of direction in three wind speed classes.

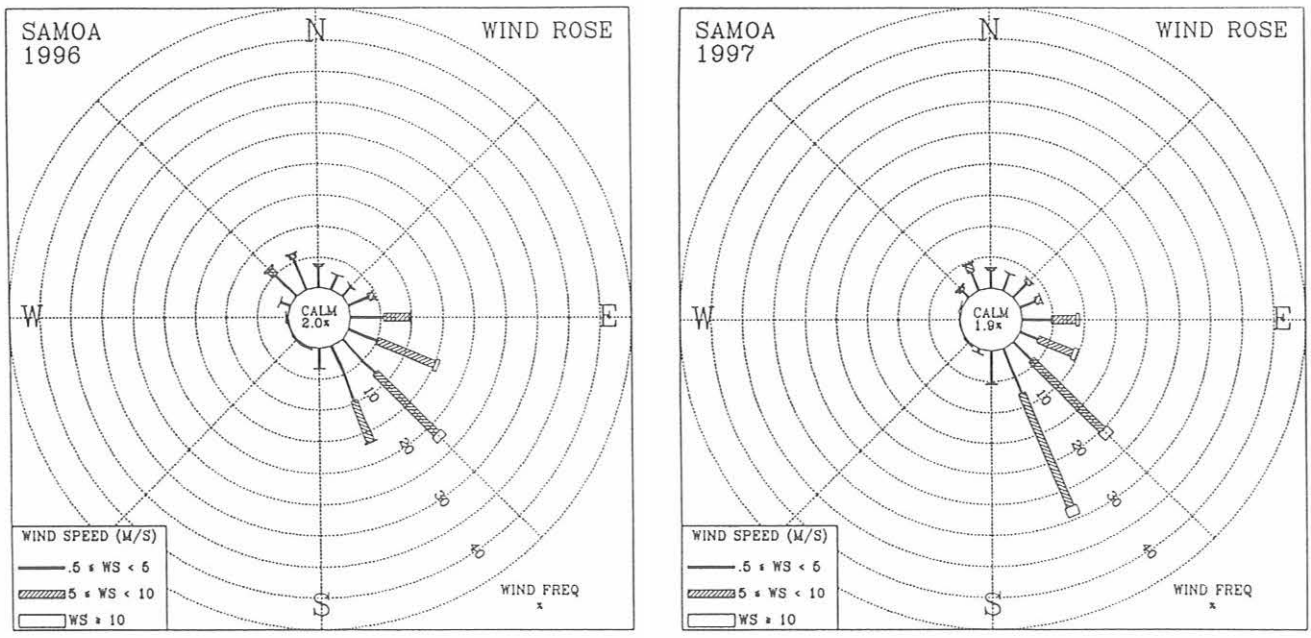

Fig. 1.6. Wind roses of surface winds for SMO for 1996 (left) and 1997 (right). The distribution of resultant wind direction and speed are given in units of percent occurrence. Wind speed is displayed as a function of direction in three speed classes.

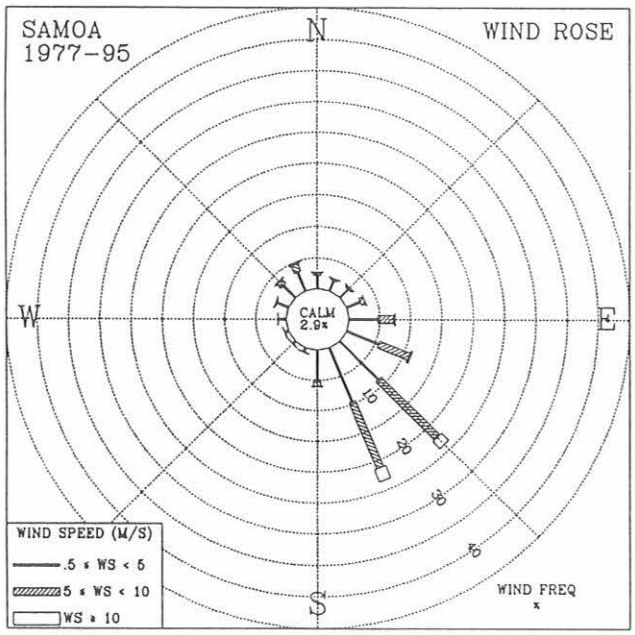

Fig. 1.7. Wind rose of surface winds for SMO for 1977 through 1995. The distribution of resultant wind direction and speed are given in units of percent occurrence for the 19-year period. Wind speed is displayed as a function of direction in three wind classes.

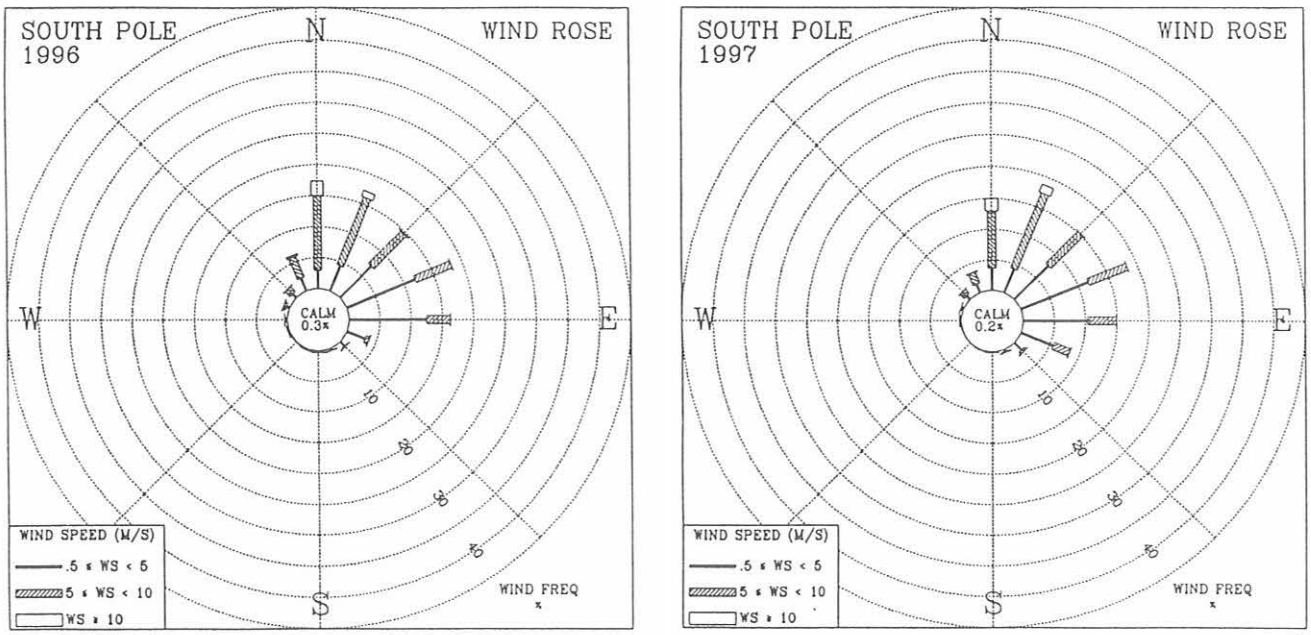

Fig. 1.8. Wind roses of surface winds for SPO for 1996 (left) and 1997 (right). The distribution of resultant wind direction and speed are given in units of percent occurrence. Wind speed is displayed as a function of direction in three speed classes.

TABLE 1.11. SMO 1996 and 1997 Monthly Climate Summary

	Jan.	Feb.	March	April	May	June	July	Aug.	Sept.	Oct.	Nov.	Dec.	Year
							1996						
Prevailing wind direction	NNW	NW	ESE	SE	SE	SE	SSE	SSE	SE	SSE	SSE	SE	SE
Average wind speed (m s^{-1})	2.8	2.8	4.0	5.3	3.8	5.4	5.6	5.6	6.6	5.2	4.0	5.0	4.7
Maximum wind speed* (m s^{-1})	8	13	14	11	13	11	10	11	14	12	10	12	14
Direction of max. wind* (deg.)	349	324	323	107	350	88	118	113	136	122	156	129	323
Average station pressure (hPa)	999.4	999.0	1000.2	1001.6	1002.4	1003.1	1003.0	1004.1	1002.2	1001.6	1000.6	998.9	1001.4
Maximum pressure* (hPa)	1005	1003	1008	1006	1007	1008	1007	1007	1006	1006	1005	1003	1008
Minimum pressure* (hPa)	996	994	993	998	997	999	999	1001	998	997	996	994	993
Average air temperature (°C)	27.9	27.6	27.6	27.5	27.3	27.2	27.1	26.1	26.1	26.1	27.1	26.9	27.0
Maximum temperature* (°C)	30	30	30	29	29	29	28	29	28	28	29	29	30
Minimum temperature* (°C)	25	24	24	24	22	24	24	24	23	22	23	23	22
Average dewpoint temperature (°C)	24.2	25.2	25.7	24.4	24.2	24.8	23.7	21.6	22.8	23.8	24.9	24.5	24.2
Maximum dewpoint temperature (°C)	26	27	28	26	26	26	26	25	26	26	27	26	28
Minimum dewpoint Temperature (°C)	22	23	23	22	21	22	21	16	19	21	21	22	16
Precipitation (mm)	144	245	377	134	221	179	81	42	154	305	157	237	2277
							1997						
Prevailing wind Direction	E	SE	NNW	ESE	SSE	SSE	SSE	SSE	SSE	SSE	SSE	SE	SSE
Average wind Speed (m s^{-1})	4.3	5.0	3.9	3.6	4.2	7.7	6.3	6.0	5.5	6.2	6.0	6.5	5.5
Maximum wind Speed* (m s^{-1})	14	11	13	7	10	13	11	12	10	12	13	11	14
Direction of max. Wind* (deg.)	349	97	325	108	155	97	147	116	147	98	139	147	349
Average station Pressure (hPa)	999.6	999.7	998.9	1001.5	1001.4	1002.3	1002.6	1002.9	1003.7	1002.1	1002.6	999.4	1001.4
Maximum pressure* (hPa)	1004	1004	1006	1006	1005	1006	1006	1007	1009	1006	1008	1004	1009
Minimum pressure* (hPa)	992	996	989	997	997	993	999	998	998	998	998	993	989
Average air Temperature (°C)	26.3	26.9	26.4	26.9	26.2	25.7	25.9	25.5	26.0	26.5	26.6	26.9	26.3
Maximum temperature* (°C)	29	29	28	29	29	27	28	28	29	29	29	29	29
Minimum temperature* (°C)	23	23	24	24	23	24	23	23	23	24	24	25	23
Average dewpoint temperature (°C)	23.5	23.9	23.5	24.1	22.3	22.3	23.7	23.3	23.2	24.1	23.7	24.4	23.5
Maximum dewpoint temperature (°C)	25	25	26	25	26	27	25	26	26	26	25	26	27
Minimum dewpoint temperature (°C)	20	21	19	23	15	17	21	19	17	20	20	22	15
Precipitation (mm)	403	201	182	65	164	60	40	98	81	58	100	52	1503

Instrument heights: wind, 13.7 m; pressure, 78.5 m (MSL); air temperature, 14.0 m; dewpoint temperature, 12.8 m. Wind and temperature instruments are on Lauagae Ridge, 110 m northeast of the main building.

*Maximum and minimum values are hourly averages.

TABLE 1.12. SPO 1996 and 1997 Monthly Climate Summary

	Jan.	Feb.	March	April	May	June	July	Aug.	Sept.	Oct.	Nov.	Dec.	Year
							1996						
Prevailing wind direction	NNE	NNE	ENE	NNW	ENE	ENE	N	N	NNE	N	N	N	ENE
Average wind speed ($m\ s^{-1}$)	3.8	4.8	5.6	4.8	5.2	5.7	7.0	6.5	5.7	5.9	5.6	5.4	5.5
Maximum wind speed* ($m\ s^{-1}$)	11	11	11	11	12	12	14	13	11	16	13	11	16
Direction of max. wind* (deg.)	296	36	345	356	316	12	6	24	12	350	6	27	350
Average station pressure (hPa)	688.6	688.7	678.9	681.2	677.3	677.4	675.3	686.8	681.3	672.4	687.7	690.3	682.1
Maximum pressure* (hPa)	706	704	690	703	692	688	687	718	695	685	708	699	718
Minimum pressure* (hPa)	679	675	670	665	667	662	661	668	663	655	674	681	655
Average air temperature (°C)	-29.1	-37.1	-56.3	-54.8	-60.3	-59.7	-55.7	-53.1	-59.6	-53.1	-35.4	-25.8	-48.3
Maximum temperature* (°C)	-19	-23	-36	-37	-42	-44	-36	-36	-48	-31	-23	-19	-19
Minimum temperature* (°C)	-35	-50	-68	-69	-72	-71	-74	-70	-70	-66	-49	-34	-74
Average dewpoint temperature (°C)	-32.9	-40.0	-56.9	-55.4	-61.0	-63.2	-59.8	-56.8	-63.1	-56.1	-39.0	-29.5	-50.1
Maximum dewpoint temperature (°C)	-23	-25	-38	-40	-46	-48	-39	-39	-51	-34	-26	-22	-22
Minimum dewpoint Temperature (°C)	-40	-53	-64	-68	-73	-73	-77	-76	-74	-68	-53	-38	-77
Precipitation (mm)	0	0	0	0	0	0	0	0	0	0	0	0	0
							1997						
Prevailing wind Direction	N	ENE	ENE	N	NNE	ENE	E	N	NNE	ENE	N	ENE	NNE
Average wind Speed ($m\ s^{-1}$)	4.2	4.8	5.8	6.4	6.2	5.4	5.0	6.7	5.8	4.5	6.6	4.1	5.5
Maximum wind Speed* ($m\ s^{-1}$)	10	9	12	13	13	14	10	14	14	10	13	9	14
Direction of max. Wind* (deg.)	7	14	32	356	355	12	1	6	19	30	7	11	12
Average station Pressure (hPa)	688.2	682.3	674.0	678.7	672.8	679.0	668.7	673.0	675.7	676.8	692.3	687.7	678.9
Maximum pressure* (hPa)	694	695	684	701	684	707	681	693	696	689	703	696	707
Minimum pressure* (hPa)	678	671	665	666	660	662	650	657	655	661	663	678	650
Average air Temperature (°C)	-28.6	-43.4	-54.8	-55.9	-57.8	-57.0	-65.1	-59.6	-59.9	-54.7	-34.0	-27.4	-50.1
Maximum temperature* (°C)	-21	-32	-42	-37	-45	-32	-34	-42	-36	-39	-25	-22	-21
Minimum temperature* (°C)	-38	-54	-68	-71	-72	-72	-76	-75	-79	-61	-53	-32	-79
Average dewpoint temperature (°C)	-32.3	-46.9	-58.5	-59.6	-61.8	-60.9	-67.7	-62.2	-63.7	-58.0	-37.4	-30.5	-53.1
Maximum dewpoint temperature (°C)	-24	-35	-45	-41	-48	-35	-37	-45	-38	-41	-28	-25	-24
Minimum dewpoint temperature (°C)	-43	-58	-72	-76	-78	-77	-79	-74	-83	-65	-57	-35	-83
Precipitation (mm)	0	0	0	0	0	0	0	0	0	0	0	0	0

Instrument heights: wind, 10.0 m; pressure, 2841 m (MSL); air temperature, 2.0 m; dewpoint temperature, 2.0 m. Wind and temperature instruments are on a tower 91.4-m grid north-northwest of the Atmospheric Research Observatory.

*Maximum and minimum values are hourly averages.

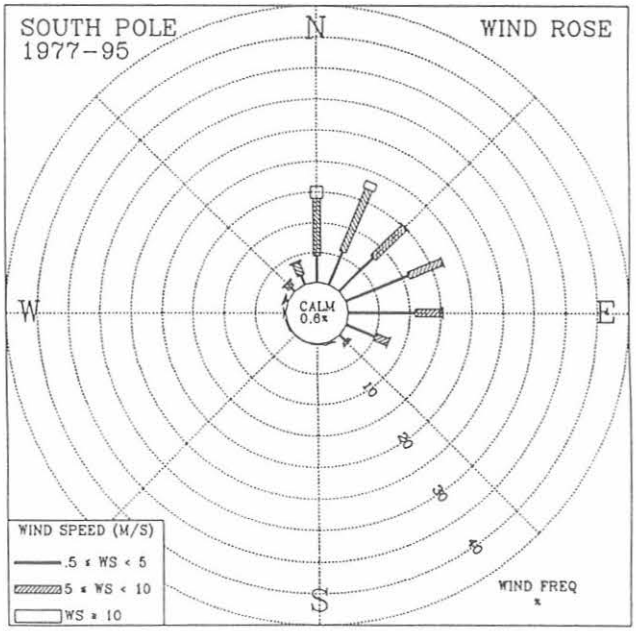

Fig. 1.9. Wind rose of surface winds for SPO for 1977 through 1995. The distribution of resultant wind direction and speed are given in units of percent occurrence for the 19-year period. Wind speed is displayed as a function of direction in three wind classes.

The average ambient temperature for 1996 (27.0°C) was close to the to 19-year average of 27.1°C while 1997 (26.3°C) was cooler than normal. The average barometric pressures for 1996 and 1997 (Table 1.11) were both 2.1 hPa above the 19-year average of 999.3 hPa. New high-pressure records were set during the months of March 1996, June 1996, September 1997, and November 1997. High-pressure records were tied during the months of January 1996 and May 1996. June 1997 set a new record low pressure for the month. The amount of precipitation in 1996 (2277 mm) was wetter than normal while 1997 (1503 mm) was considerably drier than normal.

South Pole

The distribution of the surface wind direction in 1996 and 1997 (Figure 1.8) shows a percentage of "clean air" sector (grid north-northwest through east-southeast) winds of 94.1% in 1996 and 94.2% in 1997 similar to the 19-year average (93.9%) (Figure 1.9). The percentage of winds in the 10 ms^{-1} or greater class was 4.1% in 1996 and 3.5% in 1997 compared to the 19-year average of 3.9%. The annual average wind speeds for 1996 and 1997 were both close to normal.

The average temperature for 1996 (-48.3°C) (Table 1.12) was 0.7°C warmer than the 19-year average of -49.0°C while the average temperature for 1997 (-50.1°C) was 1.1°C below normal. July 1997 tied a record high temperature and January 1997 tied a record low temperature. The minimum temperature in 1996 of -74°C occurred in July while the minimum in 1997 of -79°C occurred in September. The annual average barometric pressure for 1996 (682.1 hPa) was 3.2 hPa higher than the 19-year average while the barometric pressure for 1997 was 0.2 hPa below the long-term average. August 1996, November 1996, and June 1997 set high-pressure records. A pressure of 718.1 hPa in August 1996 was the highest ever recorded in the 21-year history of the station.

Acknowledgment. We wish to thank Mark Bieniulis who was responsible for developing software for daily data transfers and automatic data analysis, his work in setting up networks at BRW and SMO, and his dedication to the CMDL meteorology program.

1.6. REFERENCES

Peterson, J.T., and R.M. Rosson (eds.), *Climate Monitoring and Diagnostics Laboratory No. 22 Summary Report 1993*, 152 pp., NOAA Environmental Research Laboratories, Boulder, CO. 1994.

World Meteorological Organization (WMO), *Guide to Meteorological Instrumentation and Observing Practices, No. 8, Tech. Paper 3*, 347 pp., World Meteorological Organization, Geneva, 1969.

2. Carbon Cycle

P.P. TANS (EDITOR), P.S. BAKWIN, L. BRUHWILER, T.J. CONWAY, E.J. DLUGOKENCKY, D.W. GUENTHER, D.F. HURST, D.R. KITZIS, P.M. LANG, K.A. MASARIE, J.B. MILLER, P.C. NOVELLI, C. PROSTKO-BELL, K.W. THONING, B.H. VAUGHN[1], J.W.C WHITE[1], D. YAKIR[2], AND C. ZHAO

2.1. OVERVIEW

It is the goal of the Carbon Cycle Group (CCG) to improve the understanding of the factors that determine the atmospheric burdens of major trace gases influencing the Earth's climate, in particular CO_2, CH_4, and CO. The anthropogenic impact on each of these species is large, but natural cycles are involved as well. The international climate change negotiations during December 1997 in Kyoto, Japan, highlighted the fact that the world has tentatively started to take steps to try to control the steadily increasing climate forcing by anthropogenic greenhouse gases. One of the factors required for effective policies is a quantitative understanding of what controls the atmospheric concentrations.

Our main tool for studying the global budgets of the trace gases is the measurement of atmospheric spatial concentration patterns and their changes over time. Two methods have been employed from the start of the Geophysical Monitoring for Climatic Change program, the forerunner of Climate Monitoring and Diagnostics Laboratory (CMDL). Continuous measurements are made in remote clean air locations, namely the four CMDL observatories, and weekly pairs of discrete flask samples are obtained. Initially the samples were analyzed only for CO_2, but gradually more species were added (Table 2.1). The isotopic ratio measurements are being carried out at the Institute for Arctic and Alpine Research of the University of Colorado in close cooperation with CCG. Anomalous ^{17}O enrichments are measured in a small subset of the flasks by scientists at the University of California, San Diego. The global air samples provide a unique resource for narrowing uncertainties of greenhouse gas budgets as well as other atmospheric problems. We continue to investigate the feasibility of adding additional measurements.

Information on sources and sinks of the trace gases is obtained from their rates of change and from their spatial distributions. The quantitative link is provided by numerical models of atmospheric transport, operating in both two and three dimensions. Since we are working "backwards" from observed concentrations to the sources causing them, this problem is in the class of so-called inverse problems. The greatest limitation is sparseness of data, especially in regions close to important sources and sinks. Therefore the Carbon Cycle Group has gradually expanded the spatial coverage of the cooperative air sampling network. We have added isotopic analyses because different sources and sinks may be characterized by different isotopic "signatures."

TABLE 2.1. Species Analyzed in Samples of the Global Air Sampling Network

Species	Start Date	Method	Precision (One Sigma)	Collaborators
CO_2	1976	NDIR	0.05 ppm (0.02%)	
CH_4	1983	GC/FID	<1 ppb (0.07%)	
CO	1988	GC/HgO	0.5 ppb (0.5-1%)	
H_2	1988	GC/HgO	2 ppb (0.4%)	
$CO_2{}^{13}C$	1990	IRMS	0.01‰	CU/INSTAAR
$CO_2{}^{18}O$	1990	IRMS	0.03‰	CU/INSTAAR
N_2O	1996	GC/ECD	0.2 ppb (0.07%)	NOAH Group
SF_6	1996	GC/ECD	0.03 ppb (1%)	NOAH Group
$CO_2{}^{17}O$	1997	IRMS	0.03‰	UC San Diego
$CH_4{}^{13}C$	1998	GC/IRMS	0.06‰	CU/INSTAAR

CU: University of Colorado
INSTAAR: Institute for Arctic and Alpine Research, University of Colorado, Boulder
UC: University of California

To overcome the limitation of only having measurements from the remote marine boundary layer, two new approaches were initiated. One is to continuously measure a number of chemical species and atmospheric physical parameters at different heights on very tall towers. The mole fractions of many chemical species in the continental boundary layer are highly variable, making them more difficult to interpret, requiring much more auxiliary data than the traditional marine air samples. The second new approach is to obtain discrete air samples from low-cost airplanes in automated fashion from the boundary layer up to about 8 km altitude. These samples are then sent back to the laboratory in Boulder for analysis. We hope to be able to greatly expand the use of this method, especially over North America, in order to provide significant regional-scale constraints on the budgets of the gases measured.

Since the global coverage of our sampling network is unmatched, CMDL plays an active role in bringing together the measurements from many different laboratories around the world. Toward this end, measurements of standard reference gases as well as actual field samples are being intercompared. The link with the Commonwealth Scientific and Industrial Research Organization (CSIRO), Melbourne, Australia, is particularly strong in this regard. For CO_2 and CO we provide calibrated reference gas mixtures under the auspices of the World Meteorological Organization (WMO).

[1]*Institute for Arctic and Alpine Research, University of Colorado*
[2]*Visiting scientist from Weizmann Institute of Science, Rehovot, Israel*

We assembled a common database for CO_2 named GLOBALVIEW-CO_2. Its intended use is for three-dimensional (inverse) modeling. It is currently based on the measurements from laboratories in 12 countries, hopefully without significant calibration or methological discrepancies. The first release took place in 1996 and subsequent ones in 1997 and 1998. We plan to maintain and enlarge this database, as well as assemble similar ones for isotopic ratios, CH_4, CO, etc.

Full individual data records and monthly means can be obtained for each site from the CMDL World Wide Web page (www.cmdl.noaa.gov); the ftp file server's "pub" directory (ftp.cmdl.noaa.gov), from the WMO World Data Center for Greenhouse Gases in Tokyo, and from the Carbon Dioxide Information Analysis Center in Oak Ridge, Tennessee.

2.2. Carbon Dioxide

2.2.1. In Situ Carbon Dioxide Measurements

The mole fraction of atmospheric CO_2 was measured with continuously operating non-dispersive infrared analyzers (NDIR) at the four CMDL observatories during 1996 and 1997 as in previous years. Monthly and annual mean CO_2 concentrations (expressed in the WMO mole fraction scale) are given in Table 2.2. These values are provisional, pending final calibrations of station standards. Preliminary selected monthly average CO_2 mole fractions for the entire record through 1997 are plotted versus time for the four observatories in Figure 2.1.

A new data acquisition system was installed at the Barrow Observatory, Barrow, Alaska (BRW) in May 1996. This system uses a Hewlett-Packard Unix workstation to control not only the CO_2 NDIR measurements, but the CH_4 and CO in situ gas chromatograph systems as well. Data are downloaded daily from BRW to Boulder over the Internet, as well as recorded on optical disks at BRW for backup. A new data acquisition system was installed at the South Pole Observatory, Antarctica (SPO) in January 1997. This installation was done at the same time that the CO_2 in situ measurement system was moved into the new SPO Clean Air Facility. There are no CH_4 or CO gas chromatographs at SPO; only the CO_2 system is controlled by the new data acquisition system.

At both BRW and SPO modifications were made to the CO_2 system to reduce the amount of reference gas usage. The glass H_2O cryotrap was relocated between the inlet air pumps and the gas manifold with a smaller auxiliary cryotrap added in between the gas manifold and the NDIR analyzer. With this setup the first cryotrap dries only the ambient air samples, and the second cryotrap dries the reference gases and the dried ambient air. The volume of gas that the reference gases need to flush away after each gas change was greatly reduced making lower flow rates possible. The flow rate was reduced to ~150 cc min^{-1} from 300 cc min^{-1}. This change increased the life expectancy of the working reference gas tanks to about 6 months.

The SPO CO_2 NDIR analyzer experienced intermittent noise and stability problems throughout 1996 and 1997. Without success, a number of components were tested or exchanged in an attempt to pinpoint the cause of the problems. This noise problem continues to occur randomly, can last from a few minutes to many hours, and resulted in a loss of about 16% of the data for 1996 and 9% of the data for 1997. A replacement analyzer is planned for installation at SPO during austral summer 1998.

TABLE 2.2. Provisional 1996 and 1997 Monthly Mean CO_2 Mole fractions From Continuous Analyzer Data (μmol mol^{-1}, Relative to Dry Air WMO Mole Fraction Scale)

Month	BRW	MLO	SMO	SPO
		1996		
Jan.	366.59	361.82	361.10	359.28
Feb.	367.44	362.95	361.37	359.24
March	367.61	363.88	361.20	359.18
April	367.99	364.27	360.13	359.22
May	368.95	364.94	360.80	359.38
June	366.84	364.70	360.94	359.60
July	360.71	363.31	360.60	360.02
Aug.	355.49	361.17	360.76	360.43
Sept.	353.96	359.36	360.62	360.55
Oct.	361.87	359.33	360.74	360.60
Nov.	364.01	360.62	361.17	360.56
Dec.	366.60	361.96	361.58	360.52
Year	364.01	362.36	360.92	359.88
		1997		
Jan.	369.30	362.83	361.77	360.39
Feb.	369.03	363.87	362.06	360.23
March	368.60	364.24	362.37	360.22
April	369.33	366.02	361.87	360.47
May	369.22	366.47	361.12	360.63
June	366.93	365.31	361.12	360.98
July	359.17	364.07	361.93	361.30
Aug.	353.27	362.01	361.89	361.63
Sept.	356.70	360.03	361.90	361.95
Oct.	361.79	360.49	----	362.02
Nov.	366.55	362.19	362.98	362.12
Dec.	367.84	364.11	363.24	362.15
Year	364.81	363.47	362.02	361.17

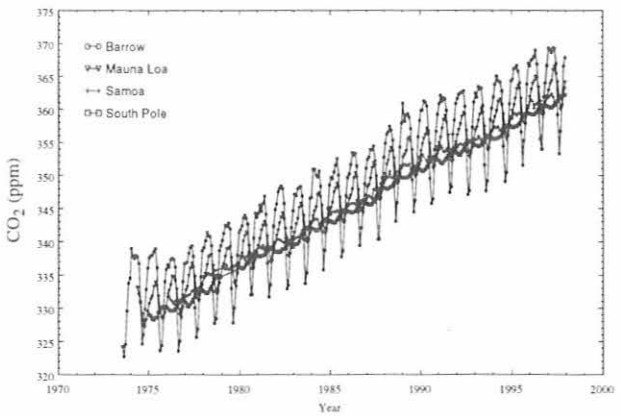

Fig. 2.1. Preliminary selected monthly mean CO_2 mole fractions in dry air expressed in μmol mol^{-1} at the four CMDL observatories.

At SMO the old data acquisition unit had several hardware problems during the second half of 1997. It failed completely at the end of September and was repaired and restarted in November.

2.2.2. Flask Sample Carbon Dioxide Measurements

Air samples collected at the CMDL global cooperative air sampling network sites (Figure 2.2) enable measurement of the atmospheric variations and distribution of trace gases (CO_2, CH_4, CO, H_2, N_2O, and SF_6) and stable isotopic ratios in CO_2 ($\delta^{13}C$ and $\delta^{18}O$). These measurements are used to document trends and help constrain estimates of sources and sinks (budgets) for these climatically and chemically important species. Carbon dioxide mole fractions were measured in 8100 samples in 1996 and 7700 samples in 1997. Methods have been described by *Conway et al.* [1994]. In January 1997 sampling was begun at Bobabeb, Namibia (23°34'S, 15°2'E) in cooperation with the Desert Research Foundation of Namibia. In June 1997 a trial air sampling program was begun at Summit, Greenland (72°35'N, 38°29'W) in cooperation with the University of Arizona Department of Hydrology and Water Resources and the National Science Foundation. This program will continue for 1 year and possibly longer if the site continues to be occupied year-round. Samples have also been collected from two sites in Kazakstan since October 1997. One of these sites, Plateau Assy (44°35'N, 77°45' E), is in the desert and the other, Sary Tkum (43°15'N, 77°45' E), is on a mountain. The cooperating agency is the Kazakh Scientific Institute of Environmental Monitoring and Climate. Sampling ended at Mould Bay, Canada (76°15'N, 199°21'W) in May 1996 when the Canadian government discontinued operations at this site. An excellent record of measurements has been obtained at Mould Bay starting in 1980. The 1995-1997 annual mean CO_2 mole fractions for the 49 network sites active in 1997 are given in Table 2.3.

In 1996 and 1997 we began converting the shipboard sampling programs from evacuated 3-L flasks to flushed and pressurized 2.5-L flasks. An automated sampling system was installed on the *Brisbane Star* of the Blue Star Ship Management Ltd. in cooperation with the University of Rhode Island. An Air Kitzis Sampler (Airkit) was installed on the M/V *Frontier Express,* a Caltex tanker, (South China Sea) in November 1997. It is hoped that the change in sampling method will lead to a higher percentage of good pairs and provide sufficient air for all analyses. The 1996-1997 annual mean CO_2 mole fractions

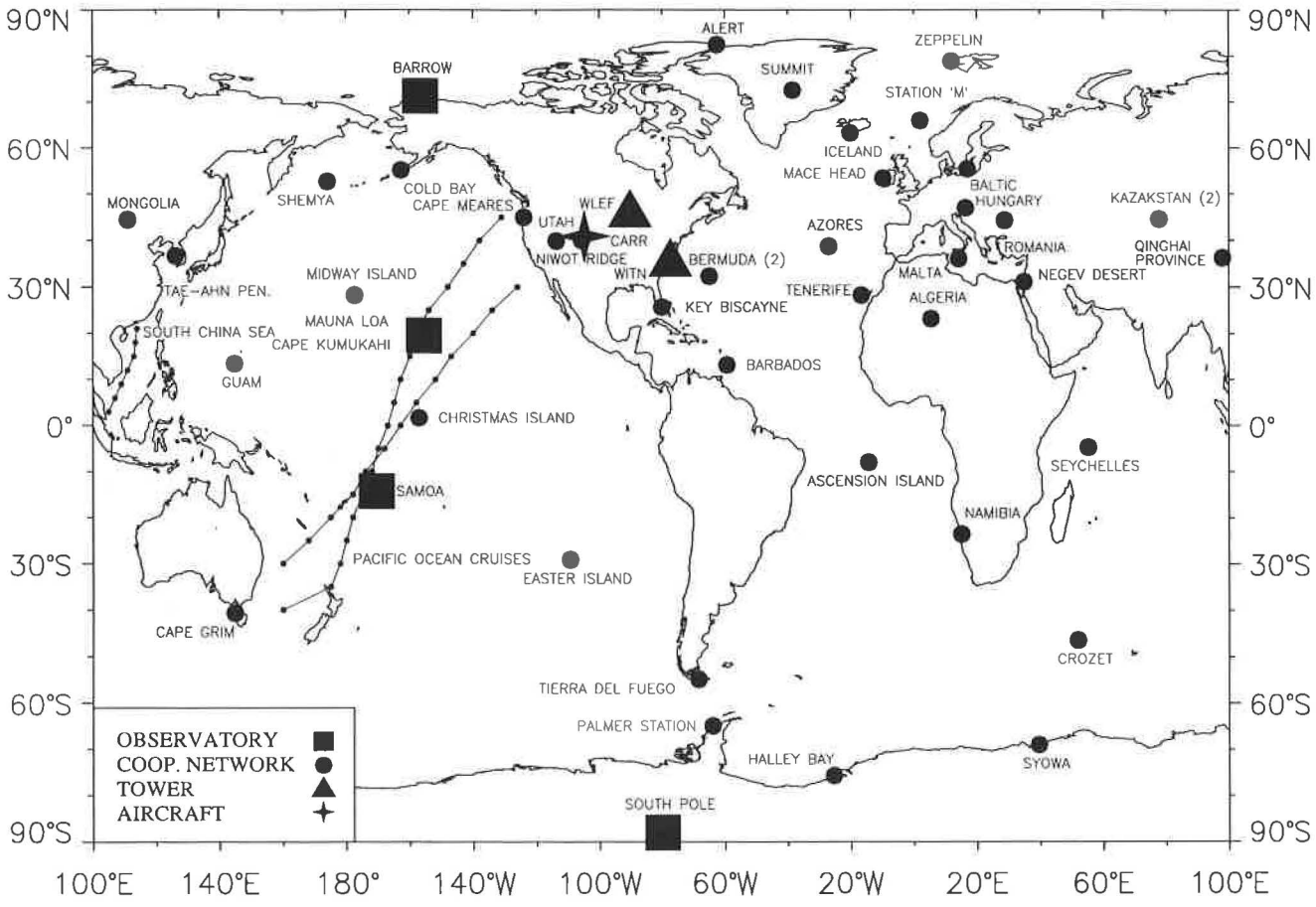

Fig. 2.2. Network of continuing measurements by the Carbon Cycle Group.

TABLE 2.3. 1995-1997 Annual Mean CO_2 Mole Fractions From Network Sites

Code	Station	CO_2 (ppm) 1995	1996	1997
ALT	Alert, N.W.T., Canada	361.5	363.6	364.4
ASC	Ascension Island	359.3	360.4	362.1
ASK	Assekrem, Algeria	[ ]	362.1	363.5
AZR	Terceira Island, Azores	359.9	363.1	363.2
BAL	Baltic Sea	364.6	367.3	366.9
BME	Bermuda (east coast)	361.4	363.3	364.2
BMW	Bermuda (west coast)	361.0	363.1	364.7
BRW	Barrow, Alaska	361.9	364.1	365.0
BSC	Constanta, Romania	[ ]	370.8	370.5
CBA	Cold Bay, Alaska	361.4	363.2	366.0
CGO	Cape Grim, Tasmania	358.0	359.7	361.0
CHR	Christmas Island	[ ]	[ ]	[ ]
CMO	Cape Meares, Oregon	361.5	363.9	364.1
CRZ	Crozet Island	357.9	359.6	[ ]
EIC	Easter Island, Chile	357.7	359.3	360.6
GMI	Guam, Mariana Islands	360.6	362.4	363.8
GOZ	Gozo Island, Malta	361.7	362.7	365.3
HBA	Halley Bay, Antarctica	358.1	359.4	[ ]
HUN	Hegyhatsal, Hungary	366.7	368.7	368.2
ICE	Vestmanaeyjar, Iceland	360.6	362.6	363.5
ITN	WITN, Grifton, North Carolina	364.4	366.6	366.8
IZO	Izana Observatory, Tenerife	361.5	363.0	363.7
KEY	Key Biscayne, Florida	362.2	363.1	364.5
KUM	Cape Kumukahi, Hawaii	360.8	362.5	364.0
KZD	Plateau Assy, Kazakstan			[ ]
KZM	Sary Taukum, Kazakstan			[ ]
LEF	WLEF, Park Falls, Wisconsin	362.9	363.5	365.9
MBC	Mould Bay, Canada	361.9	363.7	[ ]
MHT	Mace Head, Ireland	360.8	363.1	364.3
MID	Midway Island	360.9	362.8	364.1
MLO	Mauna Loa, Hawaii	360.6	362.4	363.5
NMB	Bobabeb, Namibia			[ ]
NWR	Niwot Ridge, Colorado	361.2	363.0	363.9
PSA	Palmer Station, Antarctica	358.1	359.6	361.1
QPC	Qinghai Province, China	[ ]	[ ]	363.7
RPB	Ragged Point, Barbados	360.3	362.1	363.2
SEY	Mahe Island, Seychelles	358.0	360.2	362.5
SHM	Shemya Island, Alaska	361.0	363.4	363.7
SMO	American Samoa	359.3	361.0	362.1
SPO	South Pole, Antarctica	357.9	359.5	361.1
STM	Ocean Station M	360.8	363.2	364.1
SUM	Summit, Greenland			[ ]
SYO	Syowa Station, Antarctica	358.1	360.0	[ ]
TAP	Tae-ahn Peninsula, S. Korea	364.0	366.3	368.7
TDF	Tierra del Fuego, Argentina	358.4	359.6	361.3
UTA	Wendover, Utah	361.2	363.0	364.9
UUM	Ulaan Uul, Mongolia	360.8	362.4	364.7
WIS	Sede Boker, Israel	[ ]	364.0	363.7
ZEP	Ny-Alesund, Svalbard	361.6	363.3	364.4

The square brackets indicate insufficient data to calculate annual mean. The 1997 annual means are provisional.

TABLE 2.4. 1995-1997 Annual Mean CO_2 Mixing Ratios From Pacific Ocean Cruises

Latitude	CO_2 (ppm) 1995	1996	1997
30°N	360.9	362.6	364.0
25°N	361.4	362.6	363.4
20°N	361.0	362.9	363.5
15°N	360.7	362.4	363.7
10°N	361.1	362.8	363.6
5°N	361.0	362.5	363.1
Equator	360.7	362.4	363.9
5°S	360.4	362.1	363.1
10°S	360.4	361.2	362.4
15°S	359.6	360.8	361.7
20°S	359.1	360.3	361.1
25°S	358.7	360.3	361.1
30°S	358.5	360.2	361.0
35°S	358.8	360.1	361.1

TABLE 2.5. 1995-1997 Annual Mean CO_2 Mole Fractions From South China Sea

Latitude	CO_2 (ppm) 1995	1996	1997
21°N	362.1	364.8	[ ]
18°N	362.6	365.9	[ ]
15°N	362.2	363.9	[ ]
12°N	361.4	363.7	[ ]
9°N	362.0	363.5	[ ]
6°N	361.5	363.3	[ ]
3°N	361.3	363.0	[ ]

for the Pacific Ocean cruises and for the South China Sea are reported in Tables 2.4 and 2.5.

To increase the efficiency of air sample analysis a new analytical apparatus was constructed and implemented in July 1997. This apparatus combines two gas chromatographs and an NDIR analyzer with a common sample inlet manifold to consolidate three separate analytical operations into one. This new system called MAGICC (Measurements of Atmospheric Gases Influencing Climate Change) is capable of measuring CO_2, CH_4, CO, H_2, N_2O, and SF_6 in 34 samples per 9-hour day.

The MAGICC system incorporates changes from the old CO_2 flask measurement apparatus design which appear to have eliminated small systematic losses of CO_2 that occurred in the old system. On the basis of a thorough analysis of intensive experiments and daily measurements of test flasks, we have applied corrections to all the CO_2 measurements made on the old system. These corrections are +0.10 ppm for samples measured on the old system from July 1987 through November 18, 1993, and +0.24 ppm for samples measured from November 19, 1993, until the old system was retired on April 10, 1998. We have detected no significant CO_2 offsets on MAGICC from July 1997 through April 1998.

Global fossil fuel emissions and the globally-averaged CO_2 uptake is shown in Figure 2.3. The solid line is based on the assumption that the measurements at the Mauna Loa Observatory, Hawaii (MLO) represent the global atmosphere, the gray band (including a Monte Carlo error estimate) is based on the cooperative flask sampling network. The difference between the fossil fuel emissions and the global net uptake is the atmospheric increase.

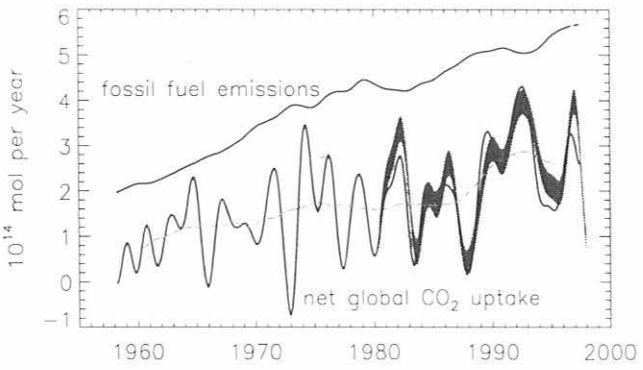

Fig. 2.3. Global rate of fossil fuel emissions and global net uptake of CO_2 by the oceans and terrestrial ecosystems combined, as determined from atmospheric measurements. Solid curve: assuming that the MLO record represents the entire atmosphere perfectly; shaded band: as determined from the global air sampling network and a two-dimensional (latitude, height) atmospheric transport model, including Monte Carlo error estimates in which the sampling network was varied.

The average atmospheric increase rate over the period of the flask network (1980-1997) is 1.47 ppm yr^{-1}. It is evident that there is significant interannual variability in uptake that is much larger than the variability in fossil fuel emissions. Understanding the processes that produce these variations is a primary goal of the air sampling program. For instance, the high rate of uptake observed in 1992-1993, particularly in the northern hemisphere, appears to have resulted from increased carbon storage in the terrestrial biosphere during the cool period following the Mount Pinatubo eruption. This conclusion is based on the spatial pattern of CO_2 during those years and on measured $^{13}C/^{12}C$ isotopic ratios. Some of this temporarily stored carbon was released back to the atmosphere in 1994 and 1995, followed by another period of as yet unexplained low CO_2 increase in 1996.

2.2.3. Carbon Dioxide Standards and Reference Gas Calibrations

A manometric absolute calibration system was developed for performing primary calibrations of the mole fraction of CO_2 in reference gas mixtures [*Zhao et al.*, 1997]. Figure 2.4 shows a schematic diagram of the system. The brief specifications are as follows:

Accuracy:	0.07 μmol mol^{-1}
Precision:	0.06 μmol mol^{-1}
Gas consumption:	15 L in 100 Kpa
Calibration time:	4 hours

There are 15 primary CO_2-in-air WMO standards in aluminum high-pressure cylinders ranging in CO_2 mole fraction from approximately 250 to 520 μmol mol^{-1}. These primary standard cylinders were analyzed by the manometric calibration system from September 1996 through February 1997. Each standard cylinder was analyzed at least three times, often with several days of separation or more between calibrations. A total of 65 individual manometric determinations were made. The results of analyses are summarized in Table 2.6. For comparison, the CO_2 mole fractions measured by the Scripps Institution of Oceanography (SIO) in these same cylinders relative to the WMO X93 scale (maintained at SIO until 1997) are also shown in Table 2.6. The mean precision of the manometric measurements indicated in Table 2.6 as the standard deviations is about 0.07 mol mol^{-1} for a total of 65 measurements. Figure 2.5 gives CO_2 mole fraction comparisons between CMDL manometric determinations and SIO total means with error bars. The concentrations analyzed by two laboratories for the primary standards in the atmospheric CO_2 concentration range of 300 to 400 μmol mol^{-1} are in good agreement, so that the switch from SIO to CMDL for the maintenance of the WMO mole fraction scale will not result in a noticeable shift of the scale. The function of the primary standards is to provide continuity to the WMO scale as well as a quality control check on the performance of the manometric system. The assigned values of the primaries are ultimately determined through the manometric analyses repeated annually.

Because we want to maximize the useful life span of the primaries, the calibration scale is transferred via NDIR measurements, approximately twice a year, to a set of secondary standards. These are in turn used to calibrate, again via NDIR comparisons, every other cylinder. During 1996 about 400 cylinders were assigned a WMO mole fraction value for CO_2 in this way. The reproducibility, in the range between 250 and 520 μmol mol^{-1}, has generally been better than 0.1 μmol mol^{-1}, and we expect the accuracy to be similar, pending a comparison with gravimetric mixtures. On request, calibrations can be performed with the manometric system well outside of the range of atmospheric CO_2 values. Cylinders prepared by CMDL with a specified CO_2 concentration have undergone the following procedures at our clean air pumping station at a high elevation on Niwot Ridge, Colorado, in the mountains east of Boulder:

New or recently hydrotested cylinder. (1) Cylinder is vented and then pressurized twice with dry natural air to about 20 atm (300 psi) and vented again. (2) Filled to about 34 atm (510 psi) with dry natural air and stored for several weeks. (3) Before the final fill the cylinder is first vented and then spiked with either 10% or zero CO_2-in-air, depending on the desired final mole fraction. (4) Final fill with ambient and dried natural air to 135 atm (2000 psi), during which the ambient CO_2 mole fraction is monitored. (5) Water vapor content of the filled cylinder is measured and must be less than 5 ppm; it is usually less than 1 ppm. Drying is accomplished through magnesium perchlorate $Mg(ClO_4)_2$. The pump is a RIX oil-less diving compressor.

Previously used cylinder. Steps 1 and 2 are replaced by venting and one fill with dry natural air to a pressure of 20 atm. Other trace gases, such as CH_4 and CO can be simultaneously targeted to specified values in the same cylinders.

2.2.4. Measurements of Stable Isotopes of Atmospheric CO_2

Since 1989 the Stable Isotope Laboratory at INSTAAR has been measuring the stable isotopic composition of CO_2 from weekly flask samples of air obtained from the CMDL

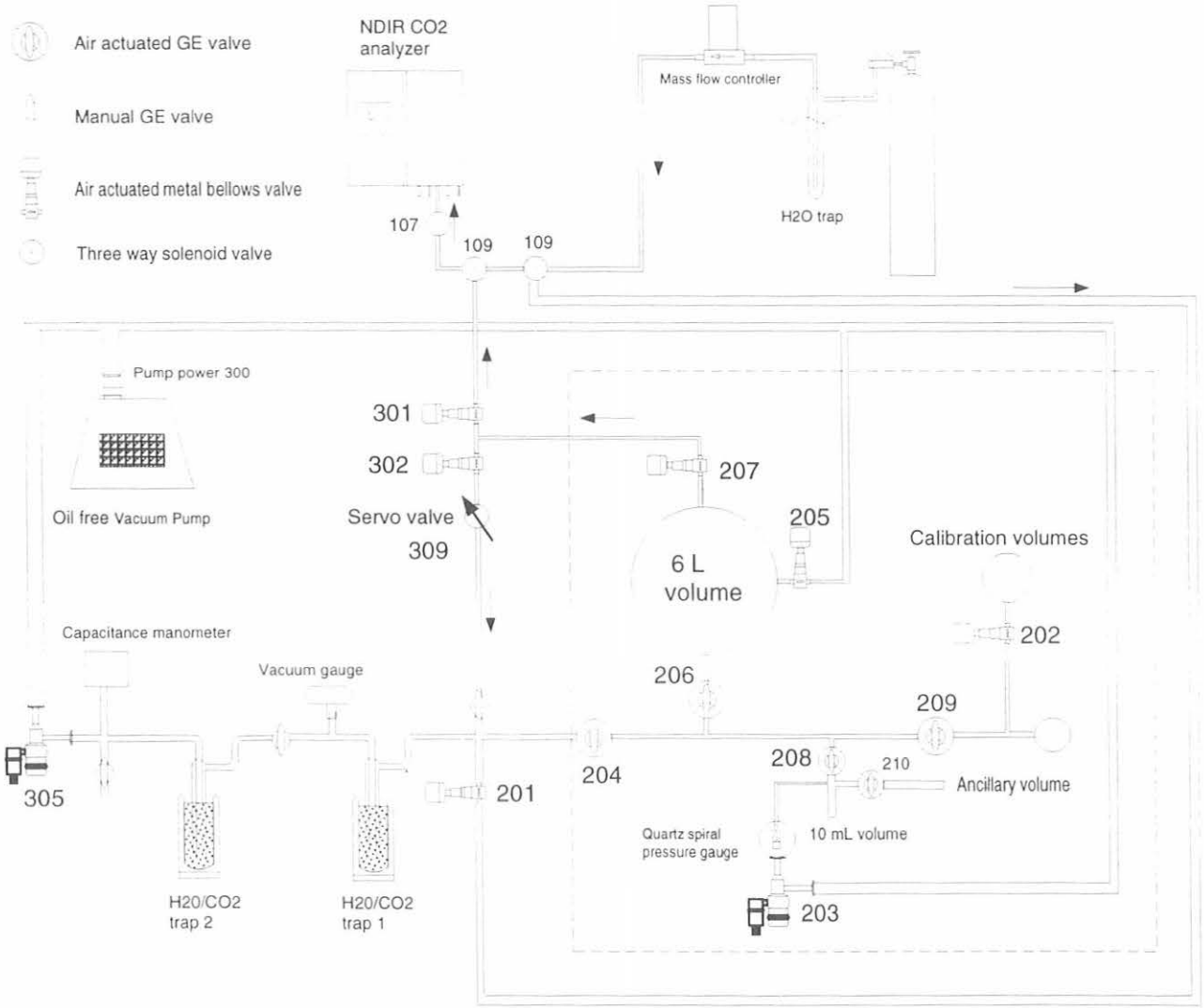

Fig. 2.4. Schematic diagram of manometric system to determine CO_2 mole fraction in samples of dry air.

network of sites. Begun with a selection of only six sites and two ships in 1990, the measurement effort has grown to include approximately 50 stationary sites in the CMDL program as well as all of the shipboard samples. During 1997 over 6400 flasks were analyzed for $\delta^{13}C$ and $\delta^{18}O$, complementing the CO_2 mole-fraction measurements made by CMDL. A description of the measurements and calibration procedures is presented by *Trolier et al. [1996]*.

Uptake of CO_2 by plants or respiratory loss from plants or herbivores changes the isotopic composition of atmospheric CO_2. In the majority of plants the process of photosynthesis discriminates against the uptake of ^{13}C relative to ^{12}C, thus producing isotopically labeled organic matter. In contrast, the exchange of CO_2 between the atmosphere and the oceans produces only a very small isotopic signature. In principle this distinction allows us to discriminate between terrestrial and oceanic sources and sinks of atmospheric CO_2. There is a group of plants, however, that employ a different photosynthetic pathway that does not produce much isotopic fractionation, making its isotopic signature look more like the oceans, and we have to account for that.

The ^{18}O signature is governed by the interaction of the carbon cycle with the hydrological cycle. Oxygen isotopic exchange takes place in liquid water and occurs during the hydration reaction $CO_2 + H_2O$ <---> H_2CO_3. Respiratory CO_2 emanating from soils equilibrates with the oxygen in soil moisture, and CO_2 diffusing in and out of photosynthesising leaves equilibrates with leaf water. Leaf water is often enriched in ^{18}O relative to soil water so that the study of ^{18}O in atmospheric CO_2 has the potential to quantitatively separate respiration from photosynthesis in carbon cycle studies. With CO_2 and $^{13}C/^{12}C$ alone one could only study the net exchanges between the atmosphere and the terrestrial biosphere and oceans.

TABLE 2.6. Measurements of NOAA Primary WMO CO_2 Standards

Cylinder	Date	CMDL	CMDL Mean	SIO Mean 1996*	Difference CMDL-SIO (1996)*
110	Nov. 16, 1996	246.56			
110	Dec. 11, 1996	246.58			
110	Dec. 29, 1996	246.56	246.57 ± 0.01	246.61 ± 0.29	-0.04
				(246.51 ± 0.28)	(0.06)
102	Dec. 8, 1996	304.28			
102	Dec. 8, 1996	304.42			
102	Dec. 11, 1996	304.22			
102	Dec. 11, 1996	304.37	304.32±0.09	304.36 ± 0.10	-0.04
				(304.35 ± 0.03)	(-0.03)
111	Aug. 29, 1996	323.82			
111	Sept. 3, 1996	323.84			
111	Sept. 5, 1996	324.12			
111	Sept. 9, 1996	324.05			
111	Jan. 16, 1997	324.04	323.97±0.14	323.98 ± 0.07	-0.01
				(323.99 ± 0.07)	(-0.03)
130	Nov. 16, 1996	337.14			
130	Nov. 17, 1996	337.21			
130	Jan. 3, 1997	337.20	337.18±0.04	337.23 ± 0.06	-0.05
				(337.27 ± 0.06)	(-0.09)
121	Sept. 8, 1996	349.21			
121	Sept. 10, 1996	349.31			
121	Dec. 30, 1996	349.46			
121	Jan. 4, 1997	349.37			
121	Jan. 5, 1997	349.41	349.35±0.10	349.29 ± 0.09	0.06
				(349.36 ± 0.03)	(-0.01)
103	Sept. 10, 1996	353.27			
103	Sept. 12, 1996	353.30			
103	Sept. 14, 1996	353.35			
103	Sept. 16, 1996	353.23			
103	Dec. 29, 1996	353.33	353.30 ± 0.05	353.13 ± 0.10	0.17
				(353.20 ± 0.04)	(0.10)
139	Sept. 17, 1996	361.03			
139	Sept. 17, 1996	360.94			
139	Sept. 18, 1996	360.85			
139	Nov. 21, 1996	360.90			
139	Dec. 08, 1996	360.89	360.92 ± 0.07	360.74 ± 0.12	0.18
				(360.85 ± 0.03)	(0.07)
105	Sept. 18, 1996	369.41			
105	Nov. 14, 1996	369.27			
105	Nov. 14, 1996	369.41			
105	Jan. 6, 1997	369.40	369.37 ± 0.07	369.27 ± 0.14	0.10
				(369.36 ± 0.07)	(0.01)
136	Sept. 3, 1996	381.23			
136	Sept. 13, 1996	381.08			
136	Sept. 13, 1996	381.31			
136	Nov. 12, 1996	381.26	381.22 ± 0.10	381.19 ± 0.17	0.03
				(381.26 ± 0.08)	(-0.04)
146	Sept. 19, 1996	389.53			
146	Nov. 13, 1996	389.43			
146	Jan. 5, 1997	389.48	389.48 ± 0.05	389.44 ± 0.20	0.04
				(389.58 ± 0.07)	(-0.10)
101	Nov. 14, 1996	395.99			
101	Dec. 13, 1996	396.28			
101	Dec. 14, 1996	396.27			
101	Dec. 15, 1996	396.25			
101	Dec. 15, 1996	396.20	396.20 ± 0.12	396.15 ± 0.19	0.05
				(396.22 ± 0.07)	(-0.02)

TABLE 2.6. Measurements of NOAA Primary WMO CO_2 Standards - Continued

Cylinder	Date	CMDL	CMDL Mean	SIO Mean 1996*	Difference CMDL-SIO (1996)*
106	Dec. 7, 1996	412.05			
106	Dec. 7, 1996	411.98			
106	Jan. 4, 1997	411.88	411.97 ± 0.09	411.87 ± 0.26	0.10
				(412.04 ± 0.05)	(-0.07)
123	Nov. 20, 1996	422.80			
123	Nov. 24, 1996	422.99			
123	Jan. 6, 1997	423.03			
123	Jan. 6, 1997	422.98	422.95 ± 0.10	422.84 ± 0.31	0.11
				(422.98 ± 0.09)	(-0.03)
107	Nov. 22, 1996	453.40			
107	Dec. 16, 1996	453.22			
107	Dec. 16, 1996	453.27			
107	Jan. 10, 1997	453.39			
107	Jan. 10, 1997	453.38			
107	Jan. 10, 1997	453.24			
107	Jan. 11, 1997	453.09	453.28 ± 0.11	452.71 ± 0.43	0.57
				(452.97 ± 0.17)	(0.31)
132	Jan. 13, 1997	521.28			
132	Jan. 13, 1997	521.31			
132	Jan. 14, 1997	521.20			
132	Jan. 14, 1997	521.33			
132	Jan. 15, 1997	521.16	521.26 ± 0.07	520.89 ± 0.83	0.37
				(521.44 ± 0.37)	(-0.18)

*Note: SIO measurements on these cylinders were performed during 1991-1993 and during 1996. Between parentheses are the means of SIO measurements during 1996 alone, perhaps a better comparison with the CMDL measurements during late 1996 and early 1997.

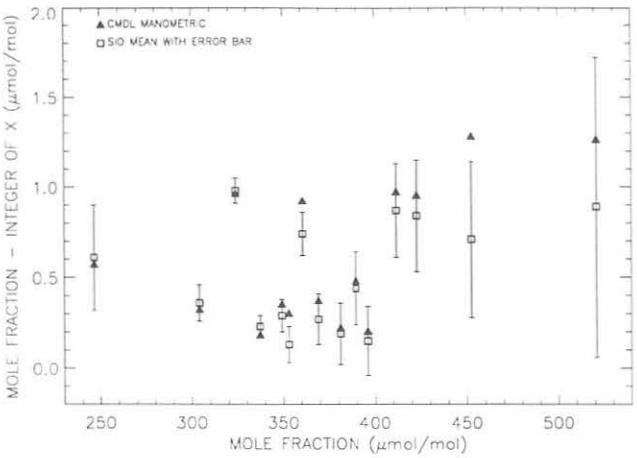

Fig. 2.5. Differences between CMDL determinations and Scripps total mean CO_2 measurements for 15 WMO primary standards. CMDL manometric determinations are shown as triangles, SIO total mean for each cylinder is shown as a square with the error bar.

The degree to which isotopic measurements made on atmospheric samples are useful is seriously constrained by the precision of the mass spectrometer used. For example, a change of just 0.024‰ $\delta^{13}C$ measured globally translates to an equivalent switch between a terrestrial or an oceanic source to the atmosphere of 1 GtC (10^{15} g C). Hence, a very high precision instrument is desirable. In 1990 we began making measurements with a VG SIRA Series 2 mass spectrometer. This instrument was capable of measurement precisions of 0.03‰ for $\delta^{13}C$ and 0.05 for $\delta^{18}O$ (one sigma). A Micromass Optima mass spectrometer was purchased and tested in 1996 and brought on line in late 1996 exclusively for making flask measurements. The overall reproducibility for the Optima system in 1997 (one sigma standard deviation for replicate analyses) is 0.012‰ for $\delta^{13}C$ and 0.031‰ for $\delta^{18}O$. This new system incorporates an automated 40-port custom manifold and a sample extraction system using all stainless steel parts and is based on the methods proven on the SIRA instrument. Air samples are extracted at a rate of 40 scc min^{-1} on both systems. However, the more efficient trapping of CO_2 and greater sensitivity of the new Optima system require 25% less sample, which shortens analysis time by a proportional amount. This also allows more air to be left in the flask for any subsequent analyses, such as isotopes of carbon in methane, or a repeat analysis should it be required. Tests have shown that with the typical amount of sample left in the flask when it arrives for isotopic analysis, only one extraction was possible with the SIRA instrument, whereas with the Optima instrument, two to three extractions are now possible with acceptable reproducibility. With further extractions the flask pressure drops below a threshold where significant isotopic fractionation occurs, possibly as a result of CO_2 coming off the flask walls with a very different $\delta^{18}O$ and $\delta^{13}C$.

The increased capacity attained with the 40-port manifold allowed us to make over 11,560 separate

analyses on flasks and reference gases in 1997. The combined effect of improved precision and increased capacity is a significant increase in the utility of the isotopic measurements towards characterizing the present day carbon cycle.

As one check on data quality, we began in late 1996 to measure three aliquots of air from a standard cylinder in the middle of each flask run on the mass spectrometer. This additional cylinder, called the "trap tank" provides for a continuous check on the performance of the entire system: the extraction of CO_2 from air, the isotopic ratio analysis, and the final corrections for N_2O and ^{17}O. Figure 2.6 shows the standard deviation for $\delta^{13}C$ values measured on three aliquots of the trap tank plotted as a 10-point running mean. The average standard deviation is slightly less than 0.01‰ and is nearly always less than 0.015‰. The same information is shown in Figure 2.7 for $\delta^{18}O$ of the trap tank. The average standard deviation is 0.03‰, and values are always less than 0.05‰. Thus most of the improvement in the isotopic measurements in moving analyses from the SIRA to the OPTIMA has been in the $\delta^{13}C$ values where standard deviations have improved by about a factor of three; $\delta^{18}O$ has improved by less than a factor of two. The difference lies, we believe, in the extraction process, which is sensitive to the presence of water in the air samples. We note that when dry air from several cylinders is intercompared, such as when standard cylinders are analyzed, the $\delta^{18}O$ standard deviations are significantly less, generally 0.015‰ or less; the $\delta^{13}C$ standard deviations are also lower, usually about 0.005‰.

A sample of the isotope data is given in Figure 2.8 which shows the time series of CO_2 mole fraction, $\delta^{13}C$, and $\delta^{18}O$ from Niwot Ridge, Colorado. The striking anti-correlation between the seasonal cycles of CO_2 and $\delta^{13}C$ is a reflection of terrestrial photosynthesis and respiration. The CO_2 absorbed by plants is depleted in ^{13}C leaving behind an atmosphere slightly enriched in ^{13}C. The $\delta^{18}O$ seasonal cycle is quite different from that of $\delta^{13}C$. For example, when the net flux from the terrestrial biosphere is already directed into the atmosphere at the end of the growing season, the respired CO_2 from soils at higher latitudes is still pulling down atmospheric $\delta^{18}O$. Soil moisture at high latitudes is very depleted in ^{18}O, a signature that is picked up by respired CO_2 [*Ciais et al.*, 1997]. Annually averaged $\delta^{18}O$ is not expected to display a decadal trend, but can change dramatically from year to year, most likely because it is subject to the strong opposing forces of respiration (depleted in ^{18}O) and photosynthesis (leaf water enriched in ^{18}O).

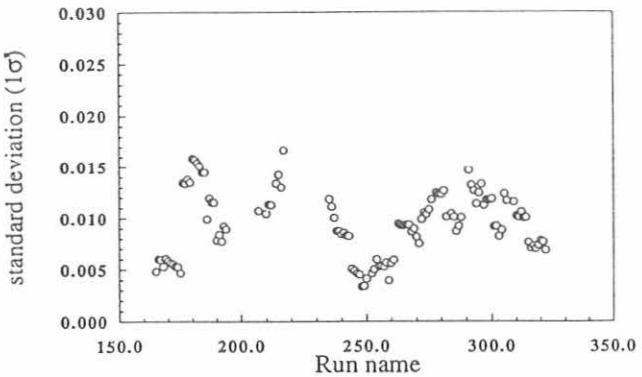

Fig. 2.6. Ten-point running mean of the standard deviation of $\delta^{13}C$ the trap tank as a function of run number in per mille. The data covers the period from June 1997 to January 1998.

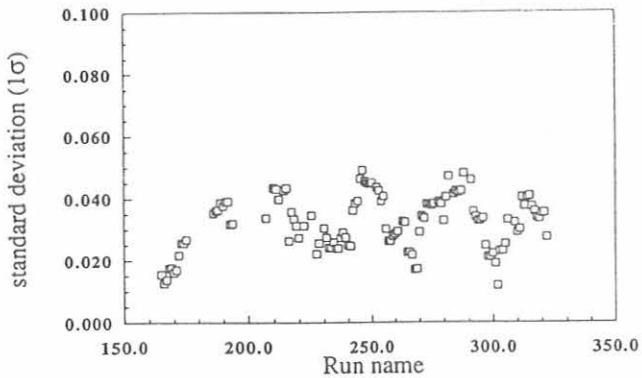

Fig. 2.7. Ten-point running mean of the standard deviation of $\delta^{18}O$ of the trap tank as a function of run number in per mille. The data covers the period from June 1997 to January 1998.

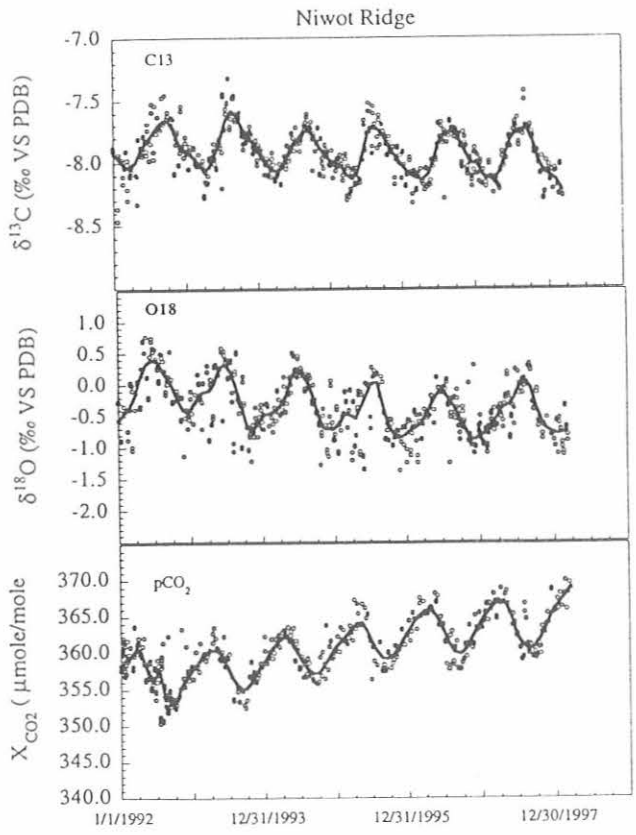

Fig. 2.8. CO_2, $\delta^{13}C$ and $\delta^{18}O$ at Niwot Ridge, Colorado.

Field testing of a new air sampling apparatus began at the Samoa Observatory, American Samoa (SMO) in September 1994 and at Cape Kumukahi, Hawaii, in May 1995. The new Airkit differs from the older Martin and Kitzis sampler (MAKS) version in two important ways. It has a thermoelectrically cooled condenser to remove most of the water vapor from the air stream, and a microprocessor to control the sampling process in order to minimize the chance for operator error. The effect of drying the air samples is most dramatic for the measurement of $^{18}O/^{16}O$ in CO_2. Without drying, $\delta^{18}O$ in the samples collected in humid tropical locations is highly variable and consistently more depleted in ^{18}O due to isotopic exchange between water and CO_2, which presumably occurs on the wall of the flask [*Gemery et al.*, 1996]. Figure 2.9 shows the improvements in the samples from SMO. For ^{18}O, the majority of the "wet" samples (MAKS) was rejected because of poor pair agreement. The fortuitously retained pairs tend to be isotopically "light." Since the samples have been dried with the Airkit the true $\delta^{18}O$ signature of CO_2 in the central equatorial Pacific is emerging. There appears to have been a small decrease, about 0.08‰ yr^{-1}, in the last 3 years. There is also an improvement in the $\delta^{13}C$ values measured in the Airkit samples. The latter samples have a defined, but small, seasonal cycle that was only vaguely hinted at in the earlier MAKS samples.

2.2.5. Measurement of the Oxygen Isotopic Ratio of Soil CO_2 and Soil-Respired CO_2

In order to better understand and eventually predict inter-annual variations in the growth rate of atmospheric carbon dioxide, the interaction between the biosphere and atmosphere must be understood in a quantitative manner. Recent advances, using the carbon isotopic ratio ($\delta^{13}C$) of atmospheric CO_2, have enabled the quantification of global Net Ecosystem Productivity (NEP), that is, the total terrestrial carbon sink. Analyzing the oxygen isotopic ratio, $\delta^{18}O$, of atmospheric CO_2 allows for the partitioning of global NEP into its two components—photosynthesis and respiration. Measuring and understanding the variations in $\delta^{18}O$ of CO_2 respired from soils is critical to such an analysis. We have designed a novel dynamic gas exchange system to measure the $\delta^{18}O$ of soil CO_2 in the laboratory. We have also developed a novel system to examine the vertical profile of $\delta^{18}O$ of soil CO_2, in situ.

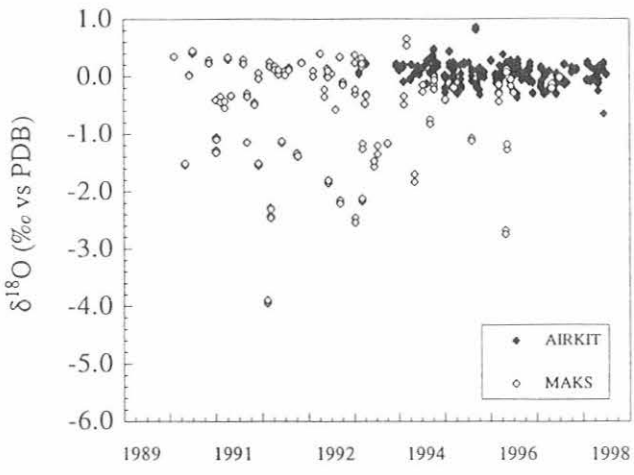

Fig. 2.9. Oxygen-18 in flask samples from Cape Matatula, Samoa.

The dynamic soil gas exchange system consists of a Lucite chamber sealed to the top of a steel box containing the soil profile. Air of a known CO_2 mole fraction and isotopic composition is pumped through the chamber at a well-defined flow rate and is allowed to interact with the soil. Soil-respired CO_2 mixes with the input air, altering its mole fraction and isotopic ratio. Air above the soil also diffuses into the soil and isotopically equilibrates with the soil water. This "invading" CO_2, now with an altered $\delta^{18}O$, diffuses back out of the soil, further altering the $\delta^{18}O$ of the CO_2 in the headspace. The mole fraction and isotopic ratios of the CO_2 entering and leaving the chamber are measured, and the $\delta^{18}O$ of the soil-respired CO_2 is calculated using a mass-balance model that takes the invasion effect into account. We found that the isotopic ratio of soil-respired CO_2 is strongly controlled by the average isotopic composition of the water in the top 10 cm of the soil which varies greatly as a function of season (run-off versus local precipitation) or short-term drying. The $\delta^{18}O$ value of the respired CO_2 is also influenced by the effective kinetic isotopic effect associated with CO_2 diffusion out of the soil. This effective fractionation factor is in fact a measure of the competition between CO_2 diffusing out of the soil and simultaneously equilibrating with soil water and was calculated using a soil CO_2 diffusion model. The theory of the processes mentioned above was described by *Tans* [1998].

The in situ soil CO_2 profile system is based on gas chromatography-isotope ratio mass spectrometry (GC-IRMS). Aliquots of soil air (200 µl) are rapidly evacuated with a fused silica probe from 1.0 to 10.0 cm depths. This air is dried with a Nafion membrane and passed directly to a porous polymer capillary column for separation of CO_2 from air and other trace species (including N_2O.) After separation the CO_2 is admitted to the IRMS, via an open split, for determination of both $\delta^{13}C$ and $\delta^{18}O$ of the CO_2. Precision is better than 0.1‰ for both ratios in an analysis time of only 6 minutes. Comparison of a soil CO_2 isotopic profile with an isotopic profile of water from the same soil showed that CO_2 and water were in full equilibrium until a depth of 4 cm, above which the CO_2 became progressively isotopically enriched towards the surface. These results were nearly identical to those predicted by a model calculation on the same soil system.

Both the dynamic soil gas exchange system and the in situ soil CO_2 profile system enabled us to examine the physical processes controlling the isotopic ratio of soil-respired CO_2 in a controlled laboratory setting. Both methods of analysis confirmed the ability of the soil CO_2 diffusion model to accurately predict the isotopic ratio of soil-respired CO_2 and the CO_2 within the soil given knowledge of soil characteristics and the oxygen isotopic profile of soil water.

2.3. METHANE

2.3.1. IN SITU METHANE MEASUREMENTS

Quasi-continuous measurements of atmospheric methane continued at MLO and BRW at a frequency of four ambient measurements each hour. The relative precision is 0.07%. Details of the measurement techniques and analysis of the in situ data through early 1994 were published in 1995 [*Dlugokencky et al.*, 1995]. Daily averaged methane mole fractions (in nanomol mol^{-1}) are plotted in Figure 2.10 for BRW (a) and MLO (b). The data have been edited for instrument malfunction using a rule-based expert system [*Masarie et al.*, 1991], but they were not selected for meteorological conditions. High CH_4 values at BRW are due to emissions from local sources. Limitations of the unselected data sets have been discussed previously by *Dlugokencky et al.* [1995].

The quasi-continuous measurements from BRW and MLO are an invaluable quality control tool when they are compared with weekly, discrete samples from these sites. They are used to illuminate sampling errors, to determine biases associated with weekly sampling, and to estimate reasonable uncertainties for monthly means, trends, and other parameters determined from the weekly samples.

Histograms of the differences between in situ and flask sample measurements are plotted in Figure 2.11.

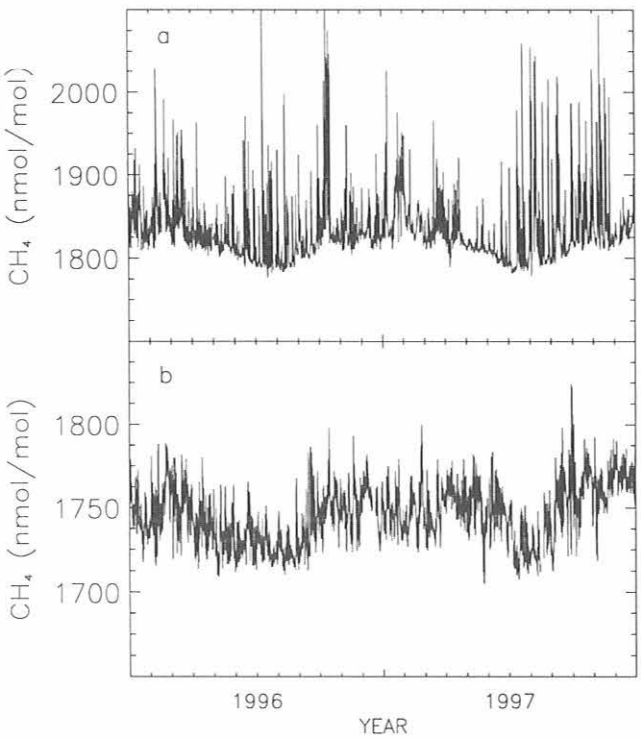

Fig. 2.10. Daily mean CH_4 mole fractions in nanomol mol^{-1} for (a) BRW and (b) MLO for 1996 and 1997. The data are unconstrained but have undergone a quality control step to ensure that the analytical instrument was working optimally when they were obtained [*Masarie et al.*, 1991].

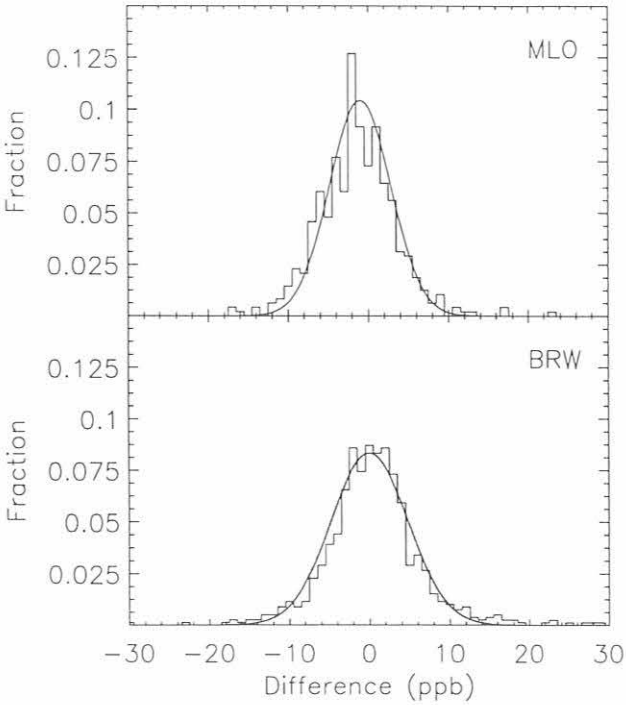

Fig. 2.11. Histograms of differences between discrete samples and in situ measurements interpolated from hourly averages for MLO (a) and BRW (b) from samples collected through 1996. The smooth curve is a normal distribution calculated from the population of differences.

Differences were determined as the difference between the average of all discrete samples collected with a unique sample date and a value interpolated from hourly averages at the time the discrete sample was collected. A smooth, normal distribution is also plotted based on the mean and standard deviation of the population of differences. The mean differences (one sigma) are -0.9 ± 4.8 ppb at MLO and 0.4 ± 6.0 ppb at BRW, where outliers greater than 3 sigma were excluded. This result gives us confidence that our sampling methods are not resulting in an offset in the CH_4 discrete sample measurements.

If we assume that high frequency sampling results in time series that accurately define the parameters of interest (e.g., trend and seasonal cycle), then a qualitative comparison of in situ and discrete sampling time series should reveal how accurately weekly sampling captures the main features in the data. In Figure 2.12 smooth curves fitted to discrete and in situ time series are plotted. Agreement is excellent. For example, trends for BRW are 6.9 ppb yr^{-1} for discrete sample and 7.4 ppb yr^{-1} for in situ, and at MLO 7.7 ppb yr^{-1} for discrete sample and 7.7 ppb yr^{-1} for in situ. Additionally, uncertainties in trends, changes in trends, and monthly averages can be calculated for the discrete sample measurements from in situ measurements using a nonparametric statistical technique called the bootstrap method, similar to what we have done for CO_2 [*Tans et al, 1990b*]. To do this, 50 "bootstrap" time series are created by randomly selecting hourly averages, one per week, from BRW and MLO in situ records. For BRW data are used only if they were

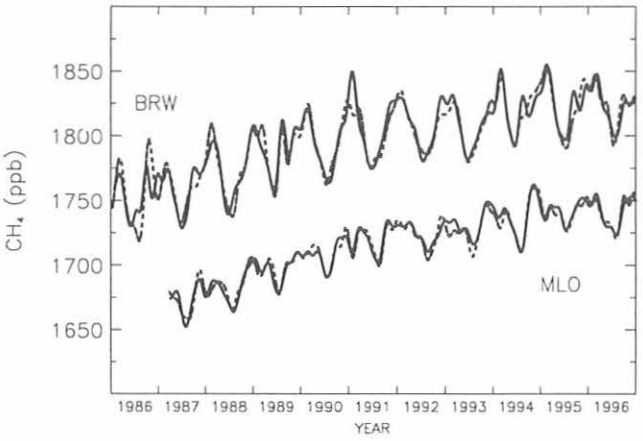

Fig. 2.12. Smooth curves fitted to discrete samples (dashed line) and in situ measurements (solid line) for BRW and MLO.

obtained when the wind was from the clean air sector, and for MLO the in situ records were constrained to downslope times. Next, the parameters of interest are determined for each "bootstrap" time series. These parameters are averaged and their standard deviation calculated; the standard deviation is used as the uncertainty for that parameter for the discrete sample data. For MLO from April 1987 through 1996, the trend is 7.7 ± 0.3 ppb yr^{-1}, changing at -1.4 ± 0.1 ppb yr^{-2}. At BRW from 1986 through 1996, the trend is 6.9 ± 0.3 ppb yr^{-1}, decreasing at -1.0 ± 0.1 ppb yr^{-2}. Uncertainties can also be calculated for mean seasonal cycles and monthly mean values.

In summary we find good agreement between discrete samples and in situ measurements at BRW and MLO suggesting that storing the discrete samples has little effect on the integrity of the samples, at least with respect to methane. Weekly samples reproduce the main features in the in situ records reasonably well at BRW and MLO. This likely holds true for most of the sites in our sampling network. Finally, using nonparametric statistical methods, in situ measurements are useful for calculating uncertainties for discrete sample records.

TABLE 2.7. Provisional 1996 and 1997 Annual Mean CH_4 Mole Fractions From the Air Sampling Network

Site Code	Station	1996 CH_4 (ppb)	1997 CH_4 (ppb)
ALT	Alert, N.W.T., Canada	1813.7	1813.9
ASC	Ascension Island	1690.3	1698.0
AZR	Terceira Island, Azores	1783.1	1784.1
BAL	Baltic Sea	1842.0	1839.5
BME	Bermuda (east coast)	1785.5	1784.1
BMW	Bermuda west coast)	1778.0	1778.6
BRW	Point Barrow, Alaska	1824.4	1825.3
BSC	Constanta, Black Sea	1929.2	1921.2
CBA	Cold Bay, Alaska	1806.9	1809.3
CGO	Cape Grim, Tasmania	1681.8	1688.0
CMO	Cape Meares, Oregon	1797.6	1796.2
CRZ	Crozet Island	1680.8	[ ]
EIC	Easter Island, Chile	1681.0	1687.4
GMI	Guam, Mariana Islands	1734.9	1749.4
GOZ	Gozo, Malta	1808.2	[ ]
HBA	Halley Bay, Antarctica	1680.2	[ ]
HUN	Hegyhatsal, Hungary	1880.4	1873.4
ICE	Heimaey, Iceland	1805.4	1806.5
ITN	WITN, North Carolina	1835.4	1834.8
IZO	Izana Observatory, Tenerife	1761.7	1764.3
KEY	Key Biscayne, Florida	1768.8	1773.6
KUM	Cape Kumukahi, Hawaii	1756.9	1759.7
LEF	WLEF, Wisconsin	1829.8	1835.6
MBC	Mould Bay, Canada	1816.5	[ ]
MHT	Mace Head, Ireland	1803.8	1802.7
MID	Midway Island	1775.2	1778.6
MLO	Mauna Loa, Hawaii	1741.2	1750.7
NWR	Niwot Ridge, Colorado	1775.7	1779.9
PSA	Palmer Station, Antarctica	1680.6	1685.6
QPC	Qinghai Province, China	1786.2	1784.8
RPB	Ragged Point, Barbados	1753.6	1751.2
SEY	Mahé Island, Seychelles	1705.6	1716.5
SHM	Shemya Island, Alaska	1807.9	1806.3
SMO	American Samoa	1691.0	1692.8
SPO	South Pole, Antarctica	1679.6	1686.2
STM	Ocean Station M	1812.6	1811.1
SYO	Syowa Station, Antarctica	1680.2	[ ]
TAP	Tae-ahn Peninsula, South Korea	1830.9	1832.7
TDF	Tierra Del Fuego	1682.5	[ ]
UTA	Wendover, Utah	1784.1	1784.2
UUM	Ulaan Uul, Mongolia	1811.8	1808.4
WIS	Negev Desert, Israel	1811.2	1807.1
ZEP	Ny-Alesund, Svalbard	1813.7	1813.1

Square brackets indicate insufficient data to calculate the annual mean.

2.3.2. Discrete Sample Measurements of Methane

During 1996-1997 the determination of the global distribution of atmospheric methane continued from 49 sampling sites of the Carbon Cycle Group's cooperative air sampling network. Sampling was started at four new sites during this 2-year period. Provisional annual mean values for 1996-1997 are given in Table 2.7.

In mid-1997 routine analysis of discrete air samples began on a new analysis system (MAGICC). For the most part, the analytical techniques remained the same. Methane is analyzed by gas chromatography with flame ionization detection using a HP 6890 GC, nearly identical to the ones used at MLO and BRW for in situ measurements. A two-column separation scheme is used to isolate CH_4 from other species in each air sample. Methane mole fractions are calculated by ratioing the peak response (area) for each sample to the average peak response of bracketing aliquots of standard gas, then multiplying this ratio by the CH_4 mole fraction assigned to the standard gas tank. Sample air is extracted from the flask and flushed through the sample loop using a metal bellows pump. When using the previous Carle 7 system, CH_4 and CO sample loops were flushed in series; now the analytical systems are set up in parallel and flushed sequentially starting with N_2O/SF_6, then CO/H_2, then CH_4, and finally CO_2.

The trend of methane is an important constraint on methane's global budget, and it impacts environmental policy. Methane has been increasing in the Earth's atmosphere since the industrial revolution, and it is clear that the increase is due to anthropogenic activities. The globally-averaged rate of increase has varied since the early-1980s, but, over the past decade, it has slowed by more than a factor of two [*Dlugokencky et al,* 1994]. The overall decline in growth rate has not been fully explained. Possibilities that could partially explain the decreased growth rate are increased OH radical concentrations due to long-term decreasing trends in stratospheric O_3, and stabilization of emissions from anthropogenic sources such as rice agriculture and cattle. A recent analysis of the CMDL global CH_4 averages shown in Figure 2.13 [*Dlugokencky et al.,* 1998] suggests that the decreasing growth rate of atmospheric methane can be explained as a chemical system approaching steady state where emissions and [OH] have remained about constant from 1983-1996.

The change in the global burden of CH_4 is given by:

$$d[CH_4]/dt = Q - [CH_4]/\tau \qquad (1)$$

where $[CH_4]$ is the global CH_4 burden (calculated directly from the CMDL globally-averaged mole fractions), Q is the sum of all emissions, and τ is the total atmospheric CH_4 lifetime. The term $[CH_4]/\tau$ is equal to the photochemical sink. Equation (1) can be rearranged to give:

$$Q = d[CH_4]/dt + [CH_4]/\tau \qquad (2)$$

The total global source, Q, and the atmospheric sink determined from our measurements are plotted in Figure 2.14a. The trend was calculated for each year from the deseasonalized curve fitted to the CH_4 global means, and the sink was calculated from the globally averaged burden for each year and constant lifetime, τ = 8.9 years [*Prinn et al.,* 1995]. Contributions to the sink from soil processes are small and have been ignored. Since [OH] is assumed constant, interannual variability in OH is accounted for in the source term. No significant long-term trend in [OH] has been detected globally [*Prinn et al.*, 1995]. Therefore, Q is really a pseudo-source since it includes deviations from the mean atmospheric lifetime. We converted from ppb in the marine boundary layer to Tg (where 1 Tg =

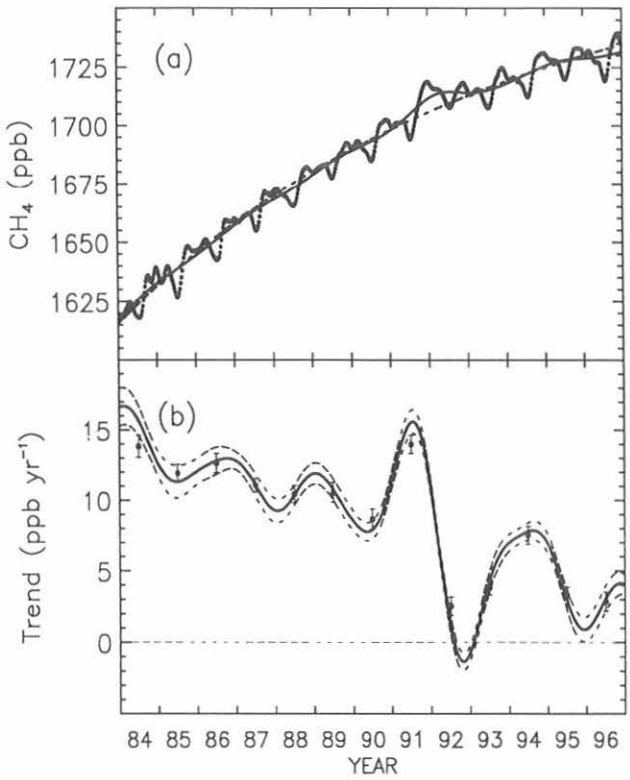

Fig. 2.13. (a) Globally averaged CH_4 mole fractions (symbols; where ppb is used to abbreviate nmol mol^{-1}). The solid line is a deseasonalized trend fitted to the global averages. The dashed line is a fit of Equation (3) to the global averages calculated using $CH_4(ss)$ = 1779 nmol mol^{-1}, $CH_4(t = t_0)$ = 1615 nmol mol^{-1}, and τ = 10 yr. (b) Instantaneous, smoothed growth rate for globally averaged atmospheric CH_4. The curve is calculated as the derivative of the solid curve in (a). Symbols are annual increases determined from the trend line above.

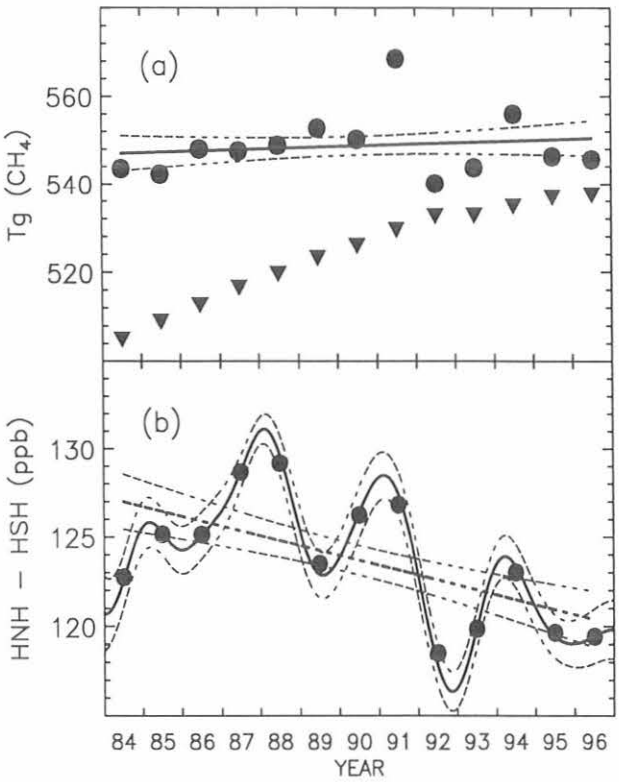

Fig. 2.14. (a) Global methane source (circles) and sink (triangles) calculated using the mass-balance equation from the global burden and annual increase determined by CMDL and CH_4 lifetime determined by *Prinn et al.* [1995]. (b) Differences between annually averaged CH_4 mole fractions in the latitude zones 30-90°N and 30-90°S. The average difference is 123.6 nmol mol^{-1}, and the trend in the difference is -0.6 ± 0.2 nmol mol^{-1} yr^{-1}.

10^{12} g) with the global conversion factor, 1 ppb = 2.767 Tg [*Fung et al.*, 1991]. There are significant interannual variations in Q, but a straight line fitted to Q gives a slope of 0.3 ± 0.6 Tg yr^{-1} for the source suggesting that over the period of our measurements a significant trend in the source was not present. The increase in the CH_4 sink is due to the increasing CH_4 burden. Therefore, it appears the long-term decrease in CH_4 growth rate is an approach to steady state where total source strength and [OH] are constant.

Alternately, consider CH_4 at steady state, where $d[CH_4]/dt = 0$, and $Q = [CH_4]_{ss}/\tau$, (the subscript "ss" implies steady state). The approach to steady state for this system, with a zeroth-order source and pseudo first-order loss of CH_4 is given by:

$$[CH_4](t) = [CH_4]_{ss} - ([CH_4]_{ss} - [CH_4]_0) \exp(-t/\tau) \qquad (3)$$

where the non-zero burden at the time our measurements started is accounted for. The terms $[CH_4]_{ss}$, $([CH_4]_{ss}-[CH_4]_0)$, and τ are determined from a nonlinear curve-fitting routine. Equation (3) was fitted to our deseasonalized global averages. A steady state CH_4 mole fraction of 1779 ppb and τ = 10.0 yr were determined, and a curve calculated using these coefficients is plotted in Figure 2.13a. Agreement between this simple kinetic model and the global averages is good. While sources have appeared to remain nearly constant, a small, yet unexplained, trend may exist in the difference in CH_4 burden between the high-northern and high-southern latitudes (Figure 2.14b).

Two data analysis methods (mass balance and kinetic expression) suggest that the global burden of CH_4 has been approaching equilibrium since the early 1980s. This has important implications for policy. If CH_4 sources and [OH] remain at 1996 levels, the global burden will increase to about 1780 ppb with a time constant of about 10 years and then stabilize. This result impacts scenarios of future climate and stratospheric O_3 (since $CH_4 + Cl \rightarrow HCl + CH_3$ is a temporary reservoir of active chlorine). We caution that quantifying small, long-term trends in specific CH_4 source strengths remains impossible, therefore, the future burden of atmospheric CH_4 cannot be predicted with certainty.

2.3.3. Measurements of $^{13}C/^{12}C$ of Methane

Partitioning atmospheric methane into its biotic and abiotic sources is possible through global measurements of its carbon isotopic ratio. Biotic sources such as wetlands have a characteristic isotopic "signature" of roughly -60‰, whereas abiotic sources such as natural gas have a "signature" near to -40‰. We have designed an automated system for the analysis of $\delta^{13}C$ in atmospheric methane. Currently the system analyzes pairs of flasks on a weekly basis from six sites of the CMDL cooperative air sampling network (Figure 2.15). The analysis technique used is gas chromatography followed by isotope ratio mass spectrometry (GC-IRMS). First, the methane is separated from over 99.99% of the air on a cryogenic pre-column (Haysep-D at -120°C). It is then cryo-focused at the head of the analytical column (Molecular Sieve 5A capillary column) where, after warming, the methane is separated from the remaining air and other trace species. The methane is then combusted to produce CO_2 and admitted to the mass spectrometer, via an open split capillary tube, for determination of its isotopic ratio. As little as 100 mL of air is used to achieve a precision of better than 0.06‰ in less than 15 minutes. The measured precision is comparable to that of systems where at least 100 times as much air is used and where analysis and separation times are more than 1 hour.

Preliminary measurements indicate a latitudinal difference of approximately -0.5‰ as measured between Pt. Barrow, Alaska, and the South Pole (Figure 2.15) during the boreal winter. The sign of this gradient is consistent with the isotopic enrichment expected in the southern hemisphere at this time of year due to enhanced destruction of methane by hydroxyl radical. (The hydroxyl radical reacts preferentially with $^{12}CH_4$). Our working air standards have not yet been linked to an international scale, therefore, we can only report our results relative to one another at this time. Our standards will be calibrated externally in the near future. An automated flask manifold is also being built so that a greater number of the network sites can be analyzed for $\delta^{13}C$ of methane.

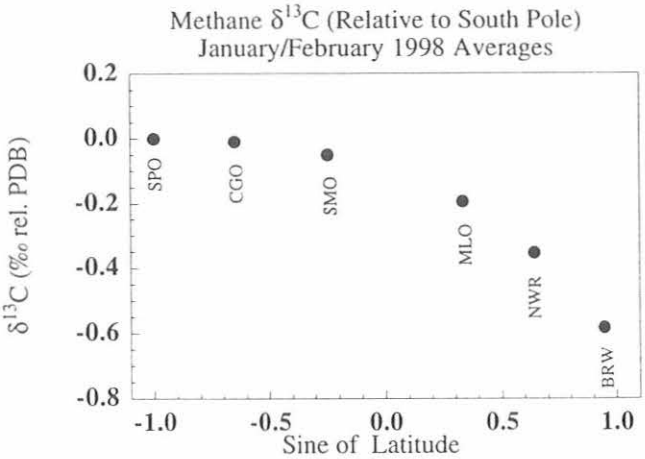

Fig. 2.15. Latitudinal gradient of $\delta^{13}C$ of methane during boreal winter.

2.4. Carbon Monoxide

2.4.1. In Situ Carbon Monoxide Measurements

Instruments based upon gas chromatography and mercuric oxide reduction and UV absorption (Reduced Gas Analyzer (RGA) from Trace Analytical Inc, Menlo Park, California) were installed at BRW and MLO in 1991 and 1992, respectively. The analytical techniques have been described previously [*Bakwin et al.*, 1994]. In brief, the analysis of samples using a RGA were compared to standards bracketing the range of mole fractions found at the site, and standards were referenced to the CMDL calibration scale. A piecewise linear calibration procedure using three standards was used to account for nonlinear instrument response. Measurements at BRW continued with only minor problems during 1996-1997. The BRW

time series shows a strong seasonal cycle with an amplitude of ~100 ppb (10^{-9} mol mol^{-1}) (Figure 2.16). The large seasonal difference found at BRW is a common feature of CO at sites throughout the Arctic (Figure 2.17a).

The RGA at MLO continued to be plagued by problems. In late 1996 chromatographic parameters of the instrument became erratic, and during the next few months various parts were replaced and columns reconditioned. After no improvement, the instrument was returned to Boulder. This instrument continues to experience reoccurring problems with its hardware and has not yet been returned to the observatory.

2.4.2. Flask Measurements of Carbon Monoxide

The expansion of the number of sites in the CMDL cooperative air sampling network from which CO was determined continued to increase during the past few years. Only glass flasks fitted with glass pistons and Teflon O-rings were used for CO analysis. These flasks have been gradually introduced to the network by replacing the previously used glass flasks, which had greased ground glass stopcocks, and by providing all new sites with the greaseless flasks. By 1996 nearly all network sites used flasks suitable for CO measurements. The annual mean CO mole fractions for 1996 and 1997 are given in Tables 2.8 and 2.9. With many more sites measuring CO than in previous years, its global distribution is now better determined. In particular, more locations in the high southern latitudes are being sampled. Mole fractions measured at the antarctic sites are typically the lowest found on Earth. As observed in the high latitudes of the northern hemisphere, the time series from individual sites in the high southern hemisphere also show very similar features (Figure 2.17b). The seasonal cycles in both the arctic and antarctic are thought to reflect the effects of both transport of polluted air from lower latitudes plus photochemical production and destruction of CO.

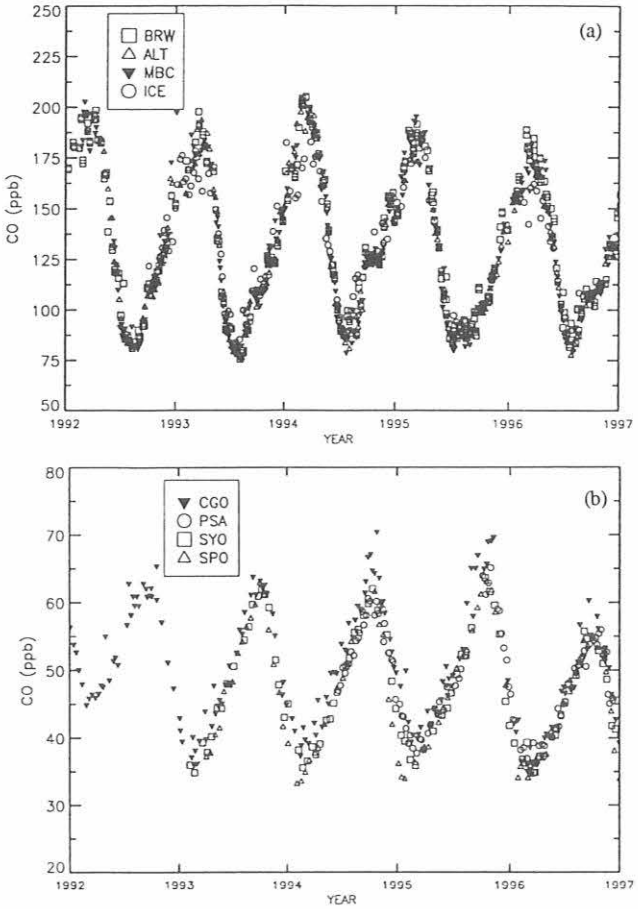

Fig. 2.17. (a) Overlay of time series determined from grab samples from Alert, Canada, Mould Bay, Canada, Point Barrow, Alaska, and Iceland. (b) Same for sites located in the high southern hemisphere.

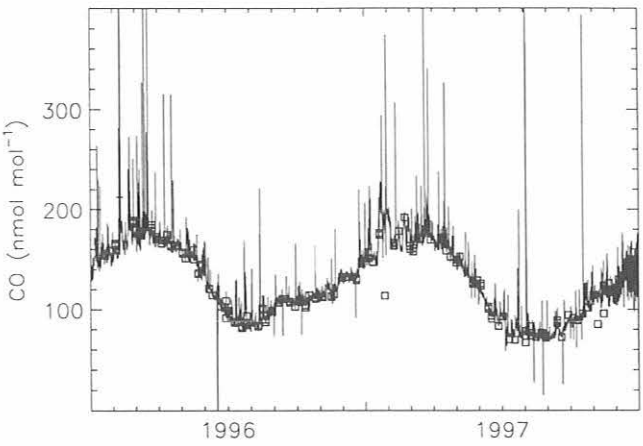

Fig. 2.16. Carbon monoxide time series determined at BRW. Solid lines are hourly means of four to five analyses per hour. Circles are mole fractions determined from grab samples.

The seasonal CO maximum in the southern hemisphere was quite depressed in 1996. However, many sites in the tropics and extratropics showed a strong recovery during 1997 (Figure 2.18). The relatively large annual mean CO values reported for 1997 in the low latitudes of the South China Sea (Table 2.9) reflect very high CO levels during August, September, and October. The magnitude of the seasonal maximum in the southern hemisphere is believed to be driven largely by seasonal biomass burning [*Novelli et al.,* 1998]. Widespread fires, fostered by dry weather typical of El Niño conditions, occurred in Indonesia during June to November 1997. The enhanced CO levels found in the south during spring 1997 most likely resulted from these fires. Samples of air collected from a commercial jet over Indochina during this period show elevated CO in the middle troposphere, presumably resulting from the vertical transport of gases from the polluted boundary layer [*Matsueda et al., 1998,* H. Matsueda, personal communication, 1998].

TABLE 2.8. Preliminary 1996 and 1997 Annual Mean CO Mole Fractions from Land Sites

Site Code	Station	Annul Mean CO (ppb) 1996	1997
ALT	Alert, Canada	127.5	124.1
ASC	Ascension Island	64.4	71.8
BAL	Baltic Sea	166.5	177.8
BME	Bermuda (east coast)	122.6	118.0
BMW	Bermuda (west coast)	118.9	122.8
BSC	Black Sea, Constanta	265.8	235.8
BRW	Point Barrow, Alaska	131.8	121.5
CBA	Cold Bay, Alaska	129.8	123.8
CGO	Cape Grim, Tasmania	45.5	47.6
CHR	Christmas Island	[ ]	[ ]
CMO	Cape Meares, Oregon	133.5	128.1
CRZ	Crozet Island	46.2	[ ]
EIC	Easter Island, Chile	55.3	52.9
GMI	Marianas Island, Guam	84.0	93.8
GOZ	Gozo, Malta	155.9	[ ]
HUN	Hegyhatsal, Hungary	261.2	235.3
ICE	Vestmannaeyjar, Iceland	125.3	121.4
ITN	Grifton, North Carolina	171.7	165.2
IZO	Izana, Tenerife	97.2	94.7
KEY	Key West, Florida	108.2	112.7
KUM	Cape Kumukahi, Hawaii	97.7	94.2
LEF	Park Falls, Wisconsin	149.8	139.3
MBC	Mould Bay, Canada	129.4	[ ]
MHT	Mace Head, Ireland	130.8	116.9
MID	Midway Island	119.8	95.8
MLO	Mauna Loa, Hawaii	83.3	94.2
NWR	Niwot Ridge, Colorado	117.4	117.3
PSA	Palmer Station	44.9	44.5
QPC	Qinghai Province, China	117.2	124.0
RPB	Ragged Point, Barbados	91.3	88.1
SEY	Seychelles	77.0	90.1
SMO	American Samoa	58.8	56.0
SPO	South Pole, Antarctica	43.5	43.6
SYO	Syowa, Antarctica	44.0	[ ]
TAP	Tae-ahn Penisula, South Korea	224.3	234.5
UUM	Ulaan Uul, Mongolia	145.8	138.8
WIS	Negev Desert, Israel	152.8	145.7
ZEP	Ny-Alesund, Svalbard	129.8	124.1

TABLE 2.9. Provisional Annual Mean CO From Shipboard Programs

Latitude	Annual Mean (ppb) 1996	1997
	*Pacific Ocean**	
N30	111.8	-
N25	114.1	-
N20	95.8	-
N15	89.8	-
N10	81.6	-
N05	66.7	-
000	61.2	-
S05	59.7	-
S10	54.4	-
S15	53.4	-
S20	52.4	-
S25	51.2	-
S30	50.0	-
S35	51.2	-
	South China Sea	
N21	247.3	221.9
N18	157.2	155.8
N15	146.1	153.5
N12	130.5	145.3
N09	124.6	154.8
N06	108.5	164.9
N03	129.3	161.6

*Annual mean values are not reported for 1997 as no samples were collected during December 1997.

It is clear that there is considerable variability in levels of tropospheric CO as is evident, for example, in the 15-year record from Cape Point, South Africa [*Scheel et al.*, 1996]. The shorter record of global measurements also shows periods of CO increase and decrease. To study global trends in CO, the time series from all marine background sampling locations were combined and smoothed to provide a surface representing tropospheric CO as a function time and latitude. From this surface, global trends were extracted. This surface also provides averaged time series for the two hemispheres and four semi-hemispheres, from which zonal trends were also calculated. After a sharp decline in global CO levels during 1992-1993 [*Novelli et al.*, 1994], there was some recovery during 1994-1995 [*Novelli et al.*, 1998]. However, the recovery in the southern hemisphere was short-lived, and another decline in CO occurred during 1996. The temporally averaged global rate of change was -2.1 ppb CO yr^{-1} from 1991 through 1996. This is equivalent to a decrease of approximately 2.4% yr^{-1} relative to average mole fractions in 1991. The zonally-averaged decrease in the northern hemisphere (-2.3 ppb yr^{-1}) was greater than that in the southern hemisphere (-1.9 ppb yr^{-1}). These decreases are believed to be due primarily to changes in emissions from fossil fuel emissions and biomass burning [*Novelli et al.*, 1994, 1998].

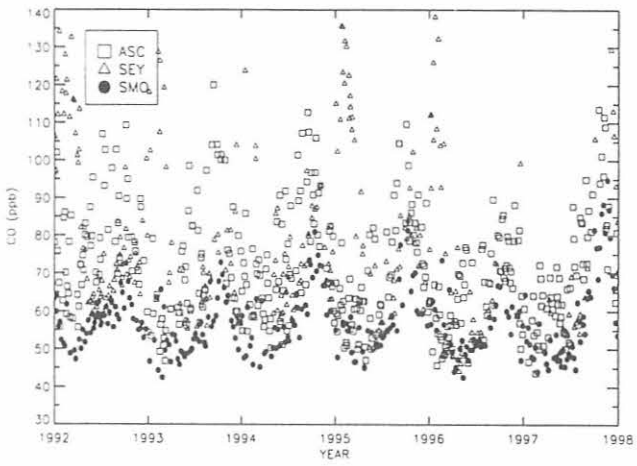

Fig. 2.18. Time series from the Seychelles (4°S), Ascension Island (8°S), and American Samoa (14°S).

2.5. HYDROGEN

Beginning in 1989 the mole fraction of molecular hydrogen (H_2) has been measured in samples of air collected as part of the CMDL air sampling network. Only glass flasks with Teflon O rings were used. The Reduced Gas Detector used for CO measurements was also used to determine H_2. The analysis included a single calibration gas with approximately 500 ppb H_2 that was compared to each sample. Multiple calibration standards were maintained through frequent intercomparisons, and although the mole fractions assigned to these standards were based upon a somewhat arbitrary scale, the standards were all internally consistent. A set of H_2-in-air standards was recently prepared by gravimetric techniques in collaboration with the CMDL Nitrous Oxide and Halocarbon (NOAH) Group. These provide a range of mole fractions between 480 and 600 ppb. All working standards were recalibrated against the gravimetric standards. The archived peak height responses from all air samples analyzed since the beginning of the program were then used to recalculate sample H_2 mole fractions using the new values assigned to the standards. The gravimetric scale was about 6% higher than the preliminary working scale. The data set now provides H_2 time series from 48 sites used to study local, regional, and global scale distributions. Annual average mole fractions from network sites are given in Table 2.10. The north-to-south gradient of increasing annual mean mole fractions is unusual; many gases with anthropogenic sources (such as CO_2, CO, and CH_4) have higher levels in the industrialized northern hemisphere.

There is about 3% more H_2 in the southern troposphere than in the north. Figure 2.19 presents the times series from two sites representative of the northern and southern hemispheres: BRW located at 71°N, and Cape Grim, Tasmania (CGO) at 41°S. The large seasonal cycle found at BRW contrasts the much smaller variation at CGO. At BRW the mole fraction ranges from approximately 460 to 530 ppb with highest levels in late winter and early spring and lowest levels in fall. At Cape Grim the amplitude of the seasonal cycle is smaller with a maximum of 550 ppb and a seasonal minimum of about 520 ppb. The differences between the two sites, and similarly between the two hemispheres, are determined primarily by the strength of the seasonal drawdown. The two main sinks

TABLE 2.10. Provisional Annual Mean H_2 Mole Fractions From Land Sites

Site Code	Station	1992	1993	1994	1995	1996
ALT	Alert, Canada	[ ]	491.8	482.2	483.4	483.1
ASC	Ascension Island	543.1	536.9	536.4	540.4	537.1
BAL	Baltic Sea	[ ]	523.0	516.9	513.0	518.0
BME	Bermuda (east coast)	533.1	523.8	519.6	524.0	529.1
BMW	Bermuda (west coast)	549.1	543.1	534.0	533.7	538.9
BRW	Point Barrow, Alaska	498.9	487.1	488.3	479.3	486.4
CBA	Cold Bay, Canada	[ ]	498.3	499.8	495.1	499.1
CGO	Cape Grim, Tasmania	536.2	532.5	530.0	536.5	536.4
CHR	Christmas Island	536.8	540.6	536.4	539.9	538.1
CMO	Cape Meares, Oregon	525.2	503.5	500.5	497.6	500.9
CRZ	Crozet Island	[ ]	[ ]	[ ]	541.9	536.8
EIC	Easter Island, Chile	[ ]	[ ]	538.5	545.7	537.9
GMI	Guam	543.7	537.1	534.1	537.9	537.5
GOZ	Gozo, Malta	[ ]	[ ]	527.4	522.1	522.3
HUN	Hegyhatsal, Hungary	[ ]	[ ]	530.2	532.7	543.8
ICE	Vestmannaeyjar, Iceland	[ ]	505.1	502.3	495.7	497.8
ITN	Grifton, North Carolina	[ ]	532.7	528.1	526.6	532.1
IZO	Izana, Tenerife	548.7	537.1	531.3	534.2	531.9
KEY	Key West, Florida	537.9	540.9	533.8	536.6	532.4
KUM	Cape Kumukahi, Hawaii	522.6	516.6	512.1	516.3	512.9
LEF	Park Falls, Wisconsin	[ ]	[ ]	[ ]	502.9	492.8
MBC	Mould Bay, Canada	489.9	487.1	488.8	483.3	486.4
MHT	Mace Head, Ireland	515.7	516.2	512.7	514.5	510.5
MID	Midway Island	533.7	523.8	525.3	525.2	525.8
MLO	Mauna Loa, Hawaii	537.7	527.3	522.0	531.0	529.0
NWR	Niwot Ridge, Colorado	528.1	528.0	519.1	515.5	518.0
PSA	Palmer Station, Antarctica	[ ]	[ ]	[ ]	536.5	536.1
QPC	Mt. Waliguan, China	503.5	498.9	505.1	512.1	502.4
RPB	Ragged Point, Barbados	[ ]	534.7	532.1	538.6	535.3
SEY	Seychelles	545.0	538.0	533.1	537.6	540.4
SMO	American Samoa	552.4	534.9	537.3	540.7	537.5
SPO	South Pole, Antarctica	[ ]	[ ]	529.7	534.6	531.8
SYO	Syowa, Antarctica	[ ]	[ ]	530.4	536.5	537.8
TAP	Tae-ahn Penisula, South Korea	537.5	527.4	527.9	512.6	528.3
UUM	Ulaan Uul, Mongolia	491.1	485.5	495.0	480.8	492.5
ZEP	Ny-Alesund, Svalbard	[ ]	[ ]	493.7	491.9	496.1

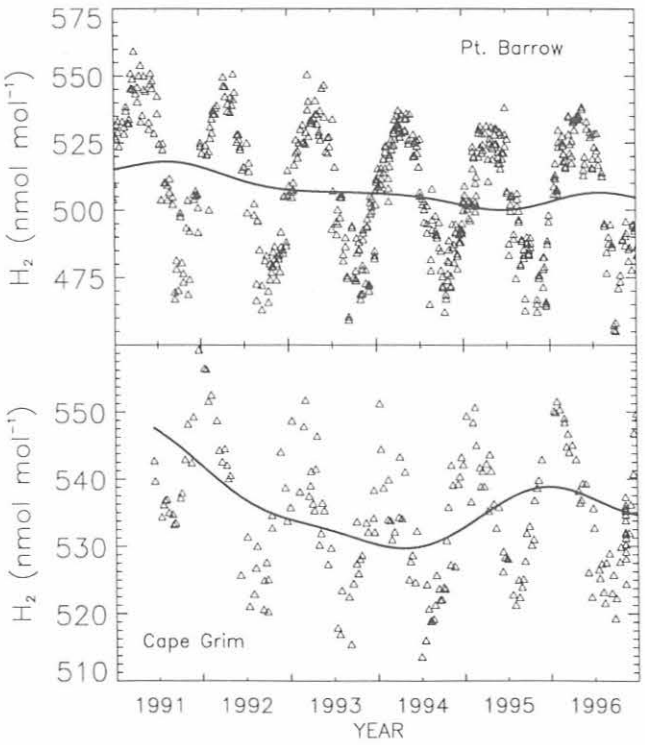

Fig. 2.19. Time series of hydrogen mole fractions: (Top) Point Barrow, Alaska, and (Bottom) Cape Grim, Tasmania.

for H_2 are believed to be reaction with OH radicals and deposition at the surface through the activities of terrestrial microbes [*Warneck,* 1988 and references therein]. Since the amount of H_2 removed by OH is approximately the same in both hemispheres, biological uptake on northern continents is the likely cause of the observed differences between the hemispheres [also see *Khalil and Rasmussen,* 1989].

Levels of H_2 have decreased at many of the network sites during the past 6 years. A smoothed surface of H_2 distributions versus latitude and time was constructed. From this surface, a globally-averaged rate of change equal to -2.33 ppb (0.44%) H_2 yr^{-1} was determined. The average decrease in the northern hemisphere was greater than that in the southern hemisphere: -2.71 ppb (0.51%) yr^{-1} and -1.96 ppb (0.36%) yr^{-1}, respectively. These differences most likely reflect either decreases in H_2 emissions from fossil fuel combustion (primarily gasolines) and/or increases in surface uptake in the northern hemisphere.

2.6. Nitrous Oxide and Sulfur Hexafluoride

The ongoing collaboration between CCG and NOAH on measurements of N_2O and SF_6 from at least a subset of the sites in the Carbon Cycle Group's cooperative air sampling network continued during 1996 and 1997. Data from Bermuda East are plotted in Figure 2.20.

A significant change in measurement procedures occurred in mid-1997. Since then, samples from all CCG network sites have been analyzed for N_2O and SF_6 using the electron capture detector (ECD) channel of the new CCG analysis system, MAGICC. The chromatographic method is the same as used previously, but the analytical instrument has changed leading to significantly improved precision. Typical precision for N_2O, determined from repeated injections of standard gas, is 0.2 ppb or 0.06% relative. Samples are now bracketed by a single standard gas and N_2O mole fractions are calculated from an instrument response curve that accounts for the highly nonlinear nature of the ECD. This curve was determined in a separate automated procedure, and it is based on three well-calibrated standards from the NOAH Group. These standards have N_2O mole fractions of 300.9, 311.8, and 335.2 ppb. The nonlinearity correction for samples is large, 0.3 ppb per 1 ppb difference from the assigned standard value. Samples are quantified for SF_6 using a single point calibration assuming linear extrapolation through zero.

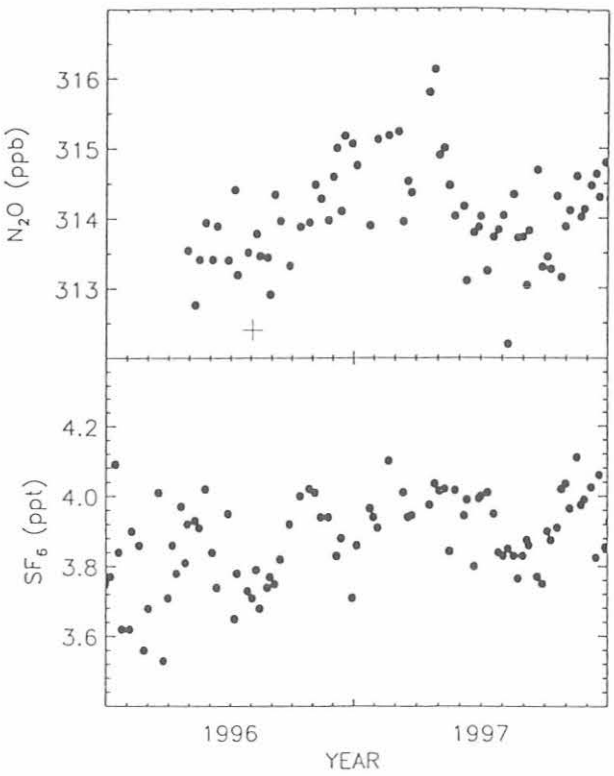

Fig. 2.20. Nitrous oxide (in nmol) and SF_6 (in pmol; abbreviated ppt) mole fractions from Bermuda East. Measurements were edited for sampling and analysis errors and selected for background conditions. One sample flagged as nonbackground is shown for N_2O. Measurements made since August 1997 were made on the MAGICC analytical system; measurements made prior to that were from the Dragons GC [*Tans et al.*, 1996, section 2.5].

2.7. MAGICC Analysis System

Though the CCG air sampling network has not expanded much in recent years, the number of people in the group has decreased, and the new MAGICC analysis system requires significantly fewer person-hours to complete measurements of all species. A schematic diagram of the

system's plumbing is shown in Figure 2.21. The analyzers used, and the precision obtained from them, are summarized in Table 2.1. A Hewlett Packard (HP) UNIX workstation is interfaced to the all components in the analysis system by a VXI bus. Air samples are introduced into the system using a custom-made sample inlet system. The operator interface is through Netscape. Samples are analyzed in groups of up to eight. MAGICC makes efficient use of the analysis day; the operator can prepare a new set of samples for analysis before the previous set has finished. For species analyzed by a gas chromatograph (GC) (all but CO_2), instrument signals are digitized using a 24-bit HP 35900 A/D and peaks are integrated by the MAGICC analysis program.

A typical analysis day is as follows. The operator makes a preliminary check of all instruments and gas cylinders, then flushes the standard gas regulators four times each. A 48-min. pre-analysis check is started to "warm-up" the analyzers. During this time up to eight samples are connected to the 8-port sample inlet system. Once the pre-analysis check is complete, a separate flask analysis program is started, and MAGICC immediately begins the first measurement of standard gas for each species. During the time the standard gases are being analyzed, MAGICC asks the operator how many flasks will be analyzed (1-8) then begins evacuating the dead volumes at the gas-tight connections where the flasks attach to the manifold, and it checks for leaks. If no leaks are found, the operator is asked to open the stopcocks. Analysis of the first flask sample begins when the first round of standards is complete. The operator can then enter flask IDs into a table (this can be done anytime before the analysis is stopped) and record system parameters (signal levels, cylinder pressures, etc.) into an electronic daily work sheet. It is important for the operator to watch the progress of the analysis cycle. Near the end of the cycle, analyzed flasks are removed and unanalyzed flasks are added to the manifold. The first sample of the next set is started without delay. Mole fractions are calculated in real time. At the end of the day, the operator stops the analysis program, and the program immediately writes all analysis information to the appropriate site and raw data files.

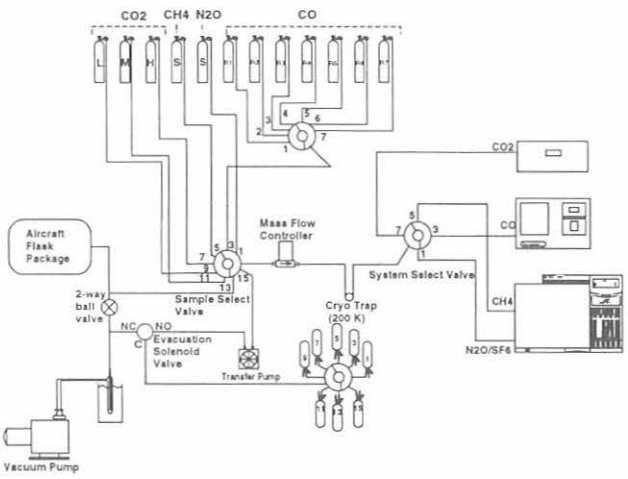

Fig. 2.21. Schematic diagram of the MAGICC analysis system.

Significant advantages that MAGICC offers over the previous systems are: (1) All analytical instruments and data acquisition systems offer the highest possible precision CCG is capable of. This is especially true of N_2O measurements where a factor of three improvement in precision was obtained. (2) One analysis system and one operator replaces three systems and operators. Samples are handled only once for the complete set of trace gas analyses. (3) The system, and its user interface (written into Netscape), are easy to learn. Using Netscape also allows the system to be accessed remotely. (4) The analysis day is used very efficiently; the instruments are not sitting idle unnecessarily.

2.8. Measurements on Tall Towers

The main goals of the tower program are to obtain regionally representative measurements of the mole fractions of CO_2 and other tracers in the continental planetary boundary layer (PBL) and to provide data to improve quantitative understanding of the processes that cause trace gas abundances over the continents to differ from those at "background" stations. For CO_2 these processes include regional fossil fuel combustion, exchange with the terrestrial biosphere (photosynthesis and respiration), and PBL dynamics and exchange of air with the overlying free troposphere (entrainment). In addition there are important feedbacks between these processes we seek to understand through our measurements. For example, vegetation has a strong influence on the surface energy budget, mainly through surface albedo and energy partitioning between sensible and latent heat, and thereby influences the daily development of the PBL and cloud-induced entrainment. Also, surface exchange (photosynthesis and respiration) and PBL mixing co-vary on diurnal and seasonal timescales as was discussed by *Denning et al.* [1996]. Continuous measurements of CO_2 in the mid-PBL, along with characterization of PBL mixing and cloud processes, are necessary observations for quantifying these effects.

The tower program consists of continuous observations of CO_2 and other tracers on two tall communications towers in the U.S.: the North Carolina (NC) tower (610 m tall, 35.37°N, 77.39°W, 9 m above sea level) in a rural area of the southeast and the Wisconsin (WI) tower (447 m tall, 45.95°N, 90.27°W, 472 m above sea level) located in a sparsely populated area of the upper Midwest (Chequamegon National Forest). The regions around the towers differ greatly in climate, land use, and human population density (Table 2.11).

Measurements began at the NC tower in June 1992 and at the WI tower in October 1994. Observations of CO_2 and basic meteorological variables (wind speed and direction, air temperature, humidity and pressure, etc.) are described by *Bakwin et al.* [1995]. We also measure CH_4, CO, H_2, CFC-11, CFC-12, CFC-113, CH_3CCl_3, CCl_4, $CHCl_3$, C_2Cl_4, SF_6, and N_2O by in situ gas chromatography (GC) in collaboration with the NOAH group, as described by *Hurst et al.* [1997]. The GC observations are of particular value for identifying

TABLE 2.11. Meteorological Data and Human Population Densities Near the North Carolina and Wisconsin Towers

	North Carolina	Wisconsin
Annual precipitation	130.2 cm	79.5 cm
Annual average temperature	16.4°C	4.1°C
Jan. average temperature	5.5°C	-12.9°C
July average temperature	25.9°C	18.9°C
Population density*	64 km^{-2}	5 km^{-2}

*Population densities are given for the counties in which the towers are located: Pitt (NC) and Price (WI).

pollution sources of CO_2 since the CFCs, other halocarbons (except $CHCl_3$), and SF_6 are only emitted from anthropogenic sources and their mole fractions are highly correlated in pollution plumes [*Bakwin et al.,* 1997]. Further, CO is a key tracer for combustion. Methane, H_2, and N_2O have significant biogenic fluxes.

The WI tower is also a component of the AmeriFlux network for long-term, ecosystem scale studies of atmosphere and surface exchange of CO_2, H_2O, and energy [see *Wofsy and Hollinger,* 1998]. We measure fluxes of CO_2, H_2O, sensible heat, and momentum using eddy covariance with sensors located 30, 122, and 396 m above the ground. Collaborative investigations (observations and modeling) are underway to characterize the biophysical environment, separate component fluxes (e.g., photosynthesis and respiration, transpiration, and evaporation), understand spatial variability of surface fluxes with reference to varied land cover types, and study dynamics of the PBL and exchange of air between the PBL and free troposphere. The overall program surrounding the WI tower is known as the Chequamegon Ecosystem/Atmosphere Study (CHEAS, see homepage at http://ra.forest.wisc.edu/cheas).

A recent paper [*Bakwin et al.,* 1998] provides an overview of CO_2 data from the WI and NC towers, compares the tower data to "background" (marine boundary layer) sites from the Globalview dataset, and suggests ways in which the results could be used in models to improve understanding of the global carbon cycle. The tower CO_2 mole fractions and meteorological data are available on the CMDL website.

Landscape scale surface fluxes of H_2 and CH_4 at the WI tower have been determined from hourly GC measurements of their vertical profiles in the PBL and from eddy covariance measurements of CO_2 surface fluxes at 30 m above ground [*Hurst et al.,* 1998]. Large vertical gradients of H_2, CH_4, and CO_2 are observed at night when surface fluxes enrich CH_4 and CO_2, and deplete H_2 in the shallow stable layer. Nighttime surface fluxes of CH_4 and H_2 are calculated using surface layer similarity theory from measured CO_2 fluxes and vertical gradients of H_2, CH_4, and CO_2. Daytime fluxes are extrapolated from nighttime data using the observed relationship between fluxes and soil temperature at 10 cm depth. Relationships with soil moisture will be explored in future work. Given the height of CO_2 flux measurements and the stability of the atmosphere at night, surface fluxes integrate over ~30 km^2 footprints that include both wet, lowland soils (bogs, fens) and dry, upland forest soils.

2.9. Aircraft Profiles

Vertical profiles of CO_2, CH_4, and CO were collected weekly over Carr, Colorado (40.9°N 104.8°W) during 1996 and 1997. The air samples were collected from a Cessna 210T starting at an altitude of approximately 7.9 km above sea level down to 2.1 km above sea level. Twenty samples were collected on each flight. During 1996 we had approximately 25 successful flights and in 1997 we increased the number of profiles to 41. Poor weather conditions, airplane problems, or pilot scheduling conflicts contributed to missing flights.

We officially terminated the Moscow, Russia, sampling site with Aviaecocentre in July 1997. During 1996, seven profiles were collected from the site located approximately 100 km southeast of Moscow (54.9°N 35.5°E). The last successful flight was in December 1996.

The costs associated with operating this site were too high for us to be able to continue sampling.

In December 1996 we started sampling near Howland, Maine [42.2°N, 68.1°W] in collaboration with the University of New Hampshire. We collected data from three flights. Sampling equipment problems caused us to suspend sampling in the summer of 1997. We may be able to restart sampling at this site in the future.

2.10. Data Integration (Globalview)

Inverse modeling efforts of recent years have made it very clear that the atmospheric data base is still very sparse for the purpose of deducing with confidence regional scale CO_2 sources and sinks from areas as large as continents. The latitudinal distribution of sources is much better constrained by the present data than any partitioning of those sources by longitude. The latter is much harder because of rapid east-west mixing in the atmosphere relative to north-south. Rapid mixing tends to erase concentration gradients. We don't know how to put quantitative constraints on large regional scale sources without making use of observed large-scale atmospheric concentration patterns. We need them as a tool to test and verify our extrapolations of knowledge and measurements of fluxes in specific locales to regional scales. The first order of business is to try integrating the data from measurement programs already existing in many nations. Thus Globalview was born.

Building on a statistical "data extension" technique to interpolate (and extrapolate!) missing data [*Masarie and Tans,* 1995], the Globalview-CO_2 database currently combines time-smoothed atmospheric CO_2 data from 13 different laboratories, with special attention devoted to calibration and methodology. The data extension is included to (partially) address the issue of biases that emerge as observational sites are added and abandoned over time. It is very transparent in the Globalview database which data sections are missing, leaving modelers the option to either use or ignore the interpolated portions. Suggested "weight" files are included which reflect, by year, the high-frequency variance (low variance equals high weight) and the number of valid data points (more data equals higher weight). Again, modelers are free to make use of the weights or not, or they may construct their own weighting scale.

One of the benefits to participating laboratories is that Globalview is also a tool to increase quality control of the measurements. Data submitted for inclusion in Globalview are plotted against a marine boundary reference curve and against data from other stations often contributed by other laboratories. Invariably, these comparisons raise scientific questions as well as increased scrutiny of the data themselves. Further motivation for quality control comes from feedback from modelers who may conclude things that, to measurement people, would appear to be over-interpretations of their data.

The first release of Globalview-CO_2 occurred in 1996, the second and third in August of 1997 and 1998, respectively. Figure 2.22 shows the number of electronic requests for the database, by month and by country.

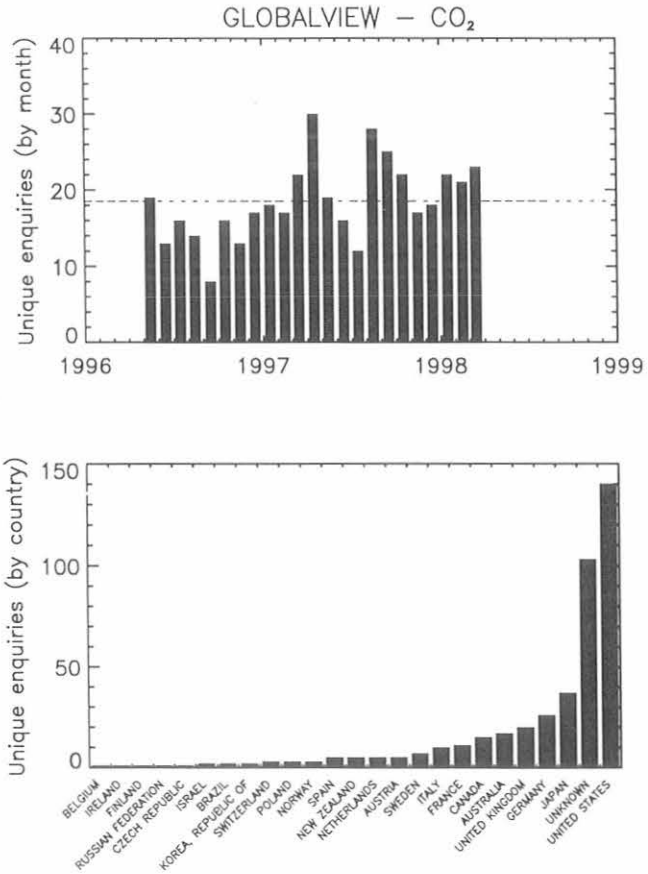

Fig. 2.22. Number of electronic requests for Globalview-CO_2.

2.11. Inverse Modeling

The success of future policies to limit atmospheric CO_2 emissions depends critically on the ability to understand and quantify the budget of CO_2, in particular the distributions of CO_2 sources and sinks. Over the past decade inverse modeling techniques, which have a long tradition of application to geophysical problems such as seismology, satellite data retrieval, and acoustic tomography, have been applied to the problem of determining the source and sink distribution of atmospheric CO_2. Early attempts were aimed at obtaining the interhemispheric gradient of the CO_2 sources and sinks [*e.g., Tans et al.,* 1989, 1990a; *Enting et al.,* 1991; *Ciais et al.,* 1995a,b; *Bousquet et al.,* 1996; *Law et al.,* 1996]. With the expansion of the CO_2 observational network, and especially after Globalview became available to the community, attempts have been made over recent years to obtain source and sink distributions over continental scales. A number of inverse techniques are currently being tested by various groups, and two common problems have emerged: (1) the calculation can be quite unstable due to the relative sparseness of the observational network, and (2) the transport models likely do not represent transport processes as realistically as desired.

Over the past few years we have developed an inverse technique and studied its performance using the TM2 model [*Heimann,* 1995]. In general, the inversion uses data from the CO_2 observational network and forward simulations of atmospheric CO_2 from 14 continental and oceanic regions, each with a standardized source strength. The linear combination of the calculated CO_2 pattern from each of the regions that provides the best fit to observations is calculated using the singular value decomposition technique.

The technique was first tested by performing forward calculations of CO_2 using source and sink distributions that were as realistic as possible [*Ramonet,* 1994]. These model calculations then provided a set of "pseudodata" that were used to test whether or not the inversion technique was capable of recovering the source and sink distributions used in the forward calculation. It was found that with a network comprised of as few as 144 regularly-spaced stations, the initial source and sink distributions could be recovered fairly accurately. The errors increased significantly when the "observational network" was reduced to 50 stations. The use of modeled CO_2 abundances at the same locations as CMDL observing sites resulted in additional error due to lack of data over large continental regions, especially Africa and South America. Preliminary results show that the error can be significantly reduced by the addition of a surface site in central Brazil.

We are participating in the multi-laboratory Carbon Modeling Consortium that aims to make more rapid progress in deciphering and predicting the global carbon cycle by bringing together atmospheric and oceanic data in a global modeling environment.

Our future work will be focused primarily on two issues: (1) interannual variability of CO_2 sources and sinks and (2) design of an optimized atmospheric observational network.

2.12. References

Bakwin, P.S., C. Zhao, W. Ussler, III, P.P. Tans, and E. Quesnell, Measurements of carbon dioxide on a very tall tower, *Tellus, 47*B, 535-549, 1995.

Bakwin, P.S. (ed.) et al., Carbon Cycle Division, Chapter 2, in *Climate Monitoring and Diagnostics Laboratory No. 22 Summary Report 1993*, edited by J.T. Peterson, and R.M. Rosson, pp. 18-30, NOAA Environ. Res. Labs., Boulder, CO., 1994.

Bakwin, P.S., D.F. Hurst, P.P. Tans, and J.W. Elkins, Anthropogenic sources of halocarbons, sulfur hexafluoride, carbon monoxide, and methane in the southeastern United States, *J. Geophys. Res., 102*, 15,915-15,925, 1997.

Bakwin, P.S., P.P. Tans, D.F. Hurst, and C. Zhao, Measurements of carbon dioxide on very tall towers: An update of the NOAA/CMDL program, submitted to *Tellus*, 1998.

Bousquet, P., P. Ciais, P. Monfray, Y. Balkanski, M. Ramonet, and P.P. Tans, Influence of two different atmospheric transport models on inferring sources and sinks of atmospheric CO_2, *Tellus, 48*(B), 568, 1996.

Ciais, P., P.P. Tans, J.W.C. White, M. Trolier, R.J. Francey, J.A. Berry, D.R. Randall, P.J. Sellers, J.G. Collatz, and D.S. Schimel, Partitioning of ocean and land uptake of CO_2 as inferred by del C13 measurements from the NOAA CMDL global air sampling network, *J. Geophys. Res., 100*, 5051-5070, 1995a.

Ciais, P., P.P. Tans, M. Trolier, J.W.C. White, and R.J. Francey, A large northern hemisphere terrestrial CO_2 sink indicated by the $^{13}C/^{12}C$ ratio of atmospheric CO_2, *Science, 269*, 1098-1102, 1995b.

Ciais, P., et al., A three-dimensional synthesis study of $\delta^{18}O$ in atmospheric CO_2. 1. Surface fluxes, *J. Geophys. Res., 102*(D5), 5857-5872, 1997.

Conway, T.J., P.P. Tans, L.S. Waterman, K.W. Thoning, D.R. Kitzis, K.A. Masarie, and N. Zhang, Evidence for interannual variability of the carbon cycle from the NOAA/CMDL global air sampling network, *J. Geophys. Res., 99*, 22,831-22,855, 1994.

Denning, A.S., D.A. Randall, G.J. Collatz, and P.J. Sellers, Simulations of terrestrial carbon metabolism and atmospheric CO_2 in a general circulation model, Part 2: Simulated CO_2 concentrations, *Tellus, 48*B, 543-567, 1996.

Dlugokencky, E.J., L.P. Steele, P.M. Lang, and K.A. Masarie, Atmospheric methane at Mauna Loa and Barrow observatories: Presentation and analysis of in situ measurements, *J. Geophys. Res., 100*, 23,103-23,113, 1995.

Dlugokencky, E.J., K.A. Masarie, P.M. Lang, P.P. Tans, L.P. Steele, and E.G. Nisbet, A dramatic decrease in the growth rate of atmospheric methane in the northern hemisphere during 1992, *Geophys. Res. Lett., 21*, 45-48, 1994.

Dlugokencky, E.J., K.A. Masarie, P.M. Lang, and P.P. Tans, Continuing decline in the growth rate of atmospheric methane, *Nature, 393*, 447-450, 1998.

Enting, I.G., and J.V. Mansbridge, Latitudinal distribution of sources and sinks of CO_2: Results of an inversion study, *Tellus, 43*(B), 156-170, 1991.

Fung, I., J. John, J. Lerner, E. Matthews, M. Prather, L.P. Steele, and P.J. Fraser, Three dimensional model synthesis of the global methane cycle, *J. Geophys. Res., 96*, 13,033-13,065, 1991.

Gemery, P.A., M. Trolier, and J.W.C. White, Oxygen isotopic exchange between carbon dioxide and water following atmospheric sampling using glass flasks, *J. Geophys. Res., 101*, 14,415-14,420, 1996.

Heimann, M., The global atmospheric tracer model TM2, *Technical Report No. 10*, 53 pp., edited by D. Klimarechenzentrum, Max Planck Institut fur Meteorologie, Germany, 1995.

Hurst, D.F., P.S. Bakwin, R.C. Myers, and J.W. Elkins, Behavior of trace gas mole fractions at a very tall tower site in North Carolina, *J. Geophys. Res., 102*, 8825-8835, 1997.

Hurst, D.F. P.S. Bakwin, K.J. Davis, and C. Zhao, Landscape-scale surface-atmosphere exchanges of methane and hydrogen in a lowland and wetland boreal forest, submitted to *Glob. Biogeochem. Cycles*, 1998.

Khalil, M.A.K., and R.A. Rasmussen, Distribution and mass balance of molecular hydrogen in the Earth's atmosphere, in *GMCC No. 17 Summary Report 1988*, edited by J.W. Elkins and R.M. Rosson, pp. 111-113, NOAA Environ. Res. Labs., Boulder, CO, 1989.

Law, R.M., and I. Simmonds, The sensitivity of deduced CO_2 sources and sinks to variations in transport and imposed surface concentrations, *Tellus, 48*(B), 613, 1996.

Masarie, K.A., Steele, L.P., and Lang, P.M., A rule-based expert system for evaluating the quality of long-term, in situ gas chromatographic measurements of atmospheric methane, *NOAA Tech. Memo. ERL CMDL-3*, Boulder, CO, 1991.

Masarie, K.A. and P.P. Tans, Extension and integration of atmospheric carbon dioxide data into a globally consistent measurement record, *J. Geophys. Res., 100*, 11,593-11,610, 1995.

Matsueda, H., H.Y. Inoue, Y. Sawa, Y. Tsutsumi, and M. Ishii, Carbon monoxide in the upper troposphere over the western Pacific between 1993 and 1996, *J. Geophys. Res.*, in press, 1998.

Novelli, P.C., K.A. Masarie, P.M. Lang, and P.P. Tans, Recent changes in atmospheric carbon monoxide, *Science, 263*, 1587-1590, 1994.

Novelli, P.C., K.A. Masarie, and P.M. Lang, Distributions and recent changes in tropospheric carbon monoxide in the lower troposphere, *J. Geophys. Res., 103*(D15), 19,015-19,033, 1998.

Prinn, R.G., R.F. Weiss, B.R. Miller, J. Huang, F.N. Alyea, D.M. Cunnold, P.J. Fraser, D.E. Hartley, and P.G. Simmonds, Atmospheric trends and lifetime of CH_3CCl_3 and global OH concentrations, *Science, 269*, 187-192, 1995.

Ramonet, M., Modelisation du transport atmospherique du dioxyde de carbone dans l'hemisphere sud, PhD. thesis, Univ. of Paris VII, 295 pp., 1994.

Schell, H.E., R. Sladkovic, and E.-G. Brunke, Temporal variations of O_3 and CO at mid-latitude sites in the Northern and Southern Hemispheres, (extended abstract), WMO-IGAG Conference on the Measurement and Assessment of Atmospheric Composition Change, Beijing, China, Oct. 9-14, 1995, WMO, Global Atmospheric Watch, No. 107, 123-127, Geneva, 1996.

Tans, P.P., T.J. Conway, and T. Nakazawa, Latitudinal distribution of the sources and sinks of atmospheric carbon dioxide derived from surface observations and atmospheric transport model, *J. Geophys. Res., 94*, 5151-5172, 1989.

Tans, P.P., I.Y. Fung, and T. Takahashi, Observational constraints on the global atmospheric carbon dioxide budget, *Science, 247*, 1431-1438, 1990a.

Tans, P.P., K.W. Thoning, W. P. Elliott, and T.J. Conway, Error estimates to background atmospheric CO_2 patterns from weekly flask samples, *J. Geophys. Res., 95*, 14,063-14,070, 1990b.

Tans, P.P., Oxygen isotopic equilibration between carbon dioxide and water in soils, *Tellus, 50B*, 163-178, 1998.

Tans, P.P. (ed.) et al., Carbon Cycle, Chapter 2, in *Climate Monitoring and Diagnostics Laboratory No. 23 Summary Report 1994-1995*, edited by D.J. Hofmann et al., pp. 29-49, NOAA Environ. Res. Labs., Boulder, CO., 1996.

Trolier, M., J.W.C. White, P.P. Tans, K.A. Masarie, and P.A. Gemery, Monitoring the isotopic composition of atmospheric CO_2: Measurements from the NOAA Global Air Sampling Network, *J. Geophys. Res., 101*, 25,897-25,916, 1996.

Warneck, P., *Chemistry of the Natural Atmosphere, International Geophysics Series*, Volume 41, R. Dmowska and J.R. Holton, eds., Academic Press, 757 pp., London, 1988.

Wofsy, S.C., and D.Y. Hollinger, Science plan for AmeriFlux: Long-term flux measurement network of the Americas, available from the AmeriFlux website: http://www.esd.ornl.gov/programs/NIGEC/scif.htm, 1998.

Zhao, C, P. Tans, and K. Thoning, A manometric system for absolute calibrations of CO_2 in dry air, *J. Geophys. Res., 102*, 5885-5894, 1997.

3. Aerosols and Radiation

3.1. Aerosol Monitoring

P. Sheridan (Editor), J. Barnes, M. Bergin, M. Doorenbosch, W. Huang, A. Jefferson, J. Ogren, and J. Wendell

3.1.1. Scientific Background

Aerosol particles affect the radiative balance of Earth both directly, by scattering and absorbing solar and terrestrial radiation, and indirectly, through their action as cloud condensation nuclei (CCN) with subsequent effects on the microphysical and optical properties of clouds. Evaluation of the climate forcing by aerosols, defined here as the perturbation of the Earth's radiation budget induced by the presence of airborne particles, requires knowledge of the spatial distribution of the particles, their optical and cloud-nucleating properties, and suitable models of radiative transfer and cloud physics. Obtaining a predictive relationship between the aerosol forcing and the physical and chemical sources of the particles additionally requires regional and global-scale chemical process, physical transformation, and transport models for calculating the spatial distributions of the major chemical species that control the optical and cloud-nucleating properties of the particles. Developing and validating these various models requires a diverse suite of in situ and remote observations of the aerosol particles on a wide range of spatial and temporal scales.

Aerosol measurements began at the CMDL baseline observatories in the mid-1970s as part of the Geophysical Monitoring for Climatic Change (GMCC) program. The objective of these "baseline" measurements was to detect a response, or lack of response, of atmospheric aerosols to changing conditions on a global scale.

Since the inception of the program, scientific understanding of the behavior of atmospheric aerosols has improved considerably. One lesson learned is that residence times of tropospheric aerosols are generally less than 1 week, and that human activities primarily influence aerosols on regional/continental scales rather than global scales. In response to this increased understanding, and to more recent findings that anthropogenic aerosols create a significant perturbation in the Earth's radiative balance on regional scales [*Charlson et al.*, 1992; *National Research Council,* 1996], CMDL expanded its aerosol research program to include regional aerosol monitoring stations. The goals of this regional-scale monitoring program are: (1) to characterize means, variabilities, and trends of climate-forcing properties of different types of aerosols, and (2) to understand the factors that control these properties.

A primary hypothesis to be tested by NOAA's aerosol research program is that the climate forcing by anthropogenic sulfate will change in response to future changes in sulfur emissions. The forcing is expected to decrease in and downwind of the United States as a result of emission controls mandated by the Clean Air Act, while continued economic development in China and other developing countries is expected to lead to an increased forcing in and downwind of those areas. Testing this hypothesis will require a coordinated research program involving modeling, monitoring, process, and closure studies. This report describes the observations that CMDL is conducting towards this goal.

No single approach to observing the atmospheric aerosol can provide the necessary data for monitoring all the relevant dimensions and spatial/temporal scales needed to evaluate the climate forcing by anthropogenic aerosols. In situ observations from fixed surface sites (like CMDL's), ships, balloons, and aircraft can provide very detailed characterizations of the atmospheric aerosol but on limited spatial scales. Remote sensing methods from satellites, aircraft, or from the surface can determine a limited set of aerosol properties from local to global spatial scales, but they cannot provide the chemical information needed for linkage with global chemical models. Fixed ground stations are suitable for continuous observations over extended time periods but lack vertical resolution. Aircraft and balloons can provide the vertical dimension, but not continuously. Only when systematically combined can these various types of observations produce a data set where point measurements can be extrapolated with models to large geographical scales where satellite measurements can be compared to the results of large-scale models, and where process studies have a context for drawing general conclusions from experiments conducted under specific conditions.

Measurements of atmospheric aerosols are used in three fundamentally different ways for aerosol/climate research: algorithm development for models and remote-sensing retrievals, parameter characterization, and model validation. Laboratory and field process studies guide the development of parameterization schemes and choice of parameter values for chemical transport models that describe the relationship between emissions and concentration fields of aerosol species. Systematic surveys and monitoring programs provide characteristic values of aerosol properties that are used in radiative transfer models for calculating the radiative effects of the aerosols, and for retrieving aerosol properties from satellites and other remote sensing platforms. And finally, monitoring programs provide spatial and temporal distributions of aerosol properties that are compared to model results to validate the models. Each of these three modes of interaction between applications and measurements require different types of data and entail different measurement strategies. *Ogren* [1995] applied the thermodynamic concept of "intensive" and "extensive" properties of a system to emphasize the relationship between measurement approach and applications of aerosol observations.

Intensive properties do not depend on the amount of aerosol present and are used as parameters in chemical transport and radiative transfer models (e.g., atmospheric residence time, single-scattering albedo). Extensive properties vary strongly in response to mixing and removal processes and are most commonly used for model validation (e.g., mass concentration, optical depth).

Intensive properties are more difficult and expensive to measure than extensive properties because they generally are defined as the ratio of two extensive properties. As a result, different measurement strategies are needed for meeting the data needs of the various applications. Measurements of a few carefully chosen extensive properties, of which aerosol optical depth and species mass concentrations are prime candidates, are needed in many locations to test the ability of the models to predict spatial and temporal variations on regional to global scales and to detect changes in aerosol concentrations resulting from changes in aerosol sources. The higher cost of determining intensive properties suggests a strategy of using a limited number of highly-instrumented sites to characterize means and variabilities of intensive properties for different regions or aerosol types, supplemented with surveys by aircraft and ships to characterize the spatial variability of these parameters. CMDL's regional aerosol monitoring program is primarily focussed on characterizing intensive properties.

CMDL's measurements provide ground truth for satellite measurements and global models, as well as key aerosol parameters for global-scale models (e.g., scattering efficiency of sulfate particles and hemispheric backscattering fraction). An important aspect of this strategy is that the chemical measurements are linked to the physical measurements through simultaneous, size-selective sampling that allows the observed aerosol properties to be connected to the atmospheric cycles of specific chemical species.

3.1.2. Experimental Methods

A number of changes were made to CMDL's aerosol sampling network during 1996-1997. Two noteworthy changes occurred as a result of collaboration with the Atmospheric Radiation Measurements (ARM) program of the U.S. Department of Energy (DOE): CMDL assumed responsibility for the aerosol observing system at ARM's site in Lamont, Oklahoma, and the aerosol sampling system at the Barrow, Alaska (BRW) baseline observatory was upgraded to use the same sampling protocols and instrumentation as at the CMDL regional monitoring sites. These changes substantially increase the number of sites where comparable measurements of aerosol intensive properties are made routinely. Routine aerosol measurements at Cheeka Peak, Washington, and Niwot Ridge, Colorado, were terminated during 1996 as a result of funding limitations, although intermittent field campaigns at Cheeka Peak have continued.

Extensive aerosol properties monitored by CMDL include the condensation nucleus (CN) concentration, aerosol optical depth (δ), and components of the aerosol extinction coefficient at one or more wavelengths (total scattering σ_{sp}, backwards hemispheric scattering σ_{bsp}, and absorption σ_{ap}). At the regional sites, size-resolved impactor and filter samples (submicrometer and supermicrometer size fractions) are obtained for gravimetric and chemical (ion chromatograph) analyses. All size-selective sampling, as well as the measurements of the components of the aerosol extinction coefficient at the regional stations, is performed at a low, controlled relative humidity (<40%) to eliminate confounding effects due to changes in ambient relative humidity. Data from the continuous sensors are screened to eliminate contamination from local pollution sources. At the regional stations, the screening algorithms use measured wind speed, direction, and total particle number concentration in real-time to prevent contamination of the chemical samples. Algorithms for the baseline stations use measured wind speed and direction to exclude data that are likely to have been locally contaminated.

Prior to 1995, data from the baseline stations were manually edited to remove spikes from local contamination. Since 1995 an automatic editing algorithm has been applied to the baseline data in addition to manual editing of local contamination spikes. For the baseline stations (BRW, Mauna Loa, Hawaii (MLO), American Samoa (SMO), and South Pole, Antarctica (SPO), as well as Sable Island (WSA)), data are automatically removed when the wind direction is from local sources of pollution (such as generators and buildings) as well as when the wind speed is less than a threshold value (0.5-1 m s^{-1}). In addition, at MLO data for upslope conditions (1800-1000 UTC) are excluded since the airmasses do not represent "background" free tropospheric air for this case. A summary of the data editing criteria is given in Table 3.1.

Integrating nephelometers are used to determine the light scattering coefficient of the aerosol. These instruments operate by illuminating a fixed sample volume from the side and observing the amount of light that is scattered by particles and gas molecules in the direction of a photomultiplier tube. The instrument integrates over scattering angles of 7-170°. Depending on the station, measurements are performed at one, three, or four wavelengths in the visible and near-infrared. Newer instruments allow determination of the hemispheric backscattering coefficient by using a shutter to prevent illumination of the portion of the instrument that yields scattering angles less than 90°. A particle filter is inserted periodically into the sample stream to measure the light scattered by gas molecules; this is subtracted from the total scattered signal to determine the contribution from the particles alone. The instruments are calibrated by filling the sample volume with a gas of known scattering coefficient; CO_2 is used for high sensitivity instruments, while CFC-12 is used for the few single-wavelength, lower sensitivity instruments still in use.

TABLE 3.1. Data Editing Summary for NOAA Baseline and Regional Stations

Station	Editing	Clean Sector
South Pole	a,b,c	0° < WD < 110°, 330°<WD < 360°
Samoa	a,b,c	0° < WD < 165°, 285°<WD < 360°
Mauna Loa	a,b,c,d	90° < WD < 270°
Barrow	a,b,c	0° < WD < 130°
Sable Island	a,b,c	0° < WD < 35°, 85° < WD < 360°
Southern Great Plains	a	
Bondville	a	

a: Manual removal of local contamination spikes;
b: Automatic removal of data not in clean sector;
c: Automatic removal of data for low wind speeds;
d: Removal of data for upslope wind conditions;
WD: Wind direction.

The aerosol light absorption coefficient is determined with a continuous light absorption photometer. This instrument continuously measures the amount of light transmitted through a quartz filter, while particles are being deposited on the filter. The rate of decrease of transmissivity, divided by the sample flow rate, is directly proportional to the light absorption coefficient of the particles. Newer instruments were calibrated in terms of the difference of light extinction and scattering in a long-path extinction cell, for laboratory test aerosols. Instruments at the baseline stations (aethalometers, Magee Scientific, Berkley, California) were calibrated by the manufacturer in terms of the equivalent amount of black carbon from which the light absorption coefficient is calculated assuming a mass absorption efficiency of the calibration aerosols of 10 m^2 g^{-1}. Preliminary results from side-by-side operation of the two methods at BRW reveal a systematic difference (see below).

Particle number concentration is determined with a CN counter that exposes the particles to a high supersaturation of butanol vapor. This causes the particles to grow to a size where they can be detected optically and counted. The instruments in use have lower particle-size detection limits of 10-20 nm diameter.

Summaries of the extensive measurements obtained at each site are given in Tables 3.2 and 3.3. Table 3.4 lists the intensive aerosol properties that can be determined from the directly-measured extensive properties. These properties are used in chemical transport models to determine the radiative effects of the aerosol concentrations calculated by the models. Inversely, these properties are used by algorithms for interpreting satellite remote-sensing data to determine aerosol amounts based on measurements of the radiative effects of the aerosol.

TABLE 3.2. CMDL Baseline Aerosol Monitoring Stations (Status as of December 1997)

Category	Baseline Arctic	Baseline Free Troposphere	Baseline Marine	Baseline Antarctic
Location	Point Barrow	Mauna Loa	American Samoa	South Pole
Designator	BRW	MLO	SMO	SPO
Latitude	71.323°N	19.539°N	14.232°S	89.997°S
Longitude	156.609°W	155.578°W	170.563°W	102.0°E
Elevation (m)	8	3397	77	2838
Responsible Institute	CMDL	CMDL	CMDL	CMDL
Status	Operational 1976. Major upgrade 1997.	Operational 1974	Operational, 1977	Operational, 1974
Sample RH	RH <40%	Uncontrolled	Uncontrolled	Uncontrolled
Sample Size Fractions	D<1 μm D<10 μm	Uncontrolled	Uncontrolled	Uncontrolled
Optical measurements	$\sigma_{sp}(3\lambda)$, $\sigma_{bsp}(3\lambda)$, σ_{ap} (1λ)	$\sigma_{sp}(4\lambda)$, $\sigma_{sp}(3\lambda)$, $\sigma_{ap}(1\lambda)$, $\delta(6\lambda)$	none	$\sigma_{sp}(4\lambda)$
Microphysical measurements	CN concentration	CN concentration	CN concentration	CN concentration
Chemical measurements	Major ions, mass	None	None	None

TABLE 3.3. CMDL Regional Aerosol Monitoring Sites (Status as of December 1997)

Category	Perturbed Marine	Perturbed Continental	Perturbed Continental	Perturbed Continental
Location	Sable Island, Nova Scotia, Canada	Bondville, Illinois	K'puszta, Keszcemet, Hungary	Lamont, Oklahoma
Designator	WSA	BND	KPO	SGP
Latitude	43.933°N	40.053°N	46.967°N	36.605°N
Longitude	60.007°W	88.372°W	19.550°E	97.489°W
Elevation (m)	5	230	180	315
Responsible Institute	CMDL	CMDL	U. Veszprem, Hungary	CMDL
Collaborating Institute	AES Canada, NOAA/PMEL	University of Illinois, Illinois State Water Survey	NOAA/CMDL	DOE/ARM
Status	Operational, August 1992	Operational, July 1994	Operational, September 1994	Operational, July 1996
Sample RH	RH <40%	RH <40%	RH <40%	RH <40%
Sample Size Fractions	D<1 μm, D<10 μm	D<1 μm, D<10 μm	D<1 μm	D<1 μm, D<10 μm
Optical measurements	$\sigma_{sp}(3\lambda)$, $\sigma_{bsp}(3\lambda)$ σ_{ap} (1λ)	$\sigma_{sp}(3\lambda)$, $\sigma_{bsp}(3\lambda)$, $\sigma_{ap}(1\lambda)$	$\sigma_{sp}(1\lambda)$, $\sigma_{ap}(1\lambda)$, $\delta(4\lambda)$	$\sigma_{sp}(3\lambda)$,$\sigma_{bsp}(3\lambda)$, $\sigma_{ap}(1\lambda)$, $\delta(7\lambda)$
Microphysical measurements	CN concentration	CN concentration	CN concentration	CN, n(D) concentration
Chemical measurements	Major ions, mass	Major ions, mass	Major ions	None

TABLE 3.4. Intensive Aerosol Properties Derived From CMDL Network

Properties	Description
$\mathring{a}$	The Ångström exponent, defined by the power-law $\sigma_{sp} \propto \lambda^{-\mathring{a}}$, describes the wavelength-dependence of scattered light. In the figures below, $\mathring{a}$ is calculated from measurements at 550 and 700 nm wavelength. Situations where the scattering is dominated by submicrometer particles typically have values around 2, while values close to 0 occur when the scattering is dominated by particles larger than a few microns in diameter.
ω_0	The aerosol single-scattering albedo, defined as $\sigma_{sp}/(\sigma_{ap} + \sigma_{sp})$, describes the relative contributions of scattering and absorption to the total light extinction. Purely scattering aerosols (e.g., sulfuric acid) have values of 1, while very strong absorbers (e.g., elemental carbon) have values around 0.3.
g, b	Radiative transfer models commonly require one of two integral properties of the angular distribution of scattered light (phase function): the asymmetry factor g or the hemispheric backscatter fraction b. The asymmetry factor is the cosine-weighted average of the phase function, ranging from a value of -1 for entirely backscattered light to +1 for entirely forward-scattered light. The hemispheric backscatter fraction b is σ_{bsp}/σ_{sp}.
α_i	The mass scattering efficiency for species i, defined as the slope of the linear regression line relating σ_{sp} and the mass concentration of the chemical species, is used in chemical transport models to evaluate the radiative effects of each chemical species prognosed by the model. This parameter has typical units of $m^2\ g^{-1}$.

3.1.3. ANNUAL CYCLES

The annual cycles of aerosol optical properties for the four baseline and three regional stations are illustrated in Figures 3.1a-d and Figures 3.2a-e. The data are presented in the form of box and whisker plots that summarize the distribution of values. Each box ranges from the lower to upper quartiles with a central bar at the median value, while the whiskers extend to the 5th and 95th percentiles. The statistics are based on hourly averages of each parameter for each month of the year, as well as for the entire year.

In general, changes in long-range transport patterns dominate the annual cycles of the baseline stations. For BRW, the highest values of CN, σ_{sp}, and σ_{ap} are observed during the spring arctic haze period when anti-cyclonic activity transports pollution from the lower latitudes of Central Europe and Russia. A more stable polar front characterizes the summertime meteorology. High cloud coverage and precipitation scavenging of accumulation mode (0.1-1.0 μm diameter) aerosols account for the annual minima in σ_{sp} and σ_{ap} from June to September. In contrast, CN values have a secondary maximum in the late summer which is thought to be the result of sulfate aerosol production from gas to particle conversion of DMS oxidation products from local oceanic emissions [*Radke et al.*, 1990]. The aerosol single-scattering albedo displays little annual variability with values between 0.90–0.98, which is indicative of highly scattering sulfate and seasalt aerosol. A September minimum is observed in $\mathring{a}$ when σ_{sp} and accumulation mode aerosols are also low but when primary production of coarse mode seasalt aerosols from open water is high. For MLO, the highest σ_{sp} and σ_{ap} values occur in the springtime and result from the long-range transport of pollution and mineral dust from Asia. However, little seasonality is seen in CN concentrations at MLO, indicating that the smallest particles (<0.1 μm diameter), which usually dominate CN concentration, are not enriched during these long-range transport events. Both the aerosol σ_{sp} and Ångström exponent display seasonal cycles at SPO with a σ_{sp} maximum and an $\mathring{a}$ minimum in winter associated with the transport of coarse mode seasalt from the antarctic coast to the interior of the continent. The summertime peaks in CN and $\mathring{a}$ are associated with fine mode sulfate aerosol and correlate with a seasonal sulfate peak found in the ice core presumably from coastal biogenic sources [*Bergin et al.*, 1998a]. The aerosol extensive properties at SMO display no distinct seasonal variation.

Based on only 2-5 years of measurements, the annual cycles for the regional stations are less certain than those of the baseline stations. The proximity of the regional sites to North American pollution sources is apparent in the results, with monthly median values of CN and σ_{sp} that are nearly two orders of magnitude higher than values from the baseline stations. The Bondville site (BND), situated in a rural agricultural region, displays autumn highs in σ_{ap} and CN and a low in ω_0 which coincide with anthropogenic and dust aerosols emitted during the harvest. As evident in the lower CN, σ_{sp}, and σ_{ap} values, the Southern Great Plains site (SGP) is more remote than BND. SGP has a similar but less pronounced annual cycle with late summer highs in CN, σ_{sp}, and σ_{ap}, and a corresponding minimum in ω_0. Little seasonal variability is observed in WSA aerosol properties. CN and $\mathring{a}$ values tend to be higher in the summer and likely result from transport of fine mode sulfate aerosol from the continent and lower coarse-mode seasalt aerosol production associated with lower summer wind speeds.

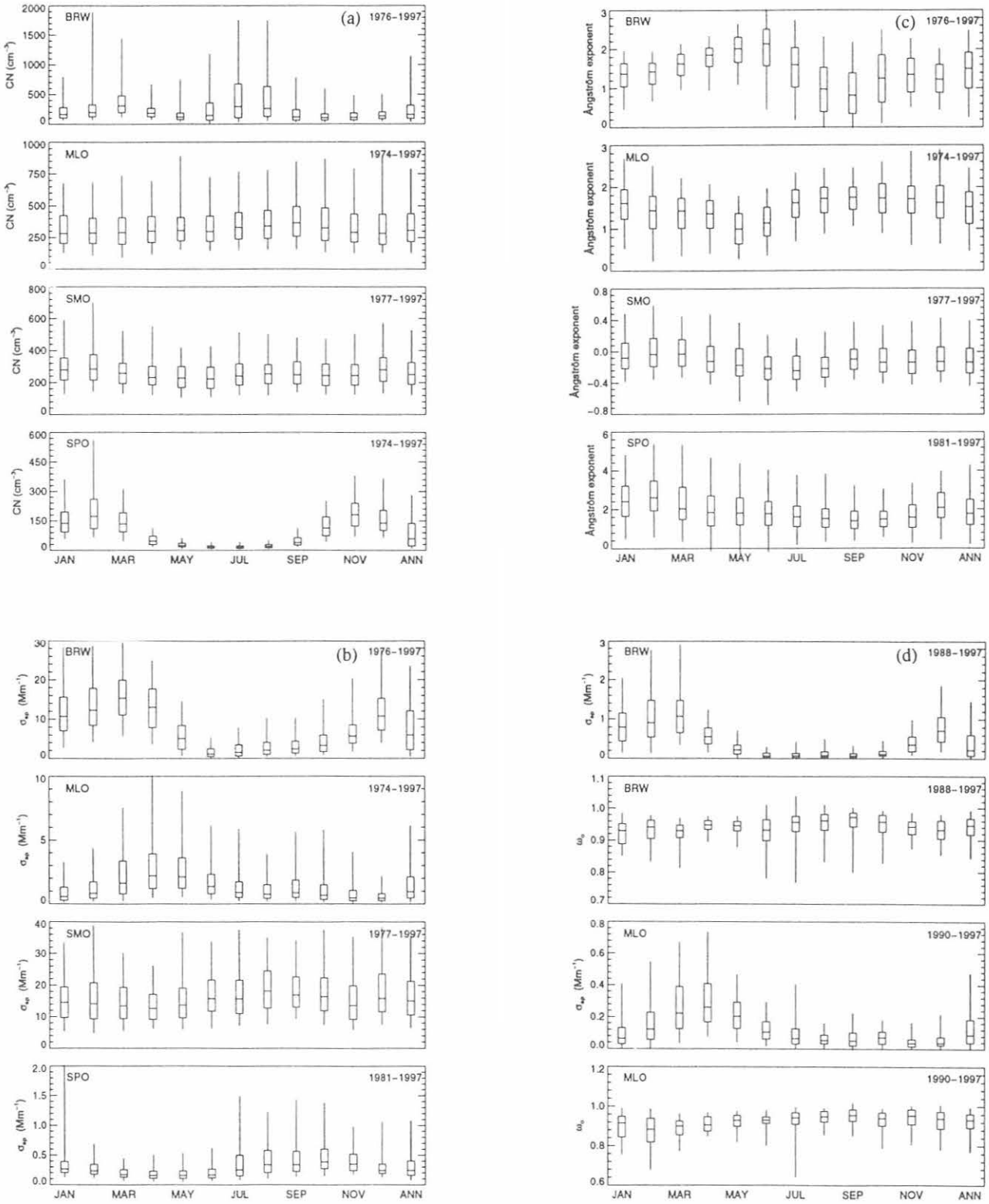

Fig. 3.1. Annual cycles for baseline stations at BRW, MLO, SMO, and SPO; values representing the entire year period, for all years in the record, are also presented (ANN): (a) CN concentrations, (b) σ_{sp} at 550 nm, (c) å (550/700 nm), and (d) Annual cycles of σ_{ap} and ω_0 for baseline stations at BRW and MLO.

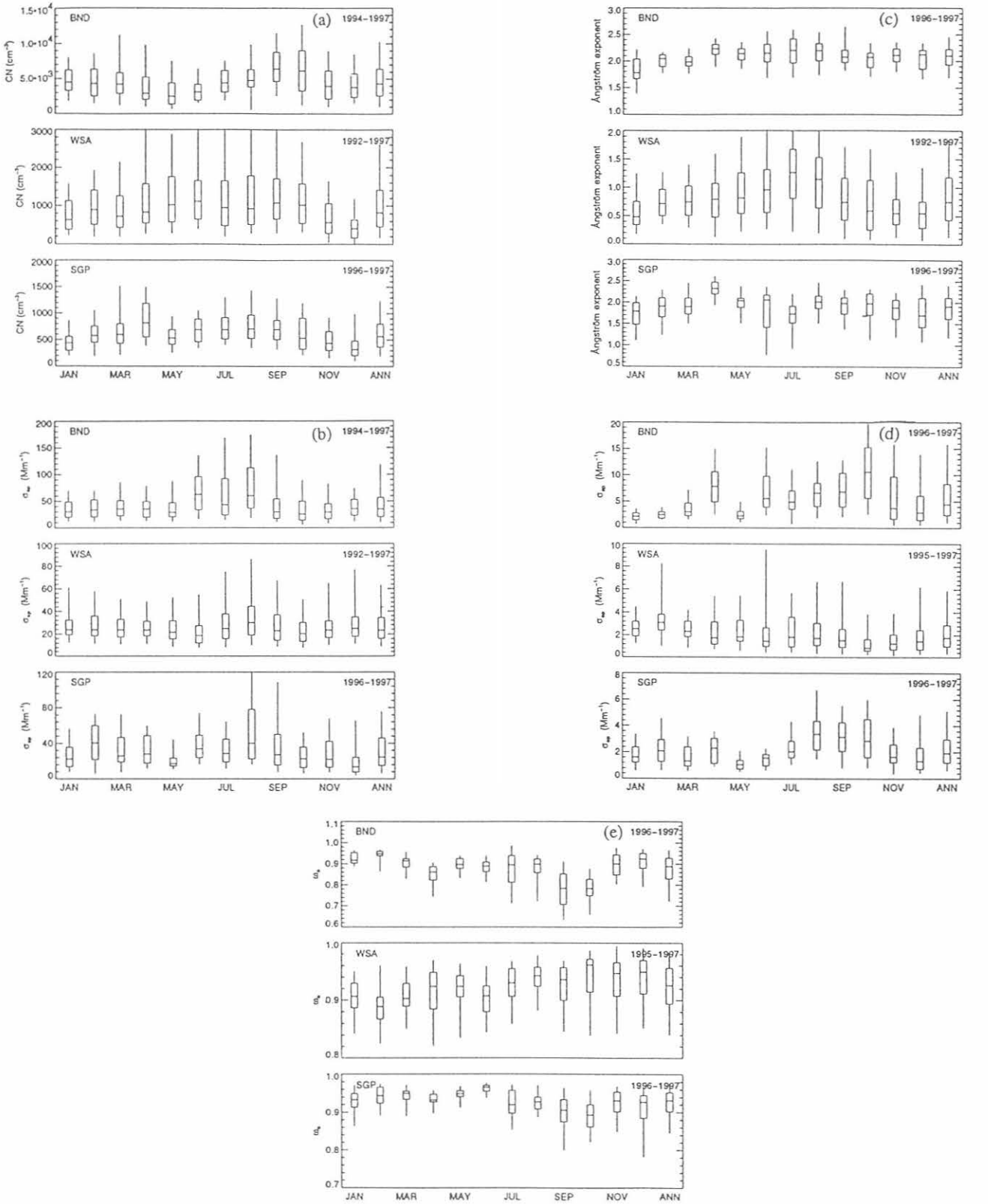

Fig. 3.2. Annual cycles for regional stations at Bondville, Illinois (BND), Sable Island, Nova Scotia (WSA), and Lamont, Oklahoma (SGP): (a) CN concentration, (b) σ_{sp} at 550 nm, (c) å, (550/70 nm), (d) σ_{ap} at 550 nm, and (e) ω_0 concentration.

3.1.4. Long-term Trends

Long-term trends in CN concentration, σ_{sp}, σ_{ap}, ω_0, and *å* are plotted in Figure 3.3a-d for the baseline observatories. The trends are plotted for the annual mean as well as for the averages for 2 months to highlight trends associated with different seasons. The aerosol properties at BRW exhibit an annual decrease in σ_{sp} of about 2% per year since 1980. This reduction in aerosol scattering has been attributed to decreased anthropogenic emissions from Europe and Russia [*Bodhaine*, 1989] and is most apparent during March when the arctic haze effect is largest. The corresponding decrease in the Ångström exponent over the same time period points to a shift in the aerosol size distribution to a larger fraction of coarse mode seasalt aerosol. *Stone* [1997] noted a long-term increase in surface temperatures and cloud coverage at BRW from 1965-1995 which derive from changing circulation patterns and may account for the reduction in σ_{sp} by enhanced scavenging of accumulation mode aerosols. In contrast to the reduction in σ_{sp} at BRW, CN concentrations, which are most sensitive to particles with diameters <0.1 μm, have increased at a rate of 3% yr^{-1} since 1976. Here, gas-to-particle conversion processes that produce these nucleation mode particles may be enhanced with respect to the decreased surface area of larger accumulation mode aerosols. The volcanic eruptions of El Chichón and Mt. Pinatubo in 1982 and 1991, respectively, seem to dominate any long-term trends in aerosol properties at MLO with peaks in CN, σ_{sp}, and σ_{ap} following these eruptions. This downward mixing of stratospheric sulfate aerosol from El Chichón and Mt. Pinatubo is also apparent at SPO with corresponding peaks in σ_{sp} in these years. The step increase in CN at SPO in 1989 is due to replacement of the CN counter with a butanol-based instrument with a lower size detection limit. The reason for the decrease in CN and increase in *å* at SMO is not readily apparent, but it could stem from changes in long-term circulation patterns.

The three regional stations, as well as BRW (since October 1997), have size-resolved sampling inlets with 1-μm and 10-μm diameter size cuts that permit the determination of the submicrometer aerosol contribution to the total aerosol optical properties. Figure 3.4 shows box and whisker plots for the different stations of the fractional contribution of submicrometer particles to scattering, backscattering, absorption, and single-scattering albedo. The size-resolved aerosol properties are part of a recent upgrade at BRW and contain data from only the last 3 months of 1997. The abundance of coarse mode seasalt aerosol at WSA is reflected in a smaller contribution of the submicrometer aerosol to the total aerosol scattering and absorption relative to the other continental sites. The spread of the WSA data suggest a highly variable air mass that changes between clean marine, polluted continental, and mixed regions. Only slight differences are apparent between the two regional continental sites.

Previous reports describing the aerosol data sets include: BRW: *Bodhaine* [1989, 1995]; *Quakenbush and Bodhaine* [1986]; *Bodhaine and Dutton* [1993]; *Barrie* [1996]; MLO: *Bodhaine* [1995]; SMO: *Bodhaine and DeLuisi* [1985]; SPO: *Bodhaine et al.* [1986, 1987, 1992]; *Bergin et al.* [1998a]; WSA: *McInnes et al.* [1998].

3.1.5. Lidar Measurements at Mauna Loa Observatory

Monitoring of the stratospheric aerosol with ruby (694 nm) and Nd:YAG (532 nm) lidars continued as part of the activities of the MLO primary site of the Network for the Detection of Stratospheric Change (NDSC). The 2-year period of 1996 through 1997 provided an excellent opportunity to observe the stratospheric aerosol layer under background conditions. The background level of about 6×10^{-5} sr^{-1} (at 694 nm) was reached in late 1995 and no further decay of the Mt. Pinatubo eruption was evident. Although this level was measured before in 1980 and 1990 by the ruby lidar, this is the first background period that the more accurate Nd:YAG lidar (532 and 1064 nm) has been in operation. Two striking features of the background aerosol are apparent with the YAG measurements that were not resolved by the ruby lidar system. One feature is a clear seasonal variation in aerosol backscatter seen in Figure 3.5. Here the total aerosol in the stratospheric layer is plotted which is dominated by the lower part of the layer above the tropopause. The source and sink balance of the stratospheric aerosol is affected by changes in the tropopause height. The variation is smaller than that seen at midlatitudes probably because the seasonal change in the tropopause is also much smaller.

Figure 3.6 shows the long-term record of the ruby lidar and the record from inception in early 1994 through 1997 for the Nd:YAG. The dominant features in the data are the major volcanic eruptions of El Chichón in 1982 and Mt. Pinatubo in 1991. A comparison of these events and an analysis of the eruption-free background period during 1996 and 1997 was recently published [*Barnes and Hofmann*, 1997].

In Figure 3.7 the aerosol backscatter above 25 km is compared with the 30 hPa tropical quasibiennial oscillation (QBO) winds; this is the second feature of the background aerosol. As the winds switch from westerly to easterly, the top of the aerosol layer changes from about 26 km to nearly 33 km. The total aerosol in the altitude range changes by a factor of 2. Although the QBO phase dominates the loading of the stratosphere at this altitude, there are episodes of transport from midlatitudes (lower aerosol loading), as in the spring of 1996, which deviate from tropical behavior.

Final results of the NDSC aerosol analysis algorithm intercomparison were presented [*Steinbrecht, et. al.*, 1996] and the MLO analysis agreed extremely well with other analyses of identical data sets. Also a lidar temperature intercomparison was conducted during the MLO3 ozone intercomparison. An error of about 3°C above 60 km was found between the MLO lidar and the other three lidars present. Below 60 km the temperatures agreed within measurement error. The discrepancy improved to about 1°C with an improved smoothing technique above 60 km. The temperature record was recalculated with this improvement. Both results were presented by *McGee et al.* [1996].

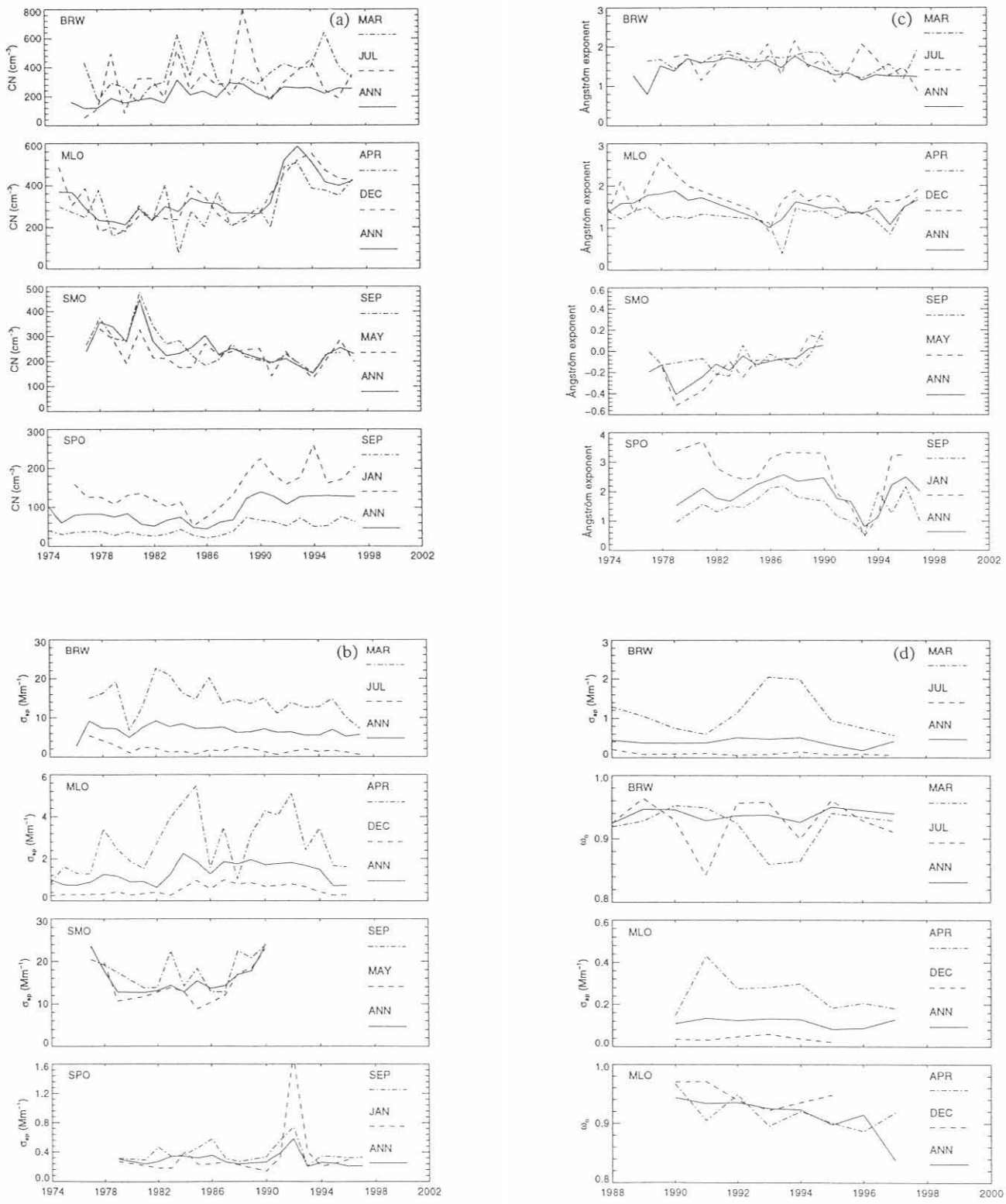

Fig. 3.3. Long-term trends for baseline stations showing months with the lowest and highest median values and annual averages for each year (ANN): (a) CN concentration, (b) σ_{sp} at 550 nm, (c) $\mathring{a}$ (550/700 nm), (d) σ_{ap} and ω_0 at BRW and MLO.

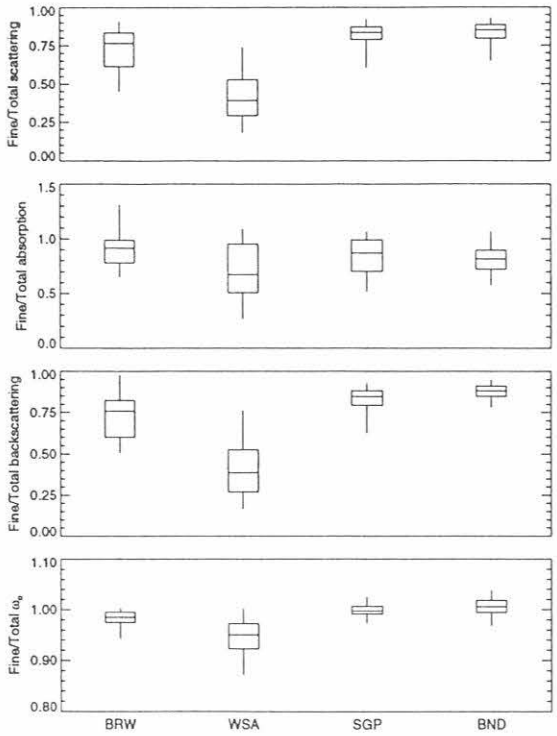

Fig. 3.4. The fractional contribution of submicrometer particles to aerosol light scattering, backscattering, absorption, and single-scattering albedo at BRW, WSA, SGP, and BND.

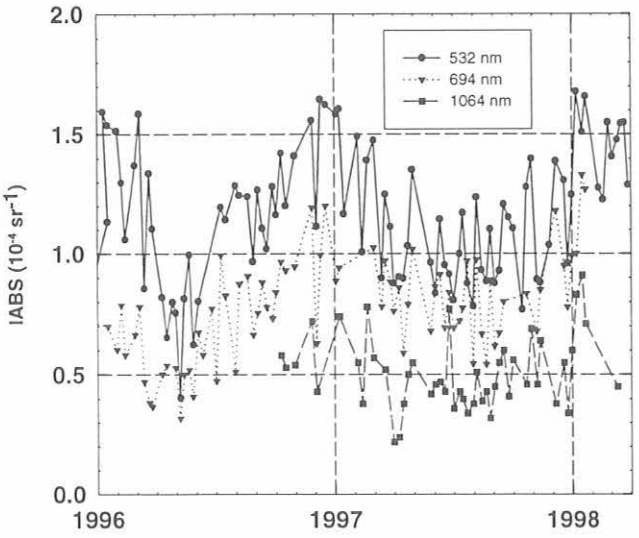

Fig. 3.5. Integrated aerosol backscatter at 532, 694, and 1064 nm.

Another test involved measuring three aerosol profiles at 532 nm simultaneously and was designed to quantify the instrument error of an aerosol measurement. Fifty-four shot periods (about 1.8 seconds) were alternately added to three different files for a total of 105 minutes (35 minutes per profile). The profiles were then analyzed normally. The standard deviation averaged 5.4% through the aerosol layer. This supports the value of 6% that has been used since initial tests were done 3 years ago. The original tests were complete profiles measured in succession that included natural variability. This test implies natural variability is smaller than 1% during periods of 1 or 2 hours.

A proposal was submitted to NASA in 1997 entitled, "Lidar measurements of Cirrus Clouds and Aerosols over Mauna Loa Observatory, Hawaii for CERES and SAGE-III Validation." The proposal used preliminary measurements of cirrus backscatter correlated with long-wave IR radiation measurements. Preliminary depolarization measurements of the clouds were also used. Although the proposal was not funded, it may be submitted again since the topic is an active area of research.

3.1.6. Special Studies

Apportionment of Light Scattering and Hygroscopic Growth to Chemical Composition at Sable Island

During a recent campaign at the CMDL monitoring station on Sable Island, a dual-nephelometer humidigraph measured the hygroscopic growth factor of aerosol scattering, $f_{RH}(\sigma_{sp})$, one of the key parameters necessary for estimating short-wave aerosol radiative forcing. Measurements revealed less growth for anthropogenically influenced aerosols than for marine, $f_{RH}(\sigma_{sp})$ of 1.7 ± 0.1 versus 2.7 ± 0.4, where $f_{RH}(\sigma_{sp}) = \sigma_{sp(85\%)}/\sigma_{sp(40\%)}$ as shown in Figure 3.8. A combined measurement-modeling approach was used to estimate σ_{sp} and its RH-dependence based on the measured particle size distribution and composition. The model suggested that differences in the particle size distribution, assuming the same aerosol composition, could not explain the observed differences in $f_{RH}(\sigma_{sp})$. We have confirmed with individual particle analysis that aerosol composition was indeed responsible for the difference in $f_{RH}(\sigma_{sp})$. In addition, the scattering contribution of organic carbon for the influenced case is at least as much as that of sulfate aerosol [*McInnes et al.*, 1998].

Barrow Upgrade

As a result of collaboration with the DOE ARM program, NOAA's aerosol measurement system at BRW was modernized and upgraded in September 1997. The original four-wavelength nephelometer was replaced with a modern, high-sensitivity, three-wavelength nephelometer that additionally determines the backwards-hemispheric component of aerosol light scattering. A continuous light absorption photometer, calibrated in terms of aerosol light absorption coefficient, replaced the original aethalometer. The aerosol inlet system was also upgraded to provide careful control of relative humidity and particle size. These upgrades were performed to meet the data requirements of the ARM program, and to provide the same parameters needed to evaluate the direct radiative forcing of climate by aerosols as are measured at CMDL's regional aerosol sites. In order to maintain continuity of the measurements, the new system will be operated in parallel with the old system until it has been proven that the results from the two systems are quantitatively

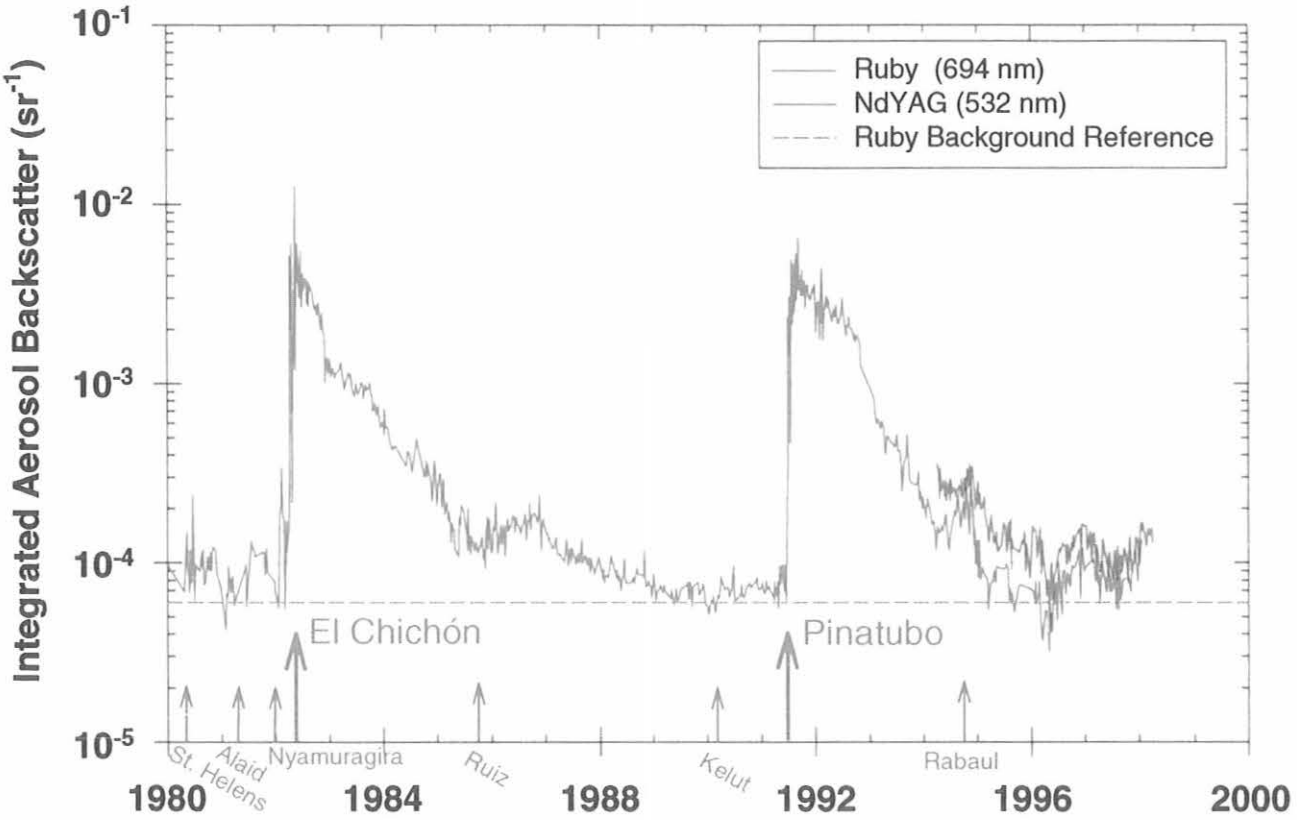

Fig. 3.6. Lidar backscatter at two wavelengths (red – 694 nm and green – 532 nm) from stratospheric aerosol between the altitudes of 15.8 and 33 km at MLO. The occurrence of volcanic eruptions which were believed to perturb the stratospheric aerosol level are indicated by arrows. The ratio of green to red backscatter decreased from 1994 to 1997 signifying a general increase in average particle size over this time period. During the background period of 1996-1997, there appears to be a QBO-related variation in the backscatter magnitude (see text).

comparable. Figure 3.9 illustrates the relationship between the aerosol absorption coefficients determined with the old aethalometer and new PSAP instrument, based on the first 3 months of simultaneous operation. Although a systematic difference is observed, the high correlation indicates that it will be possible to determine an empirical relationship linking the historical and future data sets.

Mexico City Intensive

As an exploratory step towards understanding the evolution of aerosol intensive properties during long-range transport from source regions, radiative properties of atmospheric aerosols in Mexico City were measured during 2 weeks in November 1997. The same instruments and sampling protocols as at the CMDL regional aerosol sites were used. The measurements were made at a site located in the southwest sector of the city, on a hillside 400 m above the elevation of the main metropolis. The hillside location provided a strong diurnal variation in aerosol properties as surface heating during the day raised the top of the polluted mixed layer above the elevation of the site. Urban aerosols in this region contain a large fraction of absorbing material as indicated by an average single-scattering albedo throughout the research period of 0.7. At times, the single-scattering albedo decreased to as low as 0.4, indicating that more than 50% of the aerosol light extinction was accounted for by absorption. The total light scattering during the high pollution days, when ozone typically exceeded 200 ppb, was quite high, with scattering coefficients on the order of 200 Mm^{-1}. The absorption, however, increased much less than scattering on high pollution days, and the lowest single-scattering albedos occurred on those days when rainfall and clouds kept the pollution levels much lower (Figure 3.10).

Aircraft Studies of the Vertical and Horizontal Variability of Aerosol Optical Properties

Aerosol optical properties were measured in situ during three recent field experiments from the NOAA WP-3D Orion research aircraft using an aircraft version of the ground-based CMDL aerosol measurement system. The purpose of flying this airborne package was to measure the spatial (i.e., horizontal and vertical) and temporal variability of aerosol optical properties, and thus to substantially increase the existing amount of these data collected at altitude. By performing the measurements both at very low reference altitudes (which we believe to

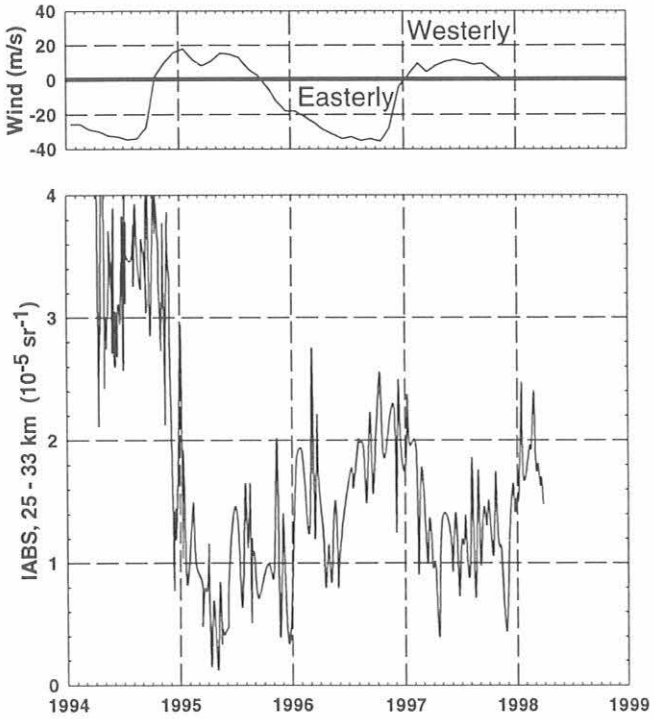

Fig. 3.7. Upper stratospheric aerosol backscatter (25-33 km) and QBO Winds (30 mbar, approximately 24 km)

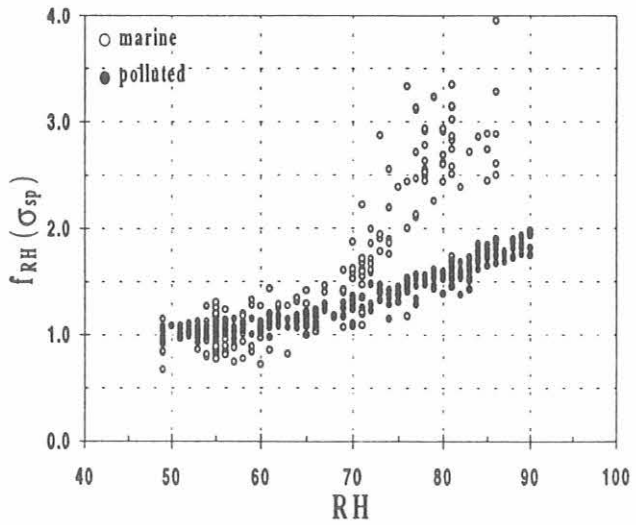

Fig. 3.8. Hygroscopic growth factor of aerosol scattering f_{RH} (σ_{sp}), measured for the marine and anthropogenically influenced cases at Sable Island.

closely reflect surface measurements) and at higher altitudes, the relationship of surface and higher altitude measurements can be made. Aerosol data from surface sites can then be properly evaluated in terms of the extent to which they represent lower column measurements. The geographical coverage of these field experiments included

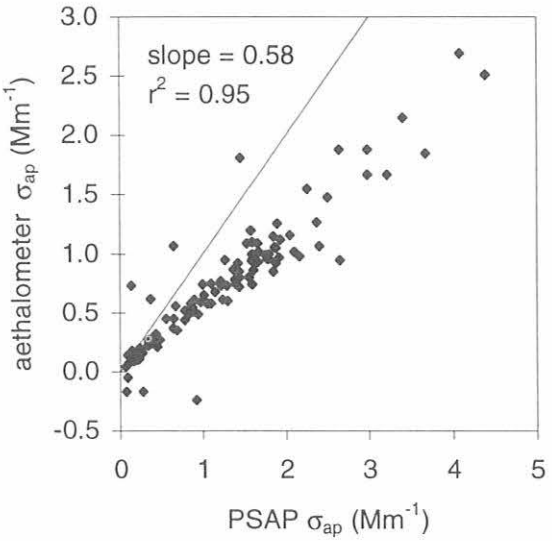

Fig. 3.9 Comparison of light absorption photometers.

much of the eastern two-thirds of the United States, the Canadian maritime provinces, and portions of the north Atlantic. Inter- and intra-regional variability of the aerosol properties for boundary layer and free tropospheric measurements was determined. As an example, Figure 3.11 shows the aerosol single-scattering albedo measurements grouped according to atmospheric layer and geographic region. The line across each box, the ends of each box, and the extent of the whiskers represent the median, the 25th and 75th percentiles, and the 10th and 90th percentiles of each distribution. Median aerosol single-scattering albedos were similar in the boundary layer of all three regions, while in the free troposphere, ω_0 was lower and showed the most variability in the East and Atlantic regions.

Relationship Between Continuous Aerosol Measurements and Firn Core Chemistry Over a 10-Year Period at SPO

Before ice core chemistry can be used to estimate past atmospheric chemistry, it is necessary to establish an

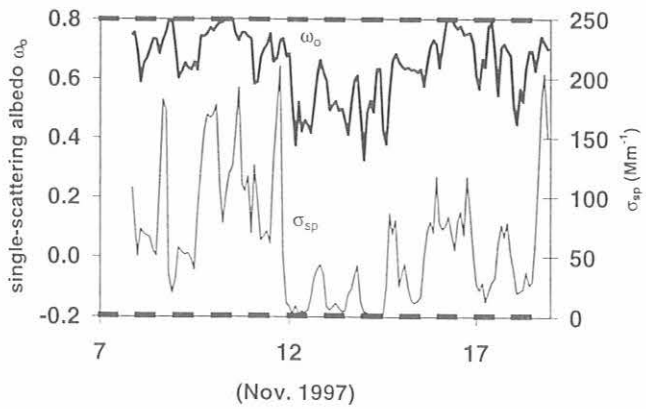

Fig. 3.10. Aerosol radiative properties in Mexico City. The solid horizontal bars indicate nighttime periods.

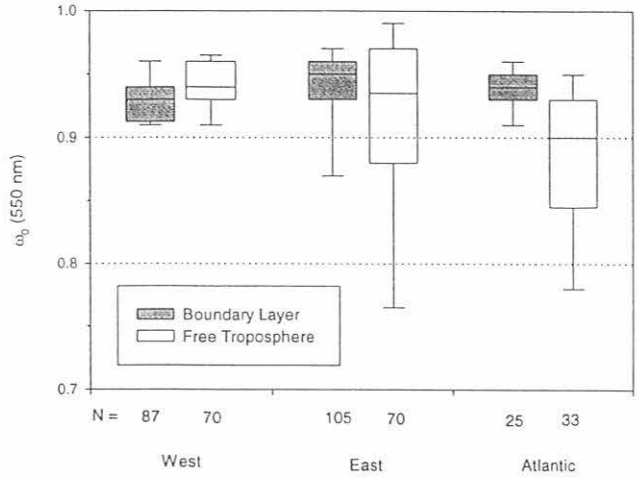

Fig. 3.11. Variability of aerosol single scattering albedo as a function of atmospheric layer and geographic region. Numbers along x-axis indicate the number of level flight segments included in each data set.

unambiguous link between concentrations of chemical species in the air and snow. For the first time a continuous long-term record of aerosol properties (σ_{sp} and *å*) at the South Pole was compared with the chemical record from a high resolution firn core (~10 samples per year) from 1981 to 1991. As shown in Figure 3.12, seasonal signals in *å*, associated with winter minima due to coarse mode seasalt and summer maxima due to accumulation mode sulfate aerosol, are reflected in the firn core $SO_4^=/Na^+$ concentration ratio. Summertime ratios of σ_{sp} and aerosol optical depth, τ, to corresponding firn core sulfur concentrations were determined and the "calibrations" were applied to sulfur concentrations in snowpits from a previous study. Results showed that σ_{sp} estimates from snowpit sulfur concentrations were in agreement with atmospheric measurements while τ estimates were significantly different, which is likely due to the lack of understanding of the processes that mix surface air with air aloft [*Bergin et al.*, 1998a].

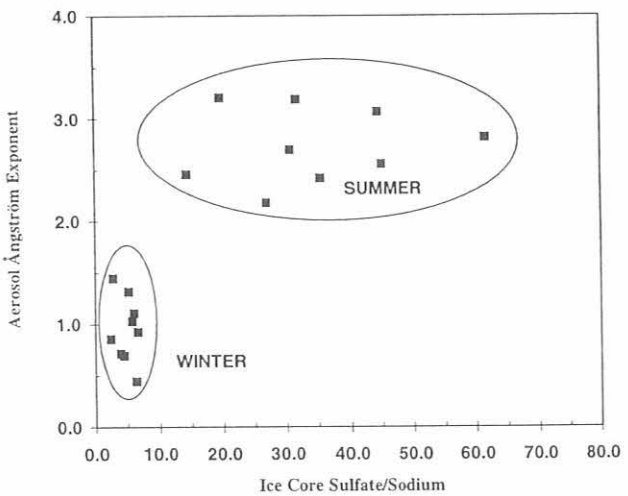

Fig. 3.12. Comparison of mean seasonal values of aerosol Ångstrom exponent and ice core sulfate/sodium from 1981-1991 at SPO.

Aerosol Evaporation in Heated Nephelometers During Sampling: A Laboratory and Modeling Study

Ammonium nitrate aerosol is ubiquitous to the atmosphere and volatile under typical ambient conditions and thus difficult to measure. In the field the scattering coefficient of the dry aerosol is measured with a nephelometer by heating the ambient aerosol to a low reference relative humidity (typically around 40%). The decrease in the light scattering coefficient of ammonium nitrate aerosol due to evaporation in a heated nephelometer was studied under laboratory conditions. Changes in the scattering coefficient of a laboratory-generated monodisperse ammonium nitrate aerosol were measured as a function of mean residence time and temperature within the nephelometer sample volume. At the same time, the change in the aerosol size distribution due to ammonium nitrate evaporation was directly measured with a laser particle counter. The changes in the aerosol size distribution and scattering coefficient were modeled as a function of mean residence time and temperature. Model results for the change in the aerosol scattering coefficient due to evaporation agree with measurements to within 10%. Application of the theory to conditions typical of NOAA field sites shown in Figure 3.13 suggests that due to the evaporation of ammonium nitrate, the decrease in the aerosol scattering coefficient is typically less than 20% [*Bergin et al.*, 1997].

Comparison of Aerosol Properties Measured at the Surface and Over the Entire Atmospheric Column at the SGP ARM Site in Oklahoma

The estimation of direct aerosol shortwave radiative forcing requires knowledge of aerosol radiative properties

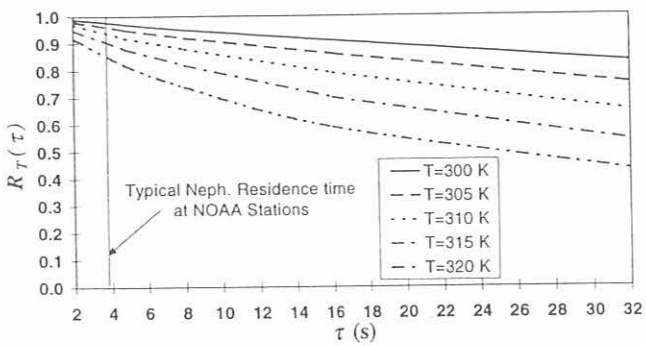

Fig. 3.13. Estimated ratio of scattering coefficient at T and τ to initial scattering coefficient, $R_T(\tau)$ versus mean residence time, τ, for ammonium nitrate size distributions having a geometric number median diameter, $D_{p,g}$, of 0.4 μm and a geometric standard deviation, GSD, of 1.6.

on relevant spatial and temporal scales. It is convenient to measure aerosol parameters associated with radiative forcing at the surface, although before these measurements can be used to quantitatively estimate direct climate forcing, it is important to determine the extent to which radiative properties represent the properties integrated over the entire column. In this study we compared measurements of the aerosol optical depth made at the SGP ARM site during several clear sky days with estimates of the aerosol optical depth based on two methods. First, the aerosol scattering coefficient measured at the surface (at a relative humidity ~20%) is multiplied by a mixing height determined from temperature profile measurements. This approach underestimates aerosol optical depth by ~70% using the dry aerosol measurements and by ~40% taking into account the estimated hygroscopic response of aerosols to ambient RH. The discrepancy is attributed to a lack of knowledge of the vertical profile of the aerosol scattering coefficient. Second, micropulse lidar (MPL) normalized aerosol backscatter profiles are used to scale the vertical profile of the aerosol scattering coefficient to surface measurements. As shown in Figure 3.14, the aerosol optical depths estimated using the dry aerosol scattering coefficient are ~30% less than measured values but are in close agreement (± ~15%) when hygroscopic growth is taken into account. These results suggest that aerosol radiative properties at the surface can be representative of radiative properties of the atmospheric column [*Bergin et al.*, 1998b].

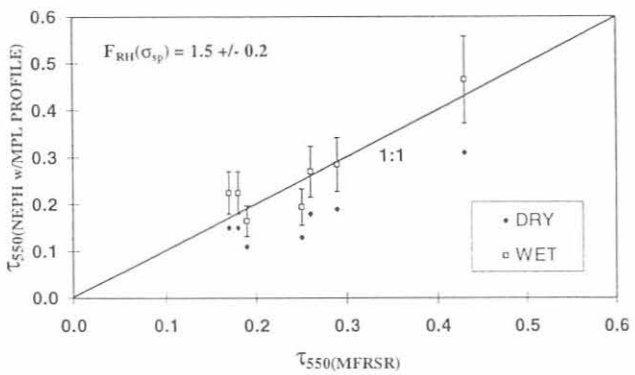

Fig. 3.14. Aerosol optical depths at 550 nm estimated for several clear sky days at 20:30 based on micropulse lidar (MPL) scaled nephelometer measurements versus radiometer measurements.

3.2. Solar and Thermal Atmospheric Radiation

B. Bodhaine (Editor), E. Dutton, B. Halter, G. Koenig, D. Longenecker, D. Nelson, R. Stone, R. Tatusko, and J. Wendell

3.2.1. Radiation Measurements

The CMDL radiation group, known as the Solar and Thermal Atmospheric Radiation (STAR) group, has undertaken several new projects in addition to the traditional surface radiation monitoring that was the primary emphasis of the group in the past. Current projects include baseline surface radiation monitoring, solar and infrared (IR) calibration facilities, spectral and wideband ultraviolet (UV) measurements, various interactions with the World Meteorological Organization (WMO) related radiation programs, validation of surface radiation budget measurements from space, instrument modification and development, polar surface and climate studies, and radiative transfer model testing and verification. This expansion of the CMDL radiation program is in response to, and partially responsible for, a general increase in interest in atmospheric radiation measurements over the past decade. Also as a result of this increased scientific interest, two relatively large programs were established by the National Aeronautics and Space Administration (NASA) and the Department of Energy (DOE) to address pressing issues in climate and radiation. The impetus for this increase in interest and the expanded role of the CMDL project has been the existence of ever improved general circulation models and satellite-derived surface radiation quantities, and the need for high quality in situ surface measurements for validation. The STAR group's movement into UV measurements resulted from many overlapping interests between the radiation/climate community and those of atmospheric chemistry.

Baseline Monitoring

Fundamental to STAR's efforts are the long-term monitoring of surface radiation components at the four CMDL baseline observatories. Upgrades to those sites continued in 1996 and 1997 as we incorporated diffuse solar irradiance into our core measurements and updated solar tracking capabilities at some sites. For the past 8 years we maintained surface radiation monitoring sites at Bermuda and Kwajalein and for the last 12 years at the Boulder Atmospheric Observatory (BAO) near Erie, Colorado. The measurement programs at these three sites and at Barrow, Alaska (BRW) and at South Pole, Antarctica (SPO) make up the CMDL contribution to the World Climate Research Program (WCRP) Baseline Surface Radiation Network (BSRN), for which CMDL also provides the international project manager.

Additional Measurement Programs

In addition to the basic monitoring activities, other major projects currently being undertaken include satellite validation and algorithm testing, operational radiometer improvements, new instrument technology testing and evaluation, spectral UV measurements, polar radiation research, aerosol optical depth studies, and cloud optical properties investigations. This report will cover the status and progress of each of the topics.

We are participating in the validation of the surface radiation quantities that will be observed and derived as part of the NASA Earth Observing System (EOS) Clouds and Earth's Radiant Energy System. The CMDL participation will be to enhance current field site observing capabilities and to provide data and analysis relative to the understanding and interpretation of the magnitude and variability of the Earth's surface radiation budget. The effort will include further refinements of field

operations and continued pursuit of full compliance with the BSRN measurement recommendations. Initial activities involve the comparison of surface-based irradiance observations with the computational procedures using radiative transfer models intended to eventually be used with the satellite data to project top-of-the-atmosphere observations to estimated surface quantities. The project is expected to last a minimum of 3 years and should help provide the information necessary to not only diagnose current climate energy but further to provide climate modeling efforts with supporting quantities against which intermediate climate predictions can be tested.

The BRW site was chosen as the third in a series of Clouds And Radiation Testbed sites of the DOE/ Atmospheric Radiation Measurements (ARM) program, which has an extensive surface irradiance measurement mission. We are cooperating with the ARM program in providing consultation and other assistance, and we are providing fast-turn-around data from our program to the ARM research team for the purpose of crosscheck and quality control. The extensive observational capability of ARM will enhance the CMDL efforts to determine the source and extent of variations in the radiation budget of the Barrow region.

In August of 1997 the STAR group hosted an intercomparison between traditional solar radiometry and developing technology. This new technology developed by the Scripps Institution of Oceanography (SIO) has begun to be used extensively by the radiation community. The purpose of the comparison was to determine how the newer instrumentation performed relative to the CMDL standards that are traceable to the international standards. Analysis of the comparison data is being performed independently so that personal specific biases would not be a factor in the conclusions. Preliminary results suggest a close agreement between the systems much of the time, even during some extreme events when midday readings on both instrument systems decreased to near <2 W m^{-2}. Differences between the instruments were generally less than 10 W m^{-2} with a few cases showing differences of about 25 W m^{-2}.

MLO Apparent Transmission

One of the longest of the radiation-related data records maintained by STAR is the Mauna Loa Atmospheric Transmission record. This record is explained by *Dutton et al.* [1985] and was updated through 1997 as shown in Figure 3.15. The principal features now evident in the record are the major impact of stratospheric aerosols from certain volcanic eruptions, an annual cycle caused by the seasonal enhanced transport of Asian dust aerosol over the central Pacific, and the lack of any pronounced or significant trend in the data over the 40-year record. This lack of a significant trend helps bound the maximum possible change that could have occurred in upper tropospheric or stratospheric aerosol. Less obvious in the record is the year-to-year variability in the annual cycle that has been shown to have a coherence with the Quasi-Biennial Oscillation [*Dutton,* 1992]. Also, not at all obvious in the record, but shown in Figure 3.15, is the fact that over the past 15 years or so, the intensity of the mean amplitude of the annual cycle has increased. This is

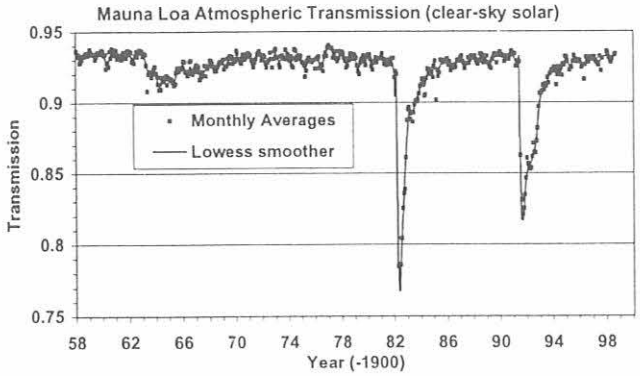

Fig. 3.15. Monthly mean (dots) of the apparent solar transmission at Mauna Loa. Apparent transmission is defined in references given in the text and is an inherently stable measure of the long-term composition of the atmosphere for those constituents that can attenuate solar wavelengths of electromagnetic radiation. A lowess smoother (solid line) was fit to the data and emphasizes the variable annual cycle in the data.

manifested in the fact that the spring minimum in transmission (maximum in aerosol content) is more consistently present in recent years. Figure 3.15 shows this in the ever increasing baseline of the amplitude of the MLO transmission annual cycle caused by the lack of the minimal amplitudes seen earlier in the record.

3.2.2. Solar Radiation Calibration Facility

Routine Operations

The Solar Radiation Calibration Facility (SRF) is responsible for all calibration activities within the STAR group. Characterized and calibrated broadband sensors were routinely supplied to the four CMDL baseline observatories plus three additional sites at Kwajalein, Bermuda, and the BAO. Each site has a complement of broadband solar radiation sensors (pyranometers and pyrheliometers) that require regular recalibration, exchange, and upgrade support. The environmental extremes at the CMDL monitoring sites also can compound the difficulty of maintaining reliable suites of monitoring instrumentation. An important SRF goal is to maintain the continuity of field site operations and constantly seek ways to enhance the reliability of the monitoring efforts and quality of the data.

Reference Cavity Comparisons

Annual participation in comparisons of cavity radiometers were conducted in 1996 and 1997. The comparisons were held during October at the National Renewable Energy Laboratory (NREL) facility in Golden, Colorado. The results are summarized and available in NREL publications and establish annual checks of the SRF cavity ratios to peer instruments, World Radiometric Reference (WRR) reproducibility, and operational behavior of cavity electronics and stability. Results of such comparisons establish and help maintain confidence in the SRF reference radiometers.

Hardware and Operational Enhancements

Implementation of operational protocols consistent with BSRN guidelines was a priority during 1996 and 1997. A focus of activity within the CMDL surface radiation monitoring effort was the improvement of sun tracking capability and the implementation of broadband solar component (direct beam and diffuse sky) measurements at all sites. A measurable improvement in tracking accuracy using existing automatic solar trackers was achieved by using a combination of a more accurate algorithm for computation of solar position plus more precise leveling of the solar tracker during installation and the use of a Global Positioning Satellite (GPS) module to provide a continuous, accurate time setting of the solar tracker control computer. The implementation of these three items resulted in tracking accuracies of one tenth of a degree over the course of a day. At remote monitoring sites this tracking accuracy reduces the demand on site personnel and contributes significantly to data quality. Diffuse-sky irradiance measurements using tracking shade disk systems mounted on automated solar trackers were initiated at the CMDL BSRN sites in Kwajalein and Bermuda during 1996, and MLO in May 1997.

Solar Radiation Site Upgrades

Pyranometers mounted on trackers equipped with shade disk systems enable more accurate measurement of the total solar irradiance because of the partitioning of the total global irradiance into two parts: the direct beam and the diffuse sky components respectively. The direct beam component is typically measured with a pyrheliometer mounted on the tracker and the diffuse is measured with a pyranometer shaded by the tracking disk system. During clear sky conditions, when a pyranometer is shaded, the measurement errors due to departures from ideal cosine response are minimized. When this measurement is summed with the direct beam measurement, which can be quite accurate if a self calibrating cavity radiometer is used (±0.3% absolute), the resulting measure of solar irradiance is the best achievable with currently deployable instrumentation.

The Bermuda instrument upgrade was completed in February 1996. Kwajalein was upgraded during April 1996. Environmental and mechanical difficulties with the Kwajalein tracker unit led to a tracker exchange in May 1997. Additional mechanical problems were experienced with the Kwajalein tracker in late 1997, and another exchange of trackers is scheduled for January 1998. The MLO upgrade was completed during May 1997. However, MLO has had diffuse measurement capability for many years using older methodology. An automated solar tracker fitted with a tracking disk system was installed to modernize the MLO installation. The original diffuse system at MLO is also being maintained to provide additional redundancy for this important measurement. During November 1997 the MLO suite of solar sensors, including the tracker, was moved to the new MLO observatory building roof platform.

At the end of 1997 all CMDL radiation measurement sites were equipped for continuous measurement of diffuse-sky irradiance using tracking disk systems mounted on automated solar trackers. The next upgrade is the implementation of direct-beam measurements using self-calibrating all-weather cavity radiometers to further reduce the uncertainties. These upgrades are scheduled for 1998 and 1999. Development and testing of all-weather cavity radiometers for CMDL radiation field sites is in progress.

Special Projects and Measurement Intensives

A prototype version of an open window all-weather cavity radiometer system was tested during the summer of 1996. The unit was based on the Eppley model AHF system and incorporated a ventilated housing unit to protect the open cavity from debris that could enter the opening. Because of size limitations and other considerations, and after additional testing, the concept of an open, all-weather cavity system was set aside in favor of a cavity fitted with a window. The presence of a window adds complexity because of spectral cutoff considerations, particularly at the long wavelength limits. At the end of 1997 the possibility of an alternative window material was being explored.

For several weeks during the winter of 1996 and 1997 and again for 2 weeks in August of 1997, an evaluation of the "solar components" method of determining total solar irradiance was conducted. This method simply uses the sum of the vertical component of the direct beam and the diffuse irradiance determined from a tracking shade disk pyranometer. This method is recommended by BSRN but has not been extensively tested. During these two periods, known as Wintertime Solar Components Evaluation Experiment (WinSCEE) and Summertime Solar Components Evaluation Experiment (SumSCEE) an array of various pyrheliometers, cavity radiometers, pyranometers, and shade disk pyranometers was assembled at the SRF.

The experiment effectively created nine duplicates of a typical installation at a CMDL radiation monitoring site. A reference irradiance was created by operating absolute cavity radiometers and then constructing a component sum using the average of the cavity radiometers and then summing it with the average from the diffuse group. A set of global irradiances operationally equivalent to typical field measurements was created by using individual pairs of pyrheliometers and tracking disk shaded pyranometers. Departures from the reference irradiance were computed by differencing the reference global irradiance and the global irradiance obtained using individual pairs of pyrheliometers and tracking disk shaded pyranometers. To demonstrate the advantages of the component summation technique for determination of global irradiances, the difference between the reference and a global irradiance obtained using a single unshaded pyranometer was also computed. The measurement intensives were conducted during winter and summer periods to examine the performance of the sensors during different seasons and solar positions. The results of this study were summarized by *Michalsky et al.* [1998], and the advantage of the component summation technique using cavity radiometers for direct-beam measurement is evident.

In summary, the results indicated that at the 95% confidence level the uncertainty in unshaded pyranometers was about 20 W m^{-2}, but for the sum of an arbitrary pyrheliometer and shade disk pyranometer the uncertainty dropped to 9 W m^{-2}, and for the combination of an

arbitrary cavity and a selected shaded diffuse the uncertainty drops to 5 W m^{-2}. This demonstrated that the cavity component sum does tend to meet the BSRN specifications of 5 W m^{-2}. These results are summarized in Figure 3.16. The process of carrying out our first WinSCEE resulted in considerable attention being paid to CMDL's Boulder measurement capabilities and resulted in extended research on the functionality of other research-grade irradiance measuring instrumentation as compared with SIO. The SCEE events also led to the identification and quantification of a phenomenon heretofore unnamed but now widely referred to as a "radiation hole" and to additional local collaboration on various aspects of cloud radiation properties.

A second experiment and measurement intensive was conducted during August 1997. The resources of the SRF were utilized to conduct a side-by-side comparison of techniques for determination of global solar irradiance. The SRF utilized absolute cavity radiometers plus tracking disk shaded pyranometers to determine the global irradiance via the component summation method. This system was operated in parallel with a pyroelectric detector radiometer system from SIO . The data from the side-by-side blind comparison are being analyzed at NASA Goddard and results are scheduled to be made available in 1998.

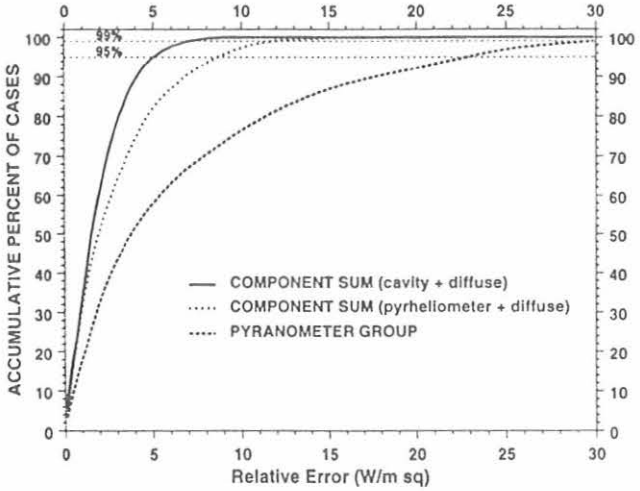

Fig. 3.16. Accumulative percentage of occurrences versus irradiance errors where the irradiance error is defined as the difference between a single instantaneous test observation and the value of a reference observation. This figure is based on over 250,000 individual observations under all sky conditions during WINSCEE. Three difference measurement techniques are compared. The merit of each measurement technique, relative to the reference, is indicated by a lower error for a given percentage of occurrence such as indicated by the 95% and 99% lines.

3.2.3. Aerosol Optical Depth Remote Sensing

Current aerosol optical depth activities include the filterwheel normal incidence phyrheliometer (FWNIP) project, the MLO Physikalisch-Meteorologisches Observatorium Davos (PMOD) sunphotometer, a small group of hand-held instruments used for special projects, and a group of multifilter rotating shadowband radiometers (MFRSRs). The FWNIP project has been discussed in earlier reports. In the near future the analysis and processing of data from the FWNIP will be upgraded to utilize a new radiative transfer model, MODTRAN 4.0. The PMOD photometer continues to collect data at MLO as it has for the past 15 years. However, the operation of the astronomical dome and the data acquisition system was updated in late 1995 and new data processing was initiated, but no newly analyzed data are available for preliminary release at this time. The hand-held instrument calibrations were conducted at MLO and in the mountains west of Boulder, Colorado. These hand-held instruments were used in the Aerosol Characterization Experiment (ACE)I and ACEII field programs as well as in the arctic and antarctic.

MFRSRs were deployed at Bermuda (February 1996), Kwajalein (April 1996), and BAO (November 1996) in conjunction with the BSRN program. The main goal of this program is to obtain a spectral optical depth time series and to maintain calibrations using Langley analysis. Data are currently downloaded from the sites and archived automatically.

3.2.4. MLO UV Spectroradiometer

A UV spectroradiometer was installed at MLO in July 1995. The first 3 months of data were described by *Bodhaine et al.* [1996], and the first complete year of data was described by *Bodhaine et al.* [1997]. The UV irradiances measured at MLO are much more intense than at low-altitude midlatitude locations. A brief introduction to the program and description of the instrument were presented in section 3.2.4 of *CMDL Summary Report No. 23*. The spectroradiometer was located on a small concrete pad just upslope from the solar radiation building for almost 2 full years (July 1995-June 1997). Here we present the 2-year data set selected for clear mornings only. Clear mornings occur at MLO approximately 60% of the time providing an excellent site for solar radiation measurements and especially Langley calibrations. All processed spectral data are available from CMDL data archives.

Instrumentation

The UV spectroradiometer was described by *McKenzie et al.* [1992] and *Bodhaine et al.* [1997]. Briefly, a diffuser designed to minimize cosine error is mounted as a horizontal incidence receptor to view the whole sky. A quartz dome protects the diffuser from the weather. A shading disk can be mounted on the instrument in order to separate the diffuse and direct radiative components. Stepper-motor driven gratings cover the spectral range of 290-450 nm with a bandpass of about 1 nm. A complete scan requires about 200 seconds. The computer control and data logging system are located in the solar radiation building.

Absolute calibration of the spectroradiometer is performed at approximately 6-month intervals using a National Institute of Standards and Technology (NIST)-traceable 1000-W FEL lamp. Weekly stability calibrations

are performed using a mercury lamp and a 45-W standard lamp. The expected long-term accuracy of the spectroradiometer system is better than ±5%. A detailed error analysis for this instrument was given by *McKenzie et al.* [1992] and was also discussed by *Bodhaine et al.* [1997].

Data Analysis

For the following analysis, UV spectroradiometer data for 45° solar zenith angle (SZA) were chosen for clear mornings at MLO during the July 1995-June 1997 time period. This comprises nearly 2 full years of data, amounting to 230 data points, and includes ozone values in the range 212-309 Dobson Units (DU).

Clear mornings at MLO were determined in the same manner as in the previous studies, that is, a day was accepted as a clear day if the sky was cloudless from dawn through the time of the 45° scan and if Dobson ozone data were available for that morning. Figure 3.17 shows 1-nm means for selected wavelengths for a SZA of 45°. At the shortest wavelengths the variations in UV irradiance are caused primarily by variations in ozone. Variations at the longer wavelengths are less influenced by ozone but may be caused by other atmospheric constituents such as Asian desert dust. Note that the large decrease evident at 325 nm in February 1997 amounts to only about 20%, whereas the corresponding decrease at 195 nm is more than 50% and is caused primarily by an increase in ozone. Missing ozone data caused the unfortunate gap in March-April 1997. Erythemal radiation data were obtained from the spectroradiometer data by applying the erythemal weighting function of *McKinlay and Diffey* [1987] and integrating over wavelength for each scan as discussed by *Bodhaine et al.* [1997]. Figure 3.18 shows the time series of erythema data and ozone data to illustrate the direct correspondence for the same 2-year period.

The radiative amplification factor (RAF), defined as the percent change of UV (erythemal) irradiance divided by the percent change of total ozone, for the 2-year peoriod is shown in Figure 3.19. Here the RAF was calculated using the power-law formulation of *Madronich* [1993]: RAF = $-\Delta\ln(I)/\Delta\ln(O_3)$, where I is UV irradiance. The RAF is simply the slope of the fit on a log-log plot, in this case 1.22. It should be noted that this value is somewhat less than the value of 1.33 found by *Bodhaine et al.* [1997] for the first year of data.

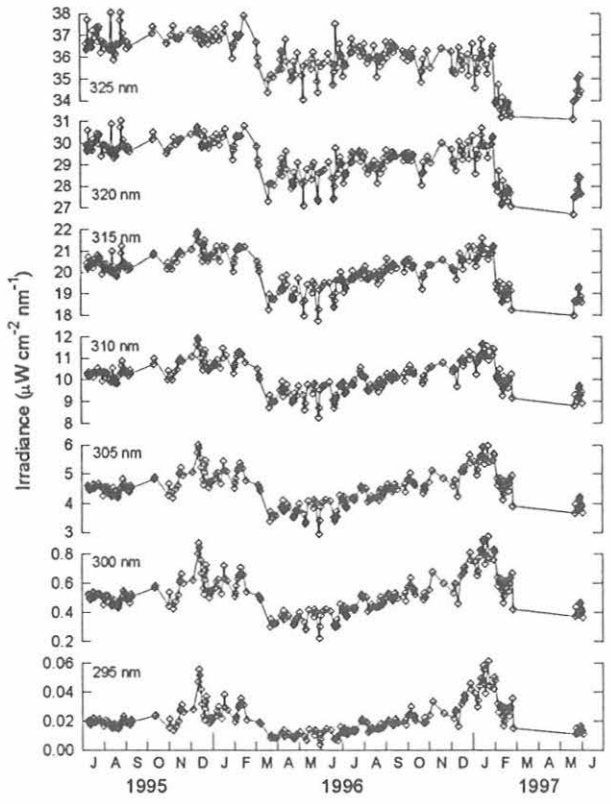

Fig. 3.17. Spectral irradiance (1-nm averages) on 230 clear sky mornings at MLO for selected wavelengths at SZA 45° over the time period July 1995-June 1997.

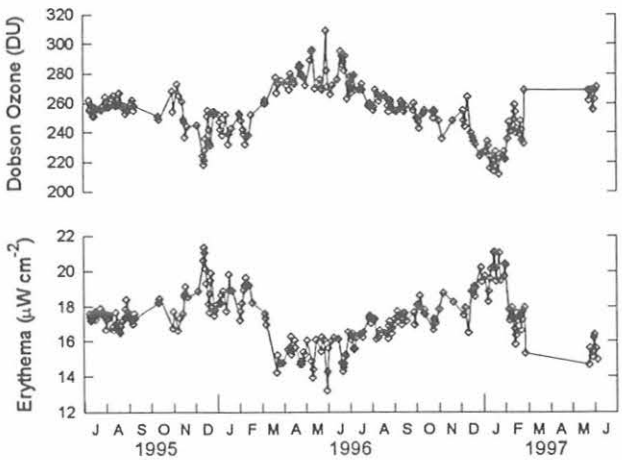

Fig. 3.18. Erythemal irradiance at SZA 45° (bottom) and total ozone (top) on 230 clear sky mornings at MLO over the time period July 1995-June 1997.

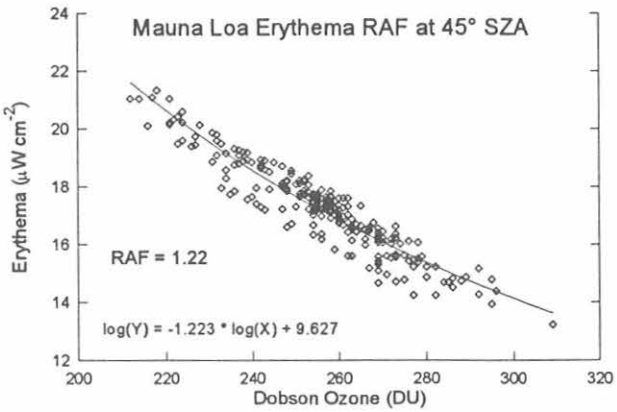

Fig. 3.19. Power law regression between erythemal irradiance at SZA 45° and Dobson total ozone for 230 clear sky mornings at MLO over the time period July 1995-June 1997. The graph is plotted on a linear scale to facilitate reading the units. The coefficient of the linear term gives the power law RAF.

In conclusion, erythema irradiance calculated from the spectroradiometer is strongly correlated (inversely) with Dobson total ozone. Spectral UV irradiance variations are strongly correlated with total ozone variations, with the highest correlations at the shortest wavelengths. The erythema RAF measured at MLO for the 2-year period is about 1.22, somewhat less than the 1.33 value reported for the first year, and no significant trend in UV irradiance may yet be inferred because of the limited time period.

3.2.5. BROADBAND UV

A broadband UV instrument (Yankee UVB-1, SN 950208) has been in operation at MLO since August 1995. Additional broadband UV instruments are being used routinely at BRW, BAO, Bermuda, and Kwajalein as part of the BSRN program. These additional instruments have all been compared at various times with the MLO instrument. A calibration procedure was developed for the broadband instruments using a long-term comparison (1 year) between the MLO UVB-1 and the MLO UV spectroradiometer that was installed at MLO in July 1995 [*Bodhaine et al.,* 1998].

One year of clear sky data was analyzed for SZA of 5°-85°, in steps of 5° and for total ozone values in the range 220-310 DU measured with a Dobson spectrophotometer. Because the erythemal response defined for human skin is significantly different than that of the broadband instrument, the calibration of the broadband instrument reporting in erythemal units is strongly dependent on total ozone. When a broadband instrument is placed in the field, it is necessary to know the calibration as a function of ozone to determine accurate erythemal irradiance. However, the manufacturers of broadband instruments do not generally provide information on the ozone dependence of the calibration. The procedure described here provides this information and does not require precise knowledge of the spectral response of the broadband instrument.

Instrumentation

The principle of operation of the UVB-1 instrument depends on a UV-sensitive phosphor that absorbs radiation in the UV-B region and re-emits in the green region. Radiation from the whole sky passes through a quartz dome and is incident on a horizontal UV broadband filter that transmits the UV to the phosphor. The green light emitted by the phosphor passes through a green filter and is measured by a photodiode that has its peak response in the green part of the spectrum. The UVB-1 is temperature stabilized at 45°C.

The manufacturer provides conversion factors for estimating various portions or weighted integrals of the UV spectrum, such as total UVB (280-315 nm or 280-320 nm), Diffey Action Spectrum, Parrish Action Spectrum, or the DNA weighted spectrum. However, these estimates can be significantly in error because of the fact that the actual spectral response of the instrument can be significantly different than the portion of the spectrum being estimated which in turn causes strong ozone dependence of the measurements. This occurs because of the strong spectral variation of ozone absorption of UV in the UVB region of the spectrum. The absolute calibration of Robertson Berger (RB)-type meters, including detailed theoretical studies of these instruments, was treated by *DeLuisi and Harris* [1981, 1983] and more recently by *Grainger et al.* [1993]; *Mayer and Seckmeyer* [1996]; and *Leszczynski et al.* [1998]. All of these authors compared broadband instruments with a collocated spectroradiometer.

The UV spectroradiometer located at MLO and used in this study was described by *McKenzie et al.* [1992] and its operation at MLO was described by *Bodhaine et al.* [1997]. This instrument uses a horizontally mounted diffuser designed to view the whole sky and minimize cosine error. The spectroradiometer is programmed to begin measurements at dawn and perform scans at 5° SZA intervals throughout the day beginning and ending at 95°, except for a period of time during the middle of the day when the system switches to a scan every 15 minutes.

The UVB-1 data set consists of 3-min means obtained from the MLO data acquisition system. The spectral response of the UVB-1 was taken from the calibration sheet supplied by the manufacturer for this particular instrument, and is shown in Figure 3.20. Also shown in Figure 3.20 is the International Commission on the Environment (CIE) erythema weighting function provided by *McKinlay and Diffey* [1987] to represent the response of human skin to UV irradiance. The two spectra in Figure 3.20 were used to construct two data sets from the spectroradiometer data by weighting and integrating over wavelength. The three data sets used here are:

UVB1: Broadband instrument voltages (V),
S(CIE): CIE spectrum weighted spectroradiometer (μW cm^{-2}),
S(UVB1): UVB-1 spectrum weighted spectroradiometer (μW cm^{-2}).

Three comparisons were done. UVB1 and S(CIE) were compared directly to derive the UVB-1 instrument calibration. The UVB1 and S(UVB1) data sets were compared to show the expected minimum effect of ozone. Also, S(UVB1) and S(CIE) were compared to show a method of simulating the different responses of the UVB-1 and the CIE spectra using spectroradiometer data.

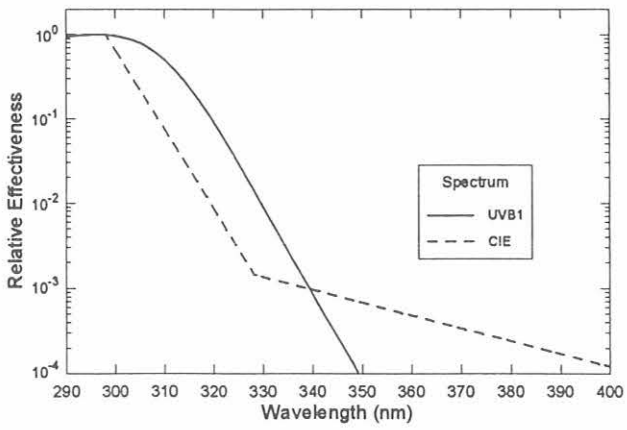

Fig. 3.20. Spectral response of the UVB-1 SN950208 (manufacturer's specifications) compared to the CIE approved spectrum for the response of human skin.

Data Analysis

For the following analysis, UV spectroradiometer data for SZA ≥ 45° were chosen for clear mornings at MLO during the July 1995 to July 1996 time period. This gives 1 full year of data, amounting to 132 data points, allowing the study of an annual cycle, and giving ozone values in the range 220-310 DU. A day was accepted as a clear day as described in the previous section. Data for SZAs smaller than 45° (sun higher in the sky) were obtained from days when morning clear conditions extended long enough, and during those times of the year when the sun was high enough in the sky. All Dobson ozone data were derived from A-D direct sun ground quartz plate observations [*Komhyr et al.*, 1993].

In order to ensure that the spectroradiometer and UVB-1 data were simultaneous, a linear interpolation was performed on the UVB-1 voltage time series in order to assign values coincident in time with spectroradiometer weighted irradiance values. In this way the three data sets could be compared at the same effective times. Finally, the three ratios (UVB1)/S(CIE), (UVB1)/S(UVB1), and S(UVB1)/S(CIE) were formed in preparation for regression against the ozone data set.

Figure 3.21b shows the ratio (UVB1)/S(CIE) plotted as a time series for the SZA 45° data. If the instruments were in exact agreement, the ratio would be equal to 1 everywhere. However, the time series show not only an offset but also an annual cycle that appears to correlate very well with the MLO ozone time series shown in Figure 3.21a. This correlation with ozone suggests that the calibration of the broadband instrument depends significantly on total ozone.

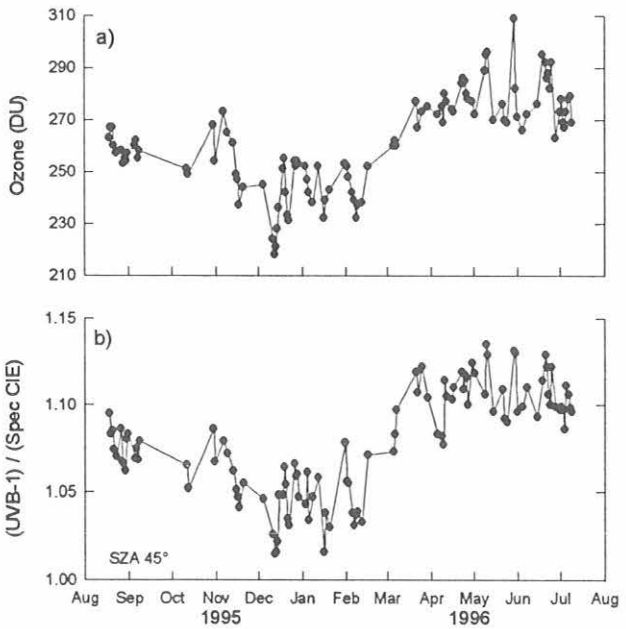

Fig. 3.21. Time series of (a) total ozone (Dobson), and (b) ratio of UVB-1 erythema to spectroradiometer erythema (CIE-weighted spectra) at SZA 45°. UVB-1 erythema values were calculated using the manufacturer's suggested calibration factor (0.141 W cm^{-2} V^{-1}). Note that the average of the erythema ratios appears to be close to the slope of the regression line in Fig. 2.

On the basis of the apparent dependence of the ratio (UVB1)/S(CIE) on total ozone, the following procedure was developed for the calibration of the UVB-1 broadband instrument in CIE erythema units. An example for SZA 45° is shown in Figure 3.22. The ratio (UVB1)/S(CIE) was regressed against the ozone data set to produce a linear equation describing the relationship. Some scatter exists about the regression line but the correlation is still fairly high. The equation relating the ratio (UVB1)/S(CIE) and ozone was then used to recover estimated erythema values, given UVB-1 voltages at the prescribed SZA (45° in this case), where total ozone is the independent variable. This process was repeated for SZAs from 5° to 85° in steps of 5°, giving a family of linear calibration equations depending only on ozone. The regression equations were expanded into an array of calibration factors depending on SZA and ozone and the results are shown in Figure 3.23 as a family of curves where different curves are given for different values of total ozone. This revealing figure shows that the ozone dependence is positive for small SZAs, becomes zero at SZA 65°, and becomes negative at large SZAs. This strange behavior is because different spectra respond differently to ozone. This effect is explained in more detail by *Bodhaine et al.* [1998].

To obtain a more complete understanding of the effects discussed here, two additional similar sets of analyses were performed. To show that the dependence on ozone is because of the different spectral responses of UVB1 and CIE, the entire analysis was repeated using the UVB1 and S(UVB1) data sets that presumably have the same spectral response. The ozone dependence was found to be small in this case [see *Bodhaine et al.*, 1998].

In the third case study S(CIE) and S(UVB1) were compared. Since the same sensor was used for these two data sets by treating the ratio S(UVB1)/S(CIE), instrumental effects are minimized. Thus this test should reveal the true ozone dependence that results from comparing the two different spectra. Figure 3.24 shows the family of curves that gives the correction factor as a function of SZA for various values of ozone. In this case the ozone dependence is almost wholly due to the two different spectra and is not significantly influenced by the use of two different sensors.

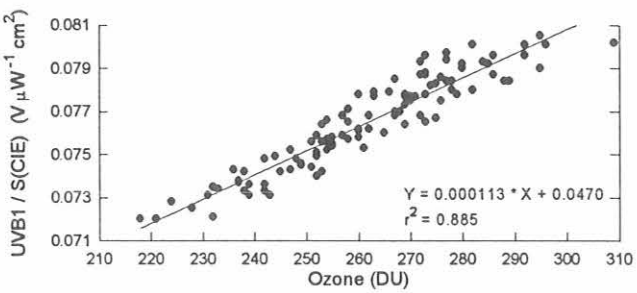

Fig. 3.22. Calibration analysis of the UVB-1 broadband instrument voltages compared to the CIE-weighted spectroradiometer data (erythema) as a function of ozone for SZA 45°. The graph shows the regression of the ratio (UVB1)/S(CIE) against ozone. Note the strong dependence on ozone.

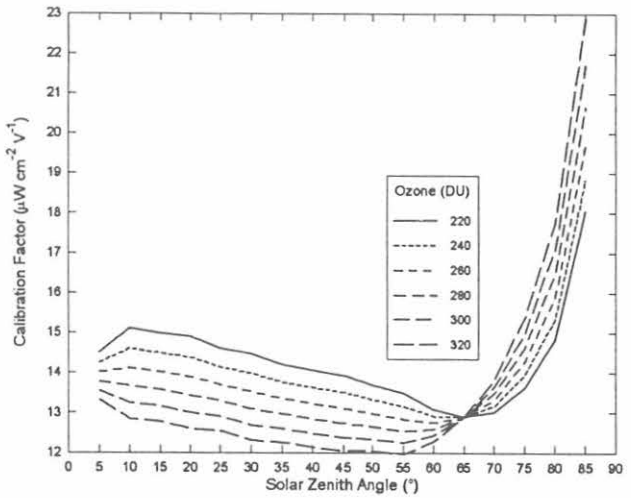

Fig. 3.23. Family of calibration factor curves as a function of SZA for various values of ozone. The calibration factor is essentially S(CIE)/(UVB1) so that multiplying the UVB-1 voltage by the calibration factor for the proper SZA and ozone value gives the predicted erythema for the broadband instrument.

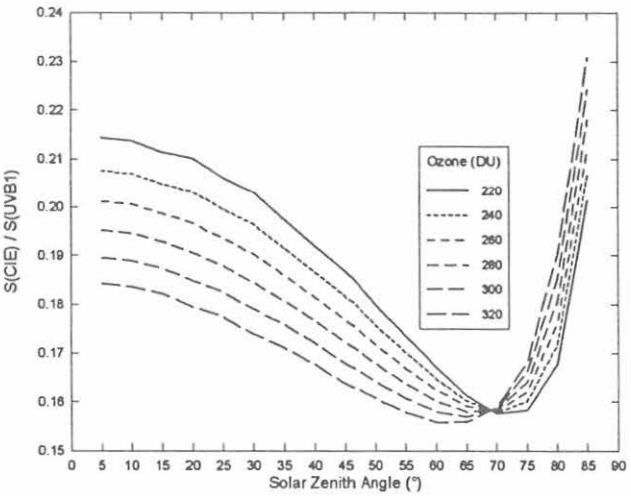

Fig. 3.24. Family of calibration factor curves as a function of SZA for various values of ozone. The calibration factor is essentially S(CIE)/S(UVB1) so that multiplying the S(UVB1) data by the calibration factor for the proper SZA and ozone value gives the predicted erythema for the broadband instrument.

Model Results

To investigate the results of the instrument comparison given previously, radiative transfer (RT) calculations simulating the above measurements were performed. Solar UV irradiances with spectral resolution similar to that of the MLO spectroradiometer were calculated for MLO atmospheric conditions using a version of DISORT [*Stamnes et al.*, 1988] that was implemented at CMDL. The model's spectral results for various SZAs and ozone amounts were weighted by the S(CIE) and S(UVB1) spectra to simulate the measurements given in Figure 3.24, and the results of the model calculations are shown in Figure 3.25. It is seen that the model calculations agree with the measurements in Figure 3.24 within about 7% and the general shape of the curves is replicated. Model calculations of a somewhat similar nature were performed by *Leszczynski et al.* [1998].

Because broadband UV sensors, such as the RB type instrument, are commonly used to estimate erythemal irradiance, it is extremely important to develop a calibration procedure applicable under a full range of field conditions. The best method of calibrating a broadband sensor is to compare it directly with a well-calibrated spectroradiometer and to integrate the resulting spectra over the same spectral response as the broadband instrument. However, a given calibration factor is only good for a particular value of SZA and a particular value of total atmospheric ozone.

This analysis shows that if, for example, total ozone concentration decreased from 300 DU to 200 DU, the calibration constant of a broadband instrument should be increased by almost 20%. Therefore, the broadband instrument would significantly underestimate the increase of erythema.

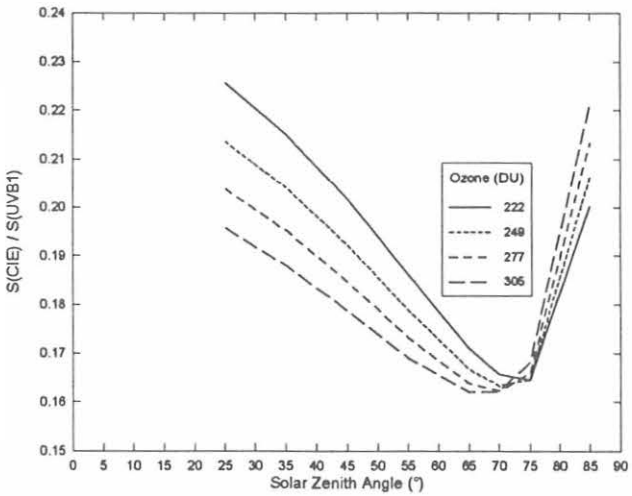

Fig. 3.25. Model calculations of the family of calibration factor curves as a function of SZA for various values of ozone using the CMDL version of DISORT to simulate S(CIE)/S(UVB1). This figure may be compared directly with Figure 3.26. Details of the model are given in the text.

3.2.6. Baseline Surface Radiation Network (BSRN)

CMDL continues to play an active role in the management of the WCRP BSRN. One of the recommendations of the BSRN is the routine use of cavity radiometers at the BSRN field sites. The requirement has proven to be particularly problematic. Our approach has been to use the cavity sparingly under supervision at the field sites and depend primarily on a calibrated pyrheliometer. This has resulted in too-infrequent field

cavity operations to meet the spirit of the BSRN recommendations. The STAR group has embarked on a course to develop an alternate approach that significantly improves upon pyrheliometer performance and only falls slightly short of the standard cavity performance. The approach is the use of an extremely wide spectral window, Supersill 300, on the front of the cavity that not only seals the interior of the cavity from the elements but protects it from adverse convective heat transfer and intrusions by particulate matter. This mode of operation was possible on earlier cavities available from Eppley Instruments, but Eppley has been working on modifications of the cavity heating cycles to account for continuous windowed operations. These modifications account for excess heat in the unwindowed version that readily escapes out the aperture. Temperature stabilization of the actual cavity area is desired. We will soon be receiving and testing one of the modified units. Radiative transfer calculations show a 5 to 7 W m^{-2} effect on the window, depending on column water vapor at SZA less than about 60° and decreasing to near 0.0 at a SZA of 90°. The full range of the variability, because of different amounts of vertical water column is about ±1 W m^{-2}, thus permitting a rather straight forward correction to the windowed measurement as a function of the SZA with a simple refinement for the water vapor amount to bring the adjusted value to within about 1 W m^{-2} of the true value.

A new BSRN activity by CMDL involved the purchase of equipment for a BSRN monitoring site at Balbina in the Amazon region of Brazil. A site visit was made during September 1997 and assistance was provided during the installation and setup of the instrumentation and data acquisition system.

3.2.7. WMO Global Atmosphere Watch (GAW) Stations

The SRF continued its contributions to the WMO Global Environment Facility (GEF) GAW effort. Components were ordered and configured for a fifth solar radiation monitoring system that will be installed at the GAW baseline station in Arembepe, Brazil. Also a solar radiation monitoring system was configured for installation at a new monitoring site located in South Africa. The CMDL equipment recommendations were forwarded to the WMO for procurement and shipment to South Africa.

3.2.8. Barrow Snow Melt Date

In order to understand global climate change more fully, an assessment of the variability of the Earth's cryosphere in response to other climatic factors is necessary. An important process that occurs each spring along the arctic cryospheric boundary is the melting of the seasonal snow pack. The timing of this event can influence the net energy budget of an entire season or year, and feedbacks involving changes in surface albedo, in turn, influence the regional temperature regime. The variability of annual snow melt at any particular location depends on many interactive processes. Although temperature is an obvious primary factor that controls the timing and rate of melt, changes in cloud conditions, thermal stability of the atmosphere, and the precipitation that occurs during the preceding seasons are also very important. The depth of accumulated snow and its influence on permafrost properties must also be considered when evaluating any long-term trends in snow extent and its seasonal duration.

An interesting feature of the spring melt in northern Alaska is that once it begins it commences at a very rapid rate (see Figure 3.26). Figure 3.26a shows the relative changes in the components of the net solar radiation balance at the surface, shortwave down (SWD) and shortwave up (SWU), respectively, for 1 year at BRW. Figure 3.26b shows the derived albedo (SWD/SWU) and indicates the "snow melt date" which at BRW is based radiometrically on a 30% albedo threshold. This value was found to be a good objective measure because once below this value, it seldom increases again until autumn except for an occasional late snowfall of brief duration. Although the decrease in albedo occurs very rapidly, typically in a matter of a few days, the period in which this occurs each spring can vary from the third week in May to the end of June.

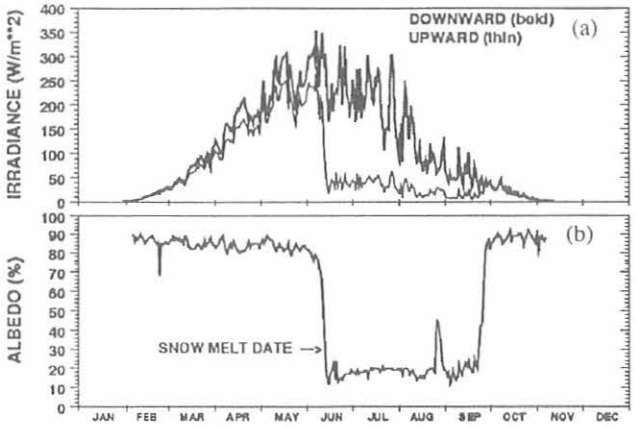

Fig. 3.26(a) Daily average downward and upward shortwave irradiance measured at BRW during 1994; (b) the snow melt date is determined radiometrically as the date when the surface albedo drops below 30% [adapted from *Stone et al.*, 1996].

More important from a climate change perspective is the suggestion that in recent decades melting has occurred earlier in the season, indicating a trend possibly related to global warming. One of the main features of global climate models that simulate the effects of increasing greenhouse gases in the atmosphere is an enhancement of warming in the arctic because of a positive feedback caused by decreasing surface albedo. The decrease results initially from the melting of ice and snow. Therefore, the date of annual melt is of great interest as a potential indicator of climate change.

Foster [1989] and *Foster et al.* [1992], on the basis of historic visual observations, claimed that the disappearance of snow in spring at Barrow showed a trend manifested by a progressively earlier melt since the 1950s and speculated that this was an indication of global

warming. *Dutton and Endres* [1991], however, took issue with Foster's conclusion suggesting that the apparent trend was in large part attributable to local urbanization effects. Their argument was based on objective, radiometric measurements made over the open tundra similar to those illustrated in Figure 3.26b. The tundra site is not likely to be influenced by urban effects because it is in a pristine location 8 km upwind of BRW. This comparison [*Dutton and Endres,* 1991] was only possible for a few years of overlapping records.

The issue is revisited in Figure 3.27 where it shows the respective time series updated through 1996. The time series were fitted using a smoothing function to indicate apparent trends. It now appears that the radiometric estimates of the snow melt date made at BRW are also tending to occur earlier in recent years. Moreover, there is a temporal correlation between the two independent observations giving credence to both data records, despite recent confirmation that the site in town is no longer representative of the surrounding tundra. It is hypothesized that earlier melting of the snow pack in the vicinity of BRW, on average, may result from less than normal accumulation of snow throughout the winter, warmer spring temperatures associated with enhanced cloudiness that accelerates ablation/melt or both. More subtle changes that affect the permafrost may also be a factor, but these are very difficult to quantify. Synoptic-scale changes in circulation patterns that have influenced northern Alaska's climate in recent years [*Stone,* 1997] probably have contributed to what appears to be a shift toward earlier spring conditions there. The interrelationship between snow distribution and other climate variables is the subject of ongoing research.

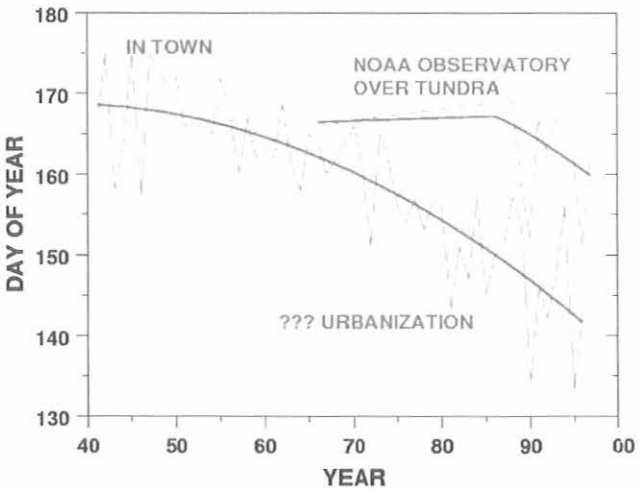

Fig. 3.27. The date of snow melt in the vicinity of Barrow is apparently occurring earlier. In town, however, the disappearance of snow is occurring earlier than at the CMDL observatory located at a remote tundra site, probably because of increased use by inhabitants and other effects of urbanization [e.g., *Dutton and Endres,* 1991].

3.2.9. Arctic UV Monitoring

In September 1997, the STAR group and the University of Alaska, Fairbanks, began an investigation of the UV-B radiation environment in the U.S. arctic by deploying two portable, inexpensive UV-measuring instruments at BRW. Rare and fragile life forms and the potential for excessive stratospheric ozone loss in the arctic make the monitoring of actual variations in the biologically sensitive regions of the UV spectrum particularly important in the Alaskan arctic and the Bering Sea region [*DeFabo,* 1995, 1997; *Nilsson,* 1997; *Madronich et al.,* 1996]. Because ozone in the stratosphere strongly absorbs energy in the UV-B portion of the solar spectrum (280 to 320 nm), any changes in the total amount of ozone affect the levels of UV-B radiation reaching the ground.

Support for this effort was received under a NOAA Arctic Research Initiative managed for NOAA by the Cooperative Institute for Arctic Research. One instrument in use is a Yankee broadband UV pyranometer that measures global solar UV-B irradiance. The other instrument is a Biospherical Instruments, Inc. (BSI) narrowband UV radiometer that measures irradiance in five optical channels (305, 313, 320, 340, and 380 nm). Figure 3.28 and Figure 3.29 show the daily average total irradiance for both instruments for September 17-November 17, 1997. Another multi-channel radiometer purchased from the Norwegian Institute for Air Research (NILU) will be installed at BRW sometime in early 1998. The BSI radiometer has compared favorably with the BSI scanning spectroradiometers linked to the U.S. National Science Foundation's polar UV monitoring network. However, the spectroradiometers are expensive and not always feasible for conducting studies in remote regions in the arctic.

Within NOAA there have been significant efforts to evaluate and calibrate UV instrumentation [*Bodhaine et al.,* 1996, 1997, 1998; *Weatherhead and Webb,* 1997; *Webb and Weatherhead,* 1996]. These efforts were well received internationally and formed the basis for continued efforts in collaboration with the Universities of Alaska (Fairbanks) and Colorado (Boulder), for 1998 and 1999 to assess the UV variability in and near the Bering Sea. The Bering Sea is an important region for biological primary production. The area has shown strong variability in biological production that, so far, is not well understood

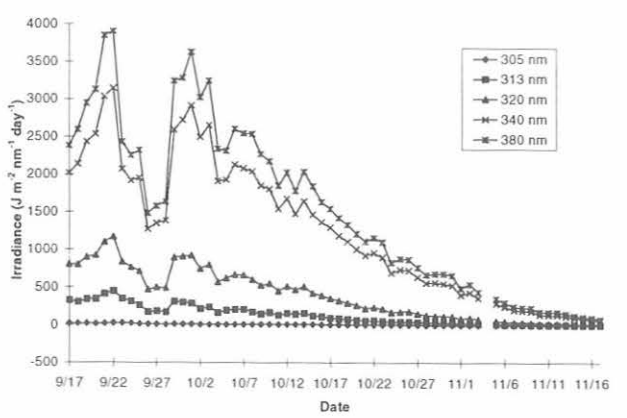

Fig. 3.28. Daily average total irradiance for the BSI radiometer at wavelengths 305, 313, 320, 340, and 380 nm for the period September 17-November 17, 1997. The data for November 4 were eliminated because the instrument may have malfunctioned that day.

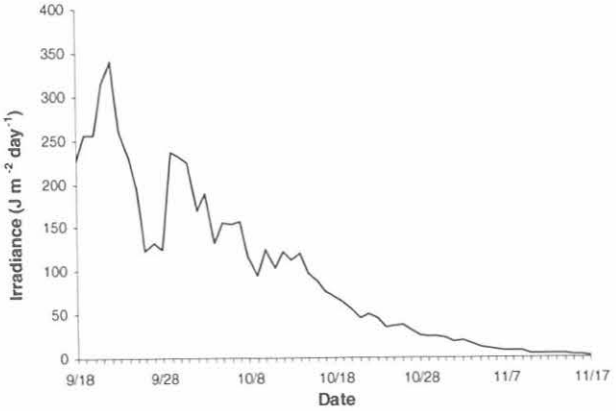

Fig. 3.29. Daily average total irradiance for the YES UV pyranometer for the period September 18-November 17, 1997.

[*DeFabo,* 1995; *Nilsson,* 1997; *Jin et al.,* 1994]. The use of UV monitoring over the next 2 years, in conjunction with other current and planned studies, should help discern if UV and photosynthetically active radiation (PAR) have a strong role in current primary production variability. In other biological studies of UV effects, the magnitude and even the sign of these effects can be linked to other stressors in the environment. The unique nature of the effects of UV with other stressors make it important for many biological studies to have access to accurate UV measurements.

In May 1998 two additional BSI radiometers will be deployed in Alaska: one on St. Paul in the Pribilof Islands (57.09°N; 170.13°W), and the other at Nome, Alaska (64.30°N; 165.26°W), in collaboration with the National Weather Service. These instruments will operate in conjunction with the BSI instruments currently at BRW and the University of Alaska, Fairbanks. The combination of Bering Sea, coastal Arctic Ocean, and internal Alaska sites will allow for a wide range of atmospheric conditions to be monitored in a fairly uniform manner.

3.3. REFERENCES

Barnes, J.E., and D.J. Hofmann, Lidar measurements of stratospheric aerosol over Mauna Loa Observatory, *Geophys. Res. Lett., 24*, 1923-1926, 1997.

Barrie, L.A., Occurrence and trends of pollution in the arctic troposphere, in *Chemical Exchange Between the Atmosphere and Snow*, edited by E.W. Wolff and R.C. Bales, pp. 93-129, Springer-Verlag, Berlin, 1996.

Bergin, M.H., S.E. Schwartz, J.A. Ogren, and L.M. McInnes, Evaporation of ammonium nitrate aerosol in a heated nephelometer: Implications for field measurements, *Environ. Sci. Technol., 31*, 2878-2883. 1997.

Bergin, M.H., E. Meyerson, J.E. Dibb, and P. Mayewski, Comparison of continuous aerosol measurements and ice core chemistry over a 10-year period at the South Pole, *Geophys. Res. Lett., 25*(8), 1189-1192, 1998a.

Bergin, M.H., R.S. Halthorne, S.E. Schwartz, J.A. Ogren, and S. Nemesure, Comparison of aerosol column properties based on nephelometer and radiometer measurements at the SGP ARM site, *J. Geophys. Res.*, submitted, 1998b.

Bodhaine, B.A., Barrow surface aerosol: 1976-1987, *Atmos. Environ., 23*(11), 2357-2369, 1989.

Bodhaine, B.A., Aerosol absorption measurements at Barrow, Mauna Loa, and South Pole, *J. Geophys. Res., 100*, 8967-8975, 1995.

Bodhaine, B.A., and J.J. DeLuisi, An aerosol climatology of Samoa, *J. Atmos. Chem., 3*, 107-122, 1985.

Bodhaine, B.A., and E.G. Dutton, A long-term decrease in arctic haze at Barrow, Alaska, *Geophys. Res. Lett., 20*, 947-950, 1993.

Bodhaine, B.A., J.M. Harris, J.A. Ogren, and D.J. Hofmann, Aerosol optical properties at Mauna Loa Observatory: Long-range transport from Kuwait?, *Geophys. Res. Lett., 19*(6), 581-584, 1992.

Bodhaine, B.A., J.J. DeLuisi, J.M. Harris, P. Houmere, and S. Bauman, Aerosol measurements at the South Pole, *Tellus, 38*B, 223-235, 1986.

Bodhaine, B.A., J.J. DeLuisi, J.M. Harris, P. Houmere, and S. Bauman, PIXE analysis of South Pole aerosol, *Nucl. Inst. Method, 22*(B), 241-247, 1987.

Bodhaine, B.A., R.L. McKenzie, P.V. Johnston, D.J. Hofmann, E.G. Dutton, R.C. Schnell, J.E. Barnes, S.C. Ryan, and M. Kotkamp, New ultraviolet spectroradiometer measurements at Mauna Loa Observatory, *Geophys. Res. Lett., 23*, 2121-2124, 1996.

Bodhaine, B.A., E.G. Dutton, D.J. Hofmann, R.L. McKenzie, and P.V. Johnston, UV Measurements at Mauna Loa: July 1995 to July 1996, *J. Geophys. Res., 102*, 19,265-19,273, 1997.

Bodhaine, B.A., E.G. Dutton, R.L. McKenzie, and P.V. Johnston, Calibrating broadband UV instruments: Ozone and solar zenith angle dependence, *J. Atmos. Oceanic Technol.*, 15, 916-925, 1998.

Charlson, R.J., S.E. Schwartz, J.M. Hales, R.D. Cess, J.A. Coakley, Jr., J.E. Hansen, and D.J. Hofmann, Climate forcing by anthropogenic aerosol, *Science, 255*, 423-430, 1992.

DeFabo, E., Effects of Increased Ultraviolet radiation in the arctic, in *Int. Arctic Science Comm. Rep. No. 2*, Oslo, Norway, 56 pp., 1995.

DeFabo, E., Ultraviolet international research centers, in *Int. Arctic Science Comm. Rep. No. 7*, Oslo, Norway, 36 pp., 1997.

DeLuisi, J.J., and J.M. Harris, Characteristics of ultraviolet radiation in the human erythema band measured with a Robertson-Berger meter and a double monochromator, *NOAA Tech. Memo. ERL ARL-99*, Air Resources Laboratories, Silver Spring, MD, 43 pp., 1981.

DeLuisi, J.J., and J.M. Harris, A determination of the absolute radiant energy of a Robertson-Berger meter sunburn unit, *Atmos. Environ., 17*, 751-758, 1983.

Dutton, E.G., A coherence between the QBO and the amplitude of the Mauna Loa atmospheric transmission annual cycle, *Int. J. Clim., 12*, 383-396, 1992.

Dutton, E.G., and D.J. Endres, Date of snow melt at Barrow, Alaska, USA, *Arc. Alp. Res., 23*, 115-119, 1991.

Dutton, E.G., J.J. DeLuisi, and A.P. Austring, Interpretation of Mauna Loa atmospheric transmission relative to aerosols, using photometric precipitable water amounts, *J. Atmos. Chem., 3*, 53-68, 1985.

Foster, J.L., The significance of the date of snow disappearance on the arctic tundra as a possible indicator of climatic change, *Arc. Alp. Res., 21*, 60-70, 1989.

Foster, J.L., J.W. Winchester, and E.G. Dutton, The date of snow disappearance on the Arctic tundra as determined from satellite, meteorological station, and radiometric in situ observations, *IEEE Transactions on Geoscience and Remote Sensing, 30*, 793-798, 1992.

Grainger, R.G., R.E. Basher, and R.L. McKenzie, UV-B Robertson-Berger meter characterization and field calibration, *Appl. Opt., 32*, 343-349, 1993.

Jin, Z., K. Stamnes and W.F. Weeks, Transport of photo-synthetically active radiation in sea ice and ocean, in *Ocean Optics XII*, edited by J. Jaffe, Proc. SPIE 2258, 954-964, 1994.

Komhyr, W. D., C. L. Mateer, and R. D. Hudson, Effective Bass-Paur 1985 ozone absorption coefficients for use with Dobson ozone spectrophotometers, *J. Geophys. Res., 98*, 20,451-20,465, 1993.

Leszczynski, K., K Jokela, L. Ylianttila, R. Visuri, and M. Blumthaler, Erythemally weighted radiometers in solar UV

monitoring: Results from the WMO/STUK intercomparison. *Photochem. Photobiol., 67*, 212-221, 1998.

Madronich, S., The atmosphere and UV-B radiation at ground level, in *Environmental UV Photobiology,* edited by A.R. Young et al., Plenum Press, New York, pp. 1-39, 1993.

Madronich, S., E. Weatherhead, and S. Flocke, Trends in UV radiation, *Int. J. Environ. Studies, 51*, 183-198, 1996.

Mayer, B., and G. Seckmeyer, All-weather comparison between spectral and broadband (Robertson-Berger) UV measurements, *Photochem. Photobiol., 64*, 792-799, 1996.

McGee, T.J., et al., Intercomparisons of lidar-derived temperatures during the MLO3 NDSC validation at Mauna Loa, HI, Proc., 18th International Laser Radar Conference, 1996.

McInnes, L.M., M.H. Bergin, J.A. Ogren, and S.E. Schwartz, Differences in hygroscopic growth between marine and anthropogenic aerosols, *Geophys. Res. Lett., 25*(4), 513-516, 1998.

McKenzie, R.L., P.V. Johnston, M. Kotkamp, A. Bittar, and J.D. Hamlin, Solar ultraviolet spectroradiometry in New Zealand: Instrumentation and sample results from 1990, *Appl. Opt., 31*, 6501-6509, 1992.

McKinlay, A.F., and B.L. Diffey, A reference action spectrum for ultraviolet induced erythema in human skin, *J. Int. Comm. Illum., 6*, 17-22, 1987.

Michalsky, J., et al., Total solar measurements: Comparison of total and component sum, *J. Atmos. Oceanic Technol.*, in press, 1998.

National Research Council (NRC), *Aerosol Radiative Forcing and Climatic Change*, National Academy Press, Washington, D.C., 161 pp., 1996.

Nilsson, A., Arctic pollution issues: A state of the environment report, in *Arctic Monitoring and Assessment Program*, Oslo, Norway, 188 pp., 1997.

Ogren, J.A., A systematic approach to in situ observations of aerosol properties, in *Aerosol Forcing of Climate*, edited by R.J. Charlson and J. Heintzenerg, John Wiley, pp. 215-226, 1995.

Quakenbush, T.K., and B.A. Bodhaine, Surface aerosols at the Barrow GMCC observatory: Data from 1976 through 1985, *NOAA Data Rep. ERL ARL-10*, 230 pp., NOAA Air Resources Laboratory, Silver Spring, MD, 1986.

Radke, L.F., C.A. Brock, R.J. Ferek, and D.J. Coffman, Summertime arctic hazes, paper A52B-03 presented at the Am. Geophys. Union Fall Annual Meeting, San Francisco, December 3-7, 1990.

Stamnes, K., S-C Tsay, W. Wiscombe, and K. Jayaweera, Numerically stable algorithm for discrete-ordinate-method radiative transfer in multiple scattering and emitting layered media, *Appl. Opt., 27*, 2502-2509, 1988.

Steinbrecht, et al., NDSC intercomparison of stratospheric aerosol processing algorithms, Proc., 18th International Laser Radar Conference, 1996.

Stone, R.S., Variations in western arctic temperatures in response to cloud-radiative and synoptic-scale Influences, *J. Geophys. Res., 102*, 21,769-21,776, 1997.

Weatherhead, E.C., and A.R. Webb, International Response to the challenge of measuring UV radiation, *Rad. Protection Dosimetry, 22*, 223-230, 1997.

Webb, A., and E. Weatherhead, Current status of UV measurements, in *Solar Ultraviolet Radiation: Modeling, Measurements and Effects,* NATO ASI Series, Vol. 52, 1996.

4. Ozone and Water Vapor

S. OLTMANS (EDITOR), M. CLARK, R. EVANS, E. HACKATHORN, J. HARRIS, B. JOHNSON, G. KOENIG, M. O'NEILL, D. QUINCY, AND H. VÖMEL

4.1. CONTINUING PROGRAMS

4.1.1. TOTAL OZONE OBSERVATIONS

Total ozone observations continued throughout 1996 and 1997 at 15 of the 16 stations that comprise the U.S. Dobson spectrophotometer network (Table 4.1). Of the 16 stations, 5 were operated by CMDL personnel, 5 by the National Weather Service (NWS), 2 are domestic cooperative stations, and 4 are foreign cooperative stations. All stations are either fully or semiautomated. A Brewer ozone spectrophotometer was operated at Boulder during this period.

The Peruvian station was still out of operation at the end of 1997, although reports indicate a new baseline monitoring station is almost completed. A date for beginning Dobson observations has not yet been established. The Tallahassee station moved from the regional airport to the Florida State University (FSU) campus when the building housing the National Weather Service Office (NSWO) was demolished. The NWSO is temporarily located in the Tallahassee airport terminal until the permanent station is completed on the FSU campus.

Provisional daily total ozone amounts, applicable to local apparent noon for the stations listed in Table 4.1, were archived at the World Ozone and Ultraviolet Radiation Data Centre (WOUDC), 4905 Dufferin Street, Ontario M3H 5T4, Canada, in *Ozone Data for the World*. Table 4.2 lists the monthly mean of the total ozone amounts measured at the various stations. (Monthly means are made for stations where observations were made on at least 10 days each month.)

An analysis of this data was made to ascertain the trend in total ozone and the results published by *Komhyr et al.* [1997]. The resultant trends are summarized in Table 4.3.

4.1.2. UMKEHR OBSERVATIONS

Umkehr observations made with the automated Dobson network instruments continued in 1996 and 1997 at Boulder, Colorado; Haute Provence, France; Lauder, New Zealand; Mauna Loa Observatory, Hawaii (MLO); Perth, Western Australia; and at the Geophysical Institute, University of Alaska. A major effort to bring the processing of Umkehr data up to date was initiated at the beginning of 1996. No data had been processed since the eruption of Mt. Pinatubo in 1991. The processing has been completed through 1997 and ozone profile data for the entire record at each site are available from the WOUDC. The data were used as part of the Stratospheric Processes and their Role in Climate/International/Ozone Commission/World Meteorological Organization (SPARC/IOC/WMO) sponsored assessment report (*Trends in the Ozone Vertical Profile,* to be published in 1998).

As part of the Mauna Loa Ozone Vertical Profile Intercomparison (MLO3) held in August and September 1995, Umkehr observations were made with MLO automated Dobson No. 76 and with World Standard Dobson No. 83. Fifteen matched profiles were obtained.

TABLE 4.1. U.S. Dobson Ozone Spectrophotometer Station Network for 1996-1997

Station	Period of Record	Instrument No.	Agency
Bismarck, North Dakota	Jan. 1, 1963-present	33	NOAA
Caribou, Maine	Jan. 1, 1963-present	34	NOAA
Wallops Is., Virginia	July 1, 1967-present	38	NOAA; NASA
SMO	Dec. 19, 1975-present	42	NOAA
Tallahassee, Florida	May 2, 1964-Nov. 30, 1989; Nov. 1, 1992-present	58	NOAA; Florida State University
Boulder, Colorado	Sept. 1, 1966-present	61	NOAA
Fairbanks, Alaska	March 6, 1984-present	63	NOAA; University of Alaska
Lauder, New Zealand	Jan. 29, 1987-present	72	NOAA; NIWA
MLO	Jan. 2, 1964-present	76	NOAA
Nashville, Tennessee	Jan. 2, 1963-present	79	NOAA
Perth, Australia	July 30, 1984-present	81	NOAA; Australian Bureau Meteorology
SPO	Nov. 17, 1961-present	82	NOAA
Haute Provence, France	Sept. 2, 1983-present	85	NOAA; CNRS
Huancayo, Peru	Feb. 14, 1964-Dec. 31, 1992	87	NOAA; IGP
BRW	June 6, 1986-present	91	NOAA
Fresno, California	June 22, 1983-March 13, 1995	94	NOAA
Hanford, California	March 15, 1995-present	94	NOAA

TABLE 4.2. Provisional 1996 Monthly Mean Total Ozone Amounts (DU)

Station	Jan.	Feb.	March	April	May	June	July	Aug.	Sept.	Oct.	Nov.	Dec.
					1996							
Bismarck, North Dakota	343	367	364	367	346	317	314	292	293	275	301	324
Caribou, Maine	353	373	377	371	391	341	333	312	291	289	289	321
Wallops Is., Virginia	320	340	339	348	338	315	304	301	286	269	282	283
SMO	240	241	237	247	244	241	245	250	256	266	257	253
Tallahassee, Florida	285	303	312	313	317	-	-	-	-	-	267	256
Boulder, Colorado	328	324	337	329	305	294	286	279	281	269	265	294
UAF-GI, Alaska	-	[377]	384	379	356	339	311	291	309	[318]	-	-
Lauder, New Zealand	259	265	262	273	289	306	329	368	356	360	344	306
MLO	245	250	268	276	280	276	267	261	256	252	239	237
Nashville, Tennessee	309	326	333	333	300	307	306	296	285	272	272	284
Perth, Australia	272	260	-	-	-	-	-	302	310	313	303	280
SPO	266	246	[238]		[222]	[234]	[230]	[193]	-	142	176	283
Haute Provence, France	338	363	337	355	349	336	334	307	317	286	290	303
Huancayo, Peru	Station closed											
BRW	-	-	394	420	362	338	315	296	293	[314]	-	-
Hanford, California	307	320	322	321	316	314	301	291	287	280	266	275
					1997							
Bismarck, North Dakota	349	353	355	371	329	325	309	293	274	283	297	333
Caribou, Maine	376	363	382	381	359	347	332	318	291	289	303	334
Wallops Is., Virginia	294	304	317	339	330	323	319	304	294	291	292	308
SMO	[244]	-	-	241	241	235	231	238	244	252	261	250
Tallahassee, Florida	[266]			300	[297]	305	299	297	289	285	291	-
Boulder, Colorado	310	323	310	348	315	302	298	284	273	280	293	310
UAF-GI, Alaska	-	[403]	386	397	[378]	327	319	280	282	[328]	-	-
Lauder, New Zealand	279	-	265	271	276	297	306	324	324	326	317	299
MLO	224	250	-	-	265	273	265	259	256	253	254	246
Nashville, Tennessee	292	295	291	322	319	[323]	301	288	280	282	297	303
Perth, Australia	258	251	270	261	257	261	275	288	307	298	292	278
SPO	277	275	-	[260]	[265]	[268]	[265]	[247]	-	136	203	274
Haute Provence, France	330	318	322	328	333	354	339	312	293	280	291	312
Huancayo, Peru	Station closed											
BRW	-	[401]	390	388	374	335	315	287	288	-	-	-
Handford, California	291	304	294	328	307	317	308	[295]	[272]	284	279	304

Monthly mean ozone values in square brackets are derived from observations made on fewer than 10 days per month.

Agreement between the profiles obtained by the two different instruments is remarkably good (Figure 4.1). The percentage of difference between the instruments (the numbers on the right side of the figure) for each layer do not exceed 4% and are generally less than 3%.

4.1.3. Calibration of Dobson Spectrophotometers

Fifteen Dobson ozone spectrophotometers were calibrated during 1996 and 1997. Table 4.4 lists all of the instruments calibrated and the resulting calibration difference expressed in percentage of ozone difference. This percentage of difference is for ozone calculated from the test instrument and the standard instrument measurements with the double wavelength pair (A and D) on the direct sun (DS) with the ground quartz plate in place (GQP) observation type at a Mu value of 2 and a total ozone value of 300 Dobson Units (DU) before any repair or calibration adjustment is made. The table also lists the place of the calibration and the standard instrument used.

As part of its role as the World Center for Dobson Calibrations, CMDL participated in international Dobson spectrophotometer calibrations at the Aerological Observatory, Tsukuba, Japan (February 26 to March 26, 1996); Perth Airport, Australia (February 3 to 14, 1997); and Stiga Ski Field, near Kalavryta, Greece (July 20 to August 8, 1997). In cooperation with the WMO Global Atmosphere Watch (GAW) program, CMDL personnel made a physical inspection and evaluation of sites operating Dobson spectrophotometers in Argentina, Uruguay, and Brazil during April 1997.

The world standard Dobson ozone spectrophotometer calibration was checked in summer campaigns (1996 and 1997) at MLO. The calibration was verified to be in error by less that 1% in both campaigns. These campaigns are a cooperative effort with NASA, and the data obtained are also used as validation for satellite measurements.

TABLE 4.3. Annual and Seasonal Trends (in % per Decade) Derived From Re-Evaluated Dobson Spectrophotometer Total Ozone Data Obtained During 1979-1996 at 16 NOAA and Cooperative Station, Allowing for Solar and QBO Equatorial Wind Effects

			Annual		Dec.-Feb.		March-May		June-Aug.		Sept.-Nov.	
Station	Latitude	Longitude	Trend	Std. Error	Trend	Std. Error	Trend	Std. Error	Trend	Std. Error	Trend	Std. Error
Caribou, Maine*	46.9°N	68.0°W	-3.75	0.64	-4.46	1.54	-4.67	1.02	-3.21	0.71	-2.28	1.02
Bismarck, North Dakota*	46.8°N	100.8°W	-2.86	0.59	-2.50	1.33	-4.81	0.93	-2.00	0.86	-1.70	0.88
Boulder, Colorado*	40.0°N	105.3°W	-3.34	0.57	-2.77	1.20	-5.94	1.11	-2.51	0.65	-1.51	0.83
Wallops Is., Virginia*	37.9°N	75.5°W	-3.52	0.66	-4.01	1.30	-4.46	1.19	-3.05	0.80	-2.29	1.04
Fresno, California*	36.8°N	86.6°W	-3.15	0.66	-3.46	1.16	-4.65	1.25	-2.46	0.86	-1.72	1.13
Tallahassee, Tennessee*		119.7°W	-3.74	1.17	-2.81	1.72	-4.27	2.53	-3.70	1.48	-4.14	1.15
Nashville, Tennessee*	36.3°N	84.3°W	-3.41	0.69	-2.10	1.21	-4.36	1.30	-3.36	1.10	-3.67	1.21
MLO*	19.5°N	155.6°W	-0.37	0.70	-0.91	1.06	-0.39	1.28	-0.17	0.86	-0.02	0.68
SMO*	14.3°S	170.6°W	-1.30	0.61	-1.37	0.85	-1.75	0.76	-1.24	0.99	-0.86	0.81
Huancayo, Peru‡	12.1°S	75.3°W	-1.85	0.43	-0.63	0.63	-1.29	0.68	-3.74	0.81	-1.64	0.73
Perth, Australia†	31.9°S	116.0°E	-0.79	0.66	-2.79	0.84	-0.80	1.35	0.96	1.52	-0.53	0.98
Lauder, New Zealand§	45.0°S	169.7°W	0.93	1.03	-3.34	1.12	-0.58	1.79	5.02	2.34	2.51	2.13
Poker Flat, Alaska†¥	65.1°N	147.5°W	-5.61	2.13	-	-	-8.70	3.20	-4.03	1.92	-1.27	4.65
BRW*¥	71.3°N	156.6°W	-3.25	1.14	-	-	-4.40	1.61	-3.01	1.19	-1.14	2.36
Haute Provence, France†	43.9°N	5.7°E	-4.31	1.08	-5.26	2.33	-7.96	1.90	-2.22	1.26	-0.25	1.43
SPO*¶	90°S	24.8°W	-12.18	2.20	-7.09	1.23	-5.90	1.81	-10.20	1.93	-19.58	4.34
Average over first five stations (1979-1996)			-3.32		-12.18	2.20	-7.09	1.23	-2.64		-1.90	
Average over first five stations (1979-1995)												
Average over first five stations (1979-1994)												

Estimated trend uncertainties are standard errors (s.e.) where 2 (s.e.) ~95% confidence interval.

*Period of record: 1979-1996

†Period of record: 1984-1996

‡Period of record: 1979-1992

§Period of record: 1987-1996

¥For Poker Flat and BRW the annual trend estimates are based on March through October data only, while "September-November" trend estimates are based on September-October data only.

¶For SPO the annual trend is based on daylight (October 15 through February) data only. The "March-November." trend is for October 15-31 and November data only.

4.1.4. SURFACE AND TROPOSPHERIC OZONE

The surface in situ ozone measurement program continued to operate in a configuration similar to previous years with some changes. Aging instrumentation continues to create data gaps at some of the stations, particularly the tropical sites at the Samoa Observatory, American Samoa (SMO) and at Barbados. After 2 years of intermittent performance, the SMO program is fully functional. A TEI Model 49 ozone monitor was installed in September 1997 and has been running in parallel to the Dasibi Model 1003AH monitor that has been running there for many years. At Barbados attempts to restart the program have not been successful and data are not available after May 1995. Intercomparisons with the network standard instrument were carried out in 1997 for all four of the CMDL baseline site ozone monitors. Based on the calibrations and reanalysis of earlier calibrations, revised surface ozone data for the Barrow Observatory, Barrow, Alaska (BRW), MLO, and the South Pole Observatory, Antarctica (SPO) are presented in **Table 4.5** for 1992-1997, which updates a similar table in *Hofmann et al.* [1996].

In February 1997, in cooperation with the New Zealand antarctic program and the Lauder Observatory of the National Institute for Water and Atmosphere (NIWA), an ozone monitor was installed at Arrival Heights near Scott Base and McMurdo station on the coast of Antarctica. We hope to use this information to better understand several years of earlier data obtained by other investigators. Records of the calibration of the instruments used to obtain much of this data are not available or non-existent. In addition, there is renewed interest in the role of halogens in destroying ozone in the lower troposphere in a manner analogous to what is seen in the arctic.

Starting in June 1997 an ozone monitor was installed at a camp on the Greenland plateau. This station is to be operated for about 10 months with the primary purpose of understanding deposition to the snow surface. This will be the first time such a camp has been operated during the winter on the plateau. The ozone observations will add to the 2 months of data obtained in Greenland from late May to July 1993.

We have recently analyzed data from a number of the longer-term surface ozone observations and tropospheric information from selected ozonesonde sites [*Oltmans et*

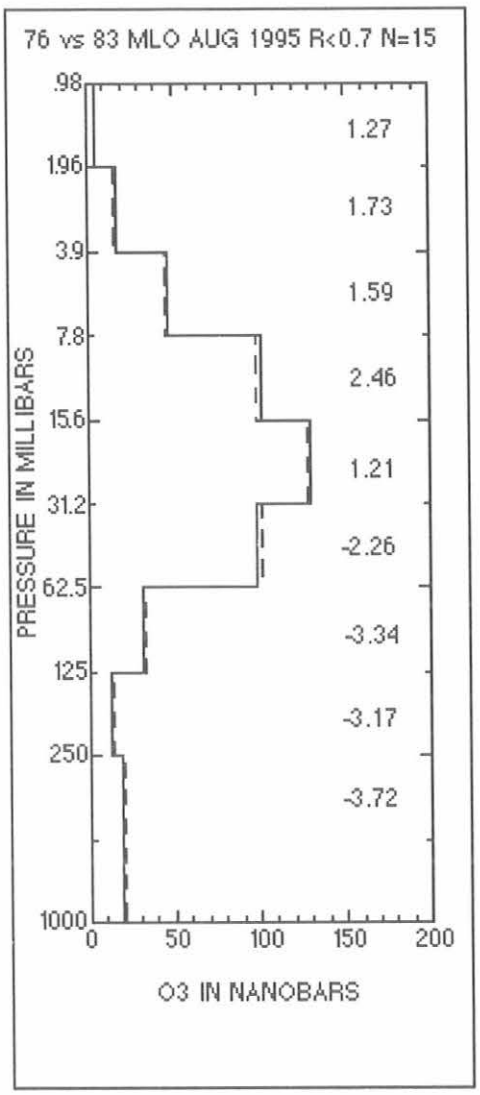

Fig. 4.1. Comparison of average ozone profiles derived from Umkehr measurements at MLO during the MLO3 campaign from two Dobson spectrophotometers (No 83 and No. 76). The profiles were obtained in August 1995. The numbers along the right side are the average percent difference in each layer.

al., 1998] to develop a fairly comprehensive picture of tropospheric ozone changes. Since 1970 significant increases were found in Europe and Japan, and at the South Pole ozone has declined markedly. Since 1980 there have been relatively small changes at all sites except in the antarctic and arctic where significant declines are evident. At the three CDML sites with long-term records and data through 1997 (Figure 4.2), several of these features are evident. At BRW ozone mixing ratios were increasing, especially during the summer, through the 1980s. Very low values in 1992-1993 following the eruption of Mt. Pinatubo seem to reflect the very reduced amounts seen in the lower stratosphere. These reduced amounts were seen through the entire tropospheric column in the Canadian arctic ozonesonde data [*Tarasick et al.*, 1995; *Oltmans et al.*, 1998]. Over the entire period of the record, ozone has increased about 3% per decade with the largest increases during the summer (Table 4.6). For 1980-1997 there has been no change. Ozone concentrations at MLO have also risen significantly since the early 1970s (Table 4.6) but have shown no growth since 1980. This result is affected somewhat by a couple of years of high amounts in the early 1980s. Four out of the last 5 years have had above-average concentrations (Figure 4.2). By contrast at SPO ozone amounts have declined by over 15% since the measurements began in 1975 (Table 4.6). This decline has taken place since the mid-1980s and seems to have paralleled the declines in the lower stratosphere [*Oltmans et al.*, 1998].

4.1.5. OZONESONDES

Table 4.7 summarizes the 1996-1997 CMDL ozonesonde projects. This includes weekly ozone soundings at NOAA long-term monitoring stations in Boulder, Colorado; Hilo, Hawaii; and SPO, as well as a new long-term site in Trinidad Head, California, funded by the NOAA "Health of the Atmosphere" program. The new west coast site started launching weekly ozonesondes on August 20, 1997. This station will provide an upstream look at ozone concentrations reaching the continent from the prevailing west to east flow. Other campaigns that CMDL participated in included Pacific Exploratory Mission in the Tropics (PEM-Tropics), Atmosphere/Ocean Chemistry Experiment (AEROCE), Photochemistry of Ozone Loss in the Arctic Region in Summer (POLARIS), and 1 month of daily ozonesondes at Sable Island, Canada, in September 1997 as part of the NOAA Climate and Global Change Program (CGCP) Atmospheric Chemistry Project.

The SPO ozonesonde program has been essential for monitoring the development of the yearly ozone hole over Antarctica. In addition, the continuous data set from 1986 to 1997 was analyzed for potential ozone hole recovery indicators by *Hofmann et al.* [1997]. The profiles from the 1996-1997 season are shown in Figure 4.3. The minimum total ozone was observed in early October, similar to past years, with 118 DU recorded in 1996 and 112 DU in 1997. The totals are above the record low of 86 DU recorded on October 12, 1993, when the effect of the Mount Pinatubo aerosol was at a maximum [*Hofmann et al.*, 1994; 1997]. However, depletion in the 14-20 km layer continues to show nearly zero ozone. In 1997 there is evidence that the altitude range of zero ozone has expanded upward.

The ongoing PEM-Tropics campaign has been investigating tropospheric chemistry related to the oxidizing capacity of the global troposphere. The focus is on the very clean atmosphere in the tropical Pacific ocean basin. CMDL participation included weekly ozonesonde flights at SMO, Tahiti, and Fiji. The frequency of ozonesondes was increased to two per week at SMO from August 1 to October 29, 1996, to coordinate with an aircraft campaign. CMDL station personnel launched ozonesondes at SMO, while personnel at Meteo, France, in Papeete, Tahiti, and the University of Southern Pacific in Suva, Fiji, were trained for launching ozonesondes at each

TABLE 4.4. Dobson Ozone Spectrophotometers Calibrated in 1996-1997

Station	Instrument Number	Calibration Date	Calibration Correction (%)	Standard Number	Place
		1996			
Manila, Philippines	52	June 1990	0.8%	116*	Tsukuba, Japan
Bangkok, Thailand	09	Oct. 1987	N/A (Instrument damaged)	116*	Tsukuba, Japan
New Delhi, India	112	Dec. 1984	0.0%	116*	Tsukuba, Japan
Seoul, Korea	124	July 1991	3.6%	116*	Tsukuba, Japan
SPO	80	NA	NA†	83	Boulder, Colorado
		1997			
Singapore	07	Sept. 1990	1.0%	83	Perth, Australia
SMO	42	Sept. 9, 1991	0.0%	83	Perth, Australia
Lauder, New Zealand	72	July 22, 1992	0.0%	83	Perth, Australia
Perth, Australia	81	July 7, 1992	-0.2%	83	Perth, Australia
Irene, South Africa	89	May 1993	-0.3%	83	Perth, Australia
Melbourne, Australia (regional standard)	105	June 29, 1992	0.0%	83	Perth, Australia
SPO	82	Aug. 27, 1992	-0.7%	83	Boulder, Colorado
Hohenpeissenberg, Germany	64	Aug. 2, 1990	-1.4%	65	Stiga Ski Field, Greece
Hradec Kralove, Czech Republic	74	Aug. 2, 1990	+1.4	65	Stiga Ski Field, Greece
Cairo, Egypt	96	July 10, 1997	-2.0%	65	Stiga Ski Field, Greece
St. Petersburg, Russia	108	May 25, 1993	-0.5%	65	Stiga Ski Field, Greece
Athens, Greece	118	Aug. 5, 1990	+0.8%	65	Stiga Ski Field, Greece
Bucharest, Romania	121	1995	N/A‡	65	Stiga Ski Field, Greece

*Although CMDL instruments were not involved, the CMDL World Dobson Calibration Center supervised the Tsukuba intercomparison.
†In 1996 the SPO instrument had a calibration defined before being sent to the station in replacement of instrument no. 82.
‡Instrument no. 121 was optically realigned and thus had no existing calibration record.

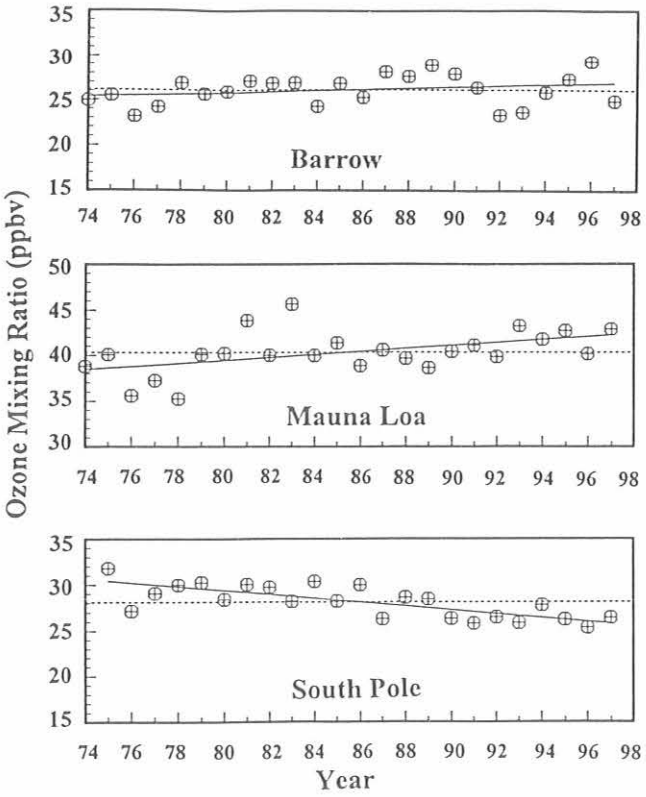

Fig. 4.2. Annual mean surface ozone mixing ratios at BRW, MLO, and SPO. The solid line is a linear regression fit to the monthly mean values. Numerical trend information is in Table 4.6.

of those sites. To date, the ozone profiles have shown typical low ozone mixing ratios of 10-20 ppbv throughout the troposphere, but layers of 80-110 ppbv ozone were observed in the middle and upper troposphere.

The AEROCE campaign in 1996 was the last of a series of springtime intensive ozonesonde launches in North American and North Atlantic sites. Since the spring of 1993, the AEROCE and North Atlantic Regional Experiment (NARE) campaigns have investigated the origin of tropospheric ozone over the North Atlantic [*Oltmans et al.*, 1996]. There were three sites located approximately 1200 km apart in West Lafayette, Indiana; Charlottesville, Virginia; and Bermuda. The University of Virginia at Charlottesville also monitored synoptic conditions and timed the daily launches in order to measure ozone behind the passing cold fronts [*Cooper et al.*, 1998].

CMDL set up, supplied, and provided training to the Geophysical Institute personnel at the University of Alaska, Fairbanks, to launch ozonesondes during POLARIS. The campaign objective was to investigate the stratospheric ozone loss rate in the spring and summer at northern latitudes. A secondary benefit from the ozonesondes was that they provided a total ozone comparison for TOMS satellite measurements during a period of low sun angle.

4.1.6. Atmospheric Water Vapor

Water vapor profile measurements continued at Boulder, Colorado. Some difficulties were experienced in adapting several replacement components in the balloonborne frost-point hygrometer. This led to a number of months in 1997

TABLE 4.5. Monthly Mean Surface Ozone Mixing Ratios (ppbv)

Year	Jan.	Feb.	March	April	May	June	July	Aug.	Sept.	Oct.	Nov.	Dec.
						BRW						
1992	29.1	27.8	27.4	15.5	16.9	19.4	18.4	18.9	24.0	27.3	28.8	26.3
1993	26.4	26.8	14.9	17.8	20.9	22.8	16.7	19.5	24.6	29.7	31.0	32.6
1994	32.3	30.6	22.4	11.4	11.8	26.6	22.3	20.2	30.7	33.0	36.1	32.7
1995	34.5	29.8	19.0	19.8	23.6	29.1	21.7	22.5	26.9	37.0	34.1	29.7
1996	32.8	33.6	30.1	9.3	29.8	26.2	22.7	26.4	32.4	32.3	39.6	36.7
1997	33.0	34.2	26.5	13.8	13.1	21.1	19.5	20.1	23.3	29.3	31.8	33.5
						MLO (nighttime only)						
1992	40.2	42.8	53.8	61.0	46.9	49.5	38.8	30.6	26.3	24.9	29.2	32.2
1993	42.2	41.3	50.0	63.3	55.2	50.6	38.0	30.6	26.6	35.3	42.7	38.3
1994	43.3	37.5	48.5	57.9	48.7	35.4	30.1	29.8	33.5	41.4	40.5	45.5
1995	34.4	42.0	51.1	50.5	52.1	44.6	34.6	45.8	42.1	36.7	30.7	35.5
1996	39.4	39.9	51.4	58.6	43.4	37.0	39.8	38.9	31.0	33.8	30.1	38.9
1997	43.1	45.9	36.1	60.2	52.2	43.3	36.8	31.6	37.9	41.1	37.9	48.5
						SPO						
1992	18.0	17.9	16.9	22.4	29.7	33.5	34.9	34.4	28.5	25.8	26.7	29.3
1993	23.4	20.1	17.5	23.1	26.4	29.7	30.7	30.3	29.1	27.5	29.7	22.9
1994	25.0	19.7	21.1	24.4	27.7	33.1	34.1	33.5	31.6	27.3	29.3	26.8
1995	25.3	18.0	18.0	19.8	24.0	28.3	34.5	33.0	31.8	26.3	29.2	26.7
1996	18.2	15.1	17.2	21.0	24.6	28.1	30.7	31.8	33.0	28.3	29.7	26.5
1997	21.2	17.6	19.2	24.1	27.0	29.3	32.0	32.0	29.5	29.0	30.3	25.8

TABLE 4.6. Annual and Seasonal Linear Trends of Surface Ozone Mixing Ratio in Percent per Year with 95% Confidence Limits

Period	Annual	Dec.-Jan.-Feb.	March-April-May	June-July-Aug.	Sept.-Oct.-Nov.
		BRW			
March 1973-Dec. 1997	+0.30 ± 0.22	+0.24 ± 0.33	-0.16 ± 0.76	+0.55 ± 0.40	+0.45 ± 0.33
Jan. 1980-Dec. 1997	-0.06 ± 0.34	+0.23 ± 0.53	-0.33 ± 1.52	-0.12 ± 0.92	+0.14 ± 0.92
		MLO			
Oct. 1973-Dec. 1997	+0.36 ± 0.11	+0.41 ± 0.33	+0.45 ± 0.52	+0.21 ± 0.63	+0.40 ± 0.48
Jan. 1980-Dec. 1997	+0.01 ± 0.28	-0.19 ± 0.46	+0.07 ± 0.79	-0.27 ± 0.97	+0.25 ± 0.75
		SMO			
Jan. 1976-Dec. 1994	+0.14 ± 0.31	-0.03 ± 0.48	-0.50 ± 1.38	+0.13 ± 0.79	+0.73 ± 0.87
		SPO			
Jan. 1975-Dec. 1997	-0.72 ± 0.17	-0.89 ± 0.41	-1.02 ± 0.40	-0.65 ± 0.57	-0.60 ± 0.38
Jan. 1980-Dec. 1997	-0.83 ± 0.24	-0.39 ± 0.51	-1.14 ± 0.58	-0.95 ± 0.87	-0.97 ± 0.55

BRW: latitude, 71.3°N; longitude, 156.6°W; elevation, 10 m
MLO: latitude, 19.5°N; longitude, 155.6°W; elevation, 3380 m
SMO: latitude, 14.3°S; longitude, 170.6°W; elevation, 30 m
SPO: latitude, 90.0°S; elevation; elevation, 2838 m

TABLE 4.7. Summary of 1994-1995 Ozonesonde Projects

Ozonesonde Sites	1996 Totals	1996 Dates	1997 Totals	1997 Dates	Project
		Station (weekly)			
Boulder, Colorado	52	Full year	52	Full year	NOAA long term
MLO	46	Full year	44	Full Year	NOAA long term
SPO	74	Full year	74	Full Year	NOAA long term
Tahiti	52	Full year	36	Full Year	PEM-Tropics
Fiji			28	Feb. 6 - Dec. 31	PEM-Tropics
SMO	61	Full year	48	Full Year	PEM-Tropics
Fairbanks, Alaska	10	Oct 29 - Dec. 2	34	April 17 – Oct. 24	POLARIS
Trinidad Head, California			21	Aug. 21 - Dec. 31	NOAA "Health of the Atmosphere"
		Intensives (~daily)			
Bermuda	33	April 1 - May 3			AEROCE
Purdue	27	March 29 - May 1			AEROCE
Virginia	30	March 22 - May 1			AEROCE
Sable Island			31	Sept. 5 - Oct. 5	NOAA Climate and Global Change

PEM-Tropics - Pacific Exploratory Mission in the Tropics (a global tropospheric experiment).
POLARIS - Photochemistry of Ozone Loss in the Arctic Region in Summer
AEROCE - Atmosphere/Ocean Chemistry Experiment

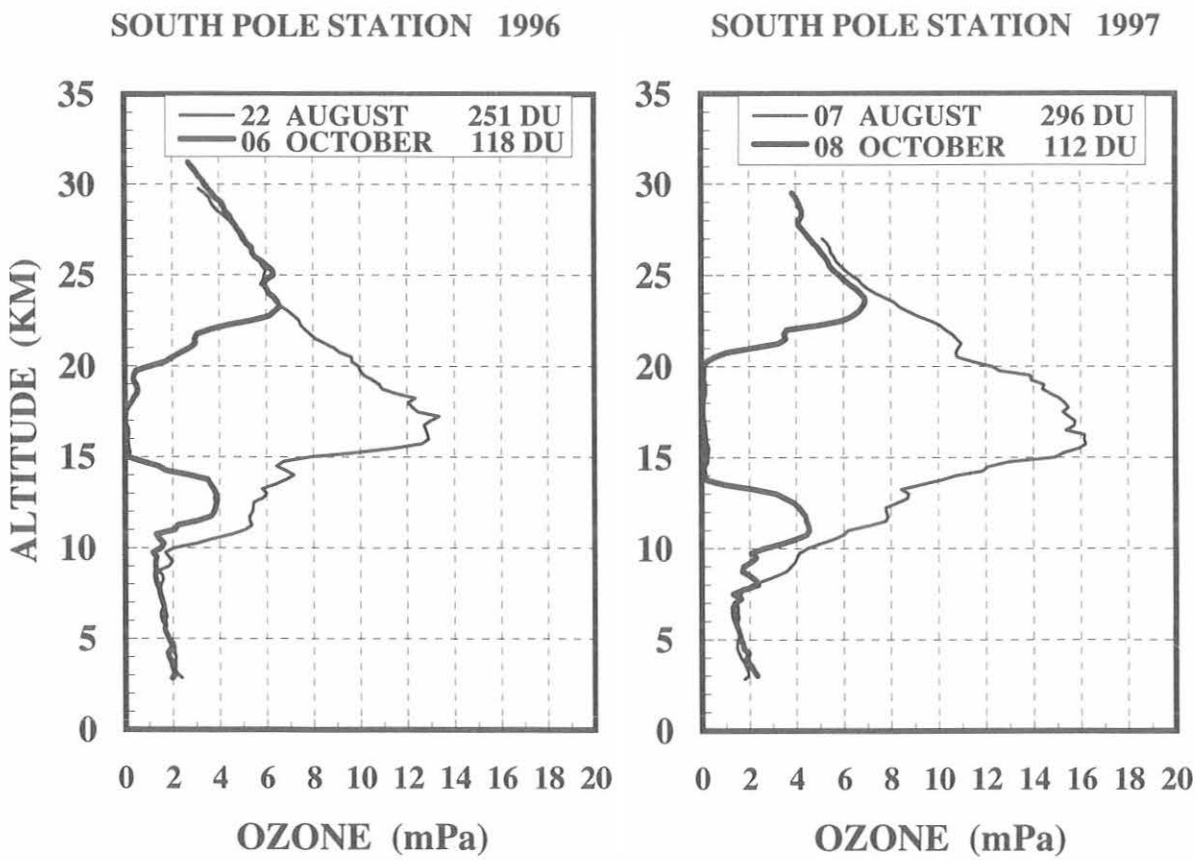

Fig. 4.3. Vertical profiles of ozone partial pressure in millipascals (mPa) at SPO during the ozone hole of 1996 and 1997. The thin line represents the predepletion profile. The thicker line is the profile observed during the minimum in total ozone.

in which profiles of acceptable quality were not obtained. As reported earlier [*Oltmans and Hofmann*, 1995; *Hofmann et al.*, 1996] stratospheric water vapor amounts have increased significantly since the beginning of the measurement program in 1981. Earlier results suggested that the increase in the vicinity was somewhat larger than that seen below 20 km. With the inclusion of recent data (Figure 4.4), the increase seems to be more uniform with altitude between 14-28 km. The increase of about 1% per year is almost twice as large as expected from the long-term increase in atmospheric methane. A plausible cause for such an increase is an enhanced injection of water vapor into the stratosphere [*Evans et al.*, 1998]. This could occur if the tropical tropopause cold-trap temperature was gradually increasing. At present, there is not strong evidence for such a change in tropopause temperatures, although this change needs to be relatively small and may be difficult to detect in the temperature record.

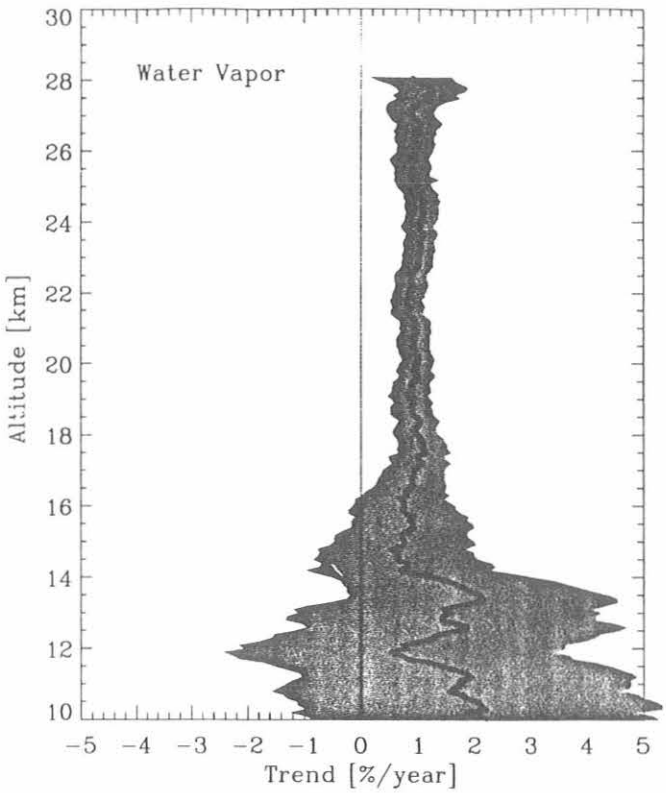

Fig. 4.4. The linear trend as a function of altitude of the water vapor mixing ratio over Boulder, Colorado, for 1981-1997. The trend is in percent per year. The shaded area is the 95% confidence interval of the trend.

4.1.7. Atmospheric Transport

CMDL supports research to identify sources and sinks of trace gases and aerosols. These efforts contribute to a better understanding of short-term variations, seasonal cycles, and long-term trends. The CMDL isentropic transport model [*Harris and Kahl*, 1994] calculates trajectories at desired elevations, including those in the stratosphere. Trajectories may be compared to data collected at the surface or data collected at elevation (sonde, aircraft, and lidar data).

One objective of this program has been to describe transport to the CMDL observatories in a detailed climatological way so that potential sources and sinks impacting the measurements are clearly defined. Seasonal changes in transport can radically alter the influence of a given source or sink throughout the year. Isobaric trajectories were first used to describe seasonal flow patterns to MLO [*Harris and Kahl*, 1990]. A more accurate picture of these flow patterns is now available using isentropic trajectories, taking into account adiabatic vertical motions encountered by air parcels. These updated seasonal transport clusters for MLO are presented in section 4.2.3 along with other transport characteristics that help determine sources and sinks affecting measurements made at MLO. SPO transport patterns were also described with isobaric trajectories [*Harris*, 1992], although an analysis of the effects of adiabatic vertical motions was included in this study. More recently, transport patterns were determined for BRW [*Harris and Kahl*, 1994] and SMO [*Harris and Oltmans*, 1997] using isentropic trajectories. Knowledge of transport characteristics has led to a better understanding of seasonal patterns in MLO methane measurements [*Harris et al.*, 1992], SMO carbon dioxide measurements [*Halter et al.*, 1988], and SMO surface ozone measurements [*Harris and Oltmans*, 1997]. An investigation into MLO's springtime tropospheric ozone maximum used transport characteristics and relationships among trace gases to link this excess ozone to a possible stratospheric source [*Harris et al.*, 1998].

Information about the isentropic transport model (methodology, description of plots, and formats of data files) is available on the Internet at http://www.cmdl.noaa.gov/traj. This home page also serves as the distribution site for "realtime" trajectories. These are trajectories calculated from data downloaded twice daily from the National Centers for Environmental Prediction (NCEP). For various CMDL baseline and regional observing sites, trajectories are thus provided within a day of when measurements are actually made. This capability is also available for any site on the globe as requested by the user with the use of a password. The transport home page (at the address above) also includes pointers to several archives of trajectory data.

A recently completed project made all trajectory programs, data files, and plots Year-2000 compliant. Data fields referring to the year have all been changed from two digits to four digits. The changes in data format are documented on the transport home page.

4.2. Special Projects

4.2.1. Characterization of the ECC Ozonesonde

Jülich Ozone Sonde Intercomparison Experiment

The CMDL ozonesonde group participated in the Jülich Ozone Sonde Intercomparsion Experiment (JOSIE) held at the Research Center Jülich GmbH, Jülich,

Germany, on February 5-16 and February 26-March 8, 1996. Eight different ozonesonde groups participated in JOSIE in order to characterize the accuracy and precision of several types of ozonesondes in an environmental simulation chamber. The sondes were tested in six computer-controlled simulation flights, representing typical midlatitude and tropical ozone and termperature profiles. The chamber accommodated four ozonesondes during each simulation. A fast response dual-beam UV-absorption photometer [*Proffitt et al.*, 1983] was used as the ozone reference for the experiments.

A summary of the tests by *Smit et al.* [1997] concluded that the electrochemical concentration cell (ECC) ozonesondes had the best precision and accuracy. However, there were differences in measured ozone among the four participating ECC groups. The NOAA ECC ozonesondes, manufactured by ENSCI Corporation, were within ±2-10% of the UV photometer in the troposphere, but in the stratosphere they started showing a positive deviation. The positive difference increased to a maximum of 15-20% greater than the UV photometer standard at the end of the 2-hour simulation. One of the midlatitude simulation results is shown in Figure 4.5.

A common, but inexact, explanation for the higher ozone is that CMDL uses individual pump flow rate efficiency curves measured in our laboratory to compute ozone concentrations. These curves have a lower efficiency than the widely used average pump efficiency curve given by *Komhyr et al.* [1986] and, therefore, result in higher ozone computations. The JOSIE results prompted additional tests at CMDL to determine why the positive deviation was observed.

CMDL Laboratory Calibration Tests

After JOSIE, a series of laboratory calibration tests were conducted to determine the accuracy of the ECC ozonesonde using a variety of sensing solution recipes. The bench top tests were done using a Thermo Environmental Instruments, Inc. 49C ozone calibrator as an ozone source. The 49C output was accurate to within 2% of a National Institute of Standards (NIST) standardized Dasibi in the 30-230 ppbv range. The calibrator ozone levels were adjusted to typical midlatitude profile levels in 12 sequential 10-min time steps, as shown in Figure 4.6. Three ozonesondes were sampling the source stream during each calibration test. We consistently observed a higher response from the ozonesondes using the standard 1% KI (potassium iodide) buffered cathode solution. The ozonesondes were from about a 2% high to 15-20% after the peak ozone level, which is similar to the JOSIE intercomparison experiments. These tests were done at surface pressure so the pump efficiency was not a factor in the higher ozone observed by the ECC ozonesondes.

The effect of different cathode solutions in ECC ozonesonde was previously addressed by *Komhyr* [1969] and *Barnes et al.* [1985]. However, the variations focused only on adjusting the KI concentration. The calibration tests at CMDL have shown that the KI is not the primary ingredient responsible for high ozone response, rather it is the sodium phosphate buffers that are added to the cathode solution. The optimum solution was found to be a 2% KI solution without buffers and without potassium bromide. Figure 4.6 also shows some average differences between the 49C calibrator profile and ozonesonde profiles using

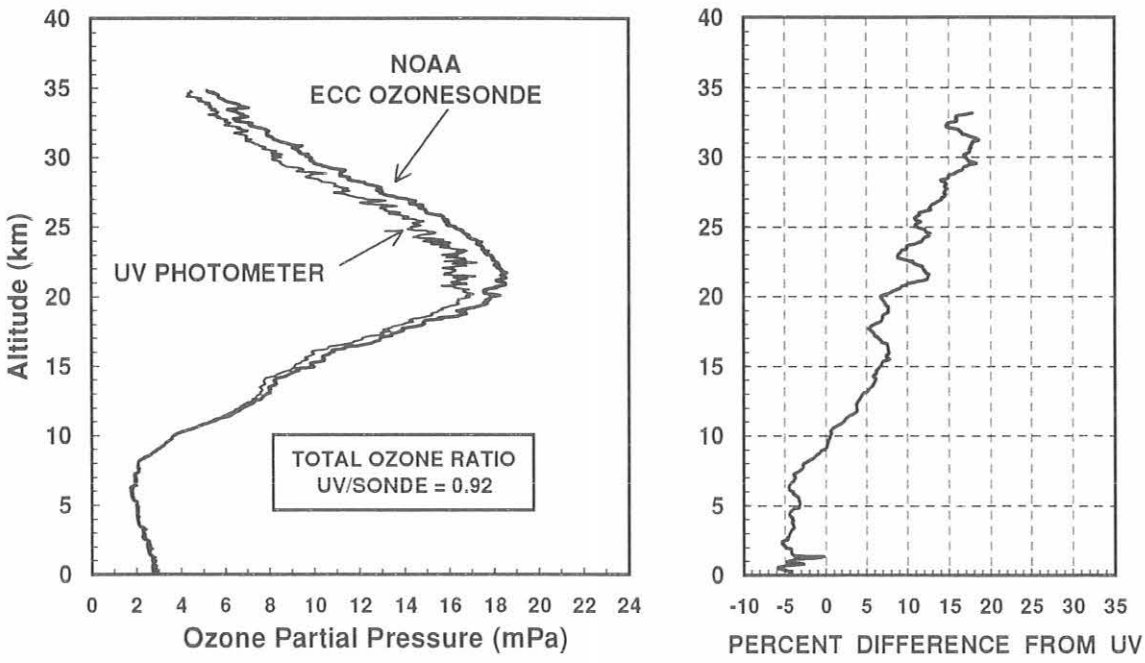

Fig. 4.5. Ozone profile measured by an ECC ozonesonde used by CMDL during a midlatitude simulation at the JOSIE ozonesonde intercomparison. A UV photometer was used as a standard. The figure on the right shows the percentage higher ozone observed by the ozonesonde compared to the UV photometer.

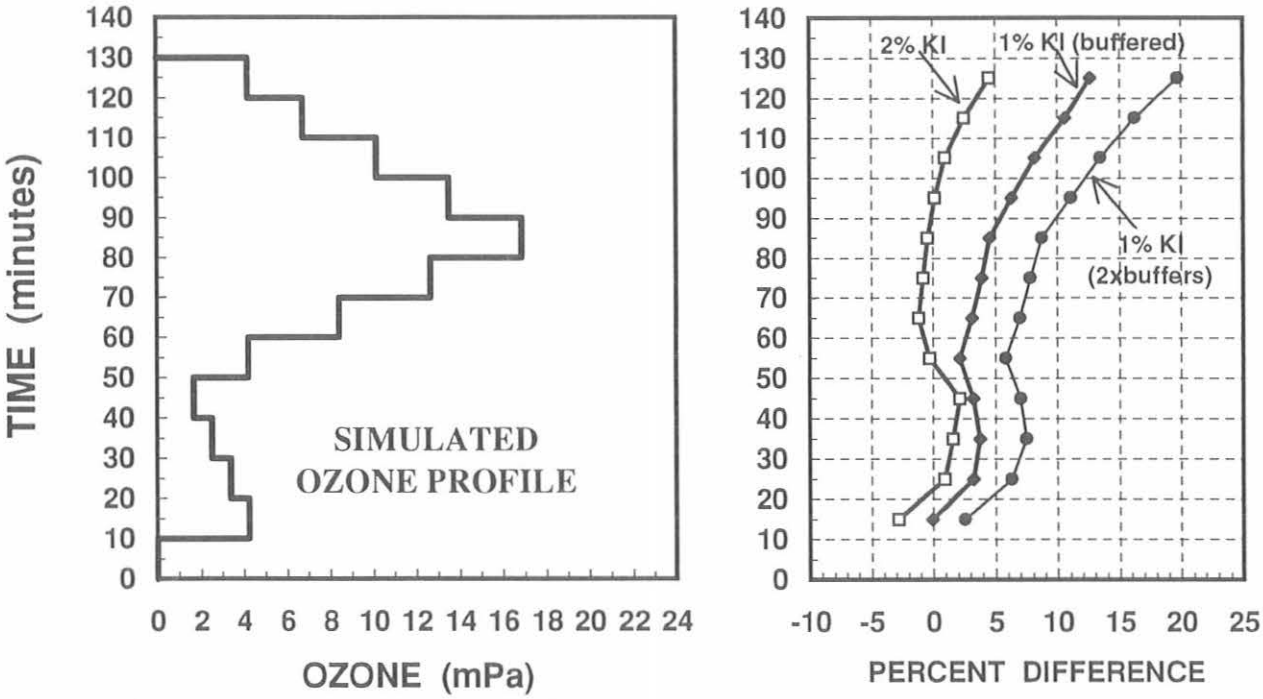

Fig. 4.6. The simulation ozone partial pressure profile generated by a TEI ozone calibrator that was used for testing various cathode solution recipes in ECC ozonesondes. The nearly 2-hour run was done in the laboratory at surface pressure. The diagram on the right shows the percentage difference (sonde-calibration)/calibration between the ECC ozonesonde measurement and the calibrator.

the 2% KI unbuffered, the standard 1% KI buffered, and the 1% KI with double the amount of buffers, to illustrate the effect of the buffers.

The Boulder ozonesonde site was switched to the 2% KI unbuffered cathode solution on August 8, 1997. Figure 4.7 shows that the total ozone ratio (Dobson/sonde) went from an average of 0.9 to nearly 1.0 after the switch. The new processing of ozonesonde data also includes a humidity correction due to evaporation that occurs when measuring the sonde pump flow rate. This increases the time for 100 mL of flow by 2% to 3.5% in Boulder. Trinidad Head has also used the 2% KI unbuffered solution since the beginning of ozonesonde launches there on August 21, 1997. The only other location that used the

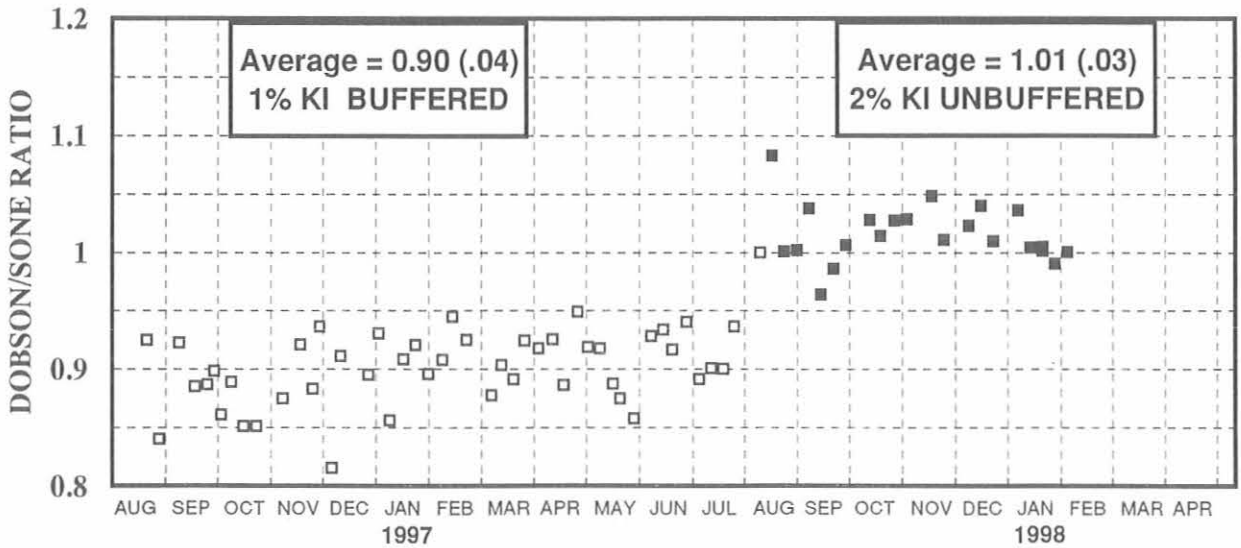

Fig. 4.7. The total ozone ratios of the Dobson spectrophotometer and ECC ozonesondes for the weekly Boulder ozonesonde flights from August 1197 to January 1998. This illustrates the better comparison the 2% KI unbuffered solution gives after the switch on August 21, 1997. The before and after average ratios and standard deviations are shown in parenthesis.

new solution was the intensive project at Sable Island in September 1997. All of the remaining stations will switch to the 2% KI unbuffered solution in early 1998. Several dual flights with the old and new solution will be necessary to obtain a correction for the previous data.

4.2.2. Stratospheric Water Vapor as Part of the Observations of the Middle Stratosphere (OMS) Program

The Observations of the Middle Stratosphere (OMS) project was established to investigate the transport of atmospheric tracers in the stratosphere at altitudes generally inaccessible to high altitude aircraft. A balloon package was developed that is capable of measuring longer-level compounds to altitudes near 35 km. We designed and developed a package for the balloon gondola to measure water vapor. In addition, we also flew free-flier balloons that were launched in conjunction with the main gondola launches. Campaigns were carried out from Fort Sumner, New Mexico, in October 1996; from Fairbanks, Alaska, in July 1997; and from Juazeiro do Norte, Brazil, in February and November 1997. Unfortunately useable data were not obtained from the Fairbanks campaign due to multiple instrument problems. In all of the campaigns the gondola water vapor instrument gave limited data because of contamination from the gondola. Several attempts at improving the performance were not successful and this instrument will not be used in future campaigns. The free-flier balloon packages, on the other hand, yielded valuable data.

The flight in February 1997 at Juazeiro do Norte, Brazil, came near the end of the northern hemisphere (NH) winter when water vapor concentrations in the tropical lowermost stratosphere are at a minimum. This corresponds to the time of coldest tropical tropopause temperatures. The cold tropopause temperature (particularly) in the western tropical Pacific impress a signal on the air passing through the tropopause by drying the air to the frost-point temperature. This mechanism is very nicely shown in several profiles obtained near the equator (Figure 4.8) including the two from Brazil. During the Central Equatorial Experiment (CEPEX) in 1993 water vapor profiles were obtained in the western and central Pacific. These profiles are similar in shape and mixing ratio except in the lowest part of the stratosphere between the 350 K and 400 K potential temperature surfaces (Figure 4.8). This is a result of the much colder tropopause temperatures in the western Pacific. The profile obtained in Brazil at roughly the same time of year (but 4 years later) is remarkably similar to the profile at Christmas Island. In particular, the minimum near 400 K and the maximum near 460 K are reproduced in each profile. The profile of November 1997 from Brazil, on the other hand, shows a different vertical structure, although a series of minima and maxima are clearly present. In November a minimum is developing near the tropopause reflecting the appearance of cold temperatures in the equatorial region. This does not reflect a local drying of the air parcels as they pass through the tropopause over Brazil, however, since the frost-point temperature is much colder than saturation at the local tropopause could produce. This is also true for February 1997 over

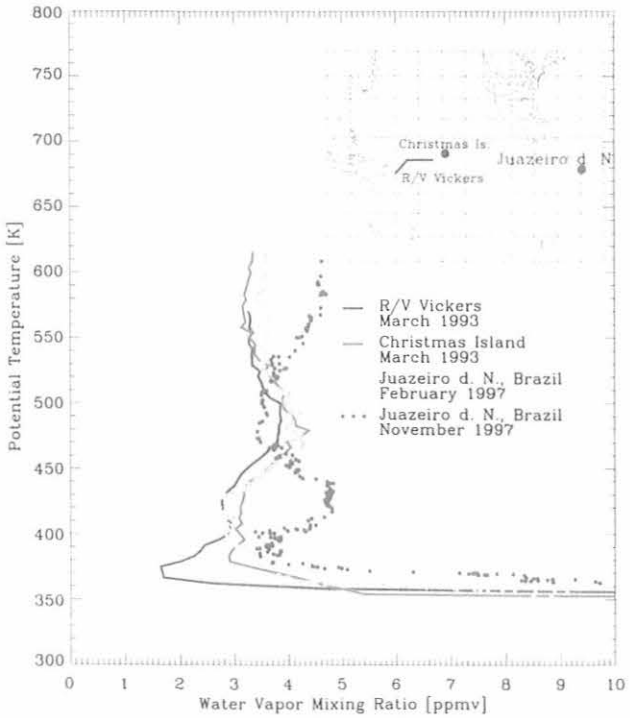

Fig. 4.8. Water vapor mixing ratio profiles from three locations along the equator.

Brazil and March 1993 over Christmas Island. In fact, only in the western Pacific do the tropopause temperatures reach the required low values. Outside of the western Pacific the mixing ratios do not maintain the very low values suggesting that the air is modified as it is mixed within the equatorial zone. During the NH summer when the equatorial tropopause temperatures are warmer, moister air passes through the tropopause. The rising air motion in the tropical stratosphere [*Holton et al.*, 1995] propagates the seasonal tropopause signature upward [*Mote et al.*, 1996]. Thus the minimum seen over Brazil at 400 K in February appears at about 460 K in November. The minima and maxima propagate upward at somewhat different rates because of the difference in the ascent rate of the air during different times of the year. These signatures can also be attenuated by lateral mixing in and out of the tropics. The ability to identify the features in individual profiles does suggest that this lateral mixing is somewhat limited, however [*Volk et al.*, 1996].

4.2.3. MLO Seasonal Transport Characteristics

Seasonal transport patterns for MLO as determined from isentropic trajectories for 1986-1997 are presented in Figure 4.9. Trajectories arrived at MLO at 3400 m, which is the approximate level of the observatory. Six average or cluster mean trajectories are also shown for each season with the percentage of trajectories that fall into each cluster. The cluster mean represents a group of trajectories that are similar in length and shape. There may be considerable variability within each cluster

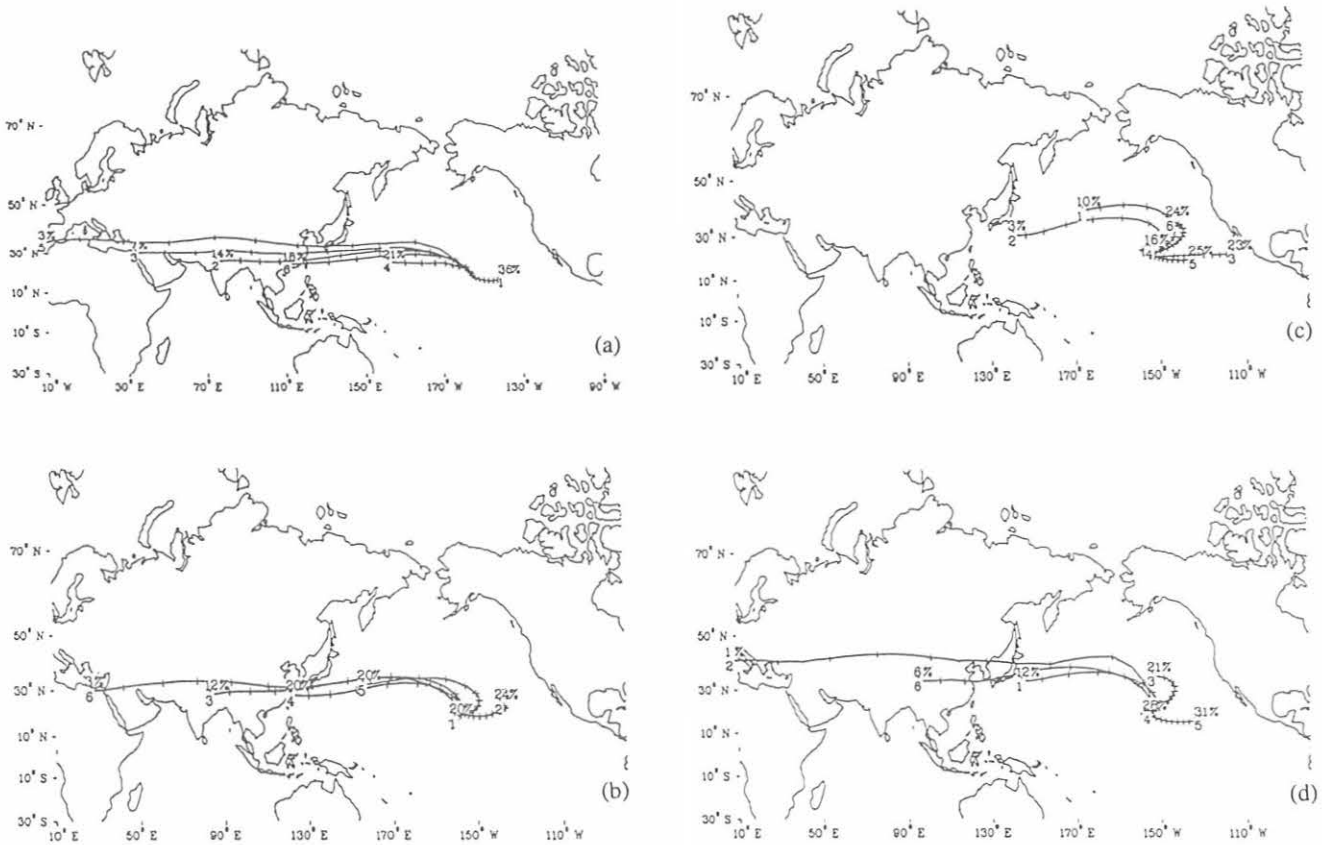

Fig. 4.9. Atmospheric flow patterns for MLO depicted by cluster-mean back trajectories for (a) Winter (December, January, February), (b) Spring (March, April, May), (c) Summer (June, July, August), and (d) Fall (September, October, November). Isentropic trajectories used in this analysis arrived at MLO at 3400 m for 1986-1997.

because of the variability of atmospheric conditions, but the cluster mean is a good way to visualize transport within that group. The four panels in Figure 4.9 show the progression of transport patterns throughout the year. During winter, westerly winds are strongest and about 40% of all trajectories have origins over Asia within 10 days. During spring, zonal flow is still prominent, although wind speeds are somewhat lighter and only 35% of trajectories have origins over Asia within 10 days. Transport during summer is dominated by easterly trade winds and MLO is mostly isolated from Asian influences. At this time of year, especially during August, some trajectories have origins over Central America within 10 days, but most easterly flow is light enough that air parcels remain over the tropical ocean. Fall is a season of transition between easterly trades and westerly flow. Every season does have a significant amount of trade wind flow, but it occurs most often in summer and least often in winter.

When considering potential sources, it is important to keep in mind the elevation of air parcels. During a recent study we examined air parcel elevation during springtime continental transport. Trajectories appeared fairly homogeneous, with all showing a strong westerly flow from Asia. The range of elevation of air parcels as they crossed the coast of the continent was large—from 3 to 8 km. Some models and aircraft experiments have found that urban pollution is mostly confined to the lower troposphere [*Banic et al.*, 1996], if not the boundary layer [*Wu et al.*, 1997; *Levy II et al.*, 1997]. At any rate, in order for Asian pollution to be detected at MLO, it would have to be mixed upward out of the boundary layer to considerable heights in the free troposphere. This may explain why a trajectory from Asia does not always result in larger trace gas amounts at MLO. The elevations of air parcels that originate over Central America are closer to surface sources ranging from 2 to 4 km. However, long transit times and photochemical modification en route to MLO could lessen the impact of sources in Central America.

Figure 4.10 shows the maximum elevation along 10-day trajectories as it varies by month. From December through April most air parcels originate above 5 km. This is largely due to subsidence around the North Pacific anticyclone. Maximum elevations during summer are close to the level of the observatory which is characteristic of trade wind flow. This transport feature is important

when considering atmospheric constituents that have strong vertical gradients or, like ozone, have a source in the upper troposphere/stratosphere.

Figure 4.11 shows the northernmost latitude along 10-day trajectories by month. This transport characteristic may be important for trace gases that have a strong north-south gradient, such as ozone, methane, and CO during springtime. Transport from the most northerly latitudes occurs during April and December when the average northerly extreme is about 35°N. During July through September air parcels originate in more southerly latitudes because of the predominance of trade wind flow.

A recent transport study investigated the cause of MLO's springtime maximum in tropospheric ozone [*Harris et al.*, 1998]. Figure 4.12 shows contours of ozone mixing ratio over Hilo, Hawaii, constructed from ozonesonde flights for 1982-1997. The springtime ozone enhancement at the level of the observatory is clear. The remarkable feature of this plot is that the enhancement is not in a well-defined transport layer, but rather the entire troposphere has more ozone in spring than in other seasons. This picture along with transport characteristics and the relationships found among ozone, CO, methane, and water vapor during spring discount Asian pollution as the main source of the ozone enhancement. A contribution from the upper troposphere/stratosphere upwind of MLO, perhaps in the baroclinically active area near Japan, is indicated. Transport across ozone gradients from the north may also contribute to the seasonal ozone maximum.

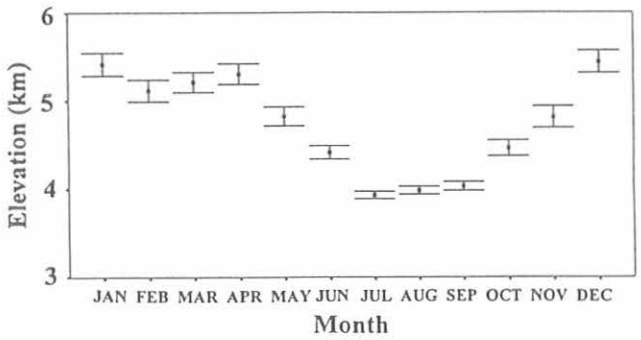

Fig. 4.10. Monthly mean maximum elevations attained by air parcels en route to MLO.

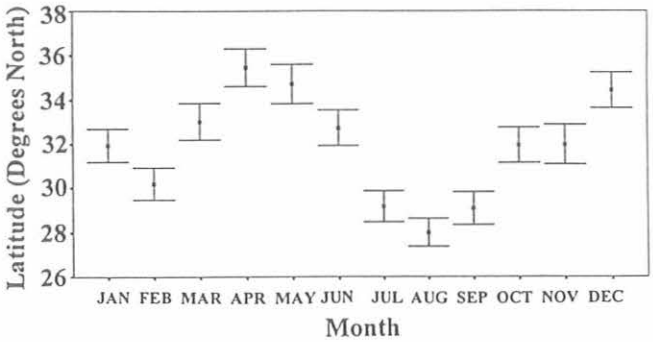

Fig. 4.11. Monthly means of the northernmost origins of air parcels en route to MLO.

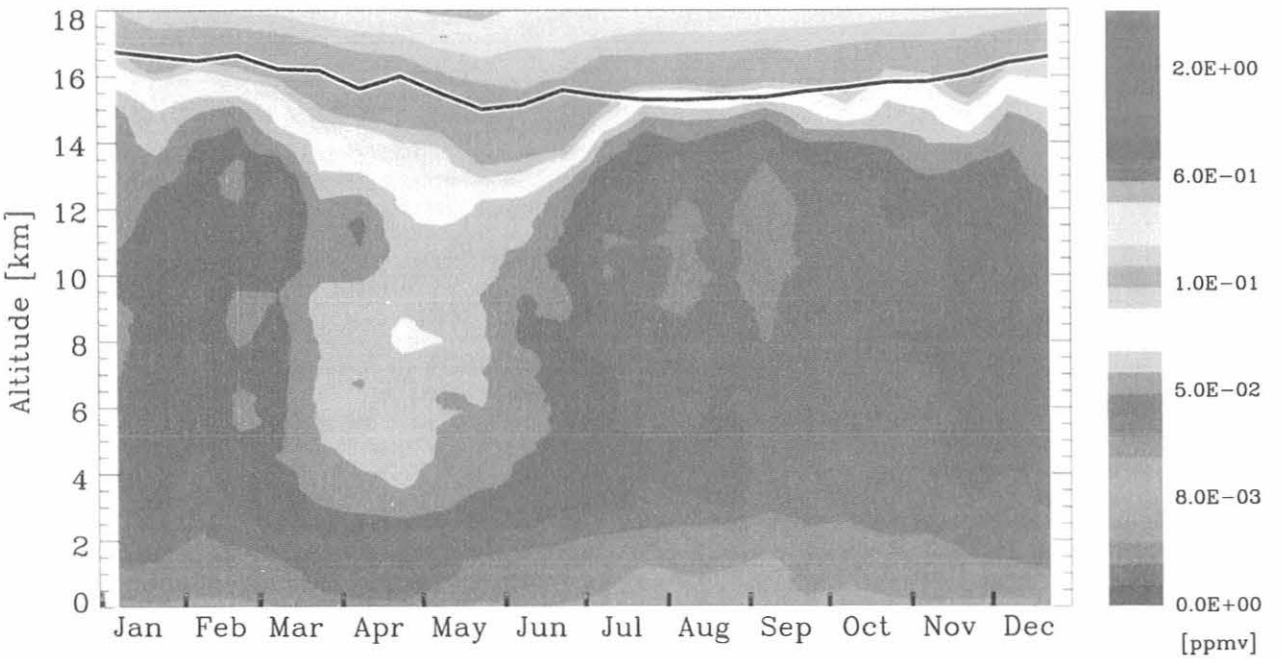

Fig. 4.12. Contours of ozone mixing ratio over Hilo, Hawaii, constructed from ozonesonde flights for 1982-1997. The dark line near the top is the climatological tropopause according to the World Meteorological Organization definition (<2 K km^{-1} for at least 2 km).

4.3. REFERENCES

Banic, C.M. W.R. Leaitch, G.A. Isaac, M.D. Couture, L.I. Kleinman, S.R. Springston, and J.I. Macpherson, Transport of ozone and sulfur to the North Atlantic atmosphere during the North Atlantic Regional Experiment, *J. Geophys. Res., 101*, 29,091-29,104, 1996.

Barnes, J.E., and D.J. Hofmann, Lidar measurements of stratospheric aerosol over Mauna Loa Observatory, *Geophys. Res. Lett.,24*, 1923-1926, 1997.

Barnes, R.A., A.R. Bandy, and A.L. Torres, Electrochemical concentration cell ozonesonde accuracy and precision, *J. Geophys. Res., 90*, 7881-7887, 1985.

Barrie, L.A., Occurrence and trends of pollution in the Arctic troposphere, in *Chemical Exchange Between the Atmosphere and Snow*, edited by E. W. Wolff and R. C. Bales, pp. 93-129, Springer-Verlag, Berlin, 1996.

Bergin, M.H., S.E. Schwartz, J.A. Ogren, and L.M. McInnes, Evaporation of ammonium nitrate aerosol in a heated nephelometer: Implications for field measurements, *Environ. Sci. Technol., 31*, 2878-2883, 1997.

Bergin, M.H., E. Meyerson, J.E. Dibb, and P. Mayewski, Comparison of continuous aerosol measurements and ice core chemistry over a 10 year period at the South Pole, *Geophys. Res. Lett., 25(8)*, 1189-1192, 1998a.

Bergin, M.H., R.S. Halthorne, S.E. Schwartz, J.A. Ogren, and S. Nemesure, Comparison of aerosol column properties based on nephelometer and radiometer measurements at the SGP ARM site, *J. Geophys. Res.*, submitted 1998b.

Bodhaine, B.A., Barrow surface aerosol: 1976-1987, *Atmos. Environ., 23(11)*, 2357-2369, 1989.

Bodhaine, B.A., Aerosol absorption measurements at Barrow, Mauna Loa, and South Pole, *J. Geophys. Res., 100*, 8967-8975, 1995.

Bodhaine, B.A., and J.J. DeLuisi, An aerosol climatology of Samoa, *J. Atmos. Chem., 3*, 107-122, 1985.

Bodhaine, B.A., and E.G. Dutton, A long-term decrease in Arctic Haze at Barrow, Alaska, *Geophys. Res. Lett., 20*, 947-950, 1993.

Bodhaine, B.A., J.M. Harris, and J.A. Ogren, Aerosol optical properties at Mauna Loa Observatory: Long-range transport from Kuwait?, *Geophys. Res. Lett., 19*, 581, 1992.

Bodhaine, B.A., J.J. DeLuisi, J.M. Harris, P. Houmere, and S. Bauman, Aerosol measurements at the South Pole, *Tellus, 38B*, 223-235, 1986.

Bodhaine, B.A., J.J. De Luisi, J.M. Harris, P. Houmere, and S. Bauman, PIXE analysis of South Pole aerosol, *Nucl. Instr. Method., 22*(B), 241-247, 1987.

Charlson, R.J., S.E. Schwartz, J.M. Hales, R.D. Cess, J.A. Coakley, Jr., J.E. Hansen, and D.J. Hofmann, Climate forcing by anthropogenic aerosols, *Science, 255*, 423-430, 1992.

Cooper, O.R., J.L. Moody, J.C. Davenport, S.J. Oltmans, B.J. Johnson, X. Chen, P.B. Shepson, J.T. Merrill, The influence of springtime weather systems on vertical ozone distributions over three North American sites, *J. Geophys. Res., 103*, 22,001-22,013, 1998.

Evans, S.J., R. Toumi, J.E. Harries, M.P. Chipperfield and J.M. Russell III, Trends in stratospheric humidity and the sensitivity of ozone to these trends, *J. Geophys. Res., 103*, 8715-8725, 1996.

Halter, B.C., J.M. Harris, and T.J. Conway, Component signals in the record of atmospheric carbon dioxide concentration at American Samoa, *J. Geophys. Res. 93(D12)*, 15,914-15,918, 1988.

Harris, J.M., An analysis of 5-day midtropospheric flow patterns for the South Pole: 1985-1989, *Tellus, 44B*, 409-421, 1992.

Harris, J.M. and J.D. Kahl, A descriptive atmospheric transport climatology for Mauna Loa Observatory, using clustered trajectories, *J. Geophys. Res., 95(D9)*, 13,651-13,667, 1990.

Harris, J.M. and J.D.W. Kahl, An analysis of 10-day isentropic flow patterns for Barrow, Alaska: 1985-1992, *J. Geophys. Res., 99(D12)*, 25,845-25,855, 1994.

Harris, J.M. and S.J. Oltmans, Variations in tropospheric ozone related to transport at American Samoa, *J. Geophys. Res., 102*(D7), 8781-8791, 1997.

Harris, J.M., S.J. Oltmans, E.J. Dlugokencky, P.C. Novelli, B.J. Johnson, and T. Mefford, An investigation into the source of the springtime tropospheric ozone maximum at Mauna Loa Observatory, *Geophys. Res. Lett., 25*, 1895-1898, 1998.

Harris, J.M., P.P. Tans, E. J. Dlugokencky, K.A. Masarie, P.M. Lang, S. Whittlestone, and L.P. Steele, Variations in atmospheric methane at Mauna Loa Observatory related to long-range transport, *J. Geophys. Res., 97(D5)*, 6003-6010, 1992.

Hofmann, D.J., J.T. Peterson, and R.M. Rosson (Eds.), *Climate Monitoring and Diagnostics Laboratory No. 23, Summary Report 1994-1995*, NOAA Environmental Research Laboratories, Boulder, CO, 161 pp., 1996.

Hofmann, D.J., S.J. Oltmans, J.M. Harris, B.J. Johnson, and J.A. Lathrop, Ten years of ozonesonde measurements at the South Pole: Implications for recovery of springtime Antarctic ozone, *J. Geophys. Res., 102(D7)*, 8931-8943, 1997.

Hofmann, D.J., S.J. Oltmans, J.A. Lathrop. J.M. Harris, and H. Vömel, Record low ozone at the South Pole in the spring of 1993, *Geophys. Res. Lett., 21*, 421-424, 1994.

Holton, J.R., P.H. Haynes, M.E. McIntyre, A.R. Douglass, R.B. Rood, and L. Pfister, Stratosphere-troposphere exchange, *Rev. Geophys., 33*, 405-439, 1995.

Komhyr, W.D., Electrochemical concentration cells for gas analysis, *Ann. Geophys., 25*, 203-210, 1969.

Komhyr, W.D., Operations handbook for ozone measurements to 40 km altitude with model 4A electrochemical concentration cell (ECC) ozonesondes (used with 1680MHz radiosondes), *NOAA Tech. Memo ERL ARL-149*, 49 pp., Air Resources Lab, Boulder, CO, 1986.

Komhyr, W.D., G.C. Reinsel, R.D. Evans, D.M. Quincy, and R.K. Leonard, Total ozone trends at sixteen NOAA/CMDL and cooperative Dobson spectrophotometer observatories during 1979-1996, *Geophys. Res. Lett., 24*, 3225-3228, 1997.

Levy II, H., P.S. Kasibhatla, W.J. Moxim, A.A. Klonecki, A.I. Hirsh, S.J. Oltmans, and W.L. Chameides, The global impact of human activity on tropospheric ozone, *Geophys. Res. Lett., 24*, 791-794, 1997.

McGee, T. J., et. al., Intercomparisons of Lidar-derived femperatures during the MLO3 NDSC validation at Mauna Loa, HI, Proc., 18th International Laser Radar Conference, 1996.

McInnes, L.M., M.H. Bergin, J.A. Ogren, and S.E. Schwartz, Differences in hygroscopic growth between marine and anthropogenic aerosols, *Geophys. Res. Lett., 25(4)*, 513-516, 1998.

Mote, P.W., et al., An atmospheric tape recorder: The imprint of tropical tropopause temperatures on stratospheric water vapor, *J. Geophys. Res., 101*, 3989-4006, 1996.

National Research Council (NRC), *Aerosol Radiative Forcing and Climatic Change*, National Academy Press, Washington, D.C., 161 pp., 1996.

Ogren, J.A., A systematic approach to in situ observations of aerosol properties, in *Aerosol Forcing of Climate*, edited by R.J. Charlson and J. Heintzenberg, John Wiley, 215-226, 1995.

Oltmans, S.J., et al., Trends of ozone in the troposphere, *Geophys. Res. Lett., 25*, 139-142, 1998.

Oltmans, S.J. and D.J. Hofmann, Increase in lower-stratospheric water vapor at a midlatitude site from 1981 to 1994, *Nature, 374*, 146-149, 1995.

Oltmans, S.J., H. Levy II, J.M. Harris, J.T. Merrill, J.L. Moody, J.A. Lathrop, E. Cuevas, M. Trainer, M.S. O'Neill, J.M. Prospero, H. Vömel, and B.J. Johnson, Summer and spring ozone profiles over the North Atlantic from ozonesonde measurements, *J. Geophys. Res., 101*, 29,179-29,200, 1996.

Proffitt, M.H., and R.J. McLaughlin, Fast response dual-beam UV-absorption photometer for use on stratospheric balloons, *Rev. Sci. Instrum., 54*, 1719-1728, 1983.

Quakenbush, T.K., and B.A. Bodhaine, Surface aerosols at the Barrow GMCC observatory: Data from 1976 through 1985, *NOAA Data Rep. ERL ARL-10,* 230 pp., NOAA Air Resources Laboratory, Silver Spring, MD, 1986.

Radke, L.F., C.A. Brock, R.J. Ferek, and D.J. Coffman, Summertime Arctic hazes, paper A52B-03 presented at the American Geophysical Union Fall Annual Meeting, San Francisco, December 3 to 7, 1990.

Steinbrecht, et. al., NDSC Intercomparison of stratospheric aerosol processing algorithms, Proc., 18th ILRC Conference, 1996.

Smit, G.J., et al., JOSIE: The 1996 WMO International Intercomparison of ozonesondes under quasi flight conditions in the environmental simulation chamber at Jülich, *J. Geophys. Res.*, submitted 1998.

Stone, R.S., Variations in western Arctic temperatures in response to cloud radiative and synoptic-scale influences, *J. Geophys. Res., 102(D18)*, 21,769-21,776, 1997.

Tarasick, D.W., D.I. Wardle, J.B. Kerr, J.J. Bellefluer, J. Davies, Tropospheric trends over Canada: 1980-1993, *Geophys. Res. Lett., 22*, 409-412, 1995.

Volk, C.M., et al., Quantifying transport between the tropical and midlatitude lower stratosphere, *Science, 272*, 1763-1768, 1996.

Wu, A., R.E. Newell, Y. Zhu, B.E. Anderson, E.V. Browell, G.L. Gregory, G.W. Sachse, and J.E. Collins Jr., Atmospheric layers measured from the NASA DC-8 during PEM-West B and comparison with PEM-West A, *J. Geophys. Res., 102*, 28,353-28,365, 1997.

5. Nitrous Oxide and Halocompounds

J.H. BUTLER (EDITOR), J.W. ELKINS, S.A. MONTZKA, T.M. THOMPSON, T.H. SWANSON, A.D. CLARKE, F.L. MOORE, D.F. HURST, P.A. ROMASHKIN, S.A. YVON-LEWIS, J.M. LOBERT, M. DICORLETO, G.S. DUTTON, L.T. LOCK, D.B. KING, R.E. DUNN, E.A. RAY, M. PENDER, P.R. WAMSLEY, AND C.M. VOLK

5.1. CONTINUING PROGRAMS

5.1.1. INTRODUCTION

Research conducted by the Nitrous Oxide and Halocompounds Group (NOAH) of CMDL in 1996 and 1997 included: (1) weekly flask sampling and analysis of air from remote locations and regionally influenced sites, (2) operation of instrumentation for hourly, in situ measurement of trace gases at the four CMDL observatories and at four regionally influenced sites, (3) preparation and maintenance of calibration gases for all measurements, (4) participation on campaigns requiring in situ stratospheric measurements from high-altitude aircraft and balloons, (5) investigation of oceanic processes influencing trace gas composition of the atmosphere, (6) in situ monitoring of air at multiple elevations from tall towers, and (7) measurement of gases in air that is archived in consolidated polar snow in Antarctica and Greenland.

The main mission of NOAH is to measure and to evaluate the distribution and trends of nitrous oxide (N_2O) and many halogenated gases in the atmosphere and ocean with the best analytical tools available. The halogenated gases, or halocompounds, include the chlorofluorocarbons (CFCs), chlorinated solvents (CCl_4, CH_3CCl_3, $CHCl_3$, etc.), hydrochlorofluorocarbons (HCFCs), hydrofluorocarbons (HFCs), methyl halides, halons, and sulfur hexafluoride (SF_6). The recent motivations for measuring these compounds are: (1) that many of the brominated and chlorinated compounds that cause ozone depletion are being phased out of production as required by the amended and adjusted Montreal Protocol [*United Nations Environmental Programme (UNEP)*, 1987, 1997], and (2) that these and many of the compounds introduced to replace them contribute to global warming. The Protocol of the Third Conference of Parties to the United Nations (UN) Framework Convention on Climate Change, held in Kyoto, Japan, December 1997, recommended future limits on the emissions of six compounds or compound groups: (1) carbon dioxide (CO_2), (2) methane (CH_4), (3) nitrous oxide (N_2O), (4) HFCs, (5) SF_6, and (6) the perfluorocarbons (PFC). The last four of these six categories are within the domain of NOAH's research.

Continuing programs within NOAH are based upon in situ or flask air sample measurements from four CMDL observatories and nine cooperative sampling sites (Figure 5.1, Table 5.1. These stations provide a robust network for evaluating global atmospheric change and hemispheric relationships for the various compounds.

One of the more significant discoveries in the past 2 years is the turnover of total anthropogenic chlorine in the atmosphere. This finding came from the combined results of flask sampling, in situ monitoring, and standards programs and is discussed in the following sections.

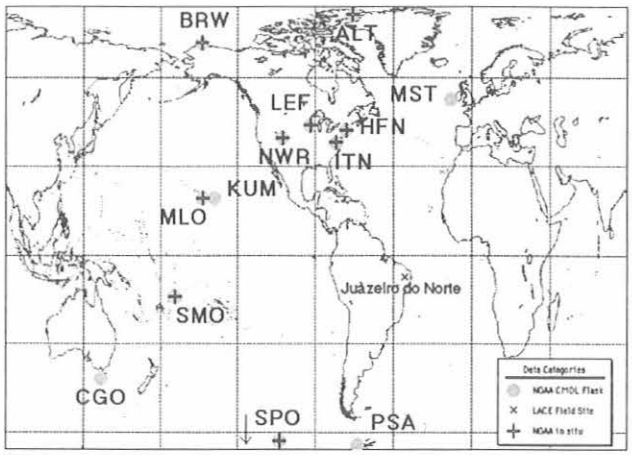

Fig. 5.1. Geographic locations of old and new stations in the NOAH flask (gray circles) and in situ (crosses) networks. The site for the tropical balloon launches, Juazeiro do Norto, Brazil, is noted by an "X."

Other significant results include the observed global increases in atmospheric N_2O and SF_6, again in both flask and in situ monitoring, the continued growth of atmospheric HCFCs and HFCs as they increasingly are used as replacements for the ozone-depleting CFCs, and the surprising, protracted growth of the halons in the atmosphere years after the cessation of their production in developed countries.

5.1.2. FLASK SAMPLES

Overview

The flask sampling program has undergone a few changes in 1996-1997 designed mainly to facilitate processing of samples and data. Over the past decade the number of gases analyzed by this group has risen from 3 to over 25 and the number of weekly sampling sites has more than doubled, from 5 to 11 (Figure 5.1, Table 5.1). Additional flasks are collected as part of special projects, including oceanic expeditions, polar firn sampling, and aircraft missions. Flasks that once were analyzed by one instrument are now analyzed by four instruments, two of which are mass spectrometers (Table 5.2). This increase in the number of flasks sampled and gases measured has resulted in a considerable increase in the laboratory workload. Attempts to offset this have focused on automation of instruments, streamlining of data processing, and improvement of quality control. In 1991 the first of the automated instruments, a three-channel gas chromatograph (GC) electron capture detector (ECD) system capable of measuring seven gases, was put in service. This system replaced the old manual, one-channel

TABLE 5.1. Geographic and Network Information on NOAH Network Sites

Code	Station	Latitude	Longitude	Elevations (m)	LST-GMT (hr)	Type
ALT	Alert, Northwest Territories, Canada (AES)*	82.45°N	62.52°W	210	-4	F, I
BRW	Point Barrow, Alaska	71.32°N	136.60°W	11	-9	F, I
MHT	Mace Head, Ireland (University College)	53.33°N	9.90°W	26	0	F
LEF	WLEF tower, Wisconsin (CMDL-CCG)	45.95°N	90.28°W	470	-6	F, I
HFM	Harvard Forest, Massachusetts (Harvard University)	42.54°N	72.18°W	340	-5	F, I
NWR	Niwot Ridge, Colorado (University of Colorado)	40.04°N	105.54°W	3013	-7	F, I
ITN	WITN tower, North Carolina (CMDL-CCG)	35.37°N	77.39°W	9	-5	F, I
MLO	Mauna Loa, Hawaii	19.54°N	155.58°W	3397	-10	F, I
KUM	Cape Kumukahi, Hawaii	19.52°N	154.82°W	3	-10	F
SMO	Tuluila, American Samoa	14.23°S	170.56°W	77	-11	F, I
CGO	Cape Grim, Tasmania, Australia†	40.41°S	144.64°E	94	+10	F
PSA	Palmer Station, Antarctica‡	64.92°S	64.00°W	10	+12	F
SPO	South Pole, Antarctica	89.98°S	102.00°E	2841	+12	F, I

Cooperative sites (F = flasks, I = in situ) with:
*In situ GC: Only N_2O and SF_6; flask sampling for all gases, however.
†Commonwealth Scientific and Industrial Research Organization (CSIRO) and Bureau of Meteorology, Australia
‡Only glass flasks used.

GC/ECD that measured only three gases [*Thompson et al.*, 1985]. After a few years of debugging and intercomparison, the old, manual GC/ECD was retired in 1996. Software for running the automated GC/ECD system was upgraded in 1995. In the past 2 years quality control programs were written and a database developed that now allows evaluation of data from samples immediately following analysis.

TABLE 5.2. Instrumentation for NOAH Flask Analysis

Instrument	Type	Gases	Frequency of Network Data
OTTO	GC/ECD, 3-channel, isothermal	N_2O, CFC's (3) ClC's (2) SF_6	Weekly
LEAPS	GC/ECD, 1-channel, temperature programmed	Halons (2) CH_3Cl CH_3Br CFC's (1)	Semi-monthly to monthly
HCFC-MS	GC/MS, 1-channel, temperature programmed	HCFCs (3) HFCs (1) CFCs (3) Halons (1) ClCs (6) BrCs (3)	Semi-monthly
HFC-MS	GC/MS, 1-channel, temperature programmed	HCFCs (5) HFCs (2) CFCs (2) Halons (2) ClCs (6) BrCs (3) ClBrCs (3)	Semi-monthly to monthly

Other efforts at automation included the GC mass spectrometer (MS) mainly responsible for measurement of HCFC's and methyl halides, and an additional GC electron capture detector (ECD) system, Low Electron Attachment Potential Species (LEAPS), mainly used for measurement of halons and methyl bromide. Programs also have been written to speed up processing of data from these instruments. Peak integration is now fully automated on both GC/MS instruments, although manual integration of peaks is still necessary on the LEAPS GC/ECD system.

Thirty-two new, 3-L sampling flasks from Meriter Corporation (San Jose, California) were purchased for inclusion in our sampling network. These flasks are constructed from no. 316 stainless steel, are highly electropolished, and have minimal internal weld exposure. Stability is excellent for most gases in these flasks, although CCl_4 and, to a lesser extent, CH_3CCl_3 can degrade over the long term as they do in all stainless steel flasks filled with dry air. Recent work with glass flasks in sampling firn air has shown that glass flasks identical to those used in the carbon cycle network can be used for sampling halocarbons over the short term. Further tests of flasks already in the network showed that many of them, depending upon their history, can be contaminated. We continue to purchase and test these in small lots as a possible option for use in special projects and for measuring gases that are less stable in selected stainless steel flasks.

A number of improvements at our flask sampling sites during 1996 and 1997 were made. At SMO the sample inlet was moved from the stack to the pump board Air-Cadet inlet system of the Radiatively Important Trace Species (RITS) GC to avoid cross contamination from other observatory instruments with inlets attached to the stack. Samples are now collected from the continuous flow, pressurized inlet at all sites except CGO, which will be changed over in 1998. Because of concerns about the durability of the Air-Cadet pumps for use with the RITS

inlet system and flask sampling, existing pumps were replaced with KNF Neuberger N-05 pumps during visits to the South Pole Observatory, Antarctica (SPO), Mauna Loa Observatory, Hawaii (MLO), Cape Kumukahi, Hawaii (KUM), and SMO. Pumps at the remaining sites will be upgraded in 1998. At KUM before November 1997, a pump system was connected upstream of the continuously flowing, Air Cadet pump to facilitate flask sampling. In November 1997 the Air cadet pump was replaced by a continuously flowing KNF Neuberger pump. Flasks can now be sampled from a simple manifold. BRW and CGO will be visited in 1998 to receive the same improvements. At NWR, AC power was installed at T-van. The battery-powered pump system will be replaced by a new system that allows flasks to be filled to higher pressures.

In addition to improvements at these sites, sampling with glass flasks was initiated at Palmer Station, Antarctica (PSA) at the end of 1997 in an attempt to understand the seasonal cycling of some of the more reactive halogens at a southern hemispheric coastal site. The objective is to compare results from this site with those from BRW where seasonal cycles are pronounced and perhaps influenced by the springtime breakup of ice. With assistance from CMDL's Carbon Cycle Group (CCG), samples are collected in glass flasks two times per month. The glass flasks are filled to about 1.3 kPa with the CCG MAKS sampling apparatus by personnel trained by CCG. Although contamination is observed for some halocarbons, pump tests and preliminary results suggest good data can be obtained for many other compounds with this technique.

CFCs and Chlorocarbons

Measurements from the automated flask GC (OTTO) show that atmospheric mixing ratios of CFC-11 and CFC-113 continued to decline through 1996 and 1997 at rates similar to those previously reported for earlier years [*Montzka et al.*, 1996], while the growth rate of CFC-12, although still positive, decreased from 5.9 to around 4 ppt yr^{-1} (see cover figure). As a result of declining concentrations and growth rates for CFCs, methyl chloroform, and CCl_4, the amount of chlorine, equivalent chlorine (chlorine + bromine weighted by an efficiency factor), and effective equivalent chlorine (equivalent chlorine weighted by destruction rates in the midlatitude stratosphere) contained within long-lived, halogenated gases (CFCs, HCFCs, CH_3CCl_3, CCl_4, and halons), peaked in 1992-1994 and declined through 1995 [*Montzka et al.*, 1996]. *Cunnold et al.* [1997] found similar results for chlorine-containing compounds measured by the Advanced Global Atmospheric Gases Experiment (AGAGE). The measurements suggest that declines in these quantities continued during 1996-1997 at rates similar to those observed in mid-1995 (Figure 5.2). Amounts observed at the end of 1997 represent a decrease of 2-4% from the peak Cl, ECl, and EECl delivered to the atmosphere from these gases in earlier years. Relative declines in the total atmospheric burden of Cl, ECl, and EECl are smaller because other gases (e.g., CH_3Cl and CH_3Br) also contribute significantly to the atmospheric burden of these quantities.

The gas contributing the most to this decline is CH_3CCl_3, which has an atmospheric lifetime of less than 5 years. As this gas is removed from the atmosphere, the overall rate of the decline in total chlorine will become slower. However, distributions and trends of this gas allow understanding of other atmospheric processes. For example, the difference in the atmospheric mixing ratio of CH_3CCl_3 between hemispheres has become dramatically smaller since 1992 as emissions have declined. The global latitudinal distribution of CH_3CCl_3 in 1992 and earlier years reflected the distribution of sources; mixing ratios in the northern hemisphere were higher than in the southern

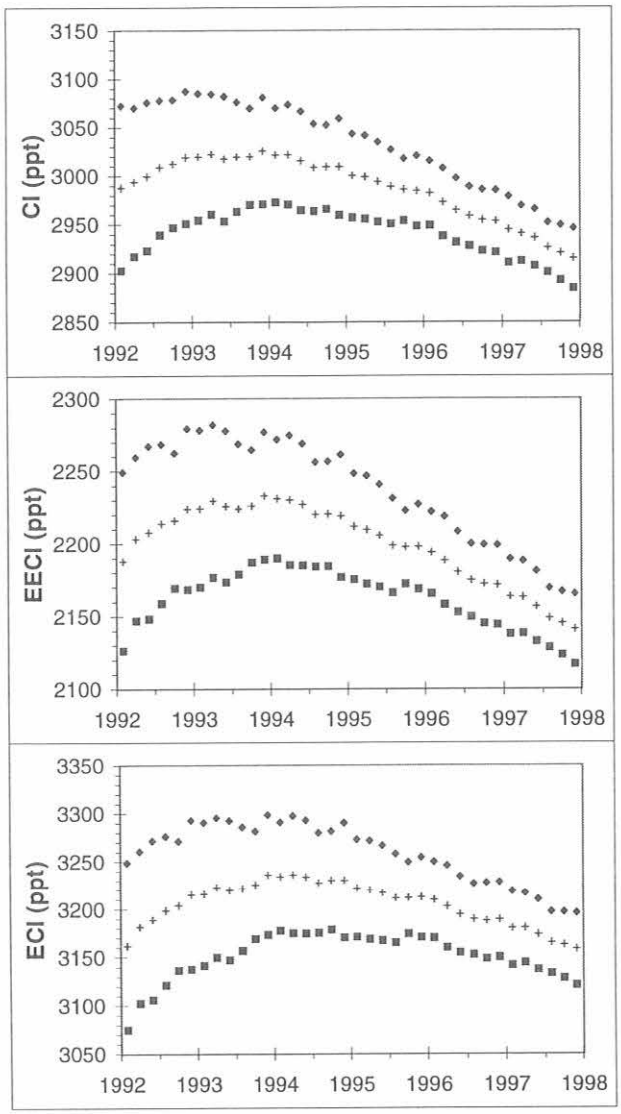

Fig. 5.2. Trends in chlorine, equivalent chlorine (chlorine + bromine multiplied by an efficiency factor of 50), and effective equivalent chlorine (equivalent chlorine where compound-specific halogen release rates are considered) from CFCs, HCFCs, halons, CCl_4, and CH_3CCl_3. Symbols refer to the northern hemisphere (filled diamonds), southern hemisphere (filled squares), and global tropospheric mean (crosses).

hemisphere because this solvent was emitted predominantly in the northern hemisphere. As emissions become insignificant, the distribution of CH_3CCl_3 will instead reflect the latitudinal distribution of sinks for this compound, which is dominated by the reaction of CH_3CCl_3 with the hydroxyl radical (Figure 5.3). Since the summer of 1996, mixing ratios at SMO have been lower than at CGO, likely as a result of the greater abundance of OH in the tropics. Continued monitoring of methyl chloroform as emissions diminish further should allow for refined estimates of the global lifetime of CH_3CCl_3 and, therefore, of other trace gases that react with OH. It also will be useful in estimating the relative mean OH abundance in the northern and southern hemispheres.

The global mixing ratio of CCl_4 is more difficult to determine from flask samples because CCl_4 (and to a much lesser extent CH_3CCl_3 and CH_3Br) can be degraded in dry air samples stored for extended periods in stainless steel flasks. This is indicated by anomalously low mixing ratios and poor flask pair agreement in many of the samples collected at SPO and less frequently from wintertime samples collected at ALT, BRW, MLO, and NWR. Nevertheless, measurements from reliable flask samples (those for which pair agreement is within acceptable limits) support the trends and abundance determined by the RITS program, showing a continued decrease of 0.8 ppt yr^{-1} for atmospheric CCl_4 through 1996 and 1997.

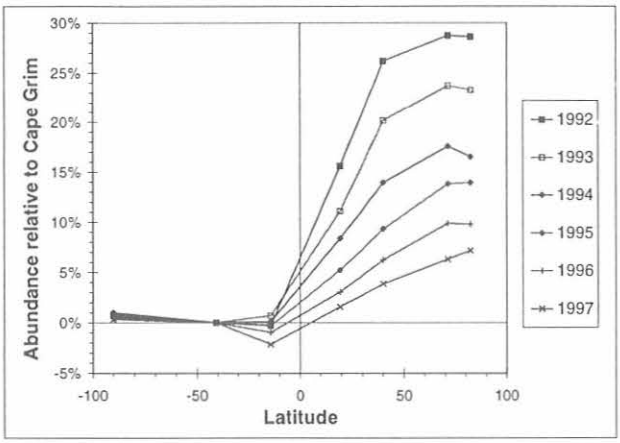

Fig. 5.3. The annual mean abundance of methylchloroform relative to the abundance at Cape Grim, Tasmania, for that year. Similar years are connected with lines to guide the eye. Mixing ratios are determined from GC/MS analysis of paired flask samples.

N_2O

The growth rate of atmospheric N_2O over the past two decades has ranged from under 0.5 to over 1.0 ppt yr^{-1}. The mean, globally-averaged growth rate of this gas from flask measurements during this time was 0.75 ± 0.03 (95% confidence limits (C.L.)) ppt yr^{-1}, which amounts to about 0.25% yr^{-1}. These data and growth rates are from 20 years of flask analyses and are corroborated by measurements with RITS in situ instrumentation over the past 11 years (section 5.1.3). The factors that cause this increase and determine the isotopic composition of atmospheric N_2O are currently unexplained [*Bouwman et al.*, 1995; *Cicerone*, 1989; *Kim and Craig*, 1993]. However, our measurements of firn air [*Battle et al.*, 1996] and other ice-core records [*Khalil and Rasmussen*, 1989; *Leuenberger and Siegenthaler*, 1992; *Machida et al.*, 1995] show clearly that N_2O has been increasing in the atmosphere for at least the past 100 years.

SF_6

SF_6 is a trace gas only recently introduced into the atmosphere. It has a lifetime of ~3200 years [*Ravishankara et al.*, 1993] and a greenhouse warming potential (GWP) of 15,000-35,000 [*Schimel et al.*, 1996], making it an extraordinarily strong greenhouse gas on a per molecule basis. SF_6 is used mainly as an insulator in electrical transformers and circuit breakers. Once leaked into the atmosphere, it will persist for millennia. Although present at low ppt levels in today's atmosphere and currently of little global consequence, SF_6 has been increasing in abundance since the early 1970s [*Geller et al.*, 1997; *Maiss and Levin*, 1994]. SF_6 data, which include archived air samples and recent samples from the flask network, show that the growth rate has not changed much over the past decade (Figure 5.4). The growth rate of 0.20 ± 0.03 (95% C.L.) ppt yr^{-1} from the flask network samples, which run from 1995-1998, does not differ

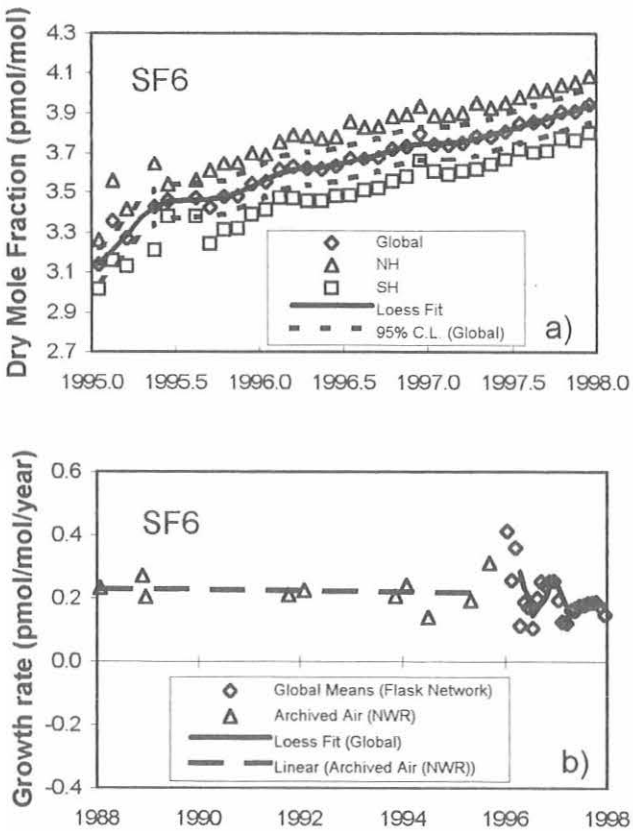

Fig. 5.4. CMDL measurements of atmospheric SF_6. (a) Global and hemispheric averages of the dry mole fraction of SF_6 in flask samples dating back to 1995. (b) Annual growth rates calculated from year-to-year differences in the global mean N_2O. The dark line is a loess smooth of the data.

significantly from the 0.22 ± 0.03 (95% C.L.) ppt yr^{-1} determined from archived NWR samples which go back to 1987. Northern hemisphere (NH), southern hemisphere (SH), and global growth rates for this gas are identical, which is to be expected for a gas with constant source strength and long lifetime.

Halons

Measurements show that the atmospheric burden of halons H-1301 and H-1211 has doubled and that of H-2402 has increased by over half during the past decade (Figure 5.5) [*Butler et al.*, 1998]. Halon mixing ratios continued to increase in recent years despite an international ban on their production and sales in developed nations effective January 1, 1994. The growth rate of H-1301 appears to have slowed recently, but it remains significant (Table 5.3, Figure 5.5a) and, within stated uncertainties, the 1997 growth rate does not differ from that reported for the end of 1996 [*Butler et al.*, 1998]. Atmospheric H-1211 is increasing at a much higher rate than H-1301 and has not shown much sign of slowing over the past decade (Table 5.3, Figure 5.5b). The 1997 tropospheric growth is virtually identical to growth over the past decade. Although the growth rate of H-2402 is substantially slower than that of the other two halons, H-2402 contains two bromine atoms per molecule. Thus the increase of Br due to growth of H-2402 in the atmosphere in 1996 is almost half that of H-1301 and about one-tenth that of H-1211.

Few measurements of halons that allow for accurate comparisons to the results presented here have been reported over the past decade. Usually such reports are associated with field missions that are limited in geographic distribution, period of sampling, or both. Some are part of stratospheric investigations, so contribute only a few values for the troposphere. Even if these differences in sampling are taken into account, it is still clear that measurements from these studies in the past have not agreed well (Figure 5.6). Such widespread disagreement among laboratories underscores the need for extensive intercalibration among investigators making these measurements. Small offsets in calibration can lead to large errors in estimates of potential ozone depletion because of the possibility of the halons offsetting gains in stratospheric ozone protection resulting from reductions in chlorocarbon emissions [*e.g., Montzka et al.*, 1996]. Small errors in estimating the atmospheric burden of halons can lead to significant errors in estimates of the atmospheric burden or trend of equivalent chlorine in the atmosphere [*Daniel et al.* 1996].

Evaluations of the growth rates and the amounts of "banked" halon available for use suggest that H-1301 emissions could continue at the present rate for another 40 years before depleting the bank of H-1301 [*Butler et al.*, 1998]. This would leave an atmospheric mixing ratio of 3.6 ppt, or 57% higher than observed today. Under the same scenario, reserves of H-1211 would be depleted in 8 to 12 years leaving an atmospheric mixing ratio of 4.6-5.0 ppt, or 31-43% higher than observed today. However, there is a significant discrepancy between H-1211 emissions calculated from production and use and emissions deduced from atmospheric measurements. The discrepancy can be reconciled by lowering estimated emissions by ~25%, reducing the atmospheric lifetime of H-1211 from the 20 years given in *Kaye et al.*, [1994] to 11 years or some combination of the two [*Butler et al.*, 1998]. These uncertainties cause considerable doubt in

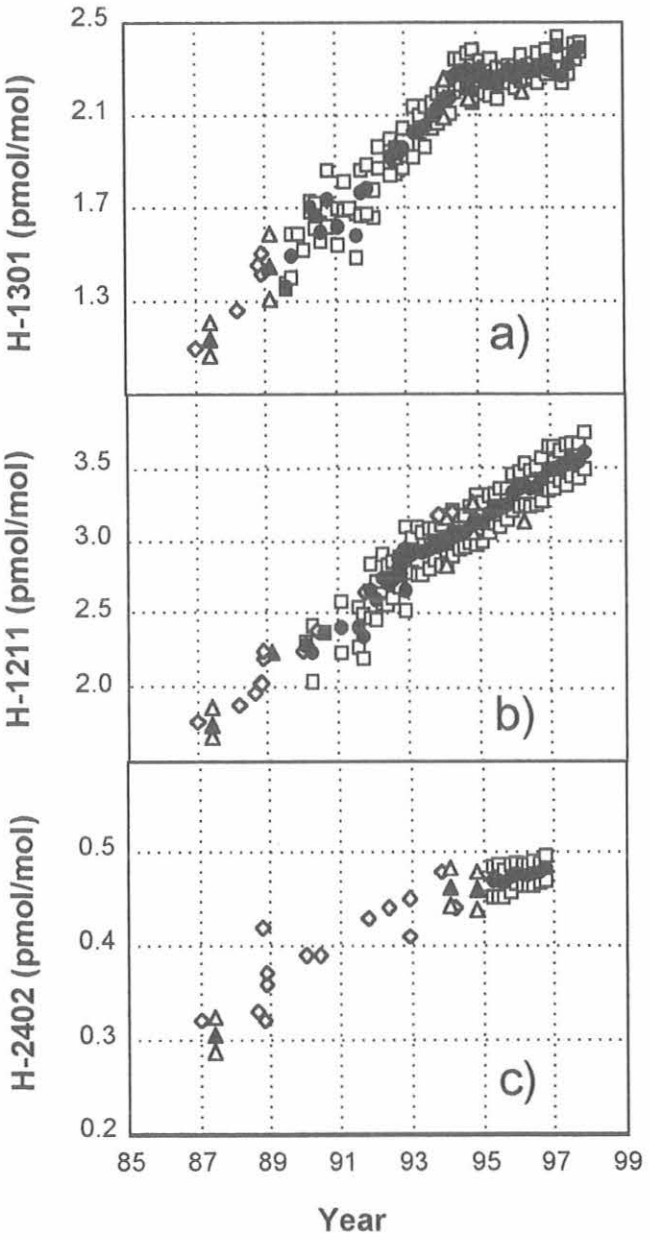

Fig. 5.5. Hemispheric and global bimonthly averages of tropospheric mole fractions of (a) H-1301, (b) H-1211, and (c) H-2402. Data are taken from the CMDL flask network (squares), research cruises (triangles), and cylinders of archived air (diamonds). Northern hemispheric results are shown as shaded symbols, southern hemispheric results as open symbols, and global means as solid symbols. Bimonthly, hemispheric averages are calculated by weighting measurements by the cosine of the sampling latitude within each hemisphere. Global averages are computed as means of the hemispheric averages.

TABLE 5.3. Atmospheric Halons

Gas	Tropospheric Mole Fraction (pmol mol^{-1})	Global Growth Rate (pmol mol^{-1} yr^{-1})
H-1301	2.4 ± 0.1	0.044 ± 0.015
H-1211	3.6 ± 0.1	0.15 ± 0.02
H-2402	0.45 ± 0.03	0.009 ± 0.001

Tropospheric mole fractions for H-1301 and H-1211 are for the end of 1997. The tropospheric mole fraction for H-2402 is for the end of 1996. Global growth rates for H-1301 and H-1211 are given as the observed change in the latitudinally weighted, global, mean mixing ratios for 1995-1997 for H-1211 and for 1995-1996 for H-2402.

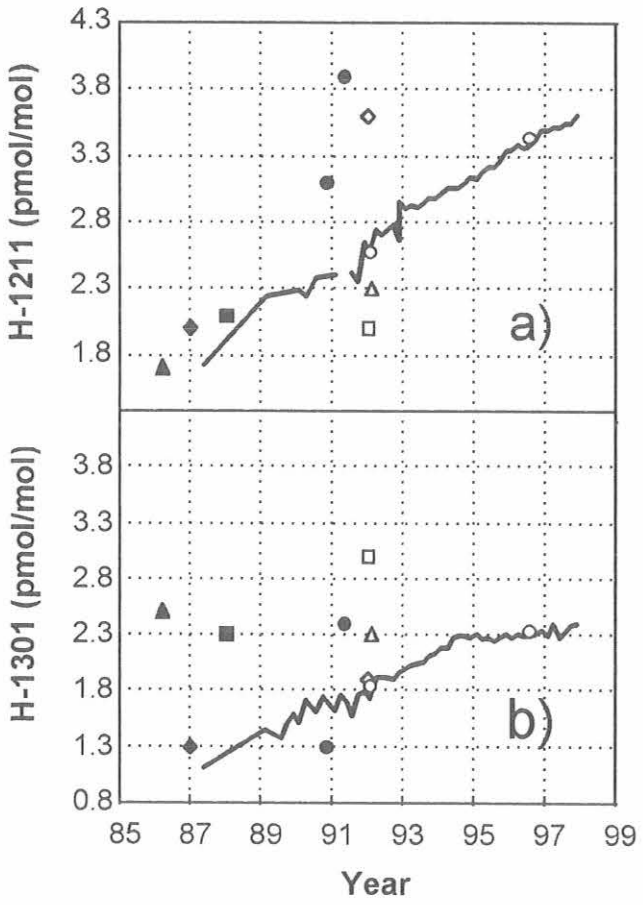

Fig. 5.6. Measurements of tropospheric halons over the past decade. Solid lines are CMDL global averages for (a) H-1211 and (b) H-1301. Symbols signify measurements by other laboratories and research groups. Filled squares represent work by Khalil and Rasmussen [*Ehhalt et al.* 1988, *Khalil and Rasmussen*, 1992], open triangles are from a study by *Singh et al.* [1988], open squares represent measurements by *Oertel* [1992], filled circles are measurements by C.J.-L. Wang, D.R. Blake, N. Blake, and F.S. Rowland, as given in *Lorenzen-Schmidt* [1994], filled diamonds are values from *Lorenzen-Schmidt* [1994], open circles are from *Schauffler et al.* [1993], and filled triangles are from *Fabian et al.* [1994].

modeled predictions of the future burden and fate of H-1211 in the atmosphere. It is not certain whether the continued rapid increase in H-1211 results from a depletion of known reserves, inordinately high fugitive emissions during its production in third world countries, or unreported production of halon.

Chlorofluorocarbon Alternatives Measurement Program (CAMP)

Measurements of chlorofluorocarbon alternatives continued on two instruments during 1996 and 1997. On average, one to three flask pairs per month from eight remote and three regional sampling locations were analyzed on the older GC-MS instrument. In addition, about one sample flask pair per month was analyzed from the remote locations on the instrument dedicated to making measurements of HFC-134a. The main changes made in this program involved automated data manipulation on both instruments as of January 1997 and automated analysis of larger flasks on the older GC-MS instrument as of September 1997.

Automated data manipulation allows results to be calculated and compiled more efficiently. This is achieved through the use of macros that determine chromatographic peak areas and calculate and compile results with a commercially-available spreadsheet software package. Automation allows for unattended analysis of up to eight flasks or four high-pressure cylinders. Flasks and secondary air standards are connected via a 16-port stream selection valve to the instrument inlet. Flows from flasks are regulated with different lengths of small diameter stainless steel tubing that are matched to the initial flask pressures. With automated analysis, agreement between replicate injections and between simultaneously filled flasks is similar to or improved over manual analysis. Results from a subset of flasks analyzed by both methods agreed for nearly all compounds. Some small offsets were observed for HCFC-142b and HCFC-141b and appear to result from problems associated with manual analysis of flasks. Protocols for routine checking of sample integrity as it passes through the multiple sampling ports are being implemented.

Mixing ratios of the most abundant HCFCs (HCFC-22, -141b, and -142b) continue to increase throughout the troposphere (Figure 5.7, Table 5.4). In mid-1997 these three gases accounted for about 5% or 150 ppt of the atmospheric burden of chlorine contained within long-lived, anthropogenic halocarbons. This amount was increasing by about 10 ppt per year in 1997 or similar to that reported for earlier years [*Elkins et al.*, 1996a; *Montzka et al.*, 1996].

Continued increases were also observed for HFC-134a, a gas for which restrictions on future use are being considered as part of the Kyoto Protocol (Figure 5.7, Table 5.4). Global mixing ratios of this CFC replacement are currently below 10 ppt. Because of laboratory air contamination and other issues, the number of good measurements made in 1997 was limited, but improvements are being implemented to avoid these problems in the future.

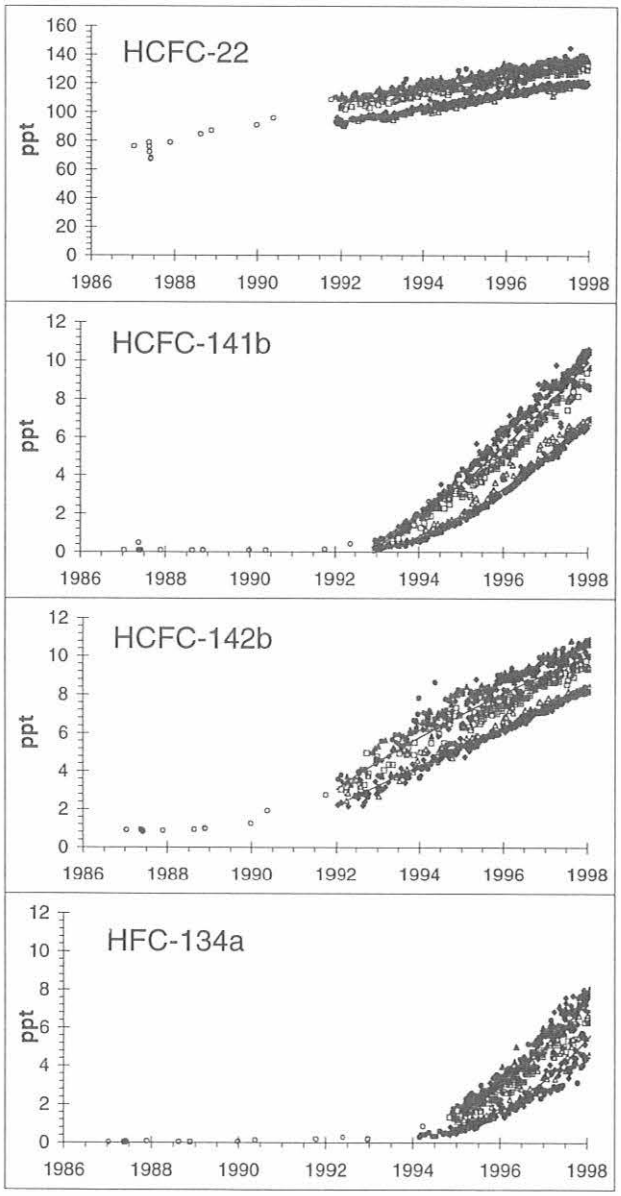

Fig. 5.7. Atmospheric dry mole fractions (ppt) of the most abundant HCFCs and HFC-134a. Each point represents the mean of two simultaneously filled flasks from one of eight stations: ALT, filled circle; BRW, filled triangle; NWR, filled diamond; KUM, crosses; MLO, open square; SMO, open triangle; CGO, filled diamond; SPO, filled circle. Also plotted are results from analysis of archived air samples (open circles) filled at NWR and in a past cruise from both hemispheres (mid-1987).

Short-Lived Gases

Measurements of CH_2Cl_2, $CHCl_3$, and C_2Cl_4 by GC-MS techniques continued from remote flask sampling locations during 1996-1997 (Figure 5.8) and as part of CAMP. Beginning in 1995 the use of a new type of flask built at Max Planck Institute for Chemistry (MPI), Mainz, Germany, allowed for more reliable measurements of CH_2Cl_2 and $CHCl_3$, and reliable measurements of CH_3Cl and CH_3Br (Figure 5.8). These MPI flasks are larger (2.4 L versus 0.8 L), made out of a higher grade stainless steel, and do not contain any seals that require Teflon tape. Results from simultaneously filled pairs of these flasks generally agree to within the instrument measurement capabilities, suggesting that mixing ratios of gases contained within the flasks do not change during storage and transport. This was not true for some gases, particularly CH_3Cl and CH_3Br in the older, 0.8-L flasks.

TABLE 5.4. Global Mid-Year Burden and Rate of Change for HCFCs, and HFC-134a

Compound	Mid-1996 Mixing Ratio (ppt)	Mid-1997 Mixing Ratio (ppt)	1996-1997 Growth Rate (ppt yr^{-1})
HCFC-22	121.6	126.0	4.9*
HCFC-141b	5.4	7.4	1.9
HCFC-142b	7.7	8.7	1.0
HFC-134a	3.1	5.4	2.1

Quantities estimated from latitudinally weighted measurements at seven remote sampling locations.

*Growth rate estimated from 1992-1997.

5.1.3. Radiatively Important Trace Species (RITS) Measurements

Operations Update

The major operational change in this program over the 2-year period of this report was the relocation of equipment to new buildings at three sites. The air line intakes were not moved during this period, but in November 1995 the tower at SPO was moved and the lines extended to accommodate construction of the Atmospheric Research Observatory (ARO). Normal equipment and software maintenance continued as usual based on failures and problems reported by the site personnel.

At the C-1 site on Niwot Ridge, Colorado, a 3 m × 5 m Tall Ranch Tuff Shed was placed at the site in early October 1995 east of the existing facility. Over the next 6 months as time and weather permitted, a window was installed and the interior of the structure was wired for electricity. The building was insulated and wall board, flooring, heating equipment, and air conditioning were installed. Finish work was done by NOAH staff. University of Colorado personnel brought power to the building and installed a fiber optic computer network. On April 3, 1996, all of the equipment was moved into the new building. As the air lines were moved, one of the lines was found to have a small hole in it about 1 m from where it entered the old building. The Dekabon tubing was cut at that point and attached to the pump in the new building. A comparison of the previous month's data shows no significant difference between the two air lines for any of the chemicals measured.

The new building at SMO was completed in early July 1996 and our equipment was the first to be moved from the old EKTO building. The equipment was checked and then

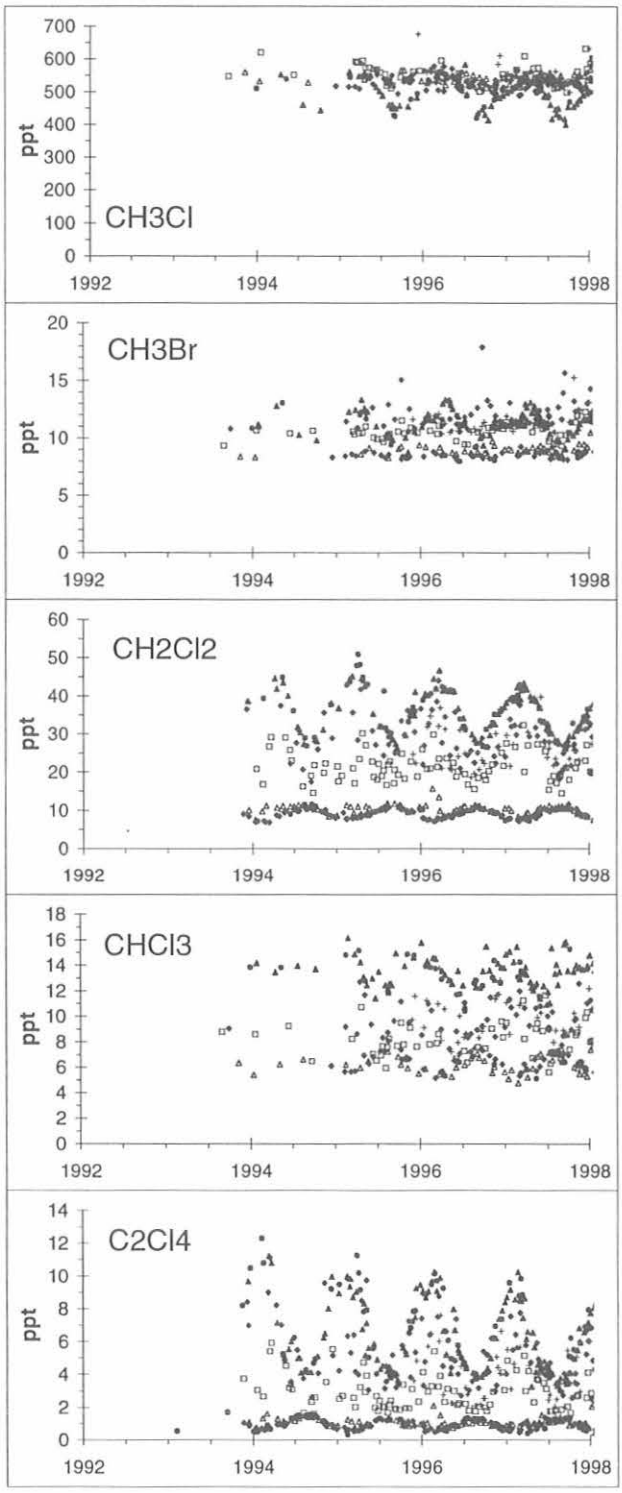

Fig. 5.8. Atmospheric dry mole fractions (ppt) determined for selected chlorinated trace gases and CH_3Br. Symbols are identical to those described in Figure 5.7. Results shown for CH_3Cl, CH_3Br, and $CHCl_3$ are from 2.4-L flasks only. Results plotted for CH_2Cl_2 and C_2Cl_4 are from both 2.4-L and 0.8-L flask samples. All results are based on preliminary calibration scales.

turned off on July 20, 1996, moved and tested, and was operational on July 25th. Because the existing air lines were too short to reach into the new building, a union fitting was put in each line and about 9 m of new Dekabon tubing was added to reach the pump board.

On January 21, 1997, the computer and GC equipment were shut down in the Clean Air Facility at SPO, crated for transport, and quickly moved to the new ARO. By January 27 all of the equipment was operational again. The very long air sampling lines were moved and cable tied above the snow with other lines on poles to avoid being crushed by people and equipment. Since the distance from the ARO to the sampling tower was closer than the Clean Air Facility to the tower, the excess air line was coiled up in the crawl space below the first floor where the equipment is located.

Three 4-channel Chromatograph for Atmospheric Trace Species (CATS) (old STEALTH system) type gas chromatographs are currently in operation at HFM, ITN, and LEF. A fourth single-channel version measures N_2O and SF_6 at ALT. The RITS 3-channel GCs will be phased out after a 6-month comparison with the CATS system. This period will be used to ensure comparable results. The first CATS system was shipped in December 1997 and was installed at SPO in January 1998.

Data Analysis

A thorough review of our current calibration scale for CFC-12 was undertaken before an intercomparison meeting with AGAGE staff in May 1997. This resulted in changes on the order of -2% to assigned mixing ratios for all calibration tanks used at the field sites from 1993 to the present. Likewise, by applying the same techniques to other gases, the calibration scales for CFC-11, nitrous oxide, methyl chloroform, and carbon tetrachloride have changed, though not dramatically. All data presented here have had these corrections applied and are our current best estimates of what is happening in the global tropospheric atmosphere.

The revised, globally averaged maximum CFC-11 mixing ratio was 272.5 ppt in late 1993 (Figure 5.9). The mixing ratio was 268.8 ppt at the end of 1997, the growth rate was -1.3 ppt yr^{-1}, and the interhemispheric difference was 2.6 ppt. The global CFC-12 mixing ratio at the end of 1997 was 531.4 ppt (Figure 5.10). The growth rate slowed until mid-1996 and now appears to be holding steady at 3.6 ppt yr^{-1}. The average interhemispheric difference continues to decline and was 7.9 ppt in late 1997.

Carbon tetrachloride has been decreasing in the troposphere over the last 6 years at the rate of -0.7 ppt yr^{-1}. At the end of 1997 the global mixing ratio was 102.0 ppt and the interhemispheric difference about 1.4 ppt (Figure 5.11). The revised calibration scale has increased mixing ratios by approximately 1% from 1993 and the rate of decrease is less than previously reported.

As noted in section 5.1.2, methyl chloroform mixing ratios continue to decrease in the atmosphere (Figure 5.12). At the end of 1997 the global mixing ratio was 76.9 ppt, and the interhemispheric gradient was near zero. The global distribution in 1997 reflects the distribution of sinks more than sources now that emissions have dropped substantially.

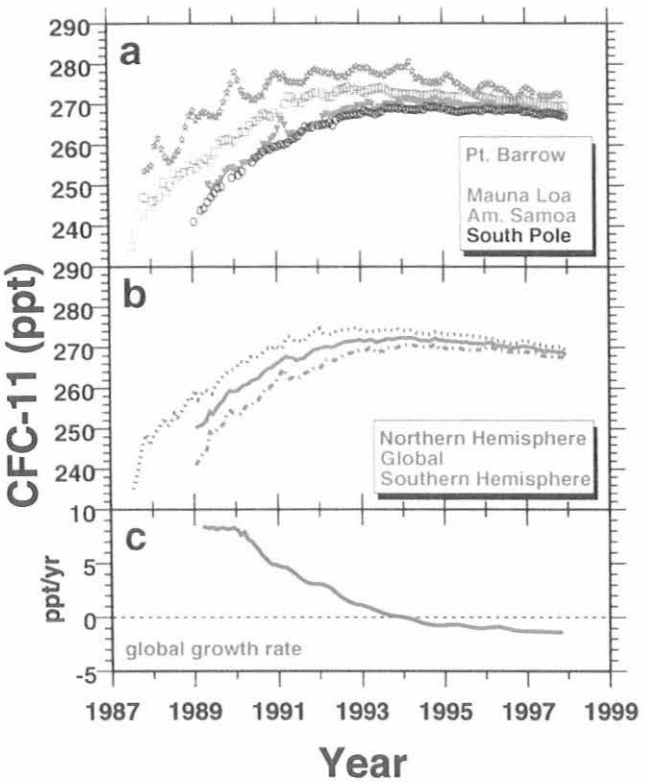

Fig. 5.9. (a) Monthly average CFC-11 mixing ratios in ppt from the in situ GCs, (b) hemispheric and global average mixing ratios, and (c) global average growth rate in ppt yr^{-1}.

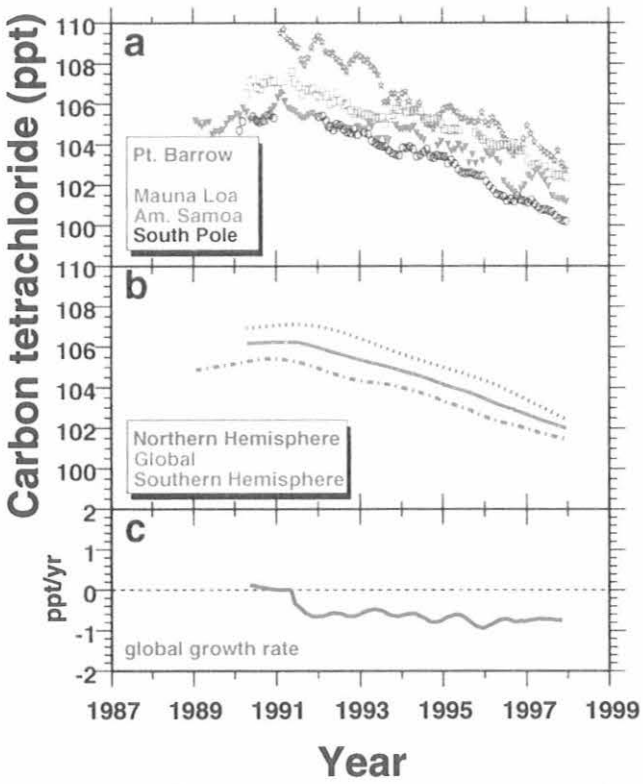

Fig. 5.11. (a) Monthly average carbon tetrachloride mixing ratios in ppt from the in situ GCs, (b) hemispheric and global average mixing ratios smoothed using a LOWESS routine, and (c) global average growth rate in ppt yr^{-1}.

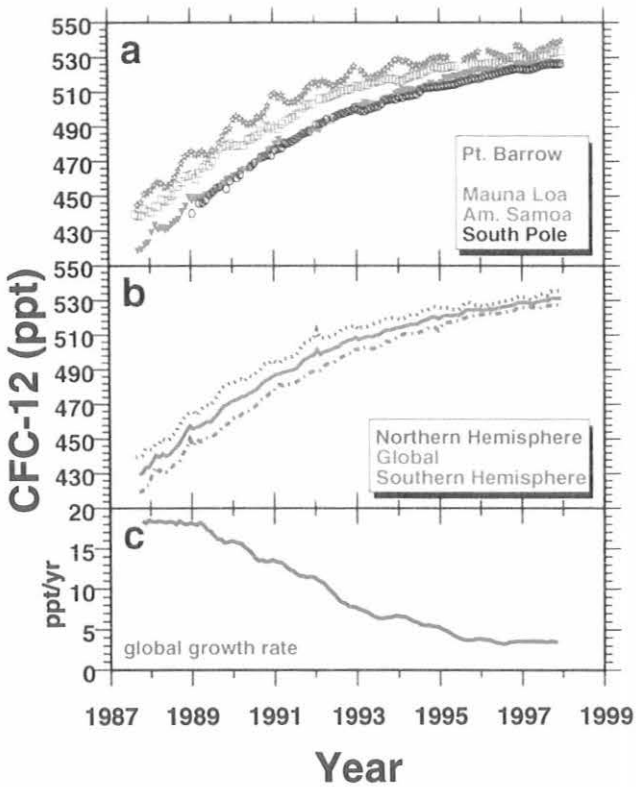

Fig. 5.10. (a) Monthly average CFC-12 mixing ratios in ppt from the in situ GCs, (b) hemispheric and global average mixing ratios, and (c) global average growth rate.

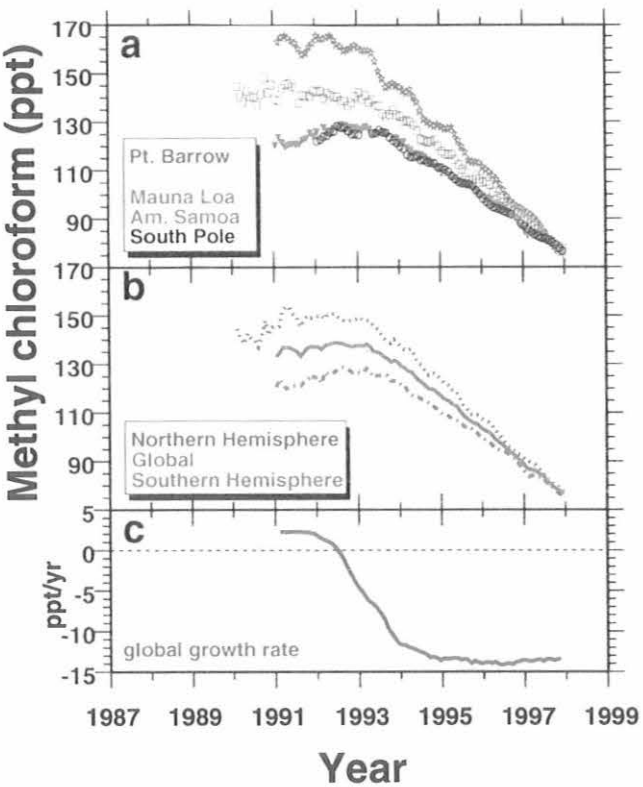

Fig. 5.12. (a) Monthly average methyl chloroform mixing ratios in ppt from the in situ GCs, (b) hemispheric and global average mixing ratios, and (c) global average growth rate.

The atmospheric burden of nitrous oxide continued to increase at an average rate of 0.68 ppb yr^{-1} (RITS measurements) over the past 4 years (Figure 5.13). The global mixing ratio at the end of 1997 was 313.1 ppb and the average hemispheric difference over the 1987-1997 period was 1.2 ppb. There is an annual cycle in the southern hemisphere that is in phase with the annual cycle in the northern hemisphere, generally peaking in the first quarter of each year.

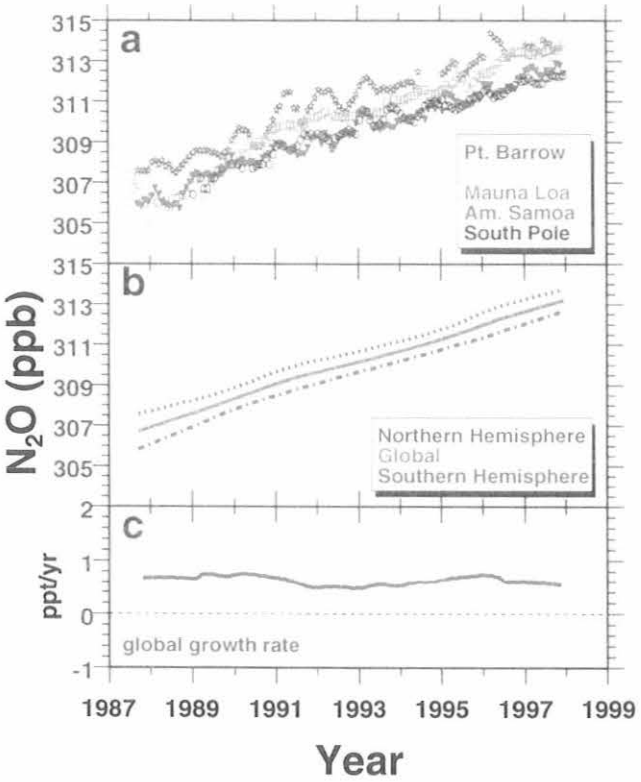

Fig. 5.13. Monthly average nitrous oxide mixing ratios in ppt from the in situ GCs, (b) hemispheric to global average mixing ratios, and (c) global average growth rate.

Chromatography and Software

Each in situ gas chromatograph system is custom designed specifically for each site. Table 5.5 lists the compounds to be sampled by the new in situ gas chromatograph at the CMDL observatories.

Chromatography is controlled and data acquired with custom programs developed on the QNX operating system run on personal computers. QNX is a UNIX-based operating system with structured C programming language support. As a multitasking operating system, QNX provides simultaneous programming functions that allow for concurrent control, data acquisition, user interface operation, and data retrieval. The enhanced capabilities of QNX have allowed the addition of features that take advantage of available technology.

TABLE 5.5. Peak Characteristics on Four-Channel GC at SPO

Compound	Channel	Retention Time (sec)	Peak Window Size (sec)
N_2O*	1	250	40
SF_6*	1	310	20
N_2O†	2	50	30
CFC-12†	2	70	30
CFC-11†	2	215	70
CFC-11‡	3	200	20
CFC-113‡	3	235	20
$CHCl_3$‡	3	350	20
CH_3CCl_3‡	3	425	30
CCl_4‡	3	485	30
TCE‡	3	590	40
PCE‡	3	1230	80
HCFC22§	4	640	30
CH_3Cl§	4	710	40
CH_3Br§	4	1148	60

*Porapak Q column
†Unibeads 1s column (replacing old Porasil a column)
‡OV101 column
§Capillary column (Poraplot Q)

The control functions of the in situ gas chromatograph fall into two categories: those controlled by a custom digital interface and those controlled by an RS-485 network. Sample selection, chromatographic valves, cut-off solenoids, and flow controllers are controlled by a custom digital interface. Temperature controllers use an RS-485 network. Two data acquisition circuit boards handle input from the gas chromatograph electrometers, temperature sensors, and pressure sensors. Chromatographic data from the electrometers and engineering data are stored in a file buffer on the hard drive of the computer. Raw chromatograms and a representative subset of the engineering data are extracted from the buffer, compressed, and stored in a retrieval sub-directory, set up as a first-in-first-out (FIFO) on the hard drive and archived on 100 mb Iomega Zip disks at the site.

A computer workstation at CMDL Boulder automatically retrieves the chromatographic and engineering data from the in situ gas chromatograph on a daily basis for processing. Routines for this retrieval were programmed using TCP/IP - Internet links. Additional programs for use in trouble-shooting and routine maintenance have been included in the QNX software. A World Wide Web (WWW) site allows scientists and technicians to determine the operational status of the instrument system over the Internet. The WWW page includes real-time and near real-time engineering and chromatographic data displayed in tabular and graphic formats. This user interface, accessed with widely available WWW browser software, adds considerable flexibility for scientists and technicians to anticipate problems to resolve quickly.

5.1.4. Gravimetric Standards

The NOAH standards project was expanded in 1996 with the addition of one full-time research assistant. A new gas chromatograph, similar to the CATS GC, was tested and

calibrated. The new GC will provide measurement of CH_3Br, CH_3Cl, and HCFC-22 in the standards laboratory and eliminate the need for three separate GCs for measuring the other seven gases. Thirty gravimetric standards were prepared during 1996-1997. A total of 132 secondary and primary gravimetric standards were analyzed in the standards laboratory. Thirty-three standards were made for outside organizations and other NOAA laboratories. The leader of the standards project left for a new position at NIST at the end of 1997.

One of the major goals of the standards program was to provide a uniform standardization between the major networks responsible for monitoring N_2O and many halocompounds in the atmosphere. A workshop was held during May 1997 in Boulder to begin this process. A series of round-robin tanks are being distributed for intercomparison. A number of tests involving cylinder stability are underway.

Calibrations for CFC-12, methyl chloroform, and carbon tetrachloride were revised since the last report [*Elkins et al.*, 1996b]. All atmospheric CFC-12 data reported after 1993 were about 2.3% higher than actual. The reason for the error was the reliance on a set of 1993 standards that deviated from the rest of the standards which were made in 1991 and 1997 (Figure 5.14). Removal of that set resulted in better agreement (within 1%) for atmospheric measurements of CFC-12 between the CMDL and AGAGE networks. New gravimetric standards were prepared for CH_3CCl_3 and CCl_4 in 1996. After comparing standards for all gases, the same 1993 set was found to have problems with these gases too (Figure 5.15). The values of the 1993 CCl_4 standards are on average 4% lower near ambient levels (102 ppt) than those made in 1991 and 1997. The net effect to atmospheric CCl_4 values (RITS GCs) reported in the last summary report is small, because a calibration tracking error in the opposite direction was found. The 1993 CH_3CCl_3 standards exhibited greater imprecision than the combined 1991 and 1996 sets but no significant offset. The atmospheric values are relatively unchanged from the last summary report. The new scales for CH_3CCl_3 and CCl_4 give atmospheric values that are about 8 ppt and 3 ppt higher in 1997 than those measured by AGAGE. An exchange of weighed pure solvents in sealed microtubes is planned to test methods used by both networks.

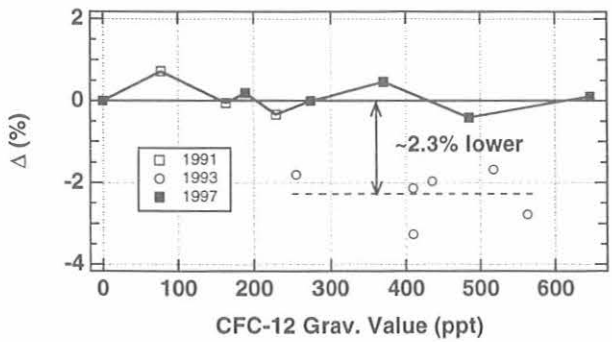

Fig. 5.14. The relative difference in percent (observed-gravimetric value) for CFC-12 standards versus the gravimetric value for those standards made in 1993 and those prepared in 1991 and 1997 for the complete range of ambient ppt mixing ratios.

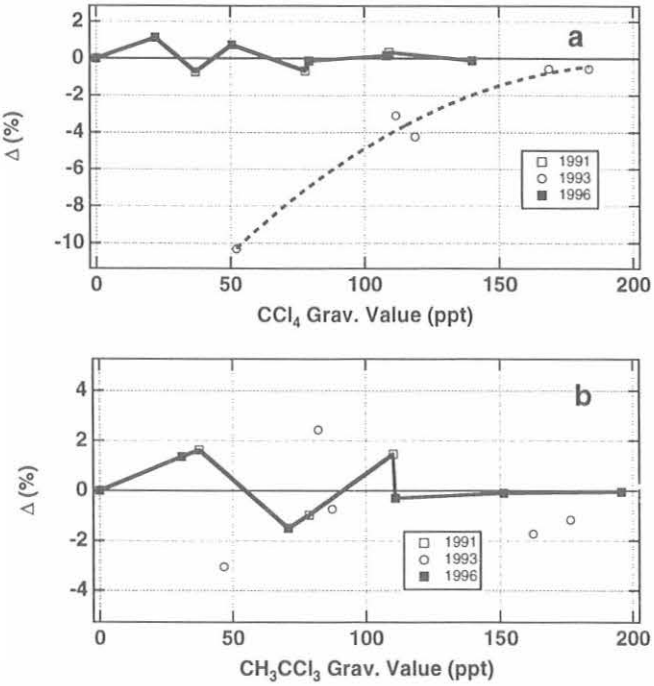

Fig. 5.15. The relative difference (%) in the observed-gravimetric value for (a) CCl_4 and (b) CH_3CCl_3 standards versus the gravimetric value for those standards made in 1993 and those prepared in 1991 and 1997 for the complete range of ambient ppt mixing ratios.

5.2. Stratospheric Measurements

5.2.1. Aircraft Projects-ACATS-IV

ASHOE/MAESA: Stratospheric and Atmospheric Lifetimes of Source Gases

The environmental impact of the measured anthropogenically-produced source gases depends, among other factors, on the rate at which they break down, releasing ozone-depleting chemicals in the stratosphere, i.e., on their stratospheric lifetimes. For many compounds studied here, there exist no significant tropospheric sinks (e.g., N_2O, CCl_4, CFCs 11, 12, and 113), so the stratospheric lifetime, defined here as the atmospheric lifetime with respect to stratospheric loss, is identical to the atmospheric lifetime for these species. A long atmospheric lifetime means a greater ozone depletion potential and a greater global warming potential than similar source gases with shorter lifetimes.

Plumb and Ko [1992] showed that in the "global diffuser" model, stratospheric transport can be described by a simple one-dimensional flux-gradient relationship. If the mixing ratios of two long-lived tracers, σ_1 and σ_2, are in steady state, then the slope of their correlation in the lower stratosphere equals the ratio of their stratospheric removal rates. Thus,

$$\frac{\tau_1}{\tau_2} \cong \frac{d\sigma_2 B_1}{d\sigma_1 B2} \qquad (1)$$

where B_i is the total atmospheric burden for species i, and τ_i is its steady-state stratospheric lifetime, equal to the steady-state atmospheric lifetime for species without tropospheric sinks. *Volk et al.*, [1997] showed that under the same conditions, steady-state stratospheric lifetimes may be derived from the gradient of the steady-state tracer mixing ratio, σ, with respect to the mean age of stratospheric air [*Hall and Plumb*, 1994], Γ, in the measured air parcels:

$$\frac{B}{\tau} = -\frac{d\sigma}{d\Gamma} M_u \qquad (2)$$

where M_u is the total number of molecules above the tropopause, and the tracer gradient with respect to age, $d\sigma/d\Gamma$, needs to be evaluated at $\Gamma = 0$ which is assumed to be the extratropical tropopause.

If the tropospheric mixing ratio of the tracer is changing with time, part of the tracer gradient at the tropopause is due to accumulation in the troposphere and $1/\tau_i$ in either equation (1) or (2) has to be replaced with $\tau_i^{-1} + B_u'/B$, where τ_i is the instantaneous lifetime and B_u' is the total accumulation rate above the tropopause. *Volk et al.* [1997] proposed an alternative method of accounting for tropospheric growth and non-steady-state mixing ratios, χ, to obtain steady-state lifetimes. In this method, one deduces the correction factors $C(\chi_i)$ for each species using the tracer gradient with respect to age at the tropopause, $d\chi_i/d\Gamma$, the time series of tropospheric mixing ratios of the respective species during a 5-year period prior to the stratospheric observations, and estimates of the width of the stratospheric age spectrum from three-dimensional transport models [*Hall and Plumb*, 1994].

Volk et al. [1997] showed that corrected steady-state correlation slopes defined as:

$$\frac{d\sigma_i}{d\sigma_{CFC-11}} = \left(\text{observed} \frac{d\chi_i}{d\chi_{CFC-11}} \right) \bullet \frac{C_i}{C_{(CFC-11)}} \qquad (3)$$

can be used in equation (1) to derive steady-state lifetimes based on a given CFC-11 reference lifetime. Mixing ratios of N_2O from the Airborne Tunable Laser Absorption Spectrometer (ATLAS) [*Loewenstein et al.*, 1989] and ACATS CFC-113 plotted against ACATS-IV CFC-11 (Figure 5.16a, b) are used to calculate the observed gradient ($d\chi_i/d\chi_{CFC-11}$) in Table 5.6. ATLAS N_2O measurements were calibrated from CMDL N_2O standards and agreed with onboard ACATS N_2O measurements to within ±2%. ATLAS N_2O data are used here to increase the number of measurements used by a factor of 2. The steady-state stratospheric lifetime for a source gas using the reference lifetime for CFC-11 is:

$$\tau = \frac{\left(\tau_{CFC-11} \frac{\bar{\sigma}}{\sigma_{CFC-11}} \right)}{\left(\frac{C_i}{C_{CFC=11} d\chi_{CFC-11}} \Big|_{[CFC-11]=\text{tropopause}} \right)} \qquad (4)$$

where $\bar{\sigma}$ is the mean atmospheric mixing ratio with the gradient calculated at the tropopause. From Figure 5.16 and Table 5.6, the steady-state atmospheric and stratospheric lifetime for N_2O is 122 ± 22 years and for CFC-113 is 100 ± 32 years using a CFC-11 reference lifetime of 45 ± 7 years using equation (4).

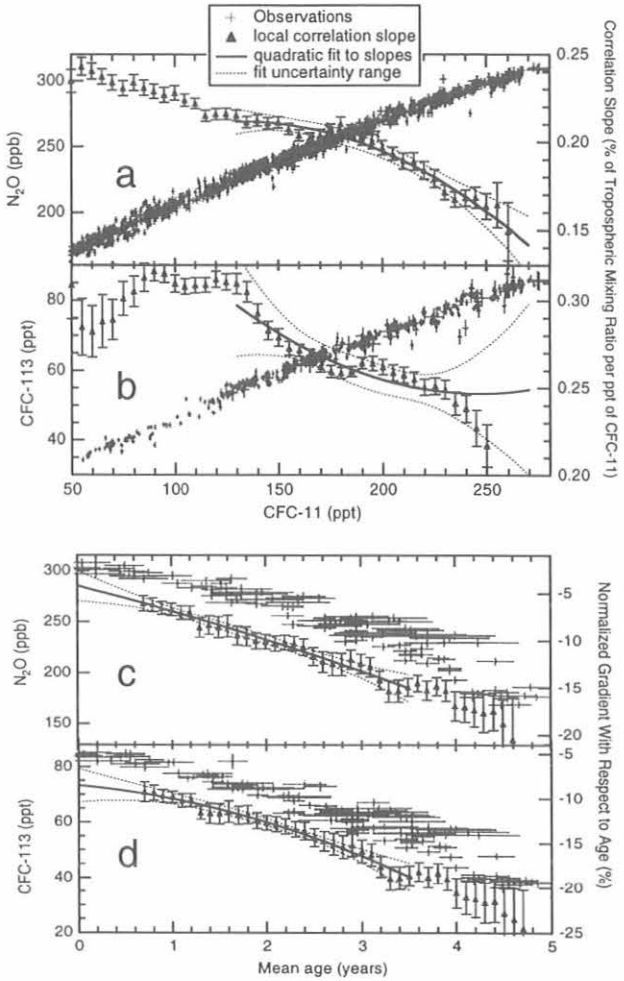

Fig. 5.16. Two methods used to calculate the stratospheric lifetimes from aircraft data. The mixing ratio and its gradient of (a) ATLAS N_2O and (b) ACATS CFC-113 against a lifetime reference molecule such as CFC-1 and the mixing ratio and its gradient of (c) ATLAS N_2O and (d) ACATS CFC-113 against the mean age of the air mass calculated from airborne SF_6 measurements. Observations (pluses, where symbol size indicates uncertainty, left axes), normalized local correlation slopes (triangles with error bars, right axes), and quadratic fits with uncertainty envelopes (lines, right axes) are shown.

The steady-state gradient, $d\sigma_i/d\Gamma$ defined as (observed $d\chi i/d\Gamma$) times $C(\chi i)$, is used in equation (2) to obtain the steady-state lifetime using the "mean age" technique. The steady-state stratospheric lifetime for a source gas based on mean age becomes

$$\tau = -\bar{\sigma} M_a \Big/ \left(M_u C \frac{d\chi}{d\Gamma}\Big|_{\Gamma=0} \right) \qquad (5)$$

TABLE 5.6. Stratospheric Steady-State Lifetimes From *Volk et al.* [1997] Compared to Current Reference Values

Source Gas	Observed $d\chi i/d\Gamma$ (ppt yr^{-1} ± %)	Steady–State Lifetime Based on Age (year)*	Observed $d\chi i/d\chi_{CFC\text{-}11}$ (ppt/ppt, ± %)	Steady-State Lifetime Based on CFC-11 (year) $\tau_{CFC\text{-}11} = 45 \pm 7$ yr^{-1}*	WMO/IPCC Reference Lifetimes (year)	Correction Factor $C(c_i)$
N_2O	-13,000 ± 38%	124 ± 49	436 ± 11%	122 ± 22	120†	0.97 ± 0.02
CH_4	-109,000±48%	84 ± 35	3230 ± 10%	93 ± 14	120‡	0.96 ± 0.02
CFC-12	-43.8 ± 25%	77 ± 26	1.29 ± 7%	87 ± 17	105†	0.77 ± 0.07
CFC-113	-7.3 ± 22%	89 ± 35	0.212 ± 20%	100 ± 32	85†	0.65 ± 0.12
CFC-11	-33.5 ± 28%	41 ± 12	(1)	(45 ± 7)	50†	0.96 ± 0.02
CCl_4	-15.9 ± 32%	32 ± 11	0.515 ± 3.6%	32 ± 6	42†	1.03 ± 0.02
CH_3CCl_3	-16.3 ± 35%	30 ± 9	0.472 ± 10%	34 ± 8	45‡	1.14 ± 0.13
H-1211	-0.84 ± 31%	20 ± 9	0.0237 ± 7%	24 ± 6	36§	0.90 ± 0.10

*Uncertainty of CFC-11 lifetime is not included in uncertainty estimate.
†[*WMO*, 1995], Table 13-1.
‡[*IPCC*, 1995b], Table 2.2.
§[*WMO*, 1992], Table 6.2, scaled to $\tau_{CFC\text{-}11}$= 45 years.

where M_a is the total atmospheric mass (5.13×10^{18} kg) and M_u is the total atmospheric mass in the upper atmosphere above the tropospause (1.1×10^{18} kg). From Figure 5.16 the steady-state atmospheric and stratospheric lifetime for N_2O is 124 ± 49 years and for CFC-113 is 89 ± 35 years based on "mean age" calculated using equation (5) (Table 5.6). The uncertainties on the lifetimes using mean age are less precise than those calculated from the reference lifetime method because SF_6 was only measured during the last quarter of the flights during ASHOE/MAESA.

Lifetime results from the two methods presented in *Volk et al.*, [1997] are consistent with each other (see Table 5.6). In most cases the calculated stratospheric lifetimes from observations are shorter than the World Meteorological Organization (WMO) or the Intergovernmental Panel on Climate Change (IPCC) reference lifetimes derived from photochemical models. Since the derived stratospheric lifetimes are identical to the atmospheric lifetimes for many of the source gases in Table 5.6, the shorter lifetimes also would imply a faster-than-predicted recovery of the ozone layer following the complete phase out of industrial halocarbons.

STRAT Campaign

The primary goal of the Stratospheric Tracers of Atmospheric Transport (STRAT) mission was to measure the morphology and dynamic properties of long-lived tracers as functions of altitude, latitude, and season to help determine the rates for global-scale transport and future stratospheric distributions of high-speed civil transport (HSCT) exhaust. ACATS-IV participated in four out of six STRAT deployments and was flown on a total of 31 flights that spanned a range of latitudes (2.1°S to 59.1°N), predominantly at 15 to 21 km altitudes (potential temperature, θ = 360 to 510 K). These flights included four southbound survey flights into the tropics from Barbers Point, Hawaii (22°N), four northbound survey flights to nearly 60°N from Moffett Field, California (38°N), and 23 midlatitude flights from both locations.

Sulfur hexafluoride has no known sinks below the stratopause (τ = 3200 years, [*Ravishankara et al.*, 1993] and has exhibited a steady rate of growth of 6.7% yr^{-1} in recent years [*Geller et al.*, 1997]. It is used to study atmospheric transport processes and the age of air masses in the upper atmosphere [*Geller et al.*, 1997; *Volk et al.*, 1997; *Wamsley et al.*, 1998]. The age of air masses at the tropical tropopause is defined as zero. Tropospheric air masses that have not yet reached the tropopause are associated with negative ages. ACATS-IV measurements of SF_6 in the northern midlatitude upper troposphere during November 1995 and December 1996 show that mixing ratios increased by approximately 0.28 ppt in 13 months, which is close to the 0.26 ppt expected from the documented growth rate (Figure 5.17). Figure 5.18 shows the convergence of the November 1995 and December 1996 data sets above θ = 450 K that are due to the increased effects of stratospheric mixing with age of the air.

In the tropics (2°S to 20°N) vertical profiles of the mixing ratios of trace gases with different lifetimes conform to the results of *Volk et al.* [1996] (that is, entrainment into a "leaky tropical pipe"). This entrainment of midlatitude air results in "proportionally mixed" tropical profiles, which for CFC-11 are shifted about 15% from the unmixed tropical model line of *Volk et al.*, [1996] shown in Figure 5.18. In the altitude range important for HSCT (16-20 km), ACATS-IV tropical data show several intrusions of midlatitude air into the tropics, denoted by several measurements that lie far to the left of the proportionally mixed tropical profiles (θ = 410-450 K and at 480 K, Figure 5.19). The trace gas mixing ratios of the intruding air masses are about 50% lower than the proportionally mixed profiles and are more typical of midlatitude air from much further aloft (θ >440 K; the midlatitude data are shown by a red line and a 95% prediction band on Figure 5.18). Similar, but weaker intrusions of midlatitude air at the same θ can also be seen in other tropical data [*Elkins et al.*, 1996a; *Volk et al.*, 1996].

The entrainment of midlatitude air into the tropics is illustrated further by looking at the age of the air in the tropical region. The age measured during the flight of December 11, 1996, reaches 1.8-2.3 years at both 410-450 and 480 K surfaces in the latitude range from 12°N to

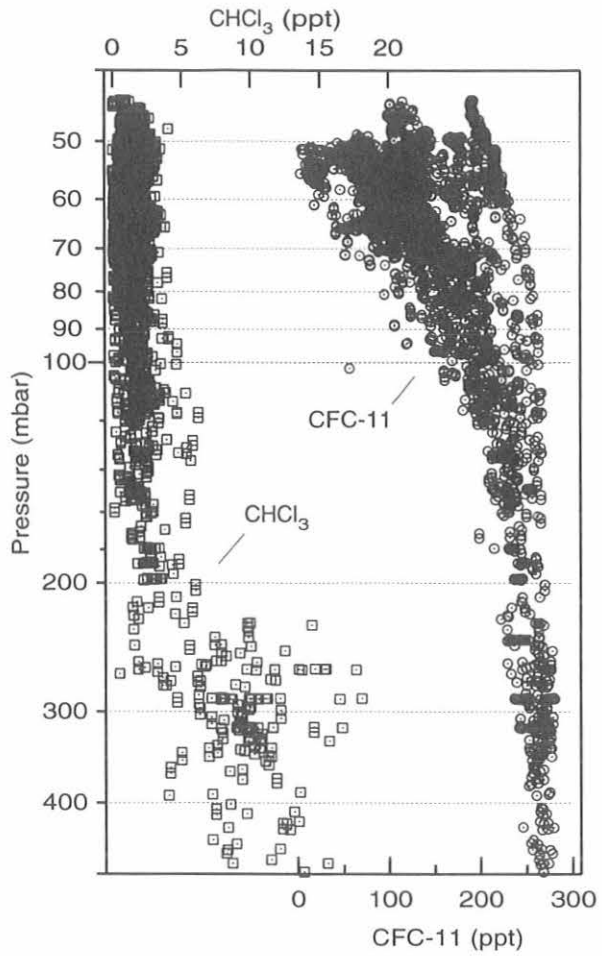

Fig. 5.21. Chloroform and CFC-11 versus pressure. CFC-11 approaches 10 ppt at 26 km and zero at about 30 km in midlatitudes.

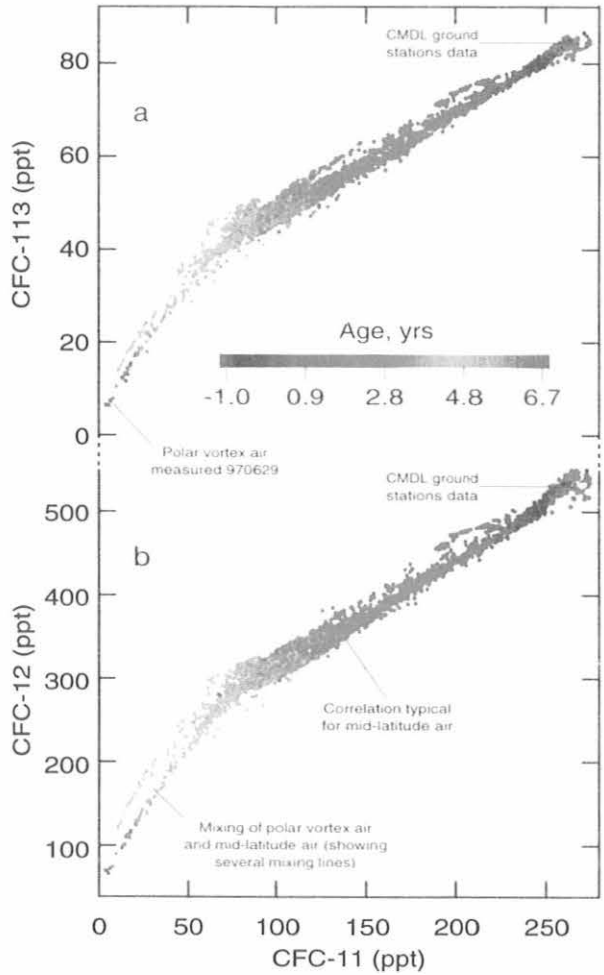

Fig. 5.22. Tracer-tracer correlations, POLARIS mission. (a) Medium-lived CFC-113 (τ = 85 years) shows some separation in the part of the plot depicting mixing; (b) Longer-lived CFC-12 (τ = 102 years.) shows several better separated lines of mixing of air parcels with different age and, subsequently, compounds ratio determined by difference in photolysis rate.

during POLARIS (Figure 5.23), calculated from ACATS-IV SF_6 measurements, demonstrates that the tropical lower stratosphere is characterized by young air (0.3 to 0.8 year average) and that the lines of stable tracer mixing ratios (isopleths) typically follow θ surfaces. Air masses older than 4 to 5 years are generally found poleward of 50°N, but in some cases were observed around 40°N. The oldest air masses encountered during POLARIS were 6.7 years at about 60-65°N in late June 1997.

5.2.2. High Altitude GC Tracer Measurements Project: OMS/STRAT/POLARIS

LACE is a relatively new, three-channel GC instrument (Figure 5.24). It was constructed to extend real time GC measurements of atmospheric tracers such as those measured with the ACATS instrument, to higher altitudes of up to 32 km where, particularly in the tropics, a larger portion of ozone production and loss takes place. The LACE instrument has also made improvements on the spatial and temporal resolution by speeding up the chromatography to obtain a sampling period of 70 seconds. Many of these improvements have now been incorporated into the ACATS instrument. During 1997 LACE obtained high-quality data from four balloon flights onboard the Observations of the Middle Stratosphere (OMS) gondola. As part of the STRAT campaign, LACE flew one midlatitude flight out of New Mexico at 35°N and two tropical flights out of Brazil at 7°S. There was also one polar flight out of Fairbanks at 65°N as part of the POLARIS campaign.

The OMS package is currently configured to make measurements pertinent to stratospheric transport issues. Toward this end, LACE has made in situ measurements from the surface to the middle stratosphere of the long lived tracers H-1211, CFC-11, -113, -12, N_2O, and SF_6

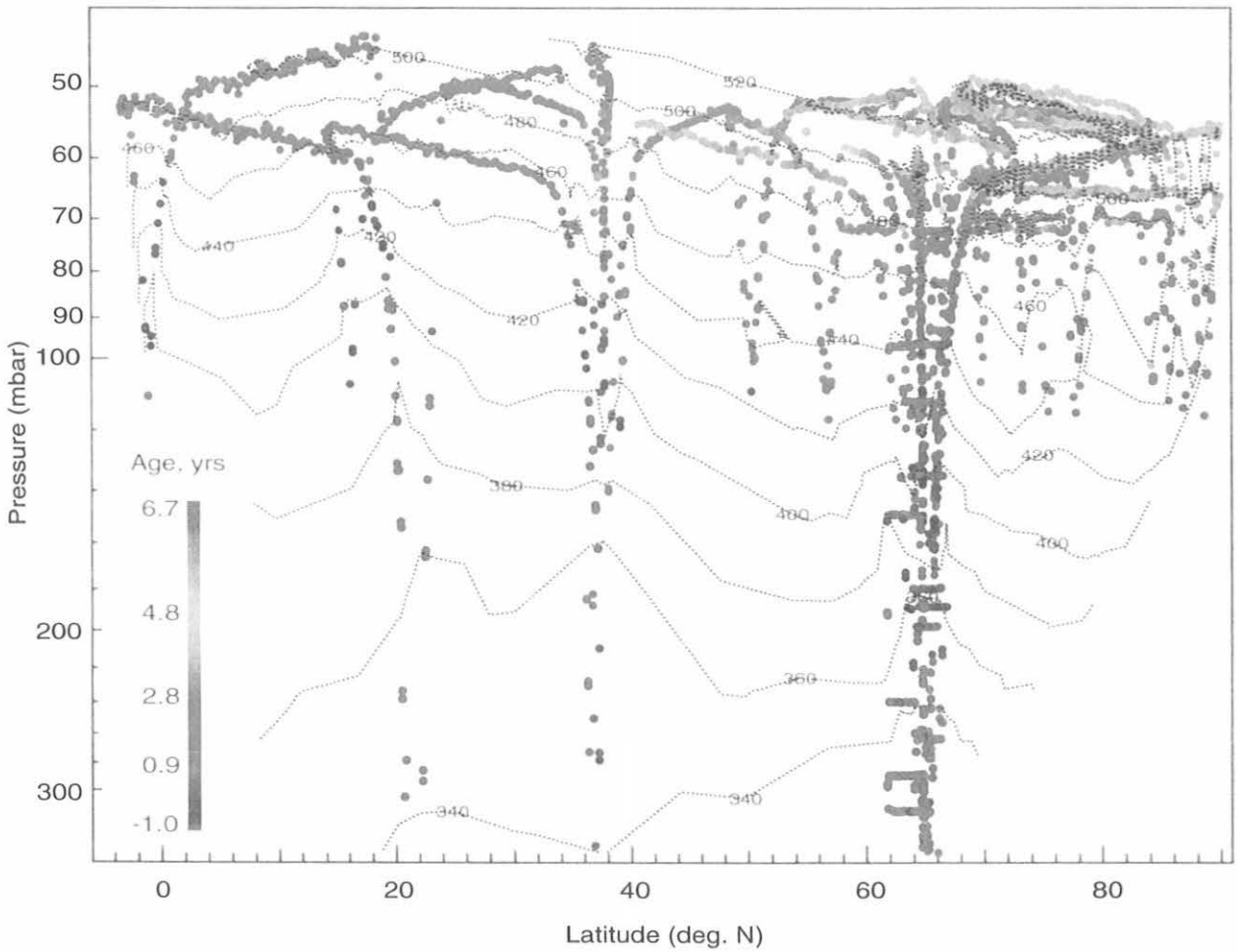

Fig. 5.23. Two-dimensional profiles of altitude and the age of the air based on POLARIS data. The oldest air masses (green) are found at high altitude in the latitude range 60-70°N; younger air is seen at the lower altitudes and latitudes. An age of zero is defined for air at the tropical tropopause, hence negative ages are associated with tropospheric data. Dotted lines show potential temperature surfaces which typically define isopleths (equal mixing ratios).

with a typical precision of between 1% and 4%. The stratospheric lifetimes of these halocarbons and nitrous oxide are dominated by simple photolysis. Their global atmospheric lifetimes span several orders of magnitude. The local photolytic lifetimes of some gases are reduced by 4 orders of magnitude from the tropopause to 32 km. This range in lifetimes covers the dynamic time scales of stratospheric transport. Gas mixing ratios are extremely sensitive to this transport with a strong dependency on vertical flow. Sulfur hexafluoride, however, does not have this altitude-dependent photo-disassociation and has a global atmospheric lifetime greater than 3200 years. Spatial and temporal gradients in the mixing ratio of SF_6 are, therefore, driven by surface emissions which are predominantly in the northern hemisphere. This leads to a large interhemispheric surface gradient and, in this instance, a nearly linear surface growth rate [*Geller et al.*, 1997]. Because there is no known stratospheric sink for SF_6, its sensitivity to transport is driven entirely by the mean transit time from this growing tropospheric source. Unlike the halocarbons, the measured gradients in the value of SF_6 in the stratosphere have only a passive sensitivity to altitude, yet maintain a strong dependency on the time scales of transport [*Volk et al.*, 1997]. Our current precision of SF_6 in the stratosphere is 2%, which translates to 3.5 months of growth.

Although this 3.5 month resolution is adequate to track stratospheric dynamics by defining a mean age of the air parcel since entering the stratosphere, it is not adequate to track transport within the free troposphere other than interhemispheric exchange. Nonetheless, tropospheric vertical gradients with both temporal and latitudinal dependence appear to persist. The interhemispheric surface gradient is believed to be transported into the free troposphere between 30°N and 30°S in a time scale comparable to or faster than this 3.5-month resolution. A measurement of these vertical gradients in the SF_6 mixing ratio below the 380 K isotherm coupled

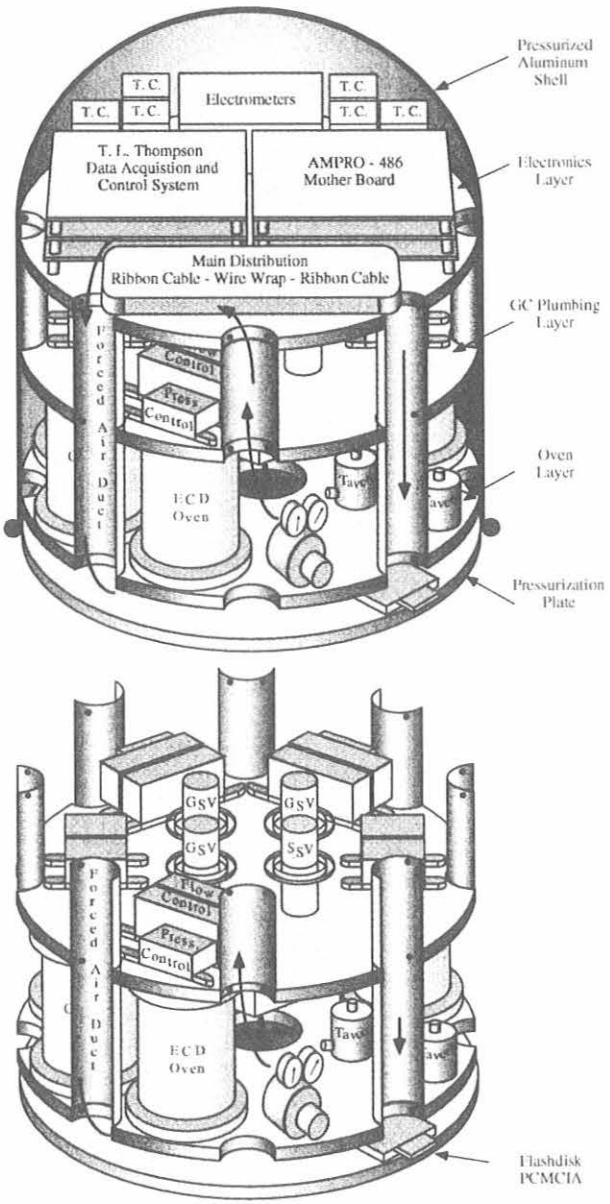

Fig. 5.24. The LACE GC is constructed in three main layers: an oven layer, a GC plumbing layer, and an electronics layer. The GC is pressurized to maintain an even redistribution of heat through convection. This is especially important at the operating altitude of 32 km. Forced air is circulated through the instrument and along the pressurized shell via air ducts to help dissipate 200 watts of heat.

with the existing measured surface gradients, can be used to quantify tropospheric transport and stratosphere-troposphere exchange. This may also be used to improve the connection between the CMDL global mean value of SF_6 and stratospheric age of the air (e.g., Figure 5.23).

Finally the CFCs and H-1211 mixing ratios represent a significant fraction of the total chlorine and bromine entering the stratosphere. As with the ACATS instrument, an estimate of total chlorine and bromine and their organic-inorganic partitioning can be made from LACE measurements.

Stratospheric Dynamics

Major strides in understanding the interactions between pollutants, production to loss of ozone, and climate forcing have been made in the last decade. Today, uncertainties in transport appear to be the limiting parameter in predictive three-dimensional models. The quality of the upcoming assessment on the environmental impact of existing aircraft and the proposed High Speed Civilian Transport (HSCT) fleet is, therefore, limited by our ability to quantify stratospheric transport. In evaluating LACE data, estimates have been made of entrainment of air from midlatitudes into the tropics, the mean age of an air parcel after crossing the tropical tropopause, and mean flow. Breakdown of the arctic vortex and the resulting cross theta "mixing surface" was also observed in the LACE measurements.

As discussed by *Plumb and Ko* [1992], tracer-tracer correlations between simple photochemical species are robust as long as quasi-horizontal mixing dominates over vertical advection, as in the global diffuser model. In the "tropical pipe" model of *Plumb* [1996] the concept of a tight tracer-tracer correlation is also valid in the midlatitudes and, to a large degree, in the tropics on the other side of the tropical barrier. Mixing across this tropical barrier, the so-called leaky pipe, connects these two regions. This mixing is a major mechanism for transport of midlatitude, lower stratospheric air into the middle and upper stratosphere. This midlatitude mixing into the tropics is also a key uncertainty in the HSCT assessment and has been a primary focus of the OMS platform.

A modified *Volk et al.* [1996] analysis, which quantifies the mixing of air from the extratropical stratosphere into the tropical pipe, has been extended to 32 km by using the new LACE CFC and SF_6 profiles. Two approaches have proven fruitful. The first approach relies on mean vertical advection rates (Q). Local chemical losses of the CFCs are dominated by simple photolysis; therefore, assuming no midlatitude influence, isolated tropical profiles can be calculated given the advection rate, photochemical lifetimes (τ), tropospheric growth rates (γ), and mixing ratios (χ) of the CFCs entering the tropical tropopause (Figure 5.25a,b; dotted black line). These isolated tropical profiles can then be evolved a second time to incorporate mixing from midlatitudes along constant potential temperature (θ) surfaces. This is done with the entrainment time (τ_{in}) assumed to be constant. The tracer continuity is governed by equation (6).

$$\frac{\partial \chi}{\partial \theta} Q = P - \frac{\chi}{\tau} - \gamma\chi - \frac{(\chi - \chi_{mid})}{\tau_{in}} \qquad (6)$$

These profiles have also been corrected for weak $O(^1D)$ chemistry and photochemical production (P) (Figure 5.25a,b).

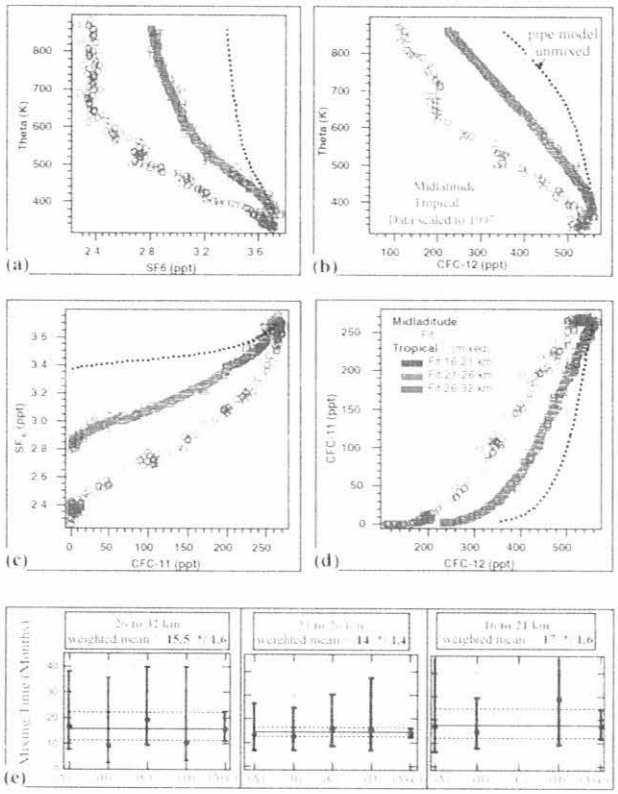

Fig. 5.25. Panels (a) and (b) show least square fits to SF_6 and CFC-12 using equation (6) over three altitude ranges. They are sensitive to uncertainties in vertical advection rates. Panels (c) and (d) show least square fits using equation (2) for CFC-11 versus. SF_6 and CFC-11 versus CFC-12 over the same three altitude ranges. They are, therefore, independent of vertical advection. Panel (e) shows a compilation of entrainment from the four fits in each of the three altitude ranges.

To evaluate whether τ_{in} varies with height, a least squares fit of this second profile to the measured profile is then performed over three altitude ranges. The entrainment time (τ_{in}) is varied as the free fit parameter and is held constant over each given altitude range to stabilize the fits.

One problem that limits this approach is the large uncertainty in the tropical advection rate. Fortunately, the advection rate can be eliminated from the calculation by using tracer-tracer correlation between molecules of differing atmospheric life times. This can be seen by taking the ratio of equation (1) for the mixing ratio Y of one molecule, to equation (1) for the mixing ratio χ of a second molecule.

$$\frac{\partial Y}{\partial X} = \frac{P_y - \left(\tau_y^{-1} + \gamma_y\right)Y - \tau_{in}^{-1}\left(Y - Y_{mid}\right)}{P_x - \left(\tau_x^{-1} + \gamma_x\right)Y - \tau_{in}^{-1}\left(X - X_{mid}\right)} \qquad (7)$$

Because this advection rate Q is common for all molecules in the same air mass moving up the tropical pipe, it drops out of equation (7) (Figure 5.25c,d).

LACE data are consistent with a constant entrainment time of $1.5^{1.9}_{1.2}$ months over the entire range up to 32 km (Figure 5.25e). By 32 km, 90% of the air in the tropical upwelling region is of midlatitude origin because of the total integrated entrainment. A comparison of the first approach (equation 6), which is sensitive to Q, with the second approach (equation 7), which is independent of Q, may help to constrain mean flow in the tropics. This work is consistent with the *Volk et al,* [1996] earlier analysis and is expected to generate a more complete picture of midlatitude intrusions into the tropics when finalized.

Data taken recently in the tropics also revealed air masses that were of midlatitude origin showing the characteristic signature of lower mixing ratios. Surprisingly, the ozone profile did not show the same midlatitude signature and remained representative of tropical air. The chemical equilibrium time for ozone at these locations is fast (weeks to a month), apparently much faster than the mixing time over the spatial scale of these midlatitude intrusions during this time of weak upwelling. These data and the chemical equilibrium time of ozone can, therefore, set lower limits on mixing within the tropical upwelling region.

Sulfur hexafloride has proven to be useful for evaluating transport in the lower and middle stratosphere. Measurements of stratospheric SF_6 permit an accurate determination of the mean age of an air parcel after it crosses the tropical tropopause. Mean age estimates are shown in Figure 5.26 for all LACE flights and three-dimensional model estimates. In general, these models underestimate the age of air as defined by SF_6 distributions. Although increased mixing from mid-latitudes could account for the older measured age in the tropics, the excessively young midlatitude model estimates imply that mean flow in these models is too high.

One important lesson from our OMS balloon launch from POLARIS in Fairbanks was the observation of unmixed and mixed remnants of the polar vortex from the earlier March 1997 arctic ozone depression. Because the remnants of this vortex lasted as late as July, these measurements show one reason why we should continue to sample the arctic. As shown in Figure 5.27, this mixed air is clearly not representative of a typical midlatitude distribution and must continually be monitored to quantify both the chemistry and dynamics that are taking place at the pole.

Atmospheric Dynamics Below the 380 K Isentropic Surface

LACE has taken highly precise measurements of several trace gases in the lowermost stratosphere and upper troposphere, regions for which very little tracer data exist. Measurements of SF_6 and CFC-11, in particular, reveal many interesting features in these regions and their vertical gradients offer constraints on transport time scales. Simulation of these tracer gradients by models is important for an accurate assessment of tracer transport in the lower stratosphere and troposphere where the impact of aircraft exhaust and the transport of greenhouse gases play a key role.

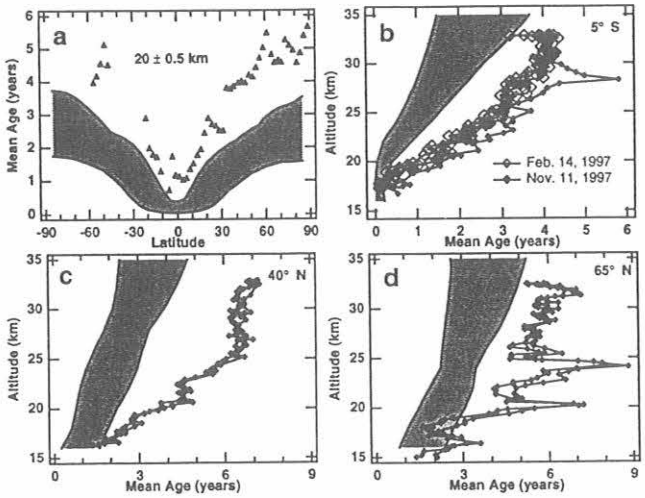

Fig. 5.26. Profiles of mean age of the air from zonally-averaged models (supplied by D. Waugh [private communication, 1998]). This modeled age is plotted with (a) ACATS measured age (triangles) against latitude, and LACE measured age (diamonds) against altitude for (b) the tropics at -5° latitude, (c) the midlatitudes at 35° latitude, and (d) the polar regions at 65° latitude. The shaded region indicates the dominant range of model results. Mean age is taken to be zero at the equator at 20.0 ± 0.5 km.

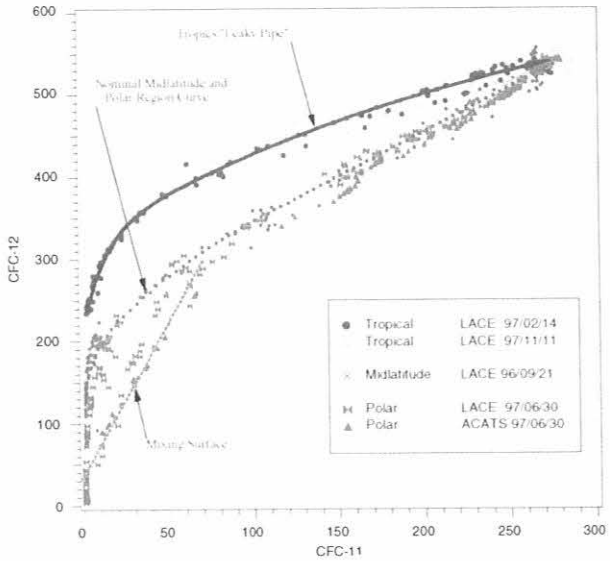

Fig. 5.27. Tracer-tracer correlation plot of CFC-12 versus CFC-11 from LACE on the OMS gondola for flights on September 21, 1996 (midlatitudes), February 14, 1997, and November 11, 1998 (tropics), and June 30, 1997 (POLARIS, polar regions). LACE data are compared against the ACATS data from the POLARIS flight of the ER-2 aircraft on June 30, 1997. The blue line indicates tropical data isolated from the mid and high latitudes by the "leaky pipe," dashed red lines represent a nominal midlatitude and/or polar profile, and the dashed gray line indicates conservative mixing across isopleths due to the anomalously late break down of the polar vortex. This mixing line can only be observed in a tracer-tracer plot over regions that have curvature in the nominal midlatitude profile.

The lowermost stratosphere is that part of the stratosphere that lies between the tropopause and the 380 K potential temperature surface. The lowermost stratosphere is a unique part of the stratosphere, since air can be exchanged isentropically between the stratosphere and troposphere. Thus the lowermost stratosphere contains a mixture of older stratospheric air that has been advected downward by the mean meridional circulation and tropospheric air that has been transported isentropically. The relative importance of downward advection and isentropic transport largely depends on season and location.

Figure 5.28 shows profiles of SF_6 and CFC-11 from the Ft. Sumner flight on September 21, 1996. The 380 K and tropopause heights are indicated on the figure and lines are drawn through the data in each height region. The two profiles have different vertical gradients in the lowermost stratosphere. CFC-11 has almost no vertical gradient below the 380 K surface, while SF_6 has a large vertical gradient in the lowermost stratosphere and a small but still noticeable gradient in the upper troposphere. The constant CFC-11 mixing ratio suggests that the gradients seen in the SF_6 profiles are of tropospheric origin. Downward advection would have a larger effect on CFC-11 because of its more rapid decrease above the 380 K surface. Weak downward flow across the 380 K surface at the time of our flight is consistent with the seasonality of the mean meridional circulation in the stratosphere and the midlatitude location.

The vertical gradient in SF_6 from the Ft. Sumner flight is, therefore, assumed to be due to an interplay between

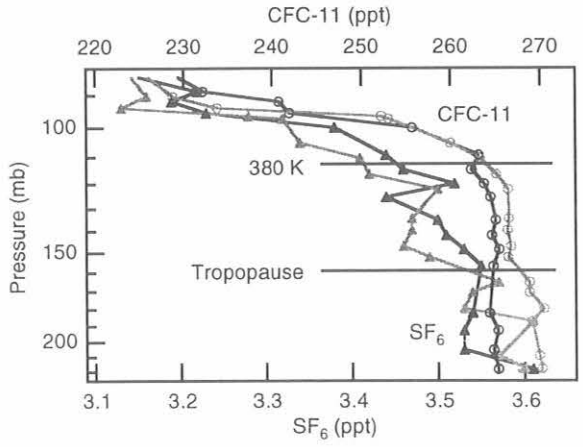

Fig. 5.28. Profiles of SF_6 and CFC-11 from the September 21, 1996, Ft. Sumner, New Mexico, flight. The tropopause and 380 K surfaces are indicated on each plot and rough linear fits to the data are included in each region.

isentropic mixing from the tropical upper troposphere and residence time of air in the lowermost stratosphere. Were it the result of growth, the vertical gradient in SF_6 would

represent a 9-month age difference over the depth of the lowermost stratosphere. The time scale of isentropic mixing between the tropopause and the northern midlatitudes is on the order of a month or less and the flushing time of the northern hemisphere lowermost stratosphere is thought to be roughly 4 or 5 months. Therefore, some of the vertical gradient in the lowermost stratosphere could be caused by transport of the interhemispheric gradient of surface SF_6 to the upper troposphere. Some portion of the interhemispheric gradient in SF_6 is likely to be mapped along the tropopause from the tropics to the midlatitudes. As tropospheric air is isentropically mixed into the midlatitude lowermost stratosphere, the latitudinal tropopause gradient will contribute to the vertical gradient of SF_6 in the lowermost stratosphere.

This gradient in SF_6 along the tropopause may have a strong dependence upon seasonal variability of tropospheric transport, coupled with the interhemispheric gradient of SF_6 at the surface. Profiles of SF_6, which have been normalized to remove the growth rate for the two Brazil flights, are shown in Figure 5.29. The February Brazil flight has SF_6 mixing ratios in the upper troposphere that are close to the global mean surface value and decrease toward the southern hemisphere surface average with decreasing height (Figure 5.29). This profile is consistent with a significant amount of northern hemispheric surface air entering the tropical upper troposphere during February. The monthly mean position of the Hadley circulation was estimated by *Oort and Yienger* [1996]. In January and February the northern hemisphere Hadley cell is shifted south and is also consistent with a significant amount of northern hemispheric surface air being transported into the tropical upper troposphere as suggested by our data.

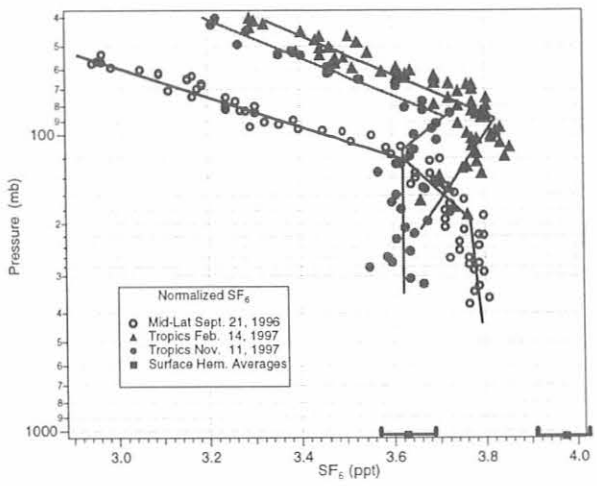

Fig. 5.29. Profiles of SF_6 from the two Brazil flights and the Ft. Sumner, New Mexico, flight normalized to remove the growth rate. Normalized northern and southern hemispheric mean surface mixing ratios from the CMDL network are also included at the bottom of the graph.

The November flight has a nearly constant mixing ratio in the upper troposphere that is close to the southern hemisphere surface average. In October and November the northern hemisphere Hadley cell is weak and shifted north of the equator so the tropical upper troposphere should be dominated by southern hemispheric air at a 7°S, again consistent with our data.

These tropical profiles suggest that the seasonal cycle of the Hadley circulation causes a seasonal cycle in the SF_6 mixing ratios in the tropical upper troposphere. This seasonal cycle will likely cause a seasonal cycle in the latitudinal gradient of SF_6 mixing ratios along the tropopause, since the mean Hadley circulation flow in the upper troposphere is poleward. For the northern hemispheric tropopause we would expect a large gradient during summer, when more southern hemispheric surface air is transported into the tropical upper troposphere, and a weak gradient during winter when mostly northern hemispheric surface air is transported into the tropical upper troposphere. Our midlatitude flight was in September at the beginning of fall when a remnant of the tropopause gradient caused by the summer tropospheric transport could have been present. This also suggests that a small seasonal correction to the connection between stratospheric age of air and the CMDL global average may be needed.

The effects of significant mean downward motion across the 380 K surface on trace gas profiles in the lowermost stratosphere can be seen in Figure 5.30. CFC-12, -11, H-1211, and SF_6 measurements from the June 30, 1997, flight over Fairbanks are shown in this figure along with the heights of the 380 K and tropopause surfaces. Mixing ratios of all four tracers decrease above the tropopause.

This decrease and the vertical gradient in the lowermost stratosphere are largest in the shortest lived tracer, H-1211, which is consistent with the expected effect of downward advection. Subsequently smaller decreases above the tropopause and vertical gradients in the lowermost stratosphere are seen in CFC-11 and CFC-12 which have longer photochemical lifetimes. SF_6 also has a large decrease above the tropopause due not to photolysis but to its growth rate. Air advected down across the 380 K surface in the high latitudes is 2 years older on average, than northern tropospheric air. Therefore the sharp decrease in SF_6 above the tropopause is a result of the growth of SF_6 in the northern high-latitude troposphere during the time air was transported to the high-latitude lowermost stratosphere.

Even though June is a time of relatively weak mean downward flow in the northern hemisphere high latitudes, the tracer data suggest that this flow is the dominant transport into this part of the lowermost stratosphere. It is interesting to note the relative compactness of the profiles above and below the 380 K surface. The lowermost stratosphere appears to be relatively well mixed compared with the stratosphere above the 380 K surface.

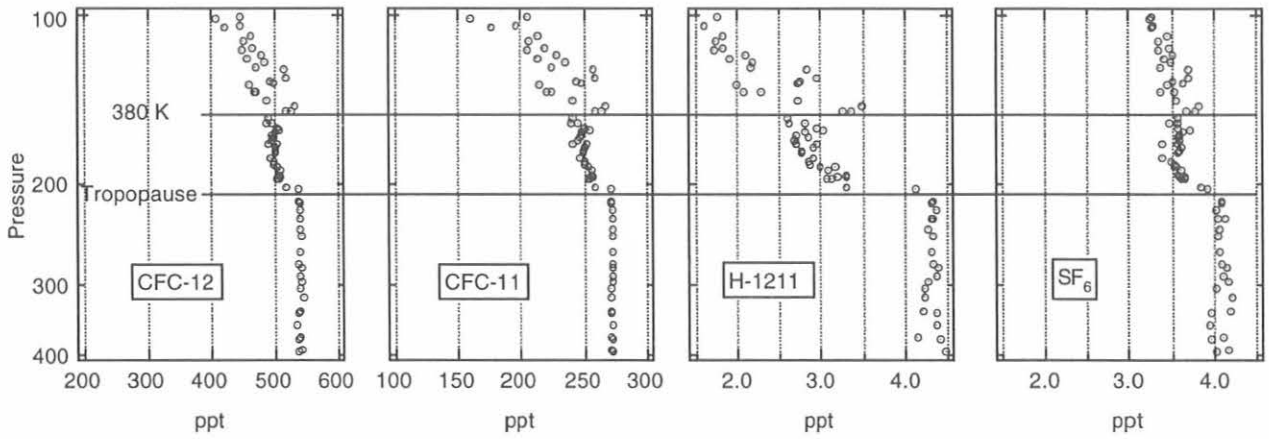

Fig. 5.30. Profiles of CFC-12, CFC-11, H-1211, and SF_6 from the Fairbanks, Alaska, flight. The tropopause and 380 K surfaces are indicated. The three distinct regions, the middle stratosphere (above 380 K), the lowermost stratosphere, and the troposphere, are clearly defined by both the gradients and spread in the data. Relationships between the time scales of mean flow and mixing can be inferred.

5.3. Ocean Projects

5.3.1. Southern Ocean Expedition - BLAST III

The flux of CH_3Br from the world's oceans has been a source of considerable controversy over recent years. Although earlier studies suggested the ocean was a large, net source of atmospheric CH_3Br [*Singh et al.*, 1983; *Singh and Kanakidou*, 1993; *Khalil et al.*, 1993], recent widespread examinations by CMDL of the saturation of CH_3Br in the east Pacific and Atlantic Oceans showed that most of the ocean was undersaturated in this gas [*Lobert et al.*, 1995, 1996; *Butler et al.*, 1995]. Extrapolation of these data indicated that the global oceans were a net sink for atmospheric CH_3Br.

Two subsequently published numerical models, however, suggested that polar and sub-polar oceans might be a large, net source of atmospheric CH_3Br [*Pilinis et al.*, 1996; *Anbar et al.*, 1996]. The two models used production rates based on data published by *Lobert et al.* [1995], presuming them to be either constant over the entire oceanic regions or a function of chlorophyll-a concentration. With chemical degradation being very slow in cold, polar waters, and a very high biological productivity during the austral summer, the predicted saturation anomalies were positive and ranged up to 500%, indicating this polar source could globally outweigh the sinks estimated by *Lobert et al.* [1995]. To resolve this question, CMDL conducted a study to measure the saturation of CH_3Br in the Southern Ocean during a time of high biological productivity (Bromine Latitudinal Air-Sea Transect (BLAST) III, Figure 5.31, *Lobert et al.* [1997]).

The shipboard GC/MS and sampling system was virtually identical to that used during the two previous cruises. On this cruise CH_3Br was also measured with a custom-built GC equipped with an ECD and different columns. Mole fractions from MS and ECD systems agreed, on average, within 0.2 ppt (Figure 5.32, Table 5.7). Measured, dry mole fractions of CH_3Br in the atmosphere were consistent with data from the BLAST I and BLAST II cruises. Most important, however, is that the ocean in this region was consistently undersaturated in CH_3Br with a mean saturation anomaly corrected for physical effects of $-33 \pm 8\%$ (Figure 5.32c, Table 5.7).

Maintaining a steady-state, ~35% undersaturation of CH_3Br in the surface waters in the presence of air-sea exchange requires a minimum in situ degradation rate of about 5.8% d^{-1}, which is a factor of 10 larger than that for chemical degradation alone. The most likely explanation of these findings is that dissolved CH_3Br is being degraded by an additional mechanism other than reaction with H_2O

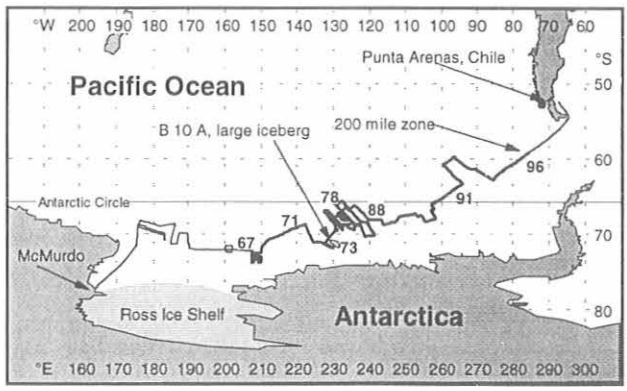

Fig. 5.31. BLAST III cruise track from McMurdo, Antarctica, to Punta Arenas, Chile, aboard the *R/V Nathaniel Palmer*, Cruise 96-02. Numbers along the cruise track indicate the Julian day of year 1996.

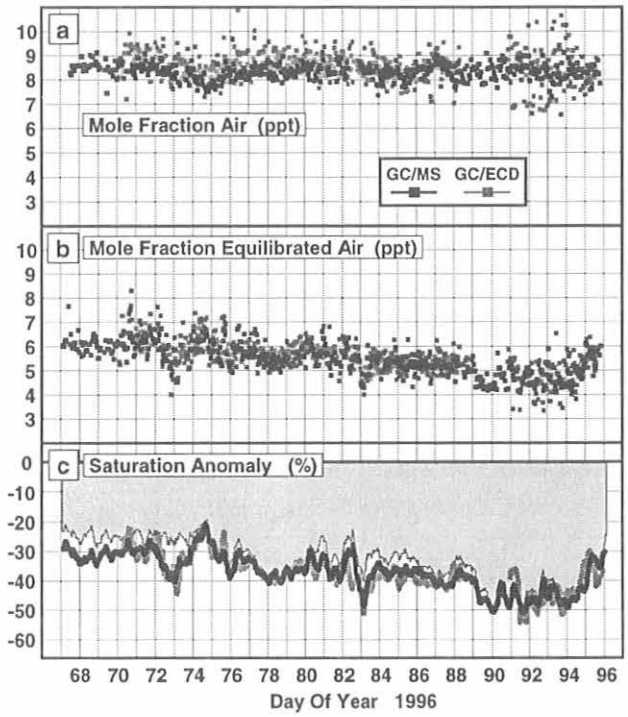

Fig. 5.32. Measurements of methyl bromide in air (a), air equilibrated with surface water (b), and the resulting saturation anomaly (c) for both the GC/MS and the GC/ECD systems. The shaded area in panel (c) represents the saturation anomaly corrected for physical effects calculated from the GC/MS saturation anomaly (black line).

TABLE 5.7. Mean Mixing Ratios of CH_3Br in Air and Equilibrated Water during BLAST III

	GC/MS (ppt)	GC/ECD (ppt)	Mean Saturation Anomaly*	Corrected Saturation Anomaly†
Air	8.3 ± 0.3	8.5 ± 0.7		
Equilibrated water	5.5 ± 0.6	5.6 ± 0.8	-36 ± 7%	-33 ± 8%

*Saturation anomaly = percent departure from equilibrium, calculated from GC/MS data.

†Corrected saturation anomaly = mean anomaly, corrected for physical effects such as those associated with mixing and warming of surface waters [e.g., *Butler et al.*, 1991].

and Cl^-. A significant biological sink for CH_3Br in subtropical waters has been identified recently [*King and Saltzman*, 1997], suggesting that the additional sink might be biological.

Several conclusions can be drawn from this study. First, the Southern Ocean, and probably most high-latitude waters, are a net sink for atmospheric CH_3Br. Second, biological processes, or some chemical processes other than reaction with H_2O or Cl^-, rapidly remove CH_3Br from surface waters. Third, CH_3Br production is neither constant over the global ocean nor strictly dependent upon chlorophyll concentration. The data from this expedition and those from BLAST I and BLAST II suggest that the global ocean is a net sink of 21 (11-31) Gg yr^{-1} for CH_3Br.

5.3.2. Oceanic Uptake of Atmospheric Trace Gases

The atmospheric lifetime of a trace gas is derived from the sum of its sinks or loss rates. Loss to the ocean is a significant sink for some gases. Over the past few years a gridded, finite-increment model was developed to determine the uptake rate constant and partial atmospheric lifetime with respect to oceanic degradation for any trace gas that reacts in seawater. The model, originally developed to study the oceanic uptake of atmospheric methyl bromide (CH_3Br) [*Butler*, 1994; *Yvon and Butler*, 1996; *Yvon-Lewis and Butler*, 1997], is used here to calculate the oceanic uptake rate and partial atmospheric lifetime of chlorocarbons, HCFCs, and HFCs (Figure 5.33, Table 5.8). The oceanic uptake rate (mol yr^{-1}) is defined in the following equation:

$$\text{Uptake} = \frac{K_W A}{H}\frac{r}{n_{tr}}\left(\frac{k_d + K_{biol} + \sqrt{D_z k_z}}{k_d + k_{biol} + \sqrt{\frac{Dk_z}{z} + \left(\frac{K_W}{z}\right)}}\right) \quad (8)$$

The rate constant (k_{ocn}) and lifetime (τ_{ocn}) for this removal process can then be calculated from the following equation:

$$k_{ocn} = \frac{1}{\tau_{ocn}} = \frac{K_W A}{H}\frac{r}{n_{tr}}\left(\frac{k_d + K_{biol} + \sqrt{D_z k_z}}{k_d + k_{biol} + \sqrt{\frac{Dk_z}{z} + \left(\frac{K_W}{z}\right)}}\right) \quad (9)$$

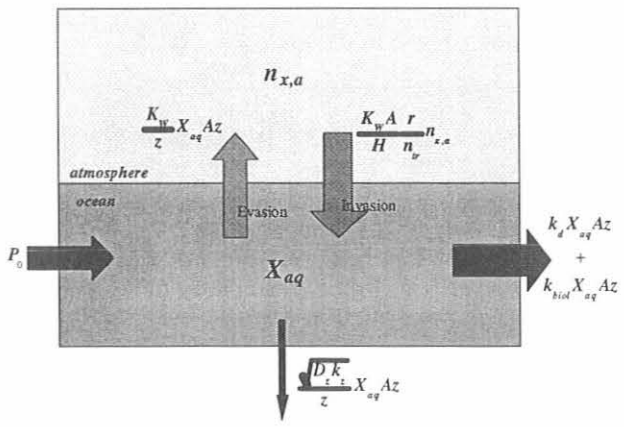

Fig. 5.33. Schematic of the air-sea flux of a trace gas. Terms are as described in Table 5.8.

Initially this equation was applied to a 2° × 2° grid of physical properties in and over the global ocean for the calculation of the partial atmospheric lifetime with respect to oceanic uptake for CH_3Br (Figure 5.34). The inclusion of both the chemical and biological degradation rates for CH_3Br in the ocean resulted in a partial atmospheric lifetime of 1.8 (1.1-3.9) years, which is substantially shorter and more certain than the 3.7 (1.4-14) year estimate calculated by *Butler* [1994], owing to the inclusion of spatial variability in oceanic physical properties and biological degradation rates. The corresponding atmospheric lifetime, including soil to atmospheric sinks for CH_3Br, is 0.7 (0.5-1.2) years.

Oceanic uptake does not appear to be a significant sink for many of the HCFCs and the HFCs (Table 5.9). Because biological degradation processes have not been investigated for most of these trace gases, the term (k_{biol}) was null in these calculations. Model results for these gases depend upon chemical degradation rates alone. The presence of any biological degradation would result in substantially reduced lifetimes. Evidence for the presence of degradation mechanisms other than the hydrolysis reaction used in this model has been observed in the saturation anomaly data for CH_3Br, CH_3Cl, and CCl_4.

The τ_{ocn} values calculated by *Wine and Chameides* [1989] are shorter than those determined by this model because the investigators neglected stratification below the mixed layer [*e.g., Butler et al.,* 1991]. At this time there are no available data on the degradation rate constants

TABLE 5.8. Definition of Terms Used in Oceanic Lifetimes Computation (Equations 2 and 9)

Parameter or Variable	Symbol or formula	Units	References for Calculations
Partial pressure of X	P_X	atm	
Oceanic concentration of X	X_{aq}	mol m^{-3}	
Gas transfer velocity	K_W	m yr^{-1}	1, 2, 3, 4
Solubility	H	m^3 atm mol^{-1}	5, 6, 7, 8, 9
Atmospheric burden of X	$n_{x,a}$	mol	
Surface area of ocean	A	m^2	
Mixed layer depth	z	m	10
Mass of the troposphere	n_{tr}	mol	
Fraction of X in troposphere	r	Unitless	11, 12, 13
Production rate of X	P_0	mol m^{-3} yr^{-1}	
Mixed layer chemical degradation rate constant	k_d	yr^{-1}	8, 14, 15, 16, 17,18, 19
Mixed layer biological degradation rate constant	k_{biol}	yr^{-1}	14,20
Thermocline diffusion coefficient	D_z	m^2 yr^{-1}	10
Thermocline chemical degradation rate constant	k_z	yr^{-1}	8, 14, 15, 16, 17,18, 19
Grid cell index	i	--	
Interhemispheric ratio multiplier (NH and SH)	R_{IHR}	Unitless	20, 21

[1]*Wanninkhof* [1992], [2]*Liss and Merlivat* [1986], [3]*DeBruyn and Saltzman* [1997a], [4]*Wilke and Chang* [1955], [5]*DeBruyn and Saltzman* [1997b], [6]*Moore et al.* [1995], [7]*Gosset* [1987], [8]McLinden [1989], [9]*Johnson and Harrison* [1986], [10]*Li et al.* [1984], [11]*Lal et al.* [1994], [12]*Fabian et al.* [1996], [13]*Chen et al.* [1994], [14]*King and Saltzman* [1997], [15]*Moelwyn-Hughes* [1938], [16]*Gerkins and Franklin* [1989], [17]*Jeffers et al.* [1989], [18]*Wine and Chameides* [1989], [19]*Elliott et al.* [1989], [20]*Lobert et al.* [1995], [21]*Montzka et al.* [1996]

TABLE 5.9. τ_{ocn} and τ for Selected Halocarbons

	τ_{ocn} (y)			τ (y)	
Trace Gas	This Study	Previous	Reference	WMO (1994)*	This Study
CH_3Cl	70(70-79)			1.5	1.46
CH_3CCl_3	94(94-123)	59-128[1]	1	4.8 [4]	4.8
CCl_4	2250			42	42
HCFC-22	2320	110[2]	2	13.3	13.3
HFC-125	10600	>1500[2]	2	36	36
HFC-134a	9100	>1100[2]	2	14	14
HFC-152a	5530	>460[2]	2	1.5	1.5
HCFC-124	1840	360[2]	2	5.9	5.9
HCFC-142b	2060	270[2]	2	19.5	19.5
HCFC-123	635	180[2]	2	1.4	1.4
HCFC-141b	2230	77-360[2]	2	9.4	9.4
$CHCl_3$	715			0.55	0.55
C_2Cl_4	2130000			0.4[5]*	
OCS	13.2	18[3]	3	4.3[6]*	3.2

*C_2Cl_4 OCS lifetimes are from the indicated manuscripts rather than *WMO* [1994]. The only value in this column that included oceanic uptake is that for CH_3CCl_3.

[1]*Butler et al.* [1991], [2]*Wine and Chameides* [1989], [3]*Ulshöfer and Andreae* [1997], [4]*Prinn et al.* [1995], [5]*Wang et al.* [1995], [6]*Chin and Davis* [1995].

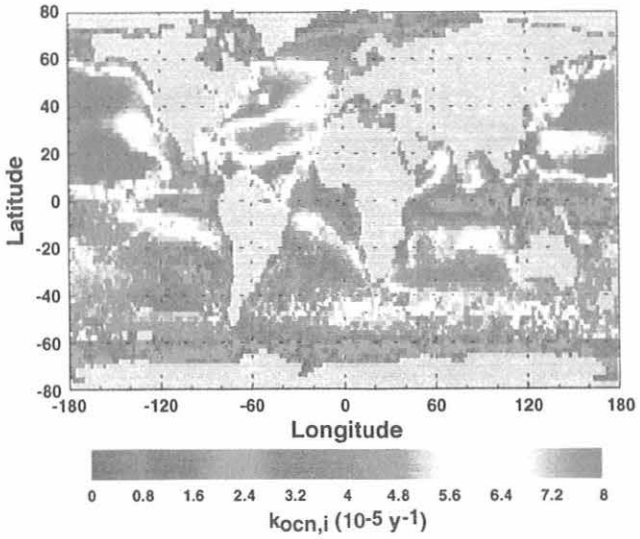

Fig. 5.34. Global distribution of the oceanic uptake rate constant, $k_{ocn,i}$, where $k_{ocn,i} = (1/\tau_{ocn})_i$ for combined chemical and biological aquatic removal of atmospheric CH_3Br. Including biological processes lowers the partial atmospheric lifetime with respect to oceanic loss from 2.7 years [*Yvon and Butler*, 1996] to 1.9 years [*Yvon-Lewis and Butler*, 1997].

and/or solubilities for many of the halocarbons found in the atmosphere. This lack of data prevents us from calculating the effect of oceanic degradation processes on the lifetimes and budgets of many trace gases. Accounting for the oceanic uptake of CH_3Cl and OCS resulted in reductions of 3% and 25% in the total atmospheric lifetimes for these species.

5.4. GC Measurements at Two Tall Towers in the U.S.

Automated, four-channel GCs have been in operation at the 610 m WITN tower in eastern North Carolina (NC) since November 1994 and at the 447-m WLEF tower in northern Wisconsin (WI) since June 1996. Every hour these instruments measure 12 trace gases (CFC-11, CFC-12, CFC-113, CH_3CCl_3, CCl_4, $CHCl_3$, C_2Cl_4, N_2O, SF_6, H_2, CH_4, and CO) at 51, 123, and 496 m above ground on the NC tower and at 30, 76, and 396 m on the WI tower. The GCs are calibrated hourly with two standards of dried, whole air stored in Aculife-treated aluminum cylinders, one of which has been diluted by 10% with zero air. The design and operation of the GC at the NC tower were described previously [*Elkins et al.*, 1996a; *Hurst et al.*, 1997a].

Trace gas mixing ratios at the two towers are variable on diurnal, synoptic, seasonal, and longer time scales. Diurnal variations result primarily from the daily development of the planetary boundary layer (PBL), which defines the mixing depth of ground-based source emissions. At night, local and regional emissions augment mixing ratios beneath a shallow (100-200 m) inversion and create significant vertical gradients. During the late morning and afternoon, this vertical structure disappears as emissions are rapidly mixed into a 1-2 km deep PBL by convection [*Hurst et al.*, 1997a, 1998]. Diurnal variability at the lower two sampling levels on each tower is greater than at the top because the nocturnal inversion consistently lies between the middle and top sampling levels.

Synoptic-scale variability is driven predominantly by the transport of pollution plumes from regional urban centers to the measurement sites. Daily mean mixing ratios (and daily standard deviations) at 496 m on the NC tower during 1996-1997 illustrate day-to-day (and diurnal-scale) variability (Figure 5.35). Daily means 5-10% above the majority of the data are regular features, especially for C_2Cl_4. Significant long-term trends in CH_3CCl_3 and SF_6 mixing ratios at the NC tower are also evident (Figure 5.35). Linear fits to regional "background" mixing ratios during 1996-1997 at the NC tower imply trends of -16.5 ± 0.5 ppt yr^{-1} for CH_3CCl_3 and 0.24 ± 0.01 ppt yr^{-1} for SF_6 [*Hurst et al.*, 1997b] which are in good agreement with background trends at remote northern hemispheric sites (Figure 5.4) [*Montzka et al.*, 1996; *Geller et al.*, 1997].

Synoptic-scale variability of trace gases at the NC tower was analyzed to identify regional-scale emission ratios [*Bakwin et al.*, 1997]. C_2Cl_4 was chosen as the reference compound because of its high ratio of atmospheric variability to measurement precision at the NC tower and its reasonably well-known emissions [*McCulloch and Midgley*, 1996]. Several statistical approaches were used for the analysis, including a method where "scores" for each trace gas were computed as the sum of its mixing ratios during pollution events >4 hours in duration. For December 1994 through August 1996, 211 pollution events of 4 to 273 hours duration were identified [*Bakwin et al.*, 1997]. Event scores for each trace gas were plotted against those for C_2Cl_4 and fit with a linear, orthogonal distance regression (Figure 5.36) to determine a regional-scale emission ratio. C_2Cl_4 correlated well with CFC-12, -11, CH_3CCl_3, SF_6, and several other gases ($r > 0.85$). North American source strengths estimated from this "score" method and a time-domain analysis of the data are in good agreement with industry estimates for $CH_3CCl_3$and CO but are 35-75% lower for CFCs. Discordance in CFC estimates may indicate that CFC emissions from the region surrounding the NC tower are not representative of North America (although CH_3CCl_3 and CO emissions appear to be) or that industry estimates of CFC emissions during 1995-1996 are too high. The latter scenario is supported by *Elkins et al.* [1993] and *Cunnold et al.* [1997] who demonstrated that global-scale observations of CFC-11 and CFC-12 mixing ratios during the 1990s are significantly lower than those calculated from emission inventories.

The synoptic-scale variability of several halogenated trace gases recently decreased at both the NC and WI towers reflecting reductions in regional-scale emissions [*Hurst et al.*, 1998]. Mixing ratio variability at all sampling heights on the towers was examined, but trends were deduced using only nighttime data from the top sampling level of each tower. This was done to minimize the influences of local sources and diurnal-scale variability, leaving regional emissions as the primary source of variability. Monthly variability, calculated as one standard deviation of monthly-binned mixing ratios with measurement errors subtracted in quadrature, was plotted as a

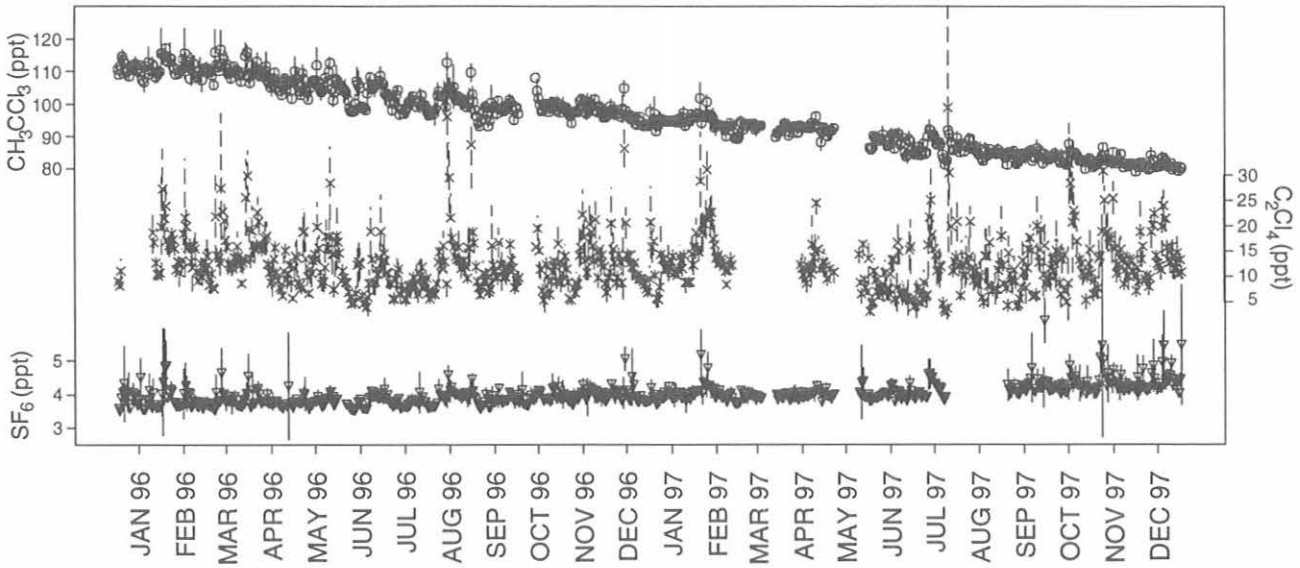

Fig. 5.35. Time series of daily mean mixing ratios of CH_3CCl_3 (circles), C_2Cl_4 (crosses), and SF_6 (inverted triangles) at the NC tower during 1996-1997. The mean mixing ratio ± one standard deviation for each day are represented by vertical bars (solid for CH_3CCl_3 and SF_6, dashed for C_2Cl_4).

time series and fit with a linear least-squares regression (Figure 5.37). Variability at the remotely-located WI tower was generally lower than at the NC tower, which is closer to large urban centers.

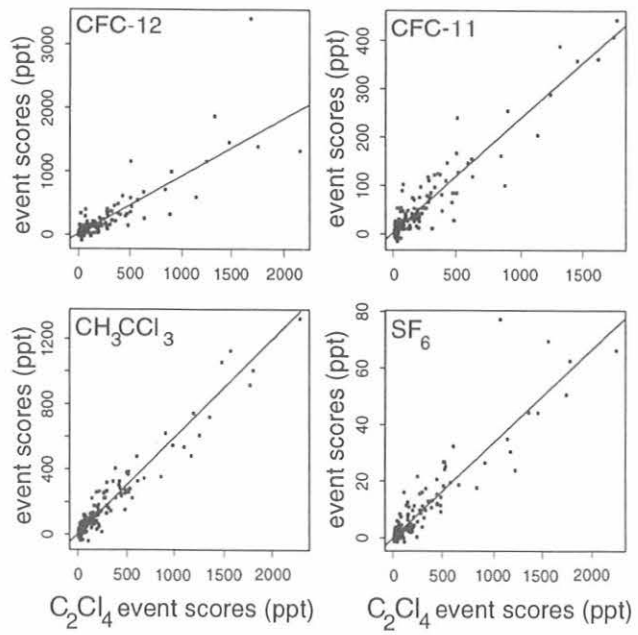

Fig. 5.36. Pollution event scores for CFC-12, CFC-11, CH_3CCl_3, and SF_6 versus scores of C_2Cl_4 at the North Carolina tower for December 1994 through August 1996. The y-axis of each panel represents event scores of the compound listed in the panel. The x-axes are scores for C_2Cl_4. Slopes of lines fit to each panel using an orthogonal distance regression reflect regional-scale emission ratios of the y-axis compound to C_2Cl_4 [from *Bakwin et al.*, 1997].

Significant decreases in the synoptic-scale variability of CFC-12, CFC-113, CH_3CCl_3, and C_2Cl_4 were observed at both towers (Table 5.10). With the exception of CH_3CCl_3, variability trends at the two towers agreed to within their quoted uncertainties. The variability trend for CH_3CCl_3 at the NC tower, -1.31 ± 0.19 ppt yr^{-1}, represents a 72 ± 11% decrease in regional emissions between early 1995 and late 1997. Trends for CFC-11, CCl_4, and SF_6 at both towers did not differ significantly from zero. However, because of the low ratios of atmospheric variability to measurement precision for these gases, only trends >25% over the entire measurement period at each tower could have been detected at a 75% level of confidence. Reductions in CFC-12, CFC-113, and CH_3CCl_3 emissions are attributed to production restrictions imposed by the Montreal Protocol. Reduced emissions of C_2Cl_4 are probably the result of recent requests to industry by the U.S. Environmental Protection Agency (EPA) to voluntarily reduce emissions of this compound because of its toxicity.

5.5. Firn Air Measurements

Past success in analyzing for halocarbons in air samples collected from firn (unconsolidated snow) at the South Pole [*Elkins et al.*, 1996a] prompted us to continue these investigations in Greenland and Antarctica. Our initial measurements of South Pole firn air were from low pressure glass flasks used in collecting air for carbon-cycle gases. Although these measurements seemed reasonable and the samples generally uncontaminated, they could only be run on two of our instruments; GC MS measurements were precluded for the South Pole samples because of a lack of available air. In April 1996 we assisted in the collection of samples from two holes at Tunu, Greenland (78°01'N, 33°59'E) and filled our usual 2.5-L stainless steel flasks to 375 kPa (yielding about 9 L of air) in

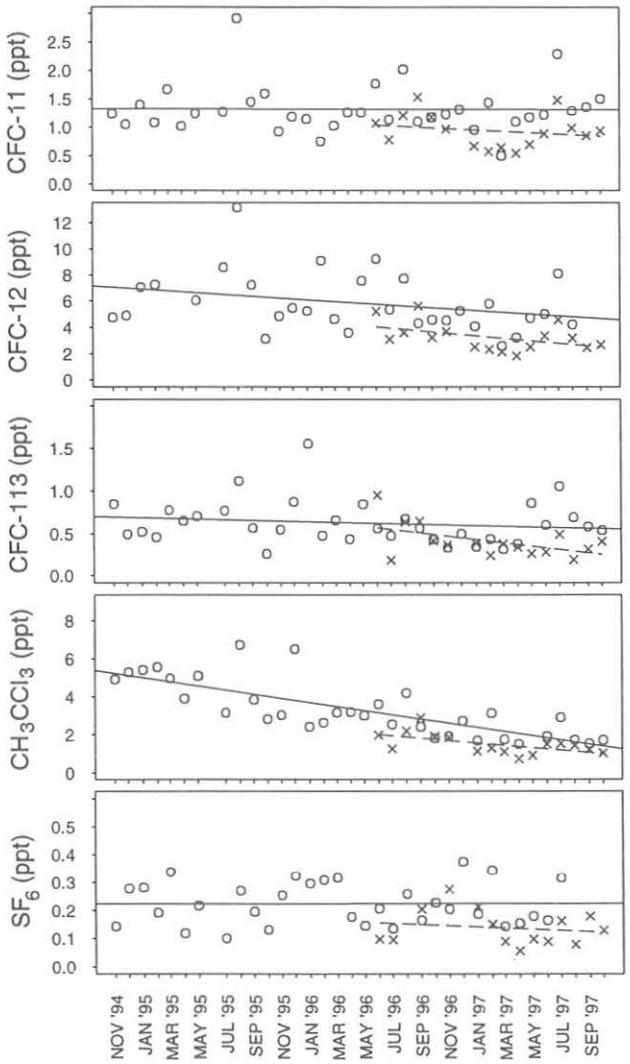

Fig. 5.37. Trends in monthly nighttime variability at the top sampling level of the North Carolina (NC) tower (circles) and Wisconsin (WI) tower (crosses). Variability was calculated as one standard deviation of nighttime mixing ratios during each month with random measurement noise removed. Lines fit to variability time series at the NC (solid) and WI (dashed) towers with least-squares regressions reflect trends in regional-scale emissions [*Hurst et al.*, 1998].

addition to the glass flasks (150 kPa, yielding only 3.8 L air, most of which is used in analyses for carbon-cycle gases by the CMDL Carbon Cycle Group). Samples were returned to Boulder for analysis on all four instruments used in flask analyses (Table 5.2). Both glass flasks and steel flasks were run on the two GC/ECD systems and steel flasks were run on the two GC/MS systems. Similarly we obtained samples in both steel and glass flasks from deep and shallow holes drilled at Siple Dome, Antarctica (81°40'S, 148°49'W), in December 1996.

Data from these sites showed that CFCs, CH_3CCl_3, CCl_4, SF_6, halons, and HCFCs were essentially absent in

TABLE 5.10. Trends in Nighttime Atmospheric Variability at the Top Sampling Levels of Tall Towers in North Carolina and Wisconsin

Compound	Trend Slope	Slope Error	Level of Confidence
NC Tower (November 1994 – October 1997)			
CFC-11	-0.09	0.13	
CFC-12	-0.82	0.48	90%
CFC-113	-0.09	0.08	76%
CH_3CCl_3	-1.31	0.19	99%
CCl_4	0.00	0.06	
C_2Cl_4	-0.63	0.38	89%
SF_6	0.00	0.02	
WI Tower (June 1996 – October 1997)			
CFC-11	-0.15	0.18	
CFC-12	-1.15	0.60	92%
CFC-113	-0.23	0.10	95%
CH_3CCl_3	-0.75	0.28	98%
CCl_4	-0.01	0.05	
C_2Cl_4	-1.19	0.73	87%
SF_6	-0.02	0.04	

the early 20th century atmosphere (Figures 5.38, 5.39, and 5.40). This is not surprising information, but these samples, which, unlike the initial South Pole samples, were collected in such a way as to avoid low-level contamination of halocarbons, are the first verification of levels of CFCs and the major chlorocarbons that do not differ significantly from zero. The data demonstrate that if natural sources of these gases do exist, they are insignificant.

Results for methyl halides were more ambiguous, although it still may be possible to derive 20th century atmospheric histories for them (Figure 5.39b and Figure 5.41). Methyl chloride in the diffusive zone is about 10% higher than it is at the bottom of the profiles suggesting that activities over the past century have elevated the mixing ratio of this gas in the atmosphere by about 50 ppt. Also, in the upper 10-12 m of the firn, CH_3Cl concentrations actually decrease toward the surface by about 30 ppt. This is consistent with seasonal cycles of CH_3Cl which are associated with photochemical cycles of tropospheric OH.

Data for CH_3Br from Siple Dome agreed well with those from the South Pole, both suggesting that atmospheric CH_3Br in the earlier part of this century was about 25% lower than it is today (Figure 5.41a). However, at Tunu, Greenland, a warmer and more coastally influenced site, CH_3Br was high near the bottom of the profile, reaching mixing ratios of nearly 50 ppt at the firn-ice transition (Figure 5.41b). Tests confirm that this elevation in concentration at depth is not an artifact of sample collection, storage, or analysis. This leads us to believe that the observed high values for CH_3Br in the firn at Tunu are real, although not necessarily of atmospheric origin. (This feature was also observed at Tunu for at least one other marine biogenic gas, CH_3I, and it was observed for $CHBr_3$ at Siple Dome where CH_3Br and CH_3I do not appear to have been produced.) A model of the

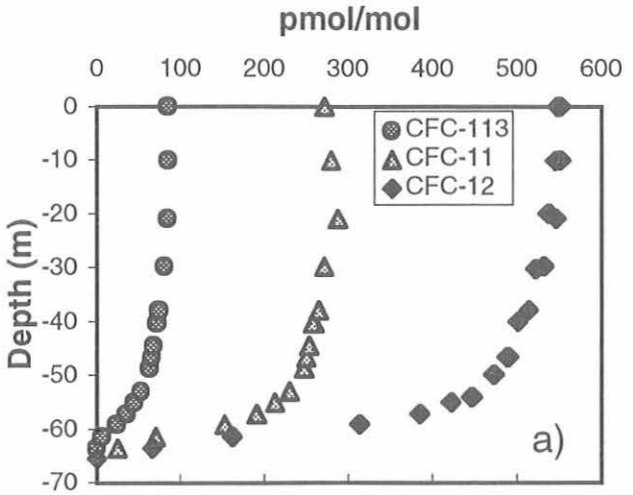

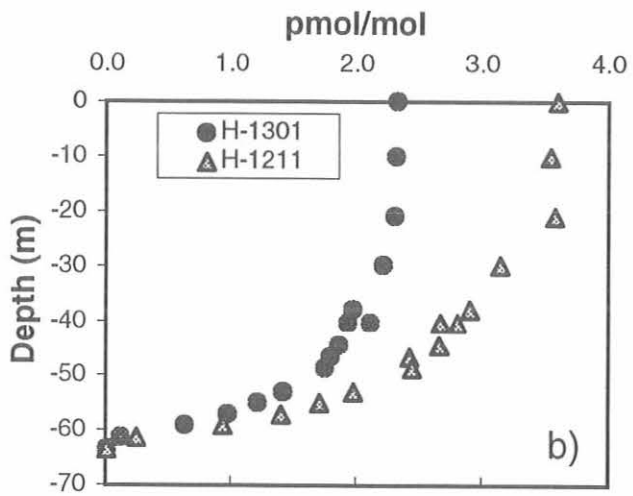

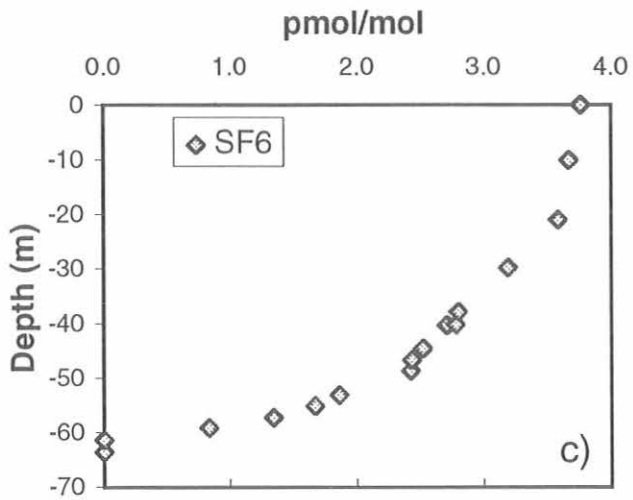

Fig. 5.38. "Conservative" gases of anthropogenic origin in Tunu firn air. (a) CFC's, (b) halons, (c) SF_6. CO_2 in air at the bottom of the Tunu, Greenland, profile corresponds to atmospheric CO_2 in the early 1930s.

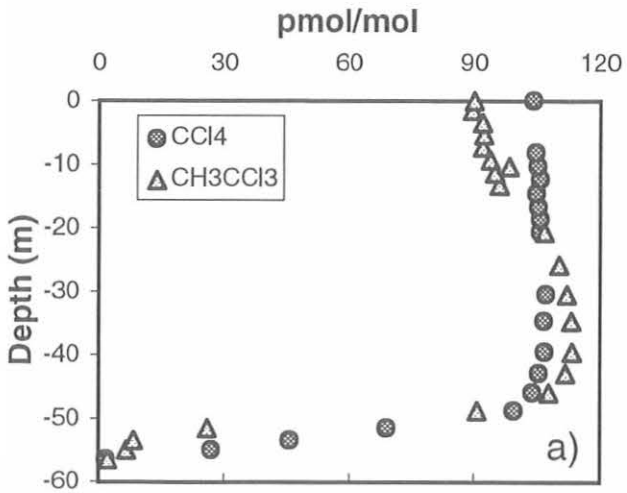

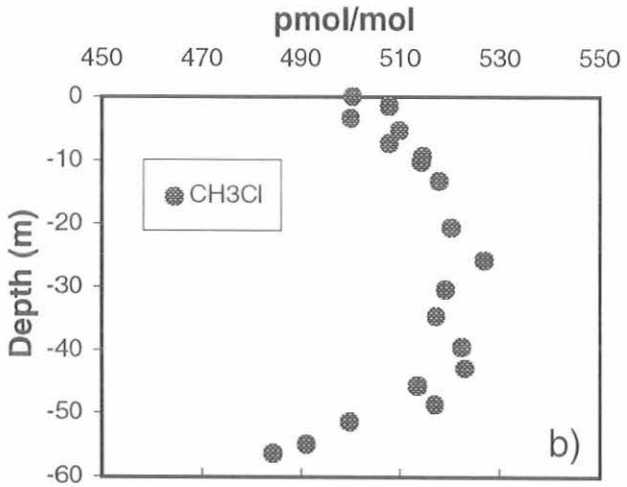

Fig. 5.39. Chlorocarbons in Siple Dome firn air. (a) CH_3CCl_3 and CCl_4, (b) CH_3Cl. CO_2 in air at the bottom of the Siple Dome profile corresponds to atmospheric CO_2 in the early 1950s.

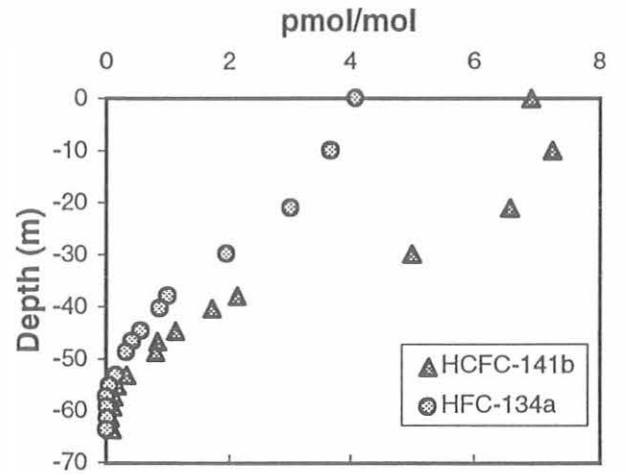

Fig. 5.40. Replacement compounds for CFCs in Tunu firn air.

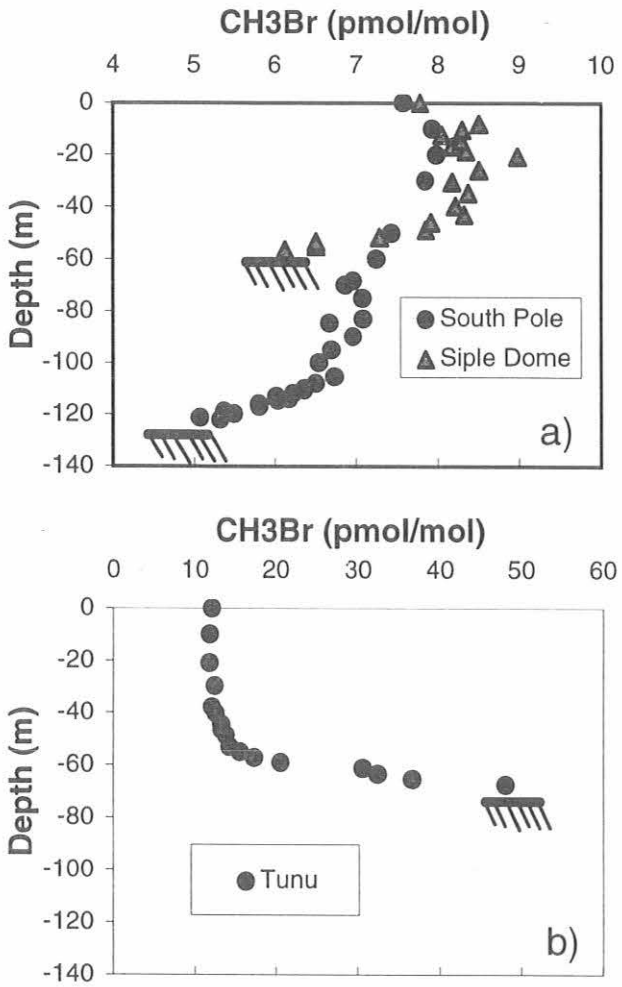

Fig. 5.41. Methyl bromide in firn air. (a) Antarctica, (b) Tunu, Greenland.

firn profiles strongly suggests that CH_3Br is produced near the firn-ice transition, a process that could not have been happening at South Pole or Siple Dome and yield the observed profiles.

Processes in the upper 10 m of firn also may affect CH_3Br concentrations. At each antarctic site, the CH_3Br concentration was elevated by as much as 1 ppt (10-15%) in samples just below the surface. This feature was consistent, though at present unexplained. Such variations did not appear throughout the profiles which suggests this may be a phenomenon limited to the upper 10 m. How this affects the overall profile is difficult to ascertain without first understanding the process. All firn samplings were conducted during the summer months thus precluding any evaluation of seasonal effects in the surface. In the fall of 1997, flasks were sent to SPO for sampling from a 15 m deep hole in winter and summer of 1998.

5.5. REFERENCES

Anbar, A.D., Y.L. Yung, and F.P. Chavez, Methyl bromide: Ocean sources, ocean sinks, and climate sensitivity, *Global Biogeochem. Cycles, 10(1)*, 175-190, 1996.

Bakwin, P.S., D.F. Hurst, P.P. Tans, and J.W. Elkins, Anthropogenic sources of halocarbons, sulfur hexafluoride, carbon monoxide, and methane in the southeastern United States, *J. Geophys. Res., 102*, 15,915-15,925, 1997.

Battle, M., M. Bender, T. Sowers, P. Tans, J. Butler, J. Elkins, J. Ellis, T. Conway, N. Zhang, P. Lang, and A. Clarke, Histories of atmospheric gases from the firn at South Pole, *Nature, 383*, 231-235, 1996.

Bouwman, A.F., K.W. Van der Hoek, and J.G.J. Olivier, Uncertainties in the global source distribution of nitrous oxide, *J. Geophys. Res., 100(D2)*, 2785-2800, 1995.

Butler, J.H., J.W. Elkins, T.M. Thompson, B.D. Hall, T.H. Swanson, and V. Koropalov, Oceanic consumption of CH_3CCl_3: Implications for tropospheric OH, *J. Geophys. Res., 96*, 22,347-22,355, 1991.

Butler, J.H., The potential role of the ocean in regulating atmospheric CH_3Br, *Geophys. Res. Lett., 21*, 185-188, 1994.

Butler, J.H., J.M. Lobert, S.A., Yvon, and L.S. Geller, The distribution and cycling of halogenated trace gases between the atmosphere and ocean, in *The Expedition ANTARKTIS XII of RV Polarstern in 1994/95, Reports of Legs ANT XII/1 and 2*, pp. 27-40, Alfred Wegener Insitut fur Polar und Meeresforschung, Bremerhaven, Germany, 1995.

Butler, J.H., S.A. Montzka, A.D. Clarke, J.M. Lobert, and J.W. Elkins, Growth and distribution of halons in the atmosphere, *J. Geophys. Res., 103(D1)*, 1503-1511, 1998.

Chen, L., Y. Makide, and T. Tominaga, Distribution and trend of chlorodifluoromethane (HCFC-22) in the atmosphere, *Chem. Lett., 12*, 2423-2426, 1994.

Chin, M., and D.D. Davis, A reanalysis of carbonyl sulfide as a source of stratospheric background sulfur aerosol, *J. Geophys. Res., 100*, 8993-9005, 1995.

Cicerone, R., Analysis of sources and sinks of atmospheric nitrous oxide (N_2O), *J. Geophys. Res., 94*, 18,265-18,271, 1989.

Cunnold, D.M., R.F. Weiss, R.G. Prinn, D. Hartley, P.G. Simmonds, P.J. Fraser, B.R. Miller, F.N. Alyea, and L. Porter, GAGE/AGAGE measurements indicating reductions in global emissions of CCl_3F and CCl_2F_2 in 1992-1994, *J. Geophys. Res., 102*, 1259-1269, 1997.

Daniel, J.S., S.M. Schauffler, W.H. Pollock, S. Solomon, A. Weaver, L.E. Heidt, R.R. Garcia, E.L. Atlas, and J.F. Vedder, On the age of stratospheric air and inorganic chlorine and bromine release, *J. Geophys. Res., 101(D11)*, 16,757-16,770, 1996.

DeBruyn W.J., and E.S. Saltzman, Diffusivity of methyl bromide in water, *Mar. Chem., 57*, 55-59, 1997a.

DeBruyn W.J., and E.S. Saltzman, The solubility of methyl bromide in pure water, 35‰ sodium chloride and seawater, *Mar. Chem., 56*, 51-57, 1997b.

Ehhalt, D.H., P.J. Fraser, D. Albritton, R.J. Cicerone, M.A.K. Khalil, M. Legrand, Y. Makide, F.S. Rowland, L.P. Steele, and R. Zander, Trends in source gases, in *Report of the International Ozone Trends Panel, 1988*, World Meteorological Organization, Geneva, 1988.

Elkins, J.W., T.M. Thompson, T.H. Swanson, J.H. Butler, B.D. Hall, S.O. Cummings, D.A. Fisher, and A.G. Raffo, Slowdown in the growth rates of atmospheric chlorofluorocarbons 11 and 12, *Nature, 364*, 780-783, 1993.

Elkins, J.W., J.H. Butler, T.M. Thompson, S.A. Montzka, R.C. Myers, J.M. Lobert, S. Yvon, P.R. Wamsley, F.L. Moore, J.M. Gilligan, D.F. Hurst, A.D. Clarke, T.H. Swanson, C.M. Volk, L.T. Lock, L.S. Geller, G.S. Dutton, R.M. Dunn, M.F. Dicorelto, T.J. Baring, and A.H. Hayden, 5. Nitrous Oxide and Halocompounds,

Climate Monitoring and Diagnostics Laboratory No. 23 Summary Report 1994-1995, D.J. Hofmann, J.T. Peterson, and R. Rosson (eds.), 84-111, NOAA Env. Res. Labs., Boulder, CO, 1996a.

Elkins, J.W., D.W. Fahey, J. M. Gilligan, G.S. Dutton, T.J. Baring, C.M. Volk, R.E. Dunn, R.C. Myers, S.A. Montzka, P.R. Wamsley, A.H. Hayden, J.H. Butler, T.M. Thompson, T.H. Swanson, E.J. Dlugokencky, P.C. Novelli, D.F. Hurst, J.M. Lobert, S.J. Ciciora, R.J. McLaughlin, T.L. Thompson, R.H. Winkler, P.J. Fraser, L.P. Steele and M.P. Lucarelli, Airborne gas chromatograph for in situ measurements of long-lived species in the upper troposphere and lower stratosphere, *Geophys. Res. Lett., 23(4)*, 347-350, 1996b.

Elliott, S., E. Lu, and F.S. Rowland, Rates and mechanisms for the hydrolysis of carbonyl sulfide in natural waters, *Environ. Sci. Technol., 23*, 458-461, 1989.

Fabian, P., R. Borchers, and K. Kourtidis, Bromine-containing source gases during EASOE, *Geophys. Res. Lett., 21(13)*, 1219-1222, 1994.

Fabian, P., R. Borchers, R. Leifer, B.H. Subbaraya, S. Lal, and M. Boy, Global stratospheric distribution of halocarbons, *Atmos. Environ., 30*, 1787-1796, 1996.

Geller, L.S., J.W. Elkins, J.M. Lobert, A.D. Clarke, D.F. Hurst, J.H. Butler, and R.C. Myers, Tropospheric SF_6: Observed latitudinal distribution and trends, derived emissions and interhemispheric exchange time, *Geophys. Res. Lett., 24(6)*, 675-678, 1997.

Gerkins, R.R., and J.A. Franklin, The rate of degradation of 1,1,1-trichloroethane in water by hydrolysis and dehydrohalogenation, *Chemosphere, 19*, 1929-1937, 1989.

Gossett, J.M., Measurement of Henry's Law constants for C_1 and C_2 chlorinated hydrocarbons, *Environ. Sci. Technol., 21(2)*, 202-208, 1987.

Hall, T.M., and R.A. Plumb, Age as a diagnostic of stratospheric transport, *J. Geophys. Res., 99*, 1059-1070, 1994.

Hurst, D.F., P.S. Bakwin, R.C. Myers, and J.W. Elkins, Behavior of trace gas mixing ratios on a very tall tower in North Carolina, *J. Geophys. Res., 102*, 8825-8835, 1997a.

Hurst, D.F., P.S. Bakwin,, and J.W. Elkins, Recent trends in halogenated trace gas mixing ratios and variance on two tall towers in the United States, *EOS Trans. AGU, 78*, Fall Meet. Suppl., F94, 1997b.

Hurst, D.F., P.S. Bakwin, and J.W. Elkins, Recent trends in the variability of halogenated trace gases over the United States, *J. Geophys. Res., 103(D19)*, 25,299-25,306, 1998.

Intergovernmental Panel on Climate Change (IPCC), Climate Change 1994: Radiative Forcing of Climate Change and An Evaluation of the IPCC IS92 Emission Scenarios, Intergovernmental Panel on Climate Change, J.T. Houghton, L.G.M. Filho, J. Bruce, H. Lee, B.A. Callander, E. Haites, N. Harris, and K. Maskell (eds.), 339 pp., Cambridge, UK, 1995.

Jeffers, P.M., L.M. Ward, L.M. Woytowitch, and N.L. Wolfe, Homogeneous hydrolysis rate constant for selected chlorinated methanes, ethanes, ethenes, and propanes, *Environ. Sci. Technol., 23*, 965-969, 1989.

Johnson, J.E., and H. Harrison, Carbonyl sulfide concentrations in the surface waters and above the Pacific Ocean, *J. Geophys. Res., 91*, 7883-7888, 1986.

Kaye, J.A., S.A. Penkett, and F.M. Ormond, Report on concentrations, lifetimes and trends of CFCs, halons and related species, *NASA RP 1339*, 248 pp., 1994.

Kaye, J.A., S.A. Penkett, F.M. Ormond, P. Fraser, D. Fisher, P. Bloomfield, S.P. Sander, and M.K.W. Ko, *Report on concentrations, lifetimes and trends of CFCs, halons and related species*, NASA, Washington, DC, 1994.

Khalil, M.A.K., and R.A. Rasmussen, Constraints imposed by the ice core data on the budgets of nitrous oxide and methane, in *28th Liege International Astrophysical Colloquium June 26-30, 1989*, edited by P.J. Crutzen, J.C. Gerard, and R. Zander, pp. 403-410, University de Liege, Liege, Belgium, 1989.

Khalil, M.A.K., and R.A. Rasmussen, Trace gases over Antarctica: Bromine, chlorine, and organic compounds involved in global change, *Ant. J. U. S., 27(5)*, 267-269, 1992.

Khalil, M.A.K., R.A. Rasmussen, and R. Gunawardena, Atmospheric methyl bromide: Trends and global mass balance, *J. Geophys. Res., 98(D2)*, 2887-2896, 1993.

Kim, K.-R., and H. Craig, Nitrogen-15 and oxygen-18 characteristics of nitrous oxide: A global perspective, *Science, 262*, 1855-1857, 1993.

King, D.B., and E.S. Saltzman, Removal of methyl bromide in coastal seawater: Chemical and biological rates, *J. Geophys. Res., 102*, 18,715-18,721, 1997.

Lal, S., R. Borchers, P. Fabian, P.K. Patra, and B.H. Subbaraya, Vertical distribution of methyl bromide over Hyderbad, India, *Tellus, 46B*, 373-377, 1994.

Leuenberger, M., and U. Siegenthaler, Ice-age atmospheric concentration of nitrous oxide from an Antarctic ice core, *Nature, 360*, 449-451, 1992.

Li, Y.H., T.H. Peng, W.S. Broecker, and H.G. Ostlund, The average vertical mixing coefficient for the oceanic thermocline, *Tellus, 36B*, 212-217, 1984.

Liss, P.S., and L. Merlivat, Air-sea gas exchange rates: Introduction and synthesis, in *The Role of Air-Sea Exchange in Geochemical Cycling*, edited by P. Buat-Menard, pp. 113-127, D. Reidel, Norwell, MA, 1986.

Lobert J.M., J.H. Butler, S.A. Montzka, L.S. Geller, R.C. Myers, and J.W. Elkins, A net sink for atmospheric CH_3Br in the East Pacific Ocean, *Science, 267*, 1002-1005, 1995.

Lobert, J.M., S.A. YvonLewis, J.H. Butler, S.A. Montzka, and R.C. Myers, Undersaturation of CH_3Br in the Southern Ocean, *Geophys. Res. Lett., 24(2)*, 171-172, 1997.

Lobert, J.M., J.H. Butler, L.S. Geller, S.A. Yvon, S.A. Montzka, R.C. Myers, A.D. Clarke, and J.W. Elkins, Blast 94: Bromine Latitudinal Air/Sea Transect, 1994, Report on Oceanic Measurements of Methyl Bromide and Other Compounds, *NOAA Tech. Memo. ERL CMDL-10*, Environmental Research Laboratories, Boulder, CO, 1996.

Loewenstein, M., J.R. Podolske, K.R. Chan, and S.E. Strahan, Nitrous oxide as a dynamical tracer in the 1987 Airborne Antarctic Ozone Experiment, *J. Geophys. Res., 94(D9)*, 11,589-11,598, 1989.

Lorenzen-Schmidt, H., Untersuchungen zur atmosphaerischen Verteilung un zum photochemischen Abbau leichtfluechtiger Bromverbindungen, Ph.D., Alfred Wegener Institute fuer Polar-und Meeresforschung, Bremerhaven, 1994.

Machida, T., T. Nakazawa, Y. Fujii, S. Aoki, and O. Watanabe, Increase in the atmospheric nitrous oxide concentration during the last 250 years, *Geophys. Res. Lett., 22(21)*, 2921-2924, 1995.

Maiss, M., and I. Levin, Global increase of SF_6 observed in the atmosphere, *Geophys. Res. Lett., 21(7)*, 569-572, 1994.

McCulloch, A., and P.M. Midgley, The production and global distribution of emissions of trichloroethene, tetrachloroethene, and dichloromethane over the period 1988-1992, *Atmos. Environ., 30*, 601-608, 1996.

McLinden, M.O., Physical properties of alternatives to the fully halogenated chlorofluorocarbons, in *Scientific Assessment of Stratospheric Ozone: 1989 Vol. II Appendix AFEAS Report*, WMO Global Ozone Research and Monitoring Project-Report No. 20, 469 pp., 1989.

Moelwyn-Hughes, E.A., The hydrolysis of methyl halides, *Proc. Roy. Soc. A, 164*, 295-306, 1938.

Montzka, S.A., J.H. Butler, R.C. Myers, T.M. Thompson, T.H. Swanson, A.D. Clarke, L.T. Lock, and J.W. Elkins, Decline in the tropospheric abundance of halogen from halocarbons: Implications for stratospheric ozone depletion, *Science, 272*, 1318-1322, 1996.

Moore, R.M., C.E. Green, and V.K. Tait, Determination of Henry's Law constants for a suite of naturally occurring halogenated methanes in seawater, *Chemosphere*, 30, 1183-1191, 1995.

Oertel, T., Verteilung leichtfluechtiger organobromver-bindungen in der marinen troposphaere un im oberflaechenwasser des Atlantiks, PhD., Universität Bremen, Germany, 1992.

Oort, A.H., and J.J. Yienger, Observed interannual variability in the Hadley circulation and its connection to ENSO, *J. Clim., 9*, 2751-2767, 1996.

Pilinis, C., D.B. King, and E.S. Saltzman, The oceans: A source or a sink of methyl bromide? *Geophys. Res. Lett., 23(8)*, 817-820, 1996.

Plumb, R.A., A "tropical pipe" model of stratospheric transport, *J. Geophys. Res., 101*, 3957-3972, 1996.

Plumb, R.A., and M.K.W. Ko, Interrelationships between mixing ratios of long-lived stratospheric constituents, *J. Geophys. Res., 97*, 10,145-10,156, 1992.

Prinn, R.G., R.F. Weiss, B.R. Miller, J. Huang, F.N. Alyea, D.M. Cunnold, P.B. Fraser, D.E. Hartley, and P.G. Simmons, Atmospheric trends and lifetime of trichloroethane and global average hydroxyl radical concentrations based on 1978-1994 ALE/GAGE measurements, *Science*, 269, 187-192, 1995.

Ravishankara, A.R., S. Solomon, A.A. Turnipseed, and R.F. Warren, Atmospheric lifetimes of long-lived halogenated species, *Science, 259*, 194-200, 1993.

Schauffler, S.M., L.E. Heidt, W.H. Pollock, T.M. Gilpin, J.F. Vedder, S. Solomon, R.A. Lueb, and E.L. Atlas, Measurements of halogenated organic compounds near the tropical tropopause. *Geophys. Res. Lett., 20(22)*, 2567-2570, 1993.

Schimel, D., D. Alves, I. Enting, M. Heimann, F. Joos, D. Raynaud, T. Wigley, M. Prather, R. Derwent, D. Ehhalt, P. Fraser, E. Sanhueza, X. Zhou, P. Jonas, R. Charlson, H. Rodhe, S. Sadasivan, K.P. Shine, Y. Fouquart, V. Ramaswamy, S. Solomon, J. Srinivasan, D. Albritton, R. Derwent, I. Isaksen, M. Lal, and D. Wuebbles, Radiative Forcing of Climate Change, in *Climate Change 1995: The Science of Climate Change*, edited by J.T. Houghton, L.G. Meira Filho, B.A. Callander, N. Harris, A. Kattenberg, and K. Maskell, pp. 65-131, Cambridge Univ. Press, U.K., 1996.

Singh, O.N., R. Borchers, P. Fabian, S. Lal, and B.H. Subbaraya, Measurements of atmospheric BrOx radicals in the tropical and mid-latitude atmosphere, *Nature, 334*, 593-595, 1988.

Singh, H.B., and M. Kanakidou, An investigation of the atmospheric sources and sinks of methyl bromide, *Geophys. Res. Lett., 20(2)*, 133-136, 1993.

Singh, H.B., L.J. Salas, and R.E. Stiles, Methyl halides in and over the eastern Pacific (40°N-32°S), *J. Geophys. Res., 88*, 3684-3690, 1983.

Thompson, T.M., W.D. Komhyr, and E.G. Dutton, Chlorofluorocarbon-11, -12, and nitrous oxide measurements at the NOAA/GMCC baseline stations (16 September 1973 to 31 December 1979), in *NOAA Tech. Rep. ERL 428-ARL 8*, 124 pp., NOAA Env. Res. Labs., Boulder, CO, 1985.

Ulshöfer, V.S. and M.O. Andreae, Carbonyl sulfide (COS) in the surface ocean and the atmospheric COS budget, *Aquat. Geochem.*, submitted, 1997.

United Nations Environmental Programme (UNEP), *Montreal Protocol on Substances that Deplete the Ozone Layer, Final Act*, 15 pp., United Nations Environmental Programme, Nairobi, 1987.

United Nations Environmental Programme (UNEP), Report of the Ninth Meeting of the Parties to the Montreal Protocol on Substances that Deplete the Ozone Layer (Montreal), United Nations Environmental Programme, New York, 1997.

Volk, C.M., J.W. Elkins, D.W. Fahey, R.J. Salawitch, G.S. Dutton, J.M. Gilligan, M.H. Profitt, M. Loewenstein, J.R. Podolske, K. Minschwaner, J.J. Margitan, and K.R. Chan, Quantifying transport between the tropical and mid-latitude lower stratosphere, *Science, 272*, 1763-1768, 1996.

Volk, C.M., J.W. Elkins, D.W. Fahey, G.S. Dutton, J.M. Gilligan, M. Loewenstein, J.R. Podolske, K.R. Chan and M.R. Gunson, Evaluation of source gas lifetime from stratospheric observations, *J. Geophys. Res., 102(D21)* , 25,543-25,564, 1997.

Wamsley, P.R., J.W. Elkins, D.W. Fahey, G.S. Dutton, C.M. Volk, R.C. Myers, S.A. Montzka, J.H. Butler, A.D. Clarke, P.J. Fraser, L.P. Steele, M.P. Lucarelli, E.L. Atlas, S.M. Schauffler, D. R. Blake, F.S. Rowland, W.T. Sturges, J.M. Lee, S.A. Penkett, A. Engel, R.M. Stimpfle, K.R. Chan, D.K. Weisenstein, M.K.W. Ko and R.J. Salawitch, Distribution of halon-1211 in the upper troposphere and lower stratosphere and the 1994 total bromine budget, *J. Geophys. Res., 103(D1)*, 1513-1526, 1998.

Wang, C. J-L., D.R. Blake, and F.S. Rowland, Seasonal variations in the atmospheric distribution of a reactive chlorine compound, tetrachloroethene (CCl2=CCl2), *Geophys. Res. Lett.*, 22, 1097-1100, 1995.

Wanninkhof, R., Relationship between wind speed and gas exchange over the ocean, *J. Geophys. Res., 97*, 7373-7382, 1992.

Wilke, C.R., and P. Chang, Correlation of diffusion coefficients in dilute solutions, *AIChE. J., 35*, 281-289, 1955.

Wine, P.H., and W.L. Chameides, Possible atmospheric lifetimes and chemical reaction mechanisms for selected HCFCs, HFCs, CH_3CCl_3, and their degradation products against dissolution and/or degradation in seawater and cloudwater, in *Scientific Assessment of Stratospheric Ozone: 1989 Vol. II Appendix AFEAS Report*, WMO Global Ozone Research and Monitoring Project-Report No. 20, 469 pp., 1989.

Woodbridge, E.L., J.W. Elkins, D.W. Fahey, L.E. Heidt, S. Solomon, T.J. Baring, T.M. Gilpin, W.H. Pollock, S.M. Schauffler, E.L. Atlas, M. Loewenstein, J.R. Podolske, C.R. Webster, R.D. May, J.M. Gilligan, S.A. Montzka, K.A. Boering and R.J. Salawitch, Estimates of total organic and inorganic chlorine in the lower stratosphere from in situ and flask measurements, *J. Geophys. Res., 100(D2)*, 3057-3064, 1995.

World Meteorological Organization (WMO), *Scientific Assessment of Ozone Depletion: 1991, Global Ozone Research and Monitoring Project, 25*, 357, WMO Geneva, 1992.

World Meteorological Organization (WMO), *Scientific Assessment of Ozone Depletion: 1994, Global Ozone Research and Monitoring Project, 37*, D.L. Albritton, and R.J. Aucamp, eds., p. 451, WMO, Geneva, 1995.

Yvon, S.A., and J.H. Butler, An improved estimate of the oceanic lifetime of atmospheric CH_3Br, *Geophys. Res. Lett., 23(1)*, 53-56, 1996.

Yvon-Lewis, S.A., and J.H. Butler, The potential effect of biological degradation on the lifetime of atmospheric CH_3Br, *Geophys. Res. Lett., 24(10)*, 1227-1230, 1997.

6. Cooperative Programs

Spectral Albedo Observation on the Snow Field at Barrow, Alaska

TERUO AOKI, TADAO AOKI, MASASHI FUKABORI, AND YUJI ZAIZEN
Meteorological Research Institute, Tsukuba, 305-0052, Japan

YOSHIHIRO TACHIBANA
Research Institute of Civilization, Tokai University, Hiratsuka 259-12, Japan

FUMIHIKO NISHIO
Hokkaido University of Education, Kushiro 085, Japan

INTRODUCTION

There are possibilities of remote sensing for snow impurities by observation of the visible albedo and the snow grain size using the near infrared albedo [*Warren*, 1982]. We will estimate the snow impurities and snow grain size with the satellite data of the next generation. The basis of these studies is a multiple scattering radiative transfer model for the atmosphere-snow system that simulates the spectral albedos at the snow surface and the top of the atmosphere. To validate this model, field observations for the spectral albedo and snow physical parameters have been done on the snow field at Barrow, Alaska, from April 14 to 27, 1997. Under a clear sky, even a gentle slope of the snow surface affects the snow albedo [*Grenfell and Warren*, 1994]. As a simpler case in which it is unnecessary to consider such an effect, the relationship between the spectral albedo and snow physical parameters under an overcast condition on April 21 after new snowfall, is discussed in this study.

OBSERVATION

The observation site was a snow field on tundra 5 km northeast of Barrow town. The snow depth was 60 cm and the surface was covered by new snow of 1 cm depth that fell the day before the observation. The grain shape of new surface snow was dendrites with crystal size (radius) of 1-2 mm and branch size (radius) of 25-50 μm. The second layer (1-24 cm snow depth) was fine-grained old snow with a grain radius of 100-150 μm, and the third layer (24-44 cm) was faceted crystals with a grain radius of 250-400 μm. The bottom layer (44-60 cm depth) was hoar crystals with a grain radius of 1-3 mm. Snow impurities were filtered within a day by Nuclepore filters with the pore size of 0.2 μm after melting the snow samples of the surface and 5-10 cm depth snow layers. The concentrations of impurities were estimated by direct weight measurements of the Nuclepore filters, before and after filtering, with a balance. The observed concentration of snow impurities was 2.46 ppmw for surface snow and 1.19 ppmw for 5-10 cm depth. The sky condition was overcast with altocumulus. Air and snow surface temperatures were −14.2°C and −11.0°C, respectively at 1200 local standard time (LST).

The spectral snow albedo was observed by a grating type spectrometer, "FieldSpec FR", made by ASD Inc. (U.S.). It is necessary to observe the downward and upward flux to obtain the albedo. The downward flux was observed by directing the optical fiber of the spectrometer toward the surface of a standard white reflection plate that is set horizontally above the snow surface. The upward flux was observed by directing the optical fiber toward the underside of the standard white reflection plate. The scanning spectral range of the spectrometer is 0.35-2.5 μm with the spectral resolution of 3 nm for the wavelength of 0.35-1.0 μm and 10 nm for 1.0-2.5 μm. The spectral snow albedo is the average of five spectral albedos obtained from five pairs of measurements for the downward and snow reflected solar fluxes. It takes several minutes to obtain these quantities.

RESULTS AND DISCUSSION

The observed spectral snow albedo was compared with the theoretical calculations by a multiple scattering model for the atmosphere-snow system in which snow grains are assumed to be mutually independent ice particles and radiative transfer processes are based on the Mie theory for single scattering and the "doubling and adding" method for multiple scattering [*Aoki et al.*, 1997]. We calculated the theoretical spectral albedos for some combinations of snow layer structure and snow impurities and obtained the best fitting of theoretical spectral albedo to the one observed (Figure 1). The theoretical calculations were carried out for two-layer snow models with three geometric depths (d_1), 2, 5, and 10 mm, with a density of 0.05 g cm^{-3} and r_{eff} = 25 μm in the first layer and semi-infinite geometric depth with r_{eff} = 100 μm in the second layer. The observed geometric depth of the surface layer was 1 cm, but we could not measure the density due to the very low density and thinness of the layer. It is known that the mean density of new snow consisting of spatial dendrites is 0.036-0.059 g cm^{-3} except in a snowstorm where the minimum is 0.02 g cm^{-3} [*Kajikawa*, 1989]. There was no snowstorm when new snow fell on the surface on April 20 at Barrow. We, therefore, assume the density of new snow to be 0.05 g cm^{-3}. For snow impurities in the theoretical calculation, the first snow layer is contaminated with a 0.1 ppmw internal soot mixture and a 2 ppmw external dust mixture. The second snow layer is contaminated by a 0.1 ppmw internal soot mixture and a 1 ppmw external dust mixture.

If the crystal grain size (r_{eff} = 250-400 μm) is assumed for snow grain size in the first layer, the theoretical spectral albedo does not agree with the observed one in the near

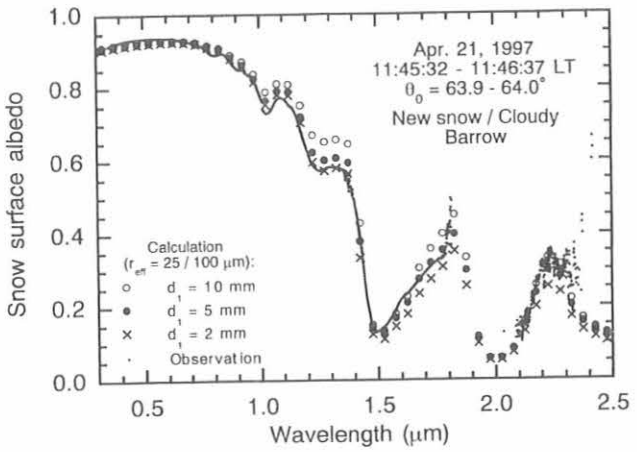

Fig. 1. Observed spectral snow albedo on April 21, 1997, at Barrow and theoretical results two-snow layer models with three geometric depths (d_1), 2, 5, and 10 mm with a density of 0.05 g cm^{-3} and r_{eff} = 25 μm in the first layer, and semi-infinite geometric depth with r_{eff} = 100 μm in the second layer. The first snow layer is contaminated by a 0.1 ppmw internal soot mixture and a 2 ppmw external dust mixture. The second snow layer is contaminated by a 0.1 ppmw internal soot mixture and a 1 ppmw external dust mixture.

infrared. It means that the optically effective snow grain size is on the order of branch size for the snow of dendrites but is not of the crystal size.

Good agreement is obtained for the model with a geometric depth of d_1 = 2 and 5 mm for the first layer at almost all wavelengths. In the case of d_1 = 10 mm, which is the value observed in this study, the theoretical spectral albedo is higher than the observed one by 0.05 to 0.1 at the wavelengths $1.0<\lambda<1.35$ μm. If we assume the value of snow density to be 0.02 g cm^{-3}, which is the minimum value of *Kajikawa* [1989], the geometric depths d_1 = 2 and 5 mm in Figure 1, respectively, become d_1 = 5 and 12.5 mm. These values are consistent with the observed geometric depth.

On the other hand, soot concentration of 0.1 ppmw with an internal mixture in both snow layers leads to good agreement between theoretical and observed spectral albedos. The arctic background concentration of snow impurities ranges from 0.005 to 0.045 ppmw [*Warren and Clarke*, 1986]. Our value of 0.1 ppmw is twice as high as the value of *Warren and Clarke* [1986]. Since our observation site was close to Barrow town, there is a possibility that the snow was polluted by locally emitted soot. Dust concentrations of 2 ppmw in the first layer and 1 ppmw in the second layer are consistent with the measured results obtained by using Nuclepore filters.

Acknowledgments. We are indebted to Y. Nakajima and Y. Tsuruga of RESTEC (Remote Sensing Technology Center), and Y. Saruya for their logistic support. We also thank D. Endres and M. Gaylord of CMDL, and G. W. Sheehan of Ukpeagvik Inupiat Corporation/Naval Arctic Research Laboratory for their help in this field experiment. Discussions with K. Stamnes, M. Jeffries, A. J. Alkezweeny and S.-I. Akasofu of the Geophysical Institute, University of Alaska Fairbanks, were fruitful for this study. This work was done as part of the ADEOS Field Campaign supported by NASDA (National Space Development Agency of Japan).

References

Aoki, Te., Ta. Aoki, and M. Fukabori, Approximations for phase function in calculating the spectral albedo of snow surface with multiple scattering. *Pap. Meteorol. Geophys., 47*, 141-156, 1997.

Grenfell, T. C., and S. G. Warren, Reflection of solar radiation by the Antarctic snow surface at ultraviolet, visible and near-infrared wavelengths. *J. Geophys. Res., 99*, 18,669-18,684, 1994.

Kajikawa, M., Relation between new snow density and shape of snow crystals, (in Japanese with English abstract) *Seppyo, 51*, 178-183, 1989.

Warren, S. G., Optical properties of snow. *Rev. Geophys. Space Phys., 20*, 67-89, 1982.

Warren, S. G., and A. D. Clarke, Soot from arctic haze: radiative effects on the arctic snowpack, *Glaciolog. Data, 18*, 73-77, 1986.

Latitudinal Tropospheric Concentration Distribution of Selected Halocarbons and Hydrocarbons

DONALD R. BLAKE AND F. SHERWOOD ROWLAND
Department of Chemistry, University of California, Irvine, 92697

Measurements of the distribution of selected halocarbons, hydrocarbons, and carbon monoxide were carried out on tropospheric air samples collected at the surface in remote locations over 2-week periods every 3 months, covering the latitudinal range from 71°N (Barrow, Alaska) to 47°S (Bluff, New Zealand). Results for CCl_4, CCl_3F, CCl_2F_2, CH_3CCl_3, and CH_4 form part of a continuing set of data from January 1978. Two halons, $CBrF_3$ and $CBrClF_2$, and methyl bromide (CH_3Br), which were added to our regular analysis in 1991, are the primary tropospheric compounds supporting increasing stratospheric bromine concentrations. Methyl bromide alone represents half of the stratospheric bromine burden, but its atmospheric chemistry is particularly complicated because of its multiple reported sources (oceanic, biomass burning, anthropogenic) and sinks (hydroxyl radical (HO), oceanic, soil), about which relatively little quantitative data are available. Numerous nonmethane hydrocarbons (NMHCs) have also been measured since the mid-1980s.

The shorter-lived gas, perchloroethene (C_2Cl_4), has a strong gradient of decreasing concentrations from the northern to southern hemisphere, with very low concentrations in the southern hemisphere throughout the year, consistent with its predominant input from the northern hemisphere. The late-winter maximum and late-summer minimum in the northern hemisphere are strongly coupled to the atmospheric abundance of HO, the only important species responsible for C_2Cl_4 removal. Using our measurements of the global atmospheric burden along with estimates of its emissions, the lifetime of C_2Cl_4 was calculated to be about 5 months [*Wang et al.*, 1994]. This is in good agreement with the 3.3 month estimate obtained by comparison of C_2Cl_4 and CH_3CCl_3 reaction rate constants, assuming an atmospheric lifetime for CH_3CCl_3 of 4.8 years. The fact that these two methods agree well suggests current global average HO concentrations obtained from the CH_3CCl_3 lifetime calculations are reasonably accurate.

Emissions of the three primary chlorofluorocarbons have slowed markedly during the 1990s in response to the regulatory restrictions of the Montreal Protocol. September 1995 ambient levels of CFC-11 and CFC-113 were decreasing. Although yearly emissions of CFC-12 estimated from our measurements have decreased by more than 60% from 1988 to 1995, the remaining emissions were still large enough to sustain a growth rate of about 4 pptv yr^{-1} at the end of 1995.

The latitudinal distribution of CH_4 has been part of this research since January, 1978 [*Blake and Rowland*, 1988]. Since 1990, there has been considerable short-term variation in the CH_4 growth rate, particularly in the northern hemisphere. The global growth rate for late 1994 and early 1995 was approximately 5 ppbv yr^{-1} but with indications of further oscillations. The reason for these short- and long-term changes has not been conclusively identified but changing natural gas emissions leakage has been reported as a partial cause.

The latitudinal and seasonal NMHC data collected for this work furnish unique information that provides an excellent record of the effects from seasonal fluctuations in HO concentrations [*Blake and Rowland* 1986]. When combined with the vertical NMHC distributions measured during the various NASA and NSF aircraft field missions that we have taken part in since 1988, we can obtain good estimates of the atmospheric burden of these gases [*Blake et al.*, 1992, 1994, 1996; *N.J. Blake* 1996, 1997]. For example, average annual burdens have been calculated as 640 ± 60 pptv for ethane; 120 ± 30 pptv for ethyne; and 150 ± 40 pptv for propane from March 1994 through March 1995. This information allows source strengths and source latitudinal distributions to be derived, which in turn can provide useful information about sources such as biomass burning, which has a significant southern hemisphere component.

REFERENCES

Blake, D.R., and F.S. Rowland, Global atmospheric concentrations and source strength of ethane, *Nature*, *321*, 231-233, 1986.

Blake, D.R., and F.S. Rowland, Continuing world-wide increase in tropospheric methane, 1978 to 1987, *Science*, *239*, 1129-1131, 1988.

Blake, D.R., D.F. Hurst, T.W. Smith, Jr., W.J. Whipple, T-Y. Chen, N.J. Blake, and F.S. Rowland, Summertime measurements of selected nonmethane hydrocarbons in the arctic and subarctic during the 1988 Arctic Boundary Layer Experiment [ABLE-3A], *J. Geophys. Res.*, *97* , 16,559-16,588, 1992.

Blake, D.R., T.W. Smith, Jr., T.-Y. Chen, W.J. Whipple, and F.S. Rowland, Effects of biomass burning on summertime nonmethane hydrocarbon concentrations in the Canadian wetlands, *J. Geophys. Res., 99*, 1699-1719, 1994.

Blake, D.R., T.-Y. Chen, T.W. Smith Jr., C.J.-L. Wang, O.W. Wingenter, N.J. Blake, F. S. Rowland, and E.W. Mayer, Three-dimensional distribution of nonmethane hydrocarbons and halocarbons over the northwestern Pacific during the 1991 Pacific Exploratory Mission [PEM-West A], *J. Geophys. Res., 101*, 1763-1778, 1996.

Blake, N.J., D.R. Blake, B.C. Sive, T.-Y. Chen, F.S. Rowland, J.E. Collins Jr., G.W. Sachse, and B.E. Anderson, Biomass burning emissions and vertical distribution of atmospheric methyl halides and other reduced carbon gases in the South Atlantic region, *J. Geophys. Res.*, *101*, 24,151-24,164, 1996.

Blake, N.J., D. R. Blake, T.-Y. Chen, J.E. Collins Jr., G.W. Sachse, B.E. Anderson, and F.S. Rowland, Distribution and seasonality of selected hydrocarbons and halocarbons over the Western Pacific Basin during PEM-West A and PEM-West B, *J. Geophys. Res.*, *102*, 28,315-28,332, 1997.

Wang, C.J.-L., D. R. Blake, and F.S. Rowland, Seasonal variations in the atmospheric distribution in remote surface locations of a reactive chlorine compound, tetrachloroethylene [CCl_2=CCl_2], *Geophys. Res. Let., 22*, 1097-1100, 1994.

Ultrahigh Resolution Infrared Solar Spectroscopy From Mauna Loa Observatory: Update

SHELLE J. DAVID AND FRANK J. MURCRAY
University of Denver, Department of Physics, Denver, Colorado 80208

An ultrahigh resolution Fourier Transform InfraRed (FTIR) solar spectrometer was installed at Mauna Loa Observatory, Hawaii (MLO) in May 1991. It was operated routinely by observatory staff from November 1991 to October 1995. In September 1995 we installed a new FTIR system that is almost completely automated. This more versatile automated system allows us to: (1) change filters and setup conditions to cover more spectral regions on a routine basis; and (2) collect data 5 days a week by starting the instrument and turning the solar tracker on and off on a computer-controlled scheduled basis.

Data collected and analyzed is reported to the Network for Detection of Stratospheric Change (NDSC). The original NDSC instrument allowed us to monitor a limited number of molecules (HCl, O_3, N_2O, HNO_3, and CFC-22). The new automated system has allowed us to add molecules such as HF, CH_4, NO, NO_2, CO, HCN, C_2H_2, C_2H_6, and N_2 to the list of routinely monitored molecules.

On June 15, 1991, Mt. Pinatubo in the Philippines erupted, injecting large amounts of aerosol and gases into the stratosphere. Lidar measurements at MLO indicated the arrival of a finger of the Mt. Pinatubo volcanic plume above the station on July 1, 1991, followed by two other pulses in July and one in August.

Approximately 6 years of spectra have been analyzed for the total vertical column amount of atmospheric nitric acid vapor (HNO_2) above MLO. We see an effect of the volcanic aerosol on HNO_3 over MLO, specifically the HNO_3 column has slowly decreased since the start of our observations.

The HNO_3 total vertical column densities obtained between November 1991 and November 1997 are presented in Figure 1, fit with an exponential decay. From November 1991 to October 1995 our original instrument collected data 1 day a week, weather permitting, at sunrise. Starting September 1991 our new system collected data 5 days a week, sunrise and sunset. The HNO_3 data collected between September 1995 and November 1997 is presented in Figure 2. The larger quantity of data collected by the automated system weighed the fit of all the data, making it necessary to give average values for the sunrise and (or sunset) data approximately 1 day a week (Figure 1).

The highest HNO_3 total vertical column density was observed on December 4, 1991, at 8.8×10^{15} molecule cm^{-2}. The high HNO_3 column amounts at the end of 1991 coincide closely with the time of maximum aerosol loading deduced from SAGE II monthly mean measurements integrated from 15 to 35 km and 10°N to 20°N in latitude. Our fit indicated an increase in the HNO_3 column of 55% due to Pinatubo and a 1/e decay time of 0.75 year since the eruption. New Zealand observed systematically higher HNO_3 amounts between September 1991 and May 1993 that were typically 1.5 to 3.5×10^{15} cm^{-2} or 10 to 30%.

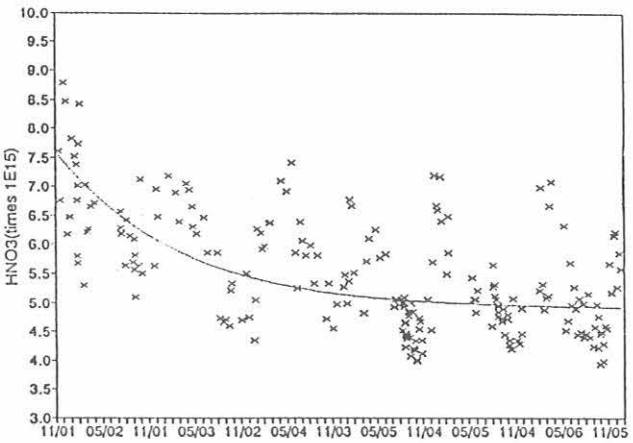

Fig. 1. The HNO_3 total vertical column densities obtained between November 1991 and November 1997.

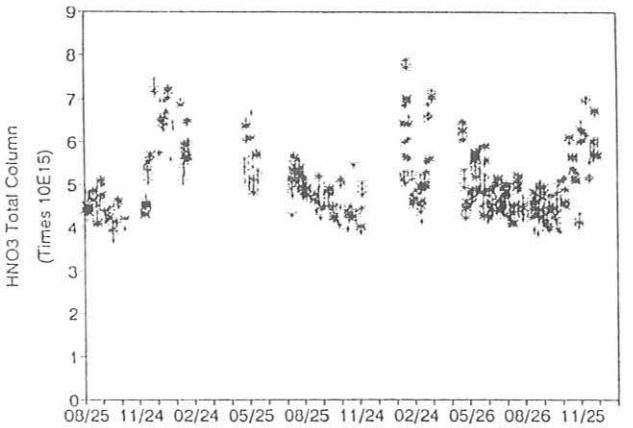

Fig. 2. The HNO_3 data collected between September 1995 and November 1997.

Polar Regions UV Spectroradiometer Monitoring Program: Observations in UV Irradiance at the South Pole and Barrow, Alaska

J. EHRAMJIAN, C.R. BOOTH, L.W. CABASUG, J.S. ROBERTSON, AND T. MESTECHKINA
Biospherical Instruments Inc., San Diego, California 92110-2621

INTRODUCTION

The antarctic ultraviolet (UV) spectroradiometer monitoring network was established by the U.S. National Science Foundation (NSF) in 1988 in response to predictions of increased UV radiation in the polar regions. The network consists of several automated, high resolution spectroradiometers; five are placed in strategic locations in Antarctica and the arctic, one is established in San Diego to collect data and serve as a training and testing facility (Table 1), and a portable system is used at instrument intercomparisons [*Seckmeyer et al.,* 1995, *Thompson et al.*1997, *Early et al.*1998]. Now in its 10th year of operation, the network continues to make measurements of UV spectral irradiance and provides a variety of biological dosage calculations of UV exposure. Biospherical Instruments Inc. (San Diego, California), under contract to Antarctica Support Associates (ASA), directed by NSF, is responsible for operating and maintaining the network and distributing data to the scientific community.

The spectroradiometers used in the system are Biospherical Instruments, Inc. Model SUV-100. Each instrument contains a diffusing irradiance collector, a double holographic grating monochromator, a photomultiplier tube (PMT), and calibration lamps. A vacuum-formed Teflon diffuser serves as an all-weather irradiance cosine collector. This collector is heated by the system to deter ice and snow accumulation. Tungsten-halogen and mercury vapor calibration lamps are used for daily automatic internal calibrations of both responsivity and wavelength registration. All instrument functions, calibration activities, and solar data acquisition are computer controlled. Further details on the spectroradiometers can be found in *Booth et al.* [1998].

UV RADIATION CLIMATE AT SPO AND BRW

Typical applications and observations that can be made from datasets produced from the network are presented. The South Pole Observatory, Antarctica (SPO) and the Barrow Observatory, Barrow, Alaska (BRW) network installations are in locations that also have CMDL facilities, and emphasis in this report is given to measurements made at these sites.

The SPO site is located away from the influence of mountains in a region of almost constant albedo. UV irradiance observations at SPO are well suited for atmospheric research because they are made in nearly constant high-albedo condition, further idealized by the air purity and high-altitude of the site. Cloud cover is also relatively infrequent and it is generally thin when it does occur. The very small hourly change in the solar zenith angle at SPO supports examination of changes in total column ozone (as estimated by UV irradiance) at 15-minute to 1-hour resolution [*Booth and Madronich*, 1993]. For example, a substantial *decrease* is seen in irradiance at 300 nm in late November 1993 (Figure 1(a)). Meanwhile, Total Ozone Mapping Spectrometer (TOMS Nimbus-7) data report a substantial *increase* in the 300 nm irradiance between November 15 and November 20, 1993.

BRW contrasts with SPO in that it is located where a significant change in surface albedo occurs due to both the springtime snowmelt [*Dutton and Endres*, 1991] and changes in sea ice coverage. Also, BRW experiences significant changes in incident irradiance during arctic storms. The contrast in irradiances between BRW and SPO is seen in Figure 1(b), which depicts the integrated local solar noontime irradiances over the UV-A spectrum (320-400 nm) from January 1993 through December 1997.

The integral of spectral irradiance from 298.507 to 303.03 nm is sensitive to changes in total ozone (and solar angle). A strong correlation between the ozone concentration and terrestrial UV irradiance is illustrated by the BRW 1997 example in Figure 2. Note the unusually low ozone over BRW in March 1997 [*Savage et al.*, 1997] as measured by the TOMS satellite. During these low ozone occurrences, the measured integral of spectral irradiance from 298.507 to 303.03 nm is the highest recorded in BRW

TABLE 1. Installation Sites

Site	Latitude	Longitude	Established	Location
South Pole	90.00°S	0°	Feb. 1988	ARO*
McMurdo	77.51°S	166.40°E	March 1988	Arrival Heights
Palmer	64.46°S	64.03°W	May 1988	T-5 Building
Ushuaia, Argentina	54.49°S	68.19°W	Nov. 1988	CADIC†
Barrow, Alaska	71.18°N	156.47°W	Dec. 1990	UIC-NARL‡
San Diego, California	32.45°N	117.11°W	Oct. 1992	Biospherical Instruments, Inc.

*ARO: Atmospheric Research Observatory, system relocated to this new, joint CMDL facility in January 1997.
†CADIC: Centro Austral de Investigaciones Cientificas, Argentina.
‡Ukpeagvik Inupiat Corporation-National Arctic Research Laboratory, Alaska.

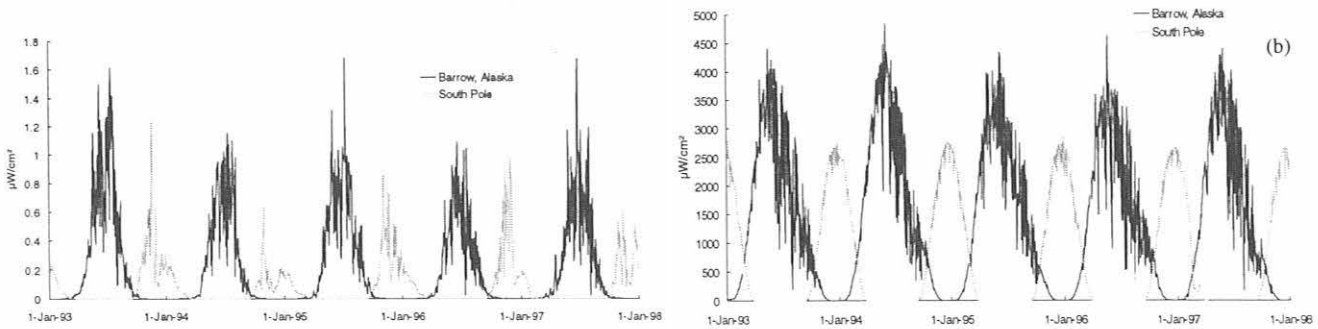

Fig. 1. Local solar noontime integrated spectral irradiance at Barrow, Alaska, and South Pole, Antarctica, from January 1993 through December 1997. The left panel shows the integrated irradiance around 300 nm (293.507-303.03 nm) and is contrasted with the right panel that illustrates the UF-A irradiance (320-400 nm). The higher irradiance values at Barrow are due to the higher sun elevation. Normally, irradiance at Barrow peaks in June, while irradiance at the South Pole peaks in December. Note that the 1997 South Pole and 1997 November-forward data are preliminary and subject to revision.

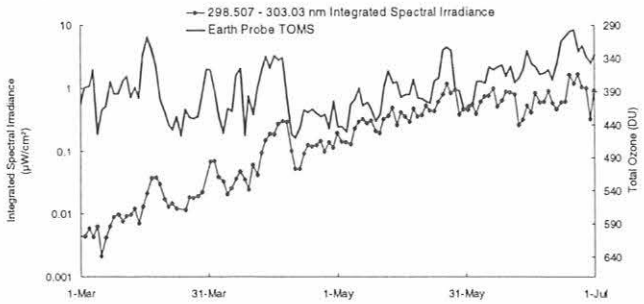

Fig. 2. Comparison of the 298.507-303.03 nm integrated spectral irradiance and TOMS total ozone measurements made at Barrow during Boreal spring 1997. Note that the left axis is a log scale to emphasize early "season" variation (lower solar zenith angles). The right axis is inverted to made the effect of decreasing ozone on increasing readily apparent.

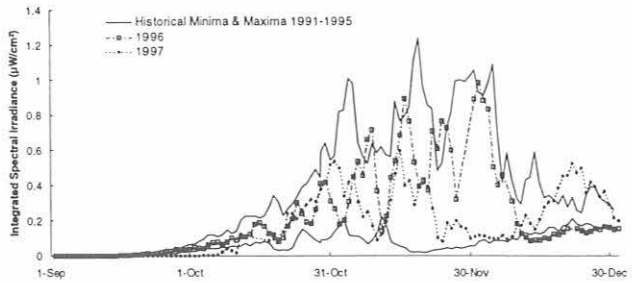

Fig. 3. Integrated 298.507 - 303.03 nm spectral irradiance at South Pole. The thin lines represent historical (1991-1995) minimum and maximum observations. The 1996 data are represented by open squares, and 1997 by filled diamonds.

for those dates. In 1996 relatively high UV levels at SPO were observed at typical times (from late October into December) during the season, with an early termination of influence of the "ozone hole" in mid-December (Figure 3). Lower overall UV levels occurred through most of the 1997 season, with some higher than typical UV levels late in the year (December), suggesting that the effects of ozone depletion lingered that year.

In addition to the production of a long time series of data, the high spectral resolution data are calculated into several spectral integrals and biological doses for the convenience of the researcher. These include several spectral integrals (UV-A_1, UV-A_2, UV-B_1, UV-B_2, Visible, etc.) and a number of dose weightings (Erythemal, Setlow, Caldwell, Hunter, etc.). A simple use of this data shows the maximum UV-B irradiances (290-320 nm) recorded at each site for 1990-1997 (Table 2.).

For the data of specific interest to the researcher, the effects of other environmental conditions can be verified using the other available integrals and doses. For instance, higher UV irradiances are sometimes observed in conditions of partial cloud cover than completely clear days, due to reflections off of cloud surfaces. This was San Diego that was verified using the Weighted Total Scene Irradiance integral [*Booth et al.*, 1998]. Another environmental factor particular to polar UV measurements is high albedo due to snow and ice coverage in addition to well-defined ozone depletion occurrences. An example of the high albedo effect on UV measurements can be seen in the Palmer Station UV-B maximum occurrence (Table 2.). It was known that ice coverage was heavy at the time of this observation.

TABLE 2. UV-B (290-320 nm) Maxima (μW/cm²)

Site	Maxima	Date	Solar Zenith Angle
Palmer	382.7	Dec. 2, 1990	44.0°
San Diego, CA	366.6	May 16, 1996	17.4°
Ushuaia, Argentina	350.5	Dec. 3, 1990	35.9°
McMurdo	236.4	Dec. 19, 1996	54.5°
Barrow, AK	199.5	June 1 1995	49.6°
South Pole	129.4	Dec. 3, 1992	67.8°

SUMMARY

High spectral resolution scanning UV spectroradiometers were established at six sites and are successfully providing multi-year data sets to the research community. Resulting data have been used to test radiative transfer models [*Lubin and Frederick*, 1992; *Smith et al.*, 1992], investigate radiation amplification [*Booth and Madronich*, 1993; *Madronich*, 1994], derive ozone concentrations [*Stamnes et al.*, 1992], investigate ozone depletion as a function of chlorofluorocarbons [*Rowland*, 1996], examine the biological impact of enhanced UV [*Cullen et al.*, 1992; *Anderson et al.*, 1993; *Benavides et al.*, 1993; *Holm-Hansen et al.*, 1993; *Madronich*, 1994; *Diaz et al.*, 1994; *Ladizesky et al.*, 1995; *Karentz et al.*, 1995, *Boucher et al.*, 1996] explore geographical differences in the UV [*Booth et al.*, 1995; *Diaz et al.*, 1994; *McKenzie et al.*, 1994; *Seckmeyer et al.*, 1995; *Bojkov et al.*, 1995], and evaluate long term trends [*Gurney*, 1998].

Data, referenced to both beginning- and end-of-season calibration constants are distributed on CD-ROM and are available to interested researchers. For more information, please contact Biospherical Instruments Inc., 5340 Riley Street, San Diego, CA 92110-2621, at www.biospherical.com for online data ordering information.

Acknowledgments. This research and monitoring activity was funded by contracts SCK-M-18914-02, SCE-M34578-01, and SFJ-M42664-01 from Antarctic Support Associates under the direction of Polly Penhale at the National Science Foundation, Office of Polar Programs. R. McPeters of the National Aeronautics and Space Administration (Goddard Space Flight Center) provided TOMS Total Ozone data for comparison purposes. Barrow (CMDL) operators are D. Endres and M. Gaylord. The Ukpeagvik Inupiat Corporation of Barrow provided assistance in the original installation. Operators at Palmer, South Pole and McMurdo were provided by ASA.

REFERENCES

Anderson, S., J. Hoffman, G. Wild, I. Bosch, and D. Karentz, Cytogenetic, cellular, and developmental responses in antarctic sea urchins (*Sterechinus neumayeri*) following laboratory ultraviolet-B and ambient solar radiation exposures, *Ant. J. U. S., 28(5)*, 115-116, 1993.

Benavides, H., L. Prado, S. Díaz, and J.I. Carreto, An exceptional bloom of *Alexandrium catenella* in the Beagle Channel, Argentina, Proc., 6th Int. Conf. on Toxic Marine Phytoplankton; Nantes, October 18-22, 1993.

Bojkov, R.D., V.E. Fioletov, and S.B. Díaz, The relationship between solar UV irradiance and total ozone from observations over southern Argentina, *Geophys. Res. Lett., 22(10)*, 1249-1252, 1995.

Booth, C.R., T.B. Lucas, T. Mestechkina, J. Shmidt, and J. Tusson, High resolution UV spectral irradiance monitoring program - contrasts in UV exposure in Antarctica and the Americas, *Ant. J. U. S., 30(5)*, 318-320, 1995.

Booth, C., J. Ehramjian,, T. Mestechkina, L. Cabasug, J. Robertson, J. Tusson IV, *NSF Polar Programs UV Spectroradiometer Network 1995-97 Operations Report*, 241 pp., Biospherical Instruments Inc., San Diego, CA, 1998.

Booth, C.R., and S. Madronich, Radiation amplification factors: Improved formulation accounts for large increases in ultraviolet radiation associated with Antarctic ozone depletion, in *Antarctic Research Series*, edited by C.S. Weiler and P.A. Penhale, *62, 39-42*, 1993.

Boucher, N.P., and B.B. Prézelin, Spectral modeling of UV inhibition of in situ antarctic primary production using a field-derived biological weighting function, *Photochem. Photobio., 64(3)*, 407-418, 1996.

Cullen, J.C., P.J. Neale, and M.P. Lesser, Biological weighting function for the inhibition of phytoplankton photosynthesis by ultraviolet radiation, *Science, 258*, 646-650, 1992.

Díaz, S.B., C.R. Booth, T.B. Lucas, and I. Smolskaia, Effects of ozone depletion on irradiances and biological doses over Ushuaia, *Arch. Hydrobiol. Beih: Ergebn. Limnol., 43*, 115-122, 1994.

Diaz, S.B., J.E. Frederick, I. Smolskaia, W. Esposito, T.B. Lucas, and C.R. Booth, Ultraviolet solar radiation in the high latitudes of South America, *Photochem. Photobiol., 60(4)*, 356-362, 1994.

Dutton, E.G., and D.J. Endres, Date of snowmelt at Barrow, Alaska, U.S.A., *Arc. Alp. Res., 23(1)*, 115-119, 1991.

Early, A., et al., The 1995 North American interagency intercomparison of ultraviolet monitoring spectroradiometers, *J. Res. Natl. Inst. Stand. Technol., 103(1)*, p. 15, 1998.

Gurney, K.R., Evidence for increasing ultraviolet irradiance at Point Barrow, Alaska, *Geophys. Res. Let., 25(6)*, 903-906, 1998.

Holm-Hansen, O., D. Lubin, and E.W. Helbling, Ultraviolet radiation and its effects on organisms in aquatic environments, in *Environmental UR Photobiology*, edited by A.R. Young et al., pp. 379-425, Plenum Press, New York, 1993.

Karentz, D., and H.J. Spero, Response of a natural Phaeocystis population to ambient fluctuations of UVB radiation caused by antarctic ozone depletion, *J. Plankton Res., 17*, 1771-1789, 1995.

Ladizesky, M., Z. Lu, B. Oliveri, N. San Roman, S. Díaz, M.E. Holick, and C. Mautalen, Solar ultraviolet B radiation and photoproduction of vitamin D_3 in central and southern areas of Argentina, *J. Bone Miner. Res., 10(4)*, 545-549, 1995.

Lubin, D., and J.E. Frederick, Observations of ozone and cloud properties from NSF ultraviolet monitor measurements at Palmer Station, Antarctica, *Ant. J. U. S., 25(5)*, 241-242, 1992.

Madronich, S., Increases in biologically damaging UV-B radiation due to stratospheric ozone reductions: A brief review. *Arch. Hydrobiol. Beih: Ergebn. Limnol., 43*, 17-30, 1994.

McKenzie, R.L., M. Blumthaler, C.R. Booth, S.B. Diaz, J.E. Frederick, T. Ito, S. Madronich, and G. Seckmeyer, Surface Ultraviolet Radiation, in *Scientific Assessment of Ozone Depletion: 1994, World Meteorological Organization Global Ozone Research Monitoring Project, 37*, 9.1-9.22, 1994.

Rowland, F.S., Stratospheric ozone depletion by chlorofluorocarbons, *Angew. Chem. Int. Ed. Engl., 35*, 1786-1798, 1996.

Savage, D., Kenitzer, A., McGehan, B., Low ozone measured over North Pole, *NASA Press Release 97-64*, (ftp://ftp.hq.nasa.gov/pub/pao/pressrel/1997/97-064.txt.), 1997.

Seckmeyer, G., et al., Geographical differences in the UV measured by intercompared spectroradiometers, *Geophys. Res. Lett., 22(14)*, 1889-1892, 1995.

Smith, R.C., Z. Wan, and K.S. Baker, Ozone depletion in Antarctica: Modeling its effect under clear-sky conditions, *J. Geophys. Res., 97*, 7383-7397, 1992.

Stamnes, K., Z. Jin, J. Slusser, C.R. Booth and T.B. Lucas, Several-fold enhancement of biologically effective ultraviolet radiation levels at McMurdo Station, Antarctica, during the 1990 ozone hole, *Geophys. Res. Lett., 19*, 1013-1017. 1992.

Thompson, A., et al., The 1994 North American interagency intercomparison of ultraviolet monitoring spectroradiometers, *J. Res. Natl. Inst. Stand. Technol., 102(3)*, 279, 1997.

The National Satellite Testbed Receiver at Mauna Loa

PER ENGE
Aeronautics and Astronautics, Stanford University, California 94305-4035

In time, the Global Positioning System (GPS) will be used for a wide variety of aircraft operations. These will include flight over oceanic routes and en route through our domestic airspace. GPS will also be used in the so-called terminal areas where flights converge in crowded metropolitan airspaces. Examples of heavily used terminal areas include the New York-Newark and the San Francisco Bay areas with their multiplicity of airports. GPS will be used on the final approach to airports; these operations demand the greatest safety and reliability. Airport approach applications include: nonprecision approach where GPS will be used solely for horizontal positioning and precision approach where GPS will be used for both horizontal and vertical position fixing. To serve all of these applications, GPS must be augmented to meet stringent requirements with respect to accuracy, integrity, continuity, and time availability. The Wide Area Augmentation System (WAAS) is currently being developed by the Federal Aviation Administration (FAA), because it will allow satellite navigation to be used as the primary means of navigation for aircraft over the United States.

The WAAS will use a ground network to develop differential corrections for the errors that limit the accuracy of SPS. The ground network includes a geographically distributed set of GPS receivers at precisely known locations. To enable the Category I precision approach of aircraft, this network must have receivers throughout the coverage area with spacings of approximately 600 km. These reference receivers send raw GPS measurements back to master control stations.

The master stations use the reference observations to develop two corrections for each monitored satellite. One correction is for the satellite clock and the other is a three-dimensional correction for the satellite location. The master station also estimates a set of corrections for the ionospheric delays. All of these corrections will be included on the WAAS broadcast and will improve GPS position accuracy from 100 m to approximately 4 m. With this vertical accuracy, WAAS will provide vertical guidance down to decision heights of 60 to 106 m.

Other countries are deploying similar wide-area augmentation systems. The Europeans are installing the European Geostationary Navigation Overlay System (EGNOS) and the Japanese are launching the Multitransport Satellite Augmentation System (MSAS) for their airspaces. This international network will provide the primary means of navigation worldwide.

The FAA has deployed a prototype of the WAAS. This system is known as the National Satellite Testbed (NSTB) and is currently being used to explore issues associated with the international use of WAAS. These issues include ionospheric effects on low and high latitude users of satellite navigation. They also include data exchange between neighboring wide-area augmentation systems such as the WAAS and the Japanese system. The receiver at the Mauna Loa Observatory, Hawaii, is an important part of this research effort.

Measurements of Short-Period Magnetic Field Data

KANJI HAYASHI
Department of Earth and Planetary Physics, The University of Tokyo, Bunkyo, 113-0033, Japan

Acquisition of short-period magnetic field data at the Pt. Barrow, Alaska, CMDL site was carried out normally throughout 1996-1997. Stable operation of the search coil magnetometer was achieved after a replacement of the data logging unit. Direct communication to the site using E-mail has also helped in quick response time to identify and fix problems.

Data up to 1.8 GB were regularly delivered by FedEx, retrieved, and stored as Unix files. Checking quick-look analysis data, all data are recorded normal. A general tendency over the years of activity of short-period geomagnetic pulsations has declined as the solar activity went into the minimum phase. The data set obtained at the Barrow site has been helpful to watch the state of short-period geomagnetic disturbances at the west-north end of our magnetometer network extending into the polar region of North America. Data requests are responded to through our web page at hpep3.geoph.s.u-tokyo.ac.jp. Some testing analysis will be prepared from the home page. This program is expected to continue until the end of this century.

Total Nitrate, NSS, and MSA Variation at Mauna Loa

B.J. HUEBERT, C.R. ADAMS, AND L. ZHUANG
Department of Oceanography, University of Hawaii, Honolulu 96822

INTRODUCTION

Much of the NO and NO_2 emitted into the atmosphere is converted to nitric acid vapor or aerosol nitrate before being removed by dry or wet deposition. This conversion to nitrate is largely complete within a few days of the odd-nitrogen's emission, so that in remote areas such as at the Mauna Loa Observatory, Hawaii (MLO) the total nitrate concentration (vapor plus aerosol) represents a fair estimate of the total odd-nitrogen concentration [*Atlas et al.*, 1992].

With support from the National Science Foundation (NSF), we have measured nitrate concentrations at MLO for several years to help identify the important sources of odd-nitrogen compounds in remote parts of the globe. In collaboration with the MLO staff, we now measure total nitrate every night from the walkup tower . We have also begun measuring methanesulfonate (MSA) and calcium aerosol. For the last decade we have also measured non-sea salt sulfate (NSS) at MLO but since the two active volcanoes on Hawaii emit sulfur dioxide that rapidly forms NSS, we have never tried to interpret it. However, this record is the only decade-long record of free tropospheric (FT) NSS in existence. Therefore, we have developed a method for identifying samples that may have been influenced by the volcanoes so that we can sort out a record of clean free tropospheric NSS. That record is now in use by seven modeling groups around the world as a test of the ability of global chemical transport models to predict FT concentrations of NSS for climate modeling.

MATERIALS AND METHODS

We use a Teflon/nylon filter pack method for collecting atmospheric nitrate. Since August 1988 one filter has been exposed each night from 2000 LST to 0800 LST. Filters are returned to the University of Hawaii for extraction and analysis by ion chromatography.

RESULTS AND DISCUSSION

During our intermittent MLO sampling prior to September 1988, we observed a sharp maximum in nitric acid and aerosol nitrate concentrations in the summer. The search for an explanation for this maximum continues to stimulate our science. The daily total nitrate values for 1996-1997 are plotted in Figure 1. The lowest sustained concentrations are still evident in the winter, with a mix of high-concentration events and cleaner periods in the spring and late summer.

Figure 2 shows monthly averages of 2000 LST to 0800 LST total nitrate concentrations from September 1988 to December 1997. The 1993 data represent the lowest (defendable) concentrations we have observed during our sampling at MLO.

The concentration of total nitrate at MLO is to a large extent controlled by precipitation scavenging of soluble material during transport from the continents [*Lee et al.*, 1993, 1994] so this interannual variability may be an indicator of changes in large-scale precipitation patterns. The apparently-monotonic decrease in summertime total nitrate from 1988 through 1991 suggests that a cyclic process, such as the southern oscillation, may be reflected in this record. It is certainly reasonable that the transport of continental materials like mineral aerosol and fixed nitrogen (which can be limiting nutrients in certain parts of the Pacific) should be sensitive to changes in large-scale atmospheric circulation patterns. Clearly we need to identify the climatological differences that cause this dramatic change in the annual cycle of nitrate from one year to the next since they may have impacts on phenomena as diverse as marine biological productivity and the earth's radiation budget.

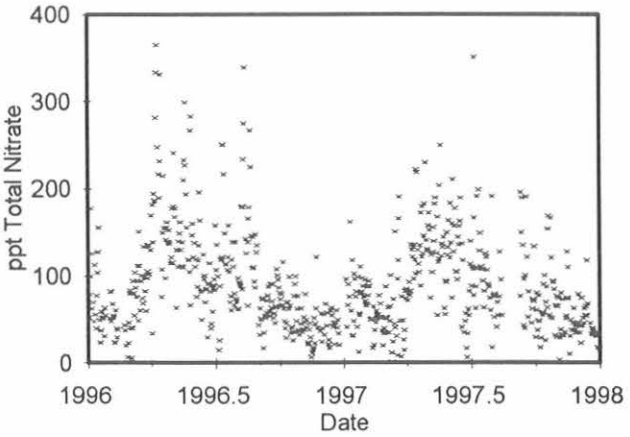

Fig. 1. Nightly concentrations of total nitrate in 1996-1997.

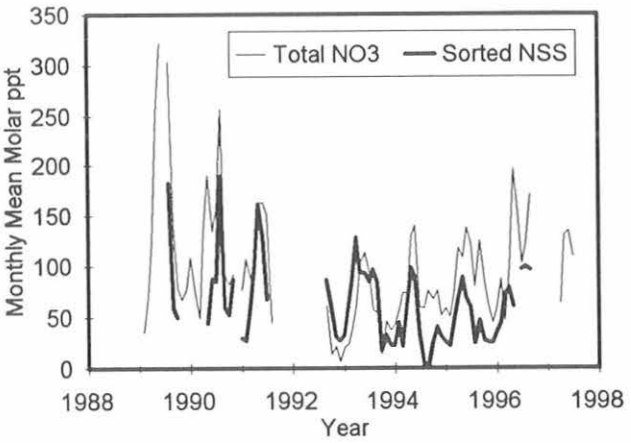

Fig. 2. Monthly average total (aerosol plus vapor) nitrate and NSS versus time.

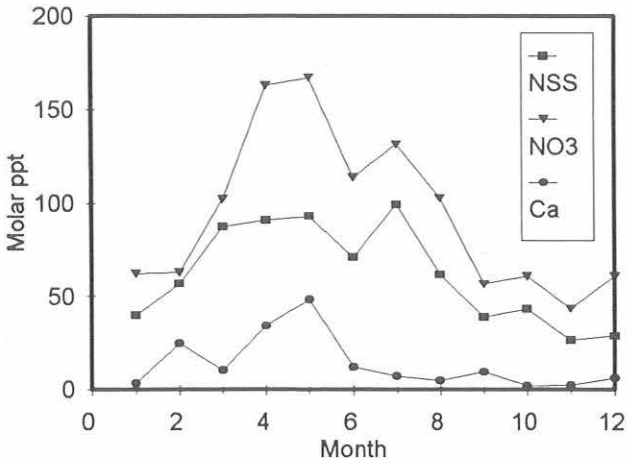

Fig. 3. Decade-mean of monthly average NSS and NO_3^- with 2 years of Ca means.

In February of 1995 we began to analyze our filter samples for MSA, since MSA is an indicator of dimethylsulfide (DMS) oxidation [*Huebert et al.*, 1996]. We are interested in the potential that DMS oxidation in the free troposphere may be responsible for much of the MSA (and some of the sulfate) found in ice-cores. The MSA data is different from either nitrate or NSS; while it varies considerably from day to day and individual months may be a bit higher or lower, the (multi-year) mean of monthly average MSA shows no annual variability. MSA averages 17.7 ± 2.5 mm (0.7 ± 0.1 inch) every month of the year. It is clear from the data that the MSA we see is not due to boundary-layer contamination of our samples since it is rarely accompanied by Cl or Na that are clear indicators of boundary-layer air.

The FT values of NSS and Ca show the same seasonality as nitrate (Figure 3). The springtime maximum suggests that Asia may be the source of much of this elevated NSS. Calcium also peaks in the spring due to the input of Asian dust.

Ongoing Research

We are continuing our nightly sampling from the tower with the help of the MLO staff. Although equipment failures and analytical problems unavoidably cause lapses in the data, a very interesting record is emerging. We intend to continue this total nitrate data record in the hopes of identifying those factors that control the form and the range of its annual cycle. We hope in the near future to add sensitive SO_2 measurements to the NSS and MSA record.

References

Atlas, E. L., B. A. Ridley, G. Hübler, M. A. Carroll, D. D. Montzka, B. Huebert, R. B. Norton, J. Walega, F. Grahek, and S. Schauffler, Partitioning and budget of NO_y species during MLOPEX, *J. Geophys. Res.*, *97*, 10,449-10,462, 1992.

Huebert, B. J., D. J. Wylie, L. Zhuang, and J. A. Heath, Production and loss of methanesulfonate and non-sea salt sulfate in the equatorial Pacific marine boundary layer, *Geophys. Res. Lett.*, *23*, 737-740, 1996.

Lee, G., L. Zhuang, B. J. Huebert, and T. P. Meyers, Concentration Gradients and Dry Deposition of Nitric Acid Vapor at Mauna Loa Observatory, Hawaii, *J. Geophys. Res.*, *98*, 12,661-12,671, 1993.

Lee, G., J. T. Merrill, and B. J. Huebert, Variation of Free Tropospheric Total Nitrate at Mauna Loa Observatory, Hawaii, *J. Geophys. Res.*, *99*, 12,821-12,831, 1994.

Monthly Average Surface Air Concentrations of ^{210}Pb and ^{7}Be at BRW, MLO, SMO, and SPO

JOHN KADA
Environmental Measurements Laboratory, U.S. Department of Energy, New York, New York 10014-3621

INTRODUCTION

High volume bulk aerosol samples have been collected for many years by CMDL personnel at the Barrow Observatory, Alaska (BRW), the Mauna Loa Observatory, Hawaii (MLO), the Samoa Observatory, American Samoa (SMO), and the South Pole Observatory, Antarctica (SPO) for the Surface Air Sampling Program (SASP), a global network of aerosol sampling sites created to determine the global distribution of artificial radionuclides released into the atmosphere by nuclear weapons tests or nuclear accidents. This network has also produced the bulk of the available data on temporal and spatial trends in the worldwide distribution of the natural radionuclides ^{7}Be and ^{210}Pb. The atmospheric production rate of ^{7}Be, a cosmogenic nuclide, increases with altitude, and thus ^{7}Be is generally considered to be a tracer of upper tropospheric and stratospheric airmasses; ^{210}Pb is a decay product of ^{222}Rn gas emanating from continental soils and thus is generally considered to be a tracer of continental airmasses. In this report we summarize data on seasonal trends in surface air ^{7}Be and ^{210}Pb concentrations at BRW, MLO, SMP, and SPO.

MATERIALS AND METHODS

Aerosol samplers drawing about 1700 standard cubic meters of air per day through polypropylene filters are in continuous operation at each site. Four samples are collected each month and mailed to our laboratory for analysis. A portion is cut from each filter and assembled into a monthly composite sample which is then subjected to gamma spectroscopic analysis. Gamma spectrometers used at our laboratory in the 1970s and 1980s were not capable of measuring ^{210}Pb, thus a considerably larger data set exists for surface air concentrations of ^{7}Be than for ^{210}Pb. Analysis for ^{210}Pb began between 1981 and 1983 at BRW, MLO, and SPO, and in 1989 at SMO; ^{7}Be analyses began in 1971 at MLO and SPO, in 1976 at BRW and in 1977 at SMO.

RESULTS

Figure 1 shows average monthly ^{7}Be and ^{210}Pb surface air concentrations at BRW, MLO, SMO, and SPO. Seasonal variations in one or both nuclides are apparent at all four sites reflecting a combination of seasonal variations in vertical mixing rates, lateral transport, and aerosol scavenging rates specific to each site. At BRW, concentrations of both ^{7}Be and ^{210}Pb exhibit clear seasonal variations. The timing of these variations suggests that the processes responsible for the arctic haze phenomenon, i.e., seasonal variations in transport from Eurasia [*Harris and Kahl*, 1994] and increased aerosol scavenging rates during the arctic summer [*Barrie et al.*, 1981], play an important role in the seasonal cycles of ^{210}Pb and ^{7}Be.

At MLO there is no clear seasonal variation in ^{7}Be concentration, however, ^{210}Pb concentrations exhibit a seasonal high from March through June coinciding with the Asian dust season [*Parrington et al.*, 1983]. The increase in ^{210}Pb concentration at MLO most likely results from the same process responsible for the influx of Asian dust: the lofting of surface air to high altitudes over Asia followed by rapid transport through the free troposphere by strong westerlies prevalent at this time of the year.

At SMO ^{7}Be and ^{210}Pb concentrations both exhibit seasonal cycles. Concentrations of both nuclides are relatively low from January through April, but the season of high ^{210}Pb concentration tends to be shorter and tends to be centered later in the year compared to the season of high ^{7}Be concentration. Seasonal variations in transport of air originating at high altitudes explain some of the seasonal variability in surface ozone concentrations [*Harris and Oltmans*, 1997] and could likewise explain some of the seasonal variability in ^{7}Be. It has also been suggested that seasonal variations in precipitation scavenging plays a role in the seasonal cycle of ^{7}Be at SMO [*Feeley*, 1989]; such variations could cause seasonal variations in ^{210}Pb at SMO as well.

At SPO ^{7}Be and ^{210}Pb concentrations exhibit similar seasonal cycles with higher concentrations of both nuclides occurring during the austral summer months. This matches the observed seasonality in crustal element concentrations at the South Pole which are thought to arise from enhanced seasonal transport of lower latitude airmasses through the midtroposphere [*Tuncel et al.*, 1989].

Acknowledgment. We wish to thank the NOAA CMDL staff at BRW, MLO, SMO, and SPO for the collection of air filter samples for SASP.

REFERENCES

Barrie L.A., R.M. Hoff, and S.M Daggupaty, The influence of midlatitudinal pollution sources on haze in the Canadian Arctic. *Atmos. Environ.*, *15*, 1407-1419, 1981.

Feely, H.W., R.J. Larsen, and C.G. Sanderson, Factors that cause seasonal variations in berylium-7 concentrations in surface air, *J. Environ. Radioact.*, *9*, 223-249, 1989.

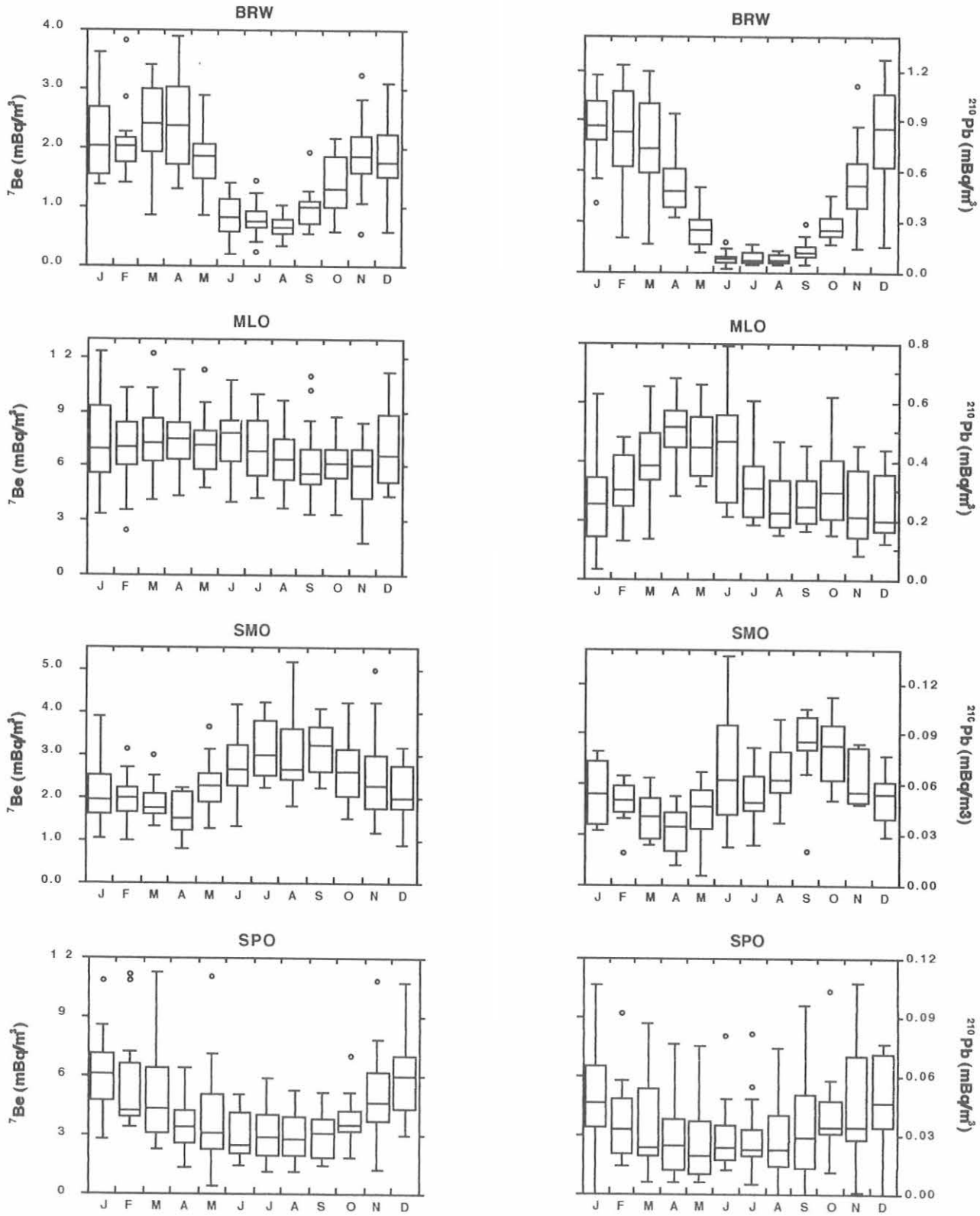

Fig. 1. Box plots of ^{7}Be and ^{210}Pb concentrations in surface air at Barrow, Mauna Loa, Samoa and the South Pole grouped by month. Each box shows the range in which the central 50% of the data fall. The box borders show the first and third quartiles and the crossbar shows the median; values exceeding the quartile values by more than factor of 1.5, the interquartile distance, are marked as circles.

Harris J.M., and J.D.W. Kahl, Analysis of 10 day isentropic flow patterns for Barrow, Alaska: 1985-1992. *J. Geophys. Res.*, *99*, 25,845-25,855, 1994.

Harris, J.M., and S.J. Oltmans, Variations in tropical ozone related to transport at Samoa, *J. Geophys. Res., 102*, 8781-8791, 1997.

Parrington J.R., W.H. Zoller, and N.K. Aras, Asian dust: Seasonal transport to the Hawaiian Islands, *Science, 220*, 195-197, 1983.

Tuncel G., N.K. Aras, and W.H. Zoller, Temporal variations and sources of elements in the South Pole atmosphere 1. Nonenriched and moderately enriched elements, *J. Geophys. Res.*, *94*, 13,025-13,038, 1989.

Operation of Brewer Instruments at Mauna Loa Observatory

J.B. KERR
Atmospheric Environment Service, Environment Canada, Downsview, Ontario Canada M3H 5T4

Brewer instrument No. 009 was installed at the Mauna Loa Observatory (MLO) on March 24, 1997, by the Atmospheric Environment Service (AES) of Environment Canada (EC). The instrument measures total ozone, the vertical profile of ozone using the Umkehr method, and UV-B radiation. An all-sky camera that records digital images of the sky every 10 minutes is mounted in the top of the instrument. These images provide information about sky conditions to assist in the data analysis, particularly the UV-B radiation.

The instrument was initially located on a concrete pad to the southeast of the present site of the Network for Detection of Stratospheric Change (NDSC) building. Supporting computer equipment for the instrument was inside the dome to the east of the NDSC building. Software operations for the instrument, such as programming and data retrieval, are carried out remotely by telephone and the Internet from AES in Toronto. On-site operations, such as hardware maintenance and routine checks, are carried out by the staff at MLO.

The instrument operated nearly flawlessly until August 15, 1997, when the observatory took a direct hit from lightning. A surge from the lightning damaged the control computer, probably through the telephone port, but left the Brewer instrument undamaged. Observations resumed on November 18, 1997, when the computer was replaced and the instrument was relocated to the deck of the NDSC building. Double monochromator Brewer instrument (No. 119) was then installed adjacent to No. 009 on the NDSC deck. Since then both instruments have been operating satisfactorily.

OZONE MEASUREMENTS

Between 20 and 30 direct sun total ozone measurements are attempted each day depending on the time of year, and a total of 5045 attempts were made during the 188 days that Brewer instrument No. 009 operated in 1997. Of these attempts, 3905 (77.4%) were of good quality and the remaining ones were usually influenced by clouds. There were only 2 days of the 188 when no good quality direct sun measurements were obtained.

Extraterrestrial calibrations for the Brewer (and Dobson) reference instruments are regularly carried out at MLO. These calibrations require several days (about 1 week) of direct sun measurements made on clear days (or half days) with airmass values between 1 and 3. The extraterrestrial calibration is the extrapolation of the daily data sets to zero airmass [see *Kerr et al.*, 1988]. The quality control on data from an instrument operating permanently at MLO is enhanced by the extraterrestrial calibration which is measured every day, so the stability of the instrument is readily monitored and the calibration can be adjusted if necessary. Figure 1 shows the record of daily mean total ozone values measured during 1997.

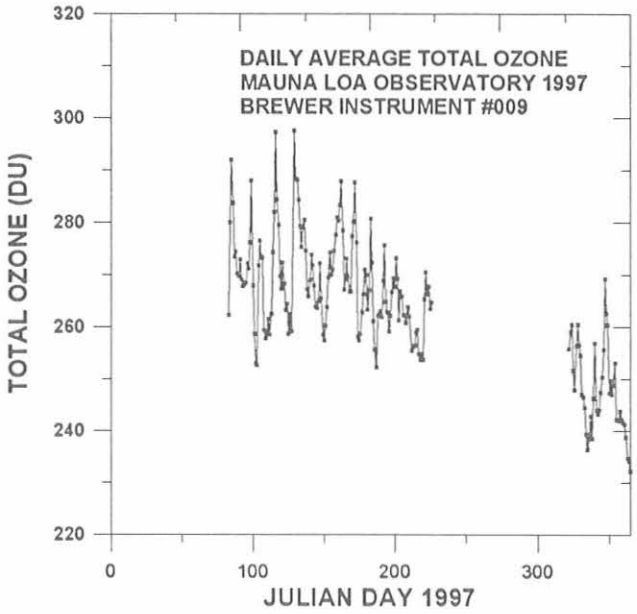

Fig. 1. Record of direct sun total ozone measurements made with Brewer instrument No. 009 at MLO during 1997.

UV-B MEASUREMENTS

Spectral measurements of UV-B global irradiance are made throughout each day two or three times per hour [*Kerr and McElroy*, 1993]. A total of 4151 spectra were made with instrument No. 009 in 1997. The data have been processed with the standard World Ozone and Ultraviolet radiation Data Centre (WOUDC) processing and quality assurance procedures [*Wardle et al.*, 1996]. The measurements are generally of high quality and about 5% of the scans have been flagged to show variability during the course of the scan, mostly due to changing cloud conditions.

Examples of analyzed UV data are shown in Figures 2 and 3 which summarize results for the entire year as functions of time of day and time of year. Figure 3 shows irradiance data in the UV-A at 324 nm, a wavelength that is negligibly absorbed by ozone. Here the irradiance values are given as the percentage of clear sky values derived from a statistical analysis of data from seven sites at lower altitude [*Fioletov et al.*, 1997]. The red and purple colors indicate clear sky conditions and the banded darker colors are for days when clouds were present. Note that most mornings are clear and clouds occur more often later in the day. Another feature seen in Figure 2 is that the sky often becomes brighter (increasing from ~100% to ~110%) near 1100 LST. This may be the result of the buildup of convective clouds below the MLO altitude causing an increase in upward scattered

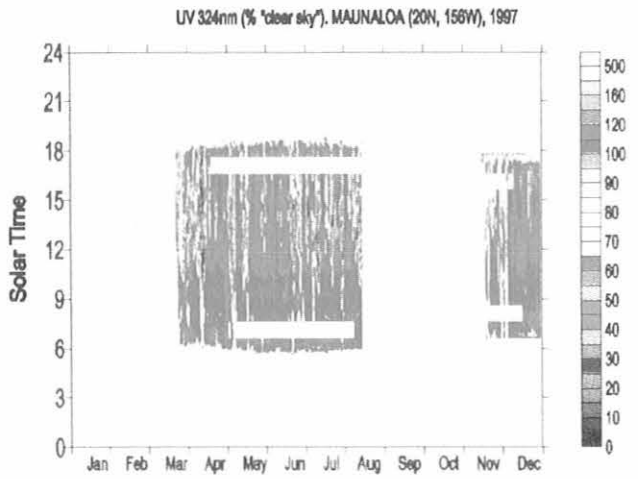

Fig. 2. Summary of UV global irradiance measurements made at 324 nm as functions of time of day and time of year for 1997. Intensity measurements are given as the percentage of clear sky values. Radiation at this wavelength is negligibly affected by ozone.

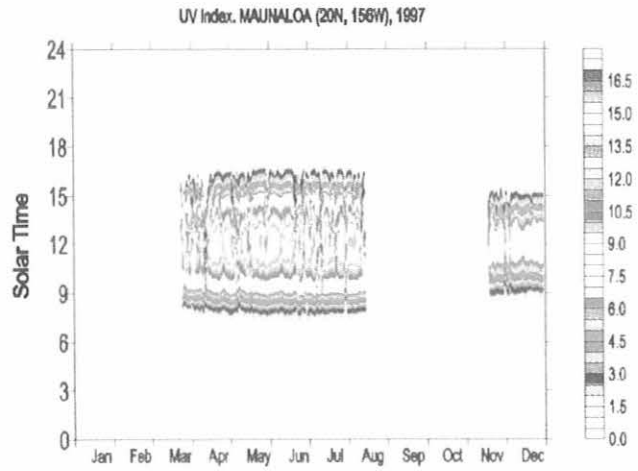

Fig. 3. Summary of measured UV Index as functions of time of day and time of year for 1997. Maximum values at noon in summer are near 16. This value is significantly more than typical values seen at mid-latitudes in summer (about 10).

radiation (similar to the enhancements caused by increased surface albedo reported in *Wardle et al.*, 1997).

Figure 3 summarizes the UV Index values as functions of time of day and time of year. At noon during the summer when the sun is directly overhead, UV Index values are typically 15 or 16. These values are significantly higher than typical summertime values of about 10 seen at midlatitudes and are due to high sun angle, clear skies, high altitude, and relatively low ozone values.

Sky Images

Figure 4 shows examples of images made by the all-sky camera mounted on Brewer instrument No. 009. The dark band from the center to the right of the images is a shade to

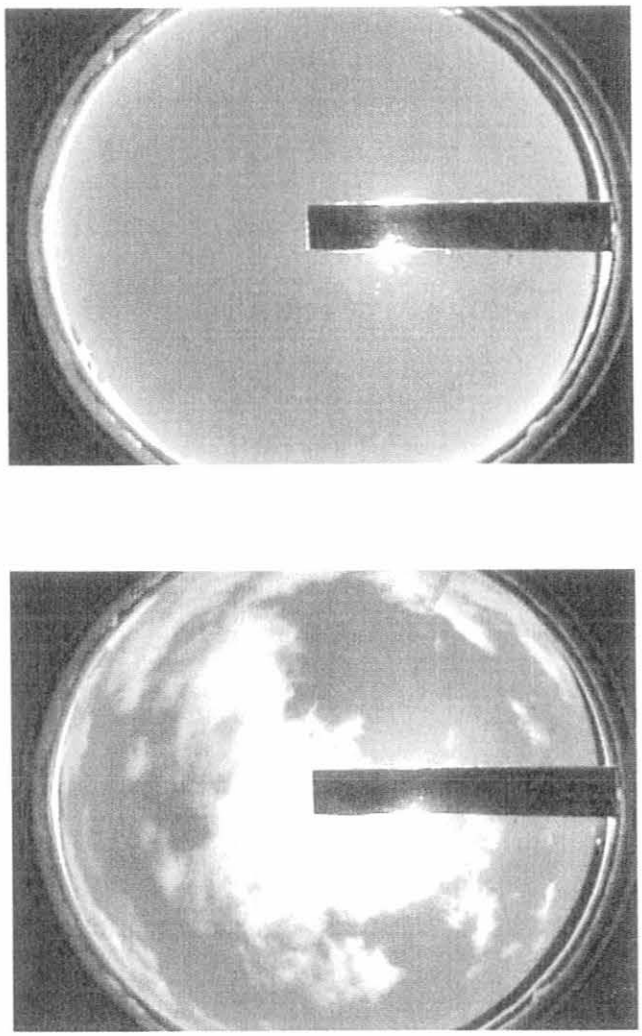

Fig. 4. Example of all sky images made with a video camera mounted on the Brewer instrument showing clear (top) and partly cloudy (bottom) situations. The Brewer instrument is normally aligned so that the shade band protects the camera from the sun and features on the horizon move clockwise around the perimeter of the image during the day. The record of sky conditions are useful for interpreting ozone and UV-B data.

prevent the sun's bright image from saturating and degrading the camera sensor. Since the Brewer instrument (and camera) follow the sun in azimuth, the shade band is always aligned with the sun. The sun rises at the eastern horizon at the right of the image behind the band. Until solar noon the sun moves behind the band toward the center of the image. After noon the sun moves back toward the right of the image until is sets on the western horizon. Throughout the day features on the horizon rotate clockwise around the perimeter of image.

The top image in Figure 1 was taken at 1147 (local standard time (LST) on March 30, 1998, when the sky was cloudless. The tower to the west of the observatory is seen on the horizon in the upper left of the image. The top of

Brewer No. 119 is seen at the lower left of the image. The bottom image in Figure 1 was taken at 1325 LST on March 20, 1998, showing convective up-slope clouds that developed in the early afternoon. At this tower is now in the upper right of the image. All images for 1997 have been archived on CD disks and are available from AES on request.

REFERENCES

Fioletov, V.E., J.B. Kerr, and D.I. Wardle, The relationship between total ozone and spectral UV irradiance from Brewer observations and its use for derivation of total ozone from UV measurements, *Geophys. Res. Lett., 24*, 2997-3000, 1997.

Kerr, J.B., I.A. Asbridge, and W.F.J. Evans, Intercomparison of total ozone measured by the Brewer and Dobson spectrophotometers at Toronto, *J. Geophys. Res., 93*, 11,129-11,140, 1988.

Kerr, J.B., and C.T. McElroy, Evidence for large upward trends of ultraviolet-B radiation linked to ozone depletion, *Science, 262*, 1032-1034, 1993.

Wardle, D.I., E.W. Hare, D.V. Barton, and C.T. McElroy, The World Ozone and Ultraviolet radiation Data Centre - content and submission, *Proc. 18th Quad. Ozone Symp.*, L'Aquila, Italy, 1996.

Wardle, D.I., J.B. Kerr, C.T. McElroy, and D.R. Francis (Eds.), Ozone science: A Canadian perspective on the changing ozone layer, *Rep. CARD 97-3*, 19 pp, Environ. Canada Int., Downsview, Ontario, 1997.

The Global Distribution of Atmospheric Methyl Chloride

M. A. K. KHALIL
Department of Physics, Portland State University, Portland, Oregon 97207-0751

R. A. RASMUSSEN
Department of Environmental Sciences and Engineering, Oregon Graduate Institute, Portland 97291

INTRODUCTION

Methyl chloride is the most abundant chlorine containing gas in the Earth's atmosphere. It is also the largest natural source of chlorine to the stratosphere. As such there is considerable interest in its global cycle which includes its sources, sinks, and trends.

We have taken measurements of methyl chloride and other gases at the polar, middle, and tropical latitudes of both hemispheres. The sites are Pt. Barrow, Alaska (71.16°N, 156.5°W); Cape Meares, Oregon (45.5°N, 124°W); Cape Kumukahi and Mauna Loa, Hawaii (19.3°N, 154.5°W); Cape Matatula, Samoa (14.1°S, 170.6°W); Cape Grim, Tasmania (42°S, 145°E); and Antarctica (South Pole at 90°S and Palmer Station at 65.46°S, 64.05°W). Most of these sites are also part of the NOAA-CMDL global monitoring network. Our present data extend back to 1981, but not all sites were sampled until 1984 or so. In this paper we will tabulate annual average concentrations of methyl chloride (1981-1996) and discuss the salient features of the data.

METHODS

Samples were collected in 0.8-L internally electropolished stainless steel canisters. These containers preserve the concentrations of most trace gases for periods much longer than the time between sample collection and analysis [*Edgerton*, 1985]. This time, between sampling and analysis, varies from site to site; it is as short as a few days for Cape Meares and can be as long as 6-9 months for samples from Antarctica. Triplicate samples are collected once per week. The samples are analyzed using a gas chromatograph equipped with an electron capture detector as described in earlier publications [*Rasmussen and Khalil*, 1980; *Rasmussen et al.*, 1980].

RESULTS

The data obtained are given in Table 1 as annual averages. These data have some noteworthy features that we will discuss next. The first is that concentrations in the tropical latitudes are higher than at middle and polar latitudes. This latitudinal bump is on average about 37 pptv or about 6% (tropics to pole difference). It was also observed in earlier work but has not been seen in certain experiments on board ship cruises or aircraft flights. One reason is that there are seasonal variations in the concentrations at various latitudes, and the latitudinal bump can virtually disappear during some seasons. Samples taken over a short period are affected by the seasonal cycle and are not directly comparable to the long-term annualized latitudinal distribution as represented in Table 1.

The general features of the latitudinal distribution suggest that the major sources of methyl chloride must be in the tropics. This conclusion is further strengthened by the fact that the abundance of hydroxyl radicals (OH) is much greater in the tropics (by a factor of 3 or so) compared to the middle latitudes. Since reaction with OH is the main process by which methyl chloride is removed from the atmosphere, it takes a large tropical source to sustain the high concentrations observed. Estimates of the total regional sources, based on these observations, suggest that some 85% of the emissions may be from the tropical regions (±30 degrees latitude, *Khalil and Rasmussen* [1997]). The total emissions needed to balance the observed concentrations are about 3.6 ± 0.4 Tg yr^{-1} and the amount of methyl chloride in the atmosphere is calculated to be 5 Tg yr^{-1}, giving an estimated average atmospheric lifetime of 1.3 years.

Another important question is whether the concentration of methyl chloride is changing over long time scales. Our data show trends, but these trends are not large enough to be unequivocal. For the 13-year period between January 1984

TABLE 1. Annually Averaged Concentrations of Methyl Chloride at Sites in the Polar, Middle and Tropical Latitudes of Both Hemispheres*

Year	Barrow	Cape Meares	Cape Kumukahi	Samoa	Tasmania	Antarctica
1981	588.7		627.4	623.3		
1982	589.8			644.5	589.5	
1983	597.7			648.1	605.1	
1984	581.4	610.0		627.5	595.0	583.0
1985	568.4	621.1	616.9	612.6	587.5	597.4
1986	591.9	618.9	598.7	597.7	576.9	573.8
1987	595.8	612.4	596.3	594.6	573.8	560.8
1988		598.8	609.3	610.6	595.6	575.9
1989		587.7	599.2	608.1	598.4	559.6
1990		584.2	598.1	600.6	577.3	559.4
1991	577.1	590.0	620.1	624.0	598.2	560.2
1992	563.1	598.4	626.3	625.3	601.1	578.1
1993	566.8	568.5	605.6	609.2	593.1	575.2
1994	558.2	568.0	604.9	599.4	587.1	565.6
1995	580.0	571.6	611.0	606.6	613.8	573.1
1996	558.3	571.2	612.1	607.6	600.4	579.4
Average	578.2	592.4	609.7	615.0	592.9	572.4

*Samples were taken at sea level. Concentrations are reported as mixing ratios in parts per trillion.

and December 1996, the trends calculated by linear regression, based on the annual average data, are shown in Figure 1 (there are data at all sites during this period). During this period there is an indication of a decrease at Barrow (-0.3 ± 0.2% yr^{-1}) and Cape Meares (-0.7 ± 0.2% yr^{-1}) representing the middle northern hemisphere latitudes. No significant trends are seen in the tropics, and a weak and barely statistically significant increase is seen at Tasmania (+0.3 ± 0.2% yr^{-1}). Trends can also be calculated by taking all years of data into account, although in this case the results are over different time periods depending on the site. The overall pattern remains nearly the same. Trends are negative at all sites except Tasmania, but are statistically significant only at Barrow (-0.3 ± 0.2 % yr^{-1}), Cape Meares (-0.7 ± 0.2% yr^{-1}) and Samoa (-0.3 ± 0.2% yr^{-1}). In all cases the trends are small and difficult to explain. We speculate that these trends are likely to be related to changes in regional biomass burning. One alternative explanation, among others, would be a slow increase in OH concentrations in the northern hemisphere. The long time series of data shown here are discussed in more detail by *Khalil and Rasmussen* [1997]. These data are currently being used to construct a budget of methyl chloride that can be further tested by field experiments.

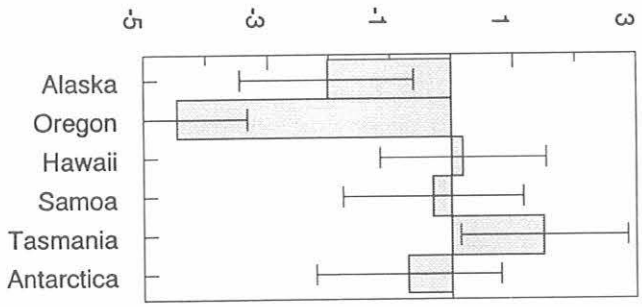

Fig. 1. The trends of methyl chloride (pptv yr^{-1}) (January 1984-December 1996).

Acknowledgments. We thank the staffs of the CMDL program, the Baseline Cape Grim Station, and CSIRO for collecting samples for us. We thank Don Stearns, Jim Mohan, Bob Dalluge (OGI), and Martha Shearer (PSU) for their contributions to this project. The analysis of the data were supported in part by the Chemical Manufacturers Association (Chlorine Chemistry Council) and the European Chemical Industry Council (Euro Chlor) through a grant to the University of Virginia as part of the Reactive Chlorine Emission Inventory activity of GEIA. Additional support was provided by the resources of the Biospherics Research Corporation and the Andarz Co.

References

Edgerton, S.A., Gaseous tracers in receptor modeling: Methylchloride emissions from wood combustion, Ph.D. dissertation, Oregon Graduate Center, Beaverton, 1985.

Khalil, M.A.K., and R.A.Rasmussen, Atmospheric methyl chloride, *Rpt. No. 01-97*, Dept. of Physics, Portland State Univ., Portland, OR, 1997.

Rasmussen, R.A., and M.A.K. Khalil, Atmospheric halocarbons: Measurements and analyses of selected trace gases, *Proc., NATO Adv. Study Ins. on Atmos. Ozone,* edited by A.C. Aikin, Department of Transportation, Washington D.C., 1980.

Rasmussen, R.A., L.E. Rasmussen, M.A.K. Khalil, and R.W. Dalluge, Concentration distribution of methylchloride in the atmosphere, *J. Geophys. Res., 85*, 7350-7356, 1980.

Artificial Windshielding of Precipitation Gauges in the Arctic

RICHARD J. MCCLURE
Soil Conservation Service, Anchorage, Alaska 99508-4362

INTRODUCTION

Precipitation gauges can provide good measurements of the water equivalent of snow precipitation, provided the gauge is protected or shielded from wind effects. Unfortunately, there are no standards for collecting snow precipitation. Gauges located in exposed and windy areas may be totally unshielded, partially shielded by one or more buildings, or equipped with one of several types of artificial shields. The various shielding options in common use, therefore, produce a wide range of gauge catch efficiency. Also, the various studies of artificial shields in the United States and Canada have produced a wide range of results. This must be, in part, due to the wide range of weather conditions under which the various studies have been conducted. A lingering problem is applying the results to the local conditions of Alaska's tundra regions.

METHODS

A study of the windshield alternatives, under the unique conditions of Alaska's arctic coastal region, was set up at the CMDL Barrow facility during September 1989. Snowfall catches from four newly installed precipitation storage gauges were compared with that from an existing storage gauge protected by a Wyoming shield [*Hanson*, 1988]. Two of the new gauges were shielded, one with a Nipher shield [*Goodison et al.*, 1983] and the other with an Alter shield [*Alter*, 1937], and two were unshielded. One of the unshielded gauges was serviced on an event basis, the same as the three shielded gauges. The other unshielded gauge was treated as if it were a remote gauge, allowing rime to build up and dissipate naturally to see what effects rime had on the overall catch. The four newly installed gauges are 20.3 cm in diameter × 100 cm tall, mounted with the orifice 2 m above the normal ground surface. The existing Wyoming-shielded gauge is 30.5 cm in diameter × 2-m tall and is equipped with a Leupold-Stevens water-level recorder. Because the anchors melted out in the permafrost, the 1993 wind storms blew over the Wyoming wind shield. An unusual wind event for that time of year. The gauge was not rebuilt.

RESULTS

The four winter seasons of total precipitation is available for comparison of the four remaining gauges in Table 1. The results continue to confirm the catch of the Alter shield are 37 to 58% of the Nipher shield with the unshielded gauges ranging from 10 to 36% of the Nipher shielded precipitation gauge.

TABLE 1. Comparison of Total Precipitation of the Four Remaining Gauges

	Nipher	Alter	Unshielded Serviced	Unshielded Unserviced
Oct. 5, 1993-June 1, 1994	76.2 mm	38.1 mm	no record	23.9 mm
% of Nipher		50%		31%
Oct. 1, 1994-June 17, 1995	104.6 mm	54.6 mm	36.3 mm	37.3 mm
% of Nipher		52%	35%	36%
Oct. 3, 1995-June 3, 1996	84.1 mm	49.3 mm	28.7 mm	23.9 mm
% of Nipher		58%	34%	28%
Oct. 3, 1996-June 5, 1997	80.8 mm	30.0 mm	10.4 mm	7.9 mm
% of Nipher		37%	13%	10%

Acknowledgment. Appreciation is expressed to D. Endres, Station Chief, Barrow, Alaska, who serviced the precipitation gauges and collected the snow samples.

REFERENCES

Alter, S.C., Shield storage precipitation gauges, *Mon. Weather Rev., 65*, 262-265, 1937.

Goodison, B.E., W.R. Turner, and J.E. Metcalfe, A Nipher-type shield for recording precipitation gauges, *Proc., 5th Symposium on Meteorological Observations and Instrumentation*, Toronto, Ontario, Canada, pp. 2-126, Am. Meteorol. Soc., Boston, 1983.

Hanson, C.L., Precipitation measured by gauges protected by the Wyoming shield and the dual-gauge system, *Proceedings, 56th Western Snow Conference*, Kalispell, MT, pp. 174-177, Colorado State University, Fort Collins, 1988.

Investigation of the Transfer Function Between Atmosphere and Snow Concentrations of Hydrogen Peroxide at South Pole

JOSEPH R. MCCONNELL AND ROGER C. BALES
Department of Hydrology and Water Resources, University of Arizona, Tucson, 85721

INTRODUCTION

A critical issue in atmospheric chemistry today is to assess the global trend in the concentration of the hydroxyl radical (OH) and hydrogen peroxide (H_2O_2). Oxidation by OH represents the main sink for a number of environmentally important atmospheric gases including methane (CH_4), carbon monoxide (CO) and the halogenated hydrocarbons involved in stratospheric ozone loss. Extensive efforts have been made over the past few years to use photochemical models to estimate past and future atmospheric concentrations of OH and hydrogen peroxide (H_2O_2) [*Thompson et al.*, 1993; *Stafflebach*, 1990]. However, these model studies of past atmospheres lack sufficient data for validation. Of the primary oxidants, only H_2O_2 is preserved in the ice, but the correspondence between atmospheric and ice core hydrogen peroxide is not well understood. To be useful for oxidant modeling, the transfer processes that relate atmosphere to snow to ice concentrations must be well defined.

Our research is an investigation of the atmosphere-ice transfer function for reversibly deposited chemical species, primarily hydrogen peroxide and formaldehyde, through laboratory, field, and computer modeling studies. Reversible implies that some fraction of the deposited mass of these species cycles between the atmosphere and snow as conditions such as atmospheric concentration and temperature change. The objective is to develop the capability to describe concentrations of reversibly deposited species in snow and ice as functions of depth and time, given concentrations and conditions in the local atmosphere and properties of the snow and ice. This modeling capability will then be inverted and used to infer possible past atmospheric concentrations from observations of what is trapped in the ice, providing additional data constraints on tropospheric modeling.

PROCEDURES

Building on similar field studies at Summit, Greenland, and Siple Dome, Antarctica, we have made measurements of H_2O_2 concentrations in the atmosphere and in the surface, near-surface and deep snow, and firn at the South Pole. What sets South Pole apart as a site for atmosphere-snow transfer studies is (a) the long-term instrumental record of meteorology and atmospheric chemistry, (b) the ongoing, year-round presence of qualified staff to make chemical and meteorological measurements, (c) the lack of a diel temperature cycle, and (d) the distance from open water and anthropogenic activity. As part of our cooperative agreement with the Climate Monitoring and Diagnostics Laboratory (CMDL), we deployed a detector for measuring H_2O_2 at the South Pole for a 3-week period in late November and early December 1994 and for a 2-week period in January 1996. Atmospheric measurements were made almost continuously during that time and a number of surface snow and shallow snow pit samples were collected and analyzed. When used for atmospheric analyses, our custom built H_2O_2 detector makes atmospheric measurements at approximately 10-minute intervals using a glass coil scrubber to transfer the peroxide from the continuous stream of air-to-water and then a chemical fluorescence method to determine the concentration in the water. For firn analyses, the samples are melted and the peroxide measurement made directly.

Since December 1994 the CMDL winterover staff have collected surface and near-surface snow samples for this project. Samples are collected approximately once a week throughout the year. Each sampling event consists of

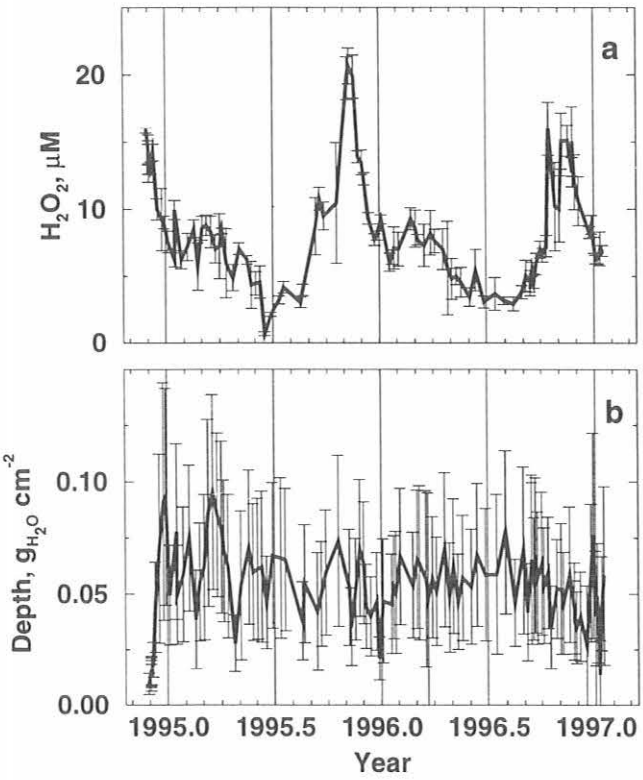

Fig. 1 (a) H_2O_2 concentrations and (b) sample depth in surface snow at the South Pole. Error bars show one standard deviation for replicated (typically six) surface snow samples [after *McConnell et al.*, 1998].

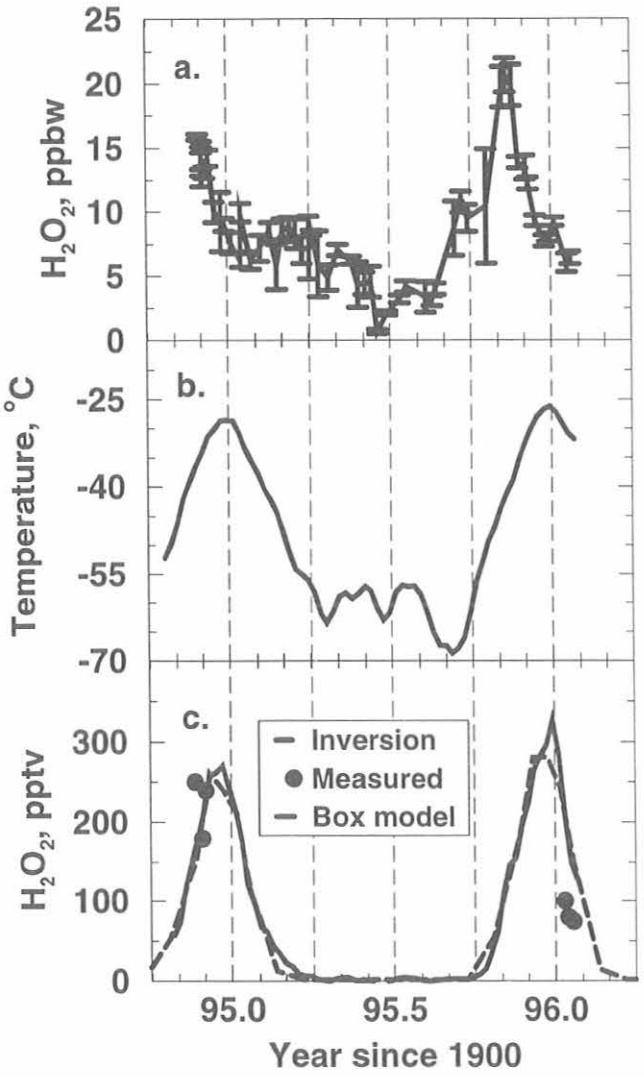

Fig. 2. (a) Measured H_2O_2 in surface snow at South Pole, (b) surface temperature, and (c) Estimated atmospheric concentration of H_2O_2 derived through inversion of surface snow samples and from photochemical modeling. Spot direct atmospheric measurements are shown as circles [after *McConnell et al.*, 1997b].

collecting approximately five surface snow and ten near-surface samples. These are returned each summer to our laboratory in Tucson for analyses of H_2O_2 and major ion concentrations and oxygen isotopes.

Results

The measured surface snow concentrations for the samples analyzed to date are shown in Figure 1. Using a physically based model for the atmosphere-snow transfer processes, and assuming rapid ventilation at the snow surface, we inverted a portion of this surface snow record to an estimate of the atmospheric concentration throughout the year (Figure 2) [*McConnell et al.*, 1997a]. The model is based on the advection-dispersion equation with the rate of uptake and release of H_2O_2 in the snow pack controlled by spherical diffusion within individual snow grains. The estimated atmospheric concentration compares favorably with both photochemical model results and with short-duration atmospheric measurements made in November-December 1994. Note that measurements made in January 1996 do not compare as favorably, perhaps, because of local pollution from construction at the new clean air facility that may have affected photochemistry.

We have extended this physically based modeling into the firn at South Pole. The physically based model was used to simulate the H_2O_2 concentration measured in snow pits where an independent estimate of accumulation history was available from snow accumulation studies [*McConnell*, 1997; *McConnell et al.*, 1997b; 1998]. The results (Figure 3) indicate that snow, which is strongly over-saturated with H_2O_2 at formation, remains generally over-saturated when buried because it is cut off from the atmosphere before it can release excess peroxide. The model results suggest that temperature and accumulation rate, along with snow's physical properties, like grain size and permeability, are the primary factors that determine preservation of H_2O_2 in the snow pack.

The snow pack model has also been used to simulate snow pit profiles from Siple Dome, Antarctica. The results (Figure 4), while preliminary, indicate that the physically based model has wide applicability since it

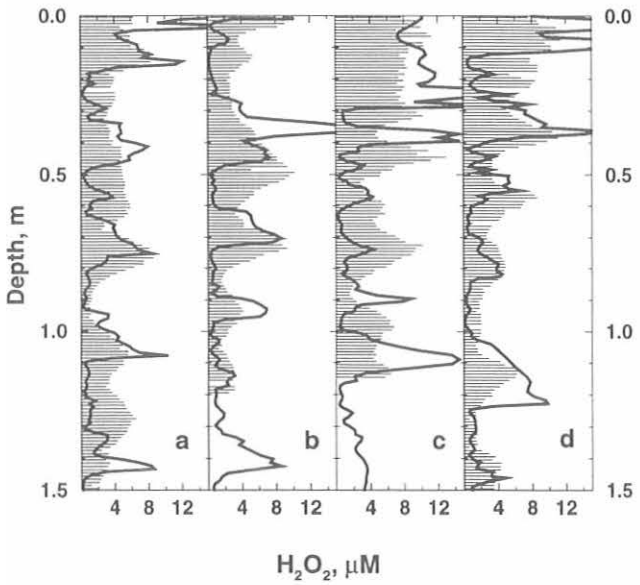

Fig. 3. Measured (horizontal bars) and simulated (solid lines) concentration profiles for four snow pits at South Pole. The pits were sampled in January 1996 and are located in a long-term snow accumulation array about 500 m from South Pole Station [after *McConnell et al.*, 1998].

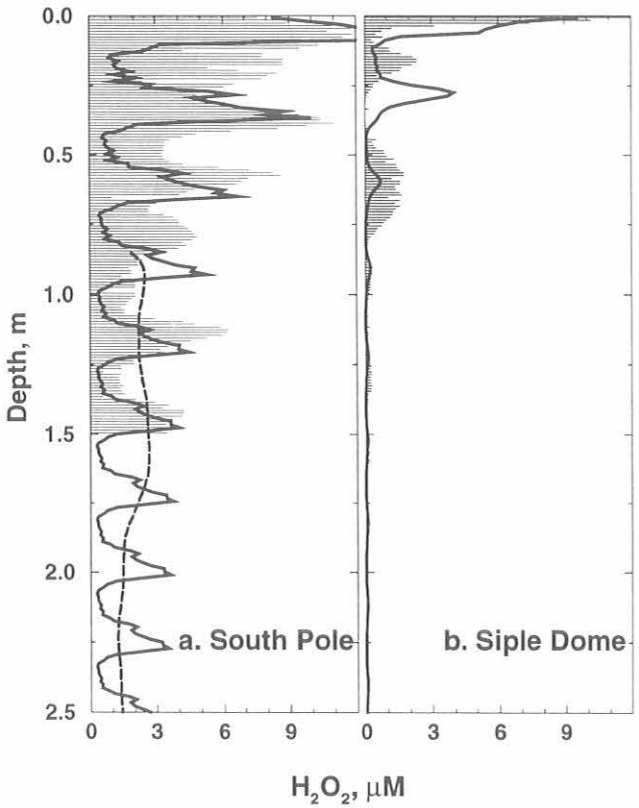

Fig. 4. Observed snow pit (horizontal bars), firn cored (dashed), and physically based model simulations (solid) of H_2O_2 concentrations in snow and firm at (a) South Pole and (b) Siple Dome, Antarctica. Annual average snow accumulation was used in the simulations so individual summer peaks and winter troughs will not coincide with observations [after *McConnell*, 1997].

correctly simulates the 4-and 40-fold decreases in H_2O_2 concentration from the surface to 1-m depth observed at South Pole and Siple Dome, respectively.

Conclusions

Our understanding of the transfer function that relates atmosphere-to-snow-to-firn concentration of reversibly deposited chemical species such as H_2O_2 has improved dramatically over the past 3-4 years. This improvement would not have been possible without the year-round surface snow and snow pit samples and atmospheric data that we have obtained through our cooperative project with CMDL.

References

McConnell, J.R., Investigation of the atmosphere-snow transfer process for hydrogen peroxide, Ph.D. Dissertation, Department of Hydrology and Water Resources, University of Arizona, 1997.

McConnell, J.R., R.C. Bales, R.W. Stewart, A.M Thompson, M.R. Albert, and R. Ramos, Physically based modeling of atmosphere-to-snow-to-firn transfer of H_2O_2 at South Pole, *J. Geophys. Res.*, in press, 1998.

McConnell, J.R., J.R. Winterle, R.C. Bales, A. M. Thompson, and R. W. Stewart, Physically based inversion of surface snow concentrations of H_2O_2 to atmospheric concentrations at South Pole, *Geophys. Res. Lett.*, *24(4)*:441-444, 1997a.

McConnell, J.R., R.C. Bales, and D.R. Davis, Recent intra-annual snow accumulation at South Pole: Implications for ice core interpretation, *J. Geophys. Res.*, *102(D18)*: 21,947-21,954, 1997b.

Staffelbach, T., *Formaldehyd- und ammonium-messungen an schnee-, firn- und eisproben aus polaren und alpinen regionen*, PhD thesis, Physikalisches Institut, Universitat Bern, 1990.

Thompson, A. M., J. A. Chappellaz, I. Y. Fung, and T. L. Kucsera, The atmospheric CH_4 increase since the last glacial maximum, 2, Interaction with oxidants, *Tellus*, *45B*, 242-257, 1993.

Middle Atmosphere Temperature Climatology at Mauna Loa From Rayleigh/Raman Lidar Measurements

STUART MCDERMID, THIERRY LEBLANC, RICHARD CAGEAO, GEORG BEYERLE AND DANIEL WALSH
Table Mountain Facility, Jet Propulsion Laboratory, California Institute of Technology, Wrightwood 92397

INTRODUCTION

The JPL Lidar at Mauna Loa Observatory (MLO) continues to make regular measurements of ozone, temperature and aerosol profiles for the Network for the Detection of Stratospheric Change (NDSC) program. This report describes the development of a temperature climatology from one aspect of the lidar results.

The temperature structure of the middle atmosphere has been studied for several decades using a variety of techniques. Temperature profiles derived from lidar measurements currently provide improved vertical resolution and accuracy making lidar one of the most suitable instruments for looking at local variations of the middle atmosphere temperature. Lidars can also provide long-term data series relatively absent of instrumental drift, and integration of the measurements over several hours removes most of the gravity wave-like short scale disturbances.

Here we describe a seasonal climatology of the middle atmosphere temperature derived from lidar measurements obtained at MLO (19.5°N). The JPL Rayleigh/Raman lidar [*McDermid et al.*, 1995] has obtained temperature measurements between ~15 and ~90 km since 1993. Most of the routine measurements comprise a 1.5 hour integration experiment, usually at the beginning of the night 4-5 nights a week, ensuring a good survey of stratospheric ozone and temperature as required by the NDSC program.

DATA ANALYSIS AND RESULTS

Lidar Temperature Record

Figure 1 shows a summary of all of the lidar temperature profiles recorded at MLO between January 1994 and July 1997.

Climatological Temperatures

Each individual lidar temperature profile was interpolated to obtain data points every 1 km. The tops of the profiles were truncated about 10 km lower than the initial tie-on altitudes so that the results containing a non negligible part of a priori information and/or noise were not used. High confidence levels are expected up to 75 km altitude. The profiles were then merged into a composite single year of data. A weighted running average with a triangular 33-day width filtering scheme was applied to each day of the composite year that a profile was available. The remaining days with no profile were filled with an interpolated profile obtained using a two-dimensional minimum curvature spline method. Although these interpolated profiles were plotted they were not retained in the numerical database in order to avoid inaccuracies in the different analyses described later. No removal of tidal structures was performed even though the role of the diurnal and semidiurnal tides may not be negligible above 80 km at MLO.

The mean annual temperature climatology is presented in Figure 2 which clearly shows a semiannual cycle at the stratopause, maximum temperature 266 K at 47 km, and an annual cycle in the lower stratosphere with a very cold minimum of 190 K at 17 km identified as the tropical tropopause. As expected at these latitudes, the amplitude of the seasonal variations is weak. At the top (80-85 km), where the effect of the mesospheric tides is the largest, the measured cold temperatures are more representative of early night temperatures than nightly (or even a 24-hour) mean temperatures.

Temperature Deviations From the Annual Mean

The annual mean temperature profile was then subtracted from each available daily composite profile to obtain the daily deviation from the annual mean. Figure 3 shows this deviation. MLO exhibits a dominant semi-annual cycle between 25 and 80 km altitude. This is not surprising since MLO is located at 19.5°N and is influenced by the equatorial dynamical pattern which in turn is affected by both northern and southern hemispheres. The semi-annual cycle observed here is almost a continuous downward propagating oscillation with an approximate vertical speed of 12 km/month and can be identified as the thermal semi-annual oscillation (SAO). The so-called mesopause and stratopause SAOs appear here as a combined single SAO propagating downward from the mesopause to 30 km with minimum amplitude at 45 km. A phase inversion is observed near 82 km similar to that observed by SME at 83 km [*Garcia and Clancy*, 1990]. The oscillation is strongly modulated with the first cycle being stronger than the second. The seasonal asymmetry of the wind and temperature SAO has been widely reported (see for example, *Garcia et al.* [1997]). One explanation of this [*Delisi and Dunkerton*, 1988] is that it is a consequence of a stronger dynamical forcing in the northern hemisphere. However, due to the relatively northward location of MLO, the late winter maxima and early summer minima of the midlatitude annual cycle and the equatorial SAO are in phase and may also cause the first oscillation of the semiannual cycle to be of larger magnitude than the second. Finally, in Figure 3 an annual cycle is observed below 25 km and a cold spot can be noted in November at 64 km.

DISCUSSION AND CONCLUSION

As has been observed in all previous middle atmospheric temperature climatologies [*Clancy and Rusch*, 1989; *Garcia and Clancy*, 1990, *Hauchecorne et al.*, 1991; *Bills and Gardner*, 1993; *Clancy et al.*, 1994; *Yu and She*, 1995, *Garcia et al.*, 1997] a semiannual cycle is dominant at lower latitudes. Below 60 km the annual cycle is in phase with the

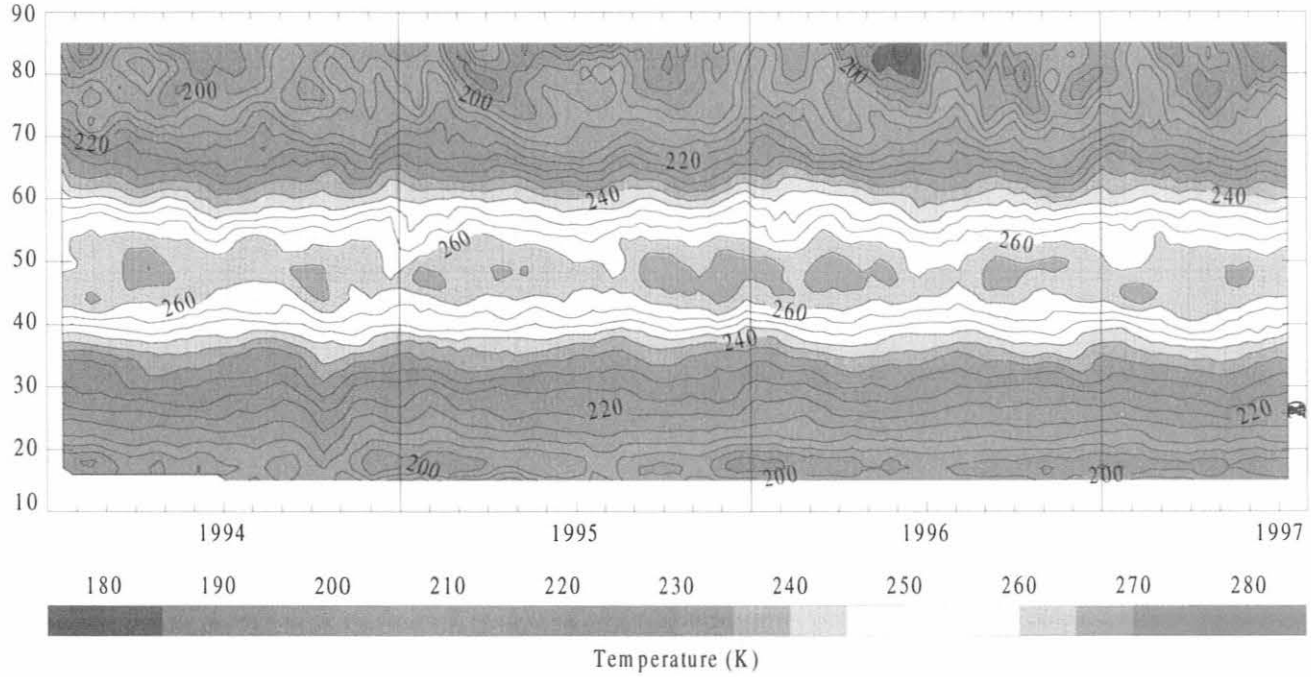

Fig. 1. Lidar temperature record at MLO.

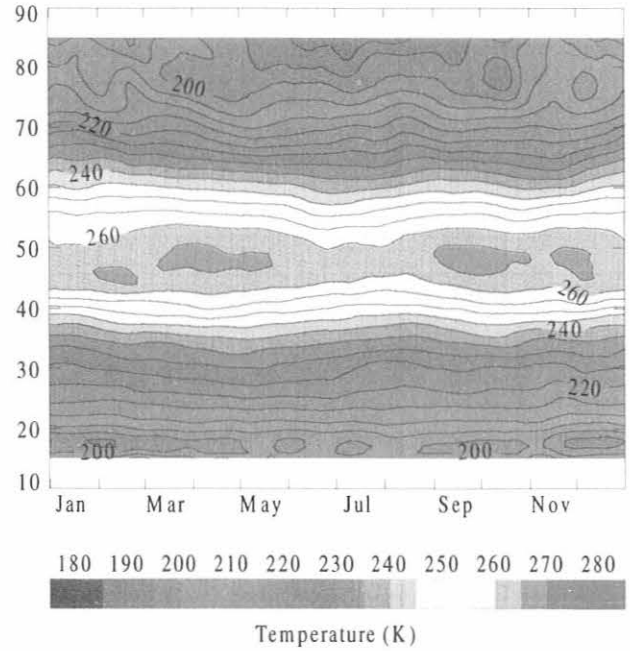

Fig. 2. Mean annual temperature climatology at MLO.

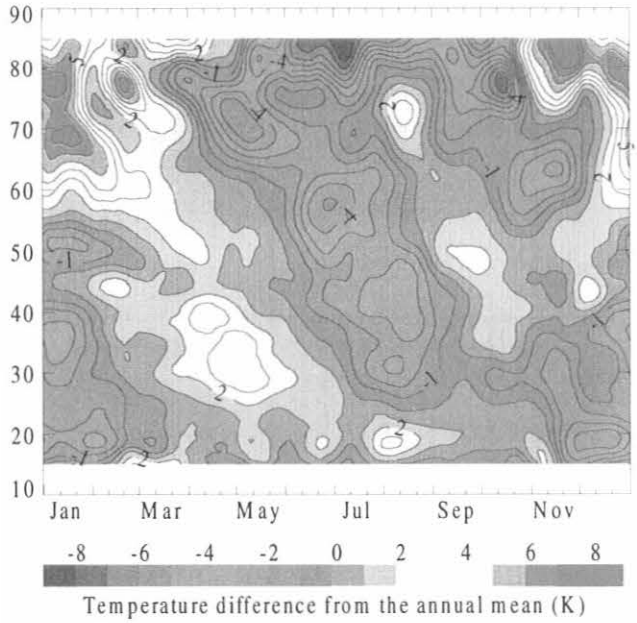

Fig. 3. Mean temperature seasonal variations at MLO.

solar flux leading to a warm summer and cold winter stratosphere and lower mesosphere as expected. Above 65 km, the annual cycle is in opposite phase to the solar flux, as a consequence of a dynamically driven mesosphere, and is characterized by a warm winter and cold summer mesosphere. The observed downward propagating

temperature behavior in the mesosphere points out the dominant wave-driven pattern, in contrast with the vertically stationary behavior observed below 50-55 km. At MLO the dominant semiannual cycle is modulated by the northern midlatitude annual cycle thus contributing, together with the well known seasonally asymmetric equatorial SAO, to the first warm-cold cycle (winter and spring) being stronger than the second (summer and fall).

Systematic departures from the CIRA-86 model were observed, **Figure 4**, which confirms the similar results of previous comparisons [*Hauchecorne et al.*, 1991; *Clancy et al.*, 1994]. In particular, too cold temperatures in the CIRA-86 model lead to a large differences (>15 K) around 90-95 km compared to lidar results, possibly due to an overestimation of non-local thermodynamic equilibrium (LTE) effects in the computation of the CIRA-86 temperatures [*Lawrence and Randel*, 1996]. On an annual basis CIRA-86 seems to be too warm around 55-60 km, too cold between 60 and 75 km, too warm between 75 and 85 km, and much too cold around 90-95 km. Using too cold CIRA-86 temperatures at 90-95 km for initialization can lead to some dramatic temperature errors at the very top of the Rayleigh lidar profiles. For this reason the JPL lidar group is currently investigating the use of different a priori temperature information to avoid such uncertainty.

The chaotic nature of the seasonal variations of the middle atmospheric temperature allows most of the discrepancies observed between the lidar and CIRA-86 climatologies, to be explained. Above MLO, it is likely that most of the observed departure in the middle and upper mesosphere is related to tidal effects and/or the mesopause thermal SAO. The amplitudes of 1-5 K predicted by tidal models [*Hagan et al.*, 1995; *Hagan*, 1996] may be underestimated [*Keckhut et al.*, 1996] and this will be investigated in more detail in the future.

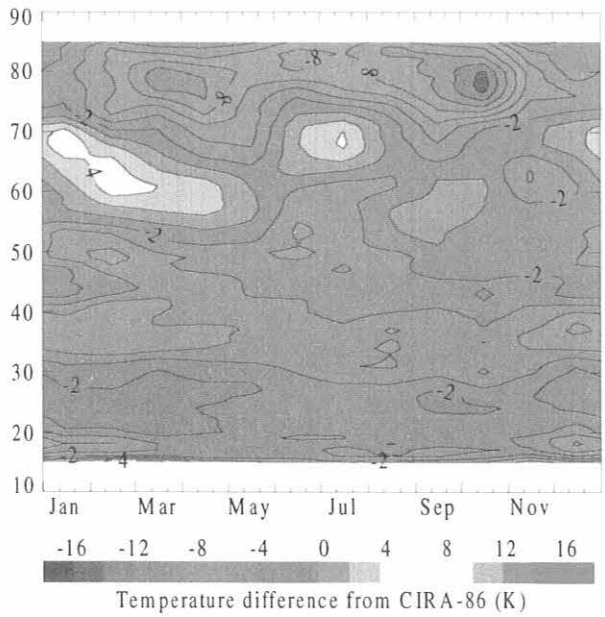

Fig. 4. Differences between the lidar and CIRA climatologies.

The climatology presented in this paper was obtained using composite temperature profiles from several years of measurements. Of course, a non-negligible interannual variability may disturb the temperature field from year to year. However, the trends already observed in previous climatologies [*Hauchecorne et al.*, 1991; *Hood et al.*, 1993] remain small compared to the seasonal variations. Also, the effect of volcanic eruptions, such Pinatubo in 1991 [*Keckhut et al.*, 1995], may have non-negligible disturbing effects. All trends, 11-year solar cycle, Quasi Biennial Oscillation (QBO), and volcanic eruption effects are currently being investigated. The use of such a complete climatology is crucial for many purposes such as providing a reference atmosphere for models and instruments, a background atmosphere for smaller scales studies, an overall comprehension of the strongly coupled lower-middle-upper atmosphere, and more. To this date, only a few instruments can provide such long-term data series. With the recent and future development of many ground based lidars within the NDSC at many latitudes, a more complete climatology of the middle atmospheric temperature should be available within few years.

Acknowledgements. The work described in this paper was carried out by the Jet Propulsion Laboratory, California Institute of Technology, under an agreement with the National Aeronautics and Space Administration.

REFERENCES

Bills, R.E., and C.S. Gardner, Lidar observations of the mesopause region temperature structure at Urbana, *J. Geophys. Res., 98*, 1011-1021, 1993.

Clancy, R.T., and D.W. Rush, Climatology and trends of mesospheric (58-90 km) temperature based upon 1982-1986 SME limb scattering profiles, *J. Geophys. Res., 94*, 3377-3393, 1989.

Clancy, R.T., D.W. Rush, and M.T. Callan, Temperature minima in the average thermal structure of the middle atmosphere (70-80 km) from analysis of 40- to 92-km SME global temperature profiles, *J. Geophys. Res., 99*, 19,001-19,020, 1994.

Delisi, D.P., and T.J. Dunkerton, Seasonal variation of the semiannual oscillation, *J. Atmos. Sci., 45*, 2772-2787, 1988.

Garcia, R.R., and R.T. Clancy, Seasonal Variation in equatorial mesospheric temperatures observed by SME, *J. Atmos. Sci., 47*, 1666-1673, 1990.

Garcia, R.R., T.J. Dunkerton, R.S. Lieberman, and R.A. Vincent, Climatology of the semiannual oscillation of the tropical middle atmosphere, *J. Geophys. Res., 102*, 26,019-26,032, 1997.

Hagan, M.E., J.M. Forbes and F. Vial, On modeling migrating solar tides, *Geophys. Res. Lett., 22*, 893-896, 1995.

Hagan, M. E., Comparative effects of migrating solar sources on tidal signatures in the middle and upper-atmosphere, *J. Geophys Res., 101*, 21,213-21,222, 1996.

Hauchecorne, A., M.L. Chanin, and P. Keckhut, Climatology and trends of the middle atmospheric temperature (33-87 km) as seen by Rayleigh lidar over the south of France, *J. Geophys. Res., 96*, 15,297-15,309, 1991.

Hood, L.L., J.L. Jirikowic, and J. P. McCormack, Quasi-decadal variability of the stratosphere: Influence of long-term solar ultraviolet variations, *J. Atmos. Sci., 50*, 3941-3958, 1993.

Keckhut, P.,A. Hauchecorne, and M.L. Chanin, Midlatitude long-term variability of the middle atmosphere: Trends and cyclic and episodic changes, *J. Geophys. Res., 100*, 18,887-18,897, 1995.

Keckhut, P., M.E. Gelman, J.D. Wild, F. Tissot, A.J. Miller, A. Hauchecorne, M.-L. Chanin, E.F. Fishbein, J. Gille, J.M. Russel III, and F.W. Taylor, Semi-diurnal and diurnal tides (30-55 km): Climatology and effect on UARS-LIDAR data comparisons, *J. Geophys. Res., 101*, 10,299-10,310, 1996.

Lawrence, B.N., and W.J. Randel, Variability in the mesosphere observed by the Nimbus 6 pressure modulator radiometer, *J. Geophys. Res., 101*, 23,475-23,489, 1996.

McDermid, I.S., T.D. Walsh, A. Deslis and M.L. White, Optical systems design for a stratospheric lidar system, *Appl. Opt., 34*, 6201-6210, 1995.

Yu, J.R., and C.Y. She, Climatology of a midlatitude mesopause region observed by a lidar at Fort Collins, Colorado (40.6°N, 105°W), *J. Geophys. Res., 100*, 7441-7452, 1995.

Intercomparison of UV-B Spectroradiometers at Mauna Loa During 1995-1996

PATRICK J. NEALE, VERNON R. GOODRICH, AND DOUGLASS R. HAYES, JR.
Smithsonian Environmental Research Center, Edgewater, Maryland 21037

INTRODUCTION

Our laboratory has been monitoring surface ultraviolet B spectral band (UV-B) irradiance at Mauna Loa Observatory, Hawaii (MLO), since the fall of 1984. The instrument (SERC-SR8) is similar to a radiometer in operation in Edgewater, Maryland, [*Correll et al.*, 1992]. The instrument measures UV-B irradiance in a series of eight, 5-nm bandpass channels with center wavelengths between 290 and 325 nm, and records 1-minute averages. Operation was continuous during August 1984 to May 1996, except for an annual break of about 1 month when the instrument was returned to Maryland for calibration. Determinations of absolute responsivity were made by recording instrument output under a 1000 W quartz-halogen standard lamp traceable to the National Institute of Standards and Technology. These responsivity determinations revealed a steady linear decrease in overall instrument responsivity of about 6% per year (since 1987) in all channels (R^2 = 0.90). However, even after adjustment of voltages for this drift, a trend of decreasing output of the instrument is apparent in long time series of clear sky irradiance at a fixed solar zenith angle (SZA) (data not shown). Thus it appears that on-site response decreased by a greater proportion than observed in the lamp calibrations conducted in Maryland. We are currently conducting experiments to determine the cause of these shifts in responsivity; the working assumption is that the malfunction is connected with high altitude operation since similar shifts have not been observed in the comparable long-term UV-B data set for Maryland [*Correll et al.*, 1992].

While the above described situation precludes any estimates of long-term changes in absolute spectral irradiance of UV-B at MLO at the present time, we have used relative signal intensity in selected channels to provide information on changes in the solar UV-B spectrum. These analyses have included estimates of atmospheric optical depth in the UV-B at MLO [*Neale et al.*, 1994] and evidence of increased incident solar UV-B during an episode of record low total column ozone at MLO during the winter of 1994-1995 [*Hofmann et al.*, 1996; *Neale et al.*, 1996]. In this latter report we presented UV irradiance measured in the 295, 300, and 305 nm channels, relative to the 325 nm channel, for clear days when the secant of the SZA was equal to 1.5 (i.e., an SZA of about 48°). The enhancement of short-wavelength UV-B observed by the SERC-SR8 was consistent with other evidence supporting higher global UV-B with decreased ozone. However, there was no direct verification that the absolute intensity of UV-B at these wavelengths actually increased.

During 1995 and 1996 another type of spectral radiometer was installed at MLO. This instrument (NIWA-SR) is based on a double monochromator and photomultiplier tube (PMT) as designed at the National Institute of Water and Atmospheric Research (NIWA) of New Zealand. The NIWA-SR made observations at a fixed series of SZAs, as well as frequent scans near midday. A description of the instrument and a report of a time series of MLO measurements for 45° SZA on clear mornings was presented by *Bodhaine et al.* [1997]. In this report we compare some of the results in this latter report to simultaneous measurements made with the Smithsonian instrument. The results show a consistent linear relationship between the outputs of the two instruments.

RESULTS AND DISCUSSION

The instrument was calibrated at SERC and sent to MLO in June 1995 and remained in operation until May 1996. On May 4, 1995, transmission spectra were measured for all eight interference filters in the instrument. The center wavelengths (wavelength midpoint between the upper and lower wavelengths at which transmission is 50% of maximum) calculated from these spectra for the 295, 300, and 305 nm channels were 295.12, 300.7, and 304.9 nm.

Spectral scans as described in [*Bodhaine et al.*, 1997] were kindly provided by CMDL. We used the 45° SZA observations for clear sky mornings for the period July 1995 to May 1996. For comparison, we used the 1-minute average from the SERC-SR8 for the time with the closest correspondence to the 45° SZA based on a computer ephemeris program. The voltages recorded at MLO were converted to provisional irradiances by application of responsivities determined under the standard lamp in May 1995. The SERC-SR8 irradiances were then compared with the readings of the NIWA-SR instrument at the wavelength closest to each channel's nominal center wavelength.

Figure 1 shows correlation plots of 295, 300 and 305 nm irradiance, which are the wavelengths presented in the *Hofmann et al.* [1996] and *Neale et al.* [1996] reports. There is a close linear relationship between the readings of the two instruments with coefficient of determination (R^2) varying between 0.87 and 0.92. The slope of the fitted relationship [E(SERC-SR8) = k E(NIWA-SR)] varies between channels (Figure 2). In the 295 channel the ratio is greater than unity, at 300 nm it is about 0.9, and for the remaining channels the ratio ranges between 0.5 to 0.6. These ratios were constant during July 1995 to March 1996 and then shifted to somewhat lower ratios (data not shown). Again, the cause for these shifts remains to be determined.

Overall, it appears that application of responsivities as measured under a standard lamp in Maryland to the SERC-SR8 voltages recorded at MLO, lead to estimates of irradiance about 55% of the irradiance recorded by the

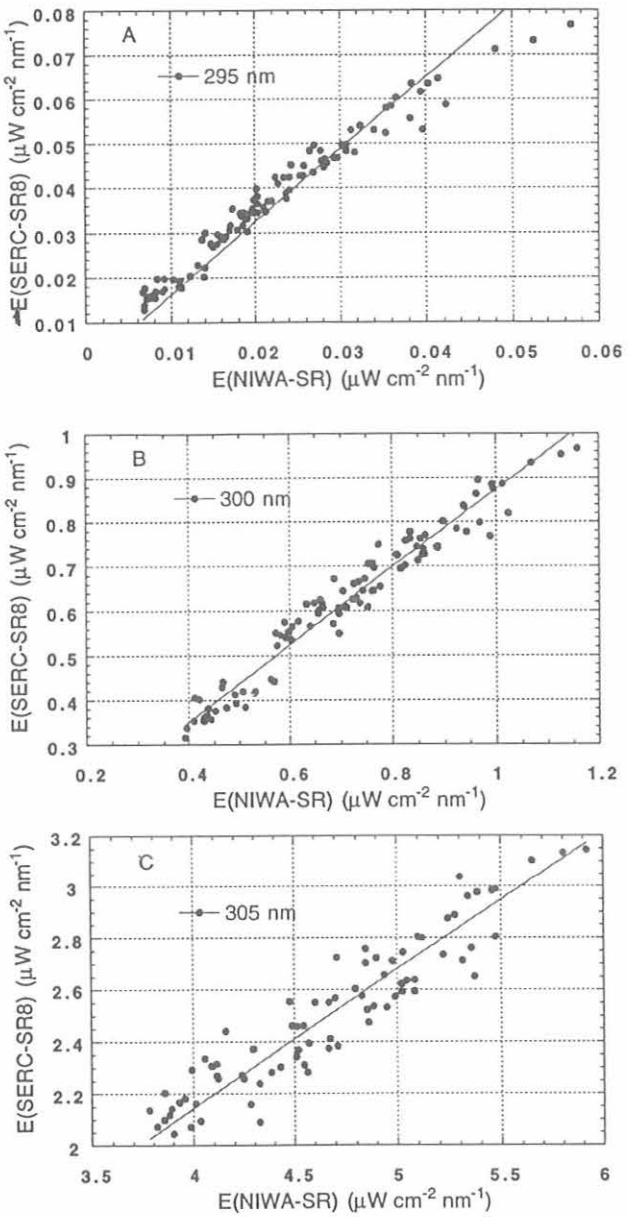

Fig. 1. Comparison of spectral irradiance (μW cm-2 nm-1) at 45° SZA on clear sky mornings at MLO measured with the SERC-SR8 and NIWA-SR instruments. (a) 295 nm, (b) 300 nm, (c) 305 nm. Each point corresponds to one morning's observation. The line indicates a fitted linear regression with the intercept forced through zero.

NIWA-SR. This is consistent with our conclusion that the on-site responsivity of the SERC-SR8 is less than that determined under a calibration lamp. However, at 295 nm, the SERC-SR8 irradiance actually appears to be higher than NIWA-SR irradiance. Also, the relationship between the two irradiances does not follow a straight proportion as well as seen for the other wavelengths (Figure 1a). This is probably due to the wide bandpass of the interference filters (nominally 5 nm, FWHM). If we performed the

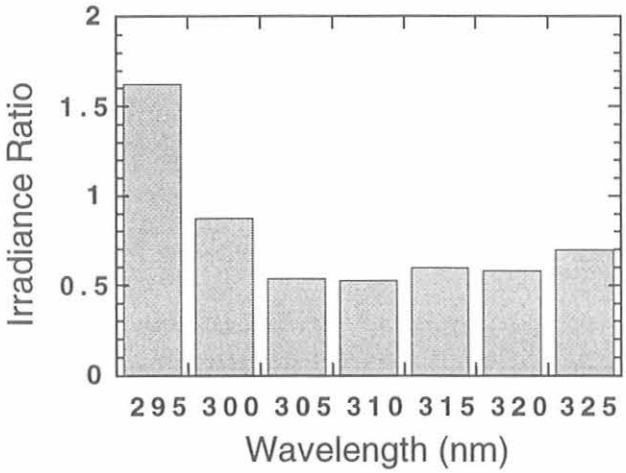

Fig. 2. Slopes of the fitted linear regression of the SERC-SR8 irradiance on the NIWA-SR irradiance (irradiance ratio, dimensionless) for each of the eight filters in the SERC-SR8 instrument.

comparison at the effective center wavelength, i.e., the filter center wavelength adjusted for the greater proportion of longer-wavelength solar irradiance within the pass band [*Correll et al.*, 1992], the proportionality between the SERC-SR8 and the NIWA-SR presumably would be lower and more linear as was the case for the longer wavelength irradiances.

Indeed, empirical determinations of effective center wavelengths could be made through a more extensive comparison between the SERC-SR8 and the NIWA-SR instruments. This is beyond the scope of the present report that had the objective of verifying the relative responsivity of the SERC-SR8. The close relationship between the two records during this intercomparison period motivates further analyses and continued engineering studies on the source of the calibration instability. In the near future it is hoped that the SERC-SR8 can be returned to MLO together with a new version of the Smithsonian UV-B radiometer, and the SERC-SR18 which has 18 interference filters with narrower (2 nm) bandwidth [*Thompson et al.*, 1997].

References

Bodhaine, B.A., E.G. Dutton, D.J. Hofmann, R.L. McKenzie, and P.V. Johnston, UV measurements at Mauna Loa: July 1995 to July 1996, *J. Geophys. Res.*, *102* (D15), 19,265-19,273, 1997.

Correll, D. L., C. O. Clark, B. Goldberg, V. R. Goodrich, D. R. Hayes Jr., W. H. Klein and W. D. Schecher, Spectral Ultraviolet-B radiation fluxes at the earth's surface: long-term variations at 39°N, 77°W, *J. Geophys. Res.*, *97*, 7579-7591, 1992.

Hofmann, D.J., S.J. Oltmans, B.A. Bodhaine, G.L. Koenig, J.M. Harris, J.A. Lathrop, R.C. Schnell, J. Barnes, J. Chin, D. Kuniyuki, S. Ryan, R. Uchida, A. Yoshinaga, P.J. Neale, D.R. Hayes, R. Goodrich, W.D. Komhyr, R.D. Evans, B.J. Johnson, D.M. Quincy, and M. Clark, Record low ozone over Mauna Loa observatory, Hawaii during the winter of 1994-1995, *Geophys. Res. Lett.*, *23* (12), 1533-1536, 1996.

Neale, P.J., D.L. Correll, V.R. Goodrich, and D.R. Hayes Jr., UV-B optical depths at Mauna Loa: Relative Contribution of Ozone

and Aerosols, in *Climate Monitoring and Diagnostics Laboratory No. 22 Summary Report*, edited by J.T. Peterson and R.M. Rosson, pp. 132-134, NOAA Environmental Research Laboratories, Boulder, CO, 1994.

Neale, P.J., D.L. Correll, V.R. Goodrich, and D.R. Hayes Jr., Early morning UV-B during the 1994-1995 record low ozone at Mauna Loa, in *Climate Monitoring and Diagnostics Laboratory No. 23 Summary Report 1994-1995*, edited by D.J. Hofmann, J.T. Peterson, and R.M. Rosson, NOAA Environmental Research Laboratories, Boulder, CO, 1996.

Thompson, A., E.A. Early, J. Deluisi, P. Disterhoft, D. Wardle, J. Kerr, J. Rives, Y. Sun, T. Lucas, T. Mestechkina, and P.J. Neale, The 1994 North American interagency intercomparison of Ultraviolet monitoring spectroradiometers, *Natl. Inst. Stds. Technol. J. Res.*, *102(3)*, 279-322, 1997.

Middle Atmospheric Water Vapor Measurements From Mauna Loa, 1996-1998

GERALD E. NEDOLUHA, RICHARD M. BEVILACQUA, R. MICHAEL GOMEZ, AND BRIAN C. HICKS
Naval Research Laboratory, Washington, D.C. 20375-5320

We present data obtained during nearly 2 years of continuous measurements of middle atmospheric water vapor from Mauna Loa, Hawaii (19.5°N, 204.4°E). The measurements are made at 22 GHz using a Naval Research Laboratory water vapor millimeter-wave spectrometer (WVMS). The data from Mauna Loa show less seasonal variation than those from WVMS instruments at Table Mountain, California (34.4°N, 242.3°E) and Lauder, New Zealand (45.0°S, 169.7°E), as is expected given the lower latitude of the Mauna Loa site. These relatively small seasonal variations, combined with the small tropospheric water vapor signal at the Mauna Loa site, make it ideal for the monitoring long term changes in water vapor.

INTRODUCTION

Water vapor is the reservoir of odd hydrogen in the middle atmosphere and thus is important to ozone chemistry. Observations by the WVMS instruments have been providing nearly continuous measurements of water vapor since 1992. *Nedoluha et al.,* [1998] showed that from 1992-1997 the WVMS instruments measured a significant increase in middle atmospheric water vapor. An average over the 40-60 km altitude range showed an increase of 0.144 ± 0.070 ppmv yr^{-1} at Table Mountain from 1993-1997 and an increase of 0.152 ± 0.070 ppmv yr^{-1} at Lauder from 1992-1997. This increase was similar to that measured by the Halogen Occultation Experiment (HALOE), which has been taking data nearly continuously since 1991. The HALOE measurements from 1991-1997 showed a global increase of 0.129 ± 0.022 ppmv yr^{-1}. Thus the trends measured from 1991-1997 were all significantly larger than those observed by *Oltmans and Hofmann* [1995] using midlatitude lower stratospheric water vapor measurements from 1981 to 1994.

WVMS MEASUREMENTS

The WVMS instrument at Mauna Loa is the third such instrument to be deployed. It is essentially identical to the WVMS2 instrument in operation at the Network for the Detection of Stratospheric Change (NDSC) site at Table Mountain since August 1993. These instruments are both very similar to the WVMS1 instrument that is deployed at the NDSC site at Lauder.

The retrieval of a vertical water vapor profile with ground-based microwave measurements relies upon the change in pressure as a function of altitude. The line width of the spectrum monotonically decreases with altitude due to the dependence on pressure broadening. Thus the resultant signal, which is the sum of the emission from all altitudes, can be deconvolved to retrieve a vertical profile. The primary difference between the WVMS2 and WVMS3 instruments and the WVMS1 instrument at the NDSC site in Lauder is the presence of an additional set of 50 kHz filters that improve the high altitude retrievals for the newer instruments. Details of the measurement technique and instrumentation are given by *Nedoluha et al.* [1995; 1996].

The 22.2 GHz transition used for these observations is optically thin in the troposphere permitting nearly continuous observation under most conditions even at low altitude sites such as Lauder. The smaller tropospheric optical depths through which observations are made from the Mauna Loa site reduces errors in the magnitude of the signal from the middle atmosphere and reduces baseline errors that can cause inaccurate stratospheric retrievals.

In Figure 1 we show the mixing ratios retrieved at several altitudes from 500 scan (~weekly) integrations. There is a summer peak in the mixing ratio at 70 and 80 km consistent with the upward motion of the atmosphere in the summer hemisphere. The annual oscillation magnitude is, however, smaller than that observed at Table Mountain or Lauder [cf. *Nedoluha et al.*, 1997]. The smaller magnitude of this oscillation should help to facilitate the identification of any interannual changes, but it will take several more years of observations to clearly distinguish the effects of quasi-biennial oscillation (QBO) related changes from any longer term trends.

Acknowledgments. We wish to thank S. McDermid and D. Walsh for their technical assistance with the Mauna Loa radiometer. This project is funded by NASA under the Upper Atmospheric Research Program.

REFERENCES

Nedoluha, G. E., et al., Ground-based measurements of water vapor in the middle atmosphere, *J. Geophys. Res., 100,* 2927-2939, 1995.

Nedoluha, G. E., et al., Measurements of water vapor in the middle atmosphere and implications for mesospheric transport, *J. Geophys. Res., 101,* 21,183-21,193, 1996.

Nedoluha, G. E., et al, A comparative study of mesospheric water vapor measurements from the ground-based Water Vapor Millimeter-wave Spectrometer and space-based instruments, *J. Geophys. Res., 102,* 16,647-16,661, 1997.

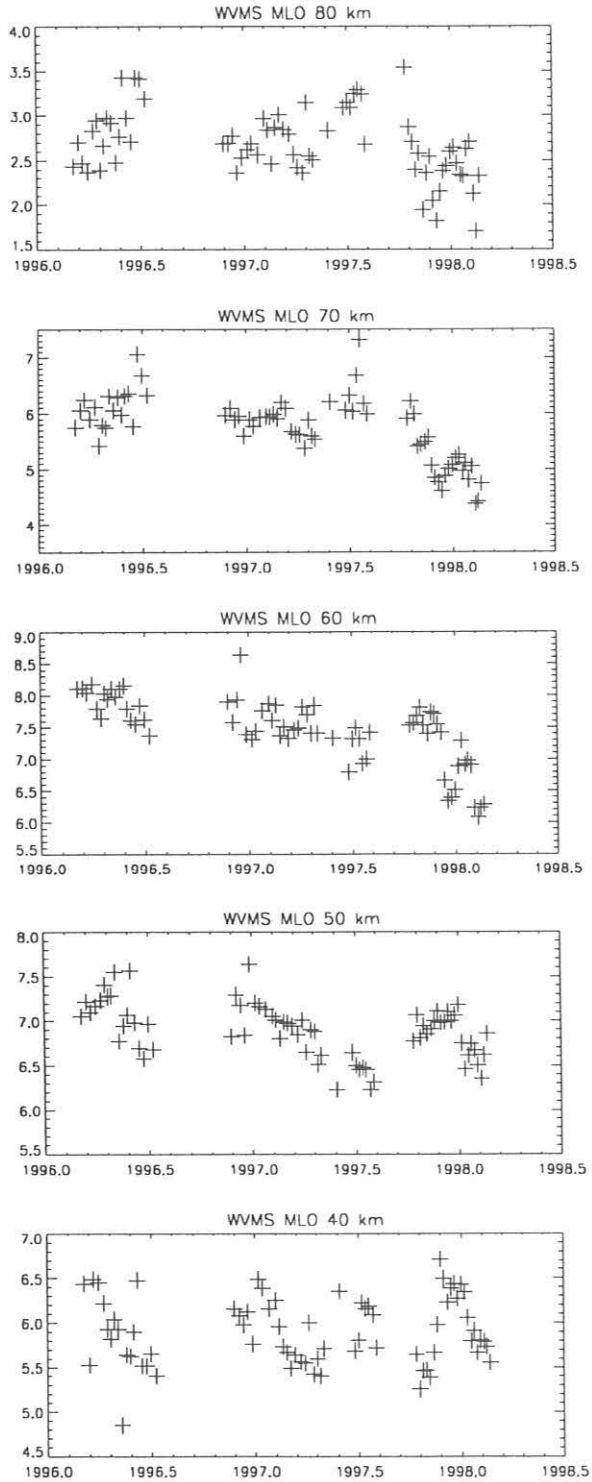

Fig. 1. Water vapor mixing ratios retrieved from WVMS3 measurements at Mauna Loa. Each scan represent approximately a week of continuous measurement.

Nedoluha, G. E., et al., Increases in middle atmospheric water vapor as observed by the ground-based water vapor millimeter-wave spectrometer and HALOE from 1991-1997, *J. Geophys. Res., 103,* 3531-3543, 1998.

Oltmans, S. J., and D. J. Hofmann, Increase in lower-stratospheric water vapor at a midlatitude northern hemisphere site from 1981 to 1994, *Nature, 374,* 146-149, 1995.

An Active Layer Thermal Regime at Barrow, Alaska

FREDERICK E. NELSON
Department of Geography, University of Delaware, Newark 19716

KENNETH M. HINKEL
Department of Geography, University of Cincinnati, Cincinnati 45221

RON PAETZOLD
U.S. Natural Resources Conservation Service, Lincoln, Nebraska 68508

INTRODUCTION

Ground temperature has been monitored at the Barrow CMDL facility and adjacent areas of the Barrow Environmental Observatory (BEO) continuously since 1993. Several thermistor strings extending through the active layer to the upper permafrost were monitored at intervals of 2 hours during this period. Extensive probing of the active layer was also performed several times during each summer. To ascertain long-term changes, frozen cores from the active layer and upper permafrost were obtained in 1994 and compared with data collected from the same locations in 1962. Instrumentation was expanded in 1995 to include readings of soil moisture at 2-hour intervals. This report summarizes the results obtained from these activities.

ACTIVE-LAYER DYNAMICS

Comparison of results from active-layer determinations at Barrow for the periods 1962-1968 and 1991-1997 reveals a strong consistency in the records from different land-cover units [*Nelson et al.*, 1998a]. The major exception involves locations that experience strong interannual variations in soil moisture content. Plotted by decade (Figure 1) the active layer shows a very strong relationship with accumulated thawing degree days. Interdecadal differences may be an artifact of changes in the stratigraphic position of segregated ice, insulation provided by organic material at the surface, soil moisture conditions, or some combination of these factors. Rather than exhibiting a simple relation with air temperature, the active-layer appears to exhibit Markovian behavior controlled by several processes in the boundary layer.

The ground temperature records from Barrow provide strong evidence that nonconductive processes are important components of the thermal regime. The thermal magnitude of these effects was estimated by *Outcalt et al.* [1998]. Comparison of the empirical record with results from a numerical model, based on conductive heat transfer with fusion, indicates that evaporative cooling and upward transfer of soil moisture cools summer temperatures in the active layer by several degrees. On an annual basis, these effects cool the average active-layer temperature by 0.4°C.

SAMPLING AND SPATIAL RELATIONSHIPS

Spatial autocorrelation analysis was performed on active-layer data obtained from a 1 km^2 area of the BEO in the summers of 1995 and 1996 [*Nelson et al.*, 1998b].

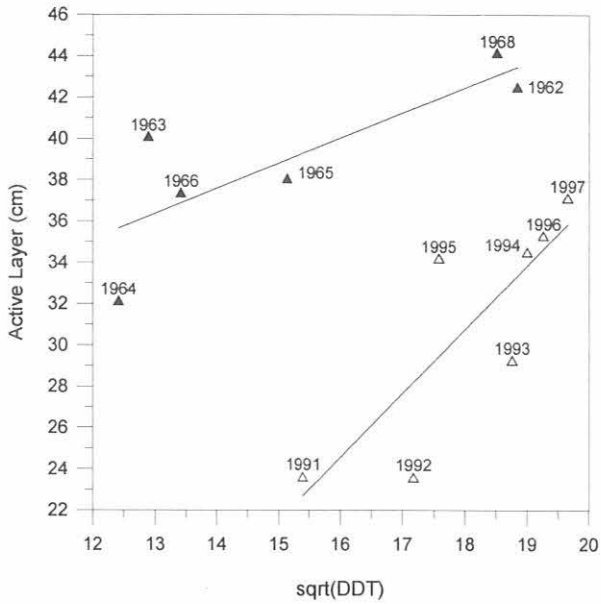

Fig. 1. Thawing degree-day accumulation versus mean active-layer thickness at a series of plots within the Barrow Environmental Observatory during the periods 1962-1968 and 1991-1997. Regression lines were computed separately for the 1960s and 1990s data [*Nelson et al.*, 1998a].

Topography, soil moisture, and active-layer thickness exhibit similar patterns, but snow-cover thickness varies at higher spatial frequencies and does not appear to affect active-layer thickness significantly over most of the area. Systematic designs involving widely separated sampling locations (e.g., 100 m) are effective on the coastal plain but are inadequate in the foothills of the Brooks Range. Because active-layer thickness is closely related to the flux of trace gases [*Waelbroeck et al.*, 1997] this result has significant implications for studies of carbon dioxide and methane fluxes.

SOIL MOISTURE

Soil moisture data were collected in 1996 and 1997 over the 1 km^2 area used to obtain active-layer thickness [*Miller et al.*, 1998]. Statistical analysis of these data indicate that (a) substantial differences occur in soil moisture and thaw depth in dissimilar terrain units; (b) soil moisture and thaw depth are relatively uniform within terrain units; (c) spatial

patterns of thaw depth are consistent within the study area on an interannual basis; and (d) patterns of soil moisture and thaw depth do not necessarily show close spatio-temporal correspondence because they fluctuate at different temporal scales. Time series of soil moisture at point locations near the CMDL facility show large variations near the surface in response to precipitation and evaporative drying. The lower part of the active layer remains near saturation throughout the summer (Figure 2).

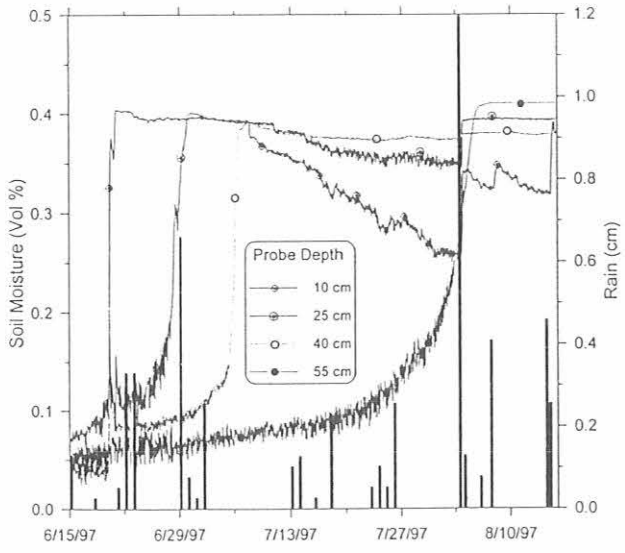

Fig. 2. Time series of volumetric soil moisture content (%) from a site within the Barrow Environmental Observatory. Hourly values at 10, 25, 40, and 55 cm are shown as traces. Vertical bars represent daily precipitation (cm) at Barrow. Note correspondence between near-surface soil moisture content and precipitation events [*Miller et al.*, 1998].

Temporal Changes in Moisture Content

Comparison of moisture content obtained from the frozen active layer and upper permafrost at Barrow indicates that the latter experienced an increase in ice content between 1962 and 1994 [*Hinkel et al.*, 1996]. This moderate increase from 57% to 62% could be an artifact of heterogeneity over short lateral distances and underscores the importance of carefully executed sampling designs.

References

Hinkel, K.M., F.E. Nelson, Y. Shur, J. Brown, and K.R. Everett, Temporal changes in moisture content of the active layer and near-surface permafrost at Barrow, Alaska: 1962-1994, *Arc. Alp. Res., 28*, 300-310, 1996.

Miller, L. L., K.M. Hinkel, F.E. Nelson, R.F. Paetzold, and S.I. Outcalt, Spatial and temporal patterns of soil moisture and thaw depth at Barrow, Alaska, *Proc., Seventh Int. Conf. Permafrost*, Centre d'Etudes Nordique, Université Laval, Québec, in press, 1998.

Nelson, F.E., S.I. Outcalt, J. Brown, and K.M. Hinkel, Spatial and temporal attributes of the active-layer thickness record, Barrow, Alaska, *Proc., Seventh Int. Conf. Permafrost*, Centre d'Etudes Nordique, Université Laval, Québec, in press, 1998a.

Nelson, F.E., K.M. Hinkel, N.I. Shiklomanov, G.R. Mueller, L.L. Miller, and D.A. Walker, Active-layer thickness in north-central Alaska: Systematic sampling, scale and spatial autocorrelation, *J. Geophys. Res.*, in press, 1998b.

Outcalt, S.I., K.M. Hinkel, F.E. Nelson, and L.L. Miller, Estimating the magnitude of coupled-flow effects in the active layer and upper permafrost, Barrow, Alaska, *Proc., Seventh Int. Conf. Permafrost*, Centre d'Etudes Nordique, Université Laval, Québec, in press, 1998.

Waelbroeck, C., P. Monfray, W.C. Oechel, S. Hastings, and G. Vourlitis, The impact of permafrost thawing on the carbon dynamics of tundra, *Geophys. Res. Lett.*, *24*, 229-232, 1997.

The NDSC Microwave Ozone Profiling Instrument at Mauna Loa Observatory

ALAN PARRISH
University of Massachusetts, Amherst 01003

B. J. CONNOR
NIWA, Lauder, New Zealand

J. J. TSOU
GATS, Inc., Hampton, Virginia 23666

We have operated a microwave instrument that measures the vertical profiles of stratospheric ozone at Mauna Loa Observatory (MLO) since July 1995. (We also operate a similar instrument at Lauder, New Zealand.) We retrieve ozone profiles covering an altitude range of 20-64 km from our measurements of a pressure-broadened spectral line produced by a rotational transition of ozone at 110.836 GHz. The vertical resolution of the measurements is 8-10 km from 20-40 km, degrading above. A typical profile, measured during the MLO ozone profile intercomparison of July-August 1995, is shown in the *Climate Monitoring and Diagnostics Laboratory No. 23 Summary Report 1994-1995*, chapter 4.2.

Measurements were made at MLO from July-September 1995; November 1995-March 1996; and from July 1996 to the present. During these periods, the instruments have generally been operated continuously in clear weather. Raw data are recorded every 20 minutes. For our standard data product, these are averaged into four time periods: midnight to just before local dawn, morning, afternoon, and evening (up to the next midnight). Fully processed and calibrated data from these measurements are deposited in the database for the Network for Detection of Stratospheric Change.

Details on the instruments and measurements may be found in the following references: The instrument, calibration, and profile retrieval: *Parrish et al.* [1992]. Technique of error analysis: *Connor et al.* [1995]. (The results of the error analysis given in this paper apply to particular early measurements; for results applicable to the current measurements, see the following reference.) Results of a long term intercomparison between one of the microwave instruments and colocated lidar and SAGE-II overpasses: *Tsou et al.* [1995].

The above references describe results from observations made at the Jet Propulsion Laboratory Table Mountain Facility in Wrightwood, California, between 1989 and 1992 with the instrument that is now in New Zealand. The MLO instrument is essentially identical.

REFERENCES

Connor, B.J., A. Parrish, J.-J. Tsou, and M.P. McCormick, Error analysis for the ground-based microwave ozone measurements during STOIC, *J. Geophys. Res., 100*(D5), 9283-9221, 1995.

Parrish, A., B.J. Connor, J.J. Tsou, I.S. McDermid, and W.P. Chu, Ground-based microwave monitoring of stratospheric ozone, *J. Geophys. Res., 97*(D2), 2541-2546, 1992.

Tsou, J.J., B.J. Connor, A. Parrish, I.S. McDermid, and W.P. Chu, Ground-based microwave monitoring of middle atmosphere ozone: Comparison to lidar and Stratospheric and Gas Experiment II satellite observations, *J. Geophys. Res., 100*(D2), 3005-3006, 1995.

NSWC Point Barrow Geomagnetic Observatory

JOHN F. SCARZELLO AND DANIEL S. LENKO
Naval Surface Warfare Center, Carderock Division, Electromagnetic Fields Branch, West Bethesda, Maryland 20817-5700

OBJECTIVE

The purpose of the observatory is to measure and characterize geomagnetic field variations using a sensitive magnetometer array for a period of at least one sunspot cycle.

BACKGROUND

The system was first installed in the spring of 1991 during Office of Naval Research (ONR Code 321SI) sponsored experiments. Three magnetometer sensor suites were placed on Air Force Long Range Radar Site Point Barrow property. The cables connected the sensors to a PC in the Climate Monitoring Diagnostics Laboratory (CMDL) Point Barrow building that controls the array and stores the magnetic information onto transportable media that is mailed to the Naval Surface Warfare Center (NSWC) for analysis.

SENSORS

Configured to form two orthogonal gradiometer axes, magnetic north-south and east-west, with a 152-m (500-ft.) baseline, each of the three magnetic sensor sites consists of two types of magnetometers. The first is the Helium-3 total field magnetometer which is an optically pumped, nuclear magnetic resonance sensing device. It provides a very accurate "absolute" measurement of the ambient magnetic field in the bandwidth from DC to about 0.1 Hz. The Helium-3 sensor can measure sub-milligamma (1 gamma = 1 nanotesla (nT) = 10^{-5} Oersted) magnetic fields when two sensors are configured as a gradiometer, to cancel out Earth's magnetic field. The dynamic range accommodates magnetic fields over 100,000 nT, but the Helium-3 sensor is gradient sensitive which can shorten the measurement time between optical pumping, leaving gaps in the otherwise continuous data. The second magnetic sensor included in each location is a triaxial fluxgate magnetometer. The three orthogonal axes measure magnetic fields in a bandwidth from DC to about 1 Hz. The digital data is appended to each of the Helium-3 sample updates (2.34 times a second) and the fluxgate sensor can resolve about 0.1 nT.

STATUS

Some of the geomagnetic noise collected has been characterized and used to develop and test noise reduction algorithms in an effort to enhance detection methods. Also, on occasions, data from the observatory were used to correlate magnetic noise events at other locations throughout the world. Because the arctic environment is quite harsh, cabling and sensor maintenance are in order. Also computer and storage media upgrades will be performed as funds permit.

FUTURE

In order to complete the current sunspot cycle, NSWC plans to support the Point Barrow observatory through at least the end of the decade.

Barrow Magnetic Observatory

JACK TOWNSHEND
U.S. Geological Survey, College Observatory, Fairbanks, Alaska 99775-5160

The Barrow Magnetic Observatory is the northernmost of the agency's 13 continuously recording, digital magnetic observatories. As such it serves as a singularly important site in a global network of observing stations whose combined data define the planetary magnetic field and track its secular change. Ground stations such as at the Barrow Observatory are controls for field modeling by harmonic analysis, essential reference stations for airborne and satellite surveys, and absolute calibration locations for field survey instrumentation. Data from Barrow are forwarded electronically to the United States Geological Survey (USGS) office in Golden, Colorado. Data are distributed by the USGS National Geomagnetic Information Center in Golden and by the international INTERMAGNET organization. Final processed data from Barrow and the other 12 USGS observatories are sent to the NOAA World Data Center A for archiving.

The primary instrumentation in operation at Barrow includes an EDA FM-100BR triaxial fluxgate magnetometer, EDA PPM-105 proton free-precession magnetometer, an Observatory Magnetometer Interface System (OMIS), and several pier-mounted instruments for absolute control observations. Data output consists of 1.0-minute values of three vector components of the Earth's magnetic field, as well as total field.

In August 1993 the USGS and NOAA negotiated a Memorandum of Agreement to have CMDL personnel at Barrow service the USGS Barrow equipment, make instrument observations, and provide some logistic support. The weekly absolute measurements and equipment service made by NOAA personnel are essential for maintaining high standards for the observatory operation and data quality.

Principal investigators for the Barrow Observatory are located in the USGS office at Fairbanks, Alaska, and at Golden Colorado. The Barrow-Magnetic Observatory receives its authorization to operate from the USGS Central Region Geologic Hazards Team in Golden, Colorado.

The ANSTO CMDL Radon Program at MLO

S. WHITTLESTONE
Australian Nuclear Science and Technology Organization, Menai, NSW 2234, Australia

D. KUNIYUKI AND S. RYAN
NOAA Mauna Loa Observatory, Hawaii

Radon is measured at the Mauna Loa Observatory, Hawaii (MLO) to characterize air masses. It is produced from the radioactive decay of radium in soils and decays with a half-life of 3.8 days, so that an air mass that has been away from land for longer than 2 weeks will contain very little radon. There are two uses for radon data: (1) as one of the parameters for selection of baseline air samples and (2) as a tracer to test the accuracy of global scale air transport models.

The latest version of the Australian Nuclear Science and Technology Organization (ANSTO) radon detector, installed at MLO in 1994, has proved to be mechanically and electronically reliable, and the calibrations were steady over a long period. The seven calibrations in 1997 had a standard deviation of 5%. The only instrumental failure was caused by a lightening strike in October 1997. Fortunately this destroyed only the automatic calibrator that was scheduled for replacement in any case.

Data are recorded directly into a data logger with a 3-month memory capacity. This logger is queried every 6 hours and the data is transferred to a computer that runs Netbeui and TCP/IP protocols under DOS for Workgroups. A program written in the BASIC language writes data to the hard drive on the local computer and to a network-shared directory residing on the server at the observatory. This allows data to be accessed in near-real time through the network by FTPing to the server or doing a map network drive from a Windows 95 or NT system. In either case a password must be given to gain access to the data directory.

The major instrumental problem has been in data retrieval. Some event, probably electrical interference from equipment elsewhere at MLO, periodically crashes the computer and sends faulty communication codes to the logger that result in corrupted data files. More robust software installed in November 1997 has reduced the effect of these events, but further work is needed.

Figures 1 and 2 show hourly radon concentrations at MLO in 1996 and 1997. At the compressed time scale of the graphs, the diurnal variation results in a band of varying width superimposed on the longer term variation of tropospheric radon from Asia. In both years, the spring and fall experienced periods of high radon with proportionally little diurnal change, whereas in summer low levels of radon with proportionally greater diurnal variation prevailed.

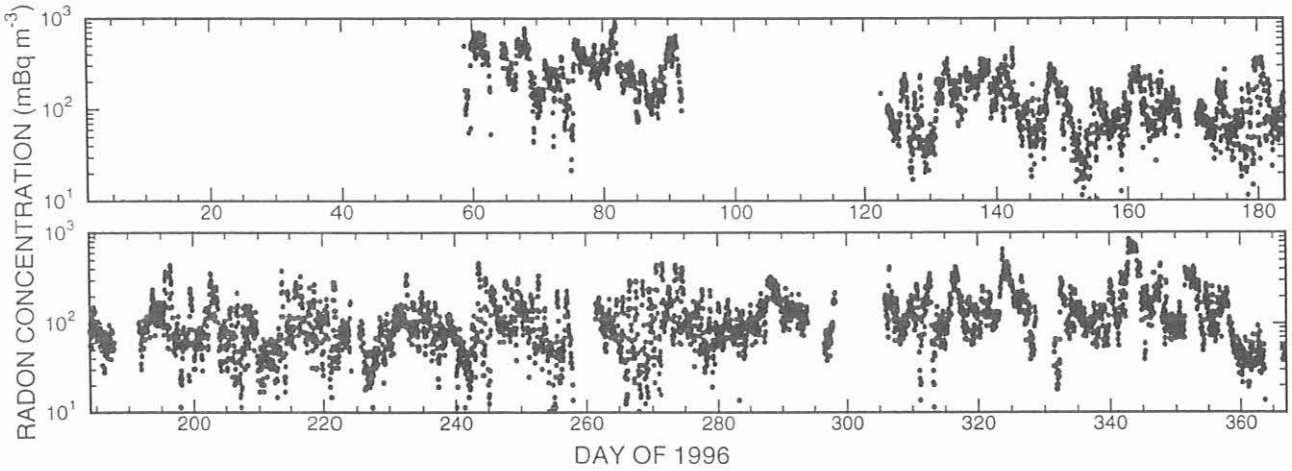

Fig. 1. Radon concentrations at MLO in 1996.

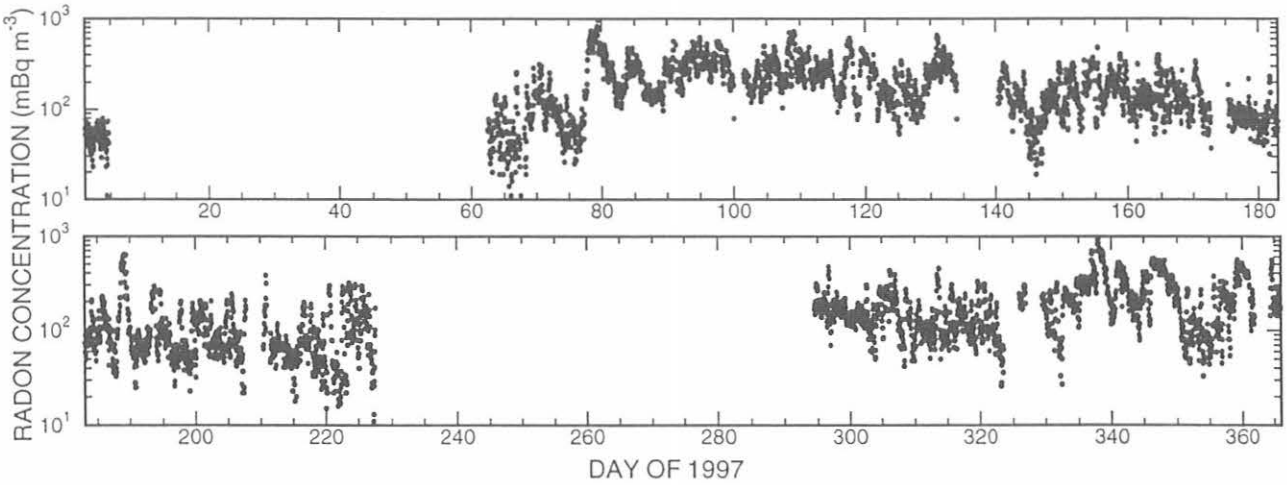

Fig. 2. Radon concentrations at MLO in 1997.

Aerosol Size Distribution and Gaseous Species in April at Barrow

Y. ZAIZEN, K. OKADA, M. IKEGAMI, T. AOKI, AND Y. SAWA
Meteorological Research Institute, 1-1 Nagamine, Tsukuba, 305-0052 Japan

F. NISHIO
Hokkaido University of Education, 1-15-55 Shiroyama, Kushiro 085-0826 Japan

Y. TACHIBANA
Research Institute of Civilization, Tokai University, 1117 Kitakaname, Hiratsuka 259-1207 Japan

INTRODUCTION

Atmospheric aerosols are one of the major components for climate through direct radiative forcing and changing radiative characteristics of clouds by acting as cloud condensation nuclei (CCN). The most effective particles for these processes are accumulation mode particles that originate from the growth of nuclei mode particles formed by homogeneous nucleation. The growth process is considered to be coagulation, heterogeneous condensation, and interaction with clouds.

In arctic regions, tropospheric aerosols are studied in relation to the arctic haze phenomena. Aerosol particles in the cases of arctic haze are mostly in the accumulation mode [*Pacyna et al.*, 1984; *Shaw*, 1985; *Lewis*, 1985]. A great majority of the arctic aerosols are in or near the accumulation mode [*Heintzenberg*, 1980; *Shaw*, 1984]. The aim of this study is to obtain the characteristics of aerosol size distributions, especially those in the smaller size range, in Barrow during April 1997 together with the concentrations of gaseous species concentrations.

OBSERVATION SITE AND INSTRUMENTS

This observation was conducted from April 13 to 27, 1997, at the NOAA CMDL Barrow Observatory, Alaska (BRW). Aerosol size distribution in the smaller size ranges ($0.004 \leq r \leq 0.13$ μm) was measured with a differential mobility analyzer (DMA), TSI, model 3071, and a condensation nucleus counter (CNC), TSI, model 3025. The size distribution in the larger size ranges ($0.15 \leq r < 5$ μm) was measured with an optical particle counter (OPC) (Dan Industry Co. Ltd., model PM-730-NS15P). Concentrations of gaseous species (SO_2, NO, and NO_2) were measured with an SO_2 analyzer (Thermo Electron, model 43S) and a NO_x analyzer (Thermo Electron, model 42S). The principal of these two instruments is chemiluminescence. Individual aerosol particles of 0.05-0.5 μm radius were collected on a carbon-covered nitrocellulose (collodion) film with a cascade impactor and examined with an electron microscope.

RESULTS

According to meteorological data and back-trajectory analyses, a polar airmass covered northern Alaska in the former part of the observational period (April 14-19, 1997) and an airmass from lower latitudes was dominant in the latter part (April 20-28, 1997).

Figure 1 shows the averaged number-size distributions during three periods. In each distribution a maximum is found in the radius range of 0.1 – 0.2 μm. The existence of this peak was reported by former investigators in Arctic areas [e.g., *Covert*, 1993]. This maximum possibly exists constantly over the arctic air in spring and is supposed to consist of well-aged particles. On the other hand, the concentrations of particles smaller than 0.005 μm radius are elevated in each size distribution, suggesting the occurrence of nucleation from gas phase material. In period A (April 13-18), the concentrations in the small size ranges (less than 0.1μm radius) are relatively low, suggesting that new particle formation is passive in the polar airmass. Besides, higher concentrations of smaller particles in period C (April 21-25) might suggest relatively active nucleation in airmass from lower latitudes. The concentrations in the larger size range ($r \geq 0.15$ μm) are higher in period A than period C. The higher concentration of large particles in period A might be due to a long residence time of aerosols in association with small exchange rates of airmass and small amounts of precipitation in polar regions. This high concentration of larger particles intends to restrict new particle formation by reducing the vapor pressure of sulfuric acid by

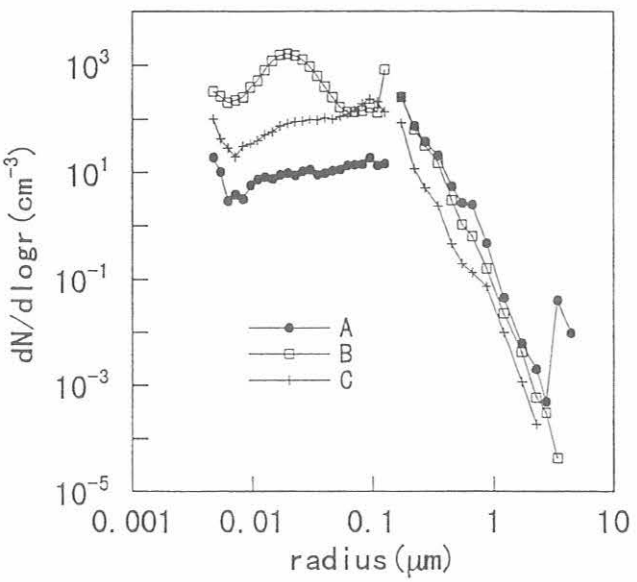

Fig. 1. Averaged number-size distributions of aerosols during period A (April 13-18), period B (April 19) and period C (April 21-25).

heterogeneous condensation on the surface of pre-existing particles. The size distribution in period B is different from others. This shape of the size distribution, with a maximum around 0.02 μm, is typical in background air of middle or low latitude [*Zaizen et. al.*, 1996].

The concentrations of precursor gases (SO_2, NO, and NO_2) were less than 50 pptv except for locally polluted air. The SO_2 concentration showed a diurnal variation with the maximum in the daytime during the latter part of the observational period. Since this type of diurnal variation is contradicted with the variation of mixing layer thickness, the variation may imply the dimethylsulfide (DMS) emission from the cracks of sea ice.

According to the morphological features of individual particles collected on April 21 and 22, most of the particles are estimated to consist of sulfuric acid or ammonium sulfate. Therefore, sulfate is considered to be one of the dominant components of accumulation mode particles in arctic regions in this season.

REFERENCES

Covert, D. S., Size distribution and chemical properties of aerosol at Ny Alesund, Svalbard, *Atmos. Environ., 27*A, 2989-2997, 1993.

Lewis, N.F., Particle-size distributions of the arctic aerosol, M. S. thesis, University of Rhode Island, 1985.

Heintzenberg, J, Particle size distribution and optical properties of Arctic Haze., *Tellus, 32*, 251-260, 1980.

Pacyna, J. M., V. Vitols and J. E. Hanssen, Size-differentiated composition of the arctic aerosol at Ny-Alesund, Spitsbergen, *Atmos. Environ., 18*, 2447-2459, 1984.

Shaw, G. E., Microparticle size spectrum of arctic haze, *Geophys. Res. Lett. 11*, 409-412, 1984.

Shaw, G. E., Aerosol measurements in central Alaska, 1982-1984, *Atmos. Environ., 19*, 2025-2031, 1985.

Zaizen, Y., M. Ikegami, Y. Tsutsumi, Y. Makino, K. Okada, J. Jensen and J. L. Gras, Number concentration and size distribution of aerosol particles in the middle troposphere over the western Pacific Ocean, *Atmos. Environ., 30*, 1755-1762, 1996.

7. Publications by CMDL Staff, 1996-1997

Anderson, B.E., G.L. Gregory, J.E. Collins Jr., G.W. Sachse, T.J. Conway, and G.P. Whiting, Airborne observations of spatial and temporal variability of tropospheric carbon dioxide, *J. Geophys. Res., 101(D1)*, 1985-1997, 1996.

Atlas, E., B. Ridley, J. Walega, J. Greenberg, G. Kok, T. Staffelbach, S. Schauffler, J. Lind, G. Hübler, R. Norton, GTE PEM-West Science Team, E. Dlugokencky, J. Elkins, S. Oltmans, G. Mackay, and D. Karecki, A comparison of aircraft and ground-based measurements at Mauna Loa Observatory, Hawaii, during GTE PEM-West and MLOPEX 2, *J. Geophys. Res., 101(D9)*, 14,599-14,612, 1996.

Bakwin, P.S., D.F. Hurst, P.P. Tans, and J.W. Elkins, Anthropogenic sources of halocarbons, sulfur hexafluoride, carbon monoxide, and methane in the southeastern United States, *J. Geophys. Res., 102(D13)*, 15,915-15,925, 1997.

Barnes, J.E., and D.J. Hofmann, Lidar measurements of stratospheric aerosol over Mauna Loa Observatory, *Geophys. Res. Lett., 24(15)*, 1923-1926, 1997.

Battle, M., M. Bender, T. Sowers, P.P. Tans, J.H. Butler, J.W. Elkins, J.T. Ellis, T. Conway, N. Zhang, P. Lang, and A.D. Clarke, Atmospheric gas concentrations over the past century measured in air from firn at the South Pole, *Nature, 383*, 231-235, 1996.

Beine, H.J., D.A. Jaffe, D.R. Blake, E. Atlas, and J. Harris, Measurements of PAN, alkyl nitrates, ozone, and hydrocarbons during spring in interior Alaska, *J. Geophys. Res., 101(D7)*, 12,613-12,619, 1996.

Bird, J.C., S.R. Pal, A.I. Carswell, D.P. Donovan, G.L. Manney, J.M. Harris, and O. Uchino, Observations of ozone structures in the Arctic polar vortex, *J. Geophys. Res., 102(D9)*, 10,785-10,800, 1997.

Bishop, J.K., W.B. Rossow, and E.G. Dutton, Surface solar irradiance from the International Satellite Cloud Climatology Project 1983-1991, *J. Geophys. Res., 102(D6)*, 6883-6910, 1997.

Bodhaine, B.A, Aerosol measurements during the Mauna Loa Photochemistry Experiment 2, *J. Geophys. Res., 101(D9)*, 14,757-14,765, 1996.

Bodhaine, B.A., Central Antarctica, atmospheric chemical composition and atmospheric transport, in *Chemical Exchange Between the Atmosphere and Polar Snow*, edited by E.W. Wolff and R.C. Bales, pp. 145-172, NATO ASI Series, 143, Springer-Verlag, Berlin, 1996.

Bodhaine, B.A., E.G. Dutton, D.J. Hofmann, R.L. McKenzie, and P.V. Johnston, UV measurements at Mauna Loa, July 1995 to July 1996, *J. Geophys. Res., 102(D15)*, 19,265-19,273, 1997.

Bodhaine, B.A., R.L. McKenzie, P.V. Johnston, D.J. Hofmann, E.G. Dutton, R.C. Schnell, J.E. Barnes, S.C. Ryan, and M. Kotkamp, New ultraviolet spectroradiometer measurements at Mauna Loa Observatory, *Geophys. Res. Lett., 23(16)*, 2121-2124, 1996.

Bodhaine, B.A., D.J. Hofmann, E.G. Dutton, R.L. McKenzie, P.V. Johnston, M. Kotkamp, R.C. Schnell, J.E. Barnes, and S.C. Ryan, Ultraviolet spectroradiometer measurements at Mauna Loa Observatory, in *IRS '96: Current Problems in Atmospheric Radiation, Proceedings of the International Radiation Symposium, Fairbanks, Alaska, 19-24 August 1996,* edited by W.L. Smith and K. Stamnes, pp. 841-844, Deepak, Hampton, VA, 1997.

Butler, J.H, Scientific uncertainties in the budget of atmospheric methyl bromide, *Atmos. Env., 30(7)*, i-iii, 1996.

Butler, J.H., and J.M. Rodriguez, Methyl bromide in the atmosphere, in *The Methyl Bromide Issue*, edited by C.H. Bell, N. Price, and B. Chakrabarati, pp. 27-90, Wiley & Sons, New York, 1996.

Chang, A.Y., R.J. Salawitch, H.A. Michelsen, M.R. Gunson, M.C. Abrams, R. Zander, C.P. Rinsland, M. Loewenstein, J.R. Podolske, M.H. Proffitt, J.J. Margitan, D.W. Fahey, R.-S. Gao, K.K. Kelly, J.W. Elkins, C.R. Webster, R.D. May, K.R. Chan, M.M. Abbas, A. Goldman, F.W. Irion, G.L. Manney, M.J. Newchurch, and G.P. Stiller, A comparison of measurements from ATMOS and instruments aboard the ER-2 aircraft, Tracers of atmospheric transport, *Geophys. Res. Lett., 23(17)*, 2389-2392, 1996.

Chang, A.Y., R.J. Salawitch, H.A. Michelsen, M.R. Gunson, M.C. Abrams, R. Zander, C.P. Rinsland, J.W. Elkins, G.S. Dutton, C.M. Volk, C.R. Webster, R.D. May, D.W. Fahey, R.-S. Gao, M. Loewenstein, J.R. Podolske, R.M. Stimpfle, D.W. Kohn, M.H. Proffitt, J.J. Margitan, K.R. Chan, M.M. Abbas, A. Goldman, F.W. Irion, G.L. Manney, M.J. Newchurch, and G.P. Stiller, A comparison of measurements from ATMOS and instruments aboard the ER-2 aircraft, halogenated gases, *Geophys. Res. Lett., 23(17)*, 2393-2396, 1996.

Darlington, J.P.E.C., P.R. Zimmerman, J. Greenberg, C. Westberg, and P. Bakwin, Production of metabolic gases by nests of the termite Macrotermes jeanneli in Kenya, *J. Trop. Ecol., 13*, 491-510, 1997.

Deshler, T., B.J. Johnson, D.J. Hofmann, and B. Nardi, Correlations between ozone loss and volcanic aerosol at altitudes below 14 km over McMurdo Station, Antarctica, *Geophy. Res. Lett., 23(D21)*, 2931-2934, 1996.

Dlugokencky, E.J., K.A. Masarie, P.P. Tans, T.J. Conway, and X. Xiong, Is the amplitude of the methane seasonal cycle changing? *Atmos. Environ., 31(1)*, 21-26,, 1997.

Dlugokencky, E.J., E.G. Dutton, P.C. Novelli, P.P. Tans, K.A. Masarie, K.O. Lantz, and S. Madronich, Changes in CH_4 and CO growth rates after the eruption of Mt. Pinatubo and their link with changes in tropical tropospheric UV flux, *Geophys. Res. Lett., 23*, 2761-2764, 1996.

Dutton, E.G., Radiative forcing of El Chichón and Pinatubo eruptions as determined from observations and radiative transfer calculations, in *IRS'96: Current Problems in Atmospheric Radiation*, edited by W. L. Smith and K. Stamnes, pp. 367-370, Deepak Publishing, Hampton, VA, 1997.

Elkins, J.W., D.W. Fahey, J.M., Gilligan, G.S. Dutton, T.J. Baring, C.M. Volk, R.E. Dunn, R.C. Myers, S.A. Montzka, P.R. Wamsley, A.H. Hayden, J.H. Butler, T.M. Thompson, T.H. Swanson, E.J. Dlugokencky, P.C. Novelli, D.F. Hurst, J.M. Lobert, S.J. Ciciora, R.J. Mc Laughlin, T.L. Thompson, R.H. Winkler, P.J. Fraser, L.P. Steele, and M.P. Lucarelli, Airborne gas chromatograph for in situ measurements of long-lived species in the upper troposphere

and lower stratosphere, *Geophys. Res. Lett., 23(4)*, 347-350, 1996.

Emmons, L.K., M.A. Carroll, D.A. Hauglustaine, G.P. Grasseur, C. Atherton, J. Penner, S. Sillman, H. Levy II, F. Rohrer, W.M.F. Wauben, P.F.J. Van Velthoven, Y. Wang, D. Jacob, P. Bakwin, R. Dickerson, B. Doddridge, C. Gerbig, R. Honrath, G. Hubler, D. Jaffe, Y. Kondo, J.W. Munger, A. Torres, and A. Voltz-Thomas, Climatologies of No_x and No_y, A comparison of data and models, *Atmos. Environ, 31(12)*, 1851-1904, 1997.

Erickson, D.J. III, P.J. Rasch, P.P. Tans, P. Friedlingstein, P. Ciais, E. Maier-Reimer, K. Six, C.A. Fischer, and S. Walters, *J. Geophys. Res., 101(D10)*, 15,079-15,097, 1996.

Flatøy, F., O. Hov, C. Gerbig, and S.J. Oltmans, Model studies of the meteorology and chemical composition of the troposphere over the North Atlantic during August 18-30, 1993, *J. Geophys. Res., 101*, 29,317-29,334, 1996.

Froidevaux, L., W.G. Read, T.A. Lungu, R.E. Cofield, E.F. Fishbein, D.A. Flower, R.F. Jarnot, B.P. Ridenoure, Z. Shippony, J.W. Waters, J.J. Margitan, I.S. McDermid, R.A. Stachnik, G.E. Peckham, G. Braathen, T. Deshler, J. Fishman, D.J. Hofmann, and S.J. Oltmans, Validation of UARS microwave limb sounder ozone measurements, *J. Geophys. Res., 101(D6)*, 10,017-10,060, 1996.

Geller, L.W., J.W. Elkins, J.M. Lobert, A.D. Clarke, D.F. Hurst, J.H. Butler, and R.C. Myers, Tropospheric SF_6: Observed latitudinal distribution and trends, derived emissions, and interhemispheric exchange time, *Geophys. Res. Lett., 24(6)*, 675-678, 1997.

Hanson, A.D.A., A.V. Polissar, R.C. Schnell, Airborne aerosol and black carbon measurements over the East Siberian Sea, Spring 1992, *Atmos. Res., 4*, 153-165, 1997.

Harris, J.M., and S.J. Oltmans, Variations in tropospheric ozone related to transport at American Samoa, *J. Geophys. Res., 102(D7)*, 8781-8791, 1997.

Harris, N.R., P., G. Ancellet, L. Bishop, D.J. Hofmann, J.B. Kerr, R.D. McPeters, M. Prendez, W.J. Randel, S. Staehelin, B.H. Subbaraya, A. Volz-Thomas, J. Zawodny, and C.S. Zerefos, Trends in stratospheric and free tropospheric ozone, *J. Geophys. Res., 102(D1)*, 1571-1590, 1997.

Hofmann, D.J., The 1996 Antarctic ozone hole, *Nature, 383*, 129, 1996.

Hofmann, D.J., Recovery of Antarctic ozone hole, *Nature, 384*, 222-223, 1996.

Hofmann, D.J., and S. Solomon, Observations and interpretation of changes in stratospheric ozone following the Pinatubo eruption, in *The Mount Pinatubo Eruption Effects on the Atmosphere and Climate*, edited by G. Fiocco, D. Fuá, and G. Visconti, pp. 177-188, *NATO ASI Series, 142*, Springer-Verlag, Berlin, 1996.

Hofmann, D.J., J.T. Peterson, and R.M. Rosson (Eds.), *Climate Monitoring and Diagnostics Laboratory No. 23 Summary Report 1994-1995*, NOAA Environmental Research Laboratories, Boulder, CO, 161 pp., 1996.

Hofmann, D.J., S.J. Oltmans, J.M. Harris, B.J. Johnson, and J.A. Lathrop, Ten years of ozonesonde measurements at the south pole, Implications for recovery of springtime Antarctic ozone. *J. Geophys. Res., 102(D7)*, 8931-8943, 1997.

Hofmann, D.J., S.J. Oltmans, G.L. Koenig, B.A. Bodhaine, J.M. Harris, J. A. Lathrop, R.C. Schnell, J. Barnes, J. Chin, D. Kuniyuki, S. Ryan, R. Uchida, A. Yoshinaga, P.J. Neale, D.R. Hayes, Jr., V.R. Goodrich, W.D. Komhyr, R.D. Evans, B.J. Johnson, D.M. Quincy, and M. Clark, Record low ozone at Mauna Loa Observatory during winter 1994-1995, A consequence of chemical and dynamical synergism? *Geophys. Res. Lett., 23(12)*, 1533-1536, 1996.

Hurst, D.F., W.T. Griffith, and G.D. Cook, Trace-gas emissions from biomass burning in Australia, in *Biomass Burning and Global Change*, Vol. 2, edited by J.S. Levine, pp. 787-792, MIT Press, Cambridge, MA, 1996.

Hurst, D.F., P.S. Bakwin, R.C. Myers, and J.W. Elkins, Behavior of trace gas mixing ratios on a very tall tower in North Carolina, *J. Geophys. Res., 102(D7)*, 8825-8835, 1997.

Kahl, J.D., D.A. Martinez, H. Kuhns, C.I. Davidson, J.-L. Jaffrezo, and J.M. Harris, Air mass trajectories to Summit, Greenland: A 44-year climatology and some episodic events, *J. Geophys. Res., 102(C12)*, 26,861-26,875, 1997.

Keeling, C.D., J.F.S. Chin, and T.P. Whorf, Increased activity of northern vegetation inferred from atmospheric CO_2 measurements, *Nature, 382*, 146-149, 1996.

Key, J.R., R.A. Silcox, and R.S. Stone, Evaluation of surface radiative flux parameterizations for use in sea ice models, *J. Geophys. Res., 101(C2)*, 3839-3849, 1996.

Kirchhoff, V.W.J.H., N.J. Schuch, D.K. Pinheiro, and J.M. Harris, Evidence for an ozone hole perturbation at 30° South, *Atmos. Environ., 30(9)*, 1481-1488, 1996.

Kley, D., P.J. Crutzen, H.G. Smit, H. Vömel, S.J. Oltmans, H. Grassl, and V. Ramanathan, Observations of near-zero ozone concentrations over the convective Pacific: Effects on air chemistry, *Science, 274*, 230-233, 1996.

Kley, D., H.G.J. Smit, H. Vömel, H. Grassl, V. Ramanathan, P.J. Crutzen, S. Williams, J. Meywerk, and S.J. Oltmans, Tropospheric water-vapor and ozone cross-sections in a zonal plane over the central equatorial Pacific Ocean, *Q. J. R. Meteorol. Soc., 123*, 2009-2040, 1997.

Komhyr, W.D., G.C. Reinsel, R.D. Evans, D.M. Quincy, R.D. Grass, and R.K. Leonard, Total ozone trends at sixteen NOAA/CMDL and cooperative Dobson spectrophotometer observatories during 1979-1996, *Geophys. Res. Lett., 24(24)*, 3225-3228, 1997.

Lahoz, W.A., M.R. Suttie, L. Froidevaux, R.S. Harwood, C.L. Lau, T.A. Lungu, G.E. Peckham, H.C. Pumphrey, W.G. Read, Z. Shippony, R.A. Suttie, J.W. Waters G.E. Nedoluha, S.J. Oltmans, J.M. Russell III, and W.A. Traub, Validation of UARS microwave limb sounder 183 GHz H_2O measurements, *J. Geophys. Res., 101(D6)*, 10,129-10,149, 1996.

LeGarrec, J.L., V. Lepage, B.R. Rowe, E.E. Ferguson, The temperature dependence of the rate constant for $O^+ + NO \rightarrow NO^+ + O$ from 23 to 3000 K, *Chem. Phys. Lett., 270*, 66-70, 1997.

Levy, H. II, P.S. Kasibhatla, W.J. Moxim, A.A. Klonecki, A.I. Hirsch, S.J. Oltmans, W.L. Chameides, The global impact of human activity on tropospheric ozone, *Geophys. Res. Lett., 24(7)*, 791-794, 1997.

Lobert, J.M., S.A. Yvon-Lewis, J.H. Butler, S.A. Montzka, and R.C. Myers, Undersaturation of CH_3Br in the Southern Ocean, *Geophys. Res. Lett., 24(2)*, 171-172, 1997.

Lobert, J.M., J.H. Butler, L.S. Geller, S.A. Yvon, S.A. Montzka, R.C. Myers, A.D. Clarke, and J.W. Elkins, BLAST94, bromine latitudinal air/sea transect 1994, report on oceanic measurements on methyl bromide and other compounds, *NOAA Tech. Memo. ERL CMDL-10*, 39 pp., NOAA Environmental Research Laboratories, Boulder, CO, 1996.

McInnes, L., D. Covert, and B. Baker, The number of sea-salt, sulfate, and carbonaceous particles in the marine atmosphere, EM measurements consistent with the ambient size distribution, *Tellus, 49*B, 300-313, 1997.

McIntosh, C.M., E.J. Dlugokencky, P.M. Lang, and K.A. Masarie, Atmospheric CH_4 seasonal cycles and latitude gradient from the NOAA CMDL cooperative air sampling network, *NOAA Tech. Memo. ERL CMDL-11*, 79 pp., NOAA Environmental Research Laboratories, Boulder, CO, 1996.

Merrill, J.T., J.L. Moody, S.J. Oltmans, and H. Levy II, Meteorological analysis of tropospheric ozone profiles at Bermuda, *J. Geophys. Res., 101*, 29,201-29,211, 1996.

Minschwaner, K., A.E. Dessler, J.W. Elkins, C.M. Volk, D.W. Fahey, M. Loewenstein, J.R. Podolske, A.E. Roche, and K.R. Chan, Bulk properties of isentropic mixing into the tropics in the lower stratosphere, *J. Geophys. Res., 101(D5)*, 9433-9439, 1996.

Montzka, S.A., R.C. Myers, J.H. Butler, and J.W. Elkins, Observations of HFC-134a in the remote troposphere, *Geophys. Res. Lett., 23(2)*, 169-172, 1996.

Montzka, S.A., J.H. Butler, R.C. Myers, T.M. Thompson, T.H. Swanson, A.D. Clarke, L.T. Lock, and J.W. Elkins, Decline in the tropospheric abundance of halogen from halocarbons: Implications for stratospheric ozone depletion, *Science, 272*, 1318-1322, 1996.

Moody, J.L., J.C. Davenport, J.T. Merrill, S.J. Oltmans, D.D. Parish, J.S. Holloway, H. Levy II, G.L. Forbes, M. Trainer, and M. Buhr, Meteorological mechanisms for transporting O_3 over the western North Atlantic Ocean: A case study for August 24-29, 1993, *J. Geophys. Res., 101*, 29,213-29,227, 1996.

Munger, J.W., S.C. Wofsy, P.S. Bakwin, S.-M. Fan, M.L. Goulden, B.C. Daube, A.H. Goldstein, K.E. Moore, and D.R. Fitzjarrald, Atmospheric deposition of reactive nitrogen oxides and ozone in a temperate deciduous forest and a subarctic woodland 1, Measurements and mechanisms, *J. Geophys. Res., 101(D7)*, 12,639-12,657, 1996.

Newman, P.A., L.R. Lait, M.R. Schoeberl, M. Seablom, L. Coy, R. Rood, R. Swinbank, M. Proffitt, M. Loewenstien, J.R. Podolski, J.W. Elkins, C.R. Webster, R.D. May, D.W. Fahey, G.S. Dutton, and K.R. Chan, Measurements of polar vortex air in the midlatitudes, *J. Geophys. Res., 101(D8)*, 12,879-12,891, 1996.

Oltmans, S.J., D.J. Hofmann, J.A. Lathrop, J.M. Harris, W.D. Komhyr, and D. Kuniyuki, Tropospheric ozone during Mauna Loa Observatory Photochemistry Experiment 2 compared to long-term measurements from surface and ozonesonde observations, *J. Geophys. Res., 101(D9)*, 14,569-14,580, 1996.

Oltmans, S.J., H. Levy II, J.M. Harris, J.T. Merrill, J.L. Moody, J.A. Lathrop, E. Cuevas, M. Trainer, M.S. O'Neill, J.M. Prospero, H. Vömel, and B.J. Johnson, Summer and spring ozone profiles over the North Atlantic from ozonesonde measurements, *J. Geophys. Res., 101(D22)*, 29,179-29,200, 1996.

Petrov, K.P., S. Waltman, E.J. Dlugokencky, M. Arbore, M.M. Fejer, F.K. Tittel, and L.W. Hollberg, Precise measurement of methane in air using diode-pumped 3.4-μm difference-frequency generation in PPLN, *Appl. Phys., 64*, 567-572, 1997.

Planet, W.G., A.J. Miller, J.J. DeLuisi, D.J. Hofmann, S.J. Oltmans, J.D. Wild, I.S. McDermid, R.D. McPeters, and B.J. Connor, Comparison of NOAA-11 SBUV/2 ozone vertical profiles with correlative measurements, *Geophys. Res. Lett., 23(3)*, 293-296, 1996.

Parungo, F., T. Kim, C. Zhu, J. Harris, R. Schnell, X. Li, D. Yang, X. Fang, P. Yan, X. Yu, M. Zhou, Z. Chen, F. Qian, and K. Park, Asian dust storms and their effects on radiation and climate, Part II, *STC Tech. Report 2959*, 80 pp., Science and Technology Corporation, Hampton, VA, 1996.

Parungo, F., R. Schnell, A. Yoshinaga, L. Pajo, Y. Kim, C. Zhu, J. Harris, B. Bodhaine, M. Zhou, Z. Chen, X. Li, D. Yang, X. Fang, P. Yan, X. Yu, and K. Park, Asian dust storms and their effects on radiation and climate, Part III, *STC Tech. Report 3111,* 95 pp., Science and Technology Corp., Hampton, VA, 1996.

Parungo, F., R. Schnell, A. Yoshinaga, L. Pajo, Y. Kim, C. Zhu, J. Harris, B. Bodhaine, X. Li, D. Yang, X. Fang, Z. He, P. Yan, X. Yu, M. Zhou, Z. Chen, F. Qian, K. Park, J. Nam, Y. Iwasaka, and S. Kwon, Asian dust storms and their effects on radiation and climate, Part IV, *STC Tech. Reort. 3134*, 124 pp., Science and Technology Corporation, Hampton, VA, 1997.

Planet, W.G., A.J. Miller, J.J. DeLuisi, D.J. Hofmann, S.J. Oltmans, J.D. Wild, I.S. McDermid, R.D. McPeters, and B.J. Connor, Comparison of NOAA-11 SBUV/2 ozone vertical profiles with correlative measurements, *Geophys. Res.Lett.,* 23(3):293-296, 1996.

Russell, P.B., J.M. Livingston, R.F. Pueschel, J.J. Bauman, J.B. Pollack, S.L. Brooks, P. Hamill, L.W. Thomason, L.L. Stowe, T. Deshler, E.G. Dutton, and R.W. Bergstrom, Global to microscale evolution of the Pinatubo volcanic aerosol derived from diverse measurements and analyses, *J. Geophys. Res., 101(D13)*, 18,745-18,763, 1996.

Ryan, S.C, The wind field around Mauna Loa derived from surface and balloon observations, *J. Geophys. Res., 102(D9)*, 10,711-10,725, 1997.

Schnell, R.C., Airflow over the island of Hawaii, *Hawaii Medical Journal, 55*, 44-45, 1996.

Seinfeld, J.H., R. Charlson, P.A. Durkee, D. Hegg, B.J. Huebert, J. Kiehl, M.P. McCormick, J.A. Ogren, J.E. Penner, V. Ramaswamy, J.H. J. and W.G.N. Slinn, *A Plan for a Research Program on Aerosol Radiative Forcing and Climate Change*, 161 pp., National Research Council, National Academy Press, Washington, D.C., 1996.

Sheridan, P.J., and R.B. Norton, A new aerosol filter inlet system for use on aircraft, *NOAA Tech. Memo. ERL CMDL-12*, 39 pp., NOAA Environmental Research Laboratories, Boulder, CO, 1997.

Stone, R.S., Variations in western Arctic temperatures in response to cloud radiative and synoptic-scale influences, *J. Geophys. Res., 102(D18)*, 21,769-21,776, 1997.

Stone, R., T. Mefford, E. Dutton, D. Longenecker, B. Halter, and D. Endres, Surface radiation and meteorological measurements, January 1992 to December 1994, *NOAA Data Report ERL-CMDL-11*, NOAA Environmental Research Laboratories, Boulder, CO, 1996.

Tans, P.P., P.S. Bakwin, and D.W. Guenther, A feasible Global Carbon Cycle Observing System, A plan to decipher today's carbon cycle based on observations, *Global Change Biol., 2*, 309-318, 1996.

Tuck, A.F., D. Baumgardner, KR. Chan, J.E. Dye, J.W. Elkins, S.J. Hovde, K.K. Kelly, M. Loewenstein, J.J. Margitan, R.D. May, J.R. Podolske, M.H. Proffitt, K.H. Rosenlof, W.L. Smith, C.R. Webster, and J.C. Wilson, The Brewer-Dobson circulation in the light of high altitude in situ aircraft observations, *Q. J. R. Meteorol. Soc., 123(537)*, 1-69, 1997.

Vömel, H., M. Rummukainen, R. Kivi, J. Karhu, T. Turunen, E. Kyro, J. Rosen, N. Kjome, and S. Oltmans, Dehydration and sedimentation of ice particles in the Arctic stratospheric vortex, *Geophys. Res. Lett., 24(7)*, 795-798, 1997.

Volk, C.M., J.W. Elkins, D.W. Fahey, G.S. Dutton, J.M. Gilligan, M. Loewenstein, J.R. Podolske, K.R. Chan, and M.R. Gunson, Evaluation of source gas lifetimes from stratospheric observations, *J. Geophys. Res., 102(D21)*, 25,543-25,564, 1997.

Volk, C.M., J.W. Elkins, D.W. Fahey, R.J. Salawitch, G.S. Dutton, J.M. Gilligan, M.H. Proffitt, M. Loewenstein, J.R. Podolske, K. Minschwaner, J.J. Margitan, and K.R. Chan, Quantifying transport between the tropical and midlatitude lower stratosphere, *Science, 272*, 1763-1768, 1996.

Vong, R.J., B.M. Baker, F.J. Brechtel, R.T. Collier, J.M. Harris, A.S. Kowalski, N.C. McDonald, and L.M. McInnes, Ionic and trace element composition of cloud water collected on the Olympic Peninsula of Washington State, *Atmos. Environ., 31(13)*, 1991-2001, 1997.

Wamsley, P.R., J.W. Elkins, D.W. Fahey, G.S. Dutton, C.M. Volk, R.C. Myers, S.A. Montzka, J.H. Butler, A.D. Clarke, P.J. Fraser, L.P. Steele, M.P. Lucarelli, E.L. Atlas, S.M. Schauffler, D.R. Blake, F.S. Rowland, W.T. Sturges, J.M. Lee, S.A. Penkett, A. Engel, R.M. Stimpfle, K.R. Chan, D.K. Weisenstein, M.K.W. Ko, and R.J. Salawitch, Distribution of halon-1211 in the upper troposphere and lower stratosphere and the 1994 total bromine budget, *J. Geophys. Res., 103(D1)*, 1997.

Waugh, D.W., T.M. Hall, W.J. Randel, P.J. Rasch, B.A. Boville, K.A. Boering, S.C. Wofsy, B.C., Daube, J.W. Elkins, D.W. Fahey, G.S. Dutton, C.M. Volk, and P.F. Vohralik, Three-dimensional simulations of long-lived tracers using winds from MACCM2, *J. Geophys. Res., 102(D17)*, 21,493-21,513, 1997.

Waugh, D.W., R.A. Plumb, J.W. Elkins, D.W. Fahey, K.A. Boering, G.S. Dutton, C.M. Volk, E. Keim, R.-S. Gao, B.C. Daube, S.C. Wofsy, M. Loewenstein, J.R. Podolske, K.R. Chan, M.H. Proffitt, K.K. Kelly, P.A. Newman, and L.R. Lait, Mixing of polar vortex air into middle latitudes as revealed by trace-tracer scatter plots, *J. Geophys. Res., 102(D11)*, 13,119-13,134, 1997.

Yvon, S.A., and J.H. Butler, An improved estimate of the oceanic lifetime of atmospheric CH_3Br, *Geophys. Res. Lett., 23(1)*, 53-56, 1996.

Yvon, S.A., and E.S. Saltzman, Atmospheric sulfur cycling in the tropical Pacific marine boundary layer (12°S, 135°W). A comparison of field data and model results 2, Sulfur dioxide, *J. Geophys. Res., 101(D3)*, 6911-6918, 1996.

Yvon, S.A., J.M.C. Plane, C.-F. Nien, D.J. Cooper, and E.S. Saltzman, Interaction between nitrogen and sulfur cycles in the polluted marine boundary layer, *J. Geophys. Res., 101(D1)*, 1379-1386, 1996.

Yvon, S.A., E.S. Saltzman, D.J. Cooper, T.S. Bates, and A.M. Thompson, Atmospheric sulfur cycling in the tropical Pacific marine boundary layer (12°S, 135°W), A comparison of field data and model results 1. Dimethylsulfide, *J. Geophys. Res., 101(D3)*, 6899-6909, 1996.

Yvon-Lewis, S.A., and J.H. Butler, The potential effect of oceanic biological degradation on the lifetime of atmospheric CH_3Br, *Geophys. Res. Lett., 24(10)*, 1227-1230, 1997.

Zhao, C.L. and P.S. Bakwin, Data acquisition and control system for measurements of carbon dioxide on WITN tower, *NOAA Tech. Memo. ERL CMDL 13*, 24 pp., NOAA Environmental Research Laboratories, Boulder, CO, 1997.

Zhao, C.L., P.S. Bakwin, and P.P. Tans, A design for unattended monitoring of carbon dioxide on a very tall tower, *J. Atmos. Oceanic Technol., 14*, 1139-1145, 1997.

Zhao, C.L., P.P. Tans, and K.W. Thoning, A high precision manometric system for absolute calibrations of CO_2 in dry air, *J. Geophys. Res., 102(D5)*, 5885-5894, 1997.